

**ANNUAL REPORTS ON
NMR SPECTROSCOPY**

Volume 24

ANNUAL REPORTS ON

NMR SPECTROSCOPY

This Page Intentionally Left Blank

ANNUAL REPORTS ON
NMR SPECTROSCOPY

Edited by

G. A. WEBB

Department of Chemistry, University of Surrey, Guildford, Surrey, England

VOLUME 24



ACADEMIC PRESS

Harcourt Brace Jovanovich, Publishers

London • San Diego • New York
Boston • Sydney • Tokyo • Toronto

ACADEMIC PRESS LIMITED
24-28 Oval Road,
LONDON NW1 7DX

U.S. Edition Published by

ACADEMIC PRESS INC.
San Diego, CA 92101

This book is printed on acid free paper

Copyright © 1992 ACADEMIC PRESS LIMITED

All Rights Reserved

No part of this book may be reproduced or transmitted in any form or by any means, electronic or mechanical, including photocopying, recording, or any information storage and retrieval system without permission in writing from the publisher

**A catalogue record for this book is available from the
British Library**

ISBN 0-12-505324-X
ISSN 0066-4103

Phototypesetting by Alden Multimedia Ltd, Northampton
Printed in Great Britain at the University Press, Cambridge

List of Contributors

N.J. Clayden, *ICI plc., Wilton Materials Research Centre, PO Box No. 90, Wilton, Middlesbrough, Cleveland TS6 8JE, UK.*

Rosalinda Contreras, *Centro de Investigacion y de Estudios Avanzados del I.P.N., Departamento de Quimica, 07000 Mexico, D.F., Mexico.*

D.G. Cory, *Bruker Instruments, Inc., 19 Fortune Drive, Billerica, MA 01821, USA.*

J. Grandjean, *University of Liege, Institute of Chemistry B6, Sart Tilman, B-4000 Liege, Belgium.*

Raj K. Gupta, *Department of Biochemistry, Albert Einstein College of Medicine, Yeshiva University, Jack and Pearl Resnick Campus, Bronx, NY 10461, USA.*

Wolfgang Meiler, *Sektion Physik, Universität Leipzig, Linnéstr. 5, 0-7010 Leipzig, Germany.*

Reinhard Meusinger, *Sektion Physik, Universität Leipzig, Linnéstr. 5, 0-7010 Leipzig, Germany.*

Joseph C. Viniero, *Department of Physiology and Biophysics, Albert Einstein College of Medicine, Yeshiva University, Jack and Pearl Resnick Campus, Bronx, NY 10461, U.S.A.*

Bernd Wrackmeyer, *Laboratorium für Anorganische Chemie der Universität Bayreuth, Postfach 101251, D-8580 Bayreuth, Germany.*

Preface

The protean nature of the applications of NMR is regularly reflected in this series of reports and Volume 24 is no exception. It is an ineluctable fact that all areas of science appear to benefit upon submission to the blandishments of NMR. The examples provided here encompass solid state NMR, solid state NMR imaging, NMR studies of interfaces, NMR investigations of cells and organisms, mercury-199 NMR and some applications of NMR in the area of coal science.

It is a pleasure for me to be able to convey my sincere thanks to all of the authors for their dedication in the preparation of their reports. The continuing success of this series depends upon the cooperation of both the contributors and the production staff which is much appreciated.

University of Surrey
Guildford

G.A. WEBB

Contents

List of contributors	v
Preface	vi

Developments in Solid State NMR

N.J. CLAYDEN

1. Introduction	2
2. Sensitivity	3
3. Chemical shift anisotropy	11
4. Dipole-dipole coupling	25
5. Quadrupole coupling	41
6. Zero field	54
7. Imaging	57
8. Multiple-quantum methods	71
References	74

Solid State NMR Imaging

D.G. CORY

1. Introduction	88
2. Imaging basics	94
3. Wide-line imaging methods	110
4. Manipulation of Hamiltonians, averaged Hamiltonians	118
5. Imaging with multiple-phase line-narrowing	127
6. Imaging with magic-angle sample spinning	145
7. Rotating frame imaging	152
8. Large samples and surface coils	157
9. Nutation studies of the skin depth in metallic samples	159
10. Slice selection and volume selected spectroscopy	160
11. Other spin = $\frac{1}{2}$ nuclei	165

12. Quadrupolar nuclei	168
13. Applications	171
Acknowledgements	174
References	174

NMR Studies of Interfacial Phenomena

J. GRANDJEAN

1. Introduction	181
2. Theory	184
3. Results	197
4. Conclusions	211
References	212

NMR Measurements of Intracellular Ions in Living Systems

JOSEPH C. VENIERO and RAJ K. GUPTA

1. Introduction	219
2. Sodium measurements	220
3. Potassium measurements	237
4. ^{19}F NMR measurements of intracellular free calcium ions	244
5. Magnesium measurements	252
6. ^{35}Cl NMR spectroscopy	258
References	262

^{199}Hg NMR Parameters

BERND WRACKMEYER and ROSALINDA CONTRERAS

1. Introduction	267
2. Experimental	268
3. Nuclear spin relaxation	271
4. Chemical shifts, $\delta^{199}\text{Hg}$	273
5. Indirect nuclear spin-spin coupling constants $^nJ(^{199}\text{HgX})$	262

6. ^{199}Hg NMR of solids	280
7. Conclusions	281
Acknowledgements	281
References	321

Applications of NMR Methods in Coal Research

WOLFGANG MEILER and REINHARD MEUSINGER

1. Introduction	331
2. NMR investigations of coal structure	332
3. Interactions between solvent molecules and coal surfaces	342
4. Thermal processes	356
Acknowledgements	360
References	361
Index	365

This Page Intentionally Left Blank

Developments in Solid State NMR

N.J. CLAYDEN

*ICI plc, Wilton Materials Research Centre, PO Box No. 90, Wilton,
Middlesbrough, Cleveland TS6 8JE, UK*

1. Introduction	2
2. Sensitivity	3
2.1. Low-temperature NMR	4
2.2. Polarization transfer	5
3. Chemical shift anisotropy	11
3.1. Magic-angle spinning	11
3.2. Determination of chemical shift tensors	15
3.3. Study of dynamic processes	20
3.4. Chemical shift correlation	25
4. Dipole-dipole coupling	25
4.1. Removal of dipole-dipole coupling	27
4.2. Reintroduction of dipole-dipole coupling	29
4.3. Nutation spectroscopy	38
4.4. Spin diffusion	39
5. Quadrupole coupling	41
5.1. Quadrupolar effects on spin- $\frac{1}{2}$ nuclei	42
5.2. Reduction and removal	43
5.3. Nutation NMR	47
5.4. Overtone NMR	49
5.5. ^2H quadrupole echo	50
5.6. Multiple-quantum excitation	54
6. Zero field	54
7. Imaging	57
7.1. Sensitive slice methods	59
7.2. High-temperature NMR imaging	60
7.3. Solid echo	60
7.4. Multiple-pulse sequences	64
7.5. Magic-angle spinning	67
7.6. Magic-angle rotating frame	68
7.7. Rare spin imaging	70
7.8. Surface coils	71
8. Multiple-quantum methods	71
References	74

1. INTRODUCTION

Solid state NMR continues to be a fertile area for research with developments in many aspects of the technique, including improved instrumentation, pulse sequences and data analysis. Much of the diversity in the experiments stems from the desire to measure or remove different nuclear spin interactions. This forms an important theme in solid state NMR. Although more emphasis is being placed on correlating nuclear spin interactions, in particular the chemical shift and dipolar coupling, it is still true to say that the main aim is to eliminate the contribution of interfering interactions in order to observe the one of interest. Even when the purpose of the experiment is to correlate the nuclear spin interactions, the unique development of one interaction in a time period has been important and hence the increased use of two-dimensional experiments. Unlike solution state NMR, though, two-dimensional experiments are not so widely used in the solid state, principally because of the low sensitivity in many of the experiments. Given this background it is logical to consider the developments as they apply in the three main nuclear spin interactions, namely the chemical shift, dipolar coupling and quadrupolar coupling. An area of potential, NMR imaging of solids, is taken separately, as are developments aimed at improving the sensitivity. In such a complex area as solid state NMR undoubtedly there will be experiments which do not adequately fit the classification adopted; however, I hope these will be kept to the minimum.

Rapid growth in the availability of commercial solid state NMR spectrometers has meant that the application of the technique to problems in chemistry, physics, biochemistry and material science have blossomed. It is therefore difficult to do justice to the review of all aspects. Consequently, I intend to restrict this review to developments in the techniques of solid state NMR and will not deal with applications, except in so far as they impinge on the technical merits. However, it would not be right to introduce the new experiments without placing them in context and to point out their strengths and weaknesses. For those interested in the applications reviews and books are available in various areas as follows: glasses and minerals,^{1,2} studies of supported metal particles both with and without adsorbed molecules,³ polymers,⁴⁻¹¹ principles of multiple-quantum NMR,¹² NMR in one and two dimensions,¹³ coherence in NMR,¹⁴ high-temperature superconductors,¹⁵ imaging of materials,¹⁶ general solid state NMR,¹⁷⁻¹⁹ solid state NMR in inorganic chemistry,^{20,21} recent developments in solid state NMR techniques,²² two-dimensional methods in polymers,²³ biochemistry,²⁴⁻²⁶ ceramics,²⁷ zeolites²⁸ and NMR microscopy.²⁹ An excellent account of some recent developments in nuclear magnetic resonance including the solid state is provided by two volumes commemorating J.S. Waugh's 60th birthday.^{30,31}

Topics covered include: high-temperature superconductors, ^2H NMR of inclusion compounds, ^1H MAS NMR imaging and heteronuclear couplings by REDOR.

2. SENSITIVITY

Arguably the single most important impediment to the wider application of solid state NMR is the low sensitivity of the technique. This arises from the small magnitude of the energy separation between the nuclear spin states in a magnetic field, giving only a small difference in populations. For a typical field of 5 T at room temperature the population ratio for ^1H is only 1.00001. The overall sensitivity of the NMR experiment can be tackled in two ways: first, by increasing the nuclear spin polarization and second, by improving the efficiency of the detection. Improvements in magnet technology are increasing the static fields, B_0 , available such that persistent high-resolution magnets of 14.1 T are now common, thereby giving a greater nuclear spin polarization. However, increasing B_0 is not a realistic way to improve the sensitivity markedly because the step changes in the field strength which are required are not foreseeable.

At the other end of the experiment one could look for a more sensitive detection device than an rf coil operating by Faraday's law. One such device is the SQUID³² which has been employed to detect low frequencies.³³⁻³⁵ With the higher frequencies more typically seen in NMR experiments, though, the advantage of the SQUID is no longer seen. Indirect detection schemes based on the optical detection of magnetic resonance (ODMR)³⁶⁻³⁸ also offer an increase in sensitivity because of the higher frequencies of the optical radiation. This is reflected in applications such as hole-electron recombinations in semiconductors.³⁹ Nevertheless, these applications are limited and optical detection methods cannot be considered a general method for sensitivity enhancement.

In essence, NMR would be more sensitive if only the polarization of the nuclei could be increased. Within the realm of conventional NMR this means low temperatures and polarization transfer methods. Polarization is most commonly transferred from electrons to the nucleus of interest or from protons to a less abundant nucleus. Highly polarized nuclei can be prepared by methods developed for producing atomic beams,^{40,41} involving multipole magnets and adiabatic rf transitions for nuclei such as ^{23}Na and ^7Li , while for the inert gases, spin transfer from an optically pumped species can be used to prepare polarizations of up to a few per cent.⁴² Because these have not been widely applied, the full capabilities are as yet unknown. In the case of ^{131}Xe the T_1 of the nuclear magnetization is sufficiently long to allow experi-

ments involving polarization and then removal to a high field magnet. This offers the possibility of studying surfaces and porous materials such as zeolites,⁴³ along the lines of previously reported experiments using normal polarization levels.^{44,45}

2.1. Low-temperature NMR

Both in principle and in practice very low temperatures < 1 K can bring about drastic improvements in the signal intensity. To achieve the most significant benefit requires temperatures as low as 10–30 mK, when the signal is 10^4 greater than at room temperature. Now we are dealing with robust signals of the order of a volt. The price to be paid for this is an enormous increase in the nuclear spin–lattice relaxation time and the experimental problems of working at low temperature. Particular attention has been paid to the mechanisms of nuclear spin relaxation and the nature of linewidths in insulators below 1 K,⁴⁶ since long relaxation times are expected because of the reduction in lattice vibrations which are important in the coupling of the nuclear spin to the lattice. If lattice vibrations were the only source of relaxation low-temperature NMR would be a curiosity; however, it has been observed that ^3He can mediate nuclear spin–lattice relaxation at surfaces.^{47–50} Moreover, coupled relaxation of surface spins is a phenomenon which occurs in all solids immersed in ^3He ; it is characterized by a temperature-independent T_1 . Have we reached a Holy Grail for NMR: high sensitivity associated with surface selectivity? In one sense, yes, when the solid has a high surface area but no if the intent is to study single crystal faces. At the millikelvin temperatures used in these experiments it can be difficult to establish the true temperature and one direct method is to use the temperature dependence of the lineshape which is evident at low temperatures.⁵¹ For example, the Pake doublet in $\text{CaSO}_4 \cdot \text{H}_2\text{O}$ becomes markedly skewed at temperatures below 50 mK (Fig. 1).

In a study of stannic oxide it has been observed that the ^{115}Sn chemical shift powder patterns were inhomogeneously broadened, which was attributed to coupling between the ^{115}Sn and paramagnetic ions. At the low temperatures used relaxation of the electron spins is also greatly inhibited. It is unclear to what extent the inhomogeneous broadening is going to restrict the applicability of ultra low-temperature NMR. Distortions can also arise in the lineshape because the Fourier transform spectrum no longer represents the steady state absorption and dispersion spectrum.⁵² This is encountered as a dependence of the lineshape on the flip angle.

Low-temperature NMR will be complicated for materials showing chemical shift inequivalence and abundant spin dipolar coupling, because all

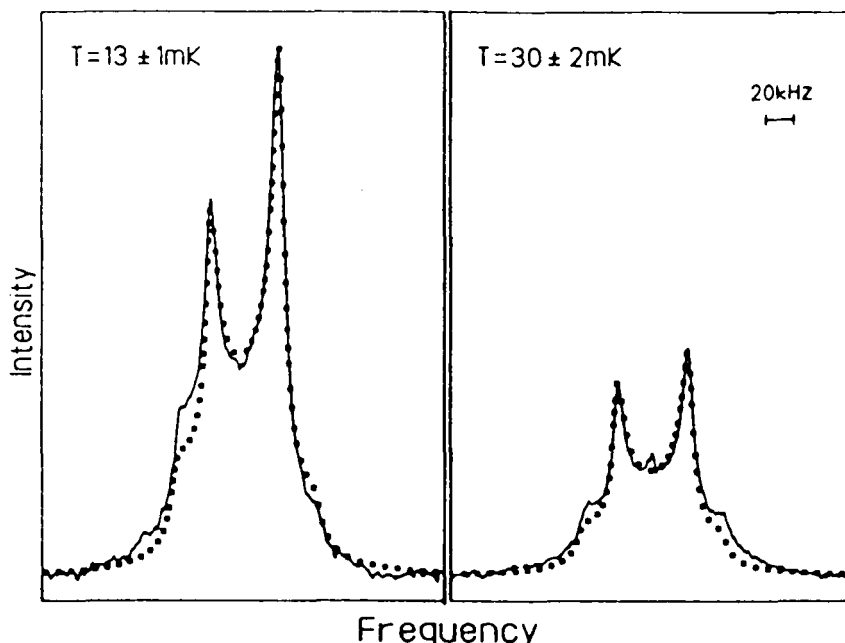


Fig. 1. Proton resonance spectra of slightly hydrated CaSO_4 powder immersed in liquid ^3He at 13 and 30 mK. The solid lines are the experimental spectra. The squares represent the best-fit theoretical spectra. (Reproduced with permission from Kulns *et al.*⁵¹)

work must be carried out on static samples and to date no multiple-pulse sequences, apart from Carr–Purcell echo trains, have been used. When a single environment is expected chemical shift powder patterns can be readily understood, as was the case for ^{13}C O adsorbed on SnO_2 at 0.01–1 K. The ^{13}C T_1 of 540 s was not outrageously long, values of the same order are seen in the crystalline phase of polyethylene.⁵³

2.2. Polarization transfer

2.2.1. Cross-polarization

The transfer of magnetization from an abundant spin, normally protons, to a rare spin, such as ^{13}C , has been of major importance in allowing the development of solid state NMR.⁵⁴ Without this increase in sensitivity the range of experiments would be greatly restricted. Cross-polarization has been achieved in three ways, shown schematically in Fig. 2; first, using adiabatic demagnetization in the rotating frame (ADRF) where dipolar order is

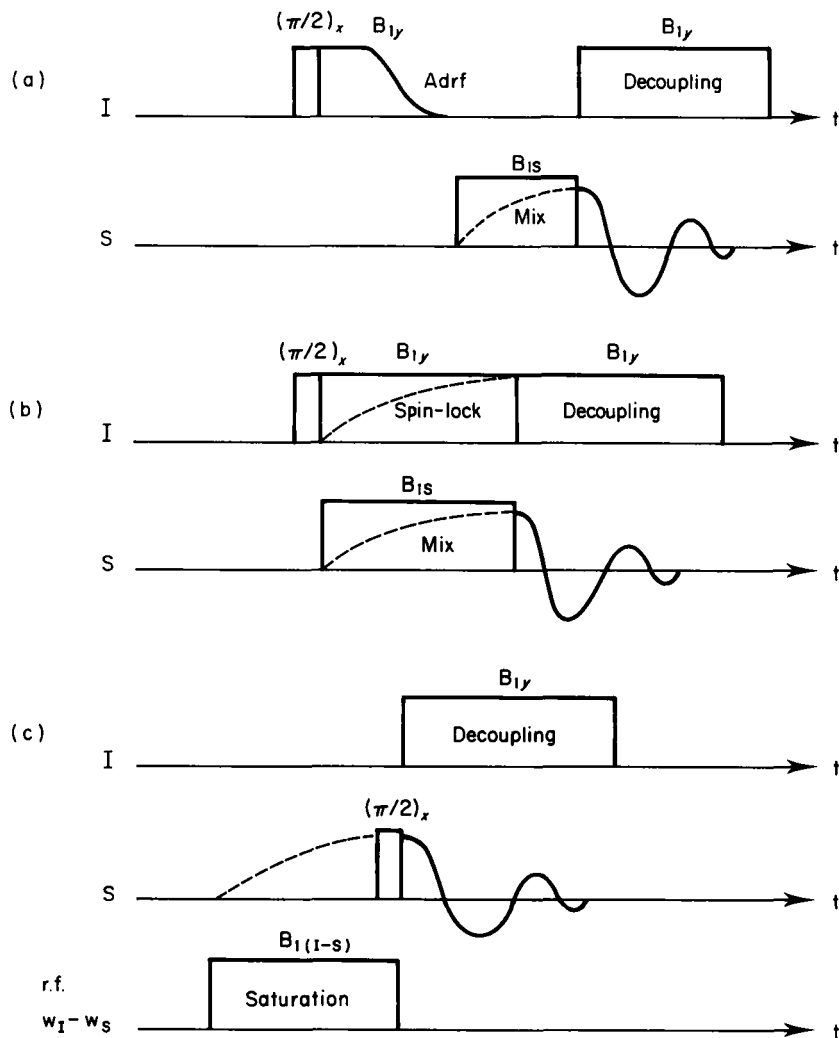


Fig. 2. Sequences for cross-polarization from an abundant spin, I, to a rare spin, S. (a) ADRF, adiabatic demagnetization in the rotating frame, (b) spin-lock and (c) nuclear solid effect.

created from the proton magnetization followed by its transfer into the rare spin;⁵⁵ second, by spin-locking in the rotating frame and transferring the magnetization by applying matched rf fields to both the spin systems meeting the so-called Hartmann-Hahn condition;⁵⁶ and third, by a solid effect involving the saturation of forbidden transitions.^{57,58} ADRF relies on the

existence of dipolar order and thus is not compatible with magic-angle spinning, which greatly reduces the relaxation time of dipolar order, and the solid effect requires a triply tuned probe. Hence the overwhelming importance of the spin-lock cross-polarization method.

A modified spin thermodynamic treatment of spin-lock cross-polarization which considered the broadening of the abundant spin energy through quantized states has led to the proposal of a new cross-polarization pulse sequence which is much less sensitive to mismatching.⁵⁹ This sequence involved the synchronous reversal of the phase on both the spin-locking rf fields. Important elements of the theoretical description were the existence of a number of spin reservoirs which were in quasi-equilibrium at different spin temperatures and the role of dipolar coupling in attaining equilibrium between these reservoirs.

Still on the theme of mismatched Hartmann-Hahn conditions, another model has been proposed to explain cross-polarization in the rotating frame involving a comparison of the rare spin rf field and the density of ^1H states.⁶⁰ The model of the density of states arising from the quantization of the dipolar energy provides a clear explanation of why only a small fraction of rare spins are polarized under mismatched conditions. In both treatments the inefficiency of cross-polarization under mismatched conditions is considered to be thermodynamic and not kinetic. When a rare spin is poorly polarized under mismatched Hartmann-Hahn conditions multiple contacts can be used to successively polarize it.⁶¹

A simple example of two spin reservoirs, and one which is discussed in the paper of Levitt *et al.*, is important in a later paper dealing with a two-stage feature in cross-polarization.⁶² Here, the authors use a depolarization sequence to show a rapid initial stage brought about by directly bonded H followed by a slower second stage when the $^{13}\text{CH}_n$ subsystems come to what they call quasi-equilibrium with the ^1H reservoir. The two reservoirs are then the isolated I-S spin pair and the remaining ^1H spins. It was noted that a turning point is seen in the variation in the intensity with depolarization time which occurs at an intensity equal to $1/(n + 1)$ of the initial value for a CH_n spin system. This was suggested as a reliable method for distinguishing between CH and CH_2 resonances in a ^{13}C NMR spectrum.

A simple modification to the basic spin-lock cross-polarization pulse sequence involving a depolarization step has been proposed,⁶³⁻⁶⁶ which can be used to distinguish between different phases in a material as well as providing an alternative to the dipolar dephasing experiment.⁶⁷ In this experiment the phase of the abundant spin rf field is shifted by 180° for a short period, typically up to $150\ \mu\text{s}$, at the end of a normal cross-polarization. During this period depolarization takes place with a time constant T_{CH} , allowing particular resonances or phases to be selected in the final spectrum. Thus for a

semicrystalline polymer the more mobile amorphous phase, which has a longer T_{CH} , can be selectively observed by nulling the crystalline component using the appropriate delay.⁶⁸ Similarly, it is possible to choose a depolarization period which will null each of the carbon resonances in a spectrum such as that of polypropene (see Fig. 3). A simple extension of the cross-depolarization method involving an additional repolarization can be used to null simultaneously methine and methylene carbons.⁶⁹ As a method for differentiating between methine and methylene carbons it suffers from the drawback that the time constants T_{CH} will vary from sample to sample and the ranges for the two types of groups overlap. Cross-polarization is normally used from the abundant spin to the rare spin to enhance the sensitivity but it is possible to carry out the polarization transfer in the reverse direction as a method of spectral assignment.^{70,71}

Although cross-polarization is an invaluable technique, care must be taken when trying to quantify the intensities in the resulting NMR spectrum. This is true even for homogeneous samples, but especially so for heterogeneous ones. For any sample the cross-polarization dynamics of a rare spin, such as ^{13}C , are defined by two time constants, T_{CH} and $T_{1\rho}$,⁷² with T_{CH} depending on the dipolar coupling between the rare and abundant spin. When the sample is homogeneous there will be a common $T_{1\rho}$ leaving only the questions, how long should the contact time be to ensure that for all carbons it is $5 * T_{CH}$, and is this attainable?⁷³

Quantifying the intensities in a heterogeneous material is, in contrast, complex. At one extreme there may be a component which is so mobile that the dipolar couplings are effectively averaged to zero, making cross-polarization totally useless. Little can be done in these circumstances except to try a lower temperature to freeze the mobile component or use single-pulse excitation. Less marked differences in T_2^* can also lead to distortions because of decay of the magnetization during the preparation pulse,⁷⁴ only in this case it is the rigid phase which will be underestimated. This effect will be most marked when a long ^1H preparation pulse is used. If the components have similar T_2^* but differ in $T_{1\rho}$ it is possible to quantify the results providing the cross-polarization dynamics are known.⁷⁵ To some extent the problems of differing $T_{1\rho}$ can be overcome by using a multiple cross-polarization method which seeks to maximize the contact time to fulfil the $5 * T_{CH}$ condition but minimize the $T_{1\rho}$ decay during the process.^{76,77} At best this increases the effectiveness of the cross-polarization by a bond length or so and is not a real answer to the problems of determining quantitative results.

Two possible advantages of the nuclear solid effect are that it can be used when the $T_{1\rho}$ is short and it is not influenced by magic-angle spinning, as is the spin-lock cross-polarization. Like the spin-lock method the maximum enhancement is a factor of γ_I/γ_S . To generate the nuclear solid effect the

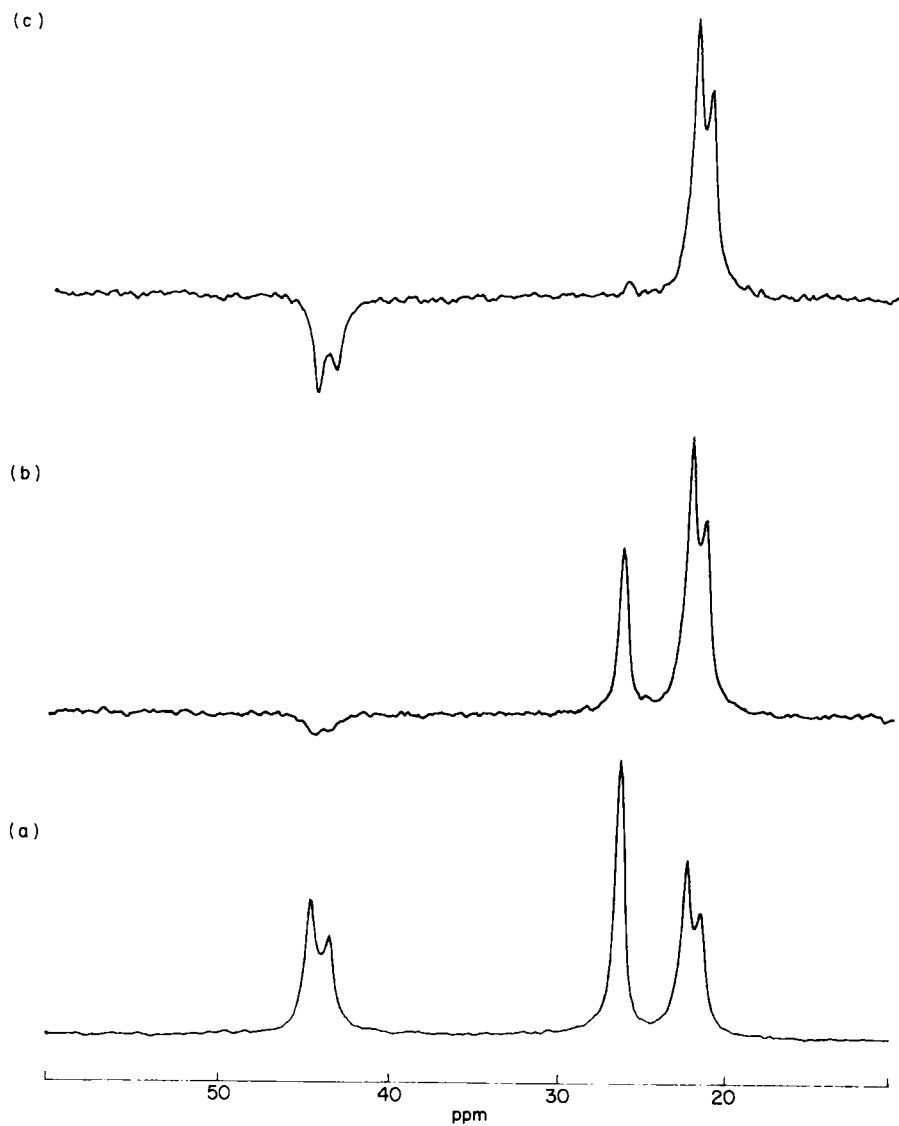


Fig. 3. Cross-depolarization of a highly crystalline polypropylene (a) showing the selective nulling of the (b) methine and (c) methylene carbon resonances.

forbidden transition at $\omega_{01} \pm \omega_{05}$ is irradiated for seconds or so with a B_1 field of about 1 mT. Clearly, a triply tuned probe is necessary if a decoupled spectrum is required at the end. Overall it was found that the nuclear solid effect gave comparable enhancements to the spin-lock method for a series of samples, better in some cases and worse in others.⁷⁸ Its main disadvantage appears to be the long irradiation times at quite high rf powers needed to increase the forbidden transition rate.

Cross-polarization can be extended from a two-spin system to a relay between three spins in a double cross-polarization.⁷⁹ Magnetization is first transferred from ^1H to ^{13}C and then to ^{15}N using a triply tuned probe. In this manner it is possible to establish the connectivity of two spin labels. A complication is that the cross-polarization dynamics can be difficult to interpret, preventing an unambiguous assignment of adjacent spin labels.

2.2.2. *Dynamic nuclear spin polarization*

The topic of dynamic nuclear spin polarization (DNP) has been reviewed recently.⁸⁰ A fundamental requirement for the experiment is that the sample contains unpaired electrons. Concentrating on the salient features of the technique, the experimental set-up differs from a standard solids NMR experiment by placing the NMR probe, either static or MAS, in a resonant microwave cavity and prior to the NMR experiment irradiating the system with microwaves. Usually the experiment has been carried out at a low B_0 because of the expense and difficulty of providing high-power microwave frequencies with an acceptable duty cycle. Two methods can be used for rare spin DNP, either enhancement of the ^1H which is then transferred to the rare spin by cross-polarization, or direct enhancement of the rare spin. Direct polarization has the effect of preferentially enhancing those rare spins close to the radical centre, while the indirect method gives a more uniform enhancement making it ideal as a method for shortening the measuring time of an experiment. The maximum enhancement observed for a range of materials was of the order of 200 for ^{13}C and 50 for ^1H , while the actual enhancement possible depends on the conditions used, the electron spin concentration and the polarization mechanism.

Perhaps the most important practical considerations are the minimal conditions required for enhancement since even an enhancement of 4, with a saving in spectrometer time of 16, could transform the feasibility of many experiments. The important factors which need to be considered are the radical concentration and its ESR linewidth and the nuclear spin relaxation parameters. An excellent illustration of the saving in time this order of enhancement gives is provided by a two-dimensional experiment correlating

the chemical shift and dipolar coupling in a pairwise doped polyacetylene. In this study the enhancement factor was only 30 but the experiment still took a day. Without DNP such an experiment would be unthinkable as it would take nearly three years!⁸¹ Typically DNP is carried out in the laboratory frame, but it is possible to obtain DNP in the rotating frame.⁸²

3. CHEMICAL SHIFT ANISOTROPY

3.1. Magic-angle spinning

The ability to correlate chemically inequivalent resonances to the structure of a material is one of the most important reasons for using solid state NMR. Hence, there is a premium on being able to resolve isotropic chemically shifted resonances in the NMR spectrum. For the most part, observing low-abundance nuclei, this can be achieved using magic-angle spinning (MAS) at speeds of up to 5 kHz with or without abundant spin decoupling.¹⁸ On the other hand, for abundant spins the much larger homonuclear dipole-dipole coupling is not adequately removed at these slow speeds so that only broad unresolved resonances are seen. Expressions for the residual linewidth in the NMR spectra of spin- $\frac{1}{2}$ nuclei, particularly ^1H , with an anisotropic chemical shift tensor combined with homo- and heteronuclear dipolar coupling have been calculated.⁸³ Two approaches have been used to overcome the poor resolution seen for abundant spins; first, very fast magic-angle spinning⁸⁴ and second, combining slower magic-angle spinning with multiple-pulse sequences.⁸⁵⁻⁸⁷ The latter technique is known as combined rotation and multiple-pulse spectroscopy (CRAMPS).

By and large the very fast MAS method involving speeds of up to 20 kHz is only applicable to ^{19}F , where it has been used to study fluoropolymers.⁸⁸ Here it was found that when the MAS speeds were the same order of magnitude as the static linewidth ($> 15\text{ kHz}$) all the significant features present in the 20 kHz NMR spectrum were already apparent. This is helpful because a commercial probe capable of 18 kHz is available.⁸⁹ A detailed comparison of very fast spinning and CRAMPS does not appear to have been carried out for ^{19}F . Such a comparison for ^1H indicated that the general quality of the MAS-only spectra, even at 21 kHz, were not as good as the CRAMPS spectra, as illustrated in Fig. 4, suggesting that the ^1H - ^1H dipolar interactions need to be rather weak before MAS-only is a viable option.⁹⁰

Despite the technical merit of the CRAMPS technique for ^1H NMR in solids it should be noted that the residual linewidths, whilst not out of line with those seen for ^{13}C ,⁹¹ still prohibit a widespread use of high-resolution ^1H NMR of solids because of the small chemical shift range for ^1H NMR.

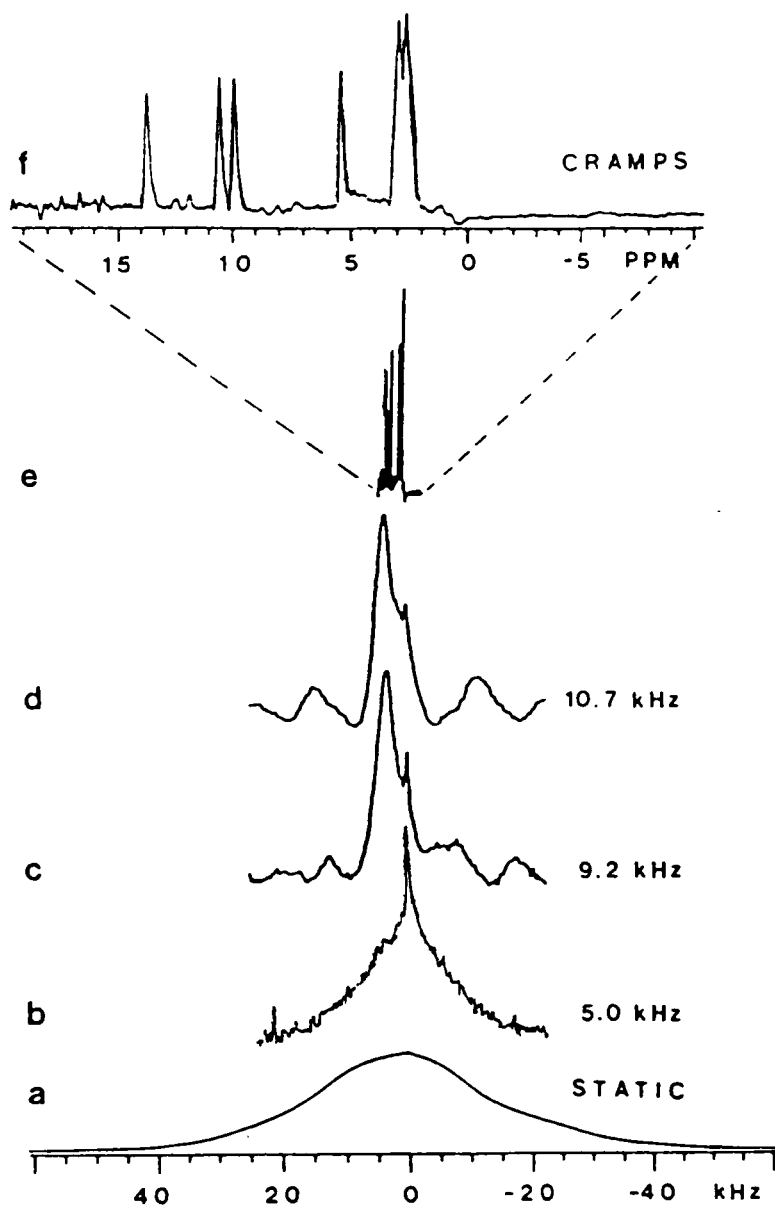


Fig. 4. Comparison of CRAMPS and MAS-only spectra for citric acid. (a) Static sample, single pulse, (b, c, d) MAS-only with the indicated MAS speed, (e) CRAMPS and (f) CRAMPS on an extended scale. (Reproduced with permission from Dec *et al.*⁹⁰)

Normally only ^1H and ^{19}F are treated as abundant spins from the point of view of requiring homonuclear decoupling. However, slow MAS is not consistent with the complete averaging of ^{31}P - ^{31}P interactions⁹² and should the highest resolution be required in a slow spinning spectrum of a material with a high phosphorus density then multiple-phase decoupling of the phosphorus might be profitable.

Even at a relatively low field of 4.7 T, 5 kHz MAS may not be sufficient to remove the spinning sidebands totally from the region of interest. This will be especially true for heavy metal nuclei such as ^{207}Pb , but is equally true for the ^{13}C NMR spectrum of an aromatic polymer with an aliphatic additive, where the 5 kHz is only 100 ppm. Clearly, having to repeat the spectra at different spinning speeds is not ideal. Furthermore, the tendency to move towards higher static magnetic field strengths will exacerbate the problem; routine spinning at 10 kHz would be necessary for ^{13}C at 9.4 T.

A partial answer is to use a spinning sideband suppression pulse sequence such as TOSS,^{93,94} which has the effect of eliminating the sidebands from the spectrum. In addition to the four-pulse TOSS a six-⁹⁵ and eight-⁹⁶ pulse variant have been suggested while an improved six-pulse version for fast MAS has also been proposed.⁹⁷ Since the spinning sideband intensity is lost and not transferred into the isotropic resonance as faster spinning would do there is inevitably a poorer signal-to-noise ratio. Moreover, accurate setting up of the sequence will be required to ensure that complete elimination of the sidebands occurs if quantitative results are sought for overlapping sidebands and isotropic resonances. A detailed examination of the effect of imperfections, such as the pulse lengths, phases and timing as well as resonance offset effects has shown that the pulse phase errors are not critical whereas errors in the pulse lengths and timings reduce the centreband intensity and leave residual spinning sidebands.⁹⁸

Another alternative to faster spinning is to scale the chemical shift anisotropy by use of a multiple-pulse sequence so that a slower spinning speed will effectively average the tensor.^{99,100} The cost here is an increased technical complexity involving a set-up routine and the possible intrusion of rotor frequency lines.¹⁰¹ For most practical purposes the solution to the problem of spinning sidebands is to spin routinely at 10 kHz or so. It must be noted though that this solution itself has drawbacks, namely the uncertainties associated with obtaining quantitative cross-polarization spectra caused by the modulation of the dipolar coupling by the magic-angle spinning.¹⁰² To some extent this can be overcome by changing the angle of the sample spinning from 90° in the cross-polarization stage to the magic angle during the detection time. The advantage of this lies in the differing modulation of the Hartmann-Hahn match at 90° as opposed to the magic angle. This modification means that the Hartmann-Hahn match will be easier to attain

and maintain.¹⁰³ In order to switch the spinning angle the magnetization is stored along the z axis after the cross-polarization. This simple storage can be used to help overcome overload of a preamplifier in a cross-polarization experiment by just leaving a delay to allow the receiver to recover without any switching of the angle.¹⁰⁴ An intriguing feature of fast spinning MAS is that it is possible to enhance the intensity of a spinning sideband using a rotary resonant field where the rotary resonance condition is $\omega_1 = N\omega_r$, with ω_1 the nutation frequency and ω_r the spinning frequency. N is an integer $-2 < N < +2$. The selected spinning sideband depends on N .¹⁰⁵ In essence, this enhancement is achieved by preparing the magnetization components with an orientation-dependent initial phase.

Low-temperature MAS is of potential value for the study of molecular rearrangements, reactive intermediates and molecular dynamics.¹⁰⁶ With the odd exception (for example, Yannoni *et al.*¹⁰⁷), all the MAS experiments have been carried out at 77 K or higher. Now MAS has been performed at 8 K,¹⁰⁸ enabling low activation energy processes and tunnelling to be studied. Only quite low spinning speeds could be managed (< 1 kHz), because of the difficulties of maintaining the low temperature with a flow of relatively warm gas. Since the experiments were performed at 15 MHz for ^{13}C the spinning sidebands were not too great a problem. Although the sensitivity was better than at ambient temperature, owing to the temperature dependence of the nuclear spin polarization, it should be stressed that the experiment was not seen as a way of improving the sensitivity of the NMR experiment.

One answer to the poor sensitivity of NMR is to use large samples and this has led to the development of a 2-cm³ spinner capable of 1–2 kHz.¹⁰⁹ A continuing area of interest is the design of rotors or rotor inserts to study sealed samples, such as adsorbed species in catalysis, or air-sensitive materials.^{110,111}

The curious, seemingly simple observation that the MAS NMR spectra of powders always give positive and absorptive intensity spinning sidebands, has only recently been explained theoretically.¹¹² This is of more than passing interest because if a single crystal is spun then a mixture of dispersion and absorption lineshapes are seen whose precise character depends on when the data acquisition begins during the rotor period.¹¹³ Starting with this behaviour for a fully ordered material a two-dimensional MAS experiment has been proposed for determining the order within a partially ordered material.¹¹⁴ Practically speaking the experiment is remarkably simple, requiring only the synchronization of the start of the acquisition time with the rotor position. The first time domain is just the time between the rotor reaching its starting position and the start of data acquisition. Order in the sample is then apparent from the presence of spinning sidebands in the frequency domain corresponding to the first time domain, as can be seen in

Fig. 5. A detailed analysis of the experiment has been presented and applied to a sample of oriented polyethylene terephthalate (PET) fibre.¹¹⁵ The technique appears to be a powerful method for studying orientation by NMR.

3.2. Determination of chemical shift tensors

An excellent illustration of the ingenuity of the NMR spectroscopist is the variety of methods which have been proposed for determining the chemical shift tensor. It is perhaps unfortunate that the same dedication has not been used in their application, for despite the extensive use of solid state NMR spectroscopy, very few references exist to the practical value of the tensorial properties except in the study of dynamic processes and orientation. When a single crystal is available the best method for determining the chemical shift tensor is through the rotation patterns of a sample with a known orientation in the magnetic field.¹¹⁶ Using these rotation patterns the principal values of the tensor can be found and, when combined with the orientation of the sample, can give the alignment of the principal axis system with the molecular axes. The collection of rotation patterns can be time-consuming, hence the value of an improved method¹¹⁷⁻¹¹⁹ involving a two-dimensional correlation with certain defined crystal orientations which gives the type of spectrum illustrated in Fig. 6.

More usually single crystals are not available, forcing us to study polycrystalline or amorphous materials. Because analytical functions exist to describe the lineshape¹²⁰ the powder pattern can be readily fitted to give the chemical shift tensor. A new approach to fitting powder patterns via a non-linear least-squares analysis has been proposed and the potential applications and limitations have been discussed.¹²¹ In the complex case of a lineshape showing dipolar coupling and chemical shift anisotropy, numerical simulation of the lineshape is necessary, involving powder averages over the orientations of the crystallites. This can be time-consuming, preventing an iterative fitting procedure to optimize the parameters. An improved method has been proposed which involves choosing orientations with a higher weighting in the powder average,¹²² increasing the speed and accuracy of the lineshape simulations. Although the example given was of a chemical shift anisotropy, in dimethoxymethane, it is expected to be of greater value when, for example, both a chemical shift and dipolar contribution are present, rather than here where, as noted above, analytical functions exist to describe pure chemical shift lineshapes.

As the number of distinct resonances, each with their own powder pattern, increases so it soon becomes impossible to analyse the overall powder

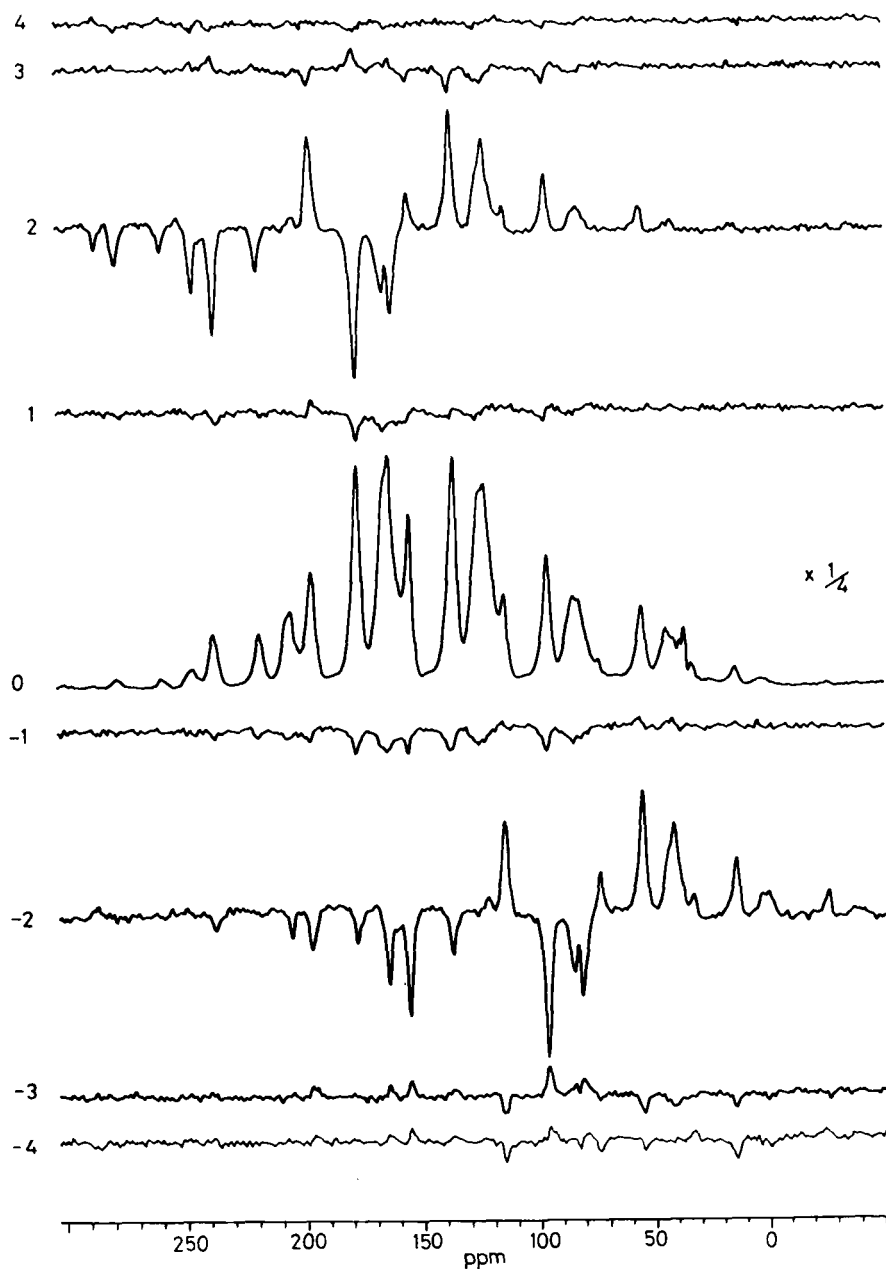


Fig. 5. Two-dimensional MAS NMR spectrum of a forward drawn sample of ICI, PEEK film. The sample was oriented with the draw direction at 90° to the rotor axis. Partial order is evident from the spinning sidebands in the $\pm M$ slices. The $M = 0$ slice corresponds to the normal MAS NMR spectrum

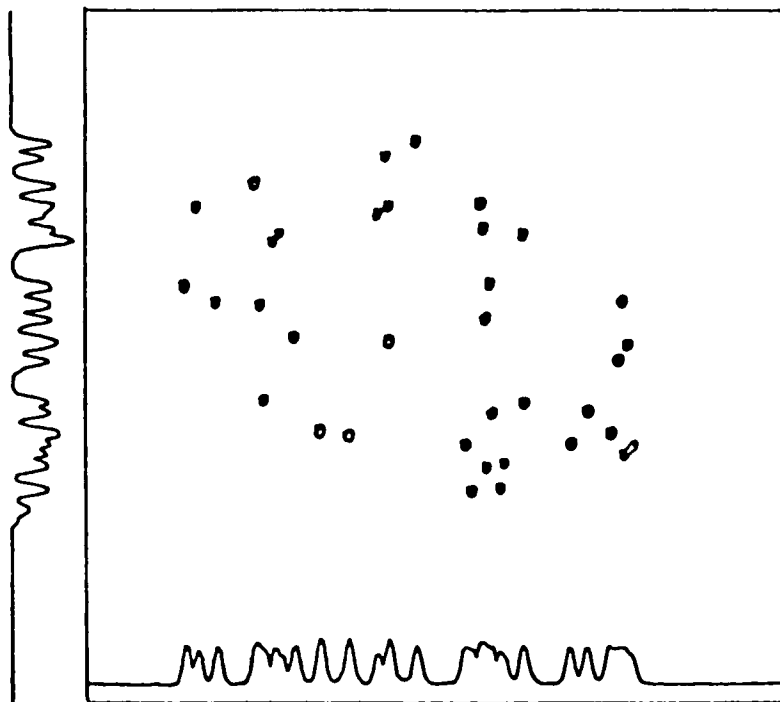


Fig. 6. Two-dimensional correlation of the resonances in a single crystal of 1,2,3-trimethoxybenzene in different orientations illustrating the dispersion in the spectra. (Reproduced with permission from Carter *et al.*¹¹⁹)

pattern. Now we must resort to MAS to improve the resolution but at the same time find some way to reintroduce the anisotropic component. It is this reintroduction of the anisotropic term which has led to the large number of methods. Some of these, as we shall see, are more instructive from the point of view of the underlying physics than their value in measuring the chemical shift tensor. We may talk about reintroducing the chemical shift anisotropy but in point of fact all we need do is not properly remove it in the first place by spinning slowly. Indeed, from the point of view of the simplicity of the experiment, ease of data interpretation and actual use, the analysis of the spinning sidebands in a slow spinning experiment represents by far and away the most important method.

Three ways have been used to obtain the tensor; moment analysis,¹¹³ the Herzfeld-Berger¹²³ and numerical simulation of the spectrum.¹²⁴ All of these methods have problems in defining the asymmetry when the tensor is nearly axial.¹²⁵ By and large this is not serious unless one is attempting to infer C3

symmetry based on an axial tensor. An analysis of spinning sideband intensities in a two-dimensional experiment has been presented,¹²⁶ as well as the spinning sidebands in paramagnetic compounds.¹²⁷ In an extension of the Herzfeld–Berger method it has been proposed that all the information contained in the spinning sidebands be used simultaneously through the use of a quantity ε , which is a function of the measured spinning sideband intensities and the theoretical values for given μ and ρ .¹²⁸

In practical terms the greatest problem with the slow spinning MAS experiment is the overlap of isotropic resonances and spinning sidebands in the spectra of complex materials.

One simple way of reintroducing the information about the anisotropy is to spin fast but off the magic angle, thereby giving a scaled powder pattern for each resonance. Since it is difficult to accurately measure the spinning angle externally, an internal reference sample with a known chemical shift tensor should be used.^{129,130} Characteristic powder-pattern-like lineshapes are also seen in the spinning sidebands if the sample is spun slowly off the magic angle.¹³¹ Although the scaling of the powder patterns improves the resolution, overlap is still possible. An obvious extension, and a common feature of the remaining methods, is to use a second dimension to spread the spectrum, giving the anisotropic chemical shifts in one dimension and the resolved isotropic chemical shifts in the other. Stated in this manner it is clear that one disadvantage of these types of experiment is going to be the total acquisition time for an adequate signal-to-noise ratio.

Mechanical manipulations, rf pulse sequences and combinations of these have all been suggested as two-dimensional experiments. As mechanical solutions we have the stop–go spinning experiment in which the powder pattern is obtained by not spinning during the first evolution period,¹³² the magic-angle hopping experiment^{133,134} and flipping of the spinning axis.^{135–137} These methods require the storage of the magnetization during the switching period and so are most suitable for samples with long T_1 . One way to reduce the experimental time, if only a limited number of anisotropies are required, is to combine the flipping axis experiment with a selective excitation pulse. Thus during the MAS phase only one resonance is selectively excited by using either a soft pulse or a more sophisticated shaped pulse. Upon flipping the spinning axis, the powder pattern of only that resonance will be seen.^{138,139}

Radiofrequency pulse methods rely on the effect of π pulses on the evolution of the chemical shift anisotropy.^{140–142} A convenient model for understanding these properties has been proposed whereby one follows the trajectory of a magnetization vector corresponding to a single crystallite defined by a set of Euler angles ($\alpha\beta\gamma$).¹⁴³ This model has been applied to the study of echo formation in rotating solids^{144,145} and the related problem of the TOSS pulse sequence for the total elimination of spinning sidebands.¹⁴⁶

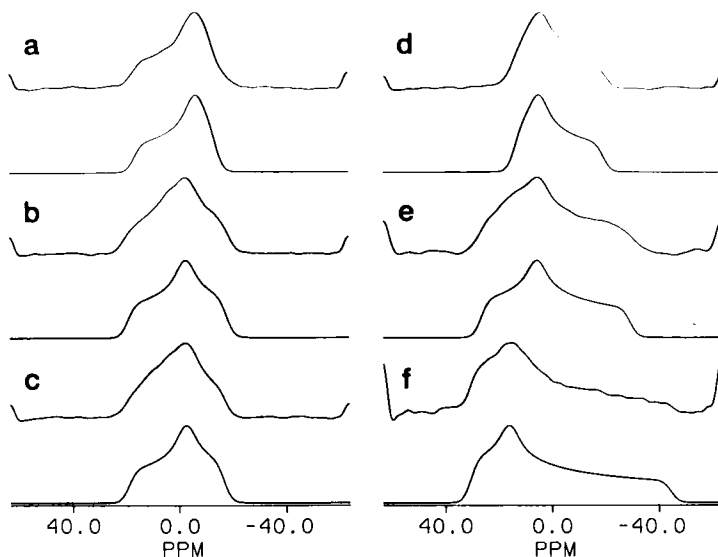


Fig. 7. A comparison of the observed and simulated chemical shift anisotropy powder patterns for methyl α -D-glucopyranoside obtained using a series of π pulses to suppress the averaging of the chemical shift: a-f correspond to the six isotropic resonances in order of increased shielding. (Reproduced with permission from Tycko *et al.*¹⁴⁷)

Perhaps a surprising feature of the π pulse sequences is that by a judicious choice of pulse spacings it is possible to prevent the chemical shift anisotropy from being averaged out by MAS.¹⁴⁷ Hence by the careful setting up and synchronization of the π pulse sequence an undistorted powder pattern can be obtained in the second dimension, as illustrated in Fig. 7.

Of the two classes the rf solution is in principle the more general because the emphasis is on the rf timing and preparation which should be applicable to commercial instrumentation, whilst the mechanical solutions mentioned above require a specialized probe. One indirect rf method is based on the resonance effect observed when a spin-lock field is applied to the nucleus being studied at ω_r or ω_{2r} whilst spinning at the magic angle. The method is indirect because the oscillations observed must be calculated for the particular chemical shift tensor.¹⁴⁸

Although the two-dimensional methods I have considered so far all try to get a powder pattern in one of the dimensions it is by no means clear that this is ideal, especially as it will tend to reduce the signal-to-noise ratio. Perhaps the simplest approach is to separate the isotropic and anisotropic chemical shift into two dimensions whilst spinning using either scaling of the chemical

shift tensor or a TOSS¹⁴⁹ sequence to suppress the spinning sidebands in one dimension.

Alternatively, rather than suppressing the chemical shift anisotropy by these methods we can choose to reduce the effective spinning speed by the effect of π pulses. Indeed a very simple spin-echo experiment has real potential, giving a spinning sideband pattern at effectively half the actual spinning speed in the first dimension,¹⁵⁰ though it should be noted that the data analysis is not so straightforward. Either the two-dimensional spectrum has to be calculated or the one-dimensional cross-sections obtained by skewing the data matrix. The advantage of the latter is that these skewed cross-sections are rigorously equivalent to the simple MAS spectrum, enabling the use of existing methods of analysis. For the reason why this experiment is useful we need to remember the problem at hand, namely the overlap of isotropic resonances and spinning sidebands forcing us to spin faster than we would wish for a spinning sideband analysis. Now it is rather rare for there not to exist any window for slower spinning, and more usually this occurs at a speed which gives low-intensity spinning sidebands. Thus, getting a spectrum at half the spinning speed may be all that is required. In a further improvement a pulse sequence has been developed, based on the extended dipolar modulation experiments, which increase the chemical shift modulation.¹⁵¹ Effectively, a sample spun at high speed will give spinning sidebands rigorously equivalent to a much slower speed in the second dimension with a reduction factor given by twice the number of rotor cycles the modulation occurs for. Hence, if a sample is spun at 4808 Hz and the three-cycle modulation is used then the effective spinning speed will be 801 Hz.

Another mechanical solution which has been suggested is to allow evolution at a slow spinning speed and then acquire the data at a high speed.¹⁵² Quite simple modifications to the spinning speed control mechanism involving a mass volume controller,¹⁵³ enabled a switch in spinning speed by a factor of 6–10. A delay of the order of 1–5 s is required for the speed to stabilize, during which the magnetization is stored along the Zeeman direction, and consequently the carbon T_1 must be at least this long for the method to be practicable. Typical spectra which can be obtained in this experiment are shown in Fig. 8.

3.3. Study of dynamic processes

The effects of dynamic processes are found in many forms in NMR and not just restricted to the chemical shift tensor. Indeed, we shall return to their manifestations through dipole–dipole and quadrupolar interactions. An

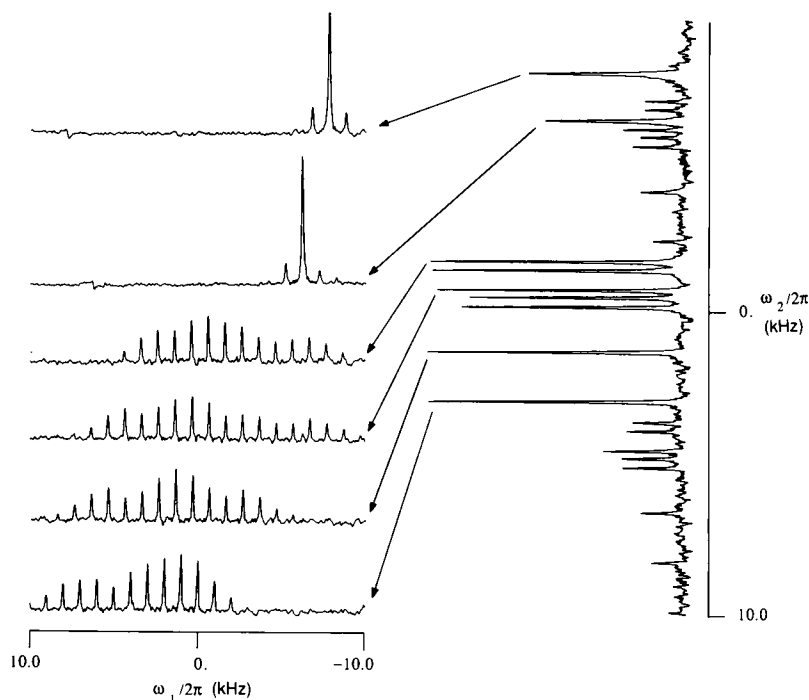


Fig. 8. Two-dimensional ^{13}C S^3 CSA spectrum of tyrosine hydrochloride at a lower speed of 1.0 kHz and a higher speed of 5.3 kHz. (Reproduced with permission from Kolbert *et al.*¹⁵²)

important difference between the chemical shift and dipolar interactions is that the chemical shift can only reflect a motional or chemical exchange, whereas the dipolar interaction can also reflect spin diffusion. In practice, for certain experiments it is not possible to eliminate the effect of spin diffusion from experiments looking at the chemical shift, thereby complicating the measurement of dynamic processes. A wide range of correlation times for dynamic events can be studied, depending on whether the sample is static or spinning and the pulse sequence used.

Fast motions are evident from averaged chemical shift tensors and averaged isotropic resonances.¹⁵⁴ The precise correlation times corresponding to the intermediate case depend on whether the isotropic chemical shifts are being averaged in a manner analogous to solution NMR¹⁵⁵ or whether the chemical shift tensor components are being averaged where rates of the order of the width of the powder pattern are important.¹⁵⁶ Dealing with more than one kind of motion can be difficult, especially when they are of the same order

of rate. The two ways of handling the problem are to take the motions sequentially or simultaneously. Sequential analysis is the more usual approach but is only valid when one motion is in the fast limit. Simultaneous analysis treats the motions at the same time and has been considered for ^{13}C lineshapes.¹⁵⁷

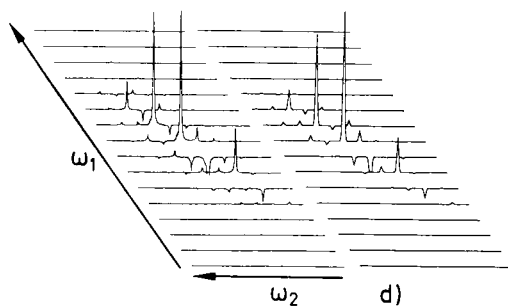
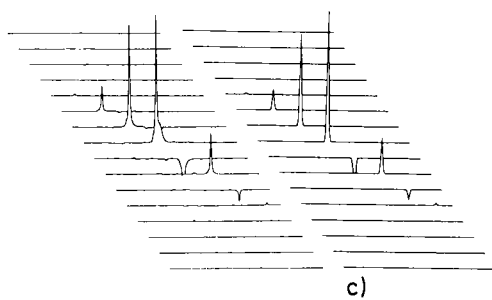
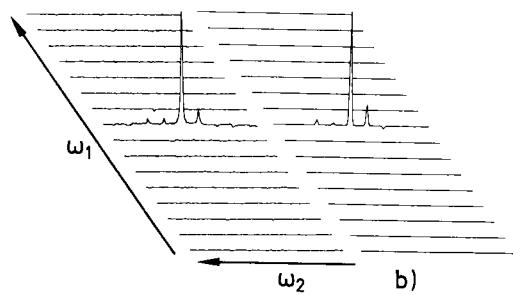
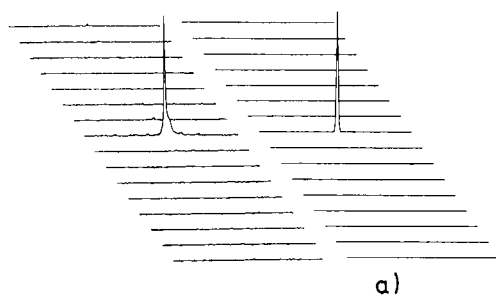
When dynamic processes are present in a sample undergoing MAS, interference effects can be seen as the correlation time for the process approaches the spinning speed, providing the motion modulates the chemical shift tensor. Typically this is observed as a line-broadening as a consequence of the dephasing between the rotational echoes.¹⁵⁸ An early treatment of the problem¹⁵⁸ considered only the isotropic resonances. This has been followed by a theoretical analysis based on Floquet theory which considers the spinning sidebands as well.¹⁵⁹ As a test example, dimethyl sulphone was chosen, and close agreement was found between the calculated and observed spectra, which allowed the rate constant to be derived and hence the activation energy for the process. At any given temperature a range of correlation times can be explored by using off-the-magic-angle spinning; as the angle moves further from the magic angle so the scaling of the powder pattern decreases and slower motions can be studied.¹⁶⁰ A novel approach has been proposed for calculating the MAS spectra of solids undergoing chemical exchange which involves replacing the original spin Hamiltonian by a set of three Hamiltonians.¹⁶¹ An earlier treatment of two-site exchange employed Floquet theory.¹⁶²

Rate constants as slow as 30 s^{-1} can cause observable changes in the MAS NMR spectra, but to see slower processes the two-dimensional chemical exchange three-pulse sequence must be used, either with static samples or MAS.^{163,164} Under suitable conditions of two-site exchange a one-dimensional analogue of this experiment, where a fixed evolution period is used, can be applied more efficiently.¹⁶⁵ With static samples there is the advantage that for certain motional models the extent of the motion can be determined directly from the spectrum. However, the attendant problems of poor sensitivity, especially with natural abundance ^{13}C , and resonance overlap restrict the usefulness of the method. Although in principle ultra slow motion can be studied using the three-pulse sequence, a major restriction is introduced by the possibility of spin diffusion. Indeed the experiment has been used to help assign resonances based on this spin diffusion.¹⁶⁶ If spin diffusion is slow, as is the case for ^{13}C , a mixing time of the order of 1–10 s can be used, enabling correspondingly slow motions to be studied. The longest mixing time which can be used depends on the rate of spin diffusion and hence the distance between the putatively exchanging sites. It is important to bear in mind that in any experiment using the three-pulse sequence there will be the problem of separating coherent magnetization transfer through an exchange process and

incoherent transfer through spin diffusion. This problem of distinguishing between spin diffusion and chemical exchange has been considered for the case of polarization transfer in crystalline meso tetratolylporphin— $^{15}\text{N}_4$.¹⁶⁷

When the two-dimensional exchange experiment is combined with slow MAS the possibility of studying the reorientation of chemically equivalent sites arises.¹⁶⁸ Care must be taken to ensure the mixing period is synchronized with the rotor period, otherwise a whole series of cross-peaks will be seen, which are unrelated to a reorientation of the molecule during the mixing period. The effect of a molecular reorientation is to give cross-peaks between the spinning sidebands in the two-dimensional spectrum. Information on the rate and type of motion is obtained by computer simulation of this spectrum. In the case of polyoxymethylene slow rotation of the helical chains over 200° has been detected in the crystalline phase.^{169,170} The main restrictions with this technique are its poor sensitivity and the complications of a complex spectrum, particularly if there is more than one set of exchange processes. A complementary technique which overcomes these problems is to use chemical shift scaling consisting of $(270_x, 270_{-x})_N$ during the first time domain. In this way the spinning sidebands are removed from the first dimension, improving the sensitivity and eliminating the need to synchronize with the rotor period.¹⁷¹ The disadvantages of this method are, first, that it is not suited for exchange between chemically equivalent but orientational inequivalent sites, and second, that it does not give relative orientations. The important feature of the slow MAS methods is to preserve the chemical shift tensor information under conditions of high sensitivity. An alternative way of achieving this is to use fast off-the-magic-angle spinning which gives scaled wide-line exchange spectra.¹⁷² For a sample such as isotactic polypropylene spectra can be obtained in 20 h using an angle of 70° .

The simple presence of slow motion can be demonstrated in a one-dimensional experiment.¹⁷³ For a fixed evolution period the spinning sidebands are suppressed using TOSS, then during a mixing period molecular motion occurs reintroducing spinning sidebands which are detected in the observation period. Phase cycling is required to obtain pure absorption mode spectra and preferably the mixing period should be an integral number of rotor periods. The beauty of this experiment is that because it detects slow molecular motion in a one-dimensional manner the motion can be correlated with some other feature by incorporating this pulse sequence into a two-dimensional experiment. A demonstration of this shown in Fig. 9 is the correlation of order and exchange in highly oriented polyethylene.^{174,175}



3.4. Chemical shift correlation

I shall consider the correlation of the chemical shift with the dipolar and quadrupolar interactions separately in the appropriate sections. Two-dimensional correlations of chemical shifts to establish spin connectivities are an important tool in modern solution NMR.¹⁷⁶ A parent of these techniques is the COSY pulse sequence,¹⁷⁷ which operates through the scalar coupling between nuclei. It is used principally for homonuclear ^1H spectra, though heteronuclear experiments are not unusual. Almost without exception it is true to say that to obtain homonuclear ^1H correlations in solids is not a realistic proposition, though this is not to dispute that certain pathologically narrow spectra could be found for which it might be feasible. Rather, the emphasis is on rare spin homonuclear^{178–181} and heteronuclear (^1H -X)^{182–185} experiments. With rare spin homonuclear correlations the major problem is sensitivity, a ^{29}Si COSY experiment on the silicate Q_8M_8 took 43 h,¹⁷⁸ mainly because too long a fixed delay was used. Initial work on a completely siliceous zeolite ZSM-39 used 80% ^{29}Si enrichment and took 23 h, even with optimization of the fixed delay for the real Si–O–Si coupling constants of around 10 Hz (Fig. 10).¹⁷⁹ Since then the experiment has been carried out at natural abundance for ^{29}Si in a zeolite ZSM-12¹⁸⁰ in a comparable time. Experiments at natural abundance for ^{13}C will be limited unless combined with techniques such as DNP.⁷⁵ On the other hand, ^{31}P should be more straightforward than ^{29}Si and yet there are few reports of ^{31}P COSY-type experiments.¹⁸¹ Heteronuclear experiments, essentially ^1H to an X nucleus, are complicated by the need for multiple-pulse decoupling of the protons. When the ^1H line is sufficiently narrowed by MAS the experiment is greatly simplified.¹⁸⁵ Unlike the solution case, heteronuclear correlations in solids do not rely on scalar coupling but instead use dipolar coupling during the transfer period. Early experiments on a single crystal demonstrated the feasibility of the technique¹⁸² which was subsequently extended to powders using MAS.^{183,184}

4. DIPOLE–DIPOLE COUPLING

Dipolar couplings are an important source of structural information because their magnitude is dependent upon the distance between the nuclear spins. This potential is not often realized because of the deleterious effects of dipolar

Fig. 9. Experimental and theoretical two-dimensional rotor synchronized TOSS MAS spectra of crystalline polyethylene. (a) Powdered sample with a zero mixing time and (b) with a mixing time of 12 s. (c) Highly oriented sample with a zero mixing time and (d) a synchronous mixing time of 12 s. (Reproduced with permission from Yang *et al.*¹⁷⁴)

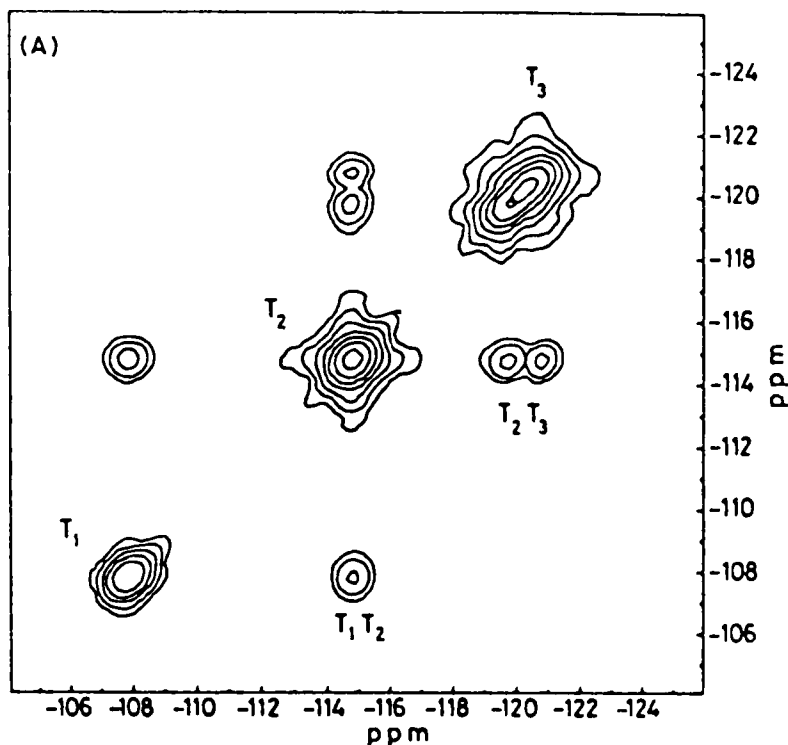


Fig. 10. ^{29}Si COSY NMR spectrum of zeolite ZSM-39. One hundred and twenty-eight experiments were performed with 64 transients each; 256 data points were used to define the FID. The fixed delay was 5 ms and a recycle delay of 10 s was used. The total experimental time was 23 h. (Reproduced with permission from Fyfe *et al.*¹⁷⁹)

couplings between many spins. For an isolated single spin pair the expected Pake doublet¹⁸⁶ can be easily analysed to give the dipolar coupling constant. However, as the number of interacting spins increases, so the lineshape tends to become featureless, and in the limit explored by van Vleck¹⁸⁷ it is only sensible to talk in terms of the moments of the lineshape. Under these circumstances the lineshape is gaussian to a good approximation. These arguments are not restricted to homonuclear dipole-dipole couplings, they apply equally to heteronuclear ones.

It is because of the severe line-broadening effects that the most common reaction to the presence of heteronuclear coupling is to remove it by the application of some decoupling scheme. This is particularly true if the dipolar broadening is obscuring the chemical shift or quadrupolar coupling information. The NMR spectra of static samples with significant dipolar broadening

have to be acquired using a solid echo technique¹⁸⁸ because of the short T_2 times and the dead time of the instrument. A windowless solid echo has been proposed as a way of preventing the spectral distortions caused by mis-setting of the pulse phases and amplitudes.¹⁸⁹

4.1. Removal of dipole–dipole coupling

When dealing with an inhomogeneous dipolar interaction the effects may be removed by magic-angle spinning, though in the case of ^1H – ^1H spin pairs quite extensive spinning sidebands can emerge because of the magnitude of the interaction. However, if the dipolar coupling is homogeneous, and in particular for coupling to ^1H , fast enough spinning is not possible and some sort of decoupling is necessary. The influence of homonuclear dipolar coupling on the residual linewidths in MAS spectra has been considered¹⁹⁰ and simulations of the MAS NMR spectra carried out using Floquet theory.¹⁹¹ Dipolar coupling can also be manifest in the NMR spectrum through line splittings as seen in the case of ^{31}P – ^{31}P dipolar coupling in sodium pyrophosphate.

We can divide decoupling methods into two classes: those aimed at removing all the dipolar coupling present and those which seek to remove the homonuclear coupling (I–I) whilst preserving the heteronuclear coupling (I–S). The motive for attempting to isolate the heteronuclear dipolar coupling from the homonuclear coupling is to simplify the spin system, ideally to a two or three spin system which will allow the dipolar coupling to be measured. Complete removal of dipolar coupling is invariably carried out using cw irradiation of the spin to be decoupled,^{192,193} while to retain the heteronuclear component pulse methods are applicable.

Various criteria need to be taken into consideration when examining the value of a decoupling scheme; in general, though, the requirement is to maximize the frequency range over which the decoupling occurs whilst minimizing the power used. This can be expressed as the residual linewidth for a given dipolar coupling, irradiation power and offset. These considerations have been presented for cw irradiation,^{194,195} where in essence a decoupling field ω_{11} must satisfy the condition

$$\omega_{11} \gg (M_2^{\text{I}})(M_2^{\text{S}})$$

entailing the use of a B_1 of > 25 kHz for ^1H irradiation. A more detailed examination of the off-resonance intermediate decoupling case where $\omega_1 = (M_2^{\text{I}})(M_2^{\text{S}})$ has revealed that not only does broadening occur but also a line splitting and frequency shift.¹⁹⁶ Off-resonance decoupling has also been reconsidered¹⁹⁷ from the point of view of correlating directly bonded ^{13}C – ^1H

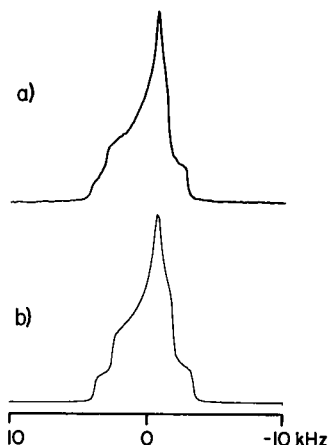


Fig. 11. An illustration of the complex lineshape resulting when the dipolar coupling ($D = 1.3$ kHz) and chemical shift tensor ($\delta = 3.2$ kHz, $\eta = 0.3$) are of the same magnitude: (a) corresponds to the observed lineshape and (b) the calculated one. The sample was 4- ^{13}C -amide- ^{15}N -asparagine. (Reproduced with permission from Munowitz *et al.*¹⁹⁸)

spin pairs in an organic solid containing chemically shifted proton resonances. Decoupling was found to be most effective for any given carbon type by irradiating exactly on resonance for the proton associated with that carbon type.

Once the dipolar coupling to an abundant spin is removed, residual dipolar coupling between other nuclei can be observed. In the case of specially enriched samples these may correspond to ^{13}C and ^{15}N spin pairs, or at natural abundance ^{13}C and ^{31}P .¹⁹⁸ Normally, the much smaller dipolar couplings are now of the same order of magnitude as the chemical shift anisotropy leading to complex powder lineshapes as demonstrated by Fig. 11. These can be simulated giving information not only on the magnitude of the tensors but also on their relative orientation.

Multiple-pulse decoupling is described in detail in a number of texts.^{17,19,199} The main multiple-pulse sequences are WAHUA,²⁰⁰ MREV-8,^{201,202} BR-24, BR-48²⁰³ and BR-52.²⁰⁴ A few new multiple-pulse sequences for homonuclear decoupling have been proposed for solid state NMR over the last ten years. These are the windowless pulse sequences such as BLEW-12 and BLEW-48,²⁰⁵ where excellent decoupling can be obtained at low power levels, TREV-8²⁰⁶ based on a "magic echo" sequence in which the time evolution of the homonuclear dipolar coupling is reversed,²⁰⁷ ALPHA-3²⁰⁸ and COMARO.²⁰⁹ For static solids the COMARO (composite magic-angle rotation) sequence was less sensitive to off-resonance effects than cw decoupling and gave good

decoupling with a relatively low rf power.²¹⁰ However, because the pulse cycle time is of the same order as a rotor period the sequence was much less efficient under MAS. Better performances are to be expected if the pulse sequence is designed taking MAS into account. Problems can be experienced in decoupling using either cw or multiple-pulse methods when the sample has a large ^1H linewidth caused by paramagnetic centres. In these circumstances it has been found that composite pulse decoupling, COMARO-2 and ALPHA-3 may be of some benefit.²¹¹

By combining MAS with a homonuclear decoupling pulse sequence it is possible to obtain spectra showing the X-H(F) scalar coupling.²¹²⁻²¹⁵ This can then be used for spectral editing in a manner analogous to solution NMR. A potential problem, namely spinning sidebands arising from the heteronuclear dipolar coupling, does not affect the spectral editing-type experiments because the scalar coupling is only used to label the multiplets in a fixed evolution period, while the detection is carried out under heteronuclear decoupling. These types of experiments, as illustrated by the SEMUT sequence,^{216,217} have typically been applied to what can be called soft samples such as camphor, adamantane and hexamethylbenzene, where the dipolar couplings are reduced by molecular motion and hence the conditions on the multiple-pulse decoupling are less stringent. For more rigid samples the conditions on the multiple-pulse decoupling, for achieving the required resolution of the scalar coupling multiplets, are harder to meet. As a consequence, spectral editing based on homonuclear decoupling is rarely used.

Predating the multiple-pulse methods for homonuclear decoupling is off-resonance coherent averaging where an offset is chosen such that the effective field satisfies the magic-angle condition, the Lee-Goldburg condition.²¹⁸ The drawback to this method is that it is difficult to satisfy the condition over the entire resonance, especially by the one-sided nature of the irradiation. Improved Lee-Goldburg decoupling can be achieved by the rapid switching of the rf carrier to opposite sides of the resonance with a synchronous π rf phase shift.²¹⁹

4.2. Reintroduction of dipole-dipole coupling

Four different classes of experiments have been proposed to reintroduce dipolar couplings into the NMR spectrum:

- (1) Homonuclear decoupling
- (2) Modulation through π pulses
- (3) Rotational resonance
- (4) Weak cw irradiation

4.2.1. *Homonuclear decoupling methods*

A variety of methods have been proposed for studying heteronuclear dipolar coupling, almost all involving multiple-phase sequences to remove the homonuclear contribution. Three considerations are important: (a) the multiple-pulse sequence to be used, (b) whether sample rotation is required, and (c) is a separation of the chemical shift and dipolar interactions necessary? The choice of multiple-pulse sequence is based on the balance between complexity and effectiveness; the standard sequence is MREV-8. From the point of view of sample rotation a number of possibilities exist; these include the use of static samples, a combination of fast or slow MAS, slow spinning off-the-magic-angle spinning and switched-angle sample spinning. A separation of the chemical shift and dipolar contributions is usually achieved using a two-dimensional experiment.

Experiments were first performed in a two-dimensional manner on a single crystal to give so-called separated local field spectra.²²⁰ Under favourable circumstances homonuclear decoupling was unnecessary to observe the heteronuclear dipolar oscillations.²²¹ The initial experiments on powders did not involve a second transform, the dipolar oscillations were examined in the time domain,^{222,244} and only later was the experiment carried out as a two-dimensional one.²²³ Such experiments give complicated spectra for powdered samples with many overlapping resonance powder patterns and, perhaps more importantly, have a poor signal-to-noise ratio.

As we have seen with the chemical shift interaction, MAS greatly improves the resolution and sensitivity of solid state NMR by concentrating the spectral intensity into a few narrow resonances. It is therefore logical to combine the separated local field experiment with MAS. In a one-dimensional MAS experiment the spinning sidebands are determined by both the chemical shift and dipolar coupling, making it difficult to extract the two tensors separately. An example of the interaction between the chemical shift, dipolar and scalar (J) tensors in the spinning sideband pattern is provided by the spectra of phosphonium iodide.²²⁴ A straightforward way to overcome this difficulty is to use a two-dimensional experiment whereby the spin system is allowed to evolve in the first time period under the influence of the heteronuclear dipolar coupling and in the second the evolution is determined only by the chemical shift interaction.^{225,226} Both multiple-pulse methods²²⁵ and off-resonance cw decoupling²²⁷ have been used to homonuclear decouple. Subsequent to the initial work a modified pulse sequence was proposed involving time reversal effects to extend the period during which the dipolar coupling is present.²²⁸ To remove the chemical shift evolution from the first time domain a refocusing π pulse is necessary which must be placed an integral number of rotor periods into the t_1 evolution. This places a constraint

on the overall t_1 evolution with the consequence that signal is lost through relaxation processes. The two major uses of this technique have been to measure bond lengths¹²⁶ and to study molecular motion.²²⁹ A simplification of the experimental spectrum can be made by eliminating the chemical shift anisotropy using chemical shift scaling and by sampling the magnetization decay only once per rotational period.²³⁰ Although most separated local field experiments are carried out using high-power decoupling, the experiment has been carried out using the BLEW-12 pulse sequence with a B_1 field giving a $\pi/2$ pulse of 5.1 ms.²³¹

In fact, it is not necessary to separate the dipolar and chemical shift evolution in the acquisition of the two-dimensional NMR spectrum.²³² Using a pulse sequence similar to the earlier ones but lacking the refocusing pulse a two-dimensional spectrum has been obtained which is related to the pure dipolar/chemical shift spectrum by a shearing transformation. Although a pure phase spectrum cannot be obtained, it is possible to suppress the phase twist by locally projecting along one axis before shearing. By obviating the need for a long fixed evolution period the signal intensity in the resulting spectrum is greatly enhanced. A similar procedure has been carried out in the fast spinning limit by applying an MREV-8 pulse sequence asynchronously with the sample spinning. In this case the phase twist problem was overcome by projecting the evolution during t_1 onto a single axis in the rotating frame by applying a pair of 90° pulses separated by a period of no decoupling.²³³ Furthermore, by working in the fast spinning limit for the chemical shift anisotropy the resulting spinning sidebands in the ω_1 dimension only result from the dipolar coupling. The authors use these spinning side patterns to assign the carbon type based on the numbers of attached protons, since the structural groups CH_n give distinctive dipolar patterns (Fig. 12). With slower spinning the dipolar patterns will show a contribution from the chemical shift, distorting the simple interpretation; even so spinning at 3 kHz at a field of 2.35 T is satisfactory.

Slow off-the-magic-angle spinning has been shown to give powder-like patterns for the spinning sidebands.^{131,321} When combined with homonuclear decoupling using an MREV-8 pulse sequence, distinctive centre patterns are seen which depend on the values of the chemical shift and dipolar tensors²³⁴ together with their mutual orientation. This, combined with the fact that it is a one-dimensional experiment, provides a particular advantage for this technique. One disadvantage, though, is that given the number of parameters which are required to define the central pattern it is not clear how easily the spectrum can be fitted. In mitigation of this the chemical shift tensor components can be found using a separate experiment leaving only four parameters: the mutual orientation, dipolar coupling constant and spinning angle. The experiment can also give the absolute sign of the one-bond scalar

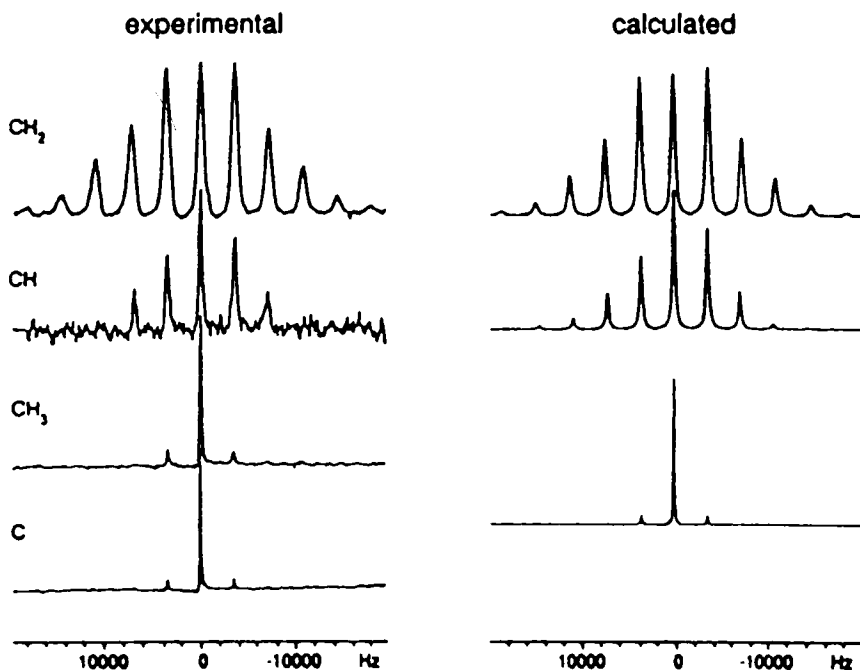


Fig. 12. Dipolar spinning sidebands resulting from fast spinning with asynchronous MREV-8 decoupling. The CH₂ pattern is from paraformaldehyde, the others are for dimethoxybenzene. Simulations based on standard dipolar and CSA tensors are shown for comparison. (Reproduced with permission from G.C. Webb and K.W. Zilm, *J. Am. Chem. Soc.*, 1989, **111**, 2455. Copyright (1989) American Chemical Society.)

coupling. Just as in the case of magic-angle spinning, the convolution of the chemical shift and dipolar interactions complicates the data interpretation. One answer to this which has been proposed is to use switched angle sample spinning (SASS)^{235,236} in conjunction with homonuclear decoupling, whereby the spinning axis is changed between the different time periods. One advantage of the off-angle method, which gives scaled powder patterns, is that it can be used in circumstances where the spinning sidebands are of low intensity by virtue of the small dipolar coupling or because of the need to spin fast to avoid resonance overlap. When the detection is at the magic angle we have the dipolar switched-angle spinning,²³⁵ while if both time periods are at the magic angle the experiment is simply a 2D-J resolved. In the general form where both angles are variable and not at the magic angle,²³⁶ scaled powder patterns are observed in both dimensions.²³⁷ Data analysis is computationally demanding but can be simplified by the use of look-up tables. In order to

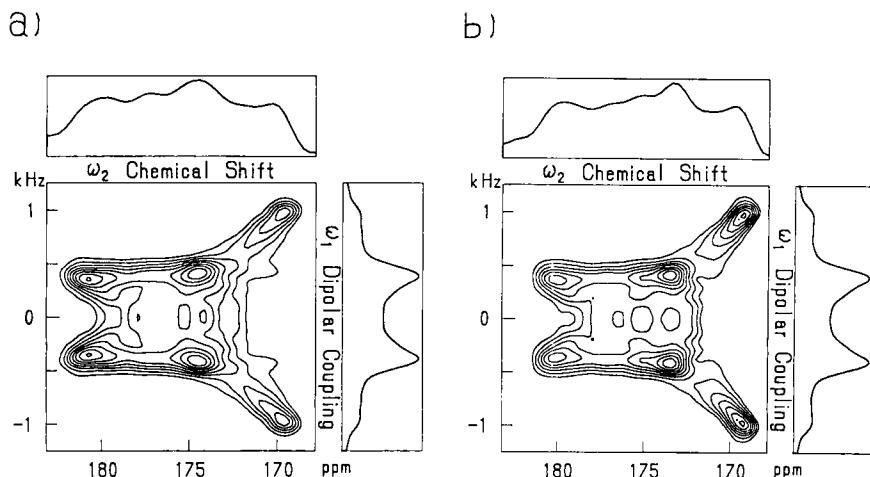


Fig. 13. Two-dimensional chemical shift/dipolar powder pattern of calcium formate obtained using off-magic-angle spinning and MREV-8 decoupling. (Reproduced with permission from Nakai *et al.*²³⁶)

obtain the proper bandwidth for the spectra it is necessary to adjust the scaling factors through the angle of the spinning axis. A typical spectrum is shown in Fig. 13. This method has been used to determine the ^{13}C chemical shift tensors in isotactic polypropylene.²³⁸ Probably the most severe restriction on this method is the need for a specialized probe.

A common feature of all the multiple-pulse homonuclear decoupling methods is that the scaling factor must be known. Generally this requires a calibration before and after the experiment of interest.

4.2.2. Modulation through π pulses

When the dipole–dipole coupling is small it is often either obscured as in the static powder pattern or averaged to zero as in a magic-angle spinning spectrum. The case most often come across is that of an S–X dipolar coupling such as ^{13}C – ^{15}N . A powerful method for establishing the presence of dipolar coupling under these circumstances is to use the effect of a π pulse on one member of the spin pair whilst observing the signal from the other. These experiments have generally been carried out for isolated heteronuclear spin pairs which may or may not be in a bath of an abundant spin. However, it is not entirely necessary that the spins be isolated, as an early example of a Cu–Co alloy shows.²³⁹ The key feature of the experiment is to use the echo modulation caused by π pulses either in a two-dimensional experiment or in a difference spectrum between two echo pulse sequences. To illustrate the

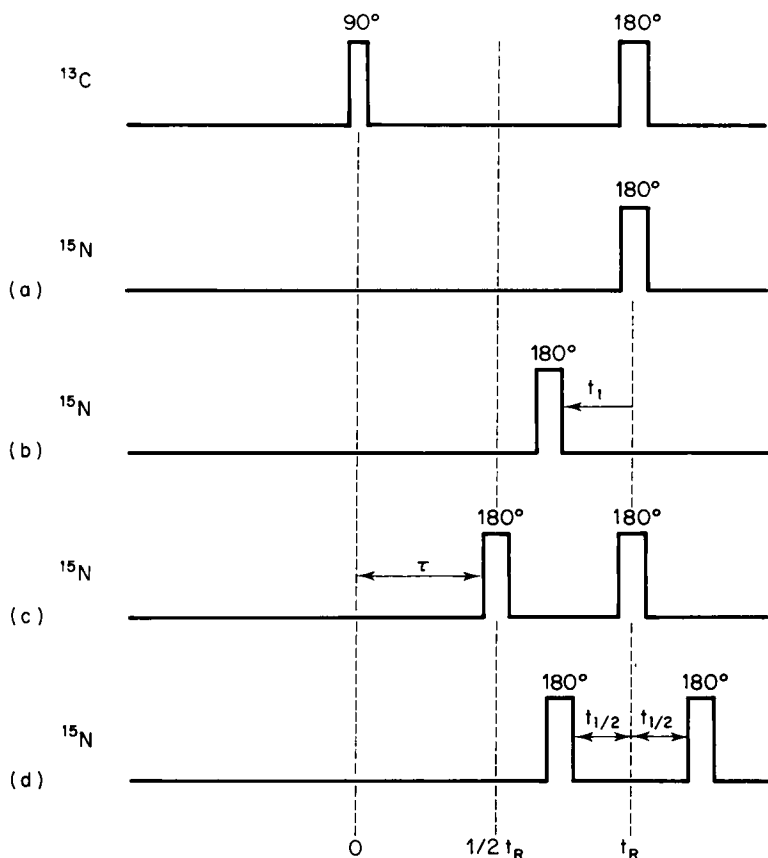


Fig. 14. Comparison of different pulse sequences proposed to study dipolar couplings. (a) Simple spin echo, (b) off-centre spin echo, in the two-dimensional form t_1 is incremented, (c) REDOR, (d) XDM a two-dimensional form of the REDOR experiment.

method I will take as an example the difference variant with the most common spin pair ^{13}C and ^{15}N . Referring to Fig. 14, in both pulse sequences the ^{13}C signal is observed, during the first echo sequence the echo is allowed to form without irradiation of the ^{15}N whilst in the second echo sequence a π pulse is applied to the ^{15}N midway through the evolution of the echo. As a consequence, the ^{13}C - ^{15}N dipolar contribution to the evolution of the ^{13}C is reversed in sign and the refocusing will be incomplete. By taking the difference spectrum between these two spectra the contribution of the dipolar coupling to the spectrum can be obtained. Clearly if the dipolar coupling is

zero then the difference spectrum will have zero intensity, and if the echo evolution is purely dipolar—the normal case for ^{13}C because of the refocusing of the chemical shift evolution—then the difference spectrum can have up to twice the intensity of the individual spectra. This spin-echo double-resonance (SEDOR) experiment has been used to establish the presence of C–O spin pairs on a Pt catalyst.^{240,241}

Starting from this basic experiment a number of modifications have been made; the relationship between these is illustrated in Fig. 14. One significant difference between the types of experiment is the use of a constant or variable dipolar evolution time. If a constant evolution time is used the detection can be optimized for a particular dipolar coupling, with the experiment being used as a filter, whilst if a variable evolution time is used then the experiment becomes a two-dimensional one. With all these pulse sequences the smallest detectable dipolar coupling is determined by the spin–spin relaxation time because the smaller the dipolar coupling the longer the evolution period that is necessary in order to build up a detectable phase difference before the magnetization has decayed. Taking the two filtering sequences first, perhaps the simplest change is to allow the ^{15}N pulse to be offset from the refocusing ^{13}C π pulse.^{242,243} For this experiment the authors estimated that given a T_2 of 1 ms the smallest detectable dipolar coupling was 100 Hz. Such a dipolar coupling should be compared with a maximum value of 2.6 kHz for an amide ^{13}C – ^{15}N . Various pulse sequences have been proposed, similar to those discussed here, to look at ^{13}C – ^{15}N dipolar couplings in single crystals and oriented samples.²⁴⁵

To extend this experiment to rotating solids an additional π pulse on the ^{15}N channel is necessary part way through the rotor period to reverse the dipolar evolution. The reason for this is because halfway during the rotor period the sign of the dipolar evolution changes in any case, as indeed must be the case if the MAS rotational echo is not to show a dipolar phase accumulation. A second ^{15}N π pulse is then applied synchronously with the rotor period, giving the rotational-echo double-resonance (REDOR) pulse sequence.²⁴⁶ Again, the dipolar coupled resonances are seen in the difference spectrum while the dipolar couplings can be found from the ratio of the spectral intensities in the REDOR difference spectrum to that of the full echo. In the limit of a long evolution time this ratio will tend to unity and clearly to measure the dipolar coupling an intermediate evolution time is required. To maximize the intensities in the REDOR experiment it is necessary to optimize the pulse location and the number of pulses. Thus, with slow spinning the greatest dephasing is seen for the P-7 sequence where the first pulse is applied one-seventh through the rotor period, but with fast spinning the P-2 sequence is to be preferred.

In view of this it is not surprising that the REDOR spectrum must be

computer-simulated before the intensities can be interpreted. This was carried out using the magnetization vector model.¹⁴⁵ A comparison with double cross-polarization⁷⁹ suggested the REDOR experiment was superior because it does not depend on the ^1H - ^1H spin flips which are difficult to interpret. In practical cases when the concentration of the ^{13}C label is small compared with the concentration of the ^{13}C from the natural abundance background, measurement of the full echo for the ^{13}C label alone can be difficult and for these cases a triple-resonance experiment has been proposed which uses a third spin to distinguish the label signal from the background.²⁴⁷

When the dipolar coupling is unknown or the ^{13}C resonances have different coupling constants then a two-dimensional experiment must be used. In the case of the MAS experiment, two modifications to the filtering pulse sequence have been suggested: the first is to use a pair of π pulses equally offset from the centre of the rotor period and then to increment the offset, giving the extended dipolar modulation two-pulse sequence XDM-R2.²⁴⁸ The second modification is to apply ^{15}N decoupling symmetrically over the two rotor intervals.²⁴⁹ In this case further differentiation is possible depending on whether a second π pulse is applied after one rotor period to the ^{15}N ; if only the ^{13}C π pulse is used this is called odd dipolar rotational spin-echo (ODRSE), while if both are used then it is even dipolar rotational spin-echo (EDRSE).

In both the XDM-R2 and ODRSE experiments the effective spinning speed shown in the dipolar spinning sidebands in the ω_1 dimension is half the actual speed, while the EDRSE spinning sidebands are at the actual spinning speed. Despite both the ODRSE and XDM-R2 having the same sideband spacing, the intensities are different because the ^{13}C - ^{15}N dipolar phase accumulation is twice as large in the XDM-R2 experiment. Thus if the XDM-R2 experiment is performed at twice the spinning speed of the ODRSE, then identical intensity dipolar spinning sideband patterns would result, differing only in absolute spacing. Data analysis is straightforward and similar for all the experiments. Since this experiment involves MAS it necessarily suffers from the problem that quite slow spinning might be necessary to get significant sideband intensity when the dipolar coupling is small. However, by analogy with the use of π pulses to suppress the chemical shift evolution it is possible to further extend the dipolar modulation by using more π pulses when pairs of π pulses are being used. Hence with six π pulses overall and four rotor periods (XDM-R4) the effective spinning speed is a quarter of the true speed. It is not possible, though, to extend the ODRSE experiment. In effect we can enhance the spinning sidebands from a small dipolar coupling. As will be apparent by now Nature gives with one hand and takes away with the other; the cost of enhancing the dipolar modulation is to lengthen the evolution time, making T_2 relaxation a severe constraint.

4.2.3. Rotational resonance

Early in the history of magic-angle spinning it was observed that cross-relaxation could occur when the spinning sideband of one resonance overlapped the isotropic resonance of another.^{250,251} Quite simply the rotational resonance condition is that

$$\Delta = n\omega_r$$

where Δ is the difference in chemical shift of the cross-relaxing resonances and ω_r is the spinning speed. This places some restrictions on the samples for which the method is applicable. For example, in ^{13}C NMR rotational resonance is feasible between the classes of aliphatic, aromatic and carbonyl but not really within these classes. Rotational resonance affects both the lineshape²⁵² and the rate of spin diffusion. Experiments have been carried out at natural abundance for ^{13}C ^{253,254} and using enriched samples.²⁵⁵

More recently this effect has been exploited as a method for determining internuclear distances.²⁵⁶ The methodology for measuring distances is first to invert selectively one of the isotropic resonances, then allow the spins to evolve for a time τ_m followed by a non-selective $\pi/2$ pulse to read the magnetizations. Initially there will be a large population difference which will decay to zero as a function of the evolution time. This decay has to be modelled theoretically, for which the chemical shift tensors, dipolar coupling (hence the distance), zero quantum T_2 and the mutual orientation of the dipolar and chemical shift tensor must all be known. Uncertainty about the zero quantum T_2 was thought to restrict the accuracy of the distance measurement. For rare spins at natural abundance the value of the experiment for examining connectivities is unclear because the statistics of the distribution of the rare spin will dominate. A detailed theoretical analysis of rotational resonance and simulations for homonuclear spin pair systems have been presented.²⁵⁷

4.2.4. Weak cw irradiation

A feature of MAS is that it is effective at removing weak dipolar couplings from the spectrum, their presence only being felt through minor perturbations in the intensities of the spinning sidebands. However, it has been shown that by irradiating one spin of a heteronuclear spin pair with a weak continuous rf field it is possible to reintroduce some heteronuclear dipolar couplings into the spectrum.²⁵⁸⁻²⁶⁰ In order to achieve this effect the irradiation frequency must be matched to the rotation frequency

$$\omega_{\text{ll}} = n\omega_r$$

The theory behind this effect has been considered²⁶⁰ but the rough explanation given is that the rotation of the spin states by the rf irradiation at the

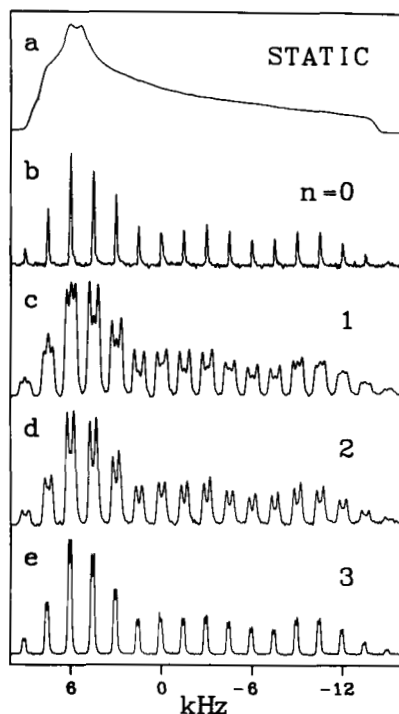


Fig. 15. Spectra showing the effect of weak cw irradiation, recoupling the ^{31}P - ^{15}N dipolar coupling removed by MAS. (a) Static ^{31}P NMR spectrum of polycrystalline ^{15}N -methyl diphenylphosphoramidate. (b) MAS spectrum with $\omega_r = 1.5$ kHz. (c-e) With rf irradiation fulfilling the rotary resonance conditions. (Reproduced with permission from Oas *et al.*²⁵⁸)

same frequency as the spinning causes the spin density to evolve much as though the sample was static. Simulations of the effect show that it can lead to line splitting or simply line-broadening with the most useful changes seen for the lower n as shown in Fig. 15. Although only the example of ^{31}P and ^{15}N was given, the effect should be more widely applicable. In practical terms since the dipolar couplings reintroduced will depend on those originally present it is apparent that for smaller dipolar couplings the actual lineshape changes may be too small to be identified, particularly if the intrinsic linewidth is large.

4.3. Nutation spectroscopy

In the nutation experiment the dipolar spectrum can be obtained free of the

chemical shift tensor. It involves a forced precession of the magnetization caused by a train of rf pulses. The signal is observed in the windows of the pulse train^{261,262} and gives a Pake doublet with a splitting reduced by a factor of 2. Such a reduction in the splitting is a disadvantage when more than one bond length is present because of the overlap of the Pake patterns. An alternative²⁶³ is to use a Carr-Purcell pulse train.²⁶⁴ Although the homonuclear dipolar coupling is again scaled, to an extent dependent upon the duty cycle, it is not as severe as in the nutation experiment. However, because of the duty cycle dependence the experiment must be carried out as a function of the duty cycle and the dipolar splitting found by extrapolating back to a zero duty cycle.

4.4. Spin diffusion

Spin diffusion is the transport of magnetization between nuclear spins in a lattice through energy-conserving spin flips. These spin flips involve the flip-flop terms in the dipole-dipole Hamiltonian, $I_{\pm} \cdot I_{\mp}$. The idea of spin diffusion was first proposed to explain how paramagnetic centres could help in nuclear spin-lattice relaxation.²⁶⁵ Two types of spin diffusion can be identified:²⁶⁶ spectral spin diffusion which consists of the diffusion of spin order in frequency space and spatial spin diffusion between equivalent spins which are spatially separated. The utility of spin diffusion rests on its dependence on the dipolar coupling and hence the internuclear distances. From a knowledge of the spin-diffusion time constant it is possible to measure these distances. When the diffusion takes place between different domains in a heterogeneous solid the domain size can be estimated given a model for the diffusion process. Natural abundance ^{13}C spin diffusion has been considered in detail, and when dealing with rare spins it is more correct to talk in terms of spin exchange rather than a true diffusion process because of the relative isolation of the spins.²⁶⁷

Simultaneous spin flips are only energy-conserving when the transition frequencies of the flip-flop processes are degenerate. When this condition is met the rate of spin diffusion is given by:²⁶⁸

$$W = 0.5\pi\omega_D^2 F(0)$$

where ω_D is the dipolar coupling and $F(0)$ the probability the single quantum transitions occur at identical frequencies. The latter term arises because in practice all resonance lineshapes are broadened either by coupling to other spins or because of a distribution in chemical shifts. Consequently, even for equivalent spins the likelihood of the flip-flop transition being energy-conserving is reduced by this joint probability distribution. More usually the

intrinsic resonance frequencies are not the same to begin with and an additional energy source must be provided to conserve the flip-flop transition energy. This is particularly true for spectral spin diffusion, where high-resolution techniques are required to observe the different resonance frequencies. For materials containing an abundant spin this is normally provided by coupling to the abundant spins; now the broadening which in the case of equivalent spins decreases the flip-flop rate acts to enhance the spin diffusion.²⁶⁹

Two other ways of conserving the transition energies are rotational resonance or rotor-driven diffusion, where the mechanical energy of the spinning is the source²⁵²⁻²⁵⁵ and rf-driven diffusion where a weak rf field supplies the energy difference.²⁷⁰ If the spectral spin-diffusion constant is to be used to measure internuclear distances it is necessary that the theoretical value can be calculated. This has been addressed by three groups, with the spin-diffusion rate constant given as a function of the difference in frequency between two resolved resonance lines.^{266,271-273} Kubo and McDowell²⁶⁶ compared the two earlier methods with the results of a third derivation and showed them to be equivalent but appertaining under different approximations. Experimentally, magic-angle spinning has been shown not to quench spin diffusion,^{274,275} however, the rate of spin diffusion does decline with spinning speed unless a rotational resonance condition is met.²⁷⁶ An illustration of the gradual quenching of the flip-flop term is the sharpening observed in the spectra of some pyrophosphates as the spinning speed increases.²⁷⁷

In a general sense spin diffusion can be studied using the two-dimensional chemical exchange pulse sequence,²⁷⁸ though this may not be the most efficient way if the diffusion pathways are limited, as with rotor-driven diffusion. If a two-dimensional experiment is not used then selective inversion or saturation of one of the resonance lines would appear to be necessary. This can be avoided by using a one-dimensional analogue of the two-dimensional experiment where the evolution period is fixed.¹⁶⁵ Selective excitation can be carried out in the solid state using DANTE pulse sequences just as in solution.^{279,280,488} The pulse sequence can be synchronized with the rotor period in MAS, in which case it has the effect of inverting all the spinning sidebands. However, it can be run asynchronously to give the excitation sidebands well outside the spectrum of interest. This has led to some contradictory statements in the use of DANTE pulse sequences in rotor-driven spin diffusion: on the one hand, the DANTE sequence was found to be compatible,²⁵³ while on the other hand, it was thought to be incompatible because of the requirement for the peaks to be separated by an integral multiple of the rotor frequency and instead a soft π pulse was used for selective inversion.²⁵² To achieve selective excitation in the ^1H NMR spectrum of a rigid solid there is the added complication of combining the DANTE-type pulse train with the

multiple-pulse sequences. This has been implemented for MREV-8 by alternating lengthened and shortened final pulses in the multiple-pulse cycle.²⁸¹ ^{13}C Spectral spin diffusion has principally been used to study connectivities,^{282,283} including the study of heterogeneity in polymer blends,²⁸⁴ while ^1H spectral spin diffusion has been used to study polymer blends in a two-dimensional experiment with homo-decoupling²⁸⁵ and by selective excitation.²⁸¹ Indirect detection involving the labelling of the ^1H spin states by the J -coupling in a J -resolved CPMAS NMR spectrum is also possible.²⁸⁶ Selective spin exchange can be arranged by combining the spin-diffusion experiment with a protonated nucleus selection interval.²⁸⁷

Spatial spin diffusion finds its greatest use in the study of the phase structure of heterogeneous materials, in particular polymers. At the qualitative level the averaging of nuclear spin relaxation times by spin diffusion can be used to place lower limits on the domain sizes.^{288,289} Quantitative information on domain sizes can be obtained by monitoring spin diffusion along a magnetization gradient generated in Goldman–Shen-type pulse sequences.²⁹⁰ A simple modification to the basic Goldman–Shen which overcomes the T_1 effect is to cycle the phase of the second pulse by 180° .^{291,292} Once the spin diffusion has been measured then the process must be modelled.^{293–296} Although the Goldman–Shen pulse sequence is useful, it is restricted to phases with different T_2 . Since many polymer blends do not show readily accessible T_2 differences but do have different $T_{1\rho}$, an extension to such cases would be invaluable.

An analogous experiment can be carried out involving spin-locking, but the spin-locking must be carried out at the magic angle to suppress spin diffusion which would otherwise occur.²⁹⁷ Other alternatives are to use the multiple-phase relaxation time T_{1xz} which eliminates spin-diffusion averaging of the relaxation time,²⁹⁵ and to detect during a dipolar narrowed Carr–Purcell sequence.²⁹³ New strategies for observing the high-resolution rare spin, or abundant spin NMR spectrum as a method of monitoring spin diffusion have been considered. These offer the prospect of a more detailed examination of heterogeneity in polymeric materials.^{298,299}

5. QUADRUPOLE COUPLING

In common with the dipolar and chemical shift interactions, the treatment of systems containing quadrupolar couplings consists of their removal, reintroduction and correlation. For the purposes of examining the various techniques involving quadrupolar nuclei it is helpful to distinguish between the integral and half-integral spins. Half-integer spins possess a central $\frac{1}{2} \rightarrow -\frac{1}{2}$ transition which is unaffected to first order by the quadrupolar

interaction, whereas for integer spins all transitions are affected. This means that for integer spins it is difficult to completely remove the quadrupolar contribution in order to see the chemical shift inequivalence, except when the nucleus is in a high-symmetry site. Even for half-integer spins the magnitude of the typical quadrupole coupling constants is often sufficient to give a significant second-order interaction obscuring the chemical shift information, requiring a simulation of the powder lineshape using both the quadrupolar and chemical shift terms³⁰⁰ as illustrated by ^{133}Cs in Cs_2CrO_4 .

In view of these problems it is rather surprising that the quadrupole parameters have not been more widely used as a structural tool. A major reason for this is that the NMR frequency is only dependent to second order on the quadrupole coupling constants, and consequently there is the tendency for all the resonances from different sites to overlap. High-field NMR does, however, offer the possibility of measuring the quadrupole parameters at a much higher sensitivity than pure NQR. One of the most important uses of the quadrupolar couplings in the NMR spectrum is, in fact, in the passive sense encountered in ^2H NMR studies of molecular dynamics. Here the important feature is that the quadrupolar tensor acts as an indicator of the motion of the $\text{X}-(^2\text{H})$ fragment. Finally, there is the possibility of correlating the quadrupolar parameters of different sites with their chemical shifts or dipolar couplings. Thus for a chemical shift correlation one can envisage a two-dimensional experiment involving the use of double axis rotation³⁰¹ in one dimension to remove the quadrupole interaction combined with magic-angle averaging in the second providing the relationship between the chemical shifts and the quadrupole couplings. As with the spin- $\frac{1}{2}$ nuclei cross-polarization can be used to enhance the signal intensity for both integral, ^{14}N ,³⁰² and half-integral, ^{23}Na ,³⁰³ ^{27}Al ,³⁰⁴ ^{17}O ³⁰⁵ nuclei. In the case of ^{23}Na the theory of cross-polarization to the $\frac{1}{2} \rightarrow -\frac{1}{2}$ transition was considered and the effect of cross-relaxation within the quadrupolar energy states.³⁰³

5.1. Quadrupolar effects on spin- $\frac{1}{2}$ nuclei

In a number of cases of spin- $\frac{1}{2}$ nuclei in close proximity to a quadrupolar nucleus asymmetric lineshapes or distorted scalar coupling multiplet structures are seen. Examples are $^{13}\text{C}-^{14}\text{N}$,³⁰⁶ $^{31}\text{P}-^{63}\text{Cu}$,³⁰⁷ $^{119}\text{Sn}-^{35}\text{Cl}$,^{308,309} and $^{75}\text{As}-^{13}\text{C}$.³¹⁰ Qualitatively, the explanation is straightforward:³¹¹ when the quadrupole coupling constant is large in comparison to the Larmor frequency of the quadrupolar nucleus then the dipolar interaction is no longer quantized along the Zeeman field direction and magic-angle spinning can no longer remove the dipolar coupling between the spin- $\frac{1}{2}$ nucleus and the

quadrupolar one. On the whole the reduction in resolution in the spin- $\frac{1}{2}$ spectrum has been treated as a nuisance to be avoided by working at higher magnetic field. In the spirit of trying to measure the quadrupole parameters the question arises can we use the effect in the spin- $\frac{1}{2}$ spectrum to do just this? On the one hand, a rigorous treatment of the ^{13}C - ^{14}N case involving the matrix diagonalization of the ^{14}N spin states has been presented,³¹¹ while on the other hand, a first-order perturbation theory has also been proposed.³¹² The latter is simpler to use and has been extended to ^2H ,³¹³ two directly bonded ^{14}N ,³¹⁴ and to the Sn-Cl and P-Cu cases.³¹⁵ However, in both cases the goal of working back to the quadrupole coupling constant is thwarted by the other unknowns such as the scalar coupling tensor or the internuclear distance. Consequently it is more appropriate to use the quadrupolar effect on the spin- $\frac{1}{2}$ spectrum to estimate, for example, the scalar coupling anisotropy using a quadrupolar coupling constant found by another method than vice versa. The question of self-decoupling of the ^{14}N in the ^{13}C CPMAS NMR spectrum has been considered.^{316,317}

5.2. Reduction and removal

For half-integer spins as noted above, the central $\frac{1}{2} \rightarrow -\frac{1}{2}$ transition is independent to first order of the quadrupolar interaction. However, to obtain accurate chemical shifts it is necessary to take into account the frequency shift caused by the second-order interaction.^{318,319} When the second-order term is negligible, MAS is effective at averaging the quadrupole interaction of the satellite transitions and, as with the chemical shift tensor, spinning sidebands will generally be visible. As the quadrupole coupling constant increases so the sidebands will be spread over a wider frequency range and correspondingly harder to see. This will be compounded by the greater sensitivity to the precise setting of the magic angle. From the intensities of the spinning sidebands it is possible to determine the quadrupolar parameters as shown for ^{27}Al and ^{23}Na ³²⁰ (see Fig. 16). In fact the quadrupole coupling constant is sufficiently small for ^2H ($< 300\text{ kHz}$) to allow narrow spinning sidebands to be seen, the intensities of which may be used in a similar manner to find the quadrupolar parameters.^{321,322} As the quadrupolar interaction increases, so the spectral width becomes such that only the central transition is excited. In addition the second-order term in the quadrupole interaction now causes the central transition to become asymmetric as illustrated by Fig. 17.^{323,324} Far too often this is seen as a drawback, whereas the limited reintroduction of the quadrupolar interaction means that the quadrupolar parameters can be measured by simulation of the lineshape.^{325,326} In order to get clear resolution

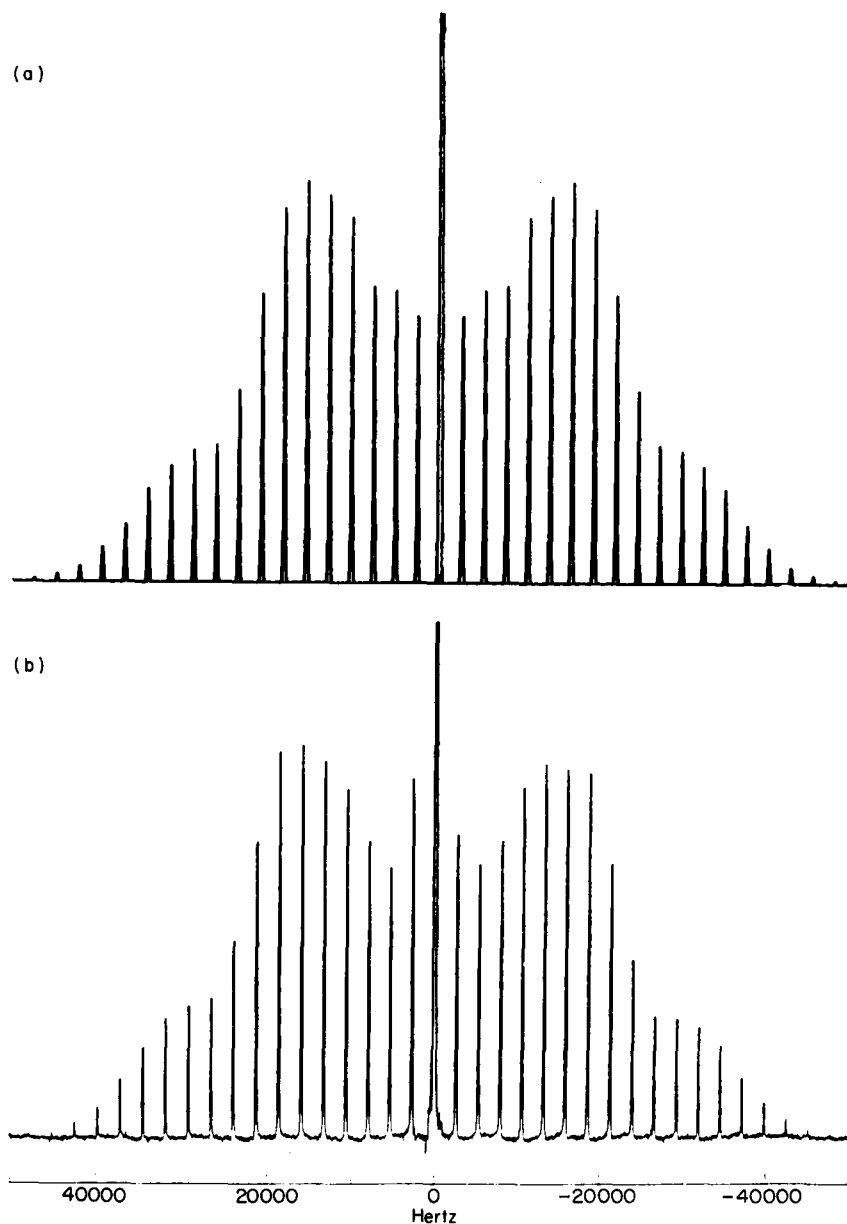


Fig. 16. ^7Li MAS NMR spectrum of a lithium complex illustrating the spinning sidebands arising from the quadrupolar coupling. The simulated spectrum was calculated using $\omega_q = 80.8$ kHz and $\eta = 0.29$.

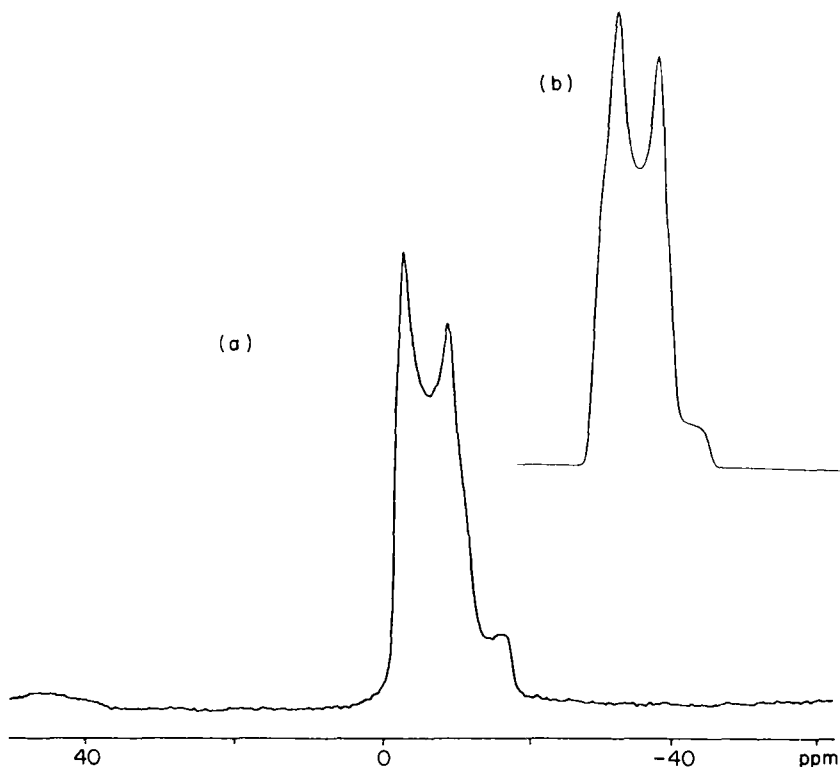


Fig. 17. The $\frac{1}{2} \rightarrow -\frac{1}{2}$ transition in the ^{23}Na MAS NMR spectrum of $\text{Na}_2\text{MoO}_4 \cdot 2\text{H}_2\text{O}$ showing the asymmetric second-order quadrupole interaction broadened lineshape (a). Simulation of the lineshape gives $\omega_q = 0.9$ MHz and $\eta = 0.28$ (b).

of the second-order lineshapes it is necessary to use fast MAS and often high magnetic fields to bring about a manageable linewidth and resolution of the central transition.³²⁷

For certain intermediate magnitudes of the quadrupole coupling constant it may be difficult to readily determine the quadrupole parameters because first, the quadrupole powder pattern may be too wide to be properly excited and hence used to measure the coupling constant, and second, the central transition may not show appreciable second-order broadening. Under these circumstances a two-pulse sequence can be used on a static sample, which has the effect of giving a reduced first-order powder pattern.^{329,330} Echo pulse sequences can also be used to observe the $\frac{1}{2} \rightarrow -\frac{1}{2}$ transition of static samples as shown for ^{39}K and ^{67}Zn salts. Appropriate phase cycling was required to remove the tails of the FIDs. Because of the low frequency, broad lineshape

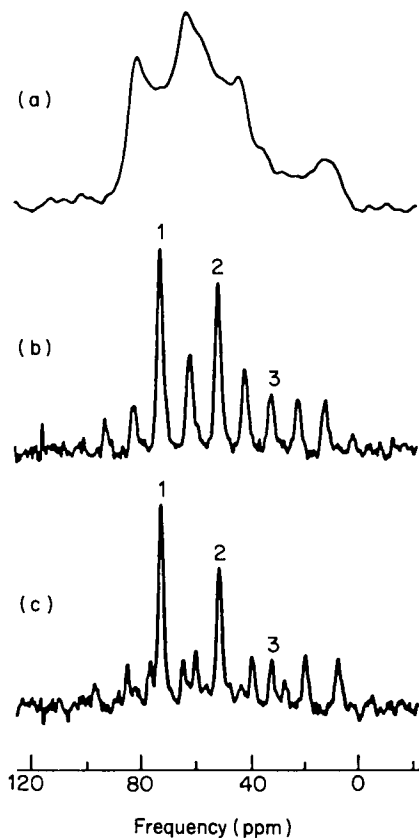


Fig. 18. ^{17}O NMR spectra of diopside, $\text{CaMgSi}_2\text{O}_6$, under conditions of (a) MAS and (b) double-rotation (DOR) at 540 Hz and (c) DOR at 680 Hz. The isotropic resonance positions are numbered. (Reproduced with permission from Chmelka *et al.*³⁰¹)

and low natural abundance many transients were required; however, in mitigation of this fast pulsing was possible.^{331,332}

Earlier attempts at improving the resolution by varying the axis of rotation, VAS,^{326,328} instead of using the magic angle have not proved to be of significant practical value. The initial theoretical treatment dealt only with the isotropic resonance, but more recently the nature of the spinning sidebands has also been considered.³²⁸ VAS can perhaps be seen as a harbinger of the more recent double-axis averaging schemes^{301,333,334} which completely average the second-order quadrupolar interaction, leaving only the fourth-order and higher terms. Figure 18 shows the removal of the second-order line-broadening from a ^{17}O NMR spectrum. A theoretical

treatment of double-angle rotation has been presented.^{333,335} The double-angle averaging techniques represent one of the most important advances in the study of quadrupolar nuclei, opening the possibility of pure chemical shift spectra for nuclei such as ^{23}Na and ^{17}O for example. Two different methods have been proposed: dynamic-angle spinning (DAS) and double rotation (DOR).

In dynamic-angle spinning the sample is spun at speeds of 3 kHz or so about an axis at an angle of 37.38° and then flipped to a new axis at an angle of 79.18° . During the flip, which takes *ca.* 35 ms the magnetization is stored along the Zeeman field. After this procedure a two-dimensional plot is obtained which contains the NMR spectrum without the second-order quadrupole coupling along the ω_1 axis. Although more readily achieved technically—a commercial probe for DAS already exists⁸⁹—DAS suffers from the drawback of requiring a two-dimensional experiment which is necessarily more time-consuming than a simple one-dimensional one.

By contrast, the double-rotation method (DOR) gives the NMR spectrum in a single dimension but requires a much more sophisticated spinning apparatus. DOR involves the simultaneous rotation of the sample about two different angles corresponding to the zeros in the second- and fourth-order Legendre polynomials, that is at 54.74° and 30.6° . Use of DOR has permitted the observation of multiple tetrahedral aluminium resonances in the aluminophosphate VPI-5.³³⁶ At present, technical problems limit the speed of the external rotor to 1 kHz or so. This is quite sufficient from the point of view of causing the lineshape to break up into a series of spinning sidebands but can lead to problems with overlapping sidebands and isotropic resonances. An improvement on this can be made by synchronizing the excitation of the sample with the external rotor position.³³⁷ If the sample is only excited when the rotor phase is 0 and 180° with the resulting spectra co-added, then the odd-numbered spinning sidebands cancel. Effectively the spinning speed of the slower outer rotor has been doubled.

5.3. Nutation NMR

Elimination of the quadrupolar coupling is one method to enhance the resolution in the NMR spectrum of a quadrupolar nucleus, particularly when there is evidence for chemically inequivalent resonances. Another approach has been to use the quadrupole coupling to disperse the NMR spectrum in two dimensions. In the two-dimensional nutation NMR experiment the first time period corresponds to the rf pulse being incremented in steps typically of $2\ \mu\text{s}$, whilst the normal acquisition time is the second time domain. After

a two-dimensional Fourier transform the projection onto the F_1 axis corresponds to the nutation spectrum showing the precession frequencies around the rf field in the rotating field.³³⁸⁻³⁴⁷ The form of the nutation spectrum depends on the ratio of the quadrupolar frequency ω_q to the applied rf field ω_{rf} . Two extreme cases are seen:

$\omega_q \ll \omega_{rf}$ —the nutation frequency is ω_{rf}

$\omega_q \gg \omega_{rf}$ —the nutation frequency is $(I + \frac{1}{2})\omega_{rf}$

When $\omega_q \approx \omega_{rf}$, the intermediate case, a complex lineshape is seen which requires numerical analysis as shown in Fig. 19.^{339,344} More recently, a theoretical description of the nutation experiment has been presented³⁴³ and graphs shown for the variation in the lineshape with the ratio ω_q/ω_{rf} against multiples of ω_{rf} . Note that the rf field must be as strong as possible to simplify the spectrum. Owing to the broad lineshapes of the intermediate case it is unclear to what extent resonances with similar quadrupole coupling constants can be resolved, but it is reasonable to assume that only a very limited number of sites could be distinguished.

Although the calculations suggest that the nutation experiment can be used to measure the quadrupole parameters, its greatest practical value has been for resolution enhancement. For example, in the ^{27}Al NMR spectrum of zeolites resonances from framework and non-framework tetrahedral sites overlap at *ca.* 60 ppm, but these can be resolved in the nutation spectrum because only the framework ^{27}Al has a negligible quadrupole coupling constant.³⁴⁵ An improvement in the resolution can be achieved by using a small spherical sample and combining the nutation pulse sequence with MAS. Under these conditions up to six lines were seen in the ^{23}Na NMR spectrum of a sodalite sample with the minimum shift differences of less than 3 ppm.³⁴⁶ For the most part, nutation spectroscopy has been applied to non-integer spins, but it can be used with integer ones such as ^2H , providing a modified pulse sequence is used to overcome the receiver deadtime.³⁴⁷

By incorporating a rotary echo into the basic nutation pulse sequence, further discrimination has been achieved³⁴⁸ because during the rotary echo delay of about $4\ \mu\text{s}$ nuclear spin relaxation occurs, defined by the time constant $T_{2\rho}$. For the sample of a zeolite NaX the linewidth in the nutation spectrum was found to be dependent on this relaxation time. A variation of nutation spectroscopy, involving two in-phase rf pulses where only the second pulse is incremented, can be used to determine the quadrupole coupling constant in a powdered sample. The experiment consists of measuring the intensity of the central transition as a function of the second pulse duration and comparing with calculated data.^{349,350}

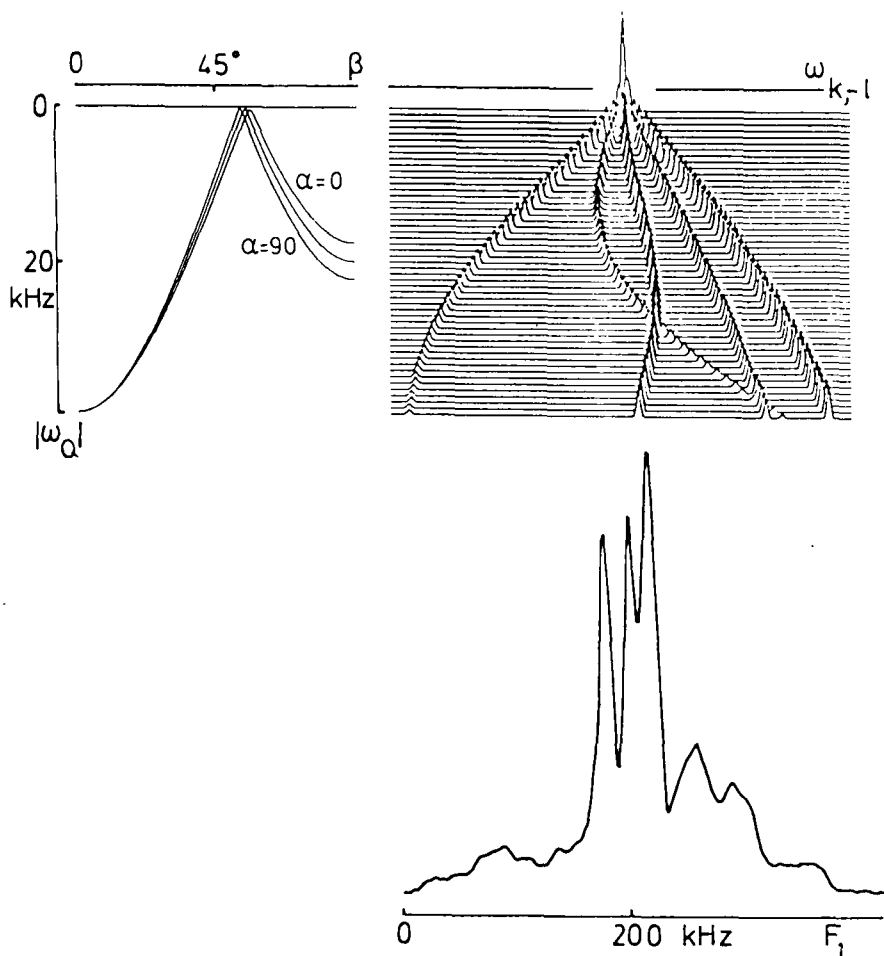


Fig. 19. The powder sample nutation spectrum of ^{55}Mn ($I = \frac{5}{2}$) in KMnO_4 at 90 MHz compared with the result of a numerical simulation. (Reproduced with permission from Samoson and Lippmaa.³⁴³)

5.4. Overtone NMR

A rather neglected nucleus for NMR structural studies has been ^{14}N because it is an $I = 1$ spin and has a large quadrupole coupling constant, though it is quite a favourable nucleus for NQR.³⁵¹ Unless the ^{14}N is found in a high-symmetry site the megahertz quadrupole coupling constants mean that the complete powder pattern cannot be acquired without retuning the

spectrometer. For single crystals observation of the ^{14}N fundamental is reasonably straightforward, though probe retuning will in general be necessary to record the whole spectrum.³⁵² Although MAS will average the first-order quadrupole interaction the intensity of the isotropic resonance will be low and acutely sensitive to the setting of the magic angle. Some progress in making ^{14}N NMR more useful has been made through the development of overtone NMR.^{302,353–355} This involves the direct excitation and detection of the ^{14}N NMR overtone transition. To first order the overtone transitions are forbidden but taking into account the second-order effects they become weakly allowed. Now in contrast to the fundamental ^{14}N NMR the total spectral width is much decreased because in the overtone NMR experiment it depends on the second-order quadrupole frequencies. Importantly, the experiment can be combined with cross-polarization to improve the sensitivity. In addition, dipolar couplings to the ^{14}N can be studied using separated local field experiments while the nutation frequency of the overtone transition is a function of the orientation of the quadrupolar tensor.

A comparison of the overtone and fundamental transition methods suggests that the sensitivity and resolution of the overtone spectra are comparable to those of the conventional spectra. For a single crystal a single resonance is seen, while for a polycrystalline material a powder pattern of the second-order quadrupole/chemical shift anisotropy is seen.³⁵³ An indirect method of detecting the ^{14}N overtone transition via the ^1H signal has been shown,³⁵⁶ as has the effect of decoupling the ^{14}N overtone on the ^{13}C NMR spectrum.³⁵⁷

5.5. ^2H Quadrupole echo

Deuterium is a popular nucleus for studying molecular motion through the characteristic changes in the lineshape.^{358,359} Proper excitation of the large spectral width requires short, intense rf pulses, fast digitization and an echo pulse sequence³⁶⁰ to overcome the receiver deadtime. In order to avoid artifacts in the resulting spectrum care must be taken in setting up the NMR spectrometer and due allowance made for the finite pulse widths on the lineshape.^{361–363} Phase cycling to remove artifacts cannot free the spectrum from the virtual FID. One possible procedure to remove the virtual FID is to make use of the echo delay dependence of the phase of this signal.³⁶² Clearly this is not possible when intermediate motion is present. Selective excitation of a subset of orientations in the ^2H powder pattern can be achieved by means of a DANTE pulse.³⁶⁴ As a method for following the reorientation of one particular initial orientation it suffers from the drawback that dynamic processes during the selective pulse will complicate the inter-

pretation. At the two extremes of motion, namely the slow and fast limit, calculation of the ^2H quadrupole echo NMR spectrum is straightforward involving the static or averaged electric field gradient tensor.³⁶⁵ On the other hand in the intermediate regime when the correlation time for the motion is of the same order as the echo delay dephasing occurs leading to spectral distortions which must be taken into account. A number of treatments have been presented,^{19,366,367} varying largely in the sophistication of the motional models which can be handled and the efficiency of the algorithm.³⁶⁷ While a yet more efficient algorithm for calculating motionally averaged powder patterns with two or three sites has been presented, it is not practical for a larger number of sites.³⁶⁸ The authors do note, though, that a simple extension of the method to overcome this limitation should be possible.

The question of the CPU time taken by these intermediate lineshape calculations is of real concern, particularly with the more complicated models. By and large specific dipolar interactions are neglected in the simulation of ^2H lineshapes because of the computational complexity. Normally a generalized line-broadening is applied. An exception to this has been the consideration of dipolar coupling between ^2H and ^{14}N in urea [^2H]₄ where it was shown that distinctive changes in the echo intensity and lineshape occurred as a function of the echo delay.³⁶⁹

One drawback to the conventional interpretation of ^2H NMR quadrupole echo spectra is the need to assume some kind of motional model, and one can never be completely sure that another more complex or indeed simpler model is not a better description of the motion. Bearing this in mind the two-dimensional exchange experiment³⁷⁰ shows significant promise since the ridges in the two-dimensional spectrum are directly related to the jump angle. This experiment consists of the combination of a modified chemical exchange pulse sequence for ^2H which gives the Zeeman correlations and a spin alignment³⁷¹ experiment which gives the quadrupolar correlations. By correctly combining these spectra a pure phase two-dimensional spectrum is obtained. An example of a typical two-dimensional spectrum is shown in Fig. 20. A comprehensive description of the experiment as well as the two-dimensional data processing is available,³⁷² with examples of dimethyl sulphone and hexamethyl benzene. In a theoretical treatment it was shown that the two-dimensional spectrum can be identified with the joint probability density function $S(\omega_1, \omega_2; \tau_m)$, that is the probability the spin has a frequency ω_1 in t_1 and a frequency ω_2 in t_2 , given a mixing time of τ_m .³⁷³ An extension of this treatment has been presented, allowing faster motions to be studied.³⁷⁴

Furthermore the computational aspects of simulating the exchange spectrum for various standard models have been dealt with.³⁷⁵ These calculations were based on a single correlation time for the motion. If more than one is present, as in the case of the example given, of polystyrene- $[\text{H}]_3$, the

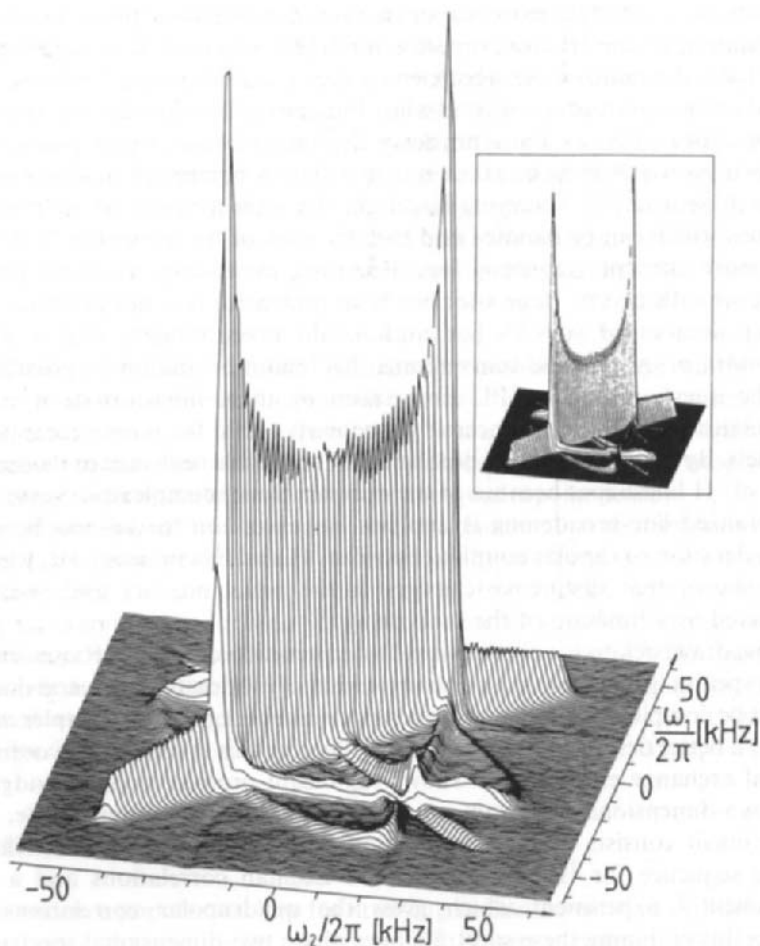


Fig. 20. ^2H two-dimensional NMR exchange spectrum of dimethyl sulphone. The inset shows the corresponding theoretical spectrum for a jump angle of $\theta = 106^\circ$. (Reproduced with permission from Schmidt *et al.*³⁷⁰)

spectra must be summed assuming some kind of distribution function. Although the suggestion earlier was that the two-dimensional exchange experiment is model-free, this is in fact an oversimplification. What is clear is that if the motion does involve a diffusive rotational reorientation then the angle for this can be found directly from the ridges in the spectrum, but if a more complex motion is involved some model must still be chosen and the spectral consequences calculated. This, combined with the computational

burden, makes this experiment of less practical value. A method to invert the experimental two-dimensional exchange spectrum into an angular distribution has been proposed which involves one assumption, namely that the spectrum can be inverted to an angular distribution function $P(\beta)$.³⁷⁶

As noted above, the conventional wisdom is that short and intense rf pulses are required for ^2H NMR, so it is rather going against the grain that a method has been proposed that uses low power and long rf pulses.³⁷⁷ Experimentally a train of low power (8–10 mW), frequency-selective pulses (1 ms long) are used together with an interleaved phase-coherent sampling. In effect, the procedure resembles cw methods. Similar lineshapes were obtained for PMMA as for the two-pulse quadrupole echo but the signal-to-noise appears to be lower. Though it should be noted that no comparison was made of the relative sensitivities nor the effect of motion during the acquisition. It was suggested that the low power levels used may find a use in solid state NMR imaging. Interesting as this approach is, for most practical ^2H experiments we are left with the need for short rf pulses, and nowhere is this more important than in inversion recovery T_1 experiments where the anisotropy in T_1 is related to the type of molecular motion.³⁷⁸ Here a complete inversion over the entire lineshape requires a pulse width of less than $3\ \mu\text{s}$ for the π pulse.³⁷⁹ Following on from work for spin- $\frac{1}{2}$ nuclei the idea of using a composite pulse sequence³⁸⁰ to compensate for the off-resonance effects was proposed, at first simply for a 90° pulse.^{381–383} Early examples of such composite pulses in quadrupole echo experiments tended to introduce artifacts as well as removing them.^{384,385} Even so, efforts have been made to develop composite inversion pulses by computer optimization which appear to give reasonable performances.³⁸⁶ The composite 90° pulse is $\overline{124}, 168, \overline{80}, 126$, which gives a similar bandwidth but is slightly shorter than previous suggestions. For the 180° pulse a composite sequence is used consisting of the sequences $79, \overline{86}, 171, \overline{73}, 41, \overline{42}$ and $\overline{17}, 62, \overline{99}, 144$, which has a larger bandwidth and is shorter than others proposed. Despite the value in such composite pulses their greater length means that it is more likely that exchange effects will be present during the excitation pulses. This can have a profound effect on the lineshape and although the consequences can be taken into account,³⁸⁷ it is at the expense of greater computational complexity. In practice there really isn't a better answer than using high rf power and small coil diameters to get the ^2H 90° pulse down to $1\text{--}2\ \mu\text{s}$.

In diamagnetic compounds it is a simple matter to assign the quadrupole doublets because of the reflection symmetry about the centre of the spectrum. This is not the case with paramagnetic compounds owing to the large paramagnetic couplings. A non-selective Jeneer–Broekaert pulse sequence³⁸⁸ is not readily applicable because of the difficulty in setting the evolution time. To resolve this problem a mixed selective and non-selective pulse sequence

was used.³⁸⁹ Hence a selective pulse was applied at one or other of the transitions followed by a non-selective pulse on resonance.

COSY-type experiments have been carried out on a single crystal of deuterated compound to deduce the sign of the quadrupole coupling constant.³⁹⁰

5.6. Multiple-quantum excitation

Different excitation pulse sequences are required depending on the magnitude of the quadrupole interaction. If the quadrupolar coupling constant is small then long soft rf pulses have been used.³⁹¹ On the other hand for large coupling constants an rf modulation technique has been used.³⁹² The general problem of using hard or soft pulses to excite multiple-quantum effects in an $I = 1$ ensemble has been considered³⁹³ and hard rf pulses used to excite ^{23}Na .³⁹⁴ Multipole spin alignment in $I = 3/2$ ³⁹⁵ and $I = 5/2$ ³⁹⁶ spin systems as a consequence of a two- or three-pulse echo sequence have been considered.

6. ZERO FIELD

A characteristic feature of the NMR spectra of powders is the poor resolution resulting from the orientation dependence of the anisotropic nuclear spin interactions. In the particular case of dipolar couplings even very simple and isolated spin systems lead to broad and featureless lineshapes. While for quadrupolar nuclei such as ^2H the small differences in quadrupole coupling constants present between inequivalent sites are rarely resolved. At zero field we can expect the NMR spectra to be greatly simplified because the couplings will no longer depend on the orientation of the molecules with respect to an applied magnetic field. This increased resolution, in principle, should allow the low-frequency couplings to be measured. It is perhaps stating the obvious but it is worth noting that at zero field all nuclei will have the same resonant frequency.

Perhaps the simplest approach for observing the zero-field spectrum is to set the spin system evolving at zero field and measure the changing magnetization directly. The evolution at zero field is initiated by the abrupt cancelling of an intermediate field by applying an opposing field.³⁹⁷ Alternatively the evolution can be initiated using an rf pulse.³⁹⁸ In practice, direct detection is difficult because the low frequencies involved mean that conventional detection methods based on Faraday's law are not sufficiently sensitive. The required sensitivity can be achieved though by use of a super-

conducting quantum interference device (SQUID),³⁹⁹ allowing the direct detection of the ^{27}Al resonance in Al_2O_3 . A review of this topic has been recently published.⁴⁰⁰

In practical terms, direct detection is severely restricted by the lack of sensitivity so that an indirect method, namely field cycling⁴⁰¹ has played a more important role in the development of zero-field NMR. By observing the zero-field evolution at high magnetic field in a point-by-point manner, the sensitivity is greatly enhanced. Both homonuclear⁴⁰² and heteronuclear⁴⁰³ dipolar couplings as well as quadrupolar couplings⁴⁰⁴ have been observed. Thus, for $\text{Ba}(\text{ClO}_3) \cdot \text{H}_2\text{O}$, a triplet is seen and from the observed splitting the internuclear separation can be determined,⁴⁰² while for perdeuterated 1,4-dimethoxybenzene, different quadrupole coupling constants can be seen for the ortho and meta deuterons.⁴⁰⁴ Having established the basic experiment, techniques analogous to those used in high-field NMR are now being introduced.

Selective excitation has been achieved by use of a d.c. magnetic field of the appropriate duration.⁴⁰⁵ This is important because it allows the indirect detection of nuclei, for example, deuterium, through protons by means of a level crossing which takes place during the field cycle. If the deuterium were not selectively excited then the interferogram observed by the high-field proton signal would also contain the proton dipolar couplings.

Two classes of two-dimensional experiment have been carried out: one involving a high-low field correlation with an example being the dipolar spectra of $\text{Ba}(\text{ClO}_3) \cdot \text{H}_2\text{O}$ ³⁹⁷ and the second a low-low field correlation such as the quadrupole transitions in diethyl terephthalate.⁴⁰⁶ To complement the series of experimental papers a more wide-ranging discussion of zero-field NMR³⁹⁷ deals with such questions as the expected lineshapes and a range of possible experiments. Recently attention has been paid to the effect of motion on the zero-field lineshapes involving features such as two-site flips⁴⁰⁷ and more general types of motion.⁴⁰⁸⁻⁴¹¹

Experimental results on the dipolar lineshapes demonstrates that resolution is still a problem, with typical linewidths of the same order as seen for single crystals. This reflects the finite spin-lattice relaxation times and the presence of unresolved splittings.³⁹⁷ Moreover, as the number of coupled spins increases, such as in squaric acid, the resolution is little different from the high field powder (see Fig. 21). To some extent this can be overcome by isotopic dilution whereby the intramolecular couplings can be enhanced by placing a protonated molecule in a perdeuterated matrix. Even so the technique would seem to be limited to small molecules and this represents a severe weakness of zero-field NMR as a general method for the determination of dipolar couplings and hence internuclear distances. Related to the overall poor resolution in a complex spin system is the difficulty in observing

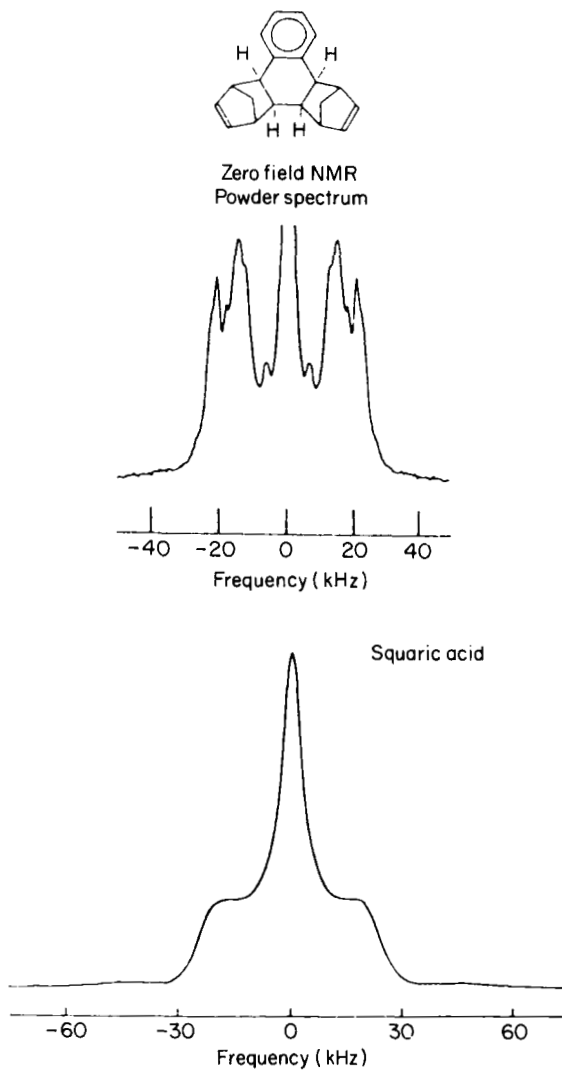


Fig. 21. Comparison of the zero-field dipolar NMR spectra of squaric acid and 1,2,3,4-tetrachloronaphthalene bis[hexachlorocyclopentadiene] adduct showing the loss in resolution in solids with a high proton density. (Adapted with permission from Zax *et al.*³⁹⁷)

small dipolar couplings because of the zero frequency peak. This can be greatly improved by suppression of the zero frequency line by use of a d.c. magnetic field pulse of a desired angle.⁴¹² Another limitation is the need for a spin-lattice relaxation time which is at least as long as the experimental cycle time, that is *ca.* 0.2 s.

Fictitious zero-field spectra can be obtained at high magnetic field by a combination of multiple-pulse sequences and spinning at angles other than the magic angle.⁴¹³⁻⁴¹⁵ Such spectra have dipolar couplings which are significantly scaled giving a spectrum only a few hundred hertz wide from a full dipolar coupling of about 2 kHz. This tends to limit the applicability of the technique to simple spin systems. An example of a ¹³C zero-field-like spectrum in high field has been provided by a couple of small molecules, one being diammonium succinate doubly enriched at the methylene carbons. In this case the observed dipolar scaling factor of 0.082 gave a splitting of 497 Hz for a bond distance of 1.55 Å.⁴¹⁶ On the basis of the observed linewidths of 12 Hz, providing that the resolution is maintained, it should be possible to measure distances of up to 4 Å.

7. IMAGING

Key to the imaging of a material is the encoding of the position of the nuclear spin as a frequency by the application of a field gradient. Consequently the simplest three-dimensional imaging pulse sequence is the one shown in Fig. 22 in which the phase encoding gradients G_z and G_y are incremented along with the read gradient G_x . Using this pulse sequence the accumulated frequency difference between adjacent volume elements in the sample will depend upon the magnitude of the field gradients and the time the spin evolves under these gradients. If the two volume elements are to be resolved in the image the difference in frequency between these elements must exceed the linewidth. Herein lies the problem for imaging a rigid solid: the ¹H linewidth can be in excess of 10 kHz while the short T_2 of the magnetization limits the time the gradient can be applied for to less than 100 μ s. Taken together, these mean that to obtain 0.1 mm resolution an applied field gradient in excess of 500 G/cm would be required. Achieving and switching such large gradients is difficult over a large sample size, especially within a superconducting magnet, making the brute force approach to the imaging of rigid solids of little practical use.

One way to overcome the switching problem which has been employed is to use a sinusoidally oscillating field gradient with the rf pulses at the null points in the gradient oscillation.⁴¹⁷ In essence, to image a rigid solid some way must be found to extend the time over which a more realistic field

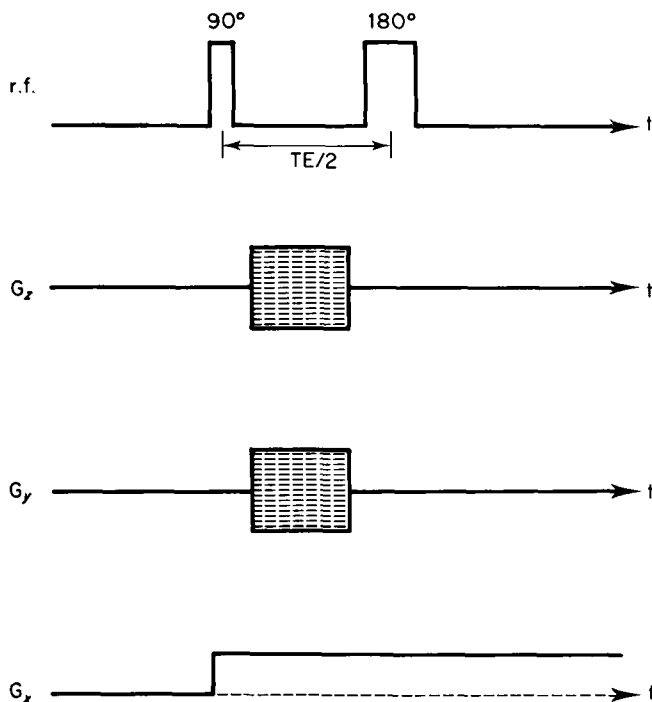


Fig. 22. Basic three-dimensional NMR imaging gradient and pulse sequence.

gradient can be applied. A problem related to the imaging of a rigid solid is that of volume selection for localized spectroscopy, in this case the short ^1H NMR relaxation times limit the spatial localization. One method which has been proposed relies on using a series of spin-lock pulses for selecting the required volume.⁴²⁴

Two fundamentally different approaches to imaging have been used: incremented time and constant time imaging. With incremented time imaging a fixed gradient is used and the variable encoding is achieved by altering the time the gradient is applied for. The advantage of this method is that gradient switching does not occur during the pulse sequence, while the main disadvantage is that projection reconstruction must be used to generate the image, necessitating the rotation of the sample or gradients. In constant time imaging a constant evolution period is used with a stepped increase in the field gradient. Images can then be obtained by a multidimensional Fourier transformation. Since the stepped gradient dimensions are constant time, the dipolar broadening drops out of these dimensions.^{418,419} By exploiting this

feature it was possible to acquire images of an adamantane phantom using only a 2 G/cm gradient and a simple $\pi/2$ pulse. Gradient switching was not a constraint here because only the signal amplitude was collected and in the presence of the field gradient. Although this overcomes the broadening associated with the dipolar coupling the effect of the short T_2 on the resolution remains because the maximum frequency spread is still defined by the T_2 and maximum field gradient, G_{\max} .

Much of the discussion on solid state NMR imaging has been concerned with the imaging of proton-containing solids, mainly polymers, with the consequent emphasis on how to overcome the large inherent linewidths. As we will see, imaging of nuclei such as ^{13}C is one possible solution for polymers. Even so, this neglects a wide range of materials, namely those with quadrupolar nuclei for which dipole-dipole couplings are absent and line-broadenings tend to be inhomogeneous. Thus for half-integral spins such as ^{23}Na and ^{79}Br the $\frac{1}{2} \rightarrow -\frac{1}{2}$ transitions are often much narrower than 2 kHz. Examples of imaging quadrupolar nuclei are: ^{23}Na for defect detection in a single crystal of NaCl,⁴²⁰ ^{23}Na diffusion in a single crystal of β -alumina⁴²¹ and ^{81}Br as a temperature probe in a KBr single crystal.⁴²² These experiments all used the $\frac{1}{2} \rightarrow -\frac{1}{2}$ transition in single crystals, constant time imaging with G_{\max} 8–15 G/cm, simple $\pi/2$ pulses and back projection to construct the image. Since the $\frac{1}{2} \rightarrow -\frac{1}{2}$ transition is independent of the quadrupolar coupling to first-order there is no reason for imaging of powders to be more difficult.

7.1. Sensitive slice methods

When intense field gradients are used it is difficult to switch them quickly, hence their common use to slice or line select rather than image, the sensitive region being defined by that region having the appropriate resonant frequency. Although in principle an image can be formed this entails moving the sample so that the sensitive region scans through the object. In one procedure⁴²³ the FIDs after a $\pi/2$ pulse are co-added whilst progressively stepping a linear gradient $G_n = n\Delta g$. One slice, the pivot, has a zero offset and is the sensitive slice. It was found that the image quality improved as the B_1 rf field strength decreased, consistent with a greater sensitivity to offset, while moving the sensitive slice gave a better resolution than Fourier transformation with respect to n .

A novel approach to the brute force method involving a sensitive layer and a superconducting magnet has been proposed.^{425–427} Near the end of a typical superconducting magnet the main magnetic field drops off drastically with distance, giving field gradients of the order of 0.01 T/mm. At this position,

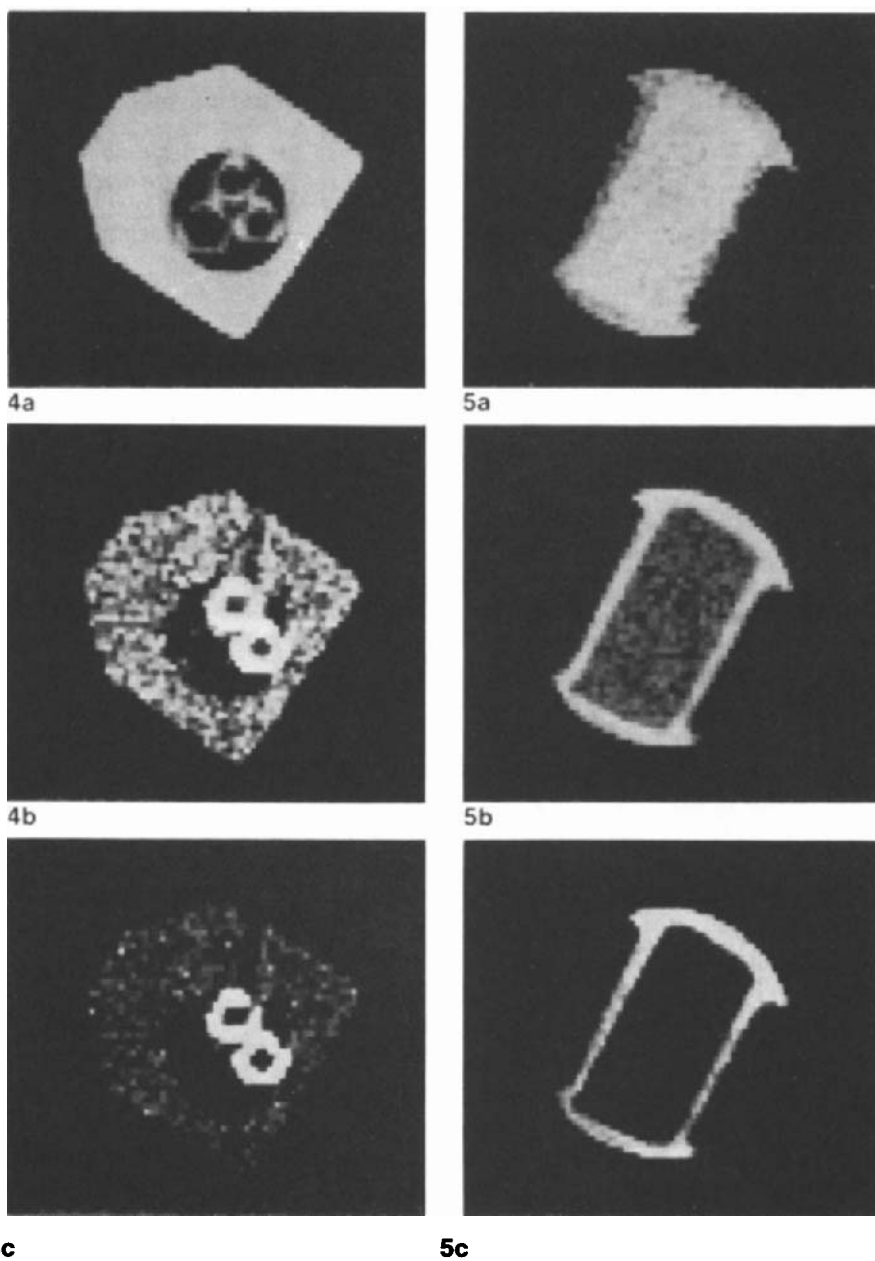
the resonant frequency for ^1H , of course, would be much lower than at the main field B_0 . In the example given, using a 4.7 T magnet, the actual resonant frequency in the sensitive layer was 100 MHz. Given the large field gradient, only a very thin layer, of the order of 200 μm will give a frequency lying within a 100 kHz bandwidth. The sample is scanned by moving it through the sensitive layer. In this manner excellent spatial resolution can be achieved in one dimension. Imaging using this technique requires that the free induction decays be obtained in a point-by-point manner by sample rotation followed by projection reconstruction as shown in Fig. 23. One possibility which can be envisaged beyond this is to design a superconducting magnet where a sensitive point is defined in space outside of the magnet by three intense field gradients from the magnet itself and this region is rapidly scanned through the sample.

7.2. High-temperature NMR imaging

Raising the temperature of a material to introduce molecular motion and thereby increase the T_2 is perhaps the simplest practical method for achieving the line-narrowing required to enable NMR imaging of solids with reasonable field gradients. Certainly for polymeric samples it is not unreasonable to raise the temperature to well above the glass transition temperature, T_g , as illustrated by the images of polypropene⁴²⁸ and elastomers⁴²⁹ which already have phases above their T_g , even at room temperature. Epoxies have been studied at temperatures above 100°C.⁴³⁰ It is worthwhile stressing the importance of the experimental set-up; in a liquids imaging experiment, an echo time, TE, of 20–40 ms is typical, while for imaging solids, a TE of less than 5 ms is desirable even at high temperature. This is important not only for imaging of a polymer matrix but also for any solvent within the matrix since short T_2 times are often seen for bound solvent. For example, tightly bound water in nylon has a T_2 of 2 ms.⁴³¹ In fact, the constraints on imaging polymer matrices has led to a tendency to image solvent absorbed by the polymer ranging from methanol in PMMA⁴³² to water in a composite material.⁴³³ Solvent uptake can be used to image defects in carbon fibre–polymer matrix composites such as ICI APC2⁴³³ (Fig. 24), taking advantage of the fact that such composites must survive hot/wet testing before being used in structures.

7.3. Solid echo

Homogeneous dipolar coupling can be refocused using a 90_x-t-90_y solid echo pulse sequence with a consequent increase in the effective T_2 . When applied



4c

5c

Fig. 23. ^1H NMR image of a mixture of polyacrylic, polypropene and polyurethane shapes using the sensitive plane method. (a–c) Correspond to images with different T_2 weighting. (Reproduced with permission from Samoilenko *et al.*⁴²⁶)

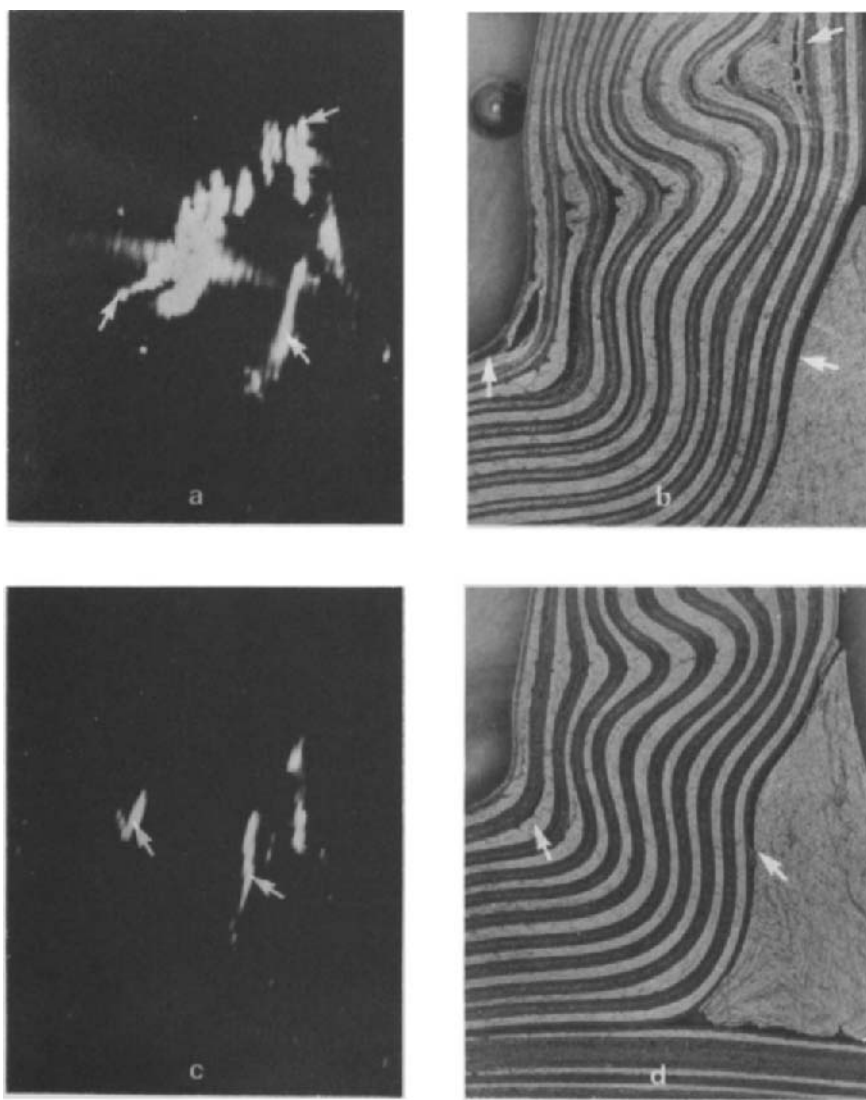


Fig. 24. Identification of defects in the lay-up of a composite material by ^1H NMR imaging. Defective areas arrowed in the NMR image (a) and (c) should be compared with the physically sectioned material (b) and (d). (Reproduced with permission from Jackson *et al.*⁴³³)

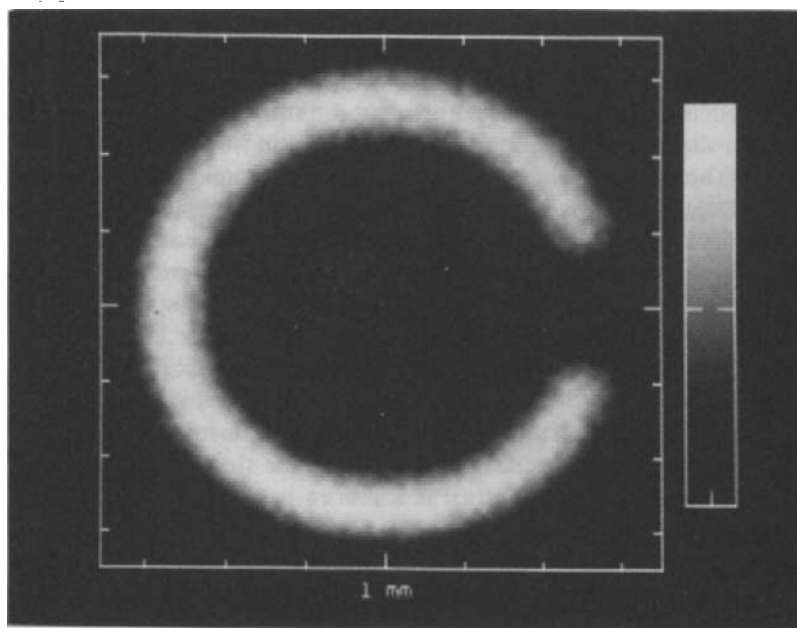


Fig. 25. ^1H NMR image of a polyacrylic annulus, 4.8 mm inner diameter and 0.8 mm wall thickness. A slit has been removed from the annulus. Reproduced with permission from Miller *et al.*⁴⁴⁰⁾

in an imaging pulse sequence with field gradients, the practical gain in the gradient evolution time is modest, approximately a doubling.⁴³⁴ For example, in the case of hexamethylbenzene the T_2 of which is $\sim 40 \mu\text{s}$, a total encoding time of $224 \mu\text{s}$ was possible. In common with the single $\pi/2$ pulse method of Emid and Creyghton,⁴¹⁹ the gradient switching was done after acquiring a single point at the top of the echo. It was found that the solid echo sequence was sensitive to slight mis-settings of the pulse lengths and phases. Although very useful, the increase in the evolution time is not adequate to image solids with a high density of rigid protons, where T_2 times of the order of $20 \mu\text{s}$ are found.

A variation on the two-pulse solid echo imaging experiment is the use of the three-pulse Jeneer–Broekaert sequence to generate dipolar order. In essence, this pulse sequence was proposed to overcome the problem of gradient switching times,⁴³⁵ but before turning to this aspect we need to consider the gradient evolution time. In the three-pulse sequence, dipolar order is created by the second pulse and read by the third pulse. To maximize the dipolar ordered state the second pulse must be applied at the time corresponding to the maximum differential change in signal intensity, which

is of the order of T_2 . Consequently, the gradient evolution time is of the order of T_2 since the spin only experiences the gradient between the first and second pulse. Clearly this does not resolve the problem of the short T_2 and is, in fact, no better than the straight $\pi/2$ pulse method. As in the case of solid echoes, the Jeneer–Broekaert pulses must be hard, limiting the size of the applied gradient. Thus if the sample is 10 cm and a 10 G/cm magnetic field gradient is applied, the frequency bandwidth is ~ 420 kHz, necessitating a $\pi/2$ pulse of less than 1 μ s.

The storage of magnetization in an ordered state during any gradient switching is a common idea. Besides the dipolar ordered state generated in the Jeneer–Broekaert pulse sequence,⁴³⁵ the magnetization can be returned to a state of Zeeman order or spin-locked.⁴³⁶ Providing the characteristic relaxation times of these states are sufficiently long, gradients can be switched and settled before the magnetization is returned to continue its course. Relaxation of the nuclear spins will indeed occur during these storage periods and may be employed to provide a contrast mechanism based on T_1 , $T_{1\rho}$ or T_{1D} .

7.4. Multiple-pulse sequences

The idea of combining multiple-pulse sequences with magnetic field gradients to image solids has a long history.^{437,438} In these early papers dating from the early 1970s the concept of NMR “diffraction” was introduced and first-order “diffraction” peaks seen for camphor. Intriguingly, it was calculated that atomic level diffraction, *ca.* 3 Å, could be seen for a typical solid T_2 if only a gradient of 10⁸ G/cm could be applied. Furthermore, based on the effective T_2 in the presence of multiple-pulse line-narrowing, it was estimated that a resolution of 4 μ m would be possible with a gradient of 100 G/cm. This does not take into account any signal-to-noise limitations.⁴³⁹ Multiple-pulse sequences have been used for three purposes in imaging: (1) line-narrowing; (2) generation of multiple-quantum coherence; and (3) forced precession.

Two considerations are of general importance when dealing with multiple-pulse sequences. First, the response to resonance offset and second, the effect of pulse length. A fundamental problem when using multiple-pulse sequences in combination with field gradients is the susceptibility of the pulse sequence to off-resonance effects which degrade the effectiveness of the coherent averaging. This appears to be caused by free precession of the magnetization during the intervals between the rf pulses in the multiple-pulse sequence.^{440,441} Most multiple-pulse sequences do not perform well with a resonance offset in excess of as little as 5 kHz and yet, as we have seen above for a 10 cm object with a very reasonable gradient of 10 G/cm, offsets in excess of 100 kHz are readily achieved. To compound this problem, quite intense field gradients are

still required, because the effective T_2 times remain short compared to liquids, of the order of a few milliseconds.

Typically, multiple-pulse sequences are less effective as the pulse length increases, with the best response requiring a pulse length of $< 5 \mu\text{s}$, though some, such as BLEW-12, are efficient with longer pulses. In practical terms this translates as a constraint on the size of the object which can be imaged because of the amount of rf power required to generate the short rf pulses. Here we can see the detrimental interplay of the various aspects of multiple-pulse imaging for solids. For a realistic power level the $\pi/2$ pulse in a large coil will be long, giving a poorer line-narrowing capability and shortening T_2 . Now, since T_2 is shorter more intense field gradients must be used to achieve a desired resolution, increasing the resonance offsets making the multiple-pulse sequence still less effective. This logic points to the use of surface coils to image large objects.⁴⁴²

7.4.1. Line-narrowing

MREV-8 has been shown to be effective for two-dimensional Fourier imaging (2DFI) when combined with the storage of the magnetization during the gradient switching times.⁴³⁶ Since the gradient settling times were of the order of 5 ms, shorter than both T_1 and $T_{1\rho}$, both Zeeman and spin-lock storage were possible. Contrast can be introduced into the image by varying the length of the storage interval. Various artifacts were noted which could be largely eliminated by the appropriate phase cycling.

Although the MREV-8 sequence is satisfactory for adamantane which has little inhomogeneous broadening, the same cannot be said for a sample such as ICI Perspex (PMMA) where over 80% of the MREV-8 linewidth is inhomogeneous. The principal origins of inhomogeneous broadening are magnetic susceptibility, chemical shift anisotropy and chemical shift dispersion. Methods have been developed, called refocused gradient imaging (RGI), for removing inhomogeneous interactions in liquids NMR imaging based on echo pulse sequences similar to Carr-Purcell pulse trains.⁴⁴³ In a solid, the inhomogeneous refocusing must be combined with a homonuclear decoupling sequence. One such combination is the reversed effective field (REF) sequence based on MREV-8 through a rotation of the reference frame.^{444,445} Rather than switching the field gradients during the multiple-pulse sequence, which would be technically difficult, the REF is applied in the presence of a sinusoidally varying gradient. To minimize off-resonance effects a small field gradient of 1.3 G/cm was used. A comparison of the RGI/REF method with the MREV-8 one suggested a marginally improved sensitivity. The necessity for removing inhomogeneous interactions arising from chemical shift and susceptibilities is to an extent a question of the static

field strength since they will scale linearly with B_0 . At low field strengths other sources of broadening, such as the residual dipolar contribution will be proportionately more important.

As the REF/RGI example illustrates, most multiple-pulse sequences are not suited to being used in combination with field gradients because of off-resonance effects. This leaves three possibilities: either to switch the gradients on and off synchronously with the rf pulses, to use a time-dependent gradient which is zero when the pulses are applied, or to develop a multiple-pulse sequence specifically for use in the presence of gradients. The first is technically difficult with largish gradient coils whilst the second is hard to achieve with pulse sequences such as WH-4 and MREV-8 where the pulse spacings are not equal. For smallish gradient coils, short (*ca.* 5 μ s) gradient pulses are possible which have been used to compensate for the off-resonance effects, while a solution to the unequal windows in the pulse sequence has been proposed involving the basic cycle $[90_{-y} 90_{-x} 90_{-x} 90_{-y} 90_{-x}]_N$.⁴⁴⁷ For hexamethylbenzene using a τ of 12 μ s, T_2 was 2 ms and the image was created by back-projection. As it stands, the experiment is only applicable to volume imaging since it does not allow for slice selection. A further modification to the pulse sequence involving the addition of the Hermitian adjunct was found to help overcome imperfections in the pulse length.

Although the use of short gradient pulses, interleaved into the multiple-pulse sequence, overcomes the problem of large offsets created by the gradients themselves, we are still left with intrinsic off-resonance effects, such as the chemical shift anisotropy. One way to eliminate these off-resonance effects is by second averaging. This consists of introducing another interaction, much larger than the off-resonance term, which is then averaged in a second frame. In practice this has been achieved using a phase-shifted MREV-8 (Fig. 25).⁴⁴⁶ Further improvements in the image resolution have been obtained with a 48-pulse cycle.⁴⁴⁸ Image resolution can also be improved by means of oversampling, that is, by collecting more than one data point per multiple-pulse cycle.⁴⁴⁹

Given the sensitivity of multiple-pulse sequences to resonance offset it is not surprising that this feature has been used to select a region in a sample.⁴⁵⁰ Rather than the standard line-narrowing sequences a train of 142° pulses was applied in the presence of sinusoidal frequency modulation. A field gradient of 20 kHz was used and a spatial resolution of 0.5 mm achieved through varying the static field to alter the resonance offset.

7.4.2. Multiple quantum

Besides applying a more intense gradient one can enhance the effect of a less intense gradient through multiple-quantum coherences.⁴⁵¹ This works

because if the single quantum transition has a frequency $\Delta\omega$ in the gradient the m th quantum transition has the frequency $m\Delta\omega$. The multiple-quantum coherences were generated by a time-reversal sequence which was capable of working in the presence of a resonance offset. No comment was made though on the extent to which it was free of off-resonance effects. For a sample of adamantane, 2 mm resolution was achieved for the $m = 8$ coherence using only a 0.48 G/cm gradient. Since the bandwidth in the detection period is narrow, the signal-to-noise ratio is good despite the great bandwidth of evolution frequencies in t_1 . One drawback immediately apparent is the spread of the multiple-quantum intensity amongst many orders of coherence, leading to a loss of sensitivity. This is unavoidable; lower-order coherences which have the poorer resolution are always excited to a greater extent. A second possible difficulty is the effect of resonance offset, since to be of real value field gradients of say 8 G/cm need to be applied.

7.4.3. *Forced precession*

A third application of multiple-pulse sequences is to bring about a forced precession of the magnetization which is independent of the resonance offset and dipolar couplings to other spins.⁴⁵² Spatial resolution is provided by making the pulse angle vary across the sample. In the proposed imaging application (no images were actually acquired) two pulse sequences need to be superimposed: one eliminates the dipolar couplings and is delivered by the rf coil, while the second causes the pulse angle to vary and is given by an rf field gradient coil. Two artifacts were seen. First, a weak θ -dependent line-broadening leading to poorer resolution at the edges of a sample, and second, a small line at $\omega = 0$, perhaps caused by the finite rise and fall time of the pulses.

Further developments in multiple-pulse techniques are sure to be based on optimizing pulse sequences for imaging purposes rather than simply taking those optimized for NMR spectroscopy.

7.5. Magic-angle spinning

Magic-angle spinning can be an effective method for increasing the effective T_2 in a solid. This is mainly through the averaging of inhomogeneous interactions, principally the chemical shift and quadrupolar interactions. Small, homogeneous dipole-dipole couplings will also be removed. For ^1H NMR imaging though, unless the ^1H lineshape is motionally averaged, MAS alone is not usually sufficient to overcome the dipolar interaction. Thus MAS must be combined with a multiple-pulse sequence for ^1H imaging of rigid solids.⁴⁵³

A critical experimental evaluation of MAS imaging and RGI-based techniques under these circumstances would be invaluable. This is rather pertinent, because in a comparison of MAS and multiple-pulse line-narrowing methods for ^1H NMR imaging it was suggested that MAS is to be preferred unless the MAS linewidth is large and/or a dramatic reduction in linewidth occurs with the multiple-pulse sequence⁴⁵⁴—precisely the conditions seen for rigid proton matrices.

Imaging of a rotating solid is possible in two ways. First, in the dynamic gradient method the gradients are spun synchronously with the sample⁴⁵⁵ so that in the rotating frame the gradients are static. In the second method, sample rotation in the presence of a defined field gradient is used as a way of scanning the spatial frequency domain, k space.^{456–458} With a ramped gradient over a number of rotor periods it was possible to perform a spiral scanning of k space. This particular experiment⁴⁵⁶ was carried out with spinning at 180 Hz and it remains to be seen how readily this can be translated into imaging a sample spinning at, say, 4 kHz in an MAS system. Prior to the start of data acquisition, it is necessary to move the origin of k space, either by a gradient switching scheme as in the original proposal or by an rf pulse method.⁴⁵⁹ Early images obtained using the static gradient method suffered from blurring, but an improved reconstruction method has been devised,⁴⁶⁰ which takes the mechanism for the blurring into account, giving satisfactory images of a phantom rotating at 102 Hz. Imperfections in the dynamic gradient experiment have been examined⁴⁶¹ and arise from four sources: imbalance in the amplitudes and non-orthogonality in the magnetic field gradients, displacement of the spinner from the centre of the field gradients and differing rotation frequencies of the rotor and gradients. These result in regions of lower intensity at the edges of one-dimensional images, though with filtered back projection distortions to the whole image will occur.

MAS is of more value in ^{13}C NMR imaging,⁴⁶² where a resolution of $\sim 100\ \mu\text{m}$ has been achieved. The limitations in the resolution are residual broadening of the MAS lineshape, off-resonance ^1H decoupling and, of lesser importance, except in systems with a large chemical shift anisotropy, interference of the coherent MAS averaging by the modulated field gradients. Despite the improvements in sensitivity brought about by use of a high Q probe and line-narrowing, ^{13}C images still take approximately 25 times longer than ^1H ones. A representative ^1H NMR image of a polymer blend⁴⁶³ is shown in Figure 26.

7.6. Magic-angle rotating frame

The feature of imaging using the magic-angle rotating frame is to narrow the dipolar-broadened ^1H lineshape by creating an effective field at the magic

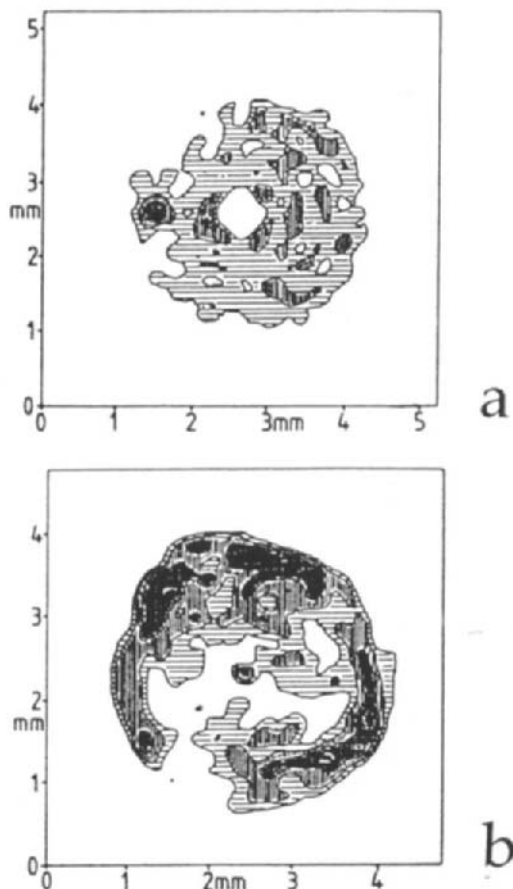


Fig. 26. ¹H NMR images of a polymer blend obtained using MAS. In (a) the blend was physically mixed and in (b) cast from a common solvent. (Modified with permission from D.G. Cory, J.C. de Boer and W.S. Veeman, *Macromolecules*, 1989, **22**, 1618. Copyright (1989) American Chemical Society.)

angle.⁴⁶⁴ Furthermore, by combining with a rotating co-ordinate frame residual dipolar broadening can be minimized. With this combination the remaining linewidth only has contributions from the dipolar coupling to second order, $O(D/\omega_e)^2$. However, in the experimental implementation the narrowing seen for adamantane was poor, with a residual linewidth of 2.5 kHz resulting in both low sensitivity and a lack of resolution.⁴⁶⁵ It is not clear whether this is a consequence of the effective field ω_e being too small (42 kHz) or because the magic-angle condition is met over only a part of the

sample through static and rf field inhomogeneity. Certainly greater line-narrowing will be necessary if this technique is to compete.

At first sight the sensitivity of the rotating frame experiment might appear to be poor because of the low detection frequencies, of the order 40 kHz. However, this is compensated for by the large number ($> 10^3$) of turns on the receiver coil. The experimental procedure involves placing the receiver coil parallel to B_0 , generating an effective field at the magic angle and two gradients for each dimension in the image, one in the laboratory frame and the other in the rf frame. An improvement to this method has been achieved by using an echo pulse sequence in the audio frequency excitation⁴⁶⁶ and images presented of adamantane.⁴⁶⁷

7.7. Rare spin imaging

In the light of the problems associated with imaging abundant spins it is to be expected that attention has been paid to NMR imaging of rare spins where the homonuclear dipolar couplings are negligible. We have already come across examples of the use of quadrupolar nuclei⁴²⁰⁻⁴²² and ^{13}C within the context of MAS line-narrowing. However, in the case of ^{13}C , once the heteronuclear coupling has been removed by decoupling, the inhomogeneous contribution does not have to be spun out, it can be simply refocused using π pulses. Various pulse sequences for 2DFI of ^{13}C have been proposed,⁴⁶⁸ all sharing the storage of ^{13}C magnetization as Zeeman order during the gradient switching. To reiterate, the fundamental constraint on rare spin imaging is the low signal intensity, which can only be partially alleviated by cross-polarization from ^1H . More drastic improvements in signal can be achieved by cross-polarization from electron spins, dynamic nuclear polarization (DNP).⁸⁰ Indeed, DNP has been combined with ^{13}C imaging⁴⁶⁹ giving an enhancement factor of 20 for a sample of pitch. In essence, the experimental set-up is analogous to that described earlier but with the addition of a field gradient.

Examples of contrast used in ^{13}C imaging of composites are the chemical shift and ^{13}C T_1 .⁴⁷⁰ The time the gradient can be applied for is controlled by T_2^* , the ^{13}C spin-spin relaxation time under strong ^1H decoupling and chemical shift refocusing which, for ICI PEEK, has been measured to be 6 ms. It was calculated that even if the ^{13}C linewidth was 5 Hz ^1H would still be more sensitive assuming a multiple-pulse line-narrowing to 0.3 ppm. Despite long accumulation times ranging from 2.1 h to 26.7 h the image quality was rather poor.

7.8. Surface coils

Surface coils are important because they can free the object from the constraint of sitting within the coil generating the intense B_1 field.⁴⁷¹ Spatial localization is achieved by using the sensitivity of the multiple-pulse sequence to the rf pulse amplitude. For a given power level and a set pulse duration the rf amplitude at a defined distance from the coil will match the condition for a $\pi/2$ pulse whilst outside of this region, line narrowing will be less effective. Somewhat surprisingly it was found that MREV-8 compensated too well for rf amplitude imperfections, resulting in poor spatial resolution.⁴⁴² In fact, what is required is a multiple-pulse sequence which is still good at line-narrowing but is more sensitive to rf amplitude and at the same time retains an insensitivity towards phase errors. Such a pulse sequence was proposed, called MAN for magic-angle nutation. Although this improved the imaging resolution near the coil it deteriorated into the sample owing to the poor dipolar decoupling of the MAN sequence, which is intolerant of long $\pi/2$ pulses. Overall the best resolution was found for a combination of MREV-8 and a pre-sequence consisting of a train of π pulses to select a sensitive plane. Greater sensitivity can be achieved by a dipolar decoupled composite inversion pulse^{440,473} coupled with the sequence $(\pi-2\pi-3\pi-\dots n\pi)_2$.⁴⁷⁴

8. MULTIPLE-QUANTUM METHODS

Multiple-quantum techniques have been used in a variety of experiments for selective detection, enhancing the effect of field gradients in NMR imaging and to study spin clustering. The basis of selective detection is analogous to the methods used in solution state NMR, while the use of multiple-quantum coherences in imaging and spin clustering are experiments with a unique solid state character. Although the principle of using a multiple-quantum filter is the same in solution and in a solid, clear differences still exist because in the solid the multiple-quantum coherences can be generated by both dipolar and scalar coupling whereas in solution only scalar coupling is used. A good example of this is the use of a double-quantum filter to remove the natural abundance resonance in the spectra of compounds with a ^{13}C - ^{13}C coupling,⁴⁷⁵ the INADEQUATE experiment, in order to highlight the connectivity of the carbon network. In solution the double-quantum coherence originates from the scalar coupling between the ^{13}C nuclei. A similar pulse sequence has been used in conjunction with magic-angle spinning for a sample of camphor.¹⁷⁸

However, to establish the correct antiphase characteristics of the doublet components an evolution time of up to 20 ms is required. For almost all

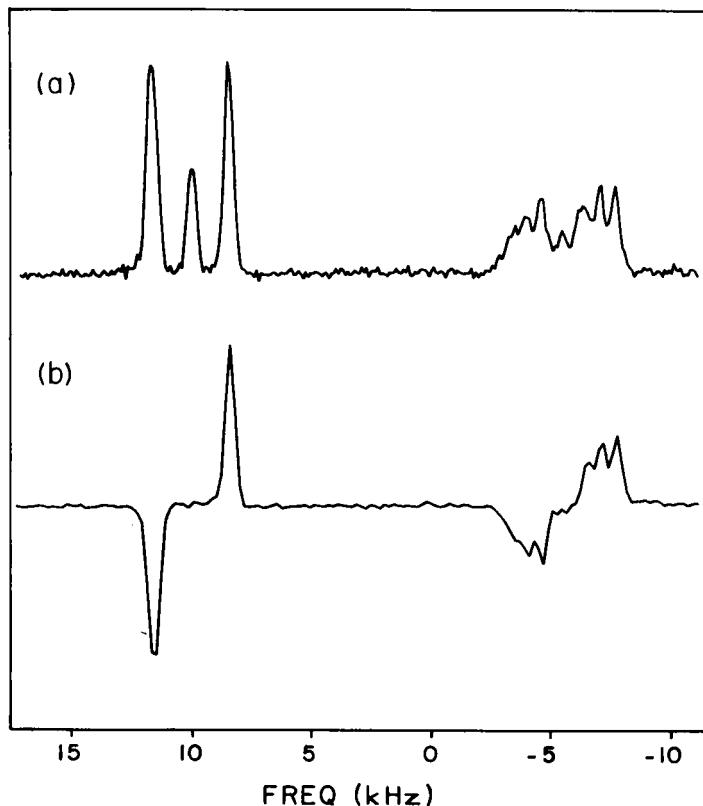


Fig. 27. Single quantum ^{13}C NMR spectrum of a 9% doubly labelled single crystal of glycine (a) and with a double-quantum filter (b). (Reproduced with permission from Menger *et al.*, 1984.⁴⁷⁶)

carbon connectivities a delay of the same order will be required; consequently the T_2 of the sample must be at least 10 ms if there is going to be any magnetization left. This in practice is quite a severe restriction. It is because the scalar couplings are rather small that the unrealistic evolution times are necessary. In contrast, the dipolar couplings between carbon nuclei are of the order of 6 kHz, meaning an evolution time of only 100–200 μs is optimal. By observing the double-quantum coherence created by dipolar coupling and using the appropriate phase cycling to remove the single-quantum transition, ^{13}C – ^{13}C dipolar couplings have been measured in a single crystal of glycine⁴⁷⁶ giving the spectrum shown in Fig. 27. The experiment was facilitated by using *ca.* 9% doubly enriched glycine.

Combining the simple 90– t –90 excitation sequence with magic-angle

spinning is expected to give rise to problems because of the interference between the spinning and the excitation. An indication of the difficulties is provided by a study of the generation of multiple-quantum coherence during magic-angle spinning.⁴⁷⁷ First of all, MAS does interfere with the effectiveness of the simple $90-t-90$ excitation sequence, leading to the poor generation of multiple-quantum coherences. Added to this the pulse sequence is resonance-offset-dependent. Superior excitation of multiple-quantum transitions can be achieved by using time-reversal pulse sequences,⁴⁷⁸ but under MAS this leads to a vanishing multiple-quantum intensity because the dipolar coupling changes sign during the rotor period.⁴⁷⁷ This has been demonstrated both experimentally, for adamantane, and by calculation. However, a relatively simple modification of the time-reversal pulse sequence to include a switch in the rf phase every half rotor period overcomes this problem. We now arrive at a third way of carrying out the INADEQUATE experiment, using a switched-phase time-reversal pulse sequence to achieve the double-quantum coherence. With a test sample of doubly 5% enriched polycrystalline zinc acetate, the double-quantum spectrum could be obtained in 1000 transients. In this paper it was estimated that under optimum conditions the natural abundance double-quantum spectrum would be only 0.1% the intensity of the normal spin-locked cross-polarization experiment. Since this sensitivity is similar for all three methods it is clear that for most, if not all, practical cases isotopic enrichment would be necessary. An intriguing observation made during this work was that line-broadening took place if any two rotational spinning sidebands of the dipolar coupled carbons overlapped. Here this causes an unnecessary loss in resolution, so steps must be taken to ensure that the overlap does not occur by altering the spinning speed appropriately. In this case there is a bright side to the phenomenon because the overlap can be used to enhance the rate of spin diffusion as we have seen earlier.

Despite the reduction in the efficiency with which double-quantum coherences can be generated using the $90-t-90$ excitation sequence when magic-angle spinning, this procedure has been used successfully to obtain a double-quantum spectrum of doubly labelled glycine.⁴⁷⁹

An aspect of multiple-quantum methods unique to solids is the idea of looking at spin clusters. In solution, the spin system is limited by the extent and nature of the scalar coupling to the size of the molecule, whereas in a solid the dipolar coupling can give rise to an essentially infinite network. The aim of the multiple-quantum experiments is to study the size of the dipolar-coupled network through the creation of higher orders of multiple-quantum coherence. This is of value when attempting to characterize an amorphous material with only a low degree of order. For example, in a polymer generated from a methane plasma do the methyl groups present cluster, so

forming a potential defect. Of course this can still be carried out in solution and the highest order of multiple-quantum coherence observed will give the size of the scalar-coupled network. Double-quantum coherence can be readily created from a state of dipolar order⁴⁸⁰ but for higher orders a more sophisticated method is required. Indeed in solids the main problem is the excitation and observation of the higher order coherences because not only does the average intensity per transition decrease rapidly with the number of spins but also the efficiency of the excitation decreases. To excite the higher orders requires longer evolution times during which time the dipole-dipole coupling will dephase the magnetization.⁴⁸¹ If the higher multiple-quantum transitions are to be seen this dephasing must be eliminated—hence time-reversal pulse sequences. Using such a pulse sequence it was possible to observe up to 22 quanta in adamantane when the excitation time was 480 μ s.⁴⁸¹ These ideas were extended to other spin systems, for example hexamethylbenzene and squaric acid, and the increase in the effective system size, or cluster, calculated using a random walk model for the time development of the density operator.⁴⁸² Further thought has been given to the description of the dynamics of the evolution of the multiple-quantum coherence in terms of discrete hops in Liouville space.^{483,484} A plateau in the number of quanta with excitation time consistent with a discrete spin cluster was found for the nematic liquid crystal *p*-cyano, *p*-pentylbiphenyl⁴⁸⁵ while in a practical application of hydrogen clusters in amorphous silicon, evidence was found for discrete clusters at a low hydrogen content becoming a continuous network at very high hydrogen contents.⁴⁸⁶

More recently a refinement of the pulse sequence has been presented involving phase incrementation.⁴⁸⁷ In essence, the phase-incremented experiment differs from the original one by keeping the evolution (excitation) period fixed and incrementing the phase of the preparation pulse in steps of 1° or so. Instrumental stability is crucial to the success of the technique both in the phase shifter and in the absence of phase transients in the multiple-pulse sequences. A key feature is that the lines in the resulting multiple-quantum spectrum are infinitely narrow, thereby enormously improving the signal-to-noise in the spectrum allowing a better spectrum to be obtained in 5 min than in an overnight accumulation using the TPPI sequence. The authors do point out though that the elimination of the multiple-quantum linewidth is not always desirable.

REFERENCES

1. P.J. Bray, S.J. Gravina, D.H. Hintenlang and R.V. Mulkern, *Magn. Reson. Rev.*, 1988, **13**, 263.
2. R.J. Kirkpatrick, *Rev. Mineral.*, 1988, **18**, 341.

3. C.P. Slichter, *Ann. Rev. Phys. Chem.*, 1986, **37**, 25.
4. R.A. Komoroski (ed), *High Resolution NMR Spectroscopy of Synthetic Polymers in Bulk*. VCH Publishers, Florida, 1986.
5. V.D. Fedotov and H. Schneider, *Structure and Dynamics of Bulk Polymers by NMR Methods*. NMR Basic Principles and Progress, Vol. 21. Springer-Verlag, Berlin, 1989.
6. D.R. Bauer, *Prog. Org. Coat.*, 1986, **14**, 45.
7. M.E.A. Cudby, *Proc. Int. Conf. Anal. Appl. Spectrosc.* (ed. C.S. Creaser and A.M.C. Davies), p. 331. Roy. Soc. Chem., London, 1988.
8. N.J. Clayden, *Topics in NMR: Basic Principles and Progress*, to be published.
9. F.A. Bovey, *Makromol. Chem., Macromol. Symp.*, 1988, **20/21**, 105.
10. J.R. Havens and J.L. Koenig, *Appl. Spectr.*, 1983, **37**, 226.
11. R. Voelkel, *Angew. Chem.*, 1988, **100**, 1525.
12. M. Munowitz and A. Pines, *Adv. Chem. Phys.*, 1987, **66**, 1.
13. R.R. Ernst, G. Bodenhausen and A. Wokaun, *Principles of Nuclear Magnetic Resonance in One and Two Dimensions*. Clarendon Press, Oxford, 1987.
14. M. Munowitz, *Coherence and NMR*. John Wiley & Sons, New York, 1988.
15. Panel Discussion of *Proc. Int. Conf. High Temperature Superconductors Physica C*, 1988, **153-155** pt 1, 75-98.
16. J.M. Listerud, S.W. Sinton and G.P. Drobny, *Anal. Chem.*, 1989, **61**, 23a.
17. B.C. Gerstein and C.R. Dybowski, *Transient Techniques in NMR of Solids: An Introduction to Theory and Practice*. Academic Press, Orlando, 1985.
18. C.A. Fyfe, *Solid State NMR For Chemists*. CFC Press, Guelph, 1985.
19. M. Mehring, *Principles of High Resolution NMR in Solids*. Springer-Verlag, Berlin, 1983.
20. N.J. Clayden, *Chem. Scripta*, 1988, **28**, 211.
21. E. Oldfield and R.J. Kirkpatrick, *Science*, 1985, **227**, 1537.
22. B.F. Chmelka and A. Pines, *Science*, 1989, **246**, 71.
23. H.W. Spiess, *Makromol. Chem., Macromol. Symp.*, 1989, **26**, 197.
24. S.J. Opella, P.L. Stewart and K.G. Valentine, *Quart. Rev. Biophys.*, 1987, **19**, 7.
25. D.A. Torchia, *Ann. Rev. Biophys. Bioeng.*, 1984, **13**, 124.
26. R.G. Griffin, *Meth. Enzymol.*, 1981, **72**, 108.
27. G.R. Hatfield and K.R. Carduner, *J. Mater. Sci.*, 1989, **24**, 4209.
28. G. Engelhardt and D. Michel, *High Resolution Solid State NMR of Silicates and Zeolites*. John Wiley & Sons, Chichester, 1987.
29. W. Kuhn, *Angew. Chem.*, 1990, **29**, 1.
30. W.S. Warren (ed.), *Adv. Magn. Reson.*, 1989, **13**.
31. W.S. Warren (ed.), *Adv. Magn. Reson.*, 1990, **14**.
32. J. Clarke and R.H. Koch, *Science*, 1988, **242**, 217.
33. T. Jach, *Appl. Phys. Lett.*, 1976, **28**, 49.
34. L.J. Friedman, A.K.M. Wennberg, S.N. Ytterboe and H.M. Bozier, *Rev. Sci. Instrum.*, 1985, **57**, 410.
35. C. Connor, J. Chang and A. Pines, *Rev. Sci. Instrum.*, 1990, **61**, 1059.
36. C. von Borczyskowski, *Adv. Magn. Reson.*, 1988, **12**, 113.
37. H. Weman, M. Godlewski and B. Monemar, *Phys. Rev. B.*, 1988, **38**, 12525.
38. G. Tastevin, P.J. Nacher, L. Wiesenfeld, M. Leduc and F. Laloe, *J. Phys. France*, 1988, **49**, 1.
39. B.C. Cavenett, *Adv. Phys.*, 1981, **30**, 475.
40. R.J. Knize, Z. Wu and W. Happer, *Adv. Atom. Mol. Phys.*, 1988, **24**, 223.
41. R.F. Haglund, *Chem. Rev.*, 1988, **88**, 697.
42. W. Happer, E. Miron, S. Schaefer, D. Schreiber, W.A. van Wijngaarden and X. Zeng, *Phys. Rev. A*, 1984, **29**, 3092.

43. Z. Wu, W. Happer and J.M. Daniels, *Phys. Rev. Lett.*, 1987, **59**, 1480.
44. M.A. Springvel-Hoet and J. Fraissard, *Chem. Phys. Lett.*, 1989, **154**, 299.
45. T. Ito and J. Fraissard, *J. Chem. Phys.*, 1982, **76**, 5225.
46. O. Gonen and J.S. Waugh, *Physica A*, 1989, **156**, 219.
47. L.J. Friedman, P. Millet and R.C. Richardson, *Phys. Rev. Lett.*, 1981, **47**, 1078.
48. O. Gonen, P.L. Kuhns, C. Zuo and J.S. Waugh, *J. Magn. Reson.*, 1989, **81**, 491.
49. P.C. Hammel, P.L. Kuhns, O. Gonen and J.S. Waugh, *Phys. Rev. B*, 1986, **34**, 6453.
50. P.L. Kuhns, O. Gonen and J.S. Waugh, *J. Magn. Reson.*, 1989, **82**, 231.
51. P.L. Kuhns, O. Gonen and J.S. Waugh, *J. Magn. Reson.*, 1987, **72**, 548.
52. J.S. Waugh, O. Gonen and P.L. Kuhns, *J. Chem. Phys.*, 1987, **86**, 3816.
53. O. Gonen, P.L. Kuhns, J.S. Waugh and J.P. Fraissard, *J. Phys. Chem.*, 1989, **93**, 504.
54. A. Pines, M.G. Gibby and J.S. Waugh, *J. Chem. Phys.*, 1973, **59**, 569.
55. A.G. Anderson and S.R. Hartmann, *Phys. Rev.*, 1960, **128**, 2023.
56. S.R. Hartmann and E.L. Hahn, *Phys. Rev.*, 1960, **128**, 2042.
57. R.A. Wind and C.S. Yannoni, *J. Magn. Reson.*, 1986, **68**, 373.
58. M. Goldman, *Spin Temperature and Nuclear Magnetic Resonance in Solids*. Oxford University Press, London, 1961.
59. M.H. Levitt, D. Suter and R.R. Ernst, *J. Chem. Phys.*, 1986, **84**, 4243.
60. S. Zhang and X. Wu, *Chem. Phys. Lett.*, 1989, **156**, 333.
61. S. Zhang, X. Wu and M. Mehring, *Chem. Phys. Lett.*, 1990, **166**, 92.
62. W. Xiaoling, Z. Shanmin and W. Xuewen, *Phys. Rev. B*, 1988, **37**, 9827.
63. X. Wu, S. Zhang and X. Wu, *J. Magn. Reson.*, 1988, **77**, 343.
64. M.T. Melchior, Poster B-29, 22nd Experimental NMR Conference, Asilomar, 1981.
65. D.G. Cory, *Chem. Phys. Lett.*, 1988, **152**, 431.
66. X. Wu and S. Zhang, *Chem. Phys. Lett.*, 1989, **156**, 79.
67. S.J. Opella and M.H. Frey, *J. Am. Chem. Soc.*, 1979, **101**, 5854.
68. D.G. Cory and W.M. Ritchey, *Macromolecules*, 1989, **22**, 1611.
69. J.S. Hartman and J.A. Ripmeester, *Chem. Phys. Lett.*, 1990, **168**, 219.
70. R.C. Crosby, R.L. Reese and J.F. Haw, *J. Am. Chem. Soc.*, 1988, **110**, 8550.
71. T.G. Neiss and J.E. Roberts, *J. Magn. Reson.*, 1990, **89**, 605.
72. M. Mehring, *Principles of High Resolution NMR in Solids*, 2nd Edn, p.151. Springer-Verlag, Berlin, 1983.
73. L.B. Alemany, D.M. Grant, R.J. Pugmire, T.D. Alger and K.W. Zilm, *J. Am. Chem. Soc.*, 1983, **105**, 2133.
74. R.H. Newman, *J. Magn. Reson.*, 1987, **72**, 337.
75. R.K. Harris, *Analyst*, 1985, **110**, 649.
76. L. Jelinski and M. Melchior, *NMR Spectroscopy Techniques* (ed. C.R. Dybowski and R. Lichter), Chap. 6. Dekker, New York, 1987.
77. N. Zumbulyadis and J.M. O'Reilly, *J. Magn. Reson.*, 1989, **82**, 613.
78. R.A. Wind and C.S. Yannoni, *J. Magn. Reson.*, 1987, **72**, 108.
79. J. Schaefer, E.O. Stejskal, J.R. Garbow and R.A. McKay, *J. Magn. Reson.*, 1984, **59**, 150.
80. R.A. Wind, M.J. Duijvestijn, C. van der Lugt, A. Manenschijn and J. Vriend, *Prog. NMR Spectrosc.*, 1985, **17**, 33.
81. M.J. Duijvestijn, A. Manenschijn, J. Smidt and R.A. Wind, *J. Magn. Reson.*, 1985, **64**, 461.
82. R.A. Wind, L. Li, H. Lock and G.E. Maciel, *J. Magn. Reson.*, 1988, **79**, 577.
83. E. Brunner, D. Freude, B.C. Gerstein and H. Pfeiffer, *J. Magn. Reson.*, 1990, **90**, 90.
84. S.F. Dec, R.A. Wind, G.E. Maciel and F.E. Anthonio, *J. Magn. Reson.*, 1986, **70**, 355.
85. B.C. Gerstein, *Phil. Trans. R. Soc. (Lond.)*, 1981, **A299**, 521.
86. R.K. Harris, P. Jackson and G.J. Nesbitt, *J. Magn. Reson.*, 1989, **85**, 294.
87. C.E. Bronnimann, B.L. Hawkins, M. Zhang and G.E. Maciel, *Anal. Chem.*, 1988, **60**, 1743.

88. S.F. Dec, R.A. Wind and G.E. Maciel, *Macromolecules*, 1987, **20**, 2754.
89. Doty Scientific Inc., 600 Clemson Road, Columbia, SC 29223, USA.
90. S.F. Dec, C.E. Bronnimann, R.A. Wind and G.E. Maciel, *J. Magn. Reson.*, 1989, **82**, 454.
91. D.L. VanderHart, W.L. Earl and A.N. Garroway, *J. Magn. Reson.*, 1981, **44**, 361.
92. R.K. Harris, P. Jackson, P.J. Wilkes and P.S. Belton, *J. Magn. Reson.*, 1987, **73**, 178.
93. W.T. Dixon, *J. Chem. Phys.*, 1982, **77**, 1800.
94. W.T. Dixon, J. Schaefer, E.O. Stejskal and R.A. McKay, *J. Magn. Reson.*, 1982, **49**, 341.
95. D.P. Raleigh, E.T. Olejniczak, S. Vega and R.G. Griffin, *J. Magn. Reson.*, 1987, **72**, 238.
96. W.T. Dixon, *J. Magn. Reson.*, 1985, **64**, 332.
97. N.C. Neilson, H. Bildsoe and H.J. Jakobsen, *J. Magn. Reson.*, 1988, **80**, 149.
98. D.P. Raleigh, A.C. Kolbert and R.G. Griffin, *J. Magn. Reson.*, 1990, **89**, 1.
99. W.P. Aue, D.J. Ruben and R.G. Griffin, *J. Chem. Phys.*, 1984, **80**, 1729.
100. D.P. Raleigh, E.T. Olejniczak, S. Vega and R.G. Griffin, *J. Am. Chem. Soc.*, 1984, **106**, 8302.
101. S. Vega, E.T. Olejniczak and R.G. Griffin, *J. Chem. Phys.*, 1984, **80**, 4832.
102. R.A. Wind, S.F. Dec, H. Lock and G.E. Maciel, *J. Magn. Reson.*, 1988, **79**, 136.
103. M. Sardashti and G.E. Maciel, *J. Magn. Reson.*, 1987, **72**, 467.
104. P. DuBois Murphy, *J. Magn. Reson.*, 1986, **70**, 307.
105. A.C. Kolbert, D.P. Raleigh, R.G. Griffin and M.H. Levitt, *J. Magn. Reson.*, 1990, **89**, 133.
106. K.W. Zilm, R.A. Merrill, M.M. Greenberg and J.A. Berson, *J. Am. Chem. Soc.*, 1987, **109**, 1567.
107. C.S. Yannoni, T.C. Clarke, R.D. Kendrick, V. Macho, R.D. Miller and P.C. Myhre, *Mol. Cryst. Liq. Cryst.*, 1983, **96**, 305.
108. A. Hackmann, H. Seidel, R.D. Kendrick, P.C. Myhre and C.S. Yannoni, *J. Magn. Reson.*, 1988, **79**, 148.
109. M. Zhang and G.E. Maciel, *J. Magn. Reson.*, 1989, **85**, 156.
110. L.J. Mathias, D.G. Powell and J.L. Bridges, *J. Magn. Reson.*, 1988, **77**, 566.
111. L.H. Merwin, A. Sebald, J.E. Espidel and R.K. Harris, *J. Magn. Reson.*, 1989, **84**, 367.
112. M.H. Levitt, *J. Magn. Reson.*, 1989, **82**, 427.
113. M.M. Maricq and J.S. Waugh, *J. Chem. Phys.*, 1979, **70**, 3300.
114. G.S. Harbison and H.W. Spiess, *Chem. Phys. Lett.*, 1986, **124**, 128.
115. G.S. Harbison, V.-D. Vogt and H.W. Spiess, *J. Chem. Phys.*, 1987, **86**, 1206.
116. W.S. Veeman, *Prog. NMR Spectrosc.*, 1984, **16**, 193.
117. C.M. Carter, D.W. Alderman and D.M. Grant, *J. Magn. Reson.*, 1987, **73**, 114.
118. M.H. Sherwood, D.W. Alderman and D.M. Grant, *J. Magn. Reson.*, 1989, **84**, 466.
119. C.M. Carter, J.C. Facelli, D.W. Alderman, D.M. Grant, N.K. Dalley and B.E. Wilson, *J. Chem. Soc., Faraday Trans. 1*, 1988, **84**, 3673.
120. N. Bloembergen and T.J. Rowland, *Acta Metal.*, 1955, **1**, 731.
121. T.G. Oas, G.P. Drobny and F.W. Dahlquist, *J. Magn. Reson.*, 1988, **78**, 408.
122. D.W. Alderman, M.S. Solum and D.G. Grant, *J. Chem. Phys.*, 1986, **84**, 3717.
123. J. Herzfeld and A.E. Berger, *J. Chem. Phys.*, 1980, **73**, 6021.
124. H.J. Jacobsen, P.D. Ellis, R.R. Inners and C.F. Jensen, *J. Am. Chem. Soc.*, 1982, **104**, 7442.
125. N.J. Clayden, C.M. Dobson, L.-Y. Lian and D.J. Smith, *J. Magn. Reson.*, 1986, **69**, 476.
126. J. Herzfeld, J.E. Roberts and R.G. Griffin, *J. Chem. Phys.*, 1987, **86**, 597.
127. A. Nayeem and J.P. Yesinowski, *J. Chem. Phys.*, 1988, **89**, 4600.
128. D. Frenze, D. Maess and H. Pfeiffer, *J. Magn. Reson.*, 1990, **88**, 172.
129. E.O. Stejskal, J. Schaefer and R.A. McKay, *J. Magn. Reson.*, 1977, **25**, 569.
130. S.J. Opella and M.H. Frey, *J. Am. Chem. Soc.*, 1979, **101**, 5854.
131. E.M. Menger, D.P. Raleigh and R.G. Griffin, *J. Magn. Reson.*, 1985, **63**, 579.
132. R.C. Zeigler, R.A. Wind and G.E. Maciel, *J. Magn. Reson.*, 1988, **79**, 299.

133. A. Bax, N.M. Szeverenyi and G.E. Maciel, *J. Magn. Reson.*, 1983, **52**, 147.
134. N.M. Szeverenyi, A. Bax and G.E. Maciel, *J. Magn. Reson.*, 1985, **61**, 440.
135. A. Bax, N.M. Szeverenyi and G.E. Maciel, *J. Magn. Reson.*, 1983, **55**, 494.
136. G.E. Maciel, N.M. Szeverenyi and M. Sardashti, *J. Magn. Reson.*, 1985, **64**, 365.
137. T. Terao, T. Fujii, T. Onodera and A. Saika, *Chem. Phys. Lett.*, 1984, **107**, 145.
138. J. Ashida, T. Nakai and T. Terao, *Chem. Phys. Lett.*, 1990, **168**, 523.
139. J.H. Iwamiya, M.F. Davis and G.E. Maciel, *J. Magn. Reson.*, 1990, **88**, 199.
140. M.A. Alla, E.I. Kundla and E. Lippmaa, *JETP Lett.*, 1978, **27**, 194.
141. Y. Yarim-Agaev, P.N. Tutunjian and J.S. Waugh, *J. Magn. Reson.*, 1982, **47**, 51.
142. A. Bax, N.M. Szeverenyi and G.E. Maciel, *J. Magn. Reson.*, 1983, **51**, 400.
143. A.C. Kolbert, D.P. Raleigh and R.G. Griffin, *J. Magn. Reson.*, 1989, **82**, 483.
144. D.P. Raleigh, A.C. Kolbert, T.G. Oas, M.H. Levitt and R.G. Griffin, *J. Chem. Soc., Faraday Trans. 1*, 1988, **84**, 3691.
145. E.T. Olejniczak, S. Vega and R.G. Griffin, *J. Chem. Phys.*, 1984, **81**, 4804.
146. D.P. Raleigh, E.T. Olejniczak and R.G. Griffin, *J. Chem. Phys.*, 1988, **89**, 1333.
147. R. Tycko, G. Dabbagh and P.A. Mirau, *J. Magn. Reson.*, 1989, **85**, 265.
148. Z.-H. Gan and D.M. Grant, *Chem. Phys. Lett.*, 1990, **168**, 304.
149. A.C. Kolbert and R.G. Griffin, *Chem. Phys. Lett.*, 1990, **166**, 87.
150. A.C. Kolbert, D.P. Raleigh, M.H. Levitt and R.G. Griffin, *J. Chem. Phys.*, 1989, **90**, 679.
151. T. Gullion, *J. Magn. Reson.*, 1989, **85**, 614.
152. A.C. Kolbert, H.J.M. de Groot and R.G. Griffin, *J. Magn. Reson.*, 1989, **85**, 60.
153. H.J.M. de Groot, V. Copie, S.O. Smith, P.J. Allen, C. Winkel, J. Lugtenburg, J. Herzfeld and R.G. Griffin, *J. Magn. Reson.*, 1988, **77**, 251.
154. N.J. Clayden, C.A. O'Mahoney and D. Williams, *J. Chem. Soc., Perkins Trans. 2*, 1990, 729.
155. M.L. Martin, J.-J. Delpuech and G.J. Martin, *Practical NMR Spectroscopy*. Heyden, London, 1980.
156. D. Wemmer, D.J. Ruben and A. Pines, *J. Am. Chem. Soc.*, 1981, **103**, 28.
157. A.K. Roy, A.A. Jones and P.T. Inglefield, *J. Magn. Reson.*, 1985, **64**, 441.
158. D. Suwelack, W.P. Rothwell and J.S. Waugh, *J. Chem. Phys.*, 1980, **73**, 2559.
159. A. Schmidt, S.O. Smith, D.P. Raleigh, J.E. Roberts, R.G. Griffin and S. Vega, *J. Chem. Phys.*, 1986, **85**, 4248.
160. A. Schmidt and S. Vega, *Chem. Phys. Lett.*, 1989, **157**, 539.
161. L. Frydman and B. Frydman, *Magn. Reson. Chem.*, 1990, **28**, 355.
162. A. Schmidt and S. Vega, *J. Chem. Phys.*, 1987, **87**, 6895.
163. H. Edzes and J.P.C. Bernards, *J. Am. Chem. Soc.*, 1984, **106**, 1515.
164. J.M. Twyman and C.M. Dobson, *Magn. Reson. Chem.*, 1990, **28**, 163.
165. C. Connor, A. Naito, K. Takegoshi and C.A. McDowell, *Chem. Phys. Lett.*, 1985, **113**, 123.
166. M.H. Frey and S.J. Opella, *J. Am. Chem. Soc.*, 1984, **106**, 4942.
167. H.H. Limbach, B. Wehrle, M. Schlabach, R. Kendrick and C.S. Yannoni, *J. Magn. Reson.*, 1988, **77**, 84.
168. A.F. de Jong, A.P.M. Kentgens and W.S. Veeman, *Chem. Phys. Lett.*, 1984, **109**, 337.
169. A.P.M. Kentgens, A.F. de Jong, E. de Boer and W.S. Veeman, *Macromolecules*, 1985, **18**, 1045.
170. A.P.M. Kentgens, E. de Boer and W.S. Veeman, *J. Chem. Phys.*, 1987, **87**, 6859.
171. G.S. Harbison, D.P. Raleigh, J. Herzfeld and R.G. Griffin, *J. Magn. Reson.*, 1985, **64**, 284.
172. B. Blumich and A. Hagemeyer, *Chem. Phys. Lett.*, 1989, **161**, 55.
173. Y. Yang, M. Schuster, B. Blumich and H.W. Spiess, *Chem. Phys. Lett.*, 1987, **139**, 239.
174. Y. Yang, A. Hagemeyer, B. Blumich and H.W. Spiess, *Chem. Phys. Lett.*, 1988, **150**, 1.
175. Y. Yang, A. Hagemeyer and H.W. Spiess, *Macromolecules*, 1989, **22**, 1004.
176. A.E. Derome, *Modern NMR Techniques for Chemistry Research*. Pergamon, Oxford, 1987.

177. L. Muller, A. Kumar and R.R. Ernst, *J. Chem. Phys.*, 1975, **63**, 5490.
178. R. Benn, H. Grondey, C. Brevard and A. Pagelot, *J. Chem. Soc., Chem. Commun.*, 1988, 102.
179. C.A. Fyfe, H. Gies and Y. Feng, *J. Chem. Soc., Chem. Commun.*, 1989, 1240.
180. C.A. Fyfe, H. Gies, Y. Feng and G.T. Kokotailo, *Nature*, 1989, **341**, 223.
181. T. Allman, *J. Magn. Reson.*, 1989, **83**, 637.
182. P. Caravatti, G. Bodenhausen and R.R. Ernst, *Chem. Phys. Lett.*, 1982, **89**, 363.
183. P. Caravatti, L. Braunschweiler and R.R. Ernst, *Chem. Phys. Lett.*, 1983, **100**, 305.
184. J.E. Roberts, S. Vega and R.G. Griffin, *J. Am. Chem. Soc.*, 1984, **106**, 2506.
185. A.J. Vega, *J. Am. Chem. Soc.*, 1988, **110**, 1049.
186. G.E. Pake, *J. Chem. Phys.*, 1948, **16**, 327.
187. J.H. Van Vleck, *Phys. Rev.*, 1948, **74**, 1168.
188. J.G. Powles and P. Mansfield, *Phys. Lett.*, 1962, **2**, 58.
189. S. Zhang and X. Wu, *Chem. Phys. Lett.*, 1989, **156**, 82.
190. E. Brunner, D. Frenze, D. Freude and H. Pfeiffer, *Chem. Phys. Lett.*, 1990, **169**, 591.
191. A. Kubo and C.A. McDowell, *J. Chem. Phys.*, 1990, **92**, 7156.
192. L.R. Sarles and R.M. Cotts, *Phys. Rev.*, 1958, **111**, 853.
193. D.E. Demco, J. Tegenfeldt and J.S. Waugh, *Phys. Rev. B*, 1975, **11**, 4133.
194. A.N. Garroway, W.B. Moniz and H.A. Resing, *ACS Symp. Ser.*, 1979, **103**, 67.
195. A.N. Garroway, D.L. VanderHart and W.L. Earl, *Phil. Trans. R. Soc. (Lond.)*, 1981, **A299**, 609.
196. K. Takegoshi and C.A. McDowell, *J. Magn. Reson.*, 1986, **66**, 14.
197. A. Bax, T.E. Early and G.E. Maciel, *J. Magn. Reson.*, 1982, **52**, 35.
198. M.G. Munowitz, T.H. Huang, C.M. Dobson and R.G. Griffin, *J. Magn. Reson.*, 1984, **57**, 56.
199. U. Haeberlen, *High Resolution NMR in Solids: Selective Averaging*, Adv. Magn. Reson. Ser., Suppl. 1, (ed. J.S. Waugh). Academic Press, New York, 1976.
200. J.S. Waugh, L.M. Huber and U. Haeberlen, *Phys. Rev. Lett.*, 1968, **20**, 180.
201. P. Mansfield, *J. Phys., C*, 1971, **4**, 1444.
202. W.K. Rhim, D.D. Elleman and R.W. Vaughan, *J. Chem. Phys.*, 1973, **58**, 1772.
203. D.P. Burum and W.K. Rhim, *J. Chem. Phys.*, 1979, **71**, 944.
204. D.P. Burum and W.K. Rhim, *J. Chem. Phys.*, 1979, **70**, 3553.
205. D.P. Burum, M. Linder and R.R. Ernst, *J. Magn. Reson.*, 1981, **44**, 173.
206. K. Takegoshi and C.A. McDowell, *Chem. Phys. Lett.*, 1985, **116**, 100.
207. W.K. Rhim, A. Pines and J.S. Waugh, *Phys. Rev. B*, 1971, **3**, 684.
208. D.L. Mui, B.M. Fung, I.R. Bonnell and E.L. Enwall, *J. Magn. Reson.*, 1985, **64**, 124.
209. K.V. Schenker, D. Suter and A. Pines, *J. Magn. Reson.*, 1987, **73**, 99.
210. D. Suter, A. Pines, J.H. Lee and G. Drobny, *Chem. Phys. Lett.*, 1988, **144**, 324.
211. T.K. Pratum, *J. Magn. Reson.*, 1990, **88**, 384.
212. T. Terao, H. Miura and A. Saika, *J. Chem. Phys.*, 1981, **75**, 1573.
213. H. Miura, T. Terao and A. Saika, *J. Magn. Reson.*, 1986, **68**, 593.
214. K.W. Zilm and D.M. Grant, *J. Magn. Reson.*, 1982, **48**, 524.
215. A.P.M. Kentgens, W.S. Veeman and J. Van Bree, *Macromolecules*, 1987, **20**, 1234.
216. H. Bildsoe, S. Donstrup, H.J. Jakobsen and O.W. Sorensen, *J. Magn. Reson.*, 1983, **53**, 154.
217. N.C. Nielsen, H. Bildsoe, H.J. Jakobsen and O.W. Sorensen, *J. Magn. Reson.*, 1988, **79**, 554.
218. M. Lee and W.I. Goldberg, *Phys. Rev.*, 1965, **140**, 1261.
219. A. Bielecki, A.C. Kolbert and M.H. Levitt, *Chem. Phys. Lett.*, 1989, **155**, 341.
220. R.K. Hester, J.L. Ackerman, B.L. Neff and J.S. Waugh, *Phys. Rev. Lett.*, 1976, **36**, 1081.
221. S. Opella and J.S. Waugh, *J. Chem. Phys.*, 1977, **66**, 4919.

222. M.E. Stoll, A.J. Vega and R.W. Vaughan, *J. Chem. Phys.*, 1976, **65**, 4093.
223. M. Linder, A. Hohener and R.R. Ernst, *J. Chem. Phys.*, 1980, **73**, 4959.
224. R.K. Harris, K.J. Packer and A.M. Thayer, *J. Magn. Reson.*, 1985, **62**, 284.
225. M.G. Munowitz, R.G. Griffin, G. Bodenhausen and T.H. Huang, *J. Am. Chem. Soc.*, 1981, **103**, 2529.
226. M.G. Munowitz and R.G. Griffin, *J. Chem. Phys.*, 1982, **76**, 2848.
227. M.H. Frey, J.A. DiVerdi and S.J. Opella, *J. Am. Chem. Soc.*, 1985, **107**, 7311.
228. M.G. Munowitz and R.G. Griffin, *J. Chem. Phys.*, 1983, **78**, 613.
229. J. Schaefer, E.O. Stejskal, R.A. McKay and W.T. Dixon, *Macromolecules*, 1984, **17**, 1479.
230. M.G. Munowitz, W.P. Aue and R.G. Griffin, *J. Chem. Phys.*, 1982, **77**, 1686.
231. T.A. Early, *J. Magn. Reson.*, 1987, **75**, 129.
232. A.C. Kolbert, M.H. Levitt and R.G. Griffin, *J. Magn. Reson.*, 1989, **85**, 42.
233. G.C. Webb and K.W. Zilm, *J. Am. Chem. Soc.*, 1989, **111**, 2455.
234. H. Miura, T. Terao and A. Saika, *J. Chem. Phys.*, 1986, **85**, 2458.
235. T. Terao, H. Miura and A. Saika, *J. Chem. Phys.*, 1986, **85**, 3816.
236. T. Nakai, J. Ashida and T. Terao, *J. Chem. Phys.*, 1988, **88**, 6049.
237. T. Nakai, T. Terao and H. Shirakawa, *Chem. Phys. Lett.*, 1988, **145**, 90.
238. T. Nakai, J. Ashida and T. Terao, *Magn. Reson. Chem.*, 1988, **27**, 666.
239. J.B. Boyce, Thesis, University of Illinois, 1972.
240. P.-K. Wang, C.P. Slichter and J.H. Sinfelt, *Phys. Rev. Lett.*, 1984, **53**, 82.
241. S.E. Shore, J.P. Ansermet, C.P. Slichter and J.H. Sinfelt, *Phys. Rev. Lett.*, 1987, **58**, 953.
242. T.G. Oas, C.J. Hartzell, T.J. McMahon, G.P. Drobny and F.W. Dahlquist, *J. Am. Chem. Soc.*, 1987, **109**, 5956.
243. T.G. Oas, C.J. Hartzell, G.P. Drobny and F.W. Dahlquist, *J. Magn. Reson.*, 1989, **81**, 395.
244. C.J. Hartzell, T.K. Pratum and G.P. Drobny, *J. Chem. Phys.*, 1987, **87**, 4324.
245. D.M. Schneider, R. Tycko and S.J. Opella, *J. Magn. Reson.*, 1987, **73**, 568.
246. T. Gullion and J. Schaefer, *J. Magn. Reson.*, 1989, **81**, 196.
247. S.M. Holl, R.A. McKay, T. Gullion and J. Schaefer, *J. Magn. Reson.*, 1990, **89**, 620.
248. T. Gullion, M.D. Poliks and J. Schaefer, *J. Magn. Reson.*, 1988, **80**, 553.
249. V. Bork, T. Gullion, A. Hing and J. Schaefer, *J. Magn. Reson.*, 1990, **88**, 523.
250. E.R. Andrew, A. Bradbury, R.G. Eades and V.T. Wynn, *Phys. Lett.*, 1963, **4**, 99.
251. E.R. Andrew, S. Clough, L.F. Farnell, T.D. Gledhill and I. Roberts, *Phys. Lett.*, 1966, **21**, 505.
252. D.P. Raleigh, G.S. Harbison, T.G. Neiss, J.E. Roberts and R.G. Griffin, *Chem. Phys. Lett.*, 1987, **138**, 285.
253. M.G. Columbo, B.H. Meier and R.R. Ernst, *Chem. Phys. Lett.*, 1988, **146**, 189.
254. W.E.J.R. Maas and W.S. Veeman, *Chem. Phys. Lett.*, 1988, **149**, 170.
255. D.P. Raleigh, M.H. Levitt and R.G. Griffin, *Chem. Phys. Lett.*, 1988, **146**, 71.
256. M.H. Levitt, D.P. Raleigh, F. Creuzet and R.G. Griffin, *J. Chem. Phys.*, 1990, **92**, 6347.
257. D.P. Raleigh, F. Creuzet, S.K. Das Gupta, M.H. Levitt and R.G. Griffin, *J. Am. Chem. Soc.*, 1989, **111**, 4502.
258. T.G. Oas, R.G. Griffin and M.H. Levitt, *J. Chem. Phys.*, 1988, **89**, 692.
259. D.P. Raleigh, A.C. Kolbert, T.G. Oas, M.H. Levitt and R.G. Griffin, *J. Chem. Soc., Faraday Trans. 1*, 1988, **84**, 3691.
260. M.H. Levitt, T.G. Oas and R.G. Griffin, *Isr. J. Chem.*, 1989, **28**, 271.
261. C.S. Yannoni and R.D. Kendrick, *J. Chem. Phys.*, 1982, **74**, 747.
262. D. Horne, R.D. Kendrick and C.S. Yannoni, *J. Magn. Reson.*, 1983, **52**, 299.
263. H.Y. Carr and E.M. Purcell, *Phys. Rev.*, 1954, **94**, 630.
264. M. Engelsberg and C.S. Yannoni, *J. Magn. Reson.*, 1990, **88**, 393.
265. N. Bloembergen, *Physica*, 1949, **15**, 95.

266. A. Kubo and C.A. McDowell, *J. Chem. Phys.*, 1988, **89**, 63.
267. D.L. VanderHart, *J. Magn. Reson.*, 1987, **72**, 13.
268. A. Abragam, *The Principles of Nuclear Magnetism*. Oxford University Press, Oxford, 1961.
269. N.J. Clayden, *J. Magn. Reson.*, 1986, **68**, 360.
270. P. Robyr, B.H. Meier and R.R. Ernst, *Chem. Phys. Lett.*, 1989, **162**, 417.
271. P.M. Henrichs, M. Linder and J.M. Hewitt, *J. Chem. Phys.*, 1986, **86**, 7077.
272. D. Suter and R.R. Ernst, *Phys. Rev. B*, 1982, **25**, 6038.
273. D. Suter and R.R. Ernst, *Phys. Rev. B*, 1985, **32**, 5608.
274. N.M. Szevenyi, M.J. Sullivan and G.E. Maciel, *J. Magn. Reson.*, 1982, **47**, 462.
275. D.L. VanderHart and A.N. Garroway, *J. Chem. Phys.*, 1979, **71**, 2773.
276. A. Kubo and C.A. McDowell, *J. Chem. Soc., Faraday Trans. 1*, 1988, **84**, 3713.
277. S. Hayashi and K. Hayamizu, *Chem. Phys. Lett.*, 1989, **161**, 158.
278. J. Jeneer, B.H. Meier, P. Bachman and R.R. Ernst, *J. Chem. Phys.*, 1979, **71**, 4546.
279. G. Bodenhausen, R. Freeman and G.A. Morris, *J. Magn. Reson.*, 1976, **23**, 171.
280. P. Caravatti, G. Bodenhausen and R.R. Ernst, *J. Magn. Reson.*, 1983, **55**, 88.
281. P. Caravatti, M.H. Levitt and R.R. Ernst, *J. Magn. Reson.*, 1986, **68**, 323.
282. V. Bork and J. Schaefer, *J. Magn. Reson.*, 1988, **78**, 348.
283. M.H. Frey and S.J. Opella, *J. Am. Chem. Soc.*, 1984, **106**, 4942.
284. P. Caravatti, J.A. Deli, G. Bodenhausen and R.R. Ernst, *J. Am. Chem. Soc.*, 1982, **104**, 5506.
285. P. Caravatti, P. Neuenschwander and R.R. Ernst, *Macromolecules* 1985, **18**, 119.
286. K. Takegoshi and C.A. McDowell, *J. Chem. Phys.*, 1986, **84**, 2084.
287. K.M. Morden and S.J. Opella, *J. Magn. Reson.*, 1986, **70**, 476.
288. D.C. Douglass and G.P. Jones, *J. Chem. Phys.*, 1966, **45**, 956.
289. V.J. McBrierty and D.C. Douglass, *J. Polym. Sci. Macromol. Rev.*, 1981, **16**, 295.
290. M. Goldman and L. Shen, *Phys. Rev.*, 1966, **144**, 321.
291. S. Zhang and M. Mehring, *Chem. Phys. Lett.*, 1989, **160**, 644.
292. R. Stannarius and H. Schmiedel, *J. Magn. Reson.*, 1989, **81**, 339.
293. T.T.P. Cheung, B.C. Gerstein, L.M. Ryan, R.E. Taylor and C.R. Dybowski, *J. Chem. Phys.*, 1980, **73**, 6059.
294. K.J. Packer, I.J.F. Poplett and M.J. Taylor, *J. Chem. Soc., Faraday Trans. 1*, 1988, **84**, 3851.
295. J.R. Havens and D.L. VanderHart, *Macromolecules*, 1985, **18**, 1663.
296. H. Tanaka and T. Nishi, *Phys. Rev. B*, 1986, **33**, 32.
297. K.J. Packer, J.M. Pope, R.R. Yeung and M.E.A. Cudby, *J. Polym. Sci. Polym. Phys. Ed.*, 1984, **22**, 589.
298. D.L. VanderHart, *Makromol. Chem. Macromol. Symp.*, 1990, **34**, 125.
299. K. Schmidt-Rohr, J. Claus, B. Blumich and H.W. Spiess, *Poly. Prepr. (Am. Chem. Soc. Div. Polym. Chem.)*, 1990, **31**, 172.
300. W.P. Power, R.E. Wasylishen, S. Mooibroek, B.A. Pettit and W. Danchura, *J. Phys. Chem.*, 1990, **94**, 591.
301. B.F. Chmelka, K.T. Mueller, A. Pines, J. Stebbins, Y. Wu and J.W. Zwanziger, *Nature*, 1989, **339**, 42.
302. R. Tycko, P.L. Stewart and S.J. Opella, *J. Am. Chem. Soc.*, 1986, **108**, 5419.
303. R.K. Harris and G.J. Nesbitt, *J. Magn. Reson.*, 1988, **78**, 245.
304. H.D. Morris and P.D. Ellis, *J. Am. Chem. Soc.*, 1989, **111**, 6045.
305. T.M. Walter and E. Oldfield, *J. Phys. Chem.*, 1989, **93**, 6744.
306. J.G. Hexem, M.H. Frey and S.J. Opella, *J. Am. Chem. Soc.*, 1981, **103**, 224.
307. E.M. Menger and W.S. Veeman, *J. Magn. Reson.*, 1982, **46**, 257.
308. R.K. Harris, *J. Magn. Reson.*, 1988, **78**, 389.

309. D.C. Apperley, B. Haiping and R.K. Harris, *Mol. Phys.*, 1989, **68**, 1277.
310. D.L. Sastry, A. Naito and C.A. McDowell, *Chem. Phys. Lett.*, 1988, **146**, 422.
311. J.G. Hexem, M.H. Frey and S.J. Opella, *J. Chem. Phys.*, 1982, **77**, 3847.
312. A.C. Olivieri, L. Frydman and L.E. Diaz, *J. Magn. Reson.*, 1988, **75**, 50.
313. A.C. Olivieri, L. Frydman, M. Grasselli and L.E. Diaz, *Magn. Reson. Chem.*, 1988, **26**, 615.
314. A.C. Olivieri, L. Frydman, M. Grasselli and L.E. Diaz, *Magn. Reson. Chem.*, 1988, **26**, 281.
315. A.C. Olivieri, *J. Magn. Reson.*, 1989, **81**, 201.
316. P. Jonsen, *J. Magn. Reson.*, 1989, **83**, 663.
317. A.C. Olivieri, *J. Magn. Reson.*, 1989, **82**, 342.
318. A. Samoson, *Chem. Phys. Lett.*, 1985, **119**, 29.
319. E. Lippmaa, A. Samoson and M. Magi, *J. Am. Chem. Soc.*, 1986, **108**, 1730.
320. H.J. Jakobsen, J. Skibsted, H. Bildsoe and N.C. Nielsen, *J. Magn. Reson.*, 1989, **85**, 173.
321. N.J. Clayden, *Chem. Phys. Lett.*, 1986, **131**, 517.
322. C. Ye, B. Sun and G.E. Maciel, *J. Magn. Reson.*, 1986, **70**, 241.
323. E. Kundla, A. Samoson and E. Lippmaa, *Chem. Phys. Lett.*, 1981, **83**, 229.
324. H.J. Behrens and B. Schnabel, *Physica B*, 1982, **114**, 185.
325. A. Samoson, E. Kundla and E. Lippmaa, *J. Magn. Reson.*, 1982, **49**, 350.
326. S. Ganapathy, S. Schramm and E. Oldfield, *J. Chem. Phys.*, 1982, **77**, 4360.
327. S.F. Dec and G.E. Maciel, *J. Magn. Reson.*, 1990, **87**, 153.
328. S. Ganapathy, J. Shore and E. Oldfield, *Chem. Phys. Lett.*, 1990, **169**, 301.
329. J. Haase and H. Pfeifer, *J. Magn. Reson.*, 1990, **86**, 217.
330. J. Haase, D. Freude, H. Pfeifer, E. Lippmaa and P. Sarv, *Chem. Phys. Lett.*, 1988, **152**, 254.
331. A.C. Kunwar, G.L. Turner and E. Oldfield, *J. Magn. Reson.*, 1986, **69**, 124.
332. E. Oldfield, H.K.C. Timkin, B. Montez and R. Ramachandran, *Nature*, 1986, **318**, 163.
333. A. Samoson, E. Lippmaa and A. Pines, *Mol. Phys.*, 1988, **65**, 1013.
334. A. Samoson and A. Pines, *Rev. Sci. Instrum.*, 1989, **60**, 3239.
335. A. Llor and J. Virlet, *Chem. Phys. Lett.*, 1988, **152**, 248.
336. Y. Wu, B.F. Chmelka, A. Pines, M.E. Davis, P.J. Grobet and P.A. Jacobs, *Nature*, 1990, **346**, 550.
337. A. Samoson and E. Lippmaa, *J. Magn. Reson.*, 1989, **84**, 410.
338. P.P. Man, *J. Magn. Reson.*, 1986, **67**, 78.
339. A. Samoson and E. Lippmaa, *Phys. Rev. B*, 1983, **28**, 6567.
340. A. Samoson and E. Lippmaa, *Chem. Phys. Lett.*, 1983, **100**, 205.
341. F.M.M. Geurts, A.P.M. Kentgens and W.S. Veeman, *Chem. Phys. Lett.*, 1985, **120**, 206.
342. A.P.M. Kentgens, K.F.M.G.J. Scholle and W.S. Veeman, *J. Phys. Chem.*, 1983, **87**, 4357.
343. A. Samoson and E. Lippmaa, *J. Magn. Reson.*, 1988, **79**, 255.
344. A.P.M. Kentgens, J.J.M. Lemmens, F.M.M. Geurts and W.S. Veeman, *J. Magn. Reson.*, 1987, **71**, 62.
345. H. Hamdan and J. Klinowski, *J. Chem. Soc. Chem. Commun.*, 1989, 240.
346. G. Engelhardt, J.C. Buhl, J. Felsche and H. Forster, *Chem. Phys. Lett.*, 1988, **153**, 3332.
347. G.-Y. Li and X.-W. Wu, *Chem. Phys. Lett.*, 1990, **168**, 518.
348. R. Janssen, G.A.H. Tjink and W.S. Veeman, *J. Chem. Phys.*, 1988, **88**, 518.
349. P.P. Man, *Mol. Phys.*, 1990, **69**, 337.
350. P.P. Man, *Chem. Phys. Lett.*, 1990, **168**, 227.
351. J.A.S. Smith, *Chem. Soc. Rev.*, 1986, **15**, 225.
352. G. Bodenhausen, R.E. Stark, D.J. Ruben and R.G. Griffin, *Chem. Phys. Lett.*, 1979, **67**, 424.
353. R. Tycko and S.J. Opella, *J. Am. Chem. Soc.*, 1986, **108**, 3531.
354. M. Bloom and M.A. Legros, *Can. J. Phys.*, 1986, **64**, 1522.
355. R. Tycko and S.J. Opella, *J. Chem. Phys.*, 1987, **86**, 1761.

356. A.N. Garroway and J.B. Miller, *J. Magn. Reson.*, 1989, **82**, 591.
357. K.V. Ramanathan and S.J. Opella, *J. Magn. Reson.*, 1988, **78**, 367.
358. H.W. Spiess, *Colloid Polym. Sci.*, 1983, **261**, 193.
359. R.G. Griffin, K. Beshah, R. Ebelhauser, T.H. Huang, E.T. Olejniczak, D.J. Siminovitch, D.M. Rice and R.J. Wittebort, NATO ASI, *The Time Domain in Surface and Structural Dynamics*, Vol. 228 (ed. G.J. Long and F. Grandjean). Kluwer, Dordrecht, 1988.
360. J.H. Davis, K.J. Jeffrey, M. Bloom, M.I. Valic and T.P. Higgs, *Chem. Phys. Lett.*, 1976, **42**, 390.
361. P.M. Henrichs, J.M. Hewitt and M. Linder, *J. Magn. Reson.*, 1984, **60**, 280.
362. A.D. Ronemus, R.L. Vold and R.R. Vold, *J. Magn. Reson.*, 1986, **70**, 416.
363. P.M. Henrichs, J.M. Hewitt and R.H. Young, *J. Magn. Reson.*, 1986, **69**, 460.
364. P. Jonsen, *Chem. Phys. Lett.*, 1990, **170**, 311.
365. J. Seelig, *Quart. Rev. Biophys.*, 1977, **10**, 353.
366. R.J. Wittebort, E.T. Olejniczak and R.G. Griffin, *J. Chem. Phys.*, 1987, **86**, 5411.
367. M.S. Greenfield, A.D. Ronemus, R.L. Vold, R.R. Vold, P.D. Ellis and T.E. Raidy, *J. Magn. Reson.*, 1987, **72**, 89.
368. D.G. Cory and W.M. Ritchey, *J. Magn. Reson.*, 1989, **81**, 383.
369. N.J. Heaton, R.R. Vold and R.L. Vold, *J. Chem. Phys.*, 1989, **91**, 56.
370. C. Schmidt, S. Wefing, B. Blumich and H.W. Spiess, *Chem. Phys. Lett.*, 1986, **130**, 84.
371. H.W. Spiess, *J. Chem. Phys.*, 1980, **72**, 6755.
372. C. Schmidt, B. Blumich and H.W. Spiess, *J. Magn. Reson.*, 1988, **79**, 269.
373. S. Wefing and H.W. Spiess, *J. Chem. Phys.*, 1988, **89**, 1219.
374. S. Kaufman, S. Wefing, D. Schaefer and H.W. Spiess, *J. Chem. Phys.*, 1990, **93**, 197.
375. S. Wefing, S. Kaufmann and H.W. Spiess, *J. Chem. Phys.*, 1988, **89**, 1234.
376. A. Hagemeyer, L. Brombacher, K. Schmidt-Rohr and H.W. Spiess, *Chem. Phys. Lett.*, 1990, **167**, 583.
377. D.W. Sindorf and V.J. Bartuska, *J. Magn. Reson.*, 1989, **85**, 581.
378. D.A. Torchia and A. Szabo, *J. Magn. Reson.*, 1982, **49**, 107.
379. N.J. Heaton, R.R. Vold and R.L. Vold, *J. Magn. Reson.*, 1988, **77**, 572.
380. M.H. Levitt, *Prog. NMR Spectrosc.*, 1986, **18**, 61.
381. D.J. Siminovitch and R.G. Griffin, *J. Magn. Reson.*, 1985, **62**, 99.
382. M.H. Levitt, D. Suter and R.R. Ernst, *J. Chem. Phys.*, 1984, **80**, 3064.
383. W. Dongsheng, L. Gengying and W. Xuewen, *J. Magn. Reson.*, 1987, **74**, 464.
384. T.M. Barbara, *J. Magn. Reson.*, 1986, **67**, 491.
385. D.J. Siminovitch, D.P. Raleigh, E.T. Olejniczak and R.G. Griffin, *J. Chem. Phys.*, 1986, **84**, 2556.
386. D.P. Raleigh, E.T. Olejniczak and R.G. Griffin, *J. Magn. Reson.*, 1989, **81**, 455.
387. T.M. Barbara, M.S. Greenfield, R.L. Vold and R.R. Vold, *J. Magn. Reson.*, 1986, **69**, 311.
388. J. Jeneer and P. Broekaert, *Phys. Rev.*, 1967, **157**, 232.
389. R.J. Wittebort, *J. Magn. Reson.*, 1989, **83**, 626.
390. H. Schlemmer and U. Haeberlen, *J. Magn. Reson.*, 1986, **70**, 436.
391. A. Wokaun and R.R. Ernst, *Mol. Phys.*, 1978, **36**, 317.
392. S. Vega, *J. Chem. Phys.*, 1978, **68**, 5518.
393. W.D. Hutchinson, F. Separovic, B. Cornell and G.J. Bowden, *Chem. Phys. Lett.*, 1988, **144**, 87.
394. G.J. Bowden, W.D. Hutchinson and F. Separovic, *J. Magn. Reson.*, 1988, **79**, 413.
395. T.K. Halstead, P.A. Osment, B.C. Sanctuary, J. Tegenfeldt and I.J. Lowe, *J. Magn. Reson.*, 1986, **67**, 267.
396. M.S. Krishan, N. Lee, B.C. Sanctuary and T.G. Halstead, *J. Magn. Reson.*, 1988, **80**, 214.

397. D.B. Zax, A. Bielecki, K.W. Zilm, A. Pines and D.P. Weitekamp, *J. Chem. Phys.*, 1985, **83**, 4877.
398. R. Kreis, D. Suter and R.R. Ernst, *Chem. Phys. Lett.*, 1986, **123**, 154.
399. J. Chang, C. Connor, E.L. Hahn, H. Huber and A. Pines, *J. Magn. Reson.*, 1989, **82**, 387.
400. N.Q. Fan, M.B. Heaney, J. Clarke, D. Newitt, L.L. Wald, E.L. Hahn, A. Bielecki and A. Pines, *IEEE Trans. Magn.*, 1989, **25**, 1193.
401. D.T. Edmonds, *Int. Rev. Phys. Chem.*, 1982, **2**, 1039.
402. D.P. Weitekamp, A. Bielecki, D.B. Zax, K.W. Zilm and A. Pines, *Phys. Rev. Lett.*, 1983, **50**, 1807.
403. D.B. Zax, A. Bielecki, K.W. Zilm and A. Pines, *Chem. Phys. Lett.*, 1984, **106**, 550.
404. J.M. Millar, A.M. Thayer, H. Zimmerman and A. Pines, *J. Magn. Reson.*, 1986, **69**, 243.
405. J.M. Millar, A.M. Thayer, A. Bielecki, D.B. Zax and A. Pines, *J. Chem. Phys.*, 1985, **83**, 934.
406. A.M. Thayer, J.M. Millar and A. Pines, *Chem. Phys. Lett.*, 1986, **129**, 55.
407. P. Jonsen, M. Lutzar, A. Pines and M. Mehring, *J. Chem. Phys.*, 1986, **85**, 4873.
408. P. Meier, G. Kothe, P. Jonsen, M. Trecocke and A. Pines, *J. Chem. Phys.*, 1987, **87**, 6867.
409. Yu.A. Serebrennikov and M.I. Majitov, *Chem. Phys. Lett.*, 1989, **157**, 462.
410. Yu.A. Serebrennikov, *Chem. Phys.*, 1987, **112**, 253.
411. J.W. Hennel, A. Birczynski, S.F. Sagnowski and M. Stachorowa, *Z. Phys. B: Condens. Matter*, 1985, **60**, 49.
412. T.P. Jarvie, K. Takegoshi, D. Suter and A. Pines, *Chem. Phys. Lett.*, 1989, **158**, 325.
413. R. Tycko, *J. Magn. Reson.*, 1987, **75**, 193.
414. R. Tycko, *Phys. Rev. Lett.*, 1988, **60**, 2734.
415. R. Tycko, *J. Chem. Phys.*, 1990, **92**, 5776.
416. R. Tycko, G. Dabbagh, J.C. Duchamp and K.W. Zilm, *J. Magn. Reson.*, 1990, **89**, 205.
417. S.P. Cottrell, M.R. Halse and J.H. Strange, *Meas. Sci. Technol.*, 1990, **1**, 624.
418. S. Emid, *Physica B&C*, 1985, **128**, 79.
419. S. Emid and J.H.N. Creighton, *Physica B&C*, 1985, **128**, 81.
420. B.H. Suits and J.L. Lutz, *J. Appl. Phys. (USA)*, 1989, **65**, 3728.
421. B.H. Suits and D. White, *Solid State Commun.*, 1984, **50**, 291.
422. B.H. Suits and D. White, *J. Appl. Phys.*, 1986, **60**, 3772.
423. M. Corti, F. Borsa and A. Rigamonti, *J. Magn. Reson.*, 1988, **79**, 21.
424. S. Hafner, E. Rommel and R. Kimmich, *J. Magn. Reson.*, 1990, **88**, 449.
425. A.A. Samoilenko, D.Yu. Artemov and L.A. Sibeldina, *JETP Lett.*, 1988, **47**, 348.
426. A.A. Samoilenko, D.Yu. Artemov and L.A. Sibeldina, *Bruker Report*, 1987, **2**, 30.
427. A.A. Samoilenko and K. Zick, *Bruker Report*, 1990, **1**, 40.
428. T.A. Carpenter, L.D. Hall, P. Jezzard, *J. Magn. Reson.*, 1989, **84**, 383.
429. C. Chang and R.A. Komoroski, *Polym. Prep. (ACS Div. Polym. Chem.)*, 1988, **29**, 94.
430. W.P. Rothwell, D.R. Holecek and J.A. Kershaw, *J. Polym. Sci. Polym. Lett.*, 1984, **22**, 241.
431. S. Blackband and P. Mansfield, *J. Phys. C*, 1986, **19**, L49.
432. L.A. Weisenberger and J.L. Koenig, *J. Polym. Sci., Part C: Polym. Lett.*, 1989, **27**, 55.
433. P. Jackson, J. Barnes, T.A. Carpenter, N.J. Clayden, P. Jezzard and L.D. Hall, *J. Mater. Sci. Lett.*, 1990, **9**, 1165.
434. P.J. McDonald, J.J. Attard and D.G. Taylor, *J. Magn. Reson.*, 1987, **72**, 224.
435. E. Rommel, S. Hafner and R. Kimmich, *J. Magn. Reson.*, 1990, **86**, 264.
436. G.C. Chingas, J.B. Miller and A.N. Garroway, *J. Magn. Reson.*, 1986, **66**, 530.
437. P. Mansfield and P.K. Grannell, *Phys. Rev. B*, 1975, **12**, 3618.
438. P. Mansfield and P.K. Grannell, *J. Phys. C*, 1973, **6**, L422.
439. C.D. Eccles and P.T. Callaghan, *J. Magn. Reson.*, 1986, **68**, 393.

440. J.B. Miller, D.G. Cory and A.N. Garroway, *Polym. Prep. (ACS Div. Polym. Chem.)*, 1990, **31**, 143.
441. J.B. Miller, D.G. Cory and A.N. Garroway, *Chem. Phys. Lett.*, 1989, **164**, 1.
442. J.B. Miller and A.N. Garroway, *J. Magn. Reson.*, 1988, **77**, 187.
443. J.B. Miller and A.N. Garroway, *J. Magn. Reson.*, 1986, **67**, 575.
444. J.B. Miller and A.N. Garroway, *Polym. Prep. (ACS Div. Polym. Chem.)*, 1988, **29**, 90.
445. J.B. Miller and A.N. Garroway, *J. Magn. Reson.*, 1989, **82**, 529.
446. D.G. Cory, J.B. Miller, R. Turner and A.N. Garroway, *Mol. Phys.*, 1990, **70**, 331.
447. P.J. McDonald and P.F. Tokarczyk, *J. Phys. E*, 1989, **22**, 948.
448. D.G. Cory, J.B. Miller and A.N. Garroway, *J. Magn. Reson.*, 1990, **90**, 205.
449. D.G. Cory, A.N. Garroway and J.B. Miller, *J. Magn. Reson.*, 1990, **87**, 202.
450. R.A. Wind and C.S. Yannoni, *J. Magn. Reson.*, 1979, **36**, 269.
451. A.N. Garroway, J. Baum, M.G. Munowitz and A. Pines, *J. Magn. Reson.*, 1984, **60**, 337.
452. H.M. Cho, C.J. Lee, D.N. Shykind and D.P. Weitekamp, *Phys. Rev. Lett.*, 1985, **55**, 1923.
453. D.G. Cory, A.M. Reichwein, J.W.M. Van Os and W.S. Veeman, *Chem. Phys. Lett.*, 1988, **143**, 467.
454. D.G. Cory and W.S. Veeman, *J. Magn. Reson.*, 1989, **84**, 392.
455. D.G. Cory, J.W.M. Van Os and W.S. Veeman, *J. Magn. Reson.*, 1988, **76**, 543.
456. S. Matsui and H. Kohno, *J. Magn. Reson.*, 1986, **70**, 157.
457. S. Matsui, K. Sekihara, H. Shiono and H. Kohno, *J. Magn. Reson.*, 1988, **77**, 182.
458. Y. Ogura and K. Sekihara, *J. Magn. Reson.*, 1989, **83**, 177.
459. D.G. Cory, *J. Magn. Reson.*, 1989, **82**, 337.
460. Y. Ogura and K. Sekihara, *J. Magn. Reson.*, 1990, **88**, 359.
461. D.G. Cory and W.S. Veeman, *J. Magn. Reson.*, 1989, **82**, 374.
462. D.G. Cory and W.S. Veeman, *J. Phys. E*, 1989, **22**, 180.
463. D.G. Cory, J.C. de Boer and W.S. Veeman, *Macromolecules*, 1989, **22**, 1618.
464. F. de Luca and B. Maraviglia, *J. Magn. Reson.*, 1986, **67**, 169.
465. F. de Luca, C. Nuccetelli, B.C. Desimone and B. Maraviglia, *J. Magn. Reson.*, 1986, **69**, 496.
466. F. de Luca, C. Nuccetelli, B.C. Desimone and B. Maraviglia, *Solid State Commun.*, 1989, **70**, 797.
467. F. de Luca, B.C. Desimone, N. Luger, B. Maraviglia and C. Nuccetelli, *J. Magn. Reson.*, 1990, **90**, 124.
468. N.M. Szeverenyi and G.E. Maciel, *J. Magn. Reson.*, 1984, **60**, 460.
469. G.E. Maciel and M.F. Davis, *J. Magn. Reson.*, 1985, **64**, 356.
470. C.G. Fry, A.C. Lind, M.F. Davis, D.W. Duff and G.E. Maciel, *J. Magn. Reson.*, 1989, **83**, 656.
471. O.C. Morse and J.R. Singer, *Science*, 1970, **170**, 440.
472. D.G. Cory, J.B. Miller, A.N. Garroway and W.S. Veeman, *J. Magn. Reson.*, 1989, **85**, 219.
473. J.B. Miller and A.N. Garroway, *J. Magn. Reson.*, 1989, **85**, 432.
474. A.J. Shaka and R. Freeman, *J. Magn. Reson.*, 1985, **64**, 145.
475. A. Bax, R. Freeman and S.P. Kempsell, *J. Am. Chem. Soc.*, 1980, **102**, 4849.
476. E.M. Menger, S. Vega and R.G. Griffin, *J. Magn. Reson.*, 1984, **56**, 338.
477. B.H. Meier and W. Earl, *J. Chem. Phys.*, 1986, **85**, 4905.
478. B.H. Meier and W. Earl, *J. Am. Chem. Soc.*, 1987, **109**, 7937.
479. E.M. Menger, S. Vega and R.G. Griffin, *J. Am. Chem. Soc.*, 1986, **108**, 2215.
480. S. Emdin, J. Smidt and A. Pines, *Chem. Phys. Lett.*, 1980, **73**, 496.
481. Y.-S. Yen and A. Pines, *J. Chem. Phys.*, 1983, **78**, 3579.
482. J. Baum, M. Munowitz, A.N. Garroway and A. Pines, *J. Chem. Phys.*, 1985, **83**, 2015.
483. M. Munowitz, A. Pines and M. Mehring, *J. Chem. Phys.*, 1987, **86**, 3172.
484. M. Munowitz and M. Mehring, *Solid State Commun.*, 1987, **64**, 605.

- 485. J. Baum and A. Pines, *J. Am. Chem. Soc.*, 1986, **108**, 7447.
- 486. J. Baum, K.K. Gleason, A. Pines, A.N. Garroway and T. Redpath, *Phys. Rev. Lett.*, 1986, **56**, 1377.
- 487. D.N. Shykind, J. Baum, S.-B. Liu, A. Pines and A.N. Garroway, *J. Magn. Reson.*, 1988, **76**, 149.
- 488. T. Nakai and C. A. McDowell, *J. Magn. Reson.*, 1990, **90**, 426.

Solid State NMR Imaging

D.G. CORY

Bruker Instruments, Inc., 19 Fortune Drive, Billerica, MA 01821, USA

1. Introduction	88
2. Imaging basics	94
2.1. Nuclear spin Hamiltonians	95
2.2. Reciprocal space and one-dimensional imaging methods	98
2.3. Limits to resolution and signal-to-noise	102
2.4. Two-dimensional images	104
2.5. Three-dimensional imaging and volume selected spectroscopy	107
2.6. Contrast	109
3. Wide-line imaging methods	110
3.1. STRAFI	110
3.2. Constant time imaging	114
3.3. Multiple-quantum imaging	116
4. Manipulation of Hamiltonians, averaged Hamiltonians	118
4.1. Average Hamiltonian theory	118
4.2. Multiple-pulse methods	120
4.3. Gradient modulation	123
4.4. Magic-angle sample spinning	126
5. Imaging with multiple-pulse line-narrowing	127
5.1. Time-independent gradients	127
5.2. Oscillating gradients	132
5.3. Pulsed gradients	134
5.4. Resolution and sensitivity for multiple-pulse imaging	139
6. Imaging with magic-angle sample spinning	144
6.1. Synchronously rotating gradients	145
6.2. CRAMPS	150
6.3. Other methods of MASS imaging	152
7. Rotating frame imaging	152
8. Large samples and surface coils	157
9. Nutation studies of the skin depth in metallic samples	159
10. Slice selection and volume selected spectroscopy	160
11. Other spin = $\frac{1}{2}$ nuclei	165
12. Quadrupolar nuclei	168
13. Applications	171
Acknowledgements	174
References	174

1. INTRODUCTION

In a remarkably short period of time since the discovery of NMR imaging in 1972 by Lauterbur^{1,2} and independently by Mansfield,³⁻⁵ medical applications of NMR imaging (MI) have established a secure position in clinical diagnosis and medical research for studying certain soft tissues. Today, commercial instrumentation yields images of great clarity for soft tissues. Furthermore, by employing special techniques, images can even be acquired in a fraction of a second.⁶⁻⁸ Many areas of non-medical NMR imaging have managed to develop nearly as fast as MI by sharing techniques and instrumentation; examples include small animal imaging, plant studies, and imaging of mobile liquids inside solid porous materials. NMR microscopy⁹⁻¹² and solid state NMR imaging,¹³⁻¹⁵ however, require a different set of techniques and hence their development has been much slower than MI. In fact the first true applications of solid state imaging are only just now appearing, and to date nearly all solid state images have been obtained on home-built equipment.

There are many non-scientific reasons why the development of NMR imaging of solids has lagged behind the development of medical imaging, foremost being that society's commitment to health care far outweighs concerns for materials studies. The issues that we will focus on, however, are the distinctions between medical and materials imaging that cause the two experiments to appear very different and to require significantly different instrumentation. Solid state imaging still shares many aspects with liquids imaging, but the large natural linewidth of solids must somehow be accommodated. This was appreciated by the founders of NMR imaging, and already in 1973 Mansfield and Grannell^{4,16} reported the first one-dimensional image of a solid phantom (shown in Fig. 1) using a multiple-pulse line-narrowing method which is still used today.

NMR imaging is based on the simple idea that a magnetic field gradient (a magnetic field which increases linearly over space) modifies the Larmor frequencies of the nuclear spins in proportion to their spatial position. Provided that the natural spread in Larmor frequencies is smaller than that imposed by the magnetic field gradient, the spread in Larmor frequencies can be inverted to yield the spatial variation in the density of nuclear spins. A problem arises since the natural linewidth of a rigid solid is on the order of 5000 times broader than the linewidth of water. This factor of 5000 difference in natural linewidths necessitates that the gradient strength be scaled up a factor of 5000 if liquid imaging techniques are to be applied. This is difficult but technically feasible. Of more concern is the fact that the receiver bandwidth must also be increased by a factor of 5000, resulting in a 5000-fold increase in the experimental time to acquire an image. This approach is often too restrictive, and in practice it is frequently easier to record images while

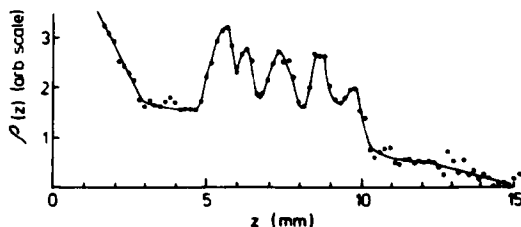


Fig. 1. A one-dimensional ^1H NMR image of five layers of solid camphor published by Mansfield and Grannell in 1975.¹⁶ The image was obtained by using a multiple-pulse sequence (MREV-8) to eliminate the normally dominant homonuclear dipolar contribution to the NMR lineshape, and acquired in the presence of a static magnetic field gradient of 0.0077 T/m. This method, while not resulting in the highest quality images, is still employed today and has the virtue of simplicity. In this classic paper Mansfield and Grannell anticipate many of the advances which were subsequently employed to change this simple experiment into a robust imaging experiment that yields high-quality images. The zero frequency contribution in the image is a spin-locked signal which is easily avoided today. (Reproduced with permission from Mansfield and Grannell.¹⁶)

manipulating the nuclear spin Hamiltonians such that the linewidth of the solid *appears* to be as small as those typically encountered in liquids.

While line-narrowing approaches may appear to be complex and difficult, they have a long and successful history in NMR spectroscopy,^{17–20} and a compact theory for describing these experiments exists in Average Hamiltonian theory.²¹ Line-narrowing schemes open up a wide range of possibilities for imaging not only solids, but also liquids. They give the experimenter the ability to manipulate the spin Hamiltonian of a sample virtually at will to increase the image resolution and sensitivity. The same approaches can be employed to introduce contrast into the image, reflecting not only relaxation times but almost any Hamiltonian of interest. Line-narrowing also is used to avoid image distortions from spatially dependent lineshapes and resonance frequencies. For solid samples the homonuclear dipolar couplings frequently lead to a blurring which can be eliminated this way; for liquid samples the most prominent distortions are from chemical shifts and susceptibility shifts. All of these can be eliminated by line-narrowing approaches.

If the experiments are made less convenient by including line-narrowing, we have the advantage over MI of freedom in sample handling and treatment. Samples are typically small and there are no limits to the static field strength, radiofrequency field strength, or duty cycle to which the sample may be subjected. Often a physical slicing of the sample can replace a slice selection sequence and preserve valuable signal-to-noise. The sample does not move and there are rarely important diffusion processes. It is

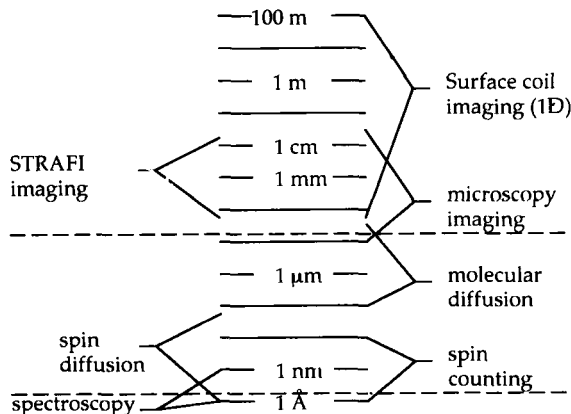


Fig. 2. A diagram outlining the range of spatial information that is available from a selection of NMR techniques. The range of spatial information spans over ten orders of magnitude, although not all samples can be studied by all of the techniques. In addition, the types of spatial information are quite different, imaging yields an absolute spatial location for each resolved spin packet, while diffusion (both molecular and spin) and spin counting techniques yield a picture of the average local geometry that is very similar to a radial distribution function. Even simple spectroscopy is a type of spatial measurement giving information about the local electron density, but in a way which is often difficult to translate into purely spatial terms.

perfectly acceptable, therefore, to spend an entire day acquiring an image provided only that the data are worth the instrument time. Physical treatment of the sample might include magic-angle sample spinning, varying the probe temperature, deformation of the sample or even isotopic enrichment of normally dilute nuclei during sample preparation.

Spatial information about solids has long been obtained via NMR; imaging methods are simply one of the latest techniques to be developed. Therefore it is appropriate to pause and see where imaging fits in with older methods. The range of spatial NMR methods is outlined in Fig. 2. These methods stretch from spectroscopic techniques that yield information on a scale of angstroms, through surface coil studies that have been applied on a scale of tens of metres.²² Spectroscopy, of course, yields information about the local electronic environment and about the near proximity of other nuclei through chemical shifts and couplings.^{23,24} Further advantage of these couplings may be made to spatially extend the technique to hundreds of angstroms by spin-counting^{25,26} or spin-diffusion^{27,28} experiments. In the case of spin counting, spatial information is obtained by generating large multiple-quantum coherences that reflect the number of proximate spins of a given type. Spin diffusion monitors the flow of magnetization from one spin

reservoir to a distinct adjacent reservoir. In all cases the measurement is of the local structure averaged over the entire sample. In addition, for these techniques detailed spectroscopic and relaxation information can be obtained simultaneously with spatial information.

At somewhat larger scales molecular diffusion²⁹⁻³² of trapped fluids can be used to characterize the geometry of the trapping solid. Again this is a local technique with only average information available, but here no spectroscopic information is available about the solid, since the solid itself is never actually observed.

Imaging allows one to determine the absolute spatial location of groups of spins and to obtain spectroscopic information about these same groups. The spatial dimensions are somewhat larger for imaging than for local techniques since each volume of spins to be resolved or voxel must contain a sufficient number of spins to be observed (typically on the order of 10^{15}).

Most images of solids are not images of spins with solid state characteristics; by far the most common approach is to add or take advantage of liquids inside the solid (see Fig. 3). The structure of the solid material is then deduced from the image of the fluid-filled spaces.³³⁻⁴⁵ As seen in the figure⁴⁵ images of astonishing clarity can be recorded in this fashion with methodologies which are not too far removed from those of medical imaging. The natural water content of wood can be similarly imaged.⁴⁶⁻⁵¹

Certain physically solid materials possess rapid molecular motion and near liquid linewidths (see Fig. 4). Rubbers⁵²⁻⁵⁹ and waxes⁶⁰⁻⁶³ are amongst the common materials whose linewidths are only 10-100 times broader than a liquid, and therefore still sharp enough that minor modifications to the spectrometer suffice to obtain reasonable images. Many of these solid materials, which are often studied as liquids, would profit from line-narrowing, but unless line-narrowing is necessary for generating the required contrast it has generally not been employed.

Heating a sample or putting it into solution are two well-known and quite robust methods of line-narrowing. Hall and coworkers^{64,65} acquired the image in Fig. 5 by heating a solid polypropylene sample while imaging it. Similarly, Koenig and coworkers⁶⁶ (Fig. 6) swelled a crosslinked rubber with a deuterated solvent to introduce sufficient motions for imaging the rubber material. Note that since the solvent was perdeuterated, Koenig could be certain that the image was from the rubber itself and not from the very mobile solvent. With non-deuterated solvents, the solvent ingress can be directly followed in polymer swelling,⁶⁷⁻⁷³ and adhesion⁷⁴⁻⁷⁸ can be followed by the removal of solvent, during the cure of the adhesive.

The above methods work quite well and have the benefit of simplicity; however, they are very restrictive in the types of samples to which they may be applied. For the remainder of this review we will concentrate on methods

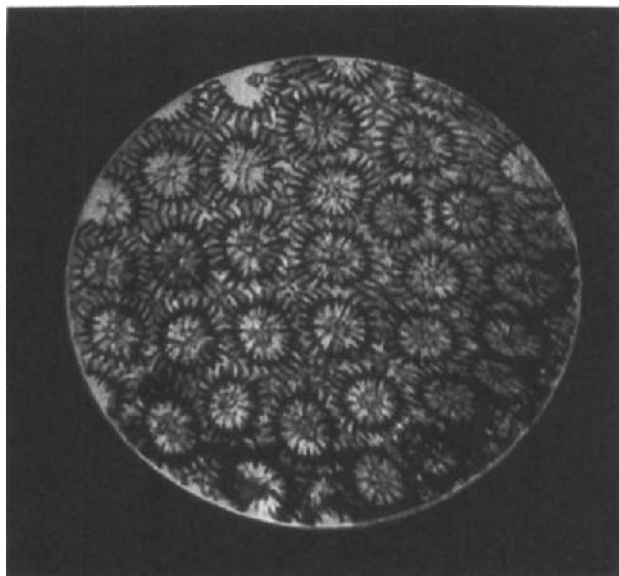


Fig. 3. A ^1H NMR image of water in a Holocene coral boundstone. The image was obtained using a commercial NMR imaging spectrometer designed for studying relatively small liquid samples. The absence of signal gives detailed information on the location of the solid coral. This is a fast, and simple method when the desired contrast is simply liquid versus solid. The displayed image has a slice thickness of $300\ \mu\text{m}$, an in-plane resolution of $100\ \mu\text{m}$ and a sample diameter of $25\ \text{mm}$. (Reproduced with permission from Woessner *et al.*⁴⁵, copyright 1990 Society of Petroleum Engineers.)

for imaging rigid solids where liquid imaging techniques break down. It is hoped that the potential of line-narrowing for improving the sensitivity and for avoiding distortions for a wider class of samples will also be recognized.

There are two general reasons for obtaining an NMR image of a solid: (1) as a means of non-destructive evaluation (NDE), or (2) to investigate the spatial variation of chemistry or physics, with the sample as a model which may be destroyed. In the latter case NMR imaging is employed because it offers forms of contrast that are unavailable from other imaging techniques. While NDE applications of solid state imaging are exciting and promising, there are a large number of unanswered questions regarding sample and experiment geometries as well as sample throughput. At this time most applications of solid state imaging have been of the latter class, involving chemical studies of model systems; common examples are studies of polymer

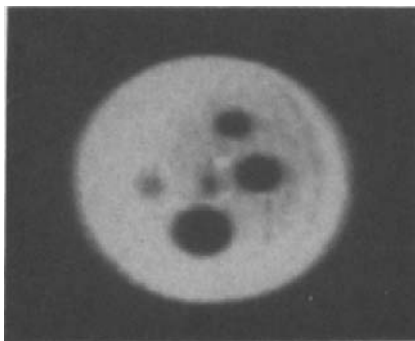


Fig. 4. A ^1H NMR image of a green ceramic obtained by Garrido *et al.*⁶³ Here the polymer binder itself is being imaged. The binder has a modestly broad linewidth of 2400 Hz, and it is just barely possible to image this material using conventional instrumentation that was modified to accommodate a short echo time. A two-dimensional spin echo imaging approach was used with an echo time of 1.98 ms and a gradient of 0.033 T/m yielding a spatial in-plane resolution of 552 μm . (Reproduced with permission from Garrido *et al.*⁶³)

and ceramic processing. NDE applications of solid state NMR imaging will not be specifically addressed in this review.

There have been a number of reviews on imaging,^{8-10,13-15,79-88} materials imaging,¹³⁻¹⁵ ESR imaging⁸⁹ and diffusion,²⁹⁻³² all of which have some relationship to the subjects covered here. In addition, we will rely very heavily on modern methods of high-resolution solid state spectroscopy.¹⁷⁻²⁰

We will begin by reviewing the full range of spin Hamiltonians that are seen in solid state NMR and some basic elements of imaging such as which parameters limit resolution and sensitivity. Then we will discuss methods for manipulating spin Hamiltonians which will lead to different classes of solid state imaging methods, followed by a selection of applications.

The required instrumentation for each experiment will be described since nearly all methods require some non-standard equipment. To implement some of these methods today does require a reasonable amount of construction, primarily of probes and gradient drivers. Nearly every technique which is discussed in this review has been successfully implemented in more than one laboratory, however, and as a physicist once informed me while I was struggling to reproduce an experiment from the literature, anything that has been done is, by definition, trivial. Clearly, one has only to point this out to one's friendly instrument manufacturer, or hard working graduate student.

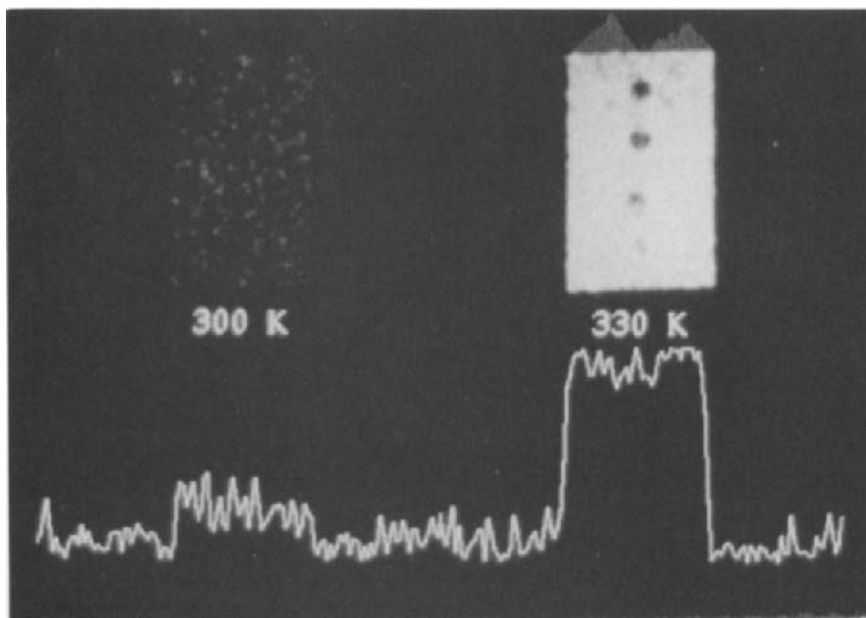


Fig. 5. Hall and coworkers⁶⁴ used heat to increase molecular mobility and hence decrease the NMR linewidth of a sample of polypropylene so that an image could be acquired using conventional methods. For this sample only a modest change in the temperature (300 K to 330 K) translates into a large variation in the sensitivity of the imaging experiment. The sample measured 12 mm \times 9 mm \times 5 mm, and has 3-mm diameter holes drilled in it to varying depths. (Reproduced with permission from Jackson *et al.*⁶⁴)

2. IMAGING BASICS

In discussing the resolution and sensitivity limits to NMR imaging, the basic interrelationships between imaging parameters and spectroscopic properties will be of interest, and also under what conditions these can be separated. As an example, one very appealing approach to NMR imaging is to “turn off” all of the Hamiltonians of the system except the gradient Hamiltonian for spatial encoding. So, for a solid sample, the dipolar, chemical shielding and susceptibility shift Hamiltonians are employed selectively to create the desired contrast and then are all switched off, resulting in an apparently narrow linewidth. An NMR image can then be collected from this narrowed line with a modest magnetic field gradient at high resolution and high sensitivity. Before returning to this experiment, the Hamiltonians of interest will be explored along with their effects on simple imaging experiments.

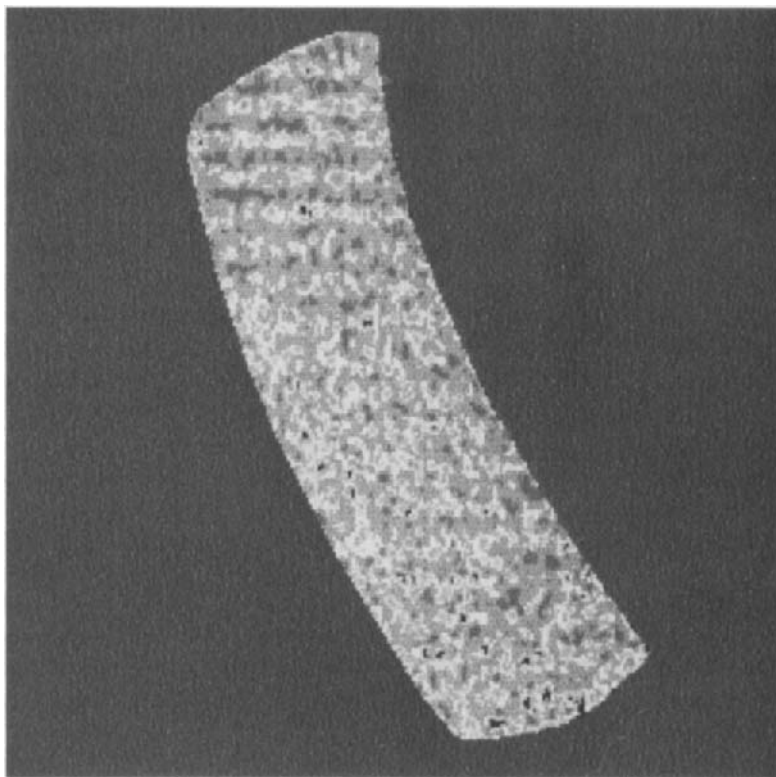


Fig. 6. Solvent swelling is another method of introducing molecular motions and thereby reducing the NMR linewidth. Koenig and coworkers swelled this sample of polybutadiene with perdeuterated cyclohexane so that a ^1H image is obtained only from the polymer. By mapping out the spatial variation of the transverse relaxation rate as a function of swelling, they were able to determine the spatial variation of the crosslink density. (Reproduced with permission from Smith and Koenig.⁶⁶)

2.1. Nuclear spin Hamiltonians

The Zeeman interaction describes the coupling of the spin angular momentum to the static magnetic field. The largest Hamiltonian for spin- $\frac{1}{2}$ systems, it splits the spin wave function into two eigenstates. The energy difference of these two states is directly proportional to the applied magnetic field. Under the influence of the Zeeman Hamiltonian, the spin's evolution is a rotation about the magnetic field at the Larmor frequency given by,

$$\omega_0 = -\gamma B_0 \quad (1)$$

The NMR experiment is normally treated as a perturbation of this motion,

and it is therefore convenient to transform all Hamiltonians to a reference system rotating at the Larmor frequency. It is only the secular components (i.e. those contributions which are along the same axis as the Zeeman interaction) of spin Hamiltonians that will therefore contribute to spin evolution. This is not only a simplification; the non-secular components are averaged by the Zeeman term and are normally not observable.¹⁷

A list of the important spin Hamiltonians is given in Table 1. There are a number of Hamiltonians which are linear in I_z and could have been lumped together; however, their effects on the image are quite different and so they will be dealt with individually. The chemical shielding Hamiltonian describes the partial shielding of the nucleus by the electrons²⁴ and is familiar from high-resolution NMR spectroscopy. Additionally, in the solid state the chemical shift is anisotropic, leading to variations in the chemical shift with changes in orientation relative to B_0 . An offset Hamiltonian could also have been included to describe the difference between the excitation frequency and the Larmor frequency, but it is convenient to include this in the chemical shielding term.

The chemical shielding may vary across a sample due to variations in chemistry. In some cases, chemical shielding anisotropy can lead to spatial changes in chemical shifts on the scale of the image resolution which are not related to chemistry (one example is bulk molecular orientation in a drawn polymer sample). Both of these effects will influence image resolution and sensitivity.

The susceptibility Hamiltonian^{90,91} describes the change in the magnetic field as one moves from one region of bulk susceptibility to another. This is a tensor quantity that is dependent on the shape of the different regions of the sample. Since any interesting sample from an imaging point of view is necessarily spatially heterogeneous, it is very likely that the bulk susceptibility will vary across the sample and hence the magnetic field will not be uniform throughout the sample. The susceptibility Hamiltonian has the same form as the chemical shielding Hamiltonian; however, their spatial dependencies are quite different. The chemical shift will, in many cases, be spatially homogeneous while the susceptibility shift is necessarily spatially heterogeneous.

The gradient Hamiltonian also has the same form as the Zeeman and chemical shielding Hamiltonians, but now the field of interest is an applied magnetic field gradient. The gradient introduces a new degree of experimental freedom in that the gradient strength and direction can be time-dependent, *vide infra*.

In NMR studies of solid state samples the dipolar couplings are often the dominant contribution to the linewidth. As seen in Table 1 the dipolar coupling Hamiltonian is bi-linear in spin operators, and in the ^1H

Table 1. Nuclear spin Hamiltonians.

		Typical size at 9.4 T
Linear in-spin operators:		
Zeeman	$H_z = -\gamma B_0 I_z$	400 MHz
Chemical shift	$H_{cs}^{(0)} = \gamma \sigma_{zz} B_0 I_z$	5 kHz
Susceptibility	$H_s^{(0)} = \gamma \sigma(\mathbf{r})_z B_0 I_z$	5 kHz
Gradient	$H_g^{(0)} = \gamma \mathbf{r} \cdot \mathbf{B}_g I_z$	Under experimental control
Radiofrequency	$H_{rf} = -\gamma B_{rf} I_k$	50 kHz
Bilinear in-spin operators:		
Indirect spin-spin coupling	$H_J = 2\pi \sum_{k < l} I_k J_{kl} I_l$	100 Hz
Direct dipolar coupling	$H_D^{(0)} = \sum_{k < l} \frac{1}{2} b_{kl} (1 - 3 \cos^2 \vartheta_{kl}) [3 I_{kz} I_{lz} - \mathbf{I}_k \cdot \mathbf{I}_l]$	50 kHz
Quadratic in-spin operators:		
Electric quadrupole	$H_Q = \omega_Q \left[(I_z^2 - \frac{1}{3} \mathbf{I}^2) + \frac{\eta}{3} (I_x^2 - I_y^2) \right]$	Varies widely with nucleous 0 for spin = $\frac{1}{2}$ nuclei

homonuclear case the contribution to the linewidth can be as large as 50 kHz for many organic samples. In the case of heteronuclear dipolar couplings, the Hamiltonian may be treated as linear in the spin operators due to the large differences in Zeeman frequencies between the coupled nuclei, giving the Hamiltonian a form similar to that of the chemical shift.

Most solid state imaging studies have been restricted to spin = $\frac{1}{2}$ nuclei and for these nuclei there are no quadrupole interactions. For nuclei with spin $> \frac{1}{2}$, where the nuclear electronic charge distribution is not spherically symmetric, there is a coupling to the gradient of the local electric potential that can be many megahertz in strength. This coupling is independent of the applied field and often so large that only the central transition (for half integer spins) of the nuclear spin states can be observed.

2.2. Reciprocal space and one-dimensional imaging methods

It has long been realized that a spatial dependence of the static magnetic field will be reflected as a spread of resonance frequencies.^{92,93} Indeed, the general usefulness of NMR for chemical analysis is a good indication of how successful instrument manufacturers have been at reducing the spatial dependence of the static magnetic field. That the gradient-induced lineshape could be calculated was also appreciated, and magnetic field gradients, which are useful for molecular diffusion studies, have been calibrated by the frequency spread they caused in a sample of known geometry.⁹⁴ Lauterbur^{1,2} and, independently, Mansfield,³⁻⁵ however, realized that the problem could be inverted for any shaped sample contained in a linear magnetic field gradient.

In general, the problem is to uncover the spin density distribution, $\rho(\mathbf{r})$, from a set of frequencies that in an ideal experiment are determined solely by a magnetic field gradient

$$\mathbf{G} = \nabla B_z = \begin{pmatrix} \frac{\partial B_z}{\partial x} \\ \frac{\partial B_z}{\partial y} \\ \frac{\partial B_z}{\partial z} \end{pmatrix} \quad (2)$$

In this simple case the spin resonance (the FID) is given by

$$s(t) = \int \rho(\mathbf{r}) \exp[i\mathbf{r} \cdot \mathbf{k}(t)] d\mathbf{r} \quad (3)$$

where \mathbf{k} is a reciprocal space vector defined as

$$\mathbf{k}(t) = \gamma \int_0^t \mathbf{G}(t') dt' \quad (4)$$

Writing the FID in terms of reciprocal space vectors makes it immediately clear that Fourier transformation of (3) will give the spin density distribution. Reciprocal space or k -space,^{16,95} allows for a simple geometric picture of imaging procedures that is not dependent on a particular sample geometry. This reciprocal space way of looking at imaging experiments will be particularly important when discussing the wide variety of two-dimensional imaging schemes.

Equation (4) may be thought of as describing the scattering of a fictitious plane wave in analogy to optical systems.¹⁶ The wavelength, λ , of the fictitious wave is then

$$\lambda = 2\pi/k \quad (5)$$

It is this wavelength which describes the limits of resolution in NMR imaging, just as in optics. One should be careful to not confuse this gradient-imposed wavelength with the wavelength of the actual radiofrequency pulse that is used to excite the spin system; the rf wavelength is much longer. The image resolution then is a product of the gradient strength and the length of the measurement. For all real samples the spin dynamics place a limit on the measurement time and the gradient strength determines the resolution. Here also we must be careful with our definitions; the measurement time is the period of spin evolution during which the gradient is present. Some examples will be discussed after the natural lineshape has been included in the imaging experiment.

Equation (3) is incomplete; the spin system has a natural response in the absence of the magnetic field gradient that must be included and noise is an important factor. Assuming that a single FID of a fully relaxed sample is recorded, and that the rf pulse excitation profile is much broader than the spread in resonance frequencies, then (3) can be rewritten to include the natural response as,

$$s(t) = \sum_j \int \rho_j(\mathbf{r}) \exp(i\mathbf{r} \cdot \mathbf{k}(t)) \sum_k \exp(i\omega_{j,k} t) \exp(-t/T_{2j,k}) d\mathbf{r} + \text{noise}(t) \quad (6)$$

where ρ_j is the spin density of compound j , $\omega_{j,k}$ is the resonance frequency of line k in compound j , $T_{2j,k}$ is the corresponding spin-spin relaxation time, and $\text{noise}(t)$ is the time-dependent noise.

The effect of having a distribution of compounds with different resonance frequencies in our sample is that one records a superposition of images. Where a single compound contains more than one resonance, the resultant

image is the convolution of the true image and these resonance frequencies. This may, in fact, be the desired result; however, where it is not the imaging experiment can be preceded by a selection process to limit the response to the resonance or compound of interest.

Similarly, the spin-spin relaxation time is a broadening which is convoluted into the image. When these distortions have the same spatial distributions, they can, in principle, be removed by deconvolution of the recorded image by the known natural response of the sample.⁹⁶⁻⁹⁹ However, the presence of noise severely limits the accuracy to which one can restore the true image. Questions of image manipulations are well-discussed outside of the NMR literature and the interested reader is referred to the recent text by Blackledge¹⁰⁰ for a readable and comprehensive discussion.

Where the observed image is a superposition of images from spatially separated distinct compounds deconvolution procedures cannot separate the image from these distinct species. Deconvolution can only be employed to sharpen an overall blurring of the image.

In addition to the distortions caused by the chemical makeup of the sample, there is a distortion caused by placing a material with a heterogeneous susceptibility inside a magnetic field.^{90,91} The different portions of the sample will generally have different bulk susceptibilities that lead to local distortions in the magnetic field. These distortions shift the resonance line and in an image make it appear that the shifted volume is elsewhere in the sample. A susceptibility gradient exists at the interface between regions of different susceptibilities. When the differences in susceptibility are large and occur over a small spatial range the susceptibility gradient can cause the portions of the sample that are near the interface to broaden into the baseline. In this way variations in susceptibility are occasionally used to amplify small features in an image which would otherwise be difficult to observe by themselves. Equation (5) is modified to include the effects of variations in the bulk susceptibility as

$$s(t) = \sum_j \int \rho_j(\mathbf{r}) \exp(i\mathbf{r} \cdot [\mathbf{k}(t) + \mathbf{k}_{bs}(t, r)]) \\ \times \sum_k \exp(i\omega_{j,k} t) \exp(-t/T_{2j,k}) d\mathbf{r} + \text{noise}(t) \quad (7)$$

where \mathbf{k}_{bs} is a reciprocal space vector which is dependent on both time and space and may be written as

$$\mathbf{k}_{bs}(t, r) = \gamma \int_0^t \mathbf{G}(t', r) dt' \quad (8)$$

For a specific geometry much more can be said about the form of (7), but since we are interested in complex geometries we will not pursue this. What

is clear, however, is that distortions arising from variations in the bulk susceptibility are not describable as simple convolutions and there is no simple processing of the data after the fact which will remove these distortions.

Equations (7) and (8) point to a simple test for the presence of susceptibility artifacts. Reorient the sample in the magnetic field and acquire a second image. In the absence of rf and gradient imperfections, variations in the two images are generally due to susceptibility artifacts.

Both the chemical shift and susceptibility shift scale as the main magnetic field strength (see Table 1), and so one practical solution to avoiding distortions from these is to record images at low magnetic field strengths with gradients which are sufficiently strong so as to mask any distortions. In other words, the gradient is made strong enough such that all distortions are contained within a single voxel (primitive volume element of an image). This is not to say that distortions within a voxel are necessarily invisible. Such distortions can lead to a variation in the intensity of the voxel in some imaging schemes.

Turning back to (5) we can ask how each of these distortions affects the observed resolution. Noise by itself has no effect on the resolution, it only places a limit on the total experiment time necessary to acquire an image with a specific signal-to-noise ratio. The spin-spin relaxation time limits the length of time during which the spin system may be observed, and therefore in a time-independent magnetic field gradient the resolution is

$$\lambda = 2\pi/T_2G \quad (9)$$

If we wish to hide a spread in resonance frequencies, Δf (such as from chemical shifts or susceptibility shifts), then the measurement time must be limited to a time short enough that the frequencies cannot be distinguished from one another, and the resolution is

$$\lambda = \Delta f/G \quad (10)$$

The above two equations simply tell us that to mask a distortion we need to apply a stronger gradient.

Molecular diffusion is also a limitation to image resolution when liquids are being studied.¹⁰¹ In a simple picture one can imagine that the liquid is moving between voxels while being imaged and that this motion during the observation time blurs the image. Once again the mean diffusion time for the liquid to traverse a voxel limits the observation window and therefore the gradient must be proportionally stronger. For solids this will rarely be a consideration, but molecular diffusion may ultimately limit the resolution in microscopic imaging of liquids.

2.3. Limits to resolution and signal-to-noise

There are many parameters which affect the sensitivity of an NMR experiment and the interested reader is referred to Freeman's recent handbook¹⁰² for a brief discussion and further references. For our purposes we will assume that the spectrometer, sample, temperature, etc. are given, and that we are only concerned with setting up the experiment to achieve the optimal sensitivity. In addition, we will want to know how much longer it will take to acquire an image with twice the resolution, or to acquire an image of a sample which has a T_2 which is half as long.

As discussed previously, we will set our voxel bandwidth equal to the NMR linewidth in order to contain all line-broadening distortions within the voxel. For simplicity we will assume that the spins are homogeneously distributed within the voxel. If we apply matched digital filter to the FID (e.g. if exponential line-broadening is used with the correct weighing factor¹⁰³), and if the receiver bandwidth is set equal to the spectral width, then the signal-to-noise is independent of the spectrum width and the digital resolution. As the resolution, and hence the gradient strength, is increased the bandwidth of the image must be increased. The noise per voxel remains the same since the voxel bandwidth is not increased; the frequency spread across a voxel remains unchanged. However, the signal is now spread amongst a larger number of voxels, proportional to the increase in the gradient strength. The signal-to-noise then is directly proportional to the gradient strength for a one-dimensional image. The signal-to-noise can be increased by averaging a number of acquisitions since the signal adds coherently while the noise adds randomly. The signal-to-noise therefore increases with the square-root of the number of acquisitions.

To record an image with twice the resolution at the same sensitivity level as a previous image, four times the number of acquisitions are necessary:

$$\text{experimental time} \approx [\text{gradient strength}]^2 \quad (11)$$

We now wish to explore a sample with twice the linewidth or equivalently a T_2 that is only half as long. The amount of signal per voxel is unaffected by the change in linewidth (at constant spatial resolution). However, the voxel bandwidth must be increased in proportion to the linewidth in order to maintain this constant spatial resolution. The noise per voxel increases as the square-root of the voxel bandwidth (the linewidth), hence the acquisition time is directly proportional to the linewidth:

$$\text{experimental time} \approx [\text{linewidth}] \quad (12)$$

This will eventually be the limitation to many approaches for solid state imaging since solid state linewidths are approximately 5000 times those of

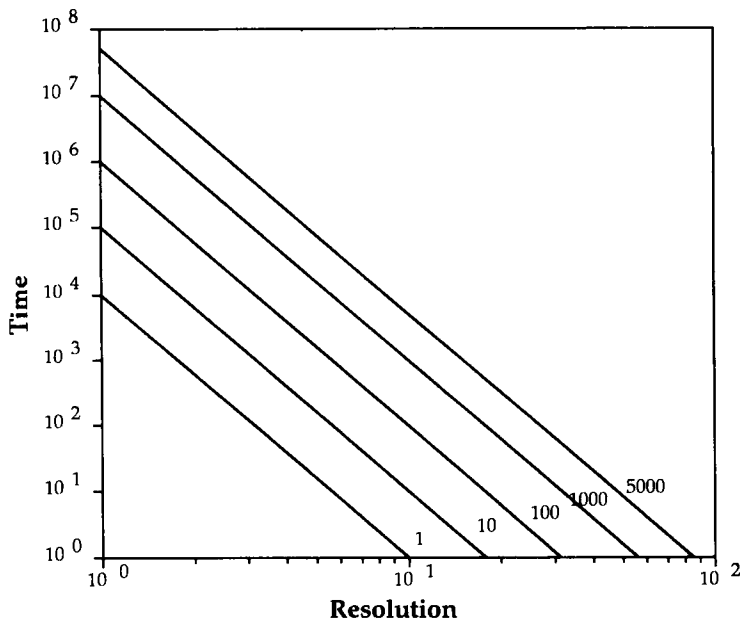


Fig. 7. Plot of the experimental time needed to obtain an image of a sample with a given linewidth versus the image resolution. The spatial resolution is assumed to be in two dimensions with the third dimension (e.g. the slice thickness) held constant. As seen, the length of an experiment increases very quickly with sample linewidth, and for rigid solids it is often preferable to employ line-narrowing rather than brute force strong gradients.

liquids. Relations (11) and (12) are valid for each imaging dimension; therefore, if the resolution is to be increased by a factor of 2 in all three dimensions simultaneously, the experimental time must be lengthened by a factor of 64. Figure 7 shows the relationships between resolution, experimental time, and linewidth for a two-dimensional imaging experiment. The most common imaging methods are two-dimensional of a previously defined slice that is frequently thicker than the in-plane resolution.

Seeing that the gradient strength affects both the sensitivity and resolution of an imaging experiment it should come as no surprise that there is an optimal gradient strength for any experiment. *The optimal gradient strength is simply the minimum gradient strength that yields the desired resolution.* The smallest voxel which can be observed varies with each technique, and therefore will be addressed for each method separately.

Mansfield and Morris⁷⁹ and Callaghan and coworkers^{11,12,91,101} have explored in great detail the sensitivity and resolution limitations to

microscopic imaging; for our purposes, however, the above simple relationships are adequate.

2.4. Two-dimensional images

Moving from one dimension to two, the goal now is to cover an area in two-dimensional k -space such that the image information can be recovered. Where previously we confined our attentions to a line in k -space here we are concerned with a plane of k -space. As in the one-dimensional case, in two dimensions one moves between k -space and real-space by Fourier transformation (FT), and the most efficient discrete FT algorithms are restricted to sets of evenly spaced points (see Fig. 8). It makes sense, therefore, to think of sampling k -space as a regular array of data points. This has the additional feature that k -space is uniformly sampled and therefore all frequency components are defined with the same precision. A problem with this simple protocol is that all experiments start at the centre of k -space, and so if we imagine acquiring data points along a set of parallel lines in k -space some time must first be spent while the experiment is offset to each line. Recalling that there is only a finite measurement window, the gradient must be made somewhat larger to accommodate this decrease in measurement time and hence some sensitivity is lost.⁷⁹

A two-dimensional Fourier imaging (2DFI) sequence¹⁰⁴ that accomplishes this k -space shifting is also shown in Fig. 8. This is only one of many possible 2DFI imaging approaches and the field of two-dimensional NMR in general is much larger. Ernst *et al.*¹⁰⁵ have recently written a clear and definitive text on two-dimensional NMR.

In Fig. 8 the 2DFI pulse sequence has been split into three periods labelled preparation, evolution and detection. At this stage the preparation period is only employed to excite the spin system. During the evolution period the spins evolve in a gradient along the y direction and no data are acquired. This corresponds to offsetting the k -space trajectory along which data acquisition will take place. During the detection period the gradient is along the x direction and data are collected along a k -space trajectory that is parallel to the k_x axis. The process is repeated for different offsets until all of k -space that is of interest has been uniformly sampled. At this point the data are of the form

$$s(t_1, t_2) = \int \rho(\mathbf{r}) \exp(i\mathbf{r} \cdot [k_y(t_1)\hat{u}_y + k_x(t_2)\hat{u}_x]) d\mathbf{r} \quad (13)$$

A two-dimensional Fourier transformation (2DFT) of the collected data yields directly the NMR spin density image.

Looking once more to (4) it is clear that a given point in k -space can be

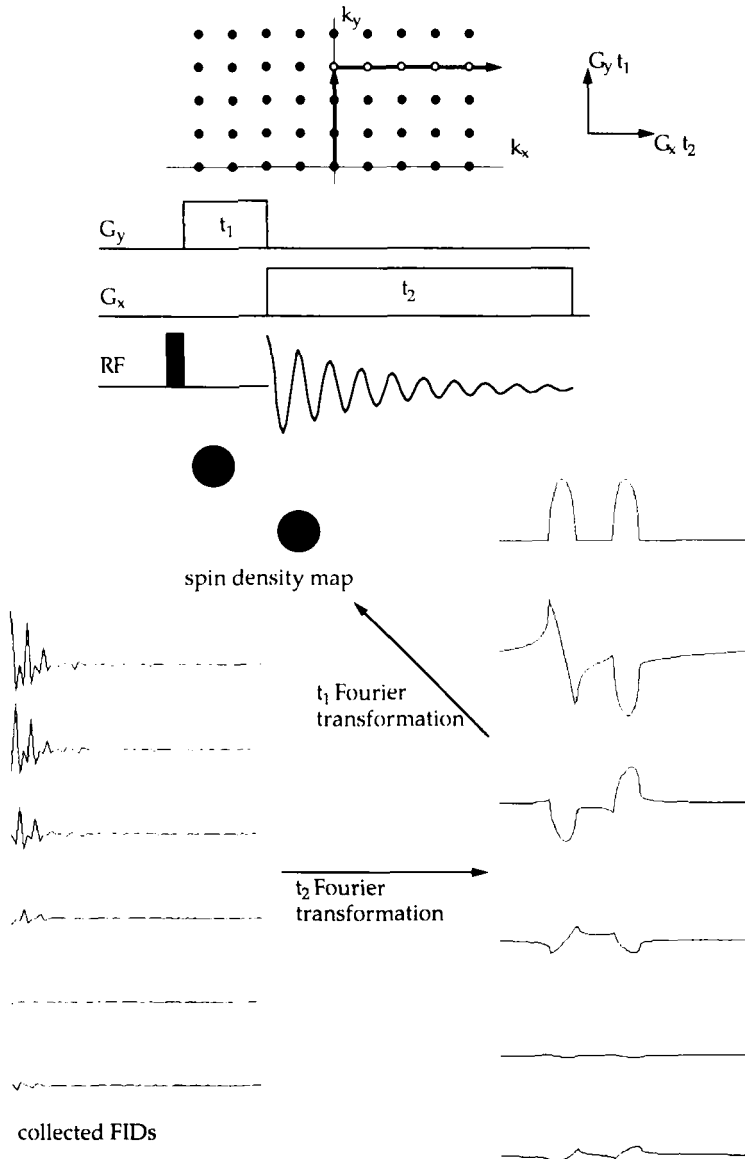


Fig. 8. Description of two-dimensional Fourier imaging showing the NMR experiment along with the corresponding k -space trajectories, and data analysis. As drawn, the data collection takes place while traversing k -space horizontally, after the experiment has been displaced vertically to the appropriate line. The data are Fourier transformed twice, once to obtain the spin density along the x axis, and a second time to obtain the spin density along the y axis.

reached by many different paths, and that in general there is a simple relationship between the time it takes to reach a point and the gradient strength during that time. A variant of 2DFI called spin-warp imaging¹⁰⁶ takes advantage of this by holding the phase encoding interval of the two-dimensional experiment constant and incrementing the gradient strength to reach the desired k-space offset. This is an example of a constant time experiment which will be discussed later.

The first NMR images were acquired by back-projection reconstruction^{1,2} in which a set of one-dimensional spin density projections are measured with the angle between the sample and the gradient incremented between each acquisition. Figure 9 shows both the k-space coverage and an example of real-space images from this procedure. This projection reconstruction approach has been predominantly replaced by two-dimensional Fourier imaging for liquid samples, but projection reconstruction is still the most widely employed technique for solid state imaging due to its inherent sensitivity advantage¹¹ and the freedom from gradient switching. Most of the sensitivity advantage arises from the lack of an evolution time which permits data collection to commence immediately following the excitation pulse.

Since there is no evolution period every acquisition must start at the k-space origin. Also, since the discussion is confined to data acquisition with a time-independent gradient, then the k-space trajectories must be straight with the only degree of freedom being the angle of the trajectory. This angle is varied by sinusoidally modulating the gradient strengths in the two quadrature gradient channels between acquisitions. Alternatively, the gradient can be left along a single direction and the sample rotated between acquisitions.

The back-projection reconstruction sampling of k-space is not on a regular grid, nor is it spaced uniformly. Neither of these characteristics represent a serious problem; by not sampling k-space on a regular grid it is impossible to apply the Fast Fourier transformation algorithm, but a discrete 2DFT could be applied to the data to recover the correct image. This would, however, require an inordinate amount of computer time. That k-space is sampled more densely near the origin results in low-frequency information in the image being better defined than high-frequency information; the coarse features of the image are better defined than the fine details. The filtered back-projection algorithm is an efficient method of obtaining the correct image from radial k-space data provided that one can measure a sufficient number of rays over half a circle (see Fig. 9). The necessary number of projections is on the order of the number of elements one wished to distinguish along a line in the resulting image.

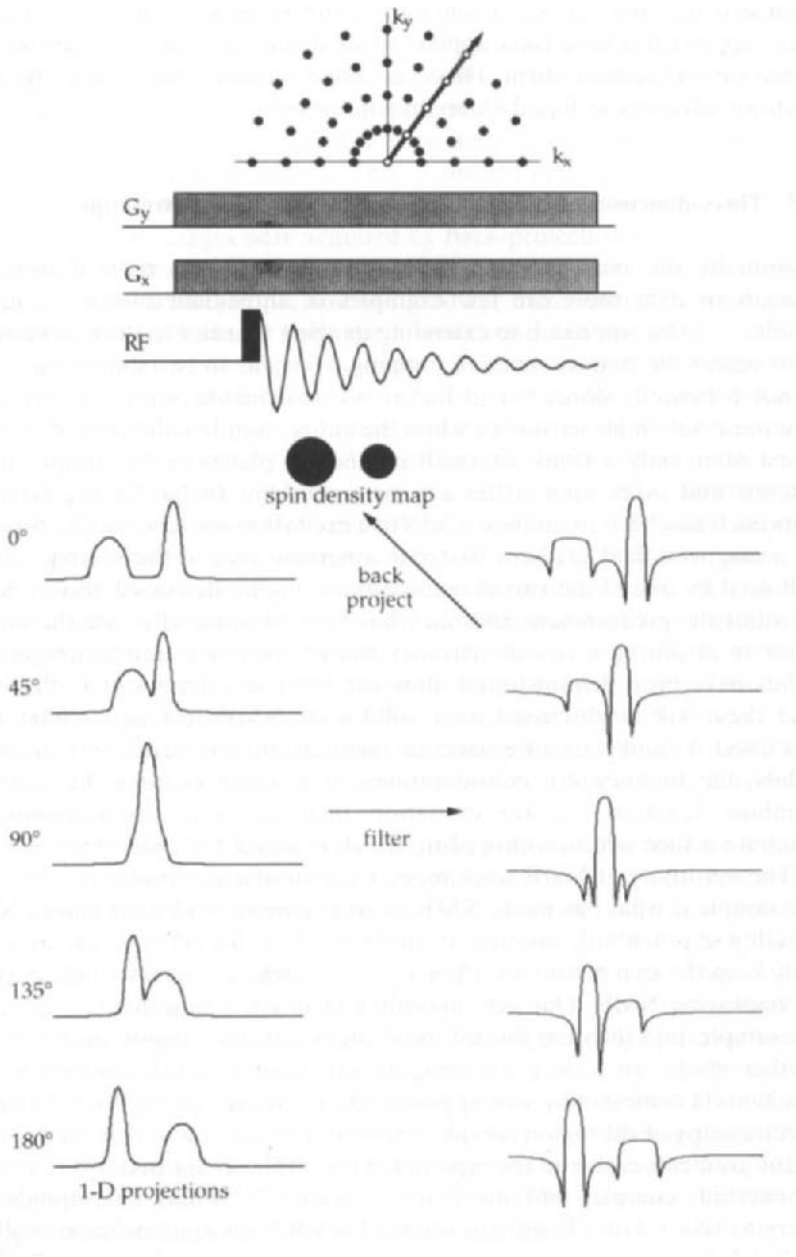
There are a variety of schemes which attempt to collect data from all of k-space in a single acquisition^{6,7} (or in a very small number of acquisitions)

such that the imaging experiment can be run extremely fast. As yet none of these approaches have been applied to solid state imaging, and to conserve space we will neglect them. However, these methods are among the most exciting advances in liquid state imaging today.⁸

2.5. Three-dimensional imaging and volume selected spectroscopy

Eventually the imaging process must be extended to three dimensions, though to date there are few examples of three-dimensional images of solids.^{107,108} One approach to extending imaging schemes to three dimensions is to repeat the step we made in jumping from one to two dimensions. This is not commonly done, but in fact it is a reasonable approach and yields comparatively high sensitivity when the entire sample volume is of interest. Most often only a single or small number of planes in the sample are of interest and other approaches are more efficient. In liquids the favoured approach has been to employ a selective excitation sequence in the presence of a magnetic field gradient to excite a narrow slice of the sample. This is followed by one of the two-dimensional techniques discussed above. So far in solids the predominant approach has been to physically slice the sample prior to acquiring a two-dimensional image. Slice selection techniques for solids have been demonstrated, however, with one-dimensional phantoms and these will be discussed after solid state NMR techniques have been discussed. Liquid state slice selection methods are not directly applicable to solids due to linewidth considerations. It is often possible, however, to combine familiar selective excitation methods with line-narrowing to generate a slice selection procedure which is useful for solid samples.

The sensitivity of NMR to changes in chemical and physical properties of the sample is what has made NMR so widely useful and what makes NMR imaging so potentially exciting. If we throw all of this information away and only keep the spin density information we are defeating much of the purpose of employing NMR. One very appealing protocol is to acquire an image of the sample, and then use this information to identify a region of interest for further study. In a way the imaging experiment is run backwards; the gradients in combination with rf pulses selectively excite a region and then the spectroscopy of the region is explored, ideally in such a way that the presence of the gradients earlier in the experiment is completely transparent. There are wonderfully complex and imaginative schemes¹⁰⁹⁻¹¹¹ under development for carrying this out on a liquid sample, but for solids the approaches are still not well-developed though some of the principles remain the same. We will neglect these liquid state studies and confine our discussion to the relatively simple solid state approaches.



2.6. Contrast

It is insufficient to arrange for good resolution and sensitivity while neglecting contrast. In an extreme case one imagines that an image is obtained which accurately depicts the exterior shape of the object but from which one is unable to discern any differences in the interior composition of the sample. An array of contrast mechanisms are given in Table 2. The pulse sequences which would be used to generate contrast by any of these methods are well-known and will not be discussed here. In one simple implementation the contrast-generating portion of the experiment precedes the imaging portion, taking place during the preparation period of a two-dimensional scheme. In other schemes contrast can be conveniently created during the evolution or mixing periods.

If the presence of the full NMR linewidth reduces the sensitivity of solid state images as compared to the liquid state, and leads to imaging methods which appear more complex, when it comes to contrast the situation is reversed. In solid state imaging we have access to a wealth of interactions including both the isotropic and anisotropic portions. The full tensor properties of all the Hamiltonians are retained so that orientations can be used to create contrast. In addition there is the strong dipolar coupling which introduces the possibility of creating large multiple-quantum coherences. Examples of most of the forms of contrast that are contained in Table 2 will be seen in the images that follow. Each imaging method is compatible with a subset of the mechanisms listed in the table, for example there must be some form of mechanical motion to distinguish the isotropic chemical shift from the anisotropic powder pattern. Images of static solids cannot, therefore, be distinguished on the basis of the isotropic chemical shift, though the bulk orientation of a sample can be studied.

Creating contrast generally costs measurement time and therefore results in a loss in the signal-to-noise ratio. De Luca and Maraviglia¹¹² have explored the question of the contrast-to-noise ratio, but it suffices to note that it is nearly always necessary to build some elements of contrast into an imaging scheme and naturally there is a price to pay which inevitably reduces the signal-to-

Fig. 9. Description of the back-projection reconstruction method of obtaining NMR images including one version of the NMR experiment with the corresponding k-space trajectories. All data collection starts at the origin of k-space and radiates outward. Unlike 2DFI, here data collection commences immediately after the excitation pulse, and only the gradient direction is varied from acquisition to acquisition. Since the data density is not uniform, a sampling artifact is convoluted into the two-dimensional data that is removed by the deconvolution step (commonly referred to as filtering). The lineshape for deconvolution corresponds to the Fourier transform of an inverse time function which is the inverse of the sampling density.

Table 2. Common contrast mechanisms.

Relaxation times	
T_1	Spectral density of molecular motions at the Larmor frequency
T_2	Range of local fields
$T_{1\rho}$	Spectral density of molecular motions at the Larmor frequency in the rotating frame (typically tens of kilohertz)
T_{1x}	Spectral density of molecular motions at a pulsed effective field frequency (typically low audiofrequencies)
Chemical shifts	
Chemical species	
Orientation	
Morphology	
Couplings	
Dipolar coupling strength	
Multiple quanta	
Spin diffusion	
Mobility	
Translational diffusion	

noise. For solids the available spin evolution time is extremely limited and one must be careful how this short interval is spent when creating contrast.

3. WIDE-LINE IMAGING METHODS

There are a number of what we will call “wide-line” techniques for solid state imaging. Wide-line methods accept the sensitivity loss associated with observing the full NMR linewidth yet can still achieve high resolution by employing large gradients. Continuous wave experiments are one obvious wide-line approach which has not to my knowledge been employed for solid state imaging. Technically acquiring an NMR image with a cw spectrometer and a strong gradient is a simple experiment, and many ESR images⁸⁹ are acquired in this fashion. The flexibility of pulsed NMR along with a recognition that the sensitivity of a cw experiment would be low have probably conspired to discourage implementing cw techniques.

Two very successful pulsed wide-line experiments which are used are STRAFI and constant time imaging.

3.1. STRAFI

Stray field imaging (STRAFI)¹¹³⁻¹¹⁵ comes closest to a cw wide-line experiment in a static magnetic field gradient. It was recognized by Samoilenko

*et al.*¹¹³ that every solenoid magnet has a region near the end of the magnet windings where there is a very large magnetic field gradient which can be used for imaging. The region corresponding to the largest magnetic field gradient has a field strength of approximately 0.4 the field strength of the homogeneous region of the magnetic field, making it very convenient to image protons by tuning the spectrometer to what would normally be the ^{31}P resonance frequency. The maximum gradient varies with the central field strength of the magnet, and is found to be 40 T/m for a 4.7-T magnet and 80 T/m for a 9.4-T magnet. This gradient is homogeneous over a disk approximately 30 mm in diameter for a wide-bore magnet.

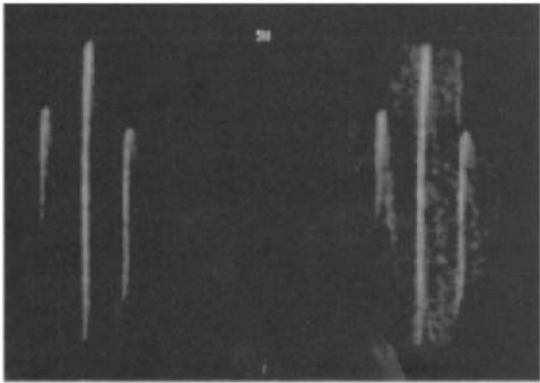
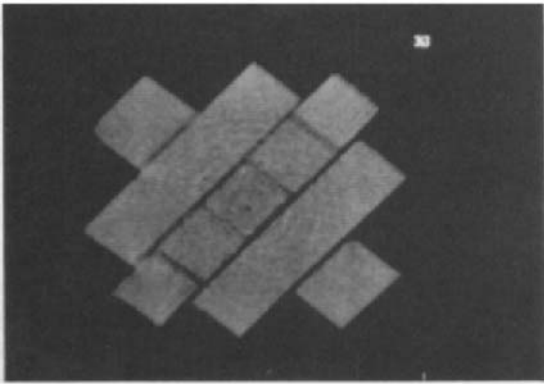
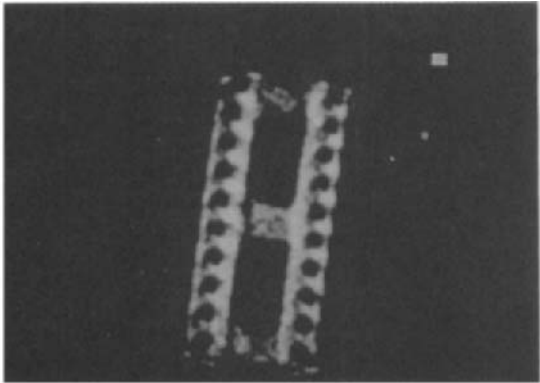
Since the gradients are extremely large, rf pulses at accessible power levels will only excite a small portion of a macroscopic sample placed in the field. The principle of STRAFI then is that a pulse train is applied to the sample as it sits in the magnetic field gradient. The pulses selectively excite a plane transverse to the gradient with the selected plane thickness being on the order of 100 μm . The sample is translated and another slice is observed, etc. Since each slice is observed separately, there is no need for a relaxation delay and the entire sample can be rapidly scanned. One version of this device can scan up to 512 slices with a separation of 60 μm in 1 s.

To enhance the sensitivity of the measurement, and as a way of introducing contrast, the signal is measured as a series of echoes in a pulsed spin-locking train. Each individual echo can be integrated and accumulated to enhance the signal-to-noise ratio. Alternatively, images from only the latter echoes can be observed to show $T_{1\rho}$ type of contrast.

A two-dimensional image is acquired by the back-projection reconstruction technique. Each scan of the sample through the selective plane yields a projection of the spin density directly (no Fourier transformation is required). The sample is then reoriented transverse to the gradient direction and scanned again. This is repeated until sufficient projections are accumulated to calculate the back-projection image. The process can be repeated in a third orthogonal direction to acquire a full three-dimensional image. So far the STRAFI technique has not been combined with slice selection, so one must resort to a full three-dimensional image, or physically slice the sample. Some examples of STRAFI images are shown in Fig. 10.

The STRAFI method is conceptually straightforward, but the probe is extremely complex, having to reorient the sample about two orthogonal axes and translate the sample along a third axis, and perform all of this in a well-controlled and reproducible manner while in a high magnet field.¹¹⁵ A diagram of the probe is shown in Fig. 11.

The spin dynamics are also not as simple as they might first appear. The slice selected by the first rf pulse is thicker than the slice at the end of a pulsed spin-locking train since the resonance offset induced by the large gradient



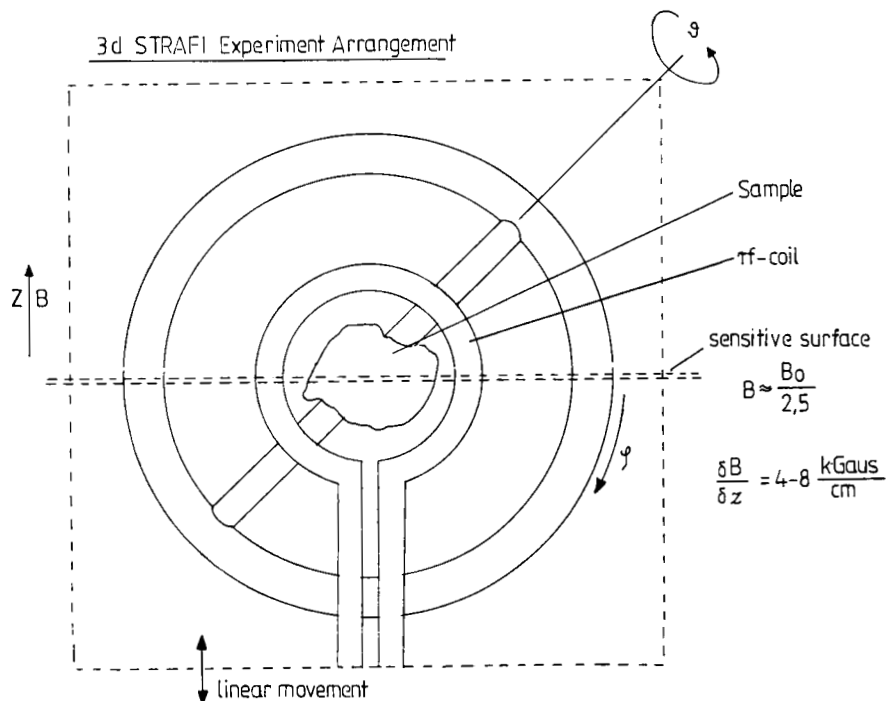


Fig. 11. A schematic description of the probe for STRAFI imaging. The sample and imaging probe are ramped through a sensitive plane in the fringe field of the magnet to acquire a one-dimensional spin density profile. To obtain a full three-dimensional image the sample is reoriented about two axes that are orthogonal to the direction of linear movement (shown by the two angles in the figure). (Figure courtesy of 4ion K. Zick.)

leads to a non-uniform relaxation rate across the slice thickness such that the edges of the excited slice relax faster than the centre. It is possible that this inhomogeneity of relaxation times can be taken to advantage to create thinner effective slices and hence higher resolution images.

Fig. 10. Some representative examples of STRAFI images including an IC socket with the metal leads still in place, a plexiglass (polymethylmethacrylate) phantom and a glass fibre reinforced composite. The PMMA phantom shows 100 μm resolution. The glass reinforced composite is a phantom which is held together by three pieces of double-sided tape. The image was collected with a 16 echo pulse train; the image on the left was reconstructed from the first four echoes, and the image on the right was reconstructed from echoes 5–16. These images demonstrate that $T_{1\rho}$ type of contrast can be built into the STRAFI technique to differentiate between hard and soft components of the sample (Figure courtesy of K. Zick.)

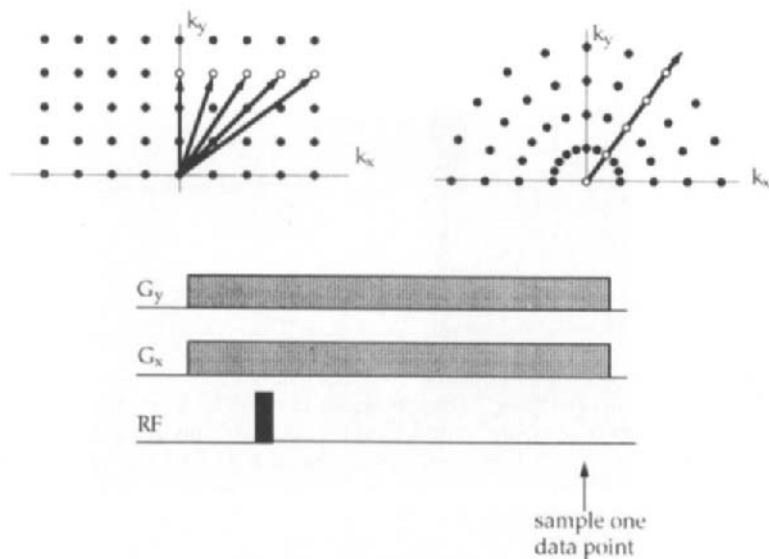


Fig. 12. A description of constant time imaging showing the NMR experiment, and the k-space trajectories. The constant time method is compatible with either BP or 2DFI, and in either case the gradient strength is varied systematically to map out the entire k-space resonance point by point. Since all of the Hamiltonians of interest commute, the chemical shift and dipolar couplings contribute a constant phase shift and attenuation so that only the variation in spin evolution due to the changing gradient field is recorded.

Finally, it should be noted that by performing the imaging experiment in a large static magnetic field gradient, some forms of contrast become unavailable; while relaxation times can be employed with some caution, spectroscopic information is generally not available.

3.2. Constant time imaging

When a system is evolving under the influence of a series of commuting Hamiltonians, the evolution is strictly the sum from each Hamiltonian (i.e. there is no interference between Hamiltonians). The secular components of the chemical shift, susceptibility, dipolar coupling and gradient Hamiltonians all commute (as can be seen from Table 1), therefore it is possible to use manipulation of the gradient strength as a means of separating the gradient Hamiltonians from all others. Emid and Creyghton¹¹⁶ suggested a wide-line imaging method, outlined in Fig. 12, for which only a modest magnetic field gradient is necessary. A two-dimensional data set is acquired

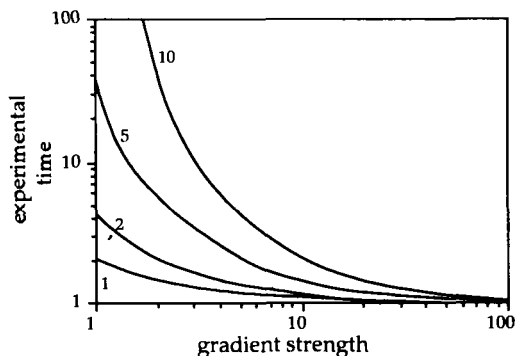


Fig. 13. A plot showing the reduction in signal-to-noise as a function of gradient strength for constant time experiments. Since the technique only gives the appearance of line-narrowing (i.e. there is no true refocusing of the magnetization), signal-to-noise is sacrificed to achieve higher resolution. Both axes of the graph are in arbitrary units.

by repeatedly measuring a single data point at a fixed evolution time. During the evolution period a gradient is applied, and in subsequent acquisitions the gradient strength is incrementally changed. The one dimension is time-independent and thus whatever spin evolution occurs due to chemical shifts, susceptibility shifts, and dipolar couplings will be constant and unobserved. However, since the gradient interaction changes from data point to data point the gradient's effect on the spin evolution will be observed. In this fashion an image can be acquired with high resolution regardless of the sample's natural linewidth.

A problem arises, however, in that while no evolution is observed from the undesired interactions, their presence is still felt as an attenuation of the signal intensity. Nothing has been done to lengthen the apparent T_2 of the sample and so there is only a very short measurement window for a typical solid. The signal-to-noise ratio therefore places a severe limit on how large the gradient must be. A plot of this reduction in sensitivity is shown in Fig. 13 for a 1-cm sample of varying linewidths. Notice that Fig. 13 shows a behaviour opposite to that displayed in Fig. 7. In a constant time experiment the signal-to-noise ratio increases with increasing gradient strength since the natural spread in resonance frequencies is assumed to be comparable to the gradient-imposed spectral width. The bandwidth of the experiment is independent of the gradient strength, and increasing the gradient allows one to move the acquisition point closer to the beginning of the FID.

The problem of sensitivity is compounded since the constant time approach is a two-dimensional experiment where the second dimension does

not contain spatial information. Every data point in k -space is phase encoded with spatial information, and collected individually so that a suitable relaxation delay must be inserted between every point in the acquisition. In practice this makes the experiment extremely time-consuming. ^1H spin-lattice relaxation times are approximately 200 ms–1 s for compounds with considerable motions such as those having methyl groups and most organic polymers. Small crystalline materials, however, often have relaxation times of many minutes. There is no need to use a 90° excitation pulse in these experiments and so normally a low tip angle pulse is used with a short recycle delay for optimum signal-to-noise ratio.

Where appropriate, the second dimension can be used to record spectroscopic information. Alternatively line-narrowing or pulsed spin-locking can be employed during the detection period to effectively reduce the receiver bandwidth and increase the sensitivity of the experiment.¹¹⁷

Line-narrowing can be introduced during the encoding delay^{116–122} to recover some of the signal-to-noise loss. Examples include solid echoes,¹¹⁹ Jeener–Broekaert echoes,¹²⁰ magic-angle sample spinning¹²¹ and multiple-pulse line-narrowing.¹²² The constant time experiment is often a good choice for the evolution period of a two-dimensional Fourier imaging scheme resulting in the spin warp modification of 2DFI. In addition, the technique is extremely insensitive to artifacts; so, though this is a slow experiment, it is very robust and a good choice when more complicated methods fail.

3.3. Multiple-quantum imaging

In the above section on constant time imaging, we saw that for signal-to-noise purposes the gradient should be as large as possible, while at the same time the bandwidth of the excitation pulse places a limit on the gradient strength (unless the gradient can be turned on after the excitation pulse). One approach to overcoming this problem is to encode the gradient evolution in a state of n -quantum coherence where it precesses n times as fast.^{123,124} A description of multiple-quantum NMR which does justice to the elegant work and understanding that has been achieved by others is beyond the scope of this review, and fortunately insightful reviews of multiple-quantum NMR have been written.^{125,126} A simple picture of why an n -quantum coherence evolves n times as rapidly in a magnetic field gradient is possible, however. The order or number of quanta that are involved in a multiple-quantum coherence is given by the difference in Zeeman quantum numbers between the spin states that the coherence connects. The single-quantum coherences with which we are familiar connect adjacent states. Each pair of connected states can be treated as a fictitious two-level system, and it is the

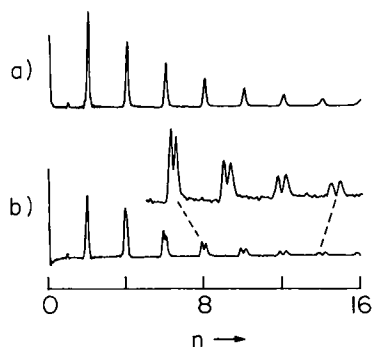


Fig. 14. A set of multiple-quantum coherences that were acquired in the presence (b) and absence (a) of a magnetic field gradient. The sample consisted of two 1.3-mm diameter tubes of adamantane with a spacing of 2 mm in a gradient of 0.048 T/m. As the order of the coherence, n , is increased, the effective magnetic field gradient also increases in proportion to n . Therefore, the higher order coherences show progressively higher spatial resolution. The vertical scale has been expanded for orders 8–14. (Reproduced with permission from Garraway *et al.*¹²⁴)

phase difference between the connected states that is of interest. This is simply a generalization of how single-quantum states are discussed and ignores for the moment how multiple-quantum states can be created. An I_z operator operating on a spin state returns the same state multiplied by the Zeeman quantum number, so an I_z rotation (a unitary operator of the form $\exp(-i\omega t I_z)$) of an n -quantum state is rotated by $n\omega t$.

The selection rules of pulsed NMR only allow single-quantum coherences to be observed,^{125,126} but it has long been known how to generate multiple-quantum coherences for a set of coupled spins and then after a multiple-quantum evolution period, to convert back to single-quantum coherence so that the effect of multiple-quantum evolution can be observed. Multiple-quantum experiments are therefore always two-dimensional or higher. The homonuclear dipolar coupling is a very convenient mechanism for generating high multiple-quantum coherences for abundant nuclei in solids.¹²⁴ Pulse cycles very similar to those employed for multiple-pulse line-narrowing are used to generate two quantum propagators that quickly lead to the creation of high quanta states.

Multiple-quantum imaging has not found much application yet, but it is an important idea to keep in mind. An example of a one-dimensional image of adamantane¹²⁴ is shown in Fig. 14. A slight twist of this experiment has been employed for ^2H imaging where it looks very promising.¹²⁷

4. MANIPULATION OF HAMILTONIANS, AVERAGED HAMILTONIANS

As was already seen with the constant time approach to imaging, it is possible to manipulate Hamiltonians during an experiment in order to keep those that are of interest and discard the remainder. There are a variety of very efficient methods for accomplishing this^{12-20,128} and average Hamiltonian theory²¹ is a simple method of describing the approaches. All Hamiltonians of interest in NMR can be split into two parts: a spin operator component, and a weighing factor which generally includes magnetic fields and geometric constants. Either of these two portions can be manipulated to obtain a desired effect. Radiofrequency pulses modulate spin operators, and the weighing factor is modulated by physically reorienting the sample or by changing the strength of an applied magnetic field. We will first introduce the basic elements of average Hamiltonian theory and then discuss multiple-pulse methods for modulating spin operators, gradient modulation techniques and sample spinning methods.

4.1. Average Hamiltonian theory

Average Hamiltonian theory (AHT) is a simple way of following the dynamics of a system that is modulated by a nearly cyclic periodic interaction. Here cyclic means that the system is returned to its original state following one modulation period. Clearly if the modulation is absolutely cyclic the experiment is of little practical interest. As the name implies, the goal of AHT is to replace a complex string of Hamiltonians with a simple effective Hamiltonian that appears to govern the dynamics of the spin system, provided that we limit the observation to particular windows. Average Hamiltonian theory saves us much effort compared to a density matrix calculation of the equations of motion for the spin system, and yields considerable insight. AHT is also not tied to a particular spin system as are density matrix calculations, and therefore AHT possibly leads to more general results than do density matrix calculations. At the allowed sampling point AHT provides the same result that the more labour-intensive methods would yield, and at every point the spin dynamics can be qualitatively followed since periodically the answer is accurately known, and between these points the spin system has only a short period of time to evolve under well-defined Hamiltonians. The total time dependence of the spin dynamics can be followed by Floquet theory¹²⁹ in a form much like AHT but at a cost of more complexity which is not warranted here.

Average Hamiltonian theory can be applied to continuously varying

Hamiltonians (an example will be given below for magic-angle sample spinning), but most applications of AHT are to piecewise constant Hamiltonians of the form,

$$H(t) = H_1 \text{ for } t_1, H_2 \text{ for } t_2, H_3 \text{ for } t_3, \dots, H_k \text{ for } t_k \quad (14)$$

where each H_i is time-independent and the total cycle time, τ_c , is given by,

$$\tau_c = t_1 + t_2 + t_3 + \dots + t_k \quad (15)$$

Each of the time-independent Hamiltonians are active in turn. The overall propagator for this set of Hamiltonians is then,

$$U(\tau_c) = \exp(-iH_k t_k) \dots \exp(-iH_2 t_2) \exp(-iH_1 t_1) \quad (16)$$

If the same set of Hamiltonians are applied repeatedly then the propagator for n repeated cycles is calculated as

$$U(n\tau_c) = U(\tau_c)^n \quad (17)$$

So from (17) it is seen that for a periodic set of Hamiltonians all that is necessary is to understand the dynamics over a single cycle, and then the spin evolution at all later times is also known. The dynamics at all times during a cycle are still quite complicated, and so we limit our observation to the end of each cycle and attempt to find an average Hamiltonian which allows (17) to be rewritten as

$$U(n\tau_c) = \exp(-i\bar{H}(\tau_c)n\tau_c) \quad (18)$$

An average Hamiltonian can be defined since the spin propagators are unitary and the product of unitary transformations is necessarily a unitary transformation. The average Hamiltonian is most directly calculated via the Baker–Campbell–Hausdorff relation for a piecewise constant Hamiltonian, and by the Magnus expansion in the more general case. The average Hamiltonian is given in terms of a series of orders with decreasing importance,

$$\bar{H}(\tau_c) = \bar{H}^{(0)} + \bar{H}^{(1)} + \bar{H}^{(2)} + \dots \quad (19)$$

where

$$\bar{H}^{(0)} = \frac{1}{\tau_c} \{H_1(t_1) + H_2(t_2) + H_3(t_3) + \dots + H_k(t_k)\} \quad (20)$$

and

$$\bar{H}^{(1)} = \frac{-i}{2\tau_c} \{[H_2(t_2), H_1(t_1)] + [H_3(t_3), H_1(t_1)] + [H_3(t_3), H_2(t_2)] + \dots\}$$

Higher order terms involve progressively higher order commutators and will not be needed for our discussions.

It is clear from (20) that if the Hamiltonian commutes with itself at all times during the cycle then the average Hamiltonian is strictly the time

average of the Hamiltonian as given by the zero-order term and all higher order terms vanish. This is the case for the constant time imaging experiment of Emid and Creyghton described above, and the arguments in that section can be directly couched in average Hamiltonian terms.

4.2. Multiple-pulse methods

Multiple-pulse methods are widely employed for averaging linear I_z Hamiltonians such as the chemical shift (for example Carr–Purcell cycles),¹³⁰ and bilinear I_z Hamiltonians such as the homonuclear dipolar coupling (for example WAHUA cycles¹³¹). A special class of multiple-pulse cycles (time-suspension cycles¹³²) aim to remove all time-independent Hamiltonians so that for a solid the observed linewidth under a perfect time-suspension cycle would be determined by the $T_{1\rho}$ of the sample ($\nu_{1/2} = (\pi T_{1\rho})^{-1}$). The spin-lattice relaxation time in the rotating frame, $T_{1\rho}$, is the general limit on the success of line-narrowing cycles, and so time-suspension cycles are particularly appealing for solid state imaging. Each of these three examples will be described briefly.

Figure 15(A) shows the familiar Carr–Purcell cycle, which refocuses linear I_z operators. In discussing the properties of multiple-pulse cycles we ignore the necessary prepulses and concentrate on averaging properties of the individual cycles. All calculations are naturally performed in the rotating reference frame, and the largest interactions are assumed to be rf pulses. Cycles are therefore defined with respect to rf pulses and all other interactions are treated as perturbations. This approach is also a great convenience since rf pulses are under our control and ideally the effects of rf pulses are uniform across the sample. A new reference frame (the toggling frame) is introduced to remove the motions due to the rf pulses so that the dynamics of smaller Hamiltonians can be followed. The toggling frame is not a continuous rotation such as the transform to the rotating frame, but is a series of discrete rotations due to rf pulses. Radiofrequency pulses only modulate the spin portion of Hamiltonians, therefore Hamiltonians are treated as classes rather than individually. Linear I_z Hamiltonians are transformed to the toggling frame as

$$\tilde{I}_z(t) = U_{\text{rf}}^{-1}(t) I_z U_{\text{rf}}(t) \quad (21)$$

where

$$U_{\text{rf}}(t) = \exp(-iH_{\text{rf}}(t)) \quad (22)$$

The toggling frame states for I_z and $I_z I'_z$ operators are shown below the pulse cycle in Fig. 15. First, notice that the cycle is indeed cyclic, that is

$$U_{\text{rf}}(\tau_c) = 1 \quad (23)$$

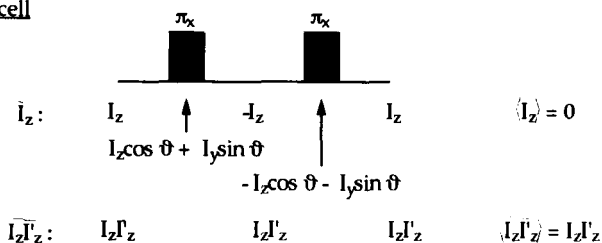
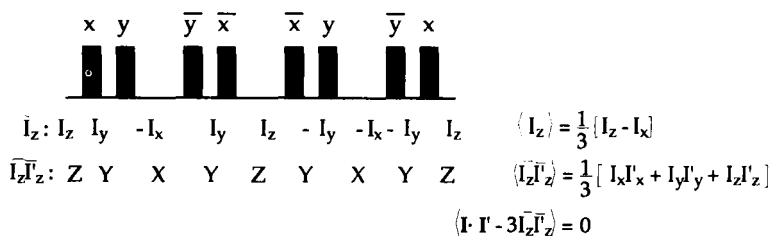
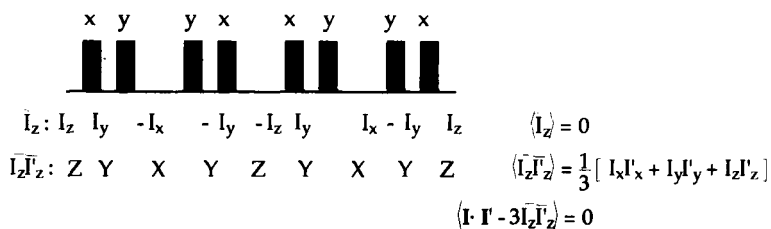
A. Carr PurcellB. MREV-8C. MG-8

Fig. 15. Common multiple-pulse cycles which are used for line-narrowing. The Carr-Purcell cycle (A) is useful for averaging time-independent I_z operators as well as heteronuclear dipolar coupling. The toggling frame states given below the cycle indicate that for delta function pulses time-independent I_z operators average to zero, and $I_z I'_z$ operators are not modulated. The MREV-8 cycle (B) averages $I_z I'_z$ operators, while only reducing the size of time-independent I_z operators. MREV-8 is frequently used for CRAMPS to remove dipolar couplings while retaining a scaled version of the chemical shift. The MG-8 cycle (C) averages both dipolar couplings and time-independent I_z operators to zero.

The angular dependence of the toggling frame state during the rf pulse is understood such that θ is linear in the pulse duration ($\theta(t) = t_p \omega_1$). The average Hamiltonian for I_z operators is calculated following (20), and the zero-order average Hamiltonian is zero including finite rf pulses. The first-order average Hamiltonian is zero if the rf pulses are approximated as delta-functions, but is non-zero for finite pulse widths.¹⁷

As seen in Fig. 15, the toggling frame states for bilinear spin operators are not modulated by the Carr–Purcell cycle in the delta-function rf pulse approximation. The Carr–Purcell cycle can be used, therefore, to suppress chemical shifts and other linear I_z operators while allowing the observation of homonuclear dipolar couplings. Yannoni¹³³ has demonstrated this application, and then used the value of the measured dipolar coupling to determine ^{13}C – ^{13}C bond lengths.

For solid state spectroscopy it is more common to suppress dipolar couplings while retaining the chemical shift. Figure 15(B) shows the MREV-8 cycle,^{134,135} which is the workhorse line-narrowing cycle for CRAMPS¹³⁶ (combined rotation and multiple-pulse spectroscopy) studies of abundant nuclei in solids. The MREV-8 cycle will only be considered in the delta-function rf pulse approximation even though this fails to do justice to the cycle, which is highly compensated for finite rf pulse widths and common rf pulse imperfections. The toggling frame states for I_z and $I_z I'_z$ are shown below the cycle in Fig. 15. The MREV-8 cycle modulates I_z operators, but the average is not zero, rather an I_z operator is transformed to an $(I_z - I_x)/3$ operator. Just as an I_z operator causes spin evolution about the z -axis in the rotating frame, an average Hamiltonian proportional to $(I_z - I_x)/3$ appears to cause spin evolution about the $(I_z - I_x)$ -axis with a frequency of $\sqrt{2}/3$ times the full Hamiltonian strength. The factor $\sqrt{2}$ originates from the length of the $(I_z - I_x)$ vector. This simple spin evolution is only apparent if the spin evolution is sampled exactly once per cycle. It is common to describe this averaging as producing an “effective” field that is oriented along the $(-1\ 0\ 1)$ axis and has a length of $\sqrt{2}/3$.

Bilinear spin operators are also modulated by the MREV-8 cycle and the spin operator $I_z I'_z$ is transformed by MREV-8 into $(I_x I'_x + I_y I'_y + I_z I'_z)/3$. This is non-zero, but recall that the dipolar Hamiltonian is proportional to $(\mathbf{I} \cdot \mathbf{I}' - 3I_z I'_z)$ (see Table 1). The dot product $\mathbf{I} \cdot \mathbf{I}' (= I_x I'_x + I_y I'_y + I_z I'_z)$ is a scalar and therefore is not modulated by rf pulses. So the MREV-8 cycle does indeed average the dipolar Hamiltonian to zero at this level of approximation. Overall, the MREV-8 cycle reduces the normally dominant homonuclear dipolar coupling to near zero and only slightly reduces the strength of the chemical shielding Hamiltonian, thereby allowing the chemical shifts to be seen without interference from the larger homonuclear dipolar couplings.

The final pulse cycle shown in Fig. 15(C) is designed to average both I_z and dipolar Hamiltonians. This cycle was suggested by Mansfield and Grannell¹⁶ and subsequently rediscovered by other workers.^{137,138} We will call it MG-8. For convenience, throughout this review we will follow the lead of MREV-8 and BR-24, and refer to un-named multiple-pulse cycles by the initials of their authors and the number of rf pulses. The toggling frame states for MG-8 are

given below the cycle and a careful examination will reveal that to zero order the cycle performs as it was designed to. In reality MG-8 is not well-compensated and performs poorly. Efficient cycles that average both linear I_z and homonuclear dipolar couplings are known and will be introduced later.

Figure 15 illustrates that multiple-pulse methods can be used for manipulating Hamiltonians and that given a set of Hamiltonians it is perfectly reasonable to design an experiment such that only the Hamiltonians of interest are preserved. In his recent book, Munowitz¹²⁸ discusses in detail this general approach of tailoring the effective Hamiltonian of a system to meet one's needs.

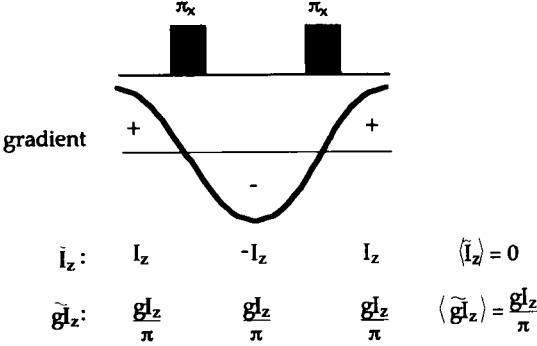
4.3. Gradient modulation

Looking back to Fig. 15 and recalling that the gradient Hamiltonian is a linear I_z operator, then it is clear that if a gradient field were present when these cycles were run, under the MREV-8 cycle the spin evolution would be a superposition of chemical shift and gradient spin evolution, while under both the Carr–Purcell cycle and MG-8 cycle no gradient evolution would be detected. In other words, a static magnetic field gradient is indistinguishable from other inhomogeneous interactions and is averaged exactly as are chemical shifts.

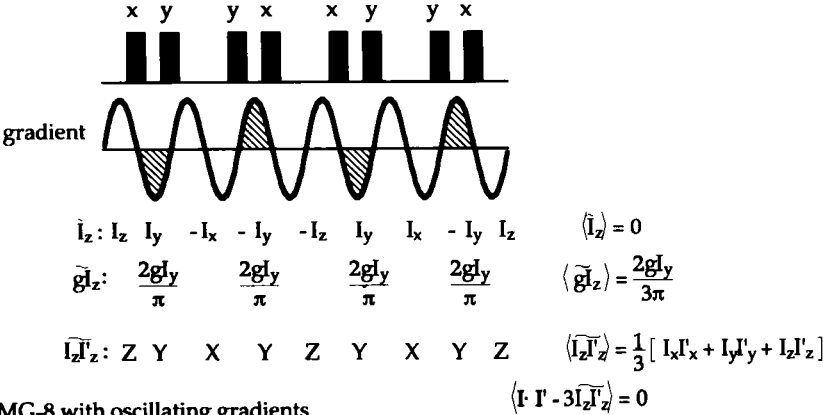
All nuclear spin Hamiltonians, including the gradient Hamiltonian, can be averaged by an appropriate multiple-pulse cycle. What is needed is a method of maintaining the gradient Hamiltonian without compromising the multiple-pulse cycle's line-narrowing efficiency. Fortunately the gradient is under experimental control, and so we can modulate the gradient strength at the same frequency that the effective field of time-independent I_z operators is modulated by the multiple-pulse cycle. This is equivalent to mixing together two identical frequencies, the result of which is a d.c. signal (along with some harmonics which are not of interest). In terms of the averaged gradient Hamiltonian, the spin operator modulation from the multiple-pulse cycle and the weighing factor modulation from the time variation of the gradient strength combine to give minimal averaging of the gradient Hamiltonian. At the same time only the spin operator portions of time-independent I_z Hamiltonians are being manipulated and the averaged Hamiltonians for these undesired Hamiltonians still vanish.

Figure 16 shows examples of gradient modulation combined with a multiple-pulse cycle for imaging and line-narrowing. The Carr–Purcell cycle, which was introduced in Fig. 15, is combined with a synchronously oscillating magnetic field gradient^{139–141} such that the gradient spin evolution is preserved while chemical shift evolution is suppressed. The toggling frame states for I_z

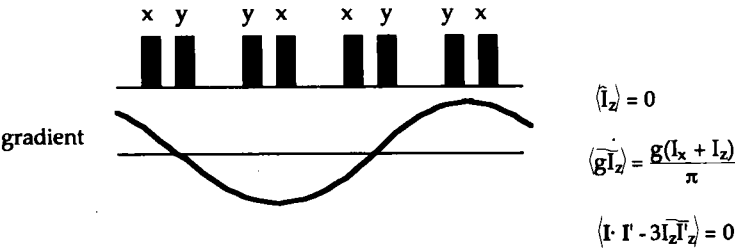
A. Carr-Purcell with oscillating gradients



B. MG-8 with oscillating gradients



C. MG-8 with oscillating gradients



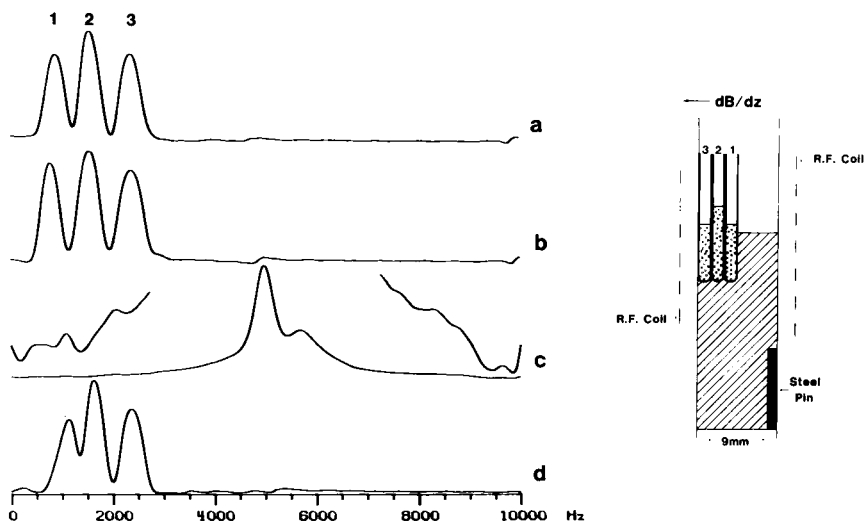


Fig. 17. A demonstration of the effectiveness of the Carr-Purcell cycle at removing time-independent linear I_z distortions from an NMR image. Using a sequence like the Carr-Purcell cycle shown in Fig. 16, Miller and Garraway were able to refocus the magnetic field distortions from a steel pin that was located within 9 mm of a water phantom while still recording the correct one-dimensional image. The figure shows the phantom geometry and four one-dimensional images of three capillary tubes containing water: (a) static gradient image without the steel pin; (b) refocused gradient image without the steel pin; (c) static gradient image with the steel pin; (d) refocused gradient image with the steel pin. The insert in (c) is magnified 15 times to display the full width of the image. (Reproduced with permission from Miller and Garraway.¹⁴¹)

and gI_z are shown below the pulse cycle. In the figure, g is the strength of the magnetic field gradient. It is clear that I_z operators are averaged to zero whereas gI_z operators are preserved. The shape of the gradient modulation enters in only as a weighing factor. This approach for separating gradient spin evolution from chemical shift and susceptibility shift spin evolution has

Fig. 16. Refocused gradient methods of imaging. The Carr-Purcell multiple-pulse cycle with a synchronously oscillating gradient to separate the gradient evolution from the chemical shift and susceptibility shift spin evolution is shown in (A). The polarity of the magnetic field gradient is modulated in step with the toggling of the effective field of the Carr-Purcell cycle resulting in the gradient effective field appearing static while time-independent I_z operators are still averaged to zero. Likewise, for the MG-8 cycle, B and C, an oscillating gradient results in a net gradient effective field, while the dipolar couplings and time-independent I_z operators vanish. The direction and strength of the gradient effective field is dependent on the frequency and phase of the oscillating magnetic field gradient.

been suggested by a number of authors; a nice demonstration by Miller and Garraway¹⁴¹ is shown in Fig. 17.

The combination of an oscillating gradient with MG-8 (Fig. 15(C)) yields a response for which both homonuclear dipolar coupling and chemical shifts are averaged to zero while the gradient evolution is only scaled see Fig. 16(B). This is the application for which MG-8 was originally suggested by Mansfield and Grannell.¹⁶ The MG-8 cycle is repeated in Fig. 16(C) with a lower frequency oscillating gradient. It is often the case that a multiple-pulse cycle is compatible with a variety of time-dependent gradients. Notice that the effective field for gradient evolution varies with the gradient modulation.

4.4. Magic-angle sample spinning

The isotropic chemical shift is one of the most valuable pieces of information from NMR, and it is therefore very desirable to have access to the isotropic chemical shift for creating contrast in solid state imaging. Volume selected spectroscopy generally will also require that the isotropic chemical shift be measured rather than the full chemical shift tensor. For solids the chemical shift for each resonance line is a second rank tensor, and in the most general case appears as a broad tent-shaped powder pattern. The width of this powder pattern depends on the chemical environment of the nuclei of interest and can well be larger than the entire range of isotropic chemical shifts. It is only through some motion that the broad powder pattern can be narrowed to the isotropic position, though as we have seen, multiple-pulse methods can completely suppress spin evolution from chemical shifts. The averaging motion can take many forms, the most common of which is magic-angle sample spinning (MASS).^{142,143} Magic-angle hopping,¹⁴⁴ a version of MASS made up from discrete rotations rather than a continuous rotation, has also been demonstrated. In solution the random molecular tumbling of molecules is responsible for removing the chemical shielding anisotropy. Mechanical sample spinning modulates the geometric weighing factors of the chemical shielding Hamiltonian. The resonance frequency of a particular spin isochromat varies as¹⁸

$$\begin{aligned}\omega(t) = & \bar{\omega} + C_1 \cos(\omega_r t + \gamma) + C_2 \cos(2\omega_r t + 2\gamma) + S_1 \sin(\omega_r t + \gamma) \\ & + S_2 \sin(2\omega_r t + 2\gamma)\end{aligned}\quad (24)$$

where the factors C_1 , C_2 , S_1 , S_2 , and γ depend on the particular isochromat of interest, and $\bar{\omega}$ is the isotropic resonance frequency. The average of (24) over one complete revolution of the spinner (i.e. $0 \leq \omega_r t \leq 2\pi$) is $\bar{\omega}$, since all of the other terms in (24) vary sinusoidally with a periodicity of 1 or $\frac{1}{2}$ a rotor period. The zero-order average Hamiltonian for a MASS experiment

where the cycle time is one rotor period is $\bar{H}_z^{(0)} = \bar{\omega}I_z$. Therefore if the spin system is observed stroboscopically once per rotor period the isotropic frequency completely describes the observed spin dynamics.¹⁴⁵ A spectral range wider than the spinner frequency is generally of interest so the spin evolution is normally sampled more often than once a rotor period, and the spinning sidebands that are observed in MASS spectra are a consequence of violating this sampling condition. Note, however, that the lineshape of the resonances does not depend on how the signal is sampled.

Mass is also useful for averaging homonuclear dipolar couplings¹⁴² provided that the spinning speed is larger than the coupling. This condition is fulfilled for some soft materials in which molecular motions reduce but do not eliminate homonuclear dipolar couplings.

5. IMAGING WITH MULTIPLE-PULSE LINE-NARROWING

As mentioned earlier, multiple-pulse line-narrowing approaches are the oldest approaches to solid state imaging and were first applied by Mansfield and coworkers.¹⁶ Multiple-pulse methods are also the most studied and in many respects the most promising for solid state imaging. Though MASS will undoubtedly be used where the isotropic chemical shift is of interest, most likely MASS will be employed in combination with multiple-pulse line-narrowing to achieve the highest possible signal-to-noise ratio and resolution. The various multiple-pulse methods will be discussed and grouped according to the type of gradient modulation since this has profound implications for the observed image.

5.1. Time-independent gradients

Time-independent gradients are the simplest to apply and are widely used in multiple-pulse imaging. Figure 1 displayed a one-dimensional image of camphor acquired early on by Mansfield and Grannell,¹⁶ and Fig. 18 shows a two-dimensional image of two pieces of coal acquired by Botto and coworkers¹⁴⁶ using the same approach with filtered back-projection reconstruction. All of these images were acquired after the gradient had been turned on and allowed to stabilize. Both groups used MREV-8 line-narrowing, so the observed spin evolution is a combination of chemical shift, susceptibility shift and gradient spin evolution. Ideally the gradient is made sufficiently large that the other contributions can be ignored. One advantage to this approach is that the gradient settling time does not enter into the imaging process.

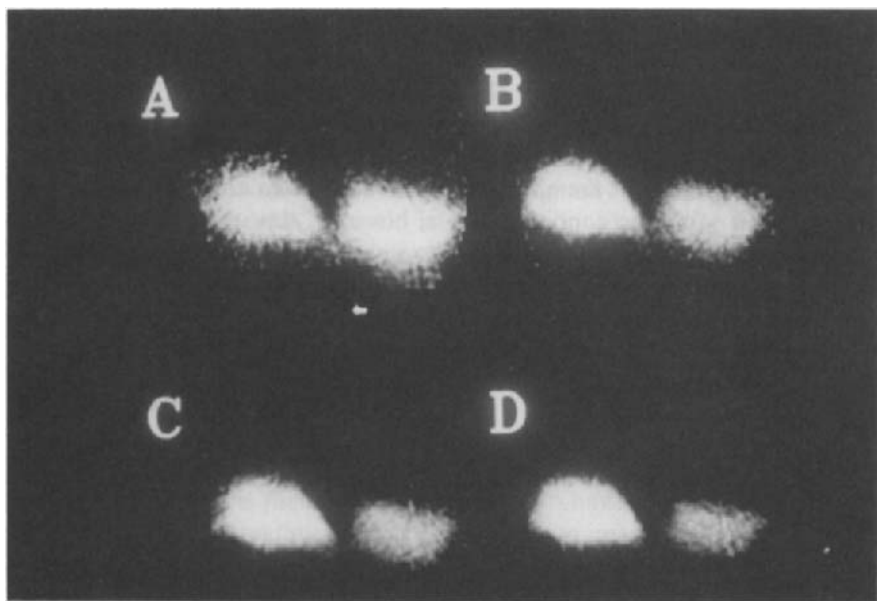


Fig. 18. A two-dimensional image of two pieces of coal collected by the static gradient multiple-pulse back-projection reconstruction technique. MREV-8 line-narrowing was employed. The phantom was constructed from a piece of retinite (left) and vitrinite (right). The four different images were obtained with recycle times of 235, 585, 1085 and 1585 ms from (A) to (D) respectively, so that the variation in image intensity reflects variations in T_1 . (Reproduced with permission from Dieckman *et al.*¹⁴⁶)

The same approach to line-narrowing can be applied as a two-dimensional Fourier imaging scheme as shown in Fig. 19. To acquire these images Chingas *et al.*¹²² used MREV-8 line-narrowing during both the evolution and detection periods of a two-dimensional imaging sequence along with gradient switching. Since 2DFI requires that the gradient direction be changed part way through the experiment (see Fig. 8), the gradient settling time represents a complication. The gradient settling time is rarely a problem in liquids imaging since it is short compared to the liquid T_2 . For solid samples, however, the T_2 is often shorter than the gradient settling time and so in the most straightforward experiment no signal would be detectable following gradient switching. Szeverenyi and Maciel¹⁴⁷ have shown that the spin magnetization can be stored, along the static magnetic field; Chingas *et al.*¹²² employed a similar storage scheme in which the static field is replaced with a spin-lock field during gradient switching to avoid image distortions from gradient settling. Magnetization storage is shown in Fig. 19 and allows

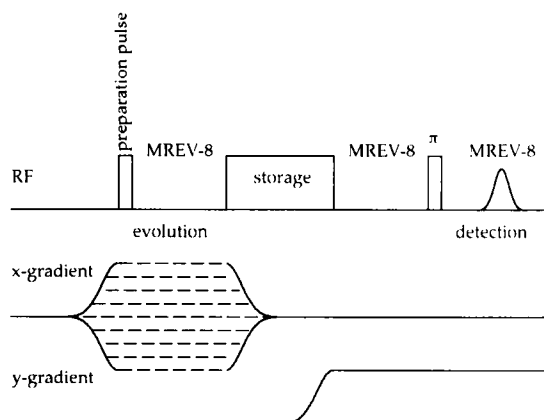
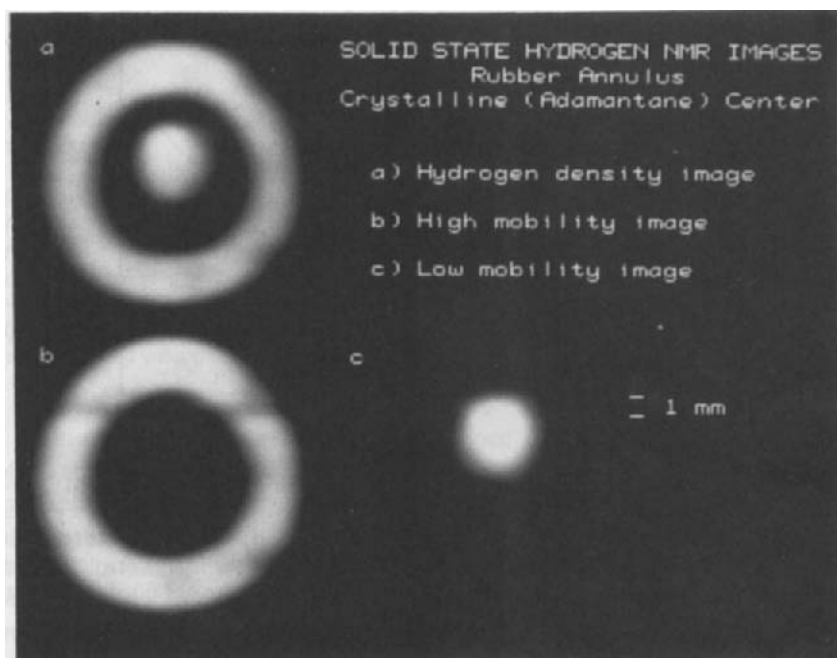


Fig. 19. A two-dimensional Fourier imaging approach to solid state imaging which utilizes the MREV-8 cycle and magnetization storage during gradient switching. The gradient was static during both the phase encoding time and the read time as indicated in the figure. The phantom consists of a neoprene hose section (12 mm o.d.) surrounding a 5 mm tube of adamantane. A combination of T_1 and $T_{1\rho}$ relaxation allowed Chingas *et al.* to record separate images of the two components. (Adapted with permission from Chingas *et al.*¹²²)

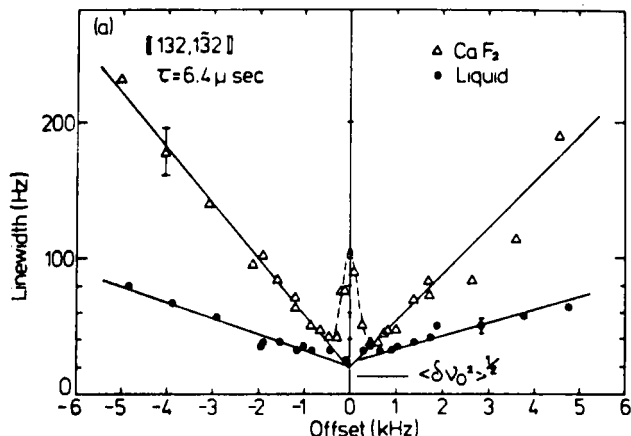


Fig. 20. Line-narrowing efficiency plotted as a function of offset for the MREV-8 multiple-pulse cycle. Ignoring the decrease in line-narrowing efficiency near resonance, MREV-8 displays a roughly quadratic dependence of the residual linewidth with offset. For imaging the implications are that the image resolution will degrade as one moves to the edges of the image. These data were obtained for a single crystal CaF_2 sample. (Reproduced with permission from Garraway *et al.*¹⁴⁸)

distortion-free images to be observed. There is a price to pay in sensitivity for using magnetization storage since only one component of the transverse magnetization can be saved at a time and the magnetization decays by T_1 or $T_{1\rho}$ during the storage interval.

There are two serious problems with a static magnetic field gradient: (1) the line-narrowing is not as efficient as it could be since time-independent I_z operators are not averaged; and (2) the line-narrowing efficiency of multiple-pulse cycles varies with resonance offset. Enough has been said on the first point, so we will concentrate here on the offset dependence of multiple-pulse cycles. When an image is acquired in the presence of a static magnetic field gradient, the frequency shift from the gradient is indistinguishable from a resonance offset. Figure 20 shows an example of the variation in line-narrowing efficiency of the MREV-8 cycle as a function of offset.¹⁴⁸

The on-resonance deterioration in line-narrowing efficiency in Fig. 20 is a consequence of small residual error terms causing spin evolution through complex trajectories which leads to dephasing. A resonance offset introduces coherent spin evolution that averages components of error terms orthogonal to the effective field to zero, while the error terms parallel to the effective field are generally too small to be apparent. This mechanism of additional line-narrowing off-resonance is commonly referred to as “second” averaging¹⁴⁹ and can be a very useful addition to line-narrowing approaches.

Table 3. Properties of common multiple-pulse cycles.

	WAHUHA	MREV-8	BR-24
Pulse sequence	$(xy)(\bar{y}x)$	$(xy)(\bar{y}x)(\bar{x}y)(\bar{y}x)$	$(xy)(\bar{y}x)(\bar{x}y)(\bar{y}x)$ $(yx)(\bar{x}y)(\bar{y}x)(yx)$ $(\bar{x}y)(\bar{y}x)(\bar{x}y)(\bar{x}y)$
$H_D^{(0)}$	$\neq 0$	4 s.e.p.p.	4 s.e.p.p.
$H_X^{(\text{odd})}$	2 s.e.p.p.	2 s.e.p.p.	12 s.e.p.p.
$H_D^{(2)}$	$\neq 0$	$\neq 0$	6 s.e.p.p.
Scaling factor	0.571	0.47	0.385

$H_D^{(0)}$ includes the effects of finite pulses.

s.e.p.p. = solid echo pulse pair.

The approximately quadratic dependence of the residual linewidth on offset complicates solid state imaging in the presence of a static magnetic field gradient. If the frequency offset in Fig. 20 is replaced by the equivalent spatial offset, it is clear that the edges of the image will have noticeably worse resolution than the centre of the image. A simple way of understanding the origins of this line-broadening is to consider a single solid echo pulse pair (made up of two rf pulses such as $\tau - (\pi/2)_x - \tau - (\pi/2)_y - \tau$), and to recognize that the presence of a magnetic field gradient during the central window is equivalent to a z-rotation of the transmitter between the two rf pulses. A phase shift of the transmitter frequency is a z-rotation in exactly the same way that a frequency offset is a continuous z-rotation. The solid echo pulse pair then in practice has the form,

$$\tau - (\pi/2)_x - \tau - (\pi/2)_{y+\phi} - \tau$$

and when ϕ is not zero the solid echo pulse pair is less effective at refocusing dipolar couplings. In this manner the gradient interferes with the line-narrowing efficiency of the multiple-pulse cycle,¹⁵⁰ and the amount of interference depends on the gradient pulse evolution. For example, if the gradient phase shift corresponds to 90° then the toggling frame states for the nominal solid echo pulse pair are I_z, I_y, I_z (rather than the expected I_z, I_y, I_x states) and this sequence of toggling frame states does not average homonuclear dipolar couplings.

The MREV-8 cycle is the most popular line-narrowing cycle for multiple-pulse imaging with static gradients, but there are many others which can be profitably employed and Table 3 lists the best known of these. In particular the BR-24¹⁵¹ sequence generally yields better resolution than MREV-8 for rigid materials. In addition to the multiple-pulse cycles listed in Table 3, there are windowless multiple-pulse cycles,¹⁵² magic-echo line-narrowing methods,^{153,154} and Lee-Goldburg line-narrowing methods,^{155,156} all of which

can be employed for solid state imaging, but so far have not been extensively explored.

The necessary instrumentation for multiple-pulse line-narrowing in the presence of a static magnetic field gradient is not particularly demanding. Commercial spectrometers have long been able to perform multiple-pulse line-narrowing, and the gradient requirements are similar to gradients which are used for NMR microscopy.

5.2. Oscillating gradients

Oscillating magnetic field gradients are an attractive replacement for static gradients for a number of reasons: (1) a sinusoidal current applied to a coil will always have the same steady state frequency, although the amplitude and phase may have changed; (2) the gradient coil can be tuned to resonate at the desired gradient frequency resulting in a very efficient transfer of power into the coil; (3) the gradient is time-dependent and therefore pulse cycles can be designed to average the chemical shift and susceptibility shift while preserving the gradient spin evolution; (4) the gradient is periodically zero and these zero points can be made to coincide with the rf pulses to avoid off-resonance effects during the rf pulses.

Table 4 lists a number of oscillating gradient imaging methods. In general it has not proven advantageous to limit the rf pulses to those times when the gradient is zero since in all oscillating gradient schemes the gradient is on between the rf pulses in every solid echo pulse pair. The gradient spin evolution between rf pulses has a greater influence on the cycles' line-narrowing efficiency than the off-resonance effects during rf pulses.¹⁵⁰ This is perhaps not surprising since the rf field strength is much stronger than the gradient field strength. Point (4) above may therefore be mainly discounted.

The most useful application of oscillating gradients is to remove chemical shifts and susceptibility shifts by using a slowly varying gradient along with an alternating effective field.^{157,158} Such images still possess a spatially varying resolution, but the methods are simple to apply and the resolution is superior to that encountered with static gradient imaging. Some of these methods may even be used with standard micro-imaging apparatus designed for materials imaging of liquid-containing samples.¹⁵⁹

The instrumentation for oscillating gradient methods is identical to that needed for static gradients where low-gradient frequencies are employed. When gradient frequencies higher than a few kilohertz are used it is beneficial to include tuning elements in the gradient circuits. The power requirements for driving the gradient are then much less since the field strength is amplified by the quality factor of the circuit.

Table 4. Oscillating gradient multiple-pulse cycles.

	MT-6	MG-8	SHRIMP	MG-24	C-48
Pulse sequence	$(\overline{xy}x\overline{xy}x)$	$(xy)(yx)(xy)(yx)$	$(xy)(yx)(xy)(yx)$ $(\overline{xy})(\overline{yx})(\overline{xy})(\overline{yx})$	$(\overline{xy})(\overline{yx})(xy)(\overline{yx})$ $(\overline{xy})(\overline{yx})(\overline{xy})(\overline{yx})$ $(xy)(\overline{yx})(\overline{xy})(\overline{yx})$	$(xy)(\overline{xy})(xy)(\overline{yx})$ $(\overline{yx})(\overline{yx})(\overline{xy})(\overline{xy})$ $(\overline{xy})(\overline{yx})(yx)(\overline{yx})$ $(\overline{xy})(\overline{xy})(\overline{xy})(yx)$ $(y\overline{x})(yx)(x\overline{y})(xy)$ $(x\overline{y})(y\overline{x})(\overline{yx})(y\overline{x})$
$H_D^{(0)}$	$\neq 0$	4 s.e.p.p.	4 s.e.p.p.	8 s.e.p.p.	3 s.e.p.p.
$H_X^{(\text{odd})}$	$\neq 0$	$\neq 0$	8 s.e.p.p.	$\neq 0$	6 s.e.p.p.
$H_D^{(2)}$	$\neq 0$	$\neq 0$	$\neq 0$	$\neq 0$	3 s.e.p.p.
Number of gradient cycles per multiple-pulse cycle	3	$\frac{6}{1}$	$\frac{12}{2}$	1	1

$H_D^{(0)}$ includes the effects of finite pulses.

s.e.p.p. = solid echo pulse pair.

5.3. Pulsed gradients

Applying the gradient in the form of short (2–5 μ s) pulses¹⁵⁰ offers the greatest experimental flexibility and the highest quality images, though at the cost of greater instrumental complexity. The primary motivation in going to the added experimental complexity that pulsed gradients represent is to avoid the spatial dependence on resolution that is normally seen with multiple-pulse methods (see Fig. 20). One can well imagine that though a static magnetic field gradient interferes with multiple-pulse line-narrowing, there are certain windows in multiple-pulse cycles that are less susceptible to interference than others. One simplistic way of thinking about pulsed gradients is to recall that the gradient Hamiltonian is an I_z operator, and so if the gradient is placed only in windows of the multiple-pulse cycle for which the toggling frame state is also along I_z then the gradient cannot interfere with the dipolar averaging, at least to zero order in average Hamiltonian theory.

An example of the benefits of using pulsed gradients is shown in Fig. 21 where a transmitter phase shift has been used to simulate a magnetic field gradient.¹⁵⁰ Also shown in Fig. 21 are two one-dimensional images comparing a static magnetic field gradient to a pulsed gradient. The resolution with pulsed gradients is clearly superior.

In the experiments shown in Fig. 21 the MREV-8 cycle was employed for line-narrowing and the gradient effective field is oriented along I_z , while the chemical shift effective field is along $I_z - I_x$. This arrangement leads to relatively complicated spin dynamics, and ideally, of course, the chemical shift should be suppressed. One approach to suppressing the chemical shift is to recognize that for ^1H observation the range of chemical shifts is reasonably small and the second averaging¹⁶⁰ mechanism discussed earlier can be used to average chemical shifts. In Fig. 22 a MREV-8 cycle is again used for imaging, but here the pulsed gradient spin evolution is oriented along the $I_z + I_x$ direction, orthogonal to the chemical shift effective field which is still along $I_z - I_x$.¹⁶⁰ In addition, a phase toggle has been introduced into the pulse sequence which adds yet another effective field that is directed parallel to the gradient effective field direction. The result is that a sum of the phase toggle and gradient Hamiltonians is observed, and provided that this sum is greater than the chemical shift term, the chemical shift vanishes. The phase toggle represents a spatial offset of the image, and since it is uniform across the sample its effect on the image may for the most part be ignored. An example of a two-dimensional image of a poly(methylmethacrylate) phantom is shown in Fig. 22 in both a stacked plot and grey scale format.

Pulsed gradients allow great flexibility in designing imaging experiments, but perhaps the most useful type of multiple-pulse cycle for imaging is one which suppresses all interactions other than the gradient Hamiltonian. Such

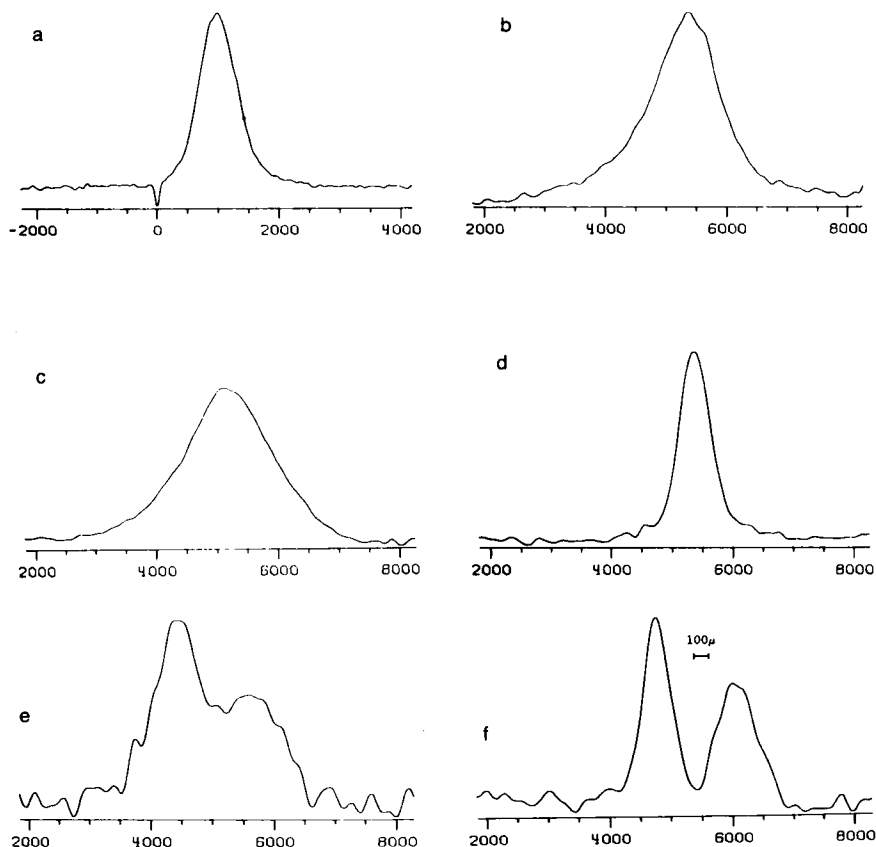


Fig. 21. The benefits of using pulsed gradients may be seen by simulating pulsed gradients as a phase shift of the transmitter. A gradient pulse corresponds to a nutation of the spin magnetization about the I_z axis, and the same result can be obtained by leaving the spin magnetization stationary while shifting the transmitter in the opposite direction. When the transmitter is offset from 2 kHz to 11.8 kHz (a–b) the linewidth of mylar film doubles under MREV-8 decoupling. Similarly if a phase shift of 15.4° is inserted 12 times per cycle to mimic a 11.8-kHz offset (c), the linewidth also approximately doubles. The same offset can be reached by using phase shifts of 49° twice per cycle (d) for which the linewidth remains sharp. This demonstrates that by carefully choosing the location of the gradient within a multiple-pulse cycle the offset dependence of the residual linewidth (see in Fig. 20) can be reduced. The images (e) and (f) are of two pieces of mylar film ($130\ \mu\text{m}$ thick) separated by $560\ \mu\text{m}$. With a static gradient (e) the two pieces are not resolved, but with pulsed gradients the two pieces are cleanly resolved. (Reproduced with permission from Miller *et al.*¹⁵⁰)

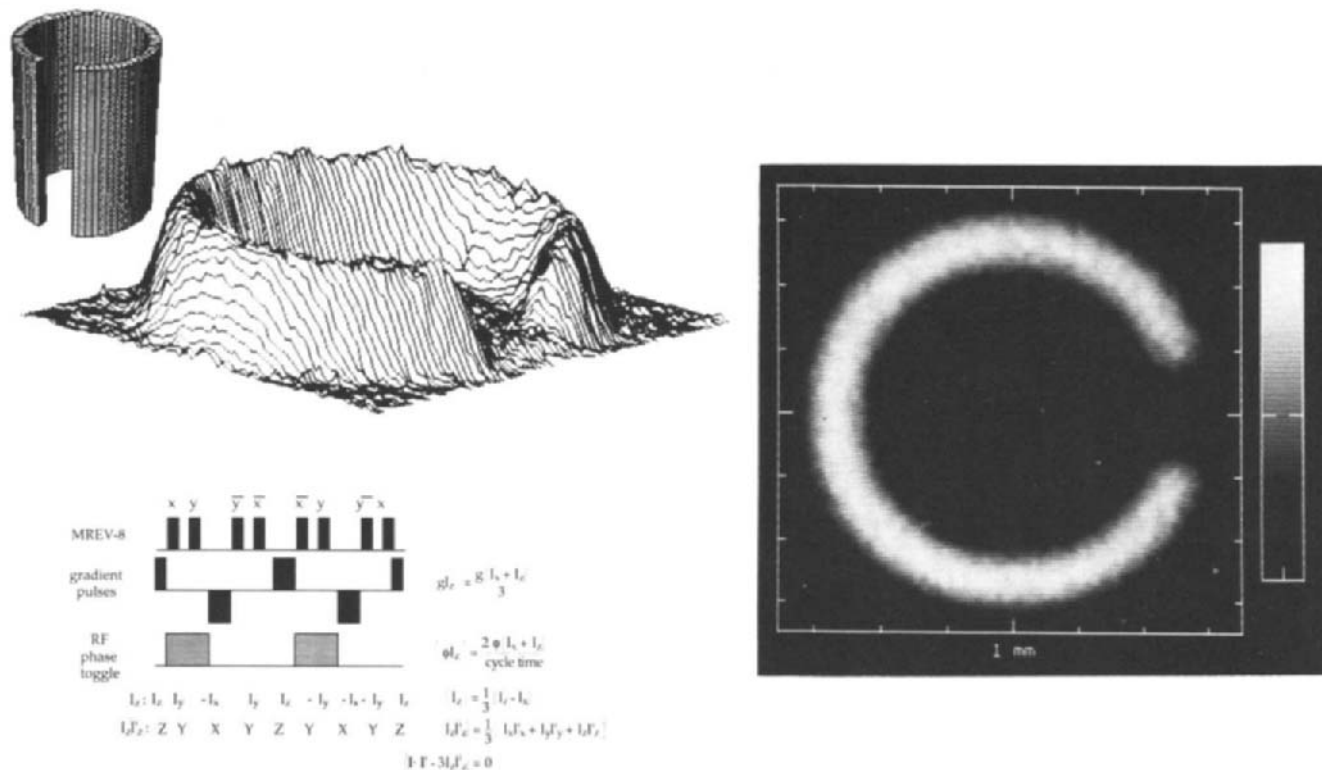


Fig. 22. Two-dimensional image of plexiglass phantom obtained with a time-suspension multiple-pulse cycle consisting of the MREV-8 cycle along with gradient pulses and a phase toggle which cause the chemical shift to vanish in a second averaging frame. The phantom is 6.35 mm o.d., has a 0.79 mm wall thickness and the slot left after removing a longitudinal section is 1.59 mm wide. The in-plane resolution of this image is just under $100 \mu\text{m}$. (Reproduced with permission from Cory *et al.*¹⁶⁰)

cycles have been termed "time-suspension" cycles¹³² since their effect is to momentarily halt spin evolution (in the absence of a pulsed gradient and irreversible effects). Table 5 lists a number of common time-suspension cycles and the average Hamiltonians associated with each. The multiple-pulse cycles which are listed in Table 4 are also time-suspension cycles and could be used with pulsed gradients in place of oscillating gradients. Compared to oscillating gradients, pulsed gradients allow more flexibility in the design of multiple-pulse cycles, though the most successful time-suspension cycle to date (CMG-48) is compatible with both pulsed and oscillating gradients.

Figure 23 shows pulsed gradient time-suspension images of two phantoms of Ultem¹⁵ and polystyrene. The polystyrene sample is actually a composite of polystyrene and polybutadiene where the polystyrene fraction of the sample has been selectively imaged. The polybutadiene fraction was suppressed on the basis of its spin-lattice relaxation time by an inversion recovery prepulse.

Table 6 gives the averaged linewidth for a variety of common NMR standards under the various time-suspension cycles. Sharper resonances correspond to improved resolution and sensitivity, and so the 48-pulse cycle¹³² looks very promising for solid state imaging.

The benefits of applying the gradient as short pulses are not limited to multiple-pulse cycles that are made up of solid echoes, this is just the area which has been most extensively explored. Recently Matsui^{161,162} has modified the magic-echo cycles of Takagashi and McDowell¹⁵⁴ to create a magic-echo time-suspension cycle. This was then combined with pulsed gradients for solid state imaging. The line-narrowing efficiency of the magic-echo cycles approximate that of the best multiple-pulse time-suspension cycles. Magic-echo cycles have larger windows for both detection and allowing better filtering of the data and therefore higher sensitivity. The gradient pulse is applied in these same windows making it somewhat easier to create short gradient pulses. It is anticipated that gradient pulses will find wide application including with Carr-Purcell cycles and frequency-switched Lee-Goldburg experiments.¹⁵⁶

The technology for creating short gradient pulses is still evolving,¹⁶³ but one approach that appears to be particularly promising is shown in Fig. 24. Here a capacitor is charged by a power supply and then discharged through a resonant coil. The pulse length is determined solely by the resonance frequency of the coil and capacitor combination, and the pulse is limited to half of a cycle by the snubber diodes. The benefit of this approach is that a very modest power supply can be employed, and the inductance of the circuit does not limit the pulse width. Naturally, the gradient coil's inductance does limit the amount of current that is realized for a given voltage and low

Table 5. Pulsed gradient multiple-pulse cycles.

	MREV-8 second-averaged	LW-24	CMG-48
Pulse sequence	$(xy)(\overline{yx})(\overline{xy})(\overline{yx})$	$(xy)(\overline{xy})(xy)(\overline{xy})$ $(xy)(\overline{xy})(\overline{yx})(\overline{yx})$ $(\overline{yx})(\overline{yx})(\overline{yx})(\overline{yx})$	$(xy)(\overline{xy})(xy)(xy)$ $(\overline{xy})(xy)(\overline{yx})(\overline{yx})$ $(\overline{yx})(\overline{yx})(yx)(\overline{yx})$ $(\overline{xy})(\overline{xy})(\overline{xy})(x\overline{y})$ $(\overline{xy})(x\overline{y})(y\overline{x})(yx)$ $(y\overline{x})(\overline{yx})(yx)(\overline{yx})$
$H_D^{(0)}$	4 s.e.p.p.	3 s.e.p.p.	3 s.e.p.p.
$H_x^{(\text{odd})}$	2 s.e.p.p.	12 s.e.p.p.	12 s.e.p.p.
$H_D^{(2)}$	$\neq 0$	3 s.e.p.p.	3 s.e.p.p.
Gradient pulses	+ - + - +	+ - + - +	+ - + - + + - + - +

inductance gradient coils¹⁶⁴ are still quite important. An oscilloscope trace of the actual rf and gradient voltages is shown in Fig. 24.

An alternative approach to employing a magnetic field gradient is to use a radiofrequency magnetic field gradient such that the nutation frequency of the spin system is spatially dependent.¹⁶⁵ This approach, which has been explored by Weitekamp and coworkers,¹³⁸ has the advantage that short rf pulses are simple to create and that an additional degree of freedom is introduced in the form of the phase of the rf gradient pulse. The difficulty of the approach is that more than one rf coil at the same resonance frequency must be placed in the probe, and these coils must be actively switched. This can be accomplished quickly via pin diode switches and two-dimensional images¹⁶⁶ have been successfully acquired by this technique. The multiple-pulse cycles which are employed are similar to the time-suspension sequences above, but now the gradient pulses are applied in different windows since they depend on operators other than I_z .

5.4. Resolution and sensitivity for multiple-pulse imaging

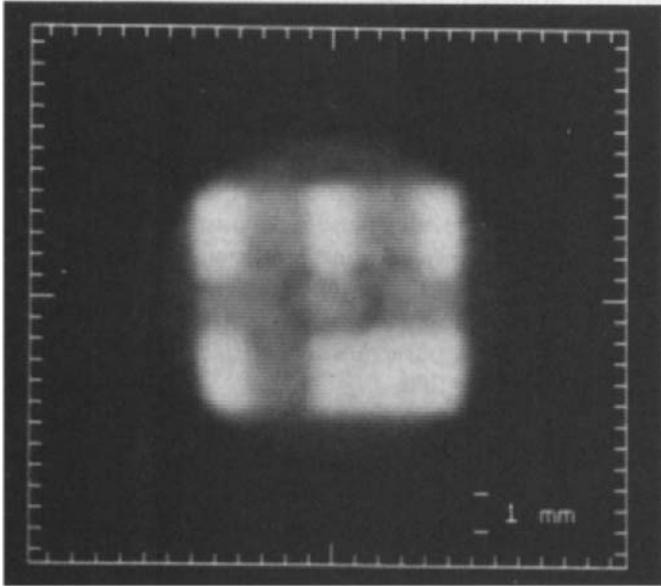
A useful criterion for the resolution of an image under multiple-pulse line-narrowing is N_e , the number of data points which can be collected in the absence of a gradient before the signal intensity has decayed by the factor e .^{157,167,168} When the gradient strength is set optimally, a reciprocal space spin-spin relaxation time, $T_{2,\text{eff}}$, may be defined as

$$T_{2,\text{eff}} = \frac{N_e}{l_s} \quad (24)$$

where l_s is the sample length along the gradient direction. The image resolution is the width at half-height of a Lorentzian corresponding to this relaxation time, or

$$\text{resolution} = \Delta\nu_{1/2} = \frac{l_s}{\pi N_e} \quad (25)$$

The number of observed data points depends on the cycle length of the various multiple-pulse cycles. Looking back to Tables 3 and 4 it is seen that generally longer cycles are more efficient at line-narrowing, but if the magnetization is only sampled once per cycle then on going from the 8-pulse MREV-8 cycle to the highly efficient 48-pulse cycle¹³² the decrease in residual linewidth would have to be more than six-fold to obtain an increase in image resolution. This difficulty is avoided by oversampling.¹⁶⁸ Rather than sampling the 48-pulse cycle once per cycle it is sampled once every six pulses, that is in every long I_z window. Likewise the MREV-8 cycle can be con-



veniently sampled once every four pulses. Oversampling leads to a small sampling modulation, but this effect is easily suppressed and for our purposes it is sufficient to state that in general time-suspension cycles for imaging can be arranged so that one can sample the magnetization at least once for every gradient pulse.¹⁶⁹

The sensitivity is a slightly more complicated affair. The magnetization is sampled stroboscopically during a "window" in the pulse cycle, only a few microseconds after a strong rf pulse. The length of the window is usually several microseconds and is determined, in part, by the sample T_2 . Thus the receiver bandwidth must be set quite wide regardless of the actual spectral width of the detected signal. This naturally introduces a large amount of noise which would normally be filtered out of the spectrum. To avoid this we would like to have an audio filter which can be switched on quickly when the signal is sampled.¹⁷⁰ A simple implementation of this filtering is to integrate the echo signal which appears in the multiple-pulse cycle.¹⁷¹ Integration naturally reduces the effective bandwidth of the receiver though not all of the way to the spectral width limit. Finally it should be recognized that every window in a multiple-pulse cycle contains useful information, and every large window should be sampled. Those groups of signals which are between gradient pulses can be combined to increase the signal-to-noise ratio of that data point.¹⁶⁹ In practice, this requires a goodly amount of spin gymnastics since the signal phase and the direction of spin evolution vary from window to window, but the principles are well-understood even if convenient hardware and software have yet to be developed.

From (25) it is seen that the resolution of multiple-pulse imaging is directly related to the residual linewidth of the sample; what then characterizes "good" and "bad" samples. Recall that these averaging techniques require a large number of spin manipulations which create a delicate balance to cancel

Fig. 23. Pulsed gradient time-suspension images of Ultem (polyether imide) and polystyrene. The Ultem image was acquired with the SHRIMP pulse cycle (see Table 4) with short gradient pulses intercalated into the long I_z toggling frame windows. The phantom comprises a circular base 9 mm in diameter by 1.9 mm thick, a rectangular layer $6.2 \times 6.5 \times 2.0$ mm thick, and a second layer of small rectangles parallel to the rectangle in the first layer. No slice selection was used, and so the small rectangles appear against the background of the larger rectangle and the cylindrical section. The resolution is $160 \mu\text{m}$. The polystyrene image was obtained with the CMG-48 pulse cycle (see Table 5) with short gradient pulses. The phantom was machined to a PS shape and looks substantially like the image. The circular region in the centre of the image is from a nylon screw which held the phantom in place. The phantom was run as a composite with the empty spaces around the machined letters filled with *cis*-polybutadiene. Prior to the imaging portion of the experiment a T_1 inversion recovery was employed to suppress the response from the polybutadiene. (The Ultem image is reproduced with permission from Miller *et al.*¹⁵)

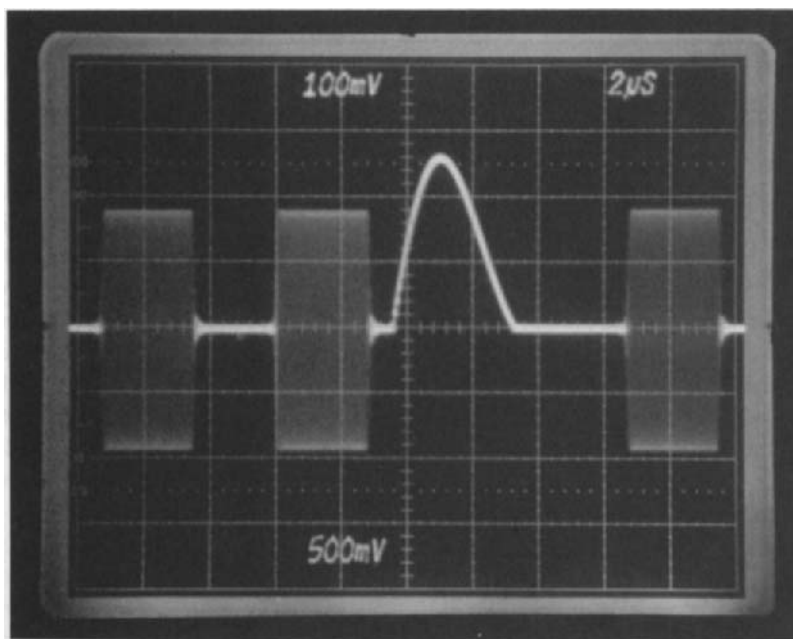
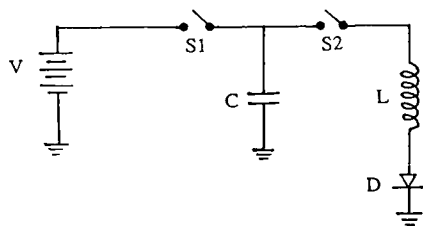


Fig. 24. A simple scheme for generating short gradient pulses is to discharge a capacitor across a resonant coil. To limit the waveform to half of a cycle, snubber diodes are included. An oscilloscope trace of the resulting waveform along with three rf pulses is shown in the figure. With this scheme the pulse length of the gradient is independent of the gradient coil's inductance, and the peak power of the gradient pulse is not determined by the power output of the voltage source. (Reproduced with permission from Conradi *et al.*¹⁶³)

to zero. Just how delicate can be seen by noting that the original dipolar couplings are on the order of 50 kHz and the residual linewidths are on the order of 25 Hz so this compensation must be good to half a part in a thousand. Other sources of modulations at frequencies similar to the cycle frequency disrupt this balance. The most common source of modulation is molecular motion which modulates both chemical shifts and dipolar couplings. Table 6 lists the linewidths of a variety of NMR standards under

Table 6. ^1H linewidths of solids under multiple-pulse time-suspension cycles.

Compound	Dipolar linewidth (Hz)	MREV-8 second-averaged (Hz)	SHRIMP (Hz)	24-pulse cycle (Hz)	CMG-48 (Hz)
Adamantane	13×10^3	34	44	28	3.5
Ferrocene	19×10^3	45	45	25	5.5
Hexamethylbenzene	21×10^3	29	52	32	8.0
Oxalic acid	58×10^3	234	186	350	67
Gypsum (single crystal)	46×10^3	176	140	349	51
High-density polyethylene	25×10^3	94	129	523	66
Pressure-crystallized polyethylene	59×10^3	335	335	350	82

Table 7. Residual linewidths (Hz) of common polymers with CMG-48 line-narrowing

<hr/>	
512 × 512 image	
<i>cis</i> -Polybutadiene	12 Hz
Polycarbonate	40
Polyethersulfone	40
Polyacetal (Delrin®)	44
Ultem®	48
Polydimethylphenyleneoxide	52
256 × 256 image	
Polybutylmethacrylate	65
Polyethyleneterephthalate	65
Cellulose acetate	65
Polystyrene	72
Polycaprolactone	72
Polyethylene, high-density	72
Polysulfone	85
Polymethylmethacrylate	86
Polyvinylacetate	98
Ethyl cellulose	102
Polyacrylamide	116
Poly α -methylstyrene	117
Nylon 6,6	119
Poly(4-methyl, 1-pentene)	120
128 × 128 image	
Nylon 12	126
Nylon 6	142
Nylon 6, 12	142
Polypropylene	143
Isotactic poly(<i>t</i> -butene)	172
<hr/>	

various averaging conditions, and Table 7 lists a series of polymers and the residual broadenings of each under the 48-pulse time-suspension cycle.¹⁷² For the most part it is seen that rigid polymers have a small residual linewidth while more mobile polymers are broader. Naturally, if the molecular motions are much faster than the multiple-pulse averaging they no longer interfere, and so the very mobile *cis*-polybutadiene has a very narrow linewidth.

Of course, this begs the question of how one records a good image of a sample that is too hard for one set of experiments and too soft for another. One possible solution is to cool the sample.

6. IMAGING WITH MAGIC-ANGLE SAMPLE SPINNING

Magic-angle sample spinning (MASS) is the most widely used approach to obtaining isotropic chemical shift spectra of solids,²⁰ so there is a strong

motivation for having imaging methods which are compatible with MASS. In addition, MASS is a simple method of averaging both homonuclear and heteronuclear dipolar couplings for those materials with small (approximately less than 10 kHz) dipolar linewidths. Therefore, for some samples MASS can replace multiple-pulse dipolar decoupling methods, and in the absence of multiple-pulse line-narrowing, MASS line-narrowing does not have a sampling bandwidth problem. So if an equivalent image can be acquired with either MASS or multiple-pulse methods, the MASS image will have a higher signal-to-noise ratio.¹⁶⁷ A variety of MASS-based imaging schemes are known^{121,167,173–179} and in many regards are quite simple to apply.

There have been many suggestions for combining MASS with imaging, but only MASS imaging schemes based on synchronously rotating gradients have been implemented, and therefore we will primarily discuss this approach which has the additional advantage of simplicity. In cases where the linewidth is too broad to be averaged by MASS alone, it is desirable to combine MASS imaging with multiple-pulse line-narrowing, and also pulsed gradients. The former has been achieved in a limited number of experiments,¹⁷⁹ while the latter has not yet been attempted.

6.1. Synchronously rotating gradients

The basic idea of MASS imaging with synchronously rotating gradients is that by rotating the magnetic field gradient at the same frequency as the spinner, each point in the sample experiences a constant magnetic field. The strength of the field depends on the position within the rotor, and since the field strength is not modulated, the imaging portion of the experiment looks exactly as it would if both the sample and the gradient were stationary. This synchronization allows any of the imaging procedures which were discussed above to be implemented directly, though the implementation is in a reference frame tied to the spinning sample rather than the laboratory frame. This basic idea was patented by Wind and Yannoni,¹⁷³ although they did not attempt the experiment.

A synchronously rotating magnetic field gradient is obtained by the method outlined in Fig. 25. The rotor frequency is optically detected and then phase-shifted, filtered, and amplitude- and phase-modulated to yield the desired gradient signals. The gradient coils are canted at the magic angle and wound around the symmetry axis of the spinner. The arrangement scales the effective magnetic field gradient by a factor of $\cos 54^\circ 44'$ (approximately 0.58).

The magnetic field gradient in a reference frame oriented at the magic angle

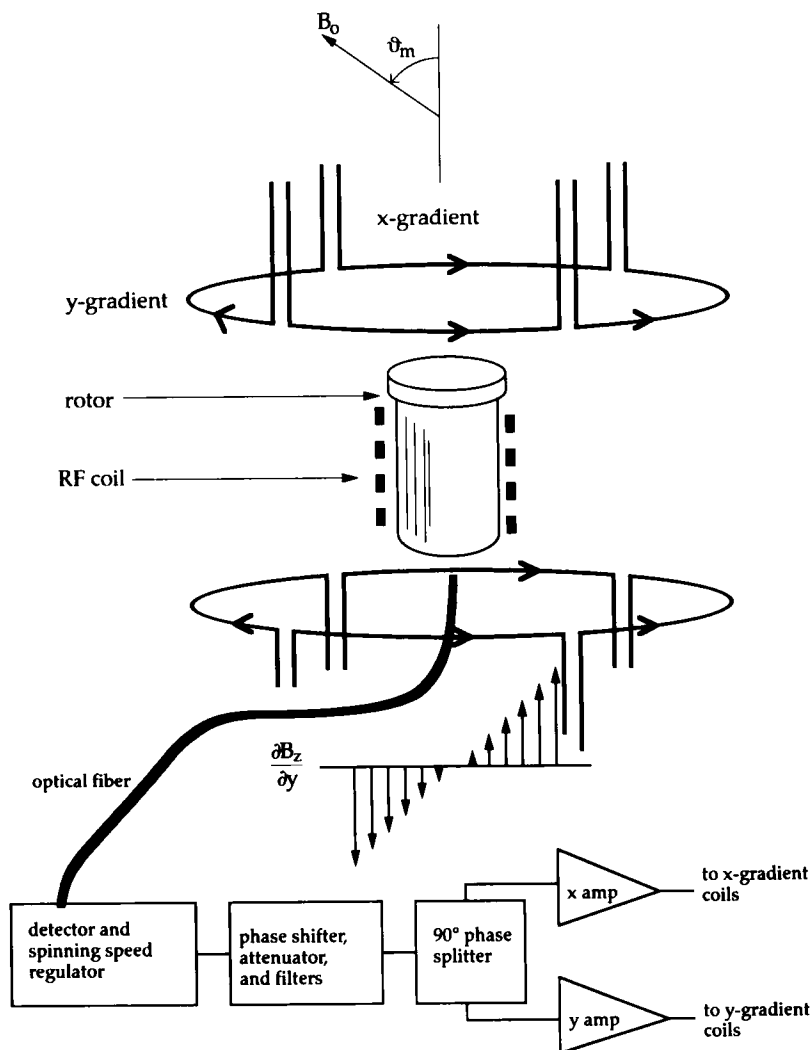


Fig. 25. A schematic representation of the probe used for MASS imaging with synchronized rotating magnetic field gradients, and a block diagram of the associated audio electronics which are used to modulate the magnetic field gradients. The semicircular current elements generate magnetic field gradients that increase along axes perpendicular to the rotor axis, and the rotating magnetic field gradient is composed of two gradients oscillating in quadrature. The rotor frequency is detected via an optical pickup, after which it is filtered, phase shifted, split into quadrature signals, and then amplified and applied to the gradient coils. The phase, and amplitude of the signals are under computer control.

rotates as,

$$\mathbf{G} = G_0[\cos(\Omega_s t + \phi)\hat{x} + \sin(\Omega_s t + \phi)\hat{y}] \quad (26)$$

where Ω_s is the rotor's angular velocity and ϕ is a phase difference between the gradient direction at time zero and the x axis. If we consider a plane in the rotor with a rotor axis system x_s, y_s, z_s which rotates about the z axis at the spinner frequency $\Omega_s/2\pi$, the rotating magnetic field gradient is transformed to this new reference frame as

$$\begin{aligned} \mathbf{G}_s = \mathbf{U}\mathbf{G} &= \begin{pmatrix} \cos(\Omega_s t + \phi_i) & \sin(\Omega_s t + \phi_i) & 0 \\ -\sin(\Omega_s t + \phi_i) & \cos(\Omega_s t + \phi_i) & 0 \\ 0 & 0 & 1 \end{pmatrix} \\ &\times \begin{pmatrix} G_0 \cos(\Omega_s t + \phi) \\ G_0 \sin(\Omega_s t + \phi) \\ 0 \end{pmatrix} \\ &= G_0[\cos(\phi - \phi_i)\hat{x}_s + \sin(\phi - \phi_i)\hat{y}_s] \end{aligned} \quad (27)$$

where \mathbf{U} is the unitary transformation from the laboratory reference frame canted at the magic angle to the reference frame which rotates with the rotor, and ϕ_i is the phase of the rotor when the first rf pulse is applied. Our definition of time starts with the first rf pulse since this is also the start of all spin evolution. The last line of (27) shows that the gradient is static as far as the spins are concerned. Furthermore, the apparent direction of the gradient is easily varied by applying a phase shift to the gradient signals derived from the rotor motion.

Figure 26 shows a list of experiments for MASS imaging including back-projection reconstruction¹⁷⁵ and two-dimensional Fourier imaging¹⁷⁶ methods. All of these experiments can be implemented with the instrumentation outlined in Fig. 25.

One of the initial worries while implementing MASS-based imaging methods was that gradient-induced modulations of the spin evolution from imperfections in the gradient coils, drivers, feedback system, etc., would lead to image distortions. Fortunately, this is not a serious problem since gradient imperfections nearly always introduce a periodic modulation of the spin evolution into the experiment which creates sidebands that are removed from the region of interest.¹⁷⁹ The experiment is even more forgiving since most of these "spinning sideband images" (SSI) have a phase relationship to the orientation of the rotor at the start of the experiment and therefore the SSIs randomly phase cancel.¹⁷⁷

As a simple example consider an imaging experiment in which the two

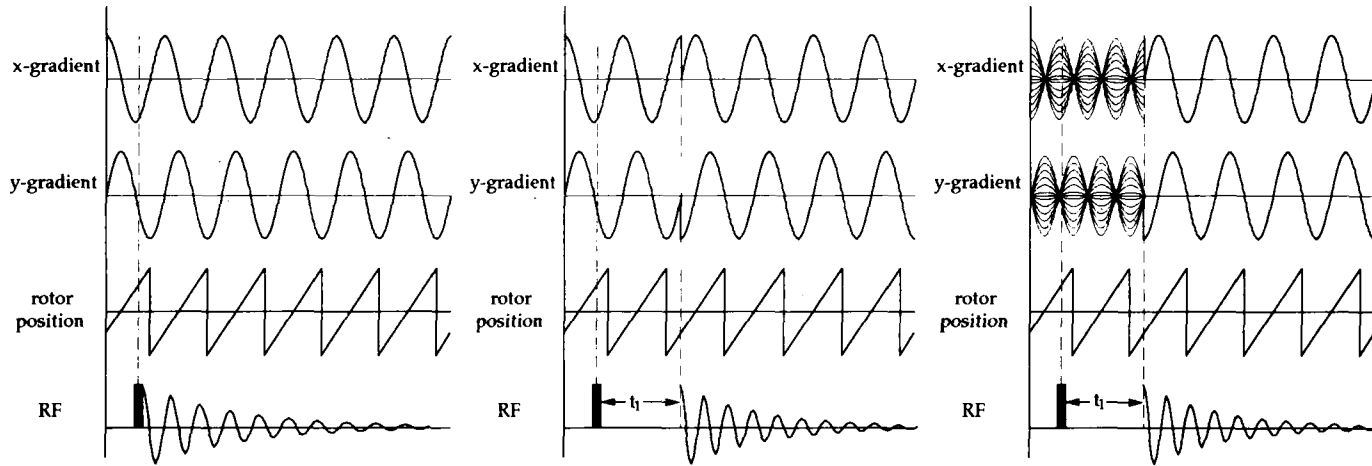


Fig. 26. The pulse sequences for three MASS imaging experiments: a back-projection experiment, a two-dimensional Fourier imaging (2DFI) experiment, and the spin warp modification of a 2DFI experiment. Always the two gradient fields are in quadrature and are synchronized to the rotor frequency. In the BP experiment, between acquisitions the phase relation between the rotor and gradients is varied incrementally to scan k -space. In both 2DFI experiments k -space is scanned by first offsetting in k -space along one trajectory and then shifting both gradients by 90° to acquire along a perpendicular line in k -space. The phase of the rotor at the start of the experiment (i.e. when the excitation pulse is applied) is immaterial for all of these experiments.

quadrature gradient channels are mis-set such that one is stronger than the other.^{177,179} During each period of the rotor every spin experiences both a static field and a field oscillating at twice the rotor frequency. This mis-set gradient can be described as

$$\mathbf{G} = (G_0 + \Delta G) \cos(\Omega_s t + \phi) \hat{x} + (G_0 - \Delta G) \sin(\Omega_s t + \phi) \hat{y} \quad (28)$$

in the tilted laboratory frame. This gradient transforms to,

$$\begin{aligned} \mathbf{G}_s = & [G_0 \cos(\phi - \phi_i) + \Delta G \cos(2\Omega_s t + \phi + \phi_i)] \hat{x}_s \\ & + [G_0 \sin(\phi - \phi_i) + \Delta G \sin(2\Omega_s t + \phi + \phi_i)] \hat{y}_s \end{aligned} \quad (29)$$

in the rotor frame. The FID of a spin at position $(r \cos(\psi), r \sin(\psi))$ in the rotor frame is a straightforward calculation,¹⁷⁹ the result of which is

$$S(t) = \sum_{k=-\infty}^{\infty} A_k J_k \left(\frac{\gamma r \Delta G}{2\Omega_s} \right) \exp(2ik\Omega_s t) S_h(t) \quad (30)$$

where

$$A_k = \exp \left(-i\gamma r \frac{\Delta G}{2\Omega_s} \sin(\phi_i + \phi + \psi) + k(\phi_i + \phi + \psi) \right) \quad (31)$$

and $S_h(t)$ is the signal for the homogeneous case ($\Delta G = 0$). The result of Fourier transforming (30) is a series of sideband images with the intensity of each given by the Bessel function of the sideband order and with an argument given by the error strength divided by twice the rotor frequency.¹⁷⁷ A_k is a phase factor which multiplies the sideband intensity, and an important point to note is that for all sidebands except the central band, this phase factor is randomly phase-modulated by the rotor position at the start of the experiment. Looking only at the central image ($k = 0$) we see that the correct image is obtained, but for a smaller effective gradient. In fact the synchronized rotating gradient method works even when only one gradient is used, though the spatial resolution is then only half of that obtained when both gradients are employed.

Most error terms in MASS imaging appear as similar spinning sideband images, and in all cases the intensity of these sidebands is proportional to a Bessel function whose argument is the modulation strength divided by a multiple of the rotor frequency. These sidebands do not distort the image so long as they are far from the central band, but they do lower the signal-to-noise ratio since some intensity ends up in the sidebands which are then averaged to zero. This is a minor problem, since even when the error modulation strength is half of the rotor frequency more than 85% of the intensity is still in the central image. Naturally, spinning faster reduces the intensity of all but the central image.

Magic-angle sample spinning accomplishes line-narrowing by modulating

the anisotropic portion of the chemical shift or dipolar coupling in such a fashion that the average is zero. Ideally, in MASS imaging the gradient rotates synchronously with the sample and therefore appears to be time-independent as viewed in the rotor frame; however, when gradient imperfections exist there is an extra modulation at the same frequency as the line-narrowing modulation and these two modulations can interfere. The dipolar averaging is not affected by gradient modulations since the dipolar coupling is not dependent on the magnetic field strength (see Table 1). The chemical shielding is dependent on the magnetic field strength, but the main magnetic field is typically 2–3 orders of magnitude stronger than the magnetic field gradient and any line-broadening that is reintroduced by the gradient modulation is not observable.

Two images of polybutadiene/polystyrene polymer blends that were acquired by MASS imaging¹²¹ are shown in Fig. 27. The samples were prepared as thin (750- μm -thick) disks which did not contain any obvious voids, and no slice selection was employed in this image. The polybutadiene fraction of the sample is sufficiently mobile that MASS alone is successful at line-narrowing and very good images may be obtained. The polystyrene fraction, on the other hand, is rigid with large homonuclear dipolar couplings and at 5 kHz MASS spinning does not narrow the styrene line. In these images, therefore, the polystyrene fraction is not observed. The image is plotted to show four levels which correspond to increasing polybutadiene content, the white areas contain predominantly polystyrene.

6.2. CRAMPS

To obtain images of rigid materials while preserving the isotropic chemical shift it is natural to combine the MASS imaging method with multiple-pulse approaches¹⁷⁹ in analogy to high-resolution CRAMPS spectra of solids. CRAMPS imaging has been implemented using a synchronous gradient and MREV-8 line-narrowing so that an image was obtained which was a combination of spatial and chemical shift information. This approach should be seen as equivalent to multiple-pulse line-narrowing with a static magnetic field gradient, and therefore leads to a spatially varying image resolution. Time-independent I_z interactions (such as the chemical shift) can be eliminated by applying an oscillating gradient approach in the rotating sample frame. In the laboratory frame such a gradient modulation could be static or conveniently implemented with the gradient synchronized to a multiple of the rotor frequency.¹⁷⁹ This has not been demonstrated, however. The most general application would be a pulsed gradient with a MASS imaging experiment. This is a technically demanding experiment and will

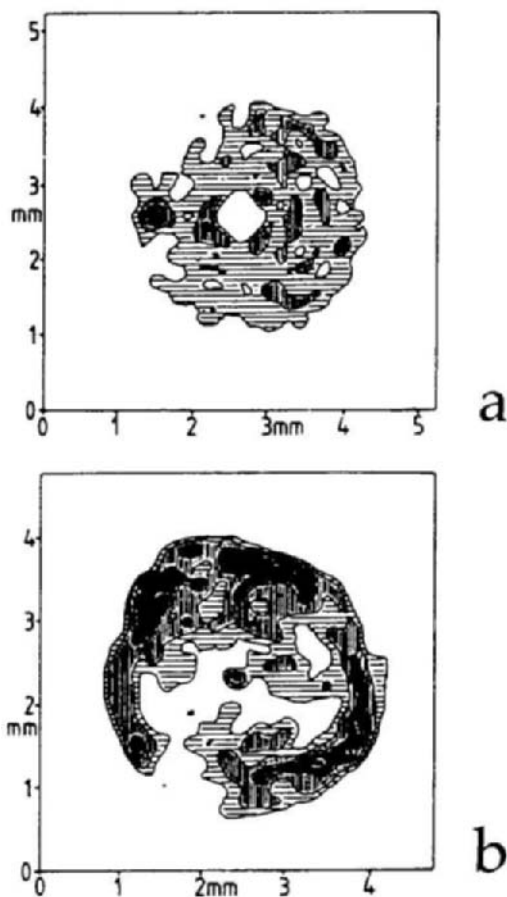


Fig. 27. Two MASS (rotor frequency = 5 kHz) images of polybutadiene/polystyrene blends: a mechanical blend (a) and a blend cast from toluene (b). Both samples were prepared as solid disks $750\text{ }\mu\text{m}$ thick and 3.5 mm in diameter. Only the resonance lines from the polybutadiene fraction of the blend is narrowed by MASS and so the polystyrene fraction is invisible in these images. Dark regions correspond to areas of predominantly polybutadiene, and white areas are predominantly polystyrene. The in-plane resolution is $50\text{ }\mu\text{m}$. (Reproduced with permission from Cory *et al.*¹²²)

most likely wait until pulsed gradient imaging methods are more widely explored.

Though the most appealing use of MASS imaging is to take advantage of the isotropic chemical shift this has yet to be demonstrated in practice. As an aside we note that there are a number of schemes which do not

require gradient switching for acquiring chemical shift resolved back-projection images.¹⁸⁰ These are all based on the idea^{181,182} that by incrementing the gradient strength in a series of spin-density profile measurements the chemical shift, which remains constant, can be differentiated from the changing gradient shift. Picture this as a pseudo constant time experiment.

6.3. Other methods of MASS imaging

Rather than synchronizing the gradients to the sample rotation such that the imaging portion of the experiment appears to be static, it is possible to use the oscillating appearance of static gradients to scan k-space on trajectories other than straight lines.^{183,184} There are many approaches to this, and we will only discuss one which demonstrates the major points. None of these alternative approaches have actually been implemented for MASS imaging though some have been applied to liquid state phantoms at slow rotor frequencies.¹⁸³ Part of the interest in developing these methods is not for MASS line-narrowing imaging but to develop novel ways of scanning k-space for liquid state imaging. Naturally, when the line-narrowing benefits of sample rotation are not necessary, the choice of rotating a gradient or the sample is only one of experimental convenience. Figure 28 shows three methods of exploring k-space with MASS imaging using the back-projection method. The first, imaging with synchronously rotating gradients, starts at the k-space origin and radiates outward. The other two methods scan k-space on semicircular paths, the differences being how the trajectory is offset to the correct starting position.⁹⁵ Rotating a sample in a static field gradient leads to a circular path in k-space, with the circumference passing through the origin. For useful imaging it is possible to first offset this circular path (as is done in 2DFI) such that the circular path is centred at the origin. After data are collected along a number of these circular paths, the data matrix is inverted and a normal filtered back-projection reconstruction yields the correct image.

Other MASS imaging approaches are based on short gradient pulsed synchronized to the rotor orientation,¹⁷⁴ and a Bessel function synthesis scheme.^{185,186}

7. ROTATING FRAME IMAGING

The rotating frame approach to line-narrowing¹⁸⁷⁻¹⁹⁰ is similar to magic-angle sample spinning but the experiment is performed in an effective field which rotates at the magic angle while the sample remains static. This rotating effective field is composed of the vector sum of an rf field and a resonance

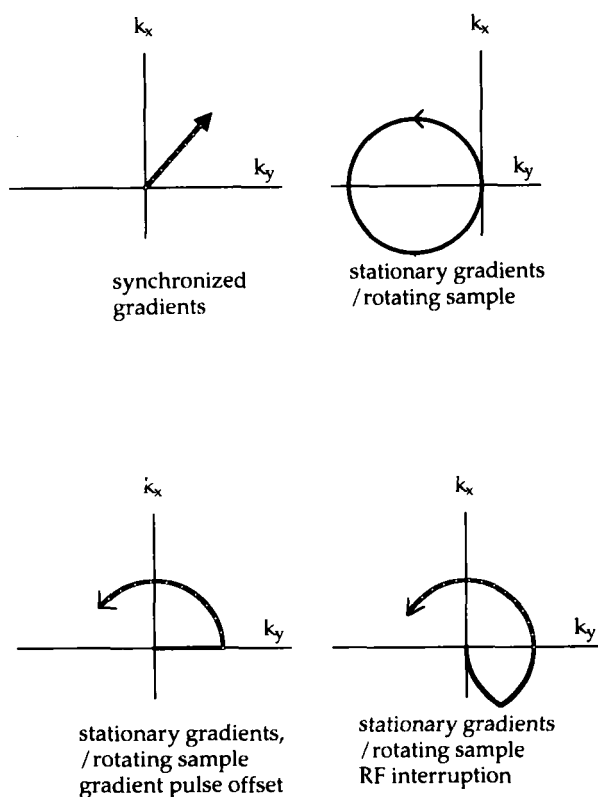


Fig. 28. The k -space trajectories for a variety of MASS imaging back-projection reconstruction methods. With the gradients synchronized to the rotor frequency the angle of the trajectory in k -space is constant and simply propagates away from the origin. This is how all MASS BP images have been acquired to date. If the gradients are left stationary then the rotor motion creates a circular trajectory in k -space; the orientation of the circular trajectory depends on the phase of the rotor at the excitation pulse. Matsui¹⁸³ realized that by offsetting the k -space trajectory this circular trajectory could be shifted such that it is centred at the k -space origin. Data collected along the trajectory could then be used for back-projection image reconstruction. This offsetting of the k -space trajectory can be conveniently accomplished by either of two methods: (1) by applying a gradient pulse which is effectively synchronized to the rotor motion; and (2) by interrupting the k -space trajectory with a second rf pulse after 1/6th of a rotor period, waiting 1/6th of a rotor period for the trajectory orientation to realign itself and then continuing the experiment by applying a third rf pulse.¹⁸⁴ In other words, the magnetization is stored while the k -space trajectory realigns itself so that it is centred at the k -space origin.

offset, so the effective resonance frequency in the magic-angle rotating frame is much lower than the Zeeman frequency in the static field, but the line-narrowing results are quite similar to the multiple-pulse results discussed above. As Redfield¹⁹⁰ showed in the very early days of NMR, bilinear interactions are scaled by the factor $(3\cos^2\vartheta - 1)$ in the presence of an off-resonance radiofrequency field, \mathbf{B}_e , of the form,

$$\mathbf{B}_e = \mathbf{B}_1 + \left[\mathbf{B}_0 - \left(\frac{\omega}{\gamma} \right) \right] \quad (32)$$

where $\mathbf{B}_1 \cos(\omega t)$ is a radiofrequency field and \mathbf{B}_0 is the main Zeeman field, and the angle between the Zeeman field and the effective field, ϑ , is given by

$$\vartheta = \tan^{-1} \left(\frac{B_1}{B_0 - (\omega/\gamma)} \right) \quad (33)$$

Linear I_z operators in this same field are scaled by $\cos \vartheta$, so when ϑ is set to the magic angle ($54^\circ 44'$) dipolar broadenings vanish, and inhomogeneous interactions are scaled by $1/\sqrt{3}$. Magic-angle rotating frame (MARF) procedures have been used for spectroscopic line-narrowing with some success, but multiple-pulse methods are more popular and simpler to apply today.

One way of looking at the MARF experiment is to recall that a frequency offset of an applied radiofrequency field is transformed to a field along the z axis by the transformation to the rotating frame. Consider a sample in a strong magnetic field such that the spin magnetization is aligned along the static magnetic field direction. For convenience we will consider a strong rf field applied half way between the x and y axis with a resonance offset such that the magic-angle condition is met ((33) $\vartheta = 54^\circ 44'$). The phase shift to place the rf field between the x and y axis has no effect on the experiment; it is simply a nice reference frame from which to view the results. The effective rf field is pointed along the body diagonal of a cube with edges along the x , y and z axes, and, of course, spin evolution occurs about this axis. A 120° spin evolution then transforms the z axis into the y axis and another 120° rotation takes the original z axis into the x axis. This is what multiple-pulse line-narrowing accomplishes, and in exactly the same fashion MARF results in a line-narrowing provided that the spin evolution is followed in the reference frame of the MARF experiment.

To carry the experiment further, before turning on the effective field the spins can be placed along the effective field direction (along the 1 1 1 axis) by an rf pulse. Now when the effective field is applied the spin magnetization is locked along this field and does not evolve. Just as an rf pulse will tip the spin magnetization out of the rotating frame z axis and allow spin evolution in a static field experiment, in the MARF experiment an audiofrequency will tip the spins out of the MARF effective field and then they will precess about it.

In this effective field, however, they will experience no dipolar couplings and the chemical shift will be reduced. The precession frequency in the MARF frame is detected by the same audio coil that was employed to excite the spins.

One reason that the MARF experiment is not widely used for spectroscopy is that each chemically shifted line has a different off-resonance behaviour, and therefore a different line-narrowing efficiency. At first glance it does not appear that MARF techniques can be used for solid state imaging since the line-narrowing condition depends on the resonance offset, and if this is made spatially varying by the presence of a magnetic field gradient then the linewidth would vary with position and the imaging approach would necessarily correspond to a sensitive point approach. De Luca and coworkers¹⁹¹⁻¹⁹⁴ realized that by superimposing a magnetic field gradient and a radiofrequency magnetic field gradient the MARF condition can be fulfilled throughout the sample simultaneously, and that the resonance frequency in the rotating frame would still be a linear function of spatial offset. Figure 29 shows a vector picture of the various magnetic fields which are necessary for this experiment.

For imaging the following two magnetic field gradients are employed

$$G_0 = \left(\frac{\partial B_0}{\partial x}, \frac{\partial B_0}{\partial y}, \frac{\partial B_0}{\partial z} \right) \quad (34)$$

and

$$G_1 = \left(\frac{\partial B_1}{\partial x} \cos \omega t, \frac{\partial B_1}{\partial y} \cos \omega t, \frac{\partial B_1}{\partial z} \cos \omega t \right) \quad (35)$$

with the added condition that

$$\left(\frac{\partial B_1 / \partial i}{\partial B_0 / \partial i} \right) = \frac{B_1}{B_0 - \omega / \gamma} = \tan \vartheta_m \quad (36)$$

Clearly, time-independent linear I_z interactions must be neglected for (36) to hold for all spins, but within this limitation the MARF condition is fulfilled for the entire sample while the sample is placed in a magnetic field gradient. The dipolar broadening also only vanishes to first order with this method,¹⁹² but the second-order contribution is small and easily swamped by the gradient.

As shown in Fig. 29 the experiment proceeds in the MARF reference frame, and within this reference system the experimenter is free to introduce any multiple-pulse cycle he chooses. For example, within the MARF frame a Carr-Purcell-type sequence for removing chemical shifts, or a solid echo-based sequence for reducing the residual dipolar broadening¹⁹⁴ can be introduced. These sequences are, of course, based on audiofrequency pulses since the effective Zeeman frequency is reduced in proportion of the effective

field to the static field. Two examples of MARF images are shown in Fig. 30 for adamantane phantoms.¹⁹⁴

The hardware that is necessary for MARF imaging is demanding and has so far only been implemented in one dimension. The images in Fig. 30 were acquired with a back-projection reconstruction technique and sample rotation. The audio coil tends to contain a large number of turns, and the two magnetic field gradients must be spatially matched. So far a single coil has served the double purpose of creating both the rf and d.c. gradients.

8. LARGE SAMPLES AND SURFACE COILS

Most of the imaging methods which have been discussed up to now are best suited for studying small samples. Multiple-pulse methods generally require strong rf fields, which are best generated in small rf coils, and magic-angle spinning methods have been limited to samples of less than 1.5 cm in diameter due to the extreme velocities at the circumference of the MASS rotor. Multiple-pulse methods can probably be scaled up to somewhat larger samples (a sample diameter of 3 cm is well within the possibilities), but if one looks at a whole-body NMR imaging apparatus it is not clear what a solid state imaging experiment on this scale would look like. Nevertheless, there has been interest expressed in imaging objects the size of airplane wings, rocket motor casings and ship hulls. Clearly different approaches are needed.

One step in this direction which has been investigated is to use a surface rf coil in a homogeneous magnetic field.¹⁹⁵⁻¹⁹⁷ With a surface coil the location of the sample is encoded in the nutation frequency¹⁶⁵ and a depth image may be obtained. All of the difficulties in dealing with broad lines remain, of course, and the trick is to combine the surface coil approach with some form

Fig. 29. The pulse sequence for one version of the MARF imaging experiment is shown along with a picture of the various fields. The experiment is performed in a reference frame which is oriented at the magic angle relative to the main magnetic field. The z axis in this frame is along the vector B_e^0 , which is composed of the off-resonance vector $B_0^0 - (\omega/\gamma)$ and the spin-locking rf field B_1^0 . In the experiment a short rf pulse is first applied to tip the spins to the magic angle and then the combination of gradients and homogeneous fields are applied to lock the spin at this orientation. To measure an image, audiofrequency pulses are applied to tip the spins into a transverse plane which is perpendicular to the spin-locking axis. For simplicity these audiofrequency pulses are applied along the z axis (vector B_1' in the figure) which results in a scaling of the effective audio field strength since only the component which is perpendicular to the spin-locking axis, B_{1n}' , contributes. Audiofrequency pulses in the MARF frame act just as rf pulses in the more usual rotating frame, and the result of a 90° - t - 180° pulse sequence is an echo at time t following the 180° pulse. The Fourier transform of the echo yields a one-dimensional spin density profile.
(Reproduced with permission from De Luca *et al.*¹⁹⁴)

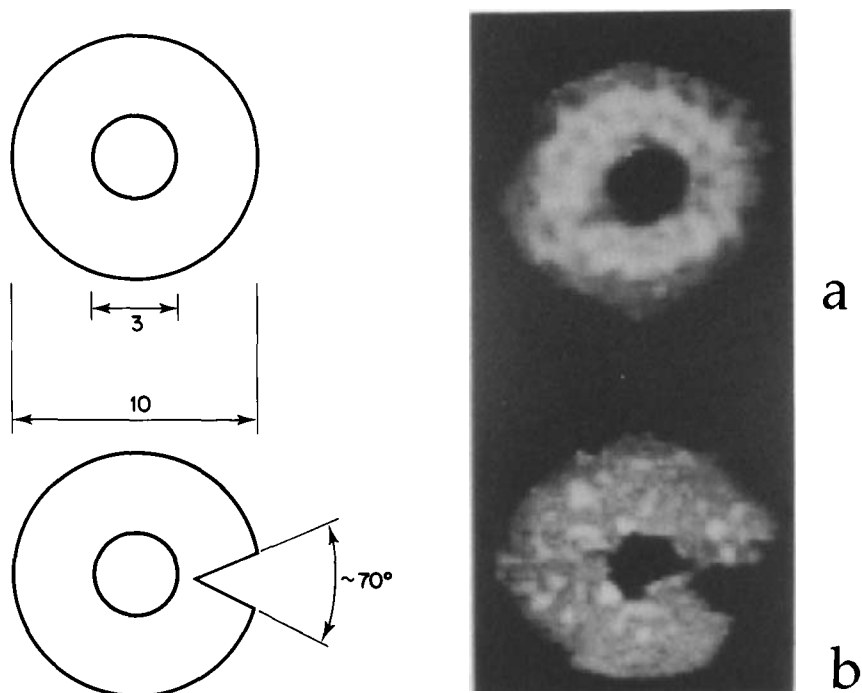


Fig. 30. MARF images of two phantoms formed by compressed adamantane. The sample for image (a) was an 8-mm-thick ring, 10 mm o.d. and 3 mm i.d., and the sample for image (b) was 6 mm thick and had an approximately 70° pie-shaped slice removed. The edges of the sample for (a) were smoothed while for (b) the edges were left rough. The images are a result of 16 projections and 100 acquisitions per projection for a total experimental time of 1.3 h. (Reproduced with permission from De Luca *et al.*¹⁹⁴)

of line-narrowing. Miller and Garroway¹⁹⁶ have demonstrated that it is possible to map out the depth profile of a solid with a surface coil using a string of composite dipolar decoupled π pulses. With the magnetization initially along the static field, a dipolar decoupled π pulse will only rotate the magnetization from the plus z axis to the minus z axis; however, since the experiment is carried out in a spatially varying rf field only selected planes experience a π pulse and for the remainder of the sample a component of the spin magnetization is left in the transverse plane following the nominal π pulse. This transverse component quickly decays and after a string of pulses only the magnetization which experienced a π pulse remains.

When a surface coil is combined with a planar or “inside-out” magnet geometry^{198–200} such that the magnet can be placed against the object of

interest, a surface coil allows a depth profile to be obtained of an arbitrarily large object, though the volume that is actually being sampled is still reasonably small. Scaling up a surface coil to dimensions large enough to look more than a few centimetres into a sample entails all of the same limitations as multiple-pulse imaging; however, the surface of larger objects can be "scanned". These techniques may prove useful for imaging objects which approximate thin sheets or shells.

Brute force methods of generating megawatt rf pulses are known (compare to the typically < 1 kW pulses which are normally employed for small-scale imaging). Since the rf field goes approximately as the square root of the rf power times the coil volume, a megawatt of rf power would allow one to scale the sample size up to approximately 5–10 cm. This may well be the limit to the sample size for the techniques discussed in this review.

9. NUTATION STUDIES OF THE SKIN DEPTH IN METALLIC SAMPLES

A closely related technique to surface coil imaging is nutation studies of the skin depth of metallic samples.²⁰¹ It has long been realized that for metallic samples the skin effect resulted in an attenuation of the rf field strength with depth²⁰² and also an associated phase shift of the observed signal.²⁰³ By measuring the rf nutation frequency of a signal then it is possible to determine from how deep within a conducting material the signal originated. Unfortunately, there are two complications, first the phase shift is a complicated function of depth and there is no known method of obtaining pure adsorption data from all depths of the sample at once, and second the extent of rf attenuation with depth is a function of the sample geometry and a depth calibration is generally not known. Recently Skibbe and Neue²⁰¹ have demonstrated a two-dimensional method of looking inside conducting samples which they call "SEEING" (skin effect imaging).

The basic experiment is a two-dimensional nutation experiment,²⁰⁴ so there are only two periods, a single rf pulse is applied to the sample for an incremented time t_1 following which an FID is collected. Provided that the rf field strength is much stronger than any inhomogeneities within the sample or in the static field, then the first interval phase encodes the rf nutation frequency and the second interval records a normal NMR spectrum of the sample. A two-dimensional Fourier transformation is applied to the data. The complex dependence of the phase with depth (or equivalently nutation frequency) is corrected for by phasing each nutation frequency constant line in the resulting two-dimensional data set by hand. The result is a two-dimensional plot of chemical shift versus nutation frequency.

In general, it is necessary to invoke the sample geometry to go further and to calibrate the nutation frequency as a function of depth. One very useful geometry is a thin ribbon of wire. For a good conductor a thin ribbon will look like an infinite conducting slab where it is known that the rf attenuation with depth is exponential and that the phase shift with depth is linear. Using this approximation the nutation axis can be recalibrated in terms of depth and the final two-dimensional data set shows chemical shift vs. depth. The depth information is a local probe of depth perpendicular to the sample surface and is not influenced by the orientation of the surface in the magnet.

The exponential decay of the rf field strength with depth results in a compression of the spatial axis and an attenuation of the observed signal intensity. For a slab geometry the two effects exactly cancel out and a uniform spin density with depth would look uniform in the displayed spin density profile.

Since the signal is measured from the entire sample at once, the SEEING technique is a local measurement as discussed in relation to Fig. 2, and there is virtually no signal-to-noise limit on the obtainable resolution. This can easily be under 1 μm . Skibbe and Neue have used this technique to investigate deuterium uptake by a palladium electrode.²⁰¹

10. SLICE SELECTION AND VOLUME SELECTED SPECTROSCOPY

At the development stage, where every phantom is made with some form of simple symmetry and just obtaining an image is an important achievement, slice selection schemes are discussed but rarely implemented. However, slice selection is, of course, crucial for studying real world samples of no known symmetry. We will briefly outline some slice selection procedures, but the techniques which eventually find widespread application may look quite different. It is possible to make a few firm statements: first, shaped pulses as they are employed for liquid state imaging are not useful due to the broad linewidths of solids, and second, almost any liquid slice selection experiment can be combined with line-narrowing to get around this problem. To demonstrate the possibility of combining liquid state slice selection with line-narrowing, we will discuss a DANTE-based imaging scheme.²⁰⁵ We don't necessarily wish to promote this particular method as an ideal slice selection technique, but rather to use it as an example of how liquid state imaging techniques can be mated with solid state line-narrowing methods.

A few wide-line slice selection techniques have been suggested, the most useful being adiabatic sweeps^{206,207} and spin-locking.^{208,210} These approaches will require strong gradients, but since there is no data acquisition there is no

sensitivity loss associated with employing strong gradients. Indeed exactly the opposite is true, the stronger the gradient, the faster a slice can be defined, and the more signal is preserved for latter portions of the experiment. These experiments are analogous to constant time imaging experiments, and the graph of experimental time vs. gradient strength in Fig. 13 applies here also.

The DANTE technique²⁰⁵ is described in Fig. 31. The idea of DANTE selectivity is that two orthogonal interactions are applied periodically to a spin system such that their net effect can be a constructive or destructive interference. Originally DANTE was employed for selective excitation of a single chemically shifted resonance by a string of hard short rf pulses. In the original example, the two orthogonal interactions are the chemical shift evolution and the rf pulses. The chemical shift is an I_z operator and therefore causes spin evolution about the I_z axis. The rf pulses will be arbitrarily placed along the y axis and therefore cause spin evolution about the y axis. For a particularly simple description of the spin dynamics, replace the spin evolution caused by the chemical shift with an equivalent phase shift of the rf transmitter. Now the sequence is a set of rf pulses with the phase from one pulse to the next incremented by a constant amount. The size of the phase shift is dependent on the chemical shift. Clearly, if the phase shift between rf pulses is an odd multiple of π , every two pulses will exactly cancel and the spin magnetization will be left along the z axis. Likewise, if the phase shift between rf pulses is an even multiple of π , each rf pulse will be given along the same axis and the overall effect will be a coherent rotation about the y axis. In between these two extremes the trajectories of the spin evolution are more complicated, but for most phase shifts the magnetization tends to stay in the neighbourhood of the z axis. The exact shape of the selectivity profile has been calculated, and approximates a sinc function.^{211,212}

To use the same approach for slice selection, the chemical shift dependence of the spin evolution between rf pulses is replaced by a gradient-induced spatial dependence.²¹¹ This is straightforward to achieve by, for example, refocusing the chemical shift and applying a magnetic field gradient for spatial encoding. Ideally the gradient is applied as pulses in between the rf pulses and the gradient is modulated in such a fashion that the gradient evolution does not vanish while the chemical shift evolution does. Refocused gradient imaging approaches are well suited to this.

For a solid sample the dipolar couplings must also be averaged for each portion of the experiment. A multiple-pulse imaging scheme can be used between the short rf pulses to yield a spatially dependent phase evolution with suppression of both chemical shifts and dipolar couplings.¹⁶⁰ Any of the multiple-pulse imaging schemes with short gradient pulses could have been chosen for this experiment; in the example shown the second averaged MREV-8 sequence was employed. The short rf pulse is also replaced by a

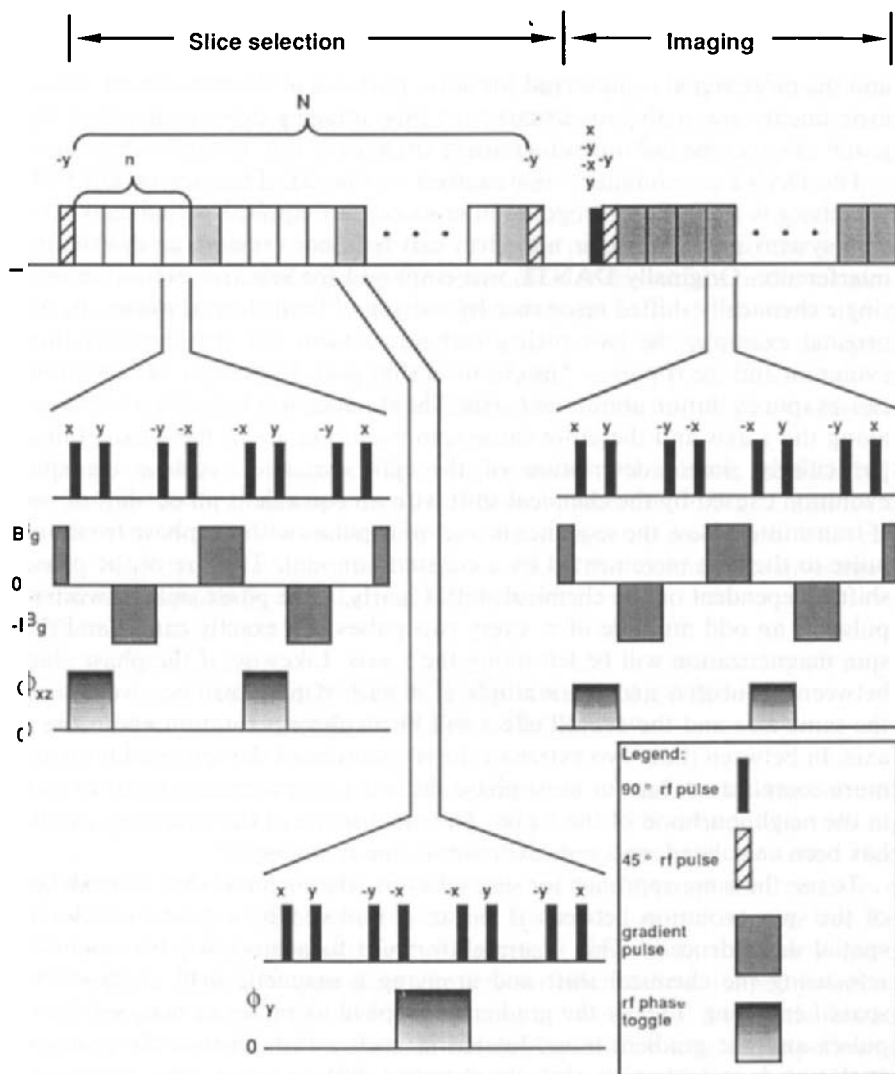


Fig. 31. Homonuclear dipolar-decoupled DANTE sequence for slice selection in solid state imaging of abundant spins with a one-dimensional imaging scheme appended to the end. The imaging portion of the sequence has been described in Fig. 23. The DANTE-style slice selection sequence is composed of an alternating series of $(I_z + I_x)$ and I_y effective fields. The gradient portion of the $(I_z + I_x)$ effective field is spatially dependent while the I_y effective field is uniform across the sample. The sequence's spatial selectivity reflects the destructive interference of the orthogonal rotations associated with these two effective fields except for where the $(I_z + I_x)$ rotation is an integral multiple of 2π . (Reproduced with permission from Cory *et al.*²⁰⁵)

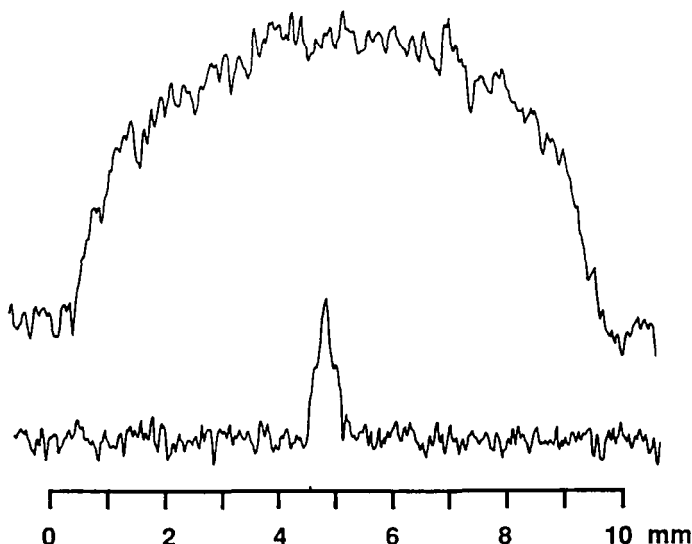


Fig. 32. An example of DANTE ^1H slice selection for a cylinder of ferrocene. The upper one-dimensional image shows a cross-section of the ferrocene sample acquired without slice selection, by the imaging scheme used in Fig. 22. The selected slice in the lower image was obtained by the sequence in Fig. 31 with $n = 4$ and $N = 10$. The average gradient field was approximately 5.5 G/cm with a gradient pulse width of 4 μs . The phase shifts were $\phi_{xz} = 20^\circ$ and $\phi_y = 9^\circ$. (Reproduced with permission from Cory *et al.*²⁰⁵)

dipolar decoupling multiple-pulse sequence that generates a small effective nutation about I_y . Ideally, this sequence should also average the chemical shift to zero, but since it will only be applied once and the chemical shifts are small this is not a stringent requirement. In Fig. 31 a second MREV-8 cycle is employed with a phase toggle that introduces a I_y rotation. This cycle has been previously employed for relaxation studies of solid polymers and for many cycles the phase toggle would lead to a second-averaging of the chemical shift.²¹³

An example of the selectivity of the above slice selection method is shown in Fig. 32 for a one-dimensional ferrocene phantom. Since the probe that this result was acquired on contained only a single gradient coil, a slice was selected and then this selected magnetization was imaged along the same axis.

The general approach of adding line-narrowing to existing slice selection methods can be employed to modify almost any liquids-based slice selection sequence into one that is usable for solid state samples. As seen in this example the final sequence appears to be quite complex, but when the

line-narrowing portions are recognized for what they are, the basic simplicity is once again revealed.

Of the wide-line approaches to slice selection, spin-locking²⁰⁸⁻²¹⁰ may be the most straightforward and simplest to apply. Wind *et al.*²⁰⁸ first suggested that a weak rf spin-locking field will selectively preserve those spins whose offsets are close to the spin-locking frequency. For a liquid sample the selectivity is of the order of the spin-locked field and therefore the stronger the applied gradient is the better the selectivity. In solids, for spin-locking to be effective, the spin-locking field must be stronger than the homogeneous linewidth which places a lower limit on this approach for solids. In principle, though, there is no limit to the maximum gradient strength since no data are collected.

Hafner, Rommel and Kimmich^{209,210} have introduced an important modification to spin-locking slice selection by incorporating the idea of magnetization storage during gradient switching. Supposing that an extremely large magnetic field gradient is used (recall that pulsed gradients of up to 1000 G/cm are routinely employed for pulsed gradient diffusion studies) then the time necessary to obtain a given selectivity is quite short and the spin magnetization is preserved in the spin-locking frame with a time constant of $T_{1\rho}$ (on the order of tens of milliseconds). It is primarily the gradient switching time that leads to a loss in signal-to-noise. This loss is circumvented by storing the magnetization along the static magnetic field during gradient switching in a manner which is similar to Maciel *et al.* use of gradient switching for solid state imaging.¹⁴⁷ Since the coherence time along the static field decays as T_1 (typically on the order of 1 s) and is independent of any magnetic field gradient across the sample, the gradient switching is no longer a problem. The LOSY slice selection scheme²⁰⁹ is then composed of turning on a gradient field, allowing it to stabilize, applying a $\pi/2$ pulse followed by a cw spin-locking field to selectively preserve a subset of the spin magnetization. Following the spin-locking interval the magnetization is returned to the z axis with another $\pi/2$ pulse. Provided that the spin-locking field, B_1^{sl} , is stronger than the local fields, and that the spin-locking time is longer than T_2^* and shorter than $T_{1\rho}$ the slice profile has the form

$$M^{sl}(x) = M_0 \cos^2 \left[\tan^{-1} \left(\frac{\omega_0 x G}{2\pi B_1^{sl}} \right) \right] \quad (37)$$

and the full width at half height of the selected slice is

$$v_{1/2} = \frac{2B_1^{sl}}{G} \quad (38)$$

If the sample has a homogeneous linewidth of 10 kHz, then a minimum spin-locking field of 10 kHz must be used and the minimum frequency spread of the selected slice is 20 kHz. To selectively excite a 100- μ m slice the gradient

must then be 460 G/cm. This is certainly a wide-line technique then, but given sufficiently strong gradients a small region of the sample may be selected.

Spin-locking is a simple method of obtaining a selective slice of modestly rigid solids with good sensitivity, and the location and width of the slice is straightforward to control. By adjusting the gradient strength, the transmitter frequency and transmitter strength, the selected slice can be offset and the width of the slice varied, but the shape of the profile will depend on the natural lineshape of the sample. Even at the point where the gradient completely dominates the lineshape, a square slice cannot be selected by this technique. So far there are no techniques for solid state imaging which allow one to control the shape of the selected region as is done with shaped rf pulses in liquid state imaging.

Adiabatic sweeps are obvious extensions to these spin-locking techniques. An adiabatic sweep reintroduces some additional selectivity into slice selection methods while retaining the favourable relaxation dependence of spin-locking. One particularly appealing approach is that of Ugurbil²⁰⁶ who combines the results from two adiabatic half passages to create an effective slice selection. This approach was originally designed for liquid samples, but has been employed with some success for solids.²⁰⁷

Any of these methods for slice selection can be employed sequentially along all three axes to generate a volume selective spectrum. This has been demonstrated with the spin-locking technique.²¹⁰ Applied as such the techniques are really run as sensitive point methods and do not allow the flexibility of selectively exciting an arbitrarily shaped region which may have been previously identified as being of interest from an image. At this point such techniques have not been demonstrated for solid state samples though a variety of approaches do exist for liquids. One final sensitive point method has been introduced by Corti *et al.*²¹⁴ in which a series of FIDs are co-added with the gradient incremented between each acquisition. The phase of those spins that are not at the zero crossing point of the gradient is thereby modulated and over a sufficient number of acquisitions the signals from these off-resonance spins average to zero.

11. OTHER SPIN = 1/2 NUCLEI

Though protons are certainly the most common nuclei for NMR imaging due to their high natural abundance, high inherent sensitivity, and chemical importance, other nuclei are also good candidates for imaging, and in particular other nuclei may offer new modes of generating contrast. ¹³C^{141,147,178,215,216} is the nucleus that first comes to mind; ¹³C is much less sensitive than ¹H, but there is generally more chemical information in a ¹³C

spectrum than in the corresponding ^1H spectrum. The overwhelming number of ^{13}C CP/MASS studies of solids as compared to ^1H CRAMPS studies demonstrates this point. In polymer science ^{13}C solid state NMR is often the method of choice for studying molecular dynamics, structure and morphology. ^{19}F images have also been obtained^{114,158,217} using techniques which are nearly identical to those employed for ^1H . Again it is polymer systems where there appears to be the most demand for ^{19}F imaging. Of course for certain polymer blends the fluorine is only present in one polymer of the mixture and a ^{19}F image will automatically display the required contrast. Primarily for biological studies, ^{31}P ^{218,219} is an important nucleus and also quite sensitive, allowing high-quality images to be obtained. For ceramics boron^{118,220} and silicon will also be important, though these nuclei have barely been explored with solid state imaging.

It may appear that the imaging experiment is greatly simplified by employing ^{13}C rather than ^1H since heteronuclear decoupling is widely considered to be simpler and more successful than homonuclear decoupling. In fact this is probably not true.^{141,178} The offset dependence of heteronuclear decoupling is very similar to that of homonuclear decoupling²²¹ and the larger residual linewidths for ^1H have more to do with chemical shift dispersion and susceptibility differences than with deficiencies in line-narrowing.²²² Be that as it may, ^{13}C resonances are generally sharper and recently multiple-pulse methods have been introduced which reduce the off-resonance dependence of ^1H heteronuclear decoupling for static samples.²²³ The greatest problem with ^{13}C imaging is that ^{13}C is about a factor of 2900 less sensitive than ^1H ; however, when the differences in the receiver bandwidths and probe Q values are factored in for solid state samples, as well as the generally narrower ^{13}C linewidth this difference in sensitivity is reduced to about a factor of 25.^{141,178} For comparison, a ^1H and ^{13}C image of the same phantom is shown in Fig. 33. Note that it is still necessary to remove chemical shift and susceptibility broadening, but this can be accomplished by Carr–Purcell sequences as discussed for refocused gradient imaging schemes. An additional benefit of the Carr–Purcell sequence is that it is an efficient means of heteronuclear decoupling.

^{13}C imaging will normally be accomplished with cross-polarization²²⁴ for increasing the signal-to-noise and in one study dynamic nuclear polarization has also been employed for additional signal-to-noise and to introduce a new contrast mechanism.²¹⁵ The full power of combining high-resolution ^{13}C spectroscopy with imaging is most simply achieved via the MASS imaging method,¹⁷⁸ and very preliminary one-dimensional examples of this approach have been demonstrated.

Ackerman and coworkers^{218,219} have explored ^{31}P imaging with the intention of studying bone. For the most part, the requirements for ^{31}P

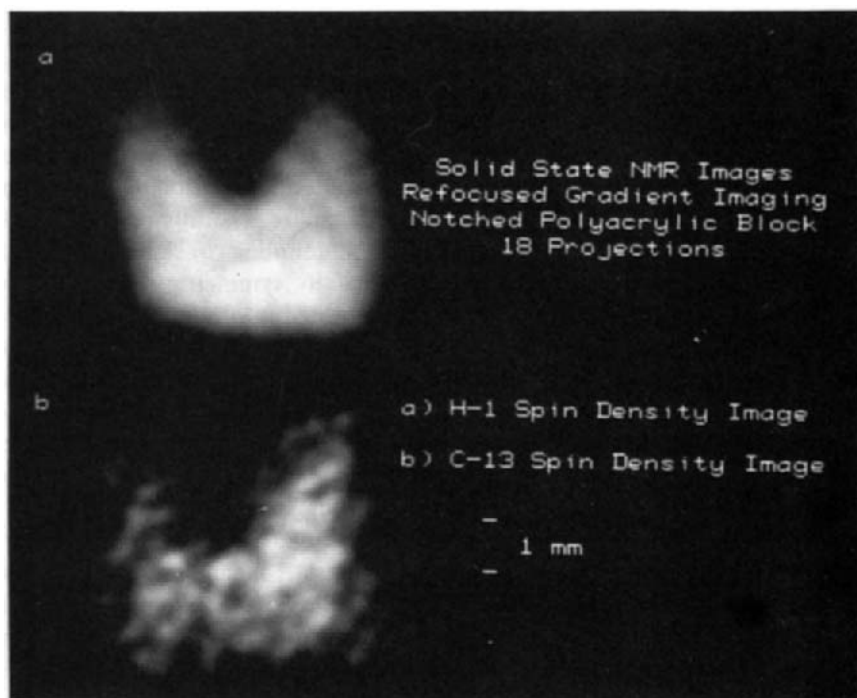


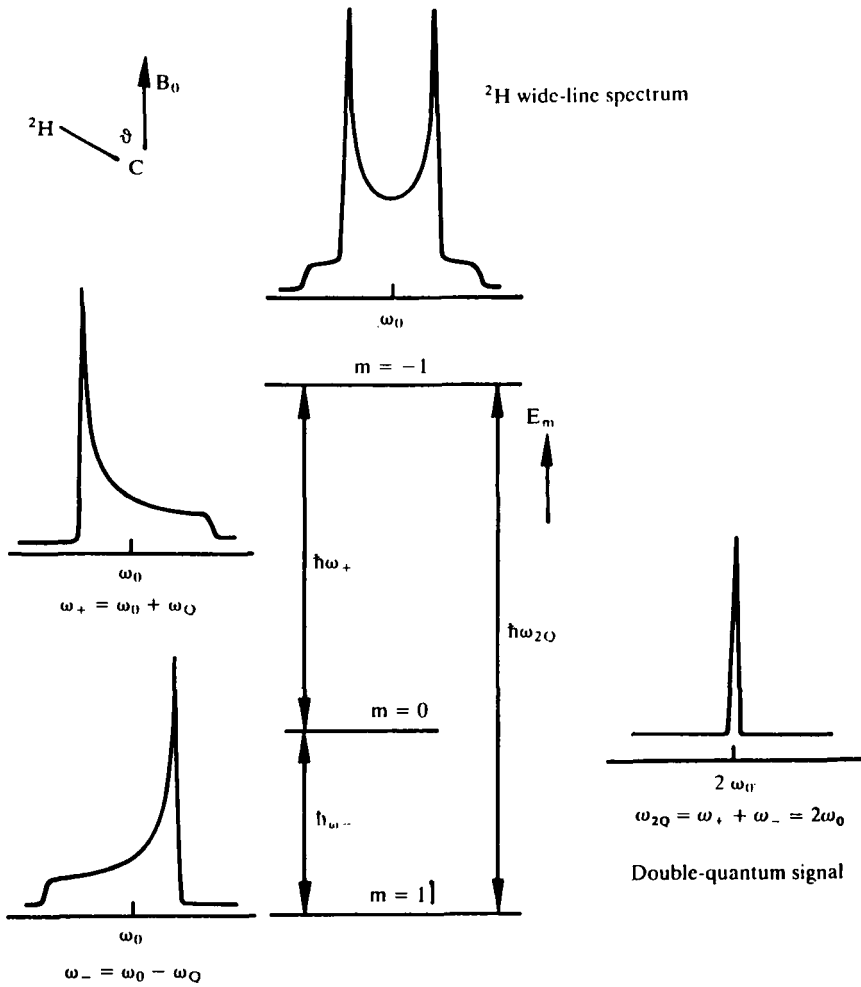
Fig. 33. A comparison of ^1H and ^{13}C images of the same polyacrylic phantom. Both images were recorded by refocused gradient techniques using a back-projection reconstruction scheme. For the ^1H image homonuclear dipolar broadenings and inhomogeneous interactions were averaged, while for ^{13}C a Carr-Purcell cycle was employed which averages both heteronuclear dipolar interactions and inhomogeneous terms. In both cases the magnetic field gradient was applied as an oscillating field. The ^1H image took 40 min to acquire and is the result of 18 projections with a one-dimensional resolution of approximately $450\ \mu\text{m}$. The ^{13}C image required 10.25 h to acquire the same 18 projections that had a one-dimensional resolution of $150\ \mu\text{m}$. The images clearly show that the ^{13}C image has higher resolution and lower signal-to-noise ratio. (Reproduced with permission from Miller and Garroway.^{141,157})

imaging are similar to those for ^{13}C . Exceptions are that ^{31}P is more sensitive than ^{13}C and phosphorus can be quite remote from protons, making spin decoupling unnecessary. As Ackerman demonstrates,²¹⁹ it is also possible to use cross-polarization dynamics as a means of creating contrast in ^{31}P imaging.

12. QUADRUPOLEAR NUCLEI

Quadrupolar nuclei are important not only because they account for most of the nuclei in the periodic table, but also because the quadrupole coupling is a very sensitive probe of the local environment. In particular, for polymer systems ^2H NMR has been used to study molecular motions²²⁵ and orientation.²²⁶ Quadrupolar lineshape analyses for ^2H are generally very accessible due to deuterium's relatively small quadrupole coupling constant and the fact that the quadrupole tensor is frequently axially symmetric with a known orientation. In addition, ^2H is easily incorporated into many materials as a site-specific probe. The quadrupole coupling is sufficiently strong that chemical shifts and other interactions can be ignored and the shape of the quadrupole powder pattern reveals the details of bulk orientations and molecular motions. Likewise, ^{27}Al NMR is valuable for studying ceramics and ceramic processing²⁰⁴ where, for example, nutation studies allow one to map out the local symmetry of aluminium sites.

A variety of images have been acquired for quadrupolar nuclei,^{117,127,227-230} and possibly the most elegant set of experiments are from the group of Spiess using ^2H NMR. Spiess and coworkers¹²⁷ realized that the double-quantum transition of ^2H is not broadened by the quadrupole coupling to first order and, therefore, by encoding the gradient spin evolution in a state of double-quantum coherence not only is the effective gradient strength doubled, but additionally the line is efficiently narrowed. Figure 34 shows an energy level diagram for a spin = 1 nuclei along with the static powder patterns from the quadrupole coupling tensor. The reader is referred to Spiess's paper¹²⁷ for the details of placing the spin system in a double-quantum state where it evolves in the presence of the magnetic field gradient, and then returning it to a single-quantum state from which the spin evolution can be measured. Recall from our previous discussions of multiple-quantum NMR that it is only the single-quantum state which is directly observable in a pulsed resonance experiment and so the double-quantum evolution is detected via a two-dimensional experiment. All three spatial directions can be encoded in the same double-quantum evolution period in a constant time phase encoding experiment; however, as Spiess *et al.* performed the experiment, only a single spatial dimension was encoded and the full quadrupolar powder pattern was observed in the detection period. As shown in Fig. 35, this allows polymers to be distinguished based on the polymer's orientation relative to the static magnetic field. In the future this should be a very powerful technique due to the very specific nature of the contrast that can be built into the image. As was the case with ^{19}F , the presence of ^2H may be itself a form of contrast in which case the ^2H lineshape contains no additional information and can be discarded.



Single quantum signals

Fig. 34. Energy levels, transitions and powder lineshapes for single ($\Delta m = \pm 1$) and double ($\Delta m = \pm 2$) quantum transitions for a spin $I = 1$, axially symmetric quadrupole coupling. To first order the width of the double-quantum line is independent of the quadrupole coupling. (Reproduced with permission from Günther *et al.*¹²⁷)

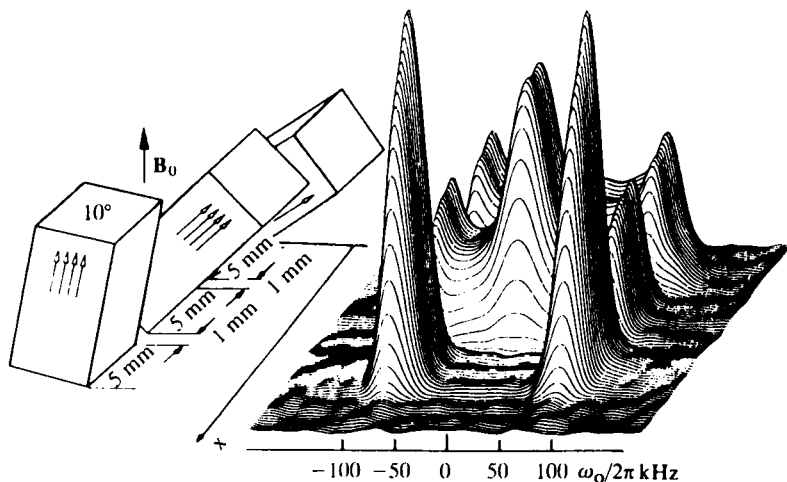


Fig. 35. The double-quantum ^2H NMR line of a phantom consisting of drawn polyethylene oriented at various angles to the main magnetic field. The stacked plot displays one spatial axis with a resolution of approximately 1 mm, and the second axis corresponds to the full single-quantum NMR lineshape. The NMR lineshape is a sensitive indicator of the relative orientation of the C-D bond to the main magnetic field. (Reproduced with permission from Günther *et al.*¹²⁷)

Ackerman and coworkers have made extensive studies of ceramics, including some initial studies of the ^{27}Al ²²⁰ which is spin = $\frac{5}{2}$. Because of the typically large quadrupole couplings, normally one only observes the $+\frac{1}{2}$ to $-\frac{1}{2}$ transition of aluminium, which is broadened by the quadrupolar interaction only in second order. Since ^{27}Al is 100% abundant with a resonance frequency near that of ^{13}C and typically has short relaxation times, it is a very appealing nucleus to image. As with ^2H , however, the most appealing feature of ^{27}Al is the very specific nature of the contrast which can be built into the image. The nutation frequency of ^{27}Al is a sensitive probe of the quadrupole interaction and therefore the local electron symmetry.²⁰⁴ This has been used by Ackerman to distinguish between alumina and an aluminate in a phantom.²²⁰

Conradi¹¹⁷ has demonstrated a constant time, refocused gradient approach to imaging which he applied to ^{27}Al . Though the experiment was demonstrated in only one dimension, in three dimensions all spatial information would still be phase encoded. To gain considerable sensitivity, Conradi applies a pulsatile spin-locking train during the detection period to essentially decrease the detection bandwidth.

Other studies of quadrupolar nuclei have mainly been restricted to systems which had naturally narrow resonances, for instance due to ionic diffusion.²²⁷

The nuclear quadrupole resonance frequency is far more sensitive to temperature and pressure variations than the nuclear Zeeman resonance frequency. This introduces the possibility of building in new types of contrast and even spatially sensitive transducers for temperature,²²⁸ and pressure. Suits and Lutz have also shown that NMR imaging of quadrupole nuclei is a very sensitive probe of defect densities in solids.²²⁹ From studies of impact-induced defects in NaCl crystals they estimate that defect densities as low as 10^6 or $10^7/\text{cm}^2$ can be observed with good signal-to-noise. This great sensitivity to defects is seen since the effects of dislocations in a crystal are experienced by other nuclei out to a radius of about 100 nm.

There has also been one report of pure quadrupole imaging (i.e. in the absence of a magnetic field).²³⁰ Here the only field was a gradient which broadened the NQR resonance since it introduced a Zeeman term to compete with the dominant quadrupolar coupling, and the experiment was run as a sensitive plane technique.

13. APPLICATIONS

To date there have been very few applications of solid state imaging, and most of these were discussed in the above sections. Though nearly every solid state imaging paper discusses potential applications, most of the work so far has been directed to developing the necessary techniques, and indeed more work along these lines is still needed before routine application can be made of solid state imaging. As I hope to have shown, however, there are robust methods of solid state imaging which do yield microscopic resolution and these can be combined with many conventional NMR experiments to display a wide range of contrasts. In this too-short section we will discuss a few areas in which solid state imaging will eventually be applied and point out some of the preliminary work that has been accomplished so far.

The area of solid state chemistry is probably the only area in which true applications have been explored, both of crystal healing²²⁷ and the spatial behaviour of a solid state reaction. Butler and coworkers²³¹ have studied the solid state reaction of ammonia gas with substituted benzoic acid crystals for both a single crystal and in a powdered bed geometry. These reactions had been previously studied by Curtin and coworkers²³² who visibly detected the anisotropy of the reaction in a single crystal. A crystal of 4-bromobenzoic acid has one face with exposed carboxylic groups along which the reaction with ammonia proceeds. Crystalline 4-bromobenzoic acid has a ^1H T_1 of 140 s, while the reaction product ammonium 4-bromobenzoate has a ^1H T_1 of 3 s. The T_1 is therefore a very convenient mechanism for generating contrast, and indeed an image of the reactant is quite difficult to obtain due

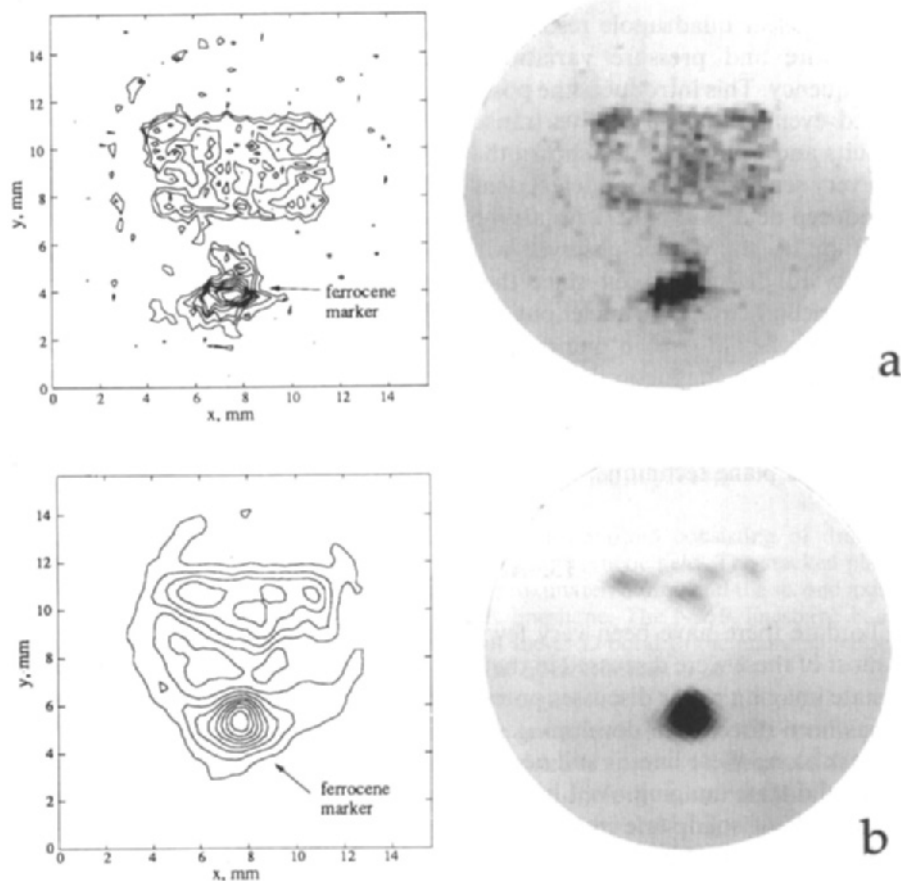


Fig. 36. Contour and grey scale NMR images of a crystal of 4-bromobenzoic acid before (A) and after (B) exposure to ammonia gas for 36 h. Both images were acquired with the CMG-48 time-suspension cycle and pulsed gradients. The first image required a relaxation delay of 180 s due to very long T_1 times. In the after image the relaxation delay is only 5 s. The ferrocene marker is included in these images for ease of alignment and as a sensitivity standard. (Figure courtesy of Les Butler.)

to the very long signal averaging times required. Figure 36 shows two images from before and after the reaction. A reaction anisotropy which is quite different from Curtin's observation is seen in these images, probably due to crystal imperfections.

Solid state NMR is widely used to characterize coals,^{146,233} and coal is one of the few areas in which there has been a continual interest in applying CRAMPS²³⁴ techniques. Since coal is heterogeneous it is natural to think of using solid state imaging to characterize the spatial variation in chemical

composition, and possibly to achieve more useful spectroscopic information by observing coal macerals one at a time. Botto and coworkers¹⁴⁶ have been using the static gradient multiple-pulse technique to characterize coal samples and there have been some initial studies of coals using the pulsed gradient technique.²³³ Though differences in coal samples are easily observed, so far these differences have been on large spatial scales and probably it is necessary to implement full three-dimensional imaging techniques on a microscopic scale before solid state imaging can be usefully applied to coal samples.

There is no doubt that the medical applications of NMR imaging have so far been the most important and so it comes as no surprise that there is interest in using solid state imaging techniques to study bones. ³¹P solid state NMR has been successfully applied to the study of bone, and bone formation.²³⁵ Ackerman and coworkers²¹⁹ have shown that constant time techniques allow good-quality images of both real bone and phantoms made of hydroxyapatite and brushite which are major components of bones. Further, this same group has demonstrated that these two components of bone can be distinguished on the basis of their response to cross-polarization and Bloch decay experiments. It is likely that techniques will be developed for *in vivo* bone studies which sacrifice some resolution for both contrast and experimental time. The demands on such an experiment are much more restrictive than materials imaging application due to sample handling and safety precautions, and the methods which are eventually employed are likely to be very different from those used for solid state materials imaging.

The area of ceramic processing is quite close to bone imaging only here we have complete freedom in how we treat the sample. Many studies have been performed looking for defects in ceramics,^{38,42,60,61,63} where the eventual goal is to follow the ceramic from the green stage through sintering. Slip-casting techniques have also been followed by NMR imaging.⁴¹ In the early stages of these processes liquid state imaging methods are adequate, and even green ceramics can be imaged without line-narrowing, though the transverse relaxation times are generally shorter than can be conveniently accommodated with commercial instruments. Small (< 2 cm) samples can be successfully studied today at microscopic resolution (< 100 μ m) and test samples of this size can be used to characterize the ceramic processing procedures. The role of NMR imaging as a non-destructive evaluation method remains an open question for larger samples and at least in the near future NDE studies are likely to be limited to expensive, critical components.

The area of polymer processing is a potential goldmine of applications for solid state NMR imaging over the next few years. Questions of polymer mixing, blending, morphology and orientation are easily followed by solid state imaging and solid state NMR has a very successful history in studies of synthetic polymers. Earlier we saw examples of the characterization of the

spatial distribution of polybutadiene in a polybutadiene/polystyrene blend, and ^2H images which displayed contrast based on both molecular mobility and orientation. The pulsed gradient technique has been explored for a wide range of polymers and so far images with a resolution of 128×128 pixels could be obtained for all of the tested polymer systems. In fact, with the exception of certain Nylon samples all polymers studied could be observed with an image resolution of 256×256 pixels. For 1-cm size samples this corresponds to a spatial resolution of $39 \mu\text{m}$ which is certainly small enough to study polymer processing. The question remains of how much contrast can be built into images of polymer systems without resorting to MASS techniques. Clearly MASS methods will continue to develop, but so far MASS has not been implemented with pulsed gradient imaging and MASS by itself is a very limited imaging approach.

From our point of view the future of solid state imaging is very bright and we have only just begun to scratch the surface of interesting applications. For those studies which can conveniently be performed in two dimensions (either due to the symmetry of the sample or by physically slicing the sample) all of the necessary techniques are in place and waiting to be exploited. Full three-dimensional approaches are still lacking, but there are no fundamental problems preventing the extension to three dimensions.

ACKNOWLEDGEMENTS

This project benefited greatly from many discussions with Joel Miller, Al Garroway, Wiebren Veeman and Sam Gravina. In particular thanks go to Joel Miller for carefully reading the entire manuscript and offering many helpful and needed suggestions. I also thank Jerry Ackerman, Bernhard Blümich, Mark Conradi, Jack Koenig, Shigeru Matsui, Dan Weitekamp, and Klaus Zick for sharing with me works prior to publication. This review was started while I was a National Research Council/Naval Research Laboratory postdoctoral associate, and was sponsored in part by the Office of Naval Research. Frank Laukien has generously given me time to complete the review while at Bruker Instruments, Inc.

REFERENCES

1. P.C. Lauterbur, *Bull. Am. Phys. Soc.*, 1972, **18**, 86.
2. P.C. Lauterbur, *Nature*, 1973, **242**, 190.
3. P. Mansfield and P.K. Grannell, *J. Phys. C: Solid State Phys.*, 1973, **6**, L422.
4. P. Mansfield, P.K. Grannell, A.N. Garroway and D.C. Stalker, *Proc. 1st Spec. Colloque Ampere*, Krakow, p. 16 (ed. J.W. Hennell), 1973.

5. P. Mansfield and P.K. Grannell, *Phys. Bull., Inst. Phys. Lond.*, 1974, **25**, 134.
6. P. Mansfield, *J. Phys. C.*, 1977, **10**, L55.
7. P. Mansfield and I.L. Pykett, *J. Magn. Reson.*, 1978, **29**, 355.
8. P. Mansfield, *J. Phys. E.: Sci. Instrum.*, 1988, **21**, 18.
9. P.T. Callaghan, *Principles of Nuclear Magnetic Resonance Microscopy*. Oxford University Press, Oxford, 1991.
10. W. Kuhn, *Angew. Chem. Int. Ed.*, 1990, **29**, 1.
11. C.D. Eccles and P.T. Callaghan, *J. Magn. Reson.*, 1986, **68**, 393.
12. P.T. Callaghan and C.D. Eccles, *J. Magn. Reson.*, 1987, **71**, 426.
13. J.M. Listerud, S.W. Sinton and G.P. Drobny, *Anal. Chem.*, 1989, **61**, 23A.
14. J.B. Miller, *Trends Anal. Chem.*, 1991, **10**, 59.
15. J.B. Miller, D.G. Cory and A.N. Garroway, *Phil. Trans. R. Soc. A*, 1990, **333**, 413.
16. P. Mansfield and P.K. Grannell, *Phys. Rev. B*, 1975, **12**, 3618.
17. U. Haeberlen, *High Resolution NMR in Solids: Selective Averaging*. Adv. Magn. Reson. suppl. 1. Academic Press, New York, 1976.
18. M. Mehring, *High Resolution NMR in Solids*. Springer-Verlag, Berlin, 1983.
19. B.C. Gerstien and C.R. Dybowski, *Transient Techniques in NMR of Solids: An Introduction to Theory and Practice*. Academic Press, Orlando, 1985.
20. C.A. Fyfe, *Solid State NMR for Chemists*. CFC Press, Guelph, 1983.
21. U. Haeberlen and J.S. Waugh, *Phys. Rev.*, 1968, **175**, 453.
22. A.G. Semenov, Abstracts from the 9th Ampere Summer School, Novosibirsk, p. 61 (1987).
23. A. Abragam, *Principles of Nuclear Magnetism*. Oxford University Press, Oxford, 1961.
24. C.P. Slichter, *Principles of Magnetic Resonance*, 2nd Edn. Springer-Verlag, Berlin, 1980.
25. J. Baum and A. Pines, *J. Am. Chem. Soc.*, 1986, **108**, 7447.
26. M. Munowitz, A. Pines and M. Mehring, *J. Chem. Phys.*, 1987, **86**, 3172.
27. P. Caravatti, P. Neuenschwander and R.R. Ernst, *Macromolecules*, 1986, **19**, 1889.
28. D.L. VanderHart, *J. Magn. Reson.*, 1987, **72**, 13.
29. P.T. Callaghan, *Aust. J. Phys.*, 1984, **37**, 359.
30. J. Kärgler, H. Pfeifer and W. Heink, *Adv. Magn. Reson.*, 1988, **12**, 1.
31. P. Stilbs, *Prog. NMR Spectrosc.*, 1987, **19**, 1.
32. D.G. Cory and A.N. Garroway, *Magn. Reson. Med.*, 1990, **14**, 435.
33. W.P. Rothwell and H.J. Vinegar, *Appl. Optics*, 1985, **24**, 3969.
34. H.J. Vinegar, *J. Petrol. Technol.*, 1986, **257**, March.
35. W.P. Rothwell, D.R. Holecek and J.A. Kershaw, *J. Polym. Sci. Polym. Lett. Ed.*, 1984, **22**, 241.
36. W.P. Rothwell, P.N. Tutunjian and H.J. Vinegar, *New Dir. Chem. Anal., Proc. Symp. Ind.-Univ. Coop. Chem. Program Dep. Chem., Tex. A&M Univ.*, 3rd, pp. 366-95 (ed. B.L. Shapiro), 1985.
37. L.D. Hall and V. Rajanayagam, *J. Magn. Reson.*, 1987, **74**, 139.
38. J.L. Ackerman, W.A. Ellingson, J.A. Koutcher and B.R. Rosen, *Nondestructive Characterization of Materials II*, p. 129. Plenum Press, New York, 1987.
39. W.A. Ellingson, J.L. Ackerman, L. Garrido, J.D. Weyand and R.A. DiMilia, *Ceram. Eng. Sci. Proc.*, 1987, **8**, 503.
40. A. Briguet, *Mol. Cryst. Liq. Cryst.*, 1987, **161** (Pt B), 413.
41. K. Hayashi, K. Kawashima, K. Kose and T. Inouye, *J. Phys. D: Appl. Phys.*, 1988, **21**, 1037.
42. J.L. Ackerman, L. Garrido, W.A. Ellingson and J.D. Weyand, *Nondestructive Testing of High-Performance Ceramics*, p. 88. American Chemical Society, 1988.
43. M.A. Horsfield, E.J. Fordham, C. Hall and L.D. Hall, *J. Magn. Reson.*, 1989, **81**, 593.

44. A.K. Gaigalas, A.C. van Orden, B. Robertson, T.H. Mareci and L.A. Lewis, *Nucl. Technol. (USA)*, 1989, **84**, 113.
45. D.E. Woessner, J.F. Gleason and C.F. Jordan, *Soc. Petrol. Engrs* (in press).
46. L.D. Hall, V. Rajanayagam, W.A. Stewart and P.R. Steiner, *Can. J. For. Res.*, 1986, **16**, 423.
47. L.D. Hall and V. Rajanayagam, *Wood Sci. Technol.*, 1986, **20**, 329.
48. L.D. Hall, V. Rajanayagam, W.A. Stewart, P.R. Steiner and S. Chow, *Can. J. For. Res.*, 1986, **16**, 684.
49. P.C. Wang and S.J. Chang, *Wood and Fiber Sci.*, 1986, **18**, 308.
50. S.J. Chang, J.R. Olson and P.C. Wang, *Forest Prod. J.*, 1989, **39**, 43.
51. L.D. Hall, V. Rajayagam and C. Hall, *J. Magn. Reson.*, 1986, **68**, 185.
52. L.W. Jelinski, M.D. Cockman, *Polym. Prep.*, 1990, **31**, 100.
53. R.W. Behling, H.K. Tubbs, M.D. Cockman and L.W. Jelinski, *Nature (Lond.)*, 1989, **341**, 321.
54. B. Blümich, *Angew. Chem.*, 1989, **100**, 1460.
55. T.A. Carpenter, L.D. Hall and P. Jezzard, *J. Magn. Reson.*, 1989, **84**, 383.
56. C. Chang and R.A. Komoroski, *Macromolecules*, 1989, **22**, 600.
57. P. Blümli and B. Blümich, *Macromolecules* (in press).
58. L. Garrido, J.E. Mark, S. Wang, J.L. Ackerman and J.M. Vevea, *Polymer (Lond.)* (in press).
59. L. Garrido, J.E. Mark, C.C. Sun, J.L. Ackerman and C. Chang, *Macromolecules* 1991, **24**, 4067.
60. L. Garrido, J.L. Ackerman, W.A. Ellingson and J.D. Weyand, *Ceram. Eng. Sci. Proc.*, 1988, **9**, 1465.
61. W.A. Ellingson, P.S. Wong, S.L. Dieckman and J.L. Ackerman, *Am. Ceram. Soc. Bull.*, 1989, **68**, 1180.
62. W.A. Ellingson, P.S. Wong, S.L. Dieckman, J.P. Pollinger, H. Yeh and M.W. Vannier, *Ceram. Eng. Sci. Proc.*, 1989, **10**, 1022.
63. L. Garrido, J.L. Ackerman and W.A. Ellingson, *J. Magn. Reson.*, 1990, **88**, 340.
64. P. Jackson, N.J. Clayden, T.A. Carpenter, L.D. Hall and P. Jezzard, Post C7, *10th Europ. Exp. NMR Conf.*, Veldoven, the Netherlands, 1990.
65. P. Jezzard, T.A. Carpenter, L.D. Hall, P. Jackson and N.J. Clayden, *Polym. Commun.*, 1991, **32**, 74.
66. S.R. Smith and J.L. Koenig, *Macromolecules* 1991, **24**, 3496.
67. L.A. Weisenberger and J.L. Koenig, *Macromolecules*, 1990, **23**, 2445.
68. L.A. Weisenberger and J.L. Koenig, *Macromolecules*, 1990, **23**, 2459.
69. S. Blackband and P. Mansfield, *J. Phys. C: Solid State Phys.*, 1986, **19**, L49.
70. T.H. Mareci, S. Donstrup and A. Rigamonti, *J. Mol. Liq.*, 1988, **38**, 185.
71. L.A. Weisenberger and J.L. Koenig, *J. Polym. Sci., Part C: Polym. Lett.*, 1989, **27**, 55.
72. L.A. Weisenberger and J.L. Koenig, *Appl. Spectrosc.*, 1989, **43**, 1117.
73. L.A. Weisenberger and J.L. Koenig, *J. Polym. Sci.: Part C: Polym. Lett.*, 1989, **27**, 55.
74. A.K. Nieminen and J.L. Koenig, *J. Adhes. Sci. Technol.*, 1988, **2**, 407.
75. A.O.K. Nieminen, J. Liu and J.L. Koenig, *J. Adhes. Sci. Technol.*, 1989, **3**, 455.
76. A.O.K. Nieminen and J.L. Koenig, *Appl. Spectrosc.*, 1989, **43**, 1358.
77. K.P. Hoh, B. Perry, G. Rotter, H. Ishida and J.L. Koenig, *J. Adhes.*, 1989, **27**, 24.
78. B.C. Perry and J.L. Koenig, *J. Polym. Sci.: Part A: Polym. Chem.*, 1989, **17**, 3429.
79. P. Mansfield and P.G. Morris, *Advances in Magnetic Resonance*, Suppl. 2. Academic Press, New York, 1982.
80. W.P. Rothwell, *Appl. Optics*, 1986, **24**, 3958.
81. P.G. Morris, *Nuclear Magnetic Resonance Imaging in Medicine and Biology*. Clarendon Press, Oxford, 1986.

82. R.R. Ernst, *Quart. Revs. Biophys.*, 1987, **19**, 183.
83. F.W. Wehrli, D. Shaw and J.B. Kneeland, *Biomedical Magnetic Resonance Imaging: Principles, Methodology and Applications*. VCH Publishers, New York, 1988.
84. S.J. Riederer, *Proc. IEEE*, 1988, **76**, 1095.
85. J.S. Taylor, *Appl. Spectr. Rev.*, 1989, **25**, 127.
86. P. Mansfield, *Physics of NMR Spectroscopy in Biology and Medicine* (ed. B. Maraviglia), p. 345. North Holland, Amsterdam, 1988.
87. B. Blümich, P. Blümli, E. Günther and G. Schauss, *Bruker Reports*, 1990 (2) 22.
88. S.L. Smith, *Anal. Chem.*, 1985, **57**, 595A.
89. L. Kevan and M.K. Bowman, *Modern Pulsed and Continuous Wave Electron Spin Resonance*. John Wiley & Sons, New York, 1990.
90. S.C.-K. Chu, Y. Xu, J.A. Balschi and C.S. Springer, Jr., *Magn. Reson. Med.*, 1990, **13**, 239.
91. P.T. Callaghan, *J. Magn. Reson.*, 1990, **87**, 304.
92. R. Gabillard, *Rev. Sci., Paris*, 1952, **90**, 307.
93. H.Y. Carr and E.M. Purcell, *Phys. Rev.*, 1954, **94**, 630.
94. J.S. Murday, *J. Magn. Reson.*, 1973, **10**, 111.
95. S. Ljunggren, *J. Magn. Reson.*, 1983, **54**, 338.
96. D.G. Cory, A.M. Reichwein and W.S. Veeman, *J. Magn. Reson.*, 1988, **80**, 259.
97. L.J. Busse, S.R. Thomas, R.G. Pratt, L.C. Clark, J.L. Ackerman, R.C. Samaritunga and R.E. Hoffman, *Med. Phys.*, 1986, **13**, 518.
98. J. Liu, A.O.K. Nieminen and J.L. Koenig, *Appl. Spectrosc.*, 1989, **43**, 1260.
99. P.A. Jansson, *Deconvolution with Applications in Spectroscopy*. Academic Press, Orlando, 1984.
100. J.M. Blackledge, *Quantitative Coherent Imaging*. Academic Press, London, 1989.
101. P.T. Callaghan and C.D. Eccles, *J. Magn. Reson.*, 1988, **77**, 1.
102. R. Freeman, *A Handbook of Nuclear Magnetic Resonance*. Longman Scientific and Technical, Essex, 1988.
103. R.R. Ernst, *Adv. Magn. Reson.*, 1966, **2**, 1.
104. A. Kumar, D. Welti and R.R. Ernst, *J. Magn. Reson.*, 1975, **18**, 69.
105. R.R. Ernst, G. Bodenhausen and A. Wokaun, *Principles of Nuclear Magnetic Resonance in One and Two Dimensions*. Clarendon Press, Oxford, 1987.
106. W.A. Edelstein, J.M.S. Hutchinson, G. Johnson and T.W. Redpath, *Phys. Med. Biol.*, 1980, **25**, 751.
107. J.H. Strange, *Phil. Trans. R. Soc. (Lond.) A*, 1990, **333**, 427.
108. R.E. Botto, S.L. Dieckman, N. Gopalsami and P. Rizo, Poster No. 239, *32nd Experimental Nuclear Magnetic Resonance Spectroscopy Conference*, April 1991, St. Louis.
109. J. Frahm, K-D. Merboldt and W. Hänicke, *J. Magn. Reson.*, 1987, **72**, 502.
110. A.J. de Crespigny, T.A. Carpenter and L.D. Hall, *J. Magn. Reson.*, 1989, **85**, 595.
111. P.G. Morris, D.J.O. McIntyre, D.E. Rourke and J.T. Ngo, *NMR Biomed.*, 1989, **2**, 257.
112. R. Campanella, C. Castieri, F. De Luca, B.C. De Simone and B. Maraviglia, *Physics of NMR Spectroscopy in Biology and Medicine* (ed. B. Maraviglia), p. 451. North Holland, Amsterdam, 1988.
113. A.A. Samoilenko, D.Yu. Artemov and L.A. Sibel'dina, *Russ. J. Phys. Chem. (UK)*, 1987, **61**, 1623.
114. A.A. Samoilenko, D. Yu Artemov and L.A. Sibel'dina, *JETP Lett.*, 1988, **47**, 417.
115. A.A. Samoilenko and K. Zick, *Bruker Reports*, 1990 (1), 41.
116. S. Emid and J.H.N. Creyghton, *Physica*, 1985, **125B**, 81.
117. M.S. Conradi, *J. Magn. Reson.* 1991, **93**, 419.
118. P. Bendel, M. Davis, E. Berman and G.W. Kabalka, *J. Magn. Reson.*, 1990, **88**, 369.
119. P.J. McDonald, J.J. Attard and D.G. Taylor, *J. Magn. Reson.*, 1987, **72**, 224.
120. E. Rommel, S. Hafner and R. Kimmich, *J. Magn. Reson.*, 1990, **86**, 264.

121. D.G. Cory, J.C. de Boer and W.S. Veeman, *Macromolecules*, 1989, **22**, 1618.
122. G.C. Chingas, J.B. Miller and A.N. Garroway, *J. Magn. Reson.*, 1986, **66**, 530.
123. D. Zax and A. Pines, *J. Chem. Phys.*, 1983, **78**, 6333.
124. A.N. Garroway, J. Baum, M.G. Munowitz and A. Pines, *J. Magn. Reson.*, 1984, **60**, 337.
125. G. Bodenhausen, *Prog. Nucl. Magn. Spectrosc.*, 1981, **14**, 137.
126. D.P. Weitekamp, *Adv. Magn. Reson.*, 1983, **11**, 111.
127. E. Günther, B. Blümich and H.W. Spiess, *Mol. Phys.*, 1990, **71**, 477.
128. M. Munowitz, *Coherence and NMR*. John Wiley & Sons, New York, 1988.
129. M.M. Maricq, *Phys. Rev.*, 1982, **B25**, 6622.
130. H.Y. Carr and E.M. Purcell, *Phys. Rev.*, 1954, **94**, 630.
131. J.S. Waugh, L.M. Huber and U. Haeberlen, *Phys. Rev. Lett.*, 1968, **20**, 180.
132. D.G. Cory, J.B. Miller and A.N. Garroway, *J. Magn. Reson.*, 1990, **90**, 205.
133. M. Engelberg and C.S. Yannoni, *J. Magn. Reson.*, 1990, **88**, 393.
134. P. Mansfield, *J. Phys. C (Solid State Phys.)*, 1971, **4**, 1444.
135. W.-K. Rhim, D.D. Elleman and R.W. Vaughan, *J. Chem. Phys.*, 1973, **58**, 1772.
136. L.M. Ryan, R.E. Taylor, A.J. Paff and B.C. Gerstein, *J. Chem. Phys.*, 1980, **72**, 508.
137. D.P. Weitekamp, J.R. Garbow and A. Pines, *J. Chem. Phys.*, 1984, **80**, 1372.
138. H.M. Cho, C.J. Lee, D.N. Shykind and D.P. Weitekamp, *Phys. Rev. Lett.*, 1985, **55**, 1923.
139. R.F. Karlicek and I.J. Lowe, *J. Magn. Reson.*, 1980, **37**, 75.
140. P. Bendel, *IEEE Trans. Med. Imaging*, 1985, **MI-4**, 114.
141. J.B. Miller and A.N. Garroway, *J. Magn. Reson.*, 1986, **67**, 575.
142. E.R. Andrew, *Prog. NMR Spectrosc.*, 1971, **8**, 1.
143. I.J. Lowe, *Phys. Rev. Lett.*, 1959, **2**, 285.
144. A. Bax, N.M. Szeverenyi and G.E. Maciel, *J. Magn. Reson.*, 1983, **52**, 147.
145. M.M. Maricq and J.S. Waugh, *J. Chem. Phys.*, 1979, **70**, 3300.
146. S.L. Dieckman, N. Gopalsami and R.E. Botto, *Energy and Fuels*, 1990, **4**, 417.
147. N.M. Szeverenyi and G.E. Maciel, *J. Magn. Reson.*, 1984, **60**, 460.
148. A.N. Garroway, P. Mansfield and D.C. Stalker, *Phys. Rev.*, 1975, **11**, 121.
149. A. Pines and J.S. Waugh, *J. Magn. Reson.*, 1975, **8**, 50.
150. J.B. Miller, D.G. Cory and A.N. Garroway, *Chem. Phys. Lett.*, 1989, **164**, 1.
151. D.P. Burum and W.-K. Rhim, *J. Chem. Phys.*, 1979, **71**, 944.
152. D.P. Burum, M. Linder and R.R. Ernst, *J. Magn. Reson.*, 1981, **44**, 173.
153. W.-K. Rhim, A. Pines and J.S. Waugh, *Phys. Rev. B*, 1971, **3**, 684.
154. K. Takagashi and C.A. McDowell, *Chem. Phys. Lett.*, 1985, **116**, 100.
155. M. Lee and W.I. Goldburg, *Phys. Rev.*, 1965, **A140**, 1261.
156. A. Bielecki, A.C. Kolbert, H.J.M. de Groot, R.G. Griffin and M.H. Levitt, *Adv. Magn. Reson.*, 1990, **14**, 111.
157. J.B. Miller and A.N. Garroway, *J. Magn. Reson.*, 1989, **82**, 529.
158. P.J. McDonald and P.F. Tokarczuk, *J. Phys. E*, 1989, **22**, 948.
159. D.G. Cory and S. Gravina, *Proceedings of the Materials Research Society*, 1990 1991, **217**, 15.
160. D.G. Cory, J.B. Miller and A.N. Garroway, *Mol. Phys.*, 1990, **70**, 331.
161. S. Matsui, *Chem. Phys. Lett.* 1991, **179**, 187.
162. S. Matsui, *J. Magn. Reson.* 1991, **95**, 149.
163. M.S. Conradi, A.N. Garroway, D.G. Cory and J.B. Miller, *J. Magn. Reson.* 1991, **94**, 370.
164. R. Turner, *J. Phys. D: Appl. Phys.*, 1986, **19**, L147.
165. D.I. Hoult, *J. Magn. Reson.*, 1977, **26**, 165.
166. M. Werner, J.A. Marohn, D.N. Shykind and D. Wietekamp, Poster No. 240, *32nd Experimental Nuclear Magnetic Resonance Spectroscopy Conference*, April 1991, St. Louis.
167. D.G. Cory and W.S. Veeman, *J. Magn. Reson.*, 1989, **84**, 392.

168. D.G. Cory, A.N. Garroway and J.B. Miller, *J. Magn. Reson.*, 1990, **87**, 202.
169. D.G. Cory, J.B. Miller and A.N. Garroway, *unpublished results*.
170. R.F. Karlicek and I.J. Lowe, *J. Magn. Reson.*, 1978, **32**, 199.
171. R.W. Vaughan, D.D. Elleman, L.M. Stacy, W.-K. Rhim and J.W. Lee, *Rev. Sci. Instrum.*, 1972, **43**, 1356.
172. D.G. Cory, J.B. Miller and A.N. Garroway, *unpublished results*.
173. R.A. Wind and C.S. Yannoni, *U.S. patent 4 301 410*, 17 November 1981.
174. J.L. Ackerman, *U.S. patent 4 654 593*, 31 March 1987.
175. D.G. Cory, J.W.M. van Os and W.S. Veeman, *J. Magn. Reson.*, 1988, **76**, 543.
176. D.G. Cory, A.M. Reichwein, J.W.M. van Os and W.S. Veeman, *Chem. Phys. Lett.*, 1988, **143**, 467.
177. D.G. Cory and W.S. Veeman, *J. Magn. Reson.*, 1989, **82**, 374.
178. D.G. Cory and W.S. Veeman, *J. Phys. E: Sci. Instrum.*, 1989, **22**, 180.
179. W.S. Veeman and D.G. Cory, *Adv. Magn. Reson.*, 1989, **13**, 43.
180. D.G. Cory, J.B. Miller, A.N. Garroway and W.S. Veeman, *J. Magn. Reson.*, 1989, **85**, 219.
181. P.C. Lauterbur, D.N. Leven and R.B. Marr, *J. Magn. Reson.*, 1984, **59**, 536.
182. M.L. Bernardo, P.C. Lauterbur and L.K. Hedges, *J. Magn. Reson.*, 1985, **61**, 168.
183. S. Matsui and H. Kohno, *J. Magn. Reson.*, 1986, **70**, 157.
184. D.G. Cory, *J. Magn. Reson.*, 1989, **82**, 337.
185. Y. Ogura and K. Sekihara, *J. Magn. Reson.*, 1989, **83**, 177.
186. Y. Ogura and K. Sekihara, *J. Magn. Reson.*, 1990, **88**, 359.
187. A.E. Mefed and V.A. Atsarkin, *Sov. Phys. JEPT*, 1978, **47**, 378.
188. V.A. Atsarkin and T.N. Khazanovich, *Sov. Phys. JEPT*, 1984, **60**, 162.
189. F. De Luca, C. Nuccetelli, B.C. De Simone and B. Maraviglia, *Solid State Commun.*, 1989, **70**, 797.
190. A.G. Redfield, *Phys. Rev.*, 1955, **98**, 1182.
191. F. De Luca, *Lettere Al Nuovo Cimento*, 1984, **39**, 390.
192. F. De Luca and B. Maraviglia, *J. Magn. Reson.*, 1986, **67**, 169.
193. F. De Luca, C. Nuccetelli, B.C. De Simone and B. Maraviglia, *J. Magn. Reson.*, 1986, **69**, 496.
194. F. De Luca, B.C. De Simone, N. Luger, B. Maraviglia and C. Nuccetelli, *J. Magn. Reson.*, 1990, **90**, 124.
195. J.B. Miller and A.N. Garroway, *J. Magn. Reson.*, 1988, **77**, 187.
196. J.B. Miller and A.N. Garroway, *J. Magn. Reson.*, 1989, **85**, 432.
197. J.B. Miller and A.N. Garroway, *Rev. Prog. Quant. Nondestructive Evaluation*, 1990, **9A**, 609.
198. R.K. Cooper and J.A. Jackson, *J. Magn. Reson.*, 1980, **41**, 400.
199. L.J. Burnett and J.A. Jackson, *J. Magn. Reson.*, 1980, **41**, 406.
200. J.A. Jackson, L.J. Burnett and J.F. Harmon, *J. Magn. Reson.*, 1980, **41**, 411.
201. U. Skibbe and G. Neue, *Colloids Surfaces*, 1990, **45**, 235.
202. M. Mehring, D. Kotzur and O. Kanert, *Phys. Status Solidi B*, 1972, **53**, 25.
203. D. Kotzur, M. Mehring and O. Kanert, *Z. Naturforsch.*, 1973, **28**, 1607.
204. A. Samoson and E. Lipmaa, *Phys. Rev. B*, 1983, **28**, 6567.
205. D.G. Cory, J.B. Miller and A.N. Garroway, *J. Magn. Reson.*, 1990, **90**, 544.
206. A.J. Johnson, M. Garwood and K. Ugurbil, *J. Magn. Reson.*, 1989, **81**, 653.
207. J.B. Miller, *unpublished results*.
208. R.A. Wind, J.H.N. Creyghton, D.J. Ligthelm and J. Smidt, *J. Phys. C: Solid State Phys.*, 1978, **11**, L223.
209. E. Rommel and R. Kimmich, *J. Magn. Reson.*, 1989, **83**, 299.
210. S. Hafner, E. Rommel and R. Kimmich, *J. Magn. Reson.*, 1990, **88**, 449.

211. G. Bodenhausen, R. Freeman and G.A. Morris, *J. Magn. Reson.*, 1976, **23**, 171.
212. G.A. Morris and R. Freeman, *J. Magn. Reson.*, 1978, **29**, 433.
213. C.R. Dybowski and R.W. Vaughan, *Macromolecules*, 1975, **8**, 50.
214. M. Corti, F. Borsa and A. Rigamonti, *J. Magn. Reson.*, 1988, **79**, 21.
215. G.E. Maciel and M.F. Davis, *J. Magn. Reson.*, 1985, **64**, 356.
216. C.G. Fry, A.C. Lind, M.F. Davis, D.W. Duff and G.E. Maciel, *J. Magn. Reson.*, 1989, **83**, 656.
217. M. Ilg, K. Albert, W. Rapp and E. Bayer, *J. Magn. Reson.*, 1990, **90**, 370.
218. J.L. Ackerman, D.P. Raleigh and M.J. Glimcher, *Magn. Reson. Med.* (in press).
219. J.L. Ackerman, J.R. Moore, Y. Wu, B. Pfeleiderer and L. Garrido, *Proc. Radiological Society of the Republic of China and International Symposium of Magnetic Resonance Imaging*, Taipei, 1991 (in press).
220. J.R. Moore, L. Garrido and J.L. Ackerman, *Ceram. Eng. Sci. Proc.*, 1990, **11**, 1302.
221. D.L. VanderHart, W.L. Earl and A.N. Garroway, *J. Magn. Reson.*, 1981, **44**, 361.
222. U. Haeberlen, *Magn. Reson. Rev.*, 1985, **10**, 81.
223. K.V. Schenker, D. Suter and A. Pines, *J. Magn. Reson.*, 1987, **73**, 99.
224. A. Pines, M. Gibby and J.S. Waugh, *J. Chem. Phys.*, 1973, **59**, 569.
225. B. Blümich and H.W. Spiess, *Angew. Chem.*, 1988, **27**, 1655.
226. H.W. Spiess, *Devel. Oriented Polym.*, 1982, **1**, 47.
227. B.H. Suits and D. White, *Solid State Commun.*, 1984, **50**, 291.
228. B.H. Suits and D. White, *J. Appl. Phys.*, 1986, **60**, 3772.
229. B.H. Suits and J.L. Lutz, *J. Appl. Phys.*, 1989, **65**, 3728.
230. S. Matsui, K. Kose and T. Inouye, *J. Magn. Reson.*, 1990, **88**, 186.
231. L.G. Butler, D.G. Cory, K.M. Dooley, J.B. Miller and A.N. Garroway *J. Am. Chem. Soc.* (in press).
232. I.C. Paul and D.Y. Curtin, *Science*, 1975, **187**, 19.
233. D.G. Cory, J.B. Miller and A.N. Garroway (to be published).
234. A. Jurkiewicz, C.E. Bronniman and G.E. Maciel, *Fuel*, 1989, **68**, 872.
235. A.H. Roufosse, W.P. Aue, J.E. Roberts, M.J. Glimcher and R.G. Griffin, *Biochemistry*, 1984, **23**, 6115.

NMR Studies of Interfacial Phenomena

J. GRANDJEAN

University of Liege, Institute of Chemistry B6, Sart Tilman, B-4000 Liege, Belgium

1. Introduction	181
2. Theory	184
2.1. Line splitting	185
2.2. Chemical shielding anisotropy	189
2.3. Relaxation	190
2.4. Self diffusion	196
3. Results	198
3.1. Interfacial molecules	198
3.2. Ions at an interface	203
3.3. Nuclei of superficial groups of phase I components	208
4. Conclusions	211
References	212

1. INTRODUCTION

Phenomena occurring at interfaces have a tremendous importance in many aspects of science. Indeed, species within this region share particular properties responsible for phenomena involved in different areas such as chromatography, heterogeneous catalysis, electrochemical experiments or membrane processes. A knowledge of the structure and dynamics of interfacial species is required for a good understanding of these phenomena. Clearly, an experimental technique cannot be used to study every interface.

A working definition of the interfacial region is necessary within the scope of this review. As shown schematically in Fig. 1, this region is located in the neighbourhood of the border between two phases. Phase I can be formed by macromolecules, aggregates or solid particles. When these components are charged, counterions in phase II will be present to preserve electroneutrality. But in a few recent investigations on the solid-solid interface, phase II is liquid. Therefore, I do not consider NMR studies on vaporized molecules adsorbed on solid material. This subject has been reviewed previously in this series.¹

There are three types of NMR studies on interfacial phenomena: (1)

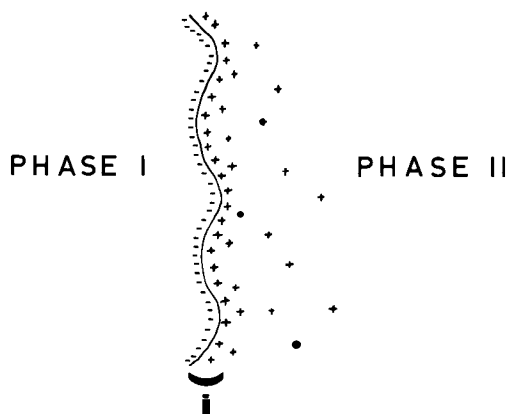


Fig. 1. Schematic representation of the interfacial region (i).

solvent or solute molecules in phase II can be observed, (2) the behaviour of ions in this phase can be studied in a similar way, and (3) nuclei of groups of phase I in contact with the solution can be observed.

Due to the ubiquitous nature of interfacial phenomena, results in this area can be found in NMR reviews devoted to many different topics such as micelles,² membrane processes,^{3,4} biological systems,^{5,6} polymers,^{7,8} clays,⁹ and liquid crystals.¹⁰

As far as neutral species in phase II are concerned, they are often more populated in the bulk liquid than in the interfacial domain. In contrast, the population of counterions near the charged surface remains important, according to mathematical theories.^{11,12} Usually, a fast exchange of these ions or molecules occurs between different environments. Therefore, the value of the observed NMR parameter is population weighted averaged. In the simplest case, NMR results are analysed in terms of a two-site exchange model, let us say, between the bulk liquid and the interface. Although such a simple model has been successfully used in the literature, other situations have also been considered to reproduce experimental data.

The most popular NMR parameter is the chemical shift; however, its isotropic value is usually not very informative in studies of concern here. Thus, this review reports mainly information deduced from line splitting, chemical shielding anisotropy, relaxation rates or self-diffusion coefficient measurements. The theory of these NMR parameters is summarized in the next section. Line splitting (Section 2.1) and chemical shielding anisotropy (Section 2.2) reveal the existence of an anisotropic medium, at least in the interfacial region. Liquid crystalline phases are the best-known examples of this behaviour but quadrupolar splittings also occur in swelling clay

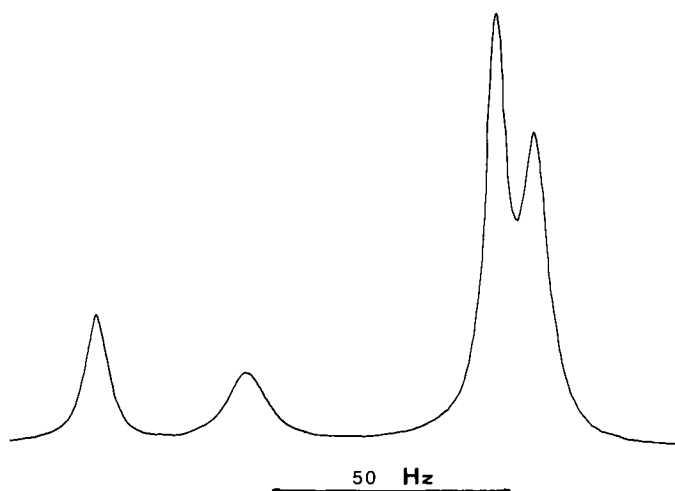


Fig. 2. ^2H NMR spectrum of a bentonite suspension in a water-methanol- d_4 mixture (87.5/12.5; V/V) at 299 K (clay content: 27 mg/ml).

suspensions.¹³⁻¹⁵ This is shown in the deuterium spectrum of a bentonite suspension in water-methanol- d_4 binary solvent (Fig. 2). Both OD (natural abundance) and CD_3 signals exhibit a quadrupolar splitting. The origin of the differential line-broadening is discussed in Section 2.3.

With quadrupolar nuclei, relaxation theory for an isotropic medium differs from that for an anisotropic solution (i.e. when a residual quadrupole splitting is observed). In the latter case, the situation is particularly complicated for nuclei with spin > 1 , where two-dimensional experiments are required for a full explanation of relaxation data. The general NMR method to determine the self-diffusion coefficient uses pulsed field gradients.¹⁶ In particular conditions, translational motion of species can be characterized otherwise, as discussed in Section 3. The theory of NMR parameters of interest here is developed in Section 2 for neutral species and counterions in phase II and for mobile groups at the surface of phase I. Because of the paramount importance of water, most studies are concerned with this molecule. The first NMR measurements recorded proton signals; however, this technique is not as informative as could be anticipated. Indeed, data analysis of proton relaxation rates is not straightforward, even with recourse to field cycling spectrometers.¹⁷ There has been renewed interest in proton NMR relaxation measurements with the development of magnetic imaging spectroscopy, however. But this subject remains highly controversial and more precise information comes from water quadrupolar nuclei. As this

review is not concerned with medical applications, the state of water is described in polyelectrolyte, surfactant, clay suspensions but not in tissues, cells or organs. Other interfacial molecules, including polymers and surfactants have been also studied by NMR and a few examples are given in Section 3.1.

When charges are present in phase I, counterions, mostly quadrupolar (^7Li , ^{23}Na , ^{35}Cl , etc.) compensate for them in phase II. Extensive results have been published for systems such as polyelectrolytes and anisotropic phases. A brief account on these studies is given in Section 3.2. Solid state NMR of cation nuclei provides further interesting results as exemplified in the same section.

In aggregates formed by amphiphile compounds, polar or charged groups are directed toward the polar medium, usually an aqueous phase. Due to the importance of phospholipids in biochemistry, associated with different NMR-sensitive nuclei, numerous studies of their polar head groups have been reported. Other interesting applications on grafted polymers or on chemically modified silica are also discussed in Section 3.3. A summary of the state of the art, together with probable trends for the future are briefly described in the last section. Finally, it should be kept in mind that, rather than providing an exhaustive account of the literature results, the main purpose of this review is to give a general insight into the different NMR approaches used in the study of interfacial phenomena.

2. THEORY

At the interface, the behaviour of molecules and ions in solution is affected by the presence of macromolecules or other macrospecies (micelles, membrane, liquid crystal, solid). Compared with their NMR parameters in bulk liquid phase, this results in an increase in the relaxation rate, a decrease in the self-diffusion coefficient and sometimes the observation of a line splitting (Fig. 2). Most NMR studies on interfacial molecules concern water. Therefore, the theory is exemplified for water nuclei but its extension to other molecules is also discussed.

Quadrupolar interaction often governs the relaxation processes of counterions. Indeed, most of them have a nucleus with half-integer spin larger than 1. The relevant NMR theories are reported hereafter both for isotropic and anisotropic media.

Exchange of molecules or counterions between different environments affects their quadrupolar (dipolar) splitting, their relaxation rates or their self-diffusion coefficient. Usually, a two-site exchange model reproduces the experimental results but other models are considered too.

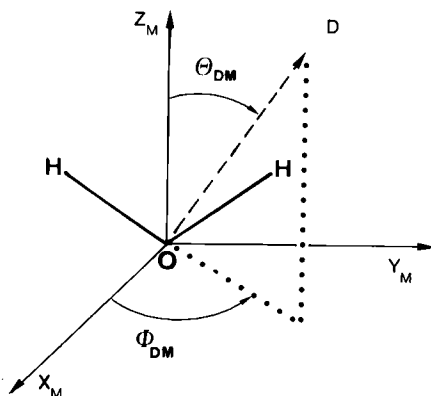


Fig. 3. Reference axes of water molecule.

Nuclei of superficial groups of the phase I component are influenced by the presence of the liquid phase. The determination of their relaxation times, the observation of line splitting or chemical shielding anisotropy provide data to characterize the structure and dynamics of these groups. A theoretical insight is also given for this, but since detailed accounts of these theories exist in the literature, only working equations are given here.

2.1. Line splitting

2.1.1. Interfacial molecules

(1) *Water molecule.* In homogeneous liquid phase, the water molecule has no preferential orientation and a single line is detected in its proton, deuteron and ^{17}O NMR spectra. In an anisotropic medium, if no processes, characteristic of the quadrupolar or dipolar interactions, are present which are rapid with respect to the coupling constant, then a constrained molecular motion may induce a line splitting. For instance, a rapid exchange of hydrogens between ordered water molecules can make the doublet in the proton spectrum invisible.¹⁸ In an anisotropic phase, water molecules near the surface of the aggregate or of the solid are preferentially oriented. To relate this to the observed splitting, the distribution of the orientational probability of the molecule should be defined. This corresponds to the distribution of Eulerian angles specifying the transformation of a coordinate system associated with the water molecule (denoted M) and another which is fixed to the rigid surface (director, denoted D) (Fig. 3).

A splitting in the proton spectrum comes from the dipolar interaction between the hydrogens of the water molecules. For quadrupolar nuclei, the

interaction of the electric field gradient at the nucleus site with the nuclear quadrupole moment also induces a line splitting in the deuteron and in the ^{17}O NMR spectrum. The principal axes characteristic of these second-rank interactions (denoted F) are not necessarily coincident with the referential of the molecule. The F coordinate system is deduced experimentally or is calculated theoretically. If the above interactions are purely intramolecular, the angles between the M and F coordinate systems are time-independent. Thus, the modulation of these interactions only occurs from the reorientational motion of the water molecule. The static part of the quadrupolar Hamiltonian may be written as:¹⁹

$$\mathbf{H}_Q = \frac{eQ}{2I(2I-1)\hbar} \sum_m (-1)^m \mathbf{A}_{-m} \mathbf{V}_m \quad (1)$$

where the \mathbf{A}_m values are the standard components of the second-rank spin tensor operator and the \mathbf{V}_m values are the irreducible components of the second-rank electric field gradient tensor (m runs from -2 to 2).

The spin operators are more easily expressed in the laboratory frame (noted L), whereas the components of the electric field gradient tensor \mathbf{V}_m are described in the F coordinate system. Therefore, the three axis transformation L-D, D-M and M-F are successively performed by using the second-rank Wigner rotation matrices.²⁰ Since the dipolar tensor has zero asymmetry parameter,^{21,22} the Wigner rotation matrices may be replaced by appropriately normalized spherical harmonics.²⁰ This mathematical treatment is closely related to the use of the ordering matrix.²³

In lamellar systems, the director is perpendicular to the surface of the aggregate or of the solid. It is assumed that the director reorientation is much slower than the water molecular motion. This implies that the first process does not influence the line splitting. For quadrupolar nuclei, the absorption line is split into $2I$ lines, separated by Δ .²⁴

$$\Delta = \frac{3e^2qQ}{4I(2I-1)\hbar} (3\cos^2\theta_{\text{LD}} - 1)A \quad (2)$$

where θ_{LD} is the angle between the z axes of the laboratory (L) and the director (D) coordinate systems and A is the residual (quadrupolar) anisotropy. The above equation postulates at least a C_3 symmetry for the director. An extra geometric term must be taken into account for a lower symmetry.²⁵ A formula similar to (2) can also be obtained for the proton-proton dipolar interaction.²⁴ Based upon the principal axes system reported in Fig. 3, Halle and Wennerström²⁴ have defined the two-order parameters occurring in NMR theory, together with their relation to the elements of the Saupe's traceless tensors \mathbf{S}_{ij} .²⁶ These expressions are:

$$S_0 = \frac{1}{2}\langle (3\cos^2\theta_{\text{DM}} - 1) \rangle = S_{33} \quad (3)$$

$$S_2 = \frac{1}{2}\sqrt{6}\langle \sin^2\theta_{DM} \cos 2\phi_M \rangle = 2(\sqrt{6})^{-1}(S_{11} - S_{22}) \quad (4)$$

where $\langle \rangle$ means the time-average value.

To perform the third principal axes transformation, the knowledge of the coordinate system associated with the (quadrupolar or dipolar) second-rank tensor is required. The z axis of the electric field gradient tensor is practically aligned along the O-D bond for deuterons and is perpendicular to the molecular plane for the ^{17}O nucleus. A short discussion on this can be found in the literature.²⁴ The interproton direction serves as the z axis for the dipolar tensor. Consequently, the Eulerian angles ϕ_M , θ_{MF} and ϕ_F are 90° , α (half of the molecular angle), 90° for deuterons; 0° , 90° , 0° for ^{17}O and 90° , 90° , 0° for protons. Assuming purely intramolecular interactions, the residual anisotropies are:²⁴

$$A(^1\text{H}) = -\frac{1}{2}S_0 - \frac{1}{4}\sqrt{6} S_2 \quad (5)$$

$$A(^2\text{H}) = \frac{1}{2}(3\cos^2\alpha - 1 + \eta\sin^2\alpha)S_0 \\ - (1/2\sqrt{6})[3\sin^2\alpha + \eta(\cos^2\alpha + 1)]S_2 \quad (6)$$

$$A(^{17}\text{O}) = -\frac{1}{2}(1 - \eta)S_0 + (1/2\sqrt{6})(3 + \eta)S_2 \quad (7)$$

where η is the asymmetry parameter defined¹⁹ as

$$\frac{V_{xx} - V_{yy}}{V_{zz}} \quad (8)$$

The components of the electric field gradient tensor are in the order $V_{zz} \geq V_{yy} \geq V_{xx}$. The above equations are valid in planar systems. In the presence of cylindrical aggregates, it has been shown that the splitting is reduced by a factor of 2.¹⁹

(2) *Other molecules.* The above formula, appropriate for a C_{2v} molecule, should be adapted to other molecular geometries. For instance, to obtain the residual quadrupolar anisotropies of acetonitrile- d_3 , one should take into account its higher C_3 symmetry. This reduces to one the number of independent order parameters.^{27,28} The principal axis of the electric field gradient tensor of ^{14}N and ^2H is coincident with the C-N bond and the C-D bond, respectively. Then, the residual anisotropies are:

$$A(^{14}\text{N}) = S_0 \quad (9)$$

$$A(^2\text{H}) = \frac{1}{2}(3\cos^2\alpha - 1 + \eta\sin^2\alpha)S_0 \quad (10)$$

For a uniaxial anisotropic medium, a five-term equation describes the residual anisotropy in the general case.²⁷⁻²⁹

(3) *Chemical exchange.* In the systems invoked here, molecules are usually

distributed among different sites. When the exchange between these environments is fast as compared with the difference in the quadrupolar splitting between these sites, the observed splitting is the population weighted average:

$$\Delta = \sum_i p_i \Delta_i \quad (11)$$

where p_i is the mole fraction in each site.

In the simplest situation, molecules are exchanged between the bulk liquid phase (no splitting) and the interface. If the largest amount of water is in the bulk, this can drastically reduce the observed splitting to a few hertz (Fig. 2). As discussed in Section 3, two sites can also show a sign reversal of the order parameter and the doublet can be zeroed in particular conditions. Therefore, according to the experimental conditions, the value of the line splitting can be found within a broad range. Although most results have been explained with a two-state exchange model, more than two sites can also be required.^{14,15}

2.1.2. Counterions

When the anisotropic mesophase or solid particles are charged, ions are present to preserve the electroneutrality of the medium. These counterion nuclei are usually quadrupolar (²³Na, ³⁵Cl, etc.) and a residual splitting occurs in their NMR spectrum if the ion mobility is not fast enough to average out the quadrupolar interaction. The above theory remains applicable. The quadrupolar splitting is given by (2) where the residual anisotropy is replaced by the order parameter S :²⁵

$$S = \frac{1}{2} \langle (3 \cos^2 \theta_{DM} - 1) \rangle + \eta \langle \sin^2 \theta_{DM} \cos 2 \phi_M \rangle \quad (12)$$

The applicability of this equation is restrained to the first-order effect. A fast chemical exchange between different sites is also described by (11), but the counterion concentration at the interface is expected to be larger.^{11,12} It should also be pointed out that the electric field gradient is of intermolecular origin. As a consequence of this, the quadrupole coupling constant strongly depends on the experimental conditions. It is known that the electric field gradient at the nucleus site is generated by the ions and dipolar molecules in the nucleus surroundings and electrostatic considerations can rationalize the experimental data.^{30,31} The intermolecular origin of the electrical field gradient precludes the simultaneous determination of both the quadrupolar coupling constant and the order parameter.

2.1.3. Nuclei at the periphery of amphiphilic aggregates

²H and, to a less extent, ¹⁴N nuclei have been used to study the behaviour of

phospholipids and other amphiphilic compounds forming anisotropic phases. As far as interfacial phenomena are concerned, we are chiefly interested in the polar head group of these molecules. In many respects, membrane in the liquid crystalline phase behaves like uniaxial crystals. In both cases, the quadrupolar splitting is expressed by an equation similar to (2).

When the plane of the membrane is aligned with the magnetic induction B_0 , the geometric term vanishes and the quadrupole splitting is given by:

$$\Delta = \frac{3e^2qQ}{4hI(2I - 1)} S \quad (13)$$

If all the orientations of the bilayer are equiprobable, a spectrum of the "powder-type" is detected but the splitting is still described by the above equation (13) with $S = 1$.³² The order parameter S is expressed by (3) where θ is the angle between the bilayer normal (director) and the principal axis of the coordinate system associated to the electric field gradient tensor (z axis is along the C-D or C-N vector). It has been shown that (13) remains valid for a rapid reorientation of the C-D (C-N) vector. Here, the origin of the electric field gradient is intramolecular and the quadrupolar coupling constant can be determined experimentally. If the motion of the C-D (C-N) vector is fast relative to the line separation, the quadrupolar interaction is partially averaged. This results in a decrease of the splitting and sometimes in a change of the lineshape.

Thus, quadrupolar (dipolar) splittings are mainly determined by the average conformation of the polar head group or by the mean orientation of ion or molecule at the interface. Therefore, they provide structural information on this region.

2.2. Chemical shielding anisotropy

Although chemical shielding anisotropy can also reflect the preferential orientation of small molecules within the interface space (see, for instance, Chachaty and Quaegebeur³³), this parameter has been chiefly used to study the orientation and the mobility of the phosphate group of phospholipids. Therefore, the theory is exemplified for the ^{31}P nucleus ($I = \frac{1}{2}$). Unsonicated phospholipid suspensions exhibit a ^{31}P "powder-type" NMR spectrum, resulting from their aggregation into a lamellar or hexagonal phase. The lineshape is caused by the chemical shielding anisotropy of the phosphorus nucleus and by the proton-phosphorus dipolar interaction.

To simplify data analysis, the phosphorus spectrum is recorded under proton decoupling. It is easy to understand intuitively that the chemical

shielding depends on the orientation of the phosphate group of the lipid with respect to the magnetic induction B_0 . Indeed, as an effect of the bonding pattern, the electron density is not isotropically distributed around the nucleus. Thus, the electronic shielding is effective to a different extent along the various molecular directions. In the absence of motion fast enough to average the static chemical shielding tensor, the three principal components σ_{11} , σ_{22} and σ_{33} should be estimated experimentally. These can be obtained from spectra resulting from the rotation of a single crystal of an appropriate compound.³⁴

Phospholipids are not easily crystallized, so the phosphodiester barium diethylphosphate has been used as a model compound. Recently, the ^{31}P chemical shielding tensor of a phospholipid has been determined, however.³⁵ In a liquid crystalline phase, this phosphate group is characterized by a fast rotation around an axis perpendicular to the bilayer surface. As a consequence, the above tensor is axially symmetric around the director axis and two components σ_{\parallel} and σ_{\perp} describe it. For a "powder-type" spectrum, it has been indicated previously, (13), that we have only to transform the second-rank tensor (here, the chemical shielding tensor) from its molecule-fixed coordinate system into the director frame. This can be achieved by the application of rotation matrices or can be expressed in terms of order parameters:^{28,34}

$$\sigma_{\parallel} = \sigma_i + 2[\mathbf{S}_{11}(\sigma_{11} - \sigma_{22}) + \mathbf{S}_{33}(\sigma_{33} - \sigma_{22})]/3 \quad (14)$$

$$\Delta\sigma = \sigma_{\parallel} - \sigma_{\perp} = 3(\sigma_{\parallel} - \sigma_i)/2 \quad (15)$$

where σ_i is the isotropic part of the chemical shielding tensor. The two components σ_{\parallel} and σ_{\perp} can be determined either directly from the spectrum or more usually by computer simulation.³⁴ The above equations apply to the lamellar (bilayer) phase. For a hexagonal phase, $\Delta\sigma$ decreases by 50% together with a sign reversal.

2.3. Relaxation

2.3.1. Interfacial molecules

Although proton magnetic resonance seems to be an adequate probe to investigate heterogeneous systems, the interpretation of water proton relaxation data remains controversial in spite of the use of NMR field cycling spectrometers.^{17,36-38} This arises from the complexity of the proton relaxation pattern which includes intra- and intermolecular effects. Furthermore, the presence of paramagnetic species also influences the relaxation process. If these paramagnetic centres are not well characterized, this renders data analysis more cumbersome yet. On the other hand, the relaxation of

quadrupolar nuclei such as ^2H and ^{17}O is purely intramolecular when these atoms are covalently bound. Since ^{17}O relaxation is not affected by deuteron exchange, in contrast with ^2H relaxation,^{39,40} it offers a means of monitoring directly the motional restraint of water molecules within the interfacial region.

The fluctuating part of the Hamiltonian which is responsible for relaxation processes may be expressed in the operator formalism:⁴²

$$\mathbf{H}(t) = \sum_m (-1)^m \mathbf{F}_m(t) \mathbf{A}_m \quad (16)$$

where the \mathbf{F}_m values are random functions of time and the \mathbf{A}_m values are operators acting on the variable. For quadrupolar relaxation, for example, the \mathbf{A}_m values are the second-rank spin tensor operator and the \mathbf{F}_m values have the same meaning as the \mathbf{V}_m values in (1). The \mathbf{F}_m values describe the reorientation of the spin, and consequently the quadrupole moment, with respect to the electric field gradient. The Fourier transform of the appropriate correlation function of $\mathbf{F}_m(t)$ gives the spectral densities.⁴² In the simplest reorientational model, this correlation function is monoexponential and therefore characterized by one single correlation time. As previously, the second-rank Wigner rotation matrix may be used for the principal axes transformation $\mathbf{F} \rightarrow \mathbf{L}$. The longitudinal R_1 and transverse R_2 relaxation rates for a $I = 1$ nucleus are given by the following equations:⁴²

$$R_1 = 3K[J(\omega_0) + 4J(2\omega_0)] \quad (17)$$

$$R_2 = 1.5K[3J(0) + 5J(\omega_0) + 2J(2\omega_0)] \quad (18)$$

with

$$K = \frac{\pi^2(e^2qQ)^2}{20h^2} (1 + \eta^2/3) \quad (19)$$

and the spectral density has the following form:

$$J(m\omega_0) = \frac{\tau_c}{1 + (m\omega_0)^2 \tau_c^2} \quad (20)$$

In the non-extreme narrowing condition ($\omega_0 \tau_c \geq 1$) and for nuclei with $I > 1$, the relaxation process is no longer governed by a monoexponential law.⁴³ This multiexponential behaviour allows multiquantum coherences to be detected.^{44,45} A few applications have used this possibility as indicated later (Section 3). For half-integer spin, the sum of the decaying exponentials is $I + \frac{1}{2}$. Analytical expressions for longitudinal and transverse relaxation rates of a $\frac{3}{2}$ -spin nucleus have been reported several years ago^{43,46} and they are expressed as a sum of a slow and a fast component:

$$R_1^{\text{tot}} = 4K[0.2J(\omega_0) + 0.8J(2\omega_0)] \quad (21)$$

$$R_2^{\text{tot}} = 2K[0.6J(0) + J(\omega_0) + 0.4J(2\omega_0)] \quad (22)$$

The relaxation behaviour of $\frac{5}{2}$ - and $\frac{7}{2}$ -spin nuclei has also been described.^{47,48}

Until now, we have implicitly assumed an isotropic medium. That means the residual quadrupolar (or dipolar for $\frac{1}{2}$ -spin) interaction is averaged out by the fluctuation of the angle θ_{LD} (see (2)). It follows that one single line is observed for each quadrupolar nucleus.

In anisotropic systems, the $2I$ transitions between Zeeman levels perturbed by the quadrupolar interaction are non-degenerate and a line splitting is detected in the spectrum. The relaxation rates differ from the result for the isotropic medium and vary with the spin number of the quadrupolar nucleus (or with coupled $\frac{1}{2}$ -spins). In the absence of cross-relaxation, the equations for a $I = 1$ nucleus have been obtained:^{49,50}

$$R_1 = 3K[J_1(\omega_0) + 4J_2(2\omega_0)] \quad (23)$$

$$R_2 = 1.5K[3J_0(0) + 3J_1(\omega_0) + 2J_2(2\omega_0)] \quad (24)$$

For nuclei with higher half-integer spin, $I + \frac{1}{2}$ equations define the longitudinal or transverse relaxation processes. Appropriate equations for the transverse relaxation rate of a $\frac{3}{2}$ -spin⁴⁵ or of a $\frac{5}{2}$ -spin²⁴ nucleus have been reported. Information on dynamics is contained in the spectral densities J . The complexity of these systems prevents any precise analysis from the relaxation times determination alone. Therefore, different NMR techniques to estimate the different spectral densities have been published for $I = 1$.⁵⁰⁻⁵³ Vold's work⁵⁰ for a spin-1 has been extended recently for a spin- $\frac{3}{2}$.⁵⁴ The response to the two-dimensional quadrupolar echo sequence⁵⁵ and to the inversion recovery experiment⁵⁶ have been developed for a $\frac{5}{2}$ -spin nucleus.

Influence of chemical exchange. In aqueous heterogeneous medium, water molecules are exchanged between different environments and relaxation, like the line splitting, is generally analysed in terms of a discrete exchange model. When the residence time of a molecule within a phase (bulk liquid or interfacial region) is longer than the reorientational timescale and shorter than the macroscopic relaxation time, an equation similar to (11) is valid for an exchange between two sites A and B:

$$R_{1,2} = (1 - p_B)R_{1,2}^A + p_B R_{1,2}^B \quad (25)$$

With large excess of water, this equation postulates a linear dependence of the observed relaxation rate on the concentration of the macrospecies (polyelectrolyte, protein, etc.), as indeed is usually found.

In heterogeneous systems, the proton, deuteron or ^{17}O NMR spectrum of water often shows one single line. Therefore, the residual interaction, dipolar

or quadrupolar, has been averaged out (see Section 2.1). The system is named isotropic in the sense described above. The extreme narrowing condition ($\omega_0\tau_c \ll 1$) is usually fulfilled with small molecules. Consequently, the spectral densities $J(m\omega)$ become field-independent (see (17) and (18)). This facilitates data analysis and the relaxation rate is governed by a mono-exponential law. In these isotropic media, molecular reorientation can be anisotropic. The motion is then described by more than one correlation time. Appropriate expressions for different molecular symmetries can be found in the literature.^{57,58} The relaxation behaviour of water nuclei has been explicitly described more recently.⁵⁹ Because the principal directions of the interaction tensors of ^{17}O and ^2H do not coincide (Fig. 3), the symmetry of water motion may be investigated.⁵⁹ As pointed out previously, information on molecular rotation is available when the dominant relaxation mechanism is purely intramolecular (^{17}O for water) and then, a difference between the transverse and the longitudinal relaxation rates implies that the extreme narrowing condition is no longer appropriate (see (17) and (18)).

To explain this observation in aqueous suspensions, a model based upon the coexistence of a fast and a slow motion of interfacial water molecules has been assumed.^{40,60} At the high fields generally used, the longitudinal relaxation time is not affected by the slow motion.⁴⁰

As noted above, a more or less complicated correlation function is assumed to explain the relaxation data. A monoexponential function represents the simplest case. To eliminate any assumption about it, relaxation time measurement must be done at four different magnetic inductions B_0 .⁶¹ The relaxation rate of quadrupolar nuclei is usually dominated by the quadrupolar interaction, therefore it allows a straightforward analysis of the data. Nevertheless, dipolar interaction can also provide interesting information but it may demand isotopically enriched compounds^{59,62} for poorly abundant nuclei such as ^{17}O .

A peculiar feature is found in the deuterium NMR spectrum of a bentonite clay suspension (Fig. 2) where a differential line-broadening is observed for the two components of the OD and the CD_3 doublets. This arises from the correlated reorientation of tensors associated with two different interactions. The involvement of dipolar interaction in these so-called cross-correlation terms has been described in the literature several years ago.^{63,64} Thus, cross terms between chemical shielding anisotropy and dipolar interaction have been displayed several times. These interference terms carry unique dynamical and/or structural information.^{65,66} As far as I know, such cross-correlation effects have only been displayed recently for interfacial species.¹³⁻¹⁵ Indeed, the deuteron spectrum of water at a clay interface exhibits a doublet with a differential broadening of the two components.^{13,14} The origin of this observation in bentonite suspensions has been asserted

both experimentally¹⁵ and theoretically:⁶⁷ the rather high iron(III) content of the clay induces a coupling between quadrupolar and paramagnetic relaxations.^{15,67}

2.3.2. Counterions

As noted in Section 2.1, when a quadrupolar nucleus is an ionic species, the electric field gradient fluctuates with the motion of the molecules in the solvation sphere. This prevents any experimental determination of this parameter and a dynamical model should be assumed for this purpose. A fast-exchange two-site model has been proposed in the literature for a $\frac{3}{2}$ -spin nucleus.⁴⁶ When the relaxation rates R_1 and R_2 and the exchange rate at one site are much larger than that at the other site, the relaxation is biexponential. This multiexponential behaviour also occurs with higher half-integer spin nuclei and tends to be more pronounced for transverse relaxation than for longitudinal relaxation.^{47,48,68} Multiple-quantum NMR spectroscopy can be useful to detect this non-exponential relaxation,⁴⁴ but it requires a high content in the observed species. Here, the two sites are assumed to be isotropic: the residual quadrupolar splitting is completely averaged out. Such a model for a spin- $\frac{3}{2}$ nucleus cannot be easily differentiated by lineshape analysis from a model which assumes an anisotropic site.⁶⁹

A model taking into account a fast exchange between three states, two isotropic and one anisotropic sites has been proposed in the literature.^{70,71} Redfield's equations based upon a second-order perturbation theory have been used in the above models. This approach is not valid when the exchange time is shorter than the rotational correlation time. Therefore, to investigate the whole range of exchange time, numerical solution of the Liouville equation have been reported recently.⁷²⁻⁷⁴ Comparison between these two theoretical treatments reveals some significant differences for the transverse relaxation process.⁷³

In all the above exchange models, an uncorrelated random walk between discrete states is assumed. Experimental data can be fitted with these discrete exchange models. Nevertheless, a continuous diffusion model has been proposed in the literature⁷⁵ but it has not been applied yet to experimental data.

Heterogeneous systems cover quite different situations. Thus all the above theories assume that the motion of small molecules (exemplified by water molecules) or ions is unrestricted, i.e. it can occur in the three-dimensional space. Sometimes, constraint forces species to move in a two-dimensional space. The relaxation behaviour is affected by this reduction in the dimensionality of the reorientational molecular motion, as has been nicely shown

experimentally.⁷⁶ Relaxation theory under these conditions has been adapted for dipolar interaction.⁷⁷⁻⁷⁹

2.3.3. Nuclei of superficial groups of phase I components

NMR relaxation can describe the dynamics of mobile components of phase I. For instance, the mobility of phospholipid head groups at the membrane-water interface or the dynamics of attached organic groups to a chemically modified solid can be characterized. Dipolar (^1H , ^{13}C , ^{31}P , etc.) and quadrupolar (^2H , ^{14}N) nuclei are adequate probes to achieve this goal.

For ^2H and ^{14}N (both spin-1 nuclei), quadrupolar relaxation is dominant. In biological membranes as well as in liquid crystals, the static or ensemble averaged Hamiltonian is not completely cancelled. Thus, each signal is observed as a doublet. The longitudinal relaxation rate is expressed, as before, by (17).⁸⁰

By analogy with liquid crystals,⁸¹⁻⁸³ it has been suggested that ^2H (^{14}N) relaxation rate in the liquid crystalline phase of saturated lipid bilayers can be written as a sum of a fast (R_{lf}) and a slow (R_{ls}) component:

$$R_1 = R_{\text{lf}} + R_{\text{ls}} \quad (26)$$

The first term represents the contribution of relatively fast motions, including chain rotational isomerization or torsional oscillation. Slow motions are associated with reorientation coupled to lateral diffusion and with collective motion involving the bilayer as a whole. Autocorrelation functions based upon different models have been obtained both for fast and slow motions.⁸⁰ An explicit form for the longitudinal relaxation rate of the i th segment has been derived:⁸⁴

$$R_1 = A\tau_{\text{f}}(i) + B(i)f(\omega_0)|S^2(i)| \quad (27)$$

where A and $B(i)$ are constant and $\tau_{\text{f}}(i)$ is an effective correlation time for fast motions of the i th segment, $f(\omega_0)$ describes the dependence of the Larmor frequency on the relaxation rate. The form of $f(\omega_0)$ changes with the assumed reorientational model for the slow motion. The bond segmental order parameter S is related to the line splitting (see (13)).

Dipolar interaction with protons provides an important mechanism for ^{13}C or ^{31}P nuclear relaxation. At low magnetic field, this contribution can be predominant for short C-H or P-H distances. Assuming isotropic reorientation, characterized by one correlation time τ_{c} , the dipolar relaxation rate R_1^{d} is given by the following equation:⁸⁵

$$R_1^{\text{d}} = F[J(\omega_{\text{H}} - \omega_i) + 3J(\omega_i) + 6J(\omega_{\text{H}} + \omega_i)] \quad (28)$$

with

$$F = h^2 \gamma_H^2 \gamma_i^2 \sum_j r_j^{-6} \quad (29)$$

where i stands for a ^{13}C or ^{31}P nucleus and h , γ and r are respectively the Planck constant, the gyromagnetic ratio and the H-C(P) distance. The spectral densities J are defined as before (see (20)).

Appropriate theory based upon models similar to those for ^2H and ^{14}N nuclei has been also derived for the ^{13}C relaxation rate and heteronuclear Overhauser enhancement.⁸⁶ The above empirical expression (28) remains applicable too. Although this theory has been chiefly used for the hydrocarbon chain in membranes and in liquid crystals, it can also be applied for mobile constituents at the surface of phase I.

At high magnetic fields ($\geq 7\text{ T}$), chemical shielding anisotropy interaction provides the dominant relaxation mechanism of the ^{31}P nucleus present in polar head groups of phospholipids. Appropriate theory to analyse these relaxation data has been reported recently.^{87,88}

Multilamellar dispersion of phospholipids exhibits the so-called powder pattern spectrum (Section 2.1). Although an angular dependence on the relaxation time may occur, this has not been displayed with these heterogeneous systems. Indeed, the lipid molecule samples all orientations with respect to the magnetic induction over the time T_1 by diffusion around the curved surface of the liposome. This averages orientational effects on ^{31}P ⁸⁹ and deuteron⁹⁰ relaxation rates. Relaxation measurements on aligned samples have revealed this orientational dependence both in ^2H ⁹⁰ and ^{31}P ⁹¹ NMR and this allows better definition of the dynamics of these groups. As the relaxation mechanism is intramolecular in nature, interaction of such mobile groups with interfacial species is reflected by changes in their relaxation parameters. Such an interaction can be directly monitored if a dominant intermolecular dipolar interaction contributes to the relaxation. In a lamellar phase formed with pyridinium octylhydrogenphosphate in water, the ^{31}P relaxation data have been analysed on the basis of the data obtained from the diffusion of the organic counterion.⁹² This model assumes the polar head group of the surfactant diffuses on an infinite plane whereas ions or molecules move within an infinite layer of finite thickness.⁹²

2.4. Self diffusion

In an isotropic homogeneous system, the self-diffusion parameter D characterizes the radial distribution function of molecules with regard to their original position. Although the average displacement in all three directions is zero, the mean-square displacement is given by the Einstein relation-

ship:

$$\langle r^2 \rangle = 6Dt \quad (30)$$

The most popular NMR method to determine D is the pulsed field gradient spin-echo experiment.⁹³ The relationship between the attenuation A at the echo time 2τ and the duration δ of the pulsed field gradient G is:

$$A(2\tau) = A(0) \exp[-(2\tau/T_2) - (\gamma\delta G)^2 D(\Delta - \delta/3)] \quad (31)$$

where Δ represents the pulsed field gradient interval, γ the gyromagnetic ratio of the observed nucleus and T_2 the transverse relaxation time. When the observed species is fast exchanged between two or more sites, the measured parameter is population weighted-averaged (see (25)).

Other techniques have also been used to circumvent the limitations of this basic experiment. For instance, a short relaxation time T_2 drastically reduces the investigated time domain. These technical aspects are discussed in two recent reviews to which interested readers can refer.^{16,94}

Obviously, the diffusion can be more complex in heterogeneous media. Restricted diffusion or anisotropic diffusion are possible for such systems. This matter is also discussed in the reviews mentioned above,^{16,94} and hereafter I mention only a few more recent adaptations. With regard to technical improvements, most articles concern modifications in different steps of known sequences.⁹⁵⁻⁹⁸ A different approach to measuring the self-diffusion coefficient has been proposed recently.⁹⁹ This employs a radio-frequency field gradient instead of a pulsed field gradient. Until now, the quality of the data obtained has been no better than those from previous methods. With regard to data analysis, restricted diffusion,¹⁰⁰ self diffusion in regions confined by adsorbing walls¹⁰¹ or the relation between the self-diffusion coefficient and the fractal dimension¹⁰² have been considered, for instance.

Both intra- and intermolecular interactions influence the dipolar relaxation rates R_1 and R_2 . This complicates the analysis of the data as already pointed out for proton relaxation. If the intermolecular interaction is dominant or can be estimated quantitatively, modulation of this dipolar interaction allows the determination of the diffusion coefficient of the mobile species. Such an example has been reported at the end of the previous subsection where ^{31}P relaxation data are related to the diffusion of the organic counterion.⁹² In the presence of paramagnetic species, the electron-nucleus dipolar interaction gives the dominant relaxation mechanism. Thus, a paramagnetic probe, fixed or tightly bound to the phase I component, can be used to determine the diffusion coefficient of interfacial species. Such studies are reported in Section 3.

3. RESULTS

3.1. Interfacial molecules

In this subsection it is shown how quadrupolar splitting reveals any change of molecular orientation in mesophases and in clay suspensions. Relaxation rates have been used to describe the state of water in different heterogeneous systems. These measurements can be used for any other molecules. This is illustrated for different molecules including polymers. A discussion on diffusion data where the echo attenuation (see (31)) follows an exponential law or not ends this subsection.

3.1.1. Line splitting studies

Numerous studies on the behaviour of water at an interface have been reported in the literature. The earliest investigations indicating a splitting of water nuclei signals were made on humid powders or on macroscopically oriented samples. We are not concerned with these results, which have been summarized previously.^{103,104} Our interest is focused on samples oriented in the presence of a strong magnetic field. For these aligned samples if the change in molecular orientation is slow enough, a splitting Δ of NMR lines is observed as a result of a residual quadrupolar (dipolar) interaction (Section 2.1). In most studies on these heterogeneous systems, $^{17}\text{O}/^2\text{H}$ and $^{17}\text{O}/^1\text{H}$ splitting ratios have been found to be nearly constant.²⁴ The insensitivity of the order parameters ratio with water orientation (see (2)–(7)) explain this. The splitting ratios are only sensitive to the shape of the orientational distribution in a narrow range of order parameters ratio.²⁴ Therefore, to describe a binding model for interfacial water molecules other data must be available.^{33,105} More recently, $^{17}\text{O}/^2\text{H}$ splitting ratios different from the usual values have been reported for appropriate water–alcohol–cationic surfactant mixtures.^{106,107} For these systems, the average orientation of water molecules with respect to the director of the mesophase (Fig. 3) can be obtained. The most plausible model indicates an interaction between the lone-pair of water oxygen and the positively charged head group.¹⁰⁶ This agrees with the conclusions deduced from relaxation data on water nuclei.^{33,105} In the presence of both a cationic and an anionic surfactant, water molecules are exchanged between these two sites which share opposite anisotropies.¹⁰⁷

In binary surfactant/water systems, studies on the change of Δ (^2H) with the water content have been reported for non-ionic,¹⁰⁸ anionic¹⁰⁹ and cationic¹¹⁰ surfactants. With a large excess of water, a linear dependence of the splitting with the concentration of the surfactant is observed, as anticipated (see (11)) (p_B varies linearly). At higher surfactant contents, the

Δ value passes through a maximum or levels off.¹⁰⁸⁻¹¹⁰ A simple model based upon the formation of a water-surfactant complex explains these observations.¹⁰⁸ The average number of bound water molecules per head group can be easily estimated after re-arrangement of (11) in terms of mole fractions of amphiphile and water. The water deuteron quadrupolar splitting is also influenced by phase transition but it is not expected to be a good probe to assert the structure of a mesophase.^{106,110}

Beside liquid crystals, clay suspensions can also be aligned in a magnetic field.¹⁵ The investigated clays are aluminosilicates of the 2/1 phyllosilicate family and are formed by platelets containing one octahedral layer sandwiched between two tetrahedral sheets. The replacement of cations in the tetrahedral or in the octahedral layer by cations with a lower charge induces the formation of negative charges in clay platelets. To preserve electroneutrality, exchangeable counterions (Na^+ , Li^+ , Ca^{2+} , etc.) are present between the platelets. In the presence of water, these aluminosilicates swell. The ^2H and ^{17}O NMR spectra of clay suspensions in heavy water display quadrupolar splittings.^{13,14} In these systems, line-broadening precludes the observation of Δ in a broad range of clay content. A linear relationship between water deuteron splitting and the amount of clay is observed, however.¹³ Also, the expected quintet in ^{17}O NMR spectra is usually not fully resolved.¹⁴ Indeed, the outer peaks are extensively broadened by the non-uniform water orientation.³³

In aqueous suspensions of a bentonite (montmorillonite), the nature and composition of exchangeable cations influence the amplitude and even the sign of the quadrupolar splitting Δ .^{14,111} If the line separation of the water deuteron doublet depends on the exchangeable monovalent cation,¹¹¹ the most important effect, i.e. a sign change of the splitting, has been observed in the joint presence of Ca^{2+} and Na^+ counterions. A direct evidence of this sign reversal comes from the different broadening of the two components of the doublet. At low $\text{Ca}^{2+}/\text{Na}^+$ ratios of exchangeable cations, the broader component is highfield, at larger ratios it is downfield^{14,15} (Fig. 4).

This observation can be explained in terms of at least two water sites at the clay interface:^{14,15} an anionic site where water molecules interact with the clay surface and a cationic site where the water-cation interaction occurs through a lone-pair on the water oxygen. This latter site is favoured by an increase in the calcium content.¹⁵ With bentonite suspensions in aqueous binary mixtures, quadrupolar splittings are displayed for deuterons of both water and organic cosolvent molecules (Fig. 2).¹⁵ Here again, the sign of Δ of both constituents is influenced by the $\text{Ca}^{2+}/\text{Na}^+$ ratio of exchangeable cations. This can also be rationalized by assuming a fast exchange between two interfacial sites of opposite anisotropies.¹⁵

Deuteron and ^{17}O quadrupolar splittings have also been observed in the

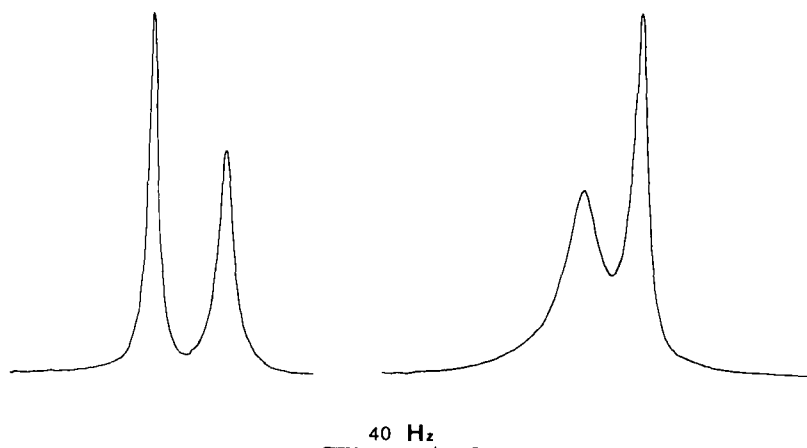


Fig. 4. Typical ^2H NMR spectra of cation-exchanged bentonites in heavy water at 299 K (clay content: 23.8 mg/ml). Ratio of exchangeable cations: $\text{Ca}^{2+}/\text{Na}^+ = 0.02$ (left); $\text{Ca}^{2+}/\text{Na}^+ = 0.13$ (right).

NMR spectra of aqueous suspensions of hectorites or saponites, two other swelling clays.¹¹² It should be pointed out that such a splitting is not expected for quite small clay platelets or spherical solid particles (silica, for instance⁴⁰). There, the residual anisotropy is averaged out (see (2)). Similarly, for aqueous solutions of small spherical aggregates such as micelles, the water deuteron spectrum shows no splitting. Then, information on the molecular reorientation is obtained from relaxation rate measurements.

3.1.2. Relaxation studies

In most NMR studies on aqueous heterogeneous systems, longitudinal and transverse relaxation rates of water deuterons or of ^{17}O are equal (extreme narrowing condition). The most detailed analysis of water relaxation data has been realized for polyelectrolyte solutions. Taking into account ^2H and ^{17}O quadrupolar relaxation, together with ^{17}O – ^1H dipolar relaxation, the water reorientational correlation time has been calculated assuming a fast exchange of water between the bulk phase and the polyelectrolyte interface. Studies with poly(ethylene oxide)¹¹³ and with polyacrylates and polystyrenesulfonates¹¹⁴ have shown a small anisotropy in water reorientation. The reduction in water motion is rather weak as compared with pure liquid. Thus, even for the two polyelectrolytes where cation condensation is present, the mobility of interfacial water which is counterion-dependent is weakly affected.¹¹⁴ A small anisotropy in water orientation has also been observed in microemulsion droplets.¹¹⁵

Linear relationships between the longitudinal relaxation rate and the amount of clay^{13,116,117} or surfactants¹¹⁸⁻¹²⁰ have been reported. This behaviour does not seem to be affected by phase transition.¹¹⁸ All these data agree with the previous conclusion, i.e. perturbation of interfacial water in these heterogeneous systems is weak (mobility decreases by a factor between 2 and 10) and of short range (one water layer or two).

A few NMR studies have reported different longitudinal and transverse relaxation times for water quadrupolar nuclei. A model assuming a slow and a fast molecular motion²⁴ for interfacial water has been used to analyse the results obtained in silica and protein solutions.^{40,41,60} Water dynamics has also been investigated in micellar systems² and the hydration number of polar head groups has been estimated. Obviously, water mobility can be influenced by the presence of compounds interacting with superficial groups of these aggregates. This can be exemplified with anaesthetics.¹²¹

Proton relaxation has been extensively used to describe the state of water in heterogeneous systems such as silica suspensions,¹²² biological media^{36,37,123,124} or polymers.¹²⁵ Particular interest in this research field is related to magnetic resonance imaging and reviews have been published on this subject.^{17,38} However, even recourse to NMR field cycling spectroscopy does not permit a complete understanding of the structure and dynamics at the interface.^{17,36-38} Data analysis is complicated by the many different contributions to the relaxation process: proton-proton exchange, inter- and intramolecular dipolar interactions, spin diffusion.

On a more applied level, water proton longitudinal relaxation times have been used to analyse the pore structure of porous solids^{126,127} and of membranes.¹²⁸ A fast exchange of water molecules between the bulk phase and the interfacial region forms the basis of this analysis (see (25)). The population in each site is related to the volume and surface of the pore, together with the number of water layers perturbed by the surface.¹²⁶⁻¹²⁸

The paramount importance of water as a solvent explains why most papers are concerned with it. However, similar studies can be performed for any other appropriate solvent or solute molecule. For instance, investigations on cetyltrimethylammonium bromide micelles in formamide indicate a slowing down of formamide motion at the interface by about a factor of 4.¹²⁰ The molecular reorientation in this state is also slightly anisotropic.¹²⁰

Adsorption of polymers from solution at a solid/liquid interface has also been studied, as reviewed previously.⁷ NMR studies can provide an estimation on the amount of adsorbed polymer, taking into account the mobility difference between adsorbed and solvated segments of the macromolecule.⁷ A more recent investigation on the adsorption of non-ionic polyacrylamide on a clay is in agreement with the above conclusions.¹²⁹ A broader ¹³C peak for the carbonyl group, indicating lower mobility, is observed for the adsorbed

polymer. In this state, the conformation of the macromolecule is rather flat as compared with that in bulk solution.¹²⁹

Copolymers adsorbed onto silica particles have also been investigated by ²H NMR of specifically labelled compounds¹³⁰ or by proton NMR.¹³¹ Comparison between relaxation data for the macromolecule in solution and that for the adsorbed copolymer suggests a rather different polymer reorientation in these two states. With copolymers of 2-vinylpyridine and styrene, the conformation in the adsorbed phase is more extended in good solvents.¹³⁰ Segments near the surface are motionally restricted and the mobility increases with the distance from the solid.

Until now, we have only considered the liquid/solid interface. The characterization of a solid/solid interface is more difficult to determine. Obviously, it often requires techniques appropriate to solid compounds, and details on these techniques can be found in the literature.¹³² The interfacial region between amorphous and crystalline polyethylene has been examined by ¹³C NMR spectroscopy. Resolved signals are seen for amorphous, crystalline and interfacial regions.¹³³ ¹³C relaxation time measurement has been used to study the interface in glass-filled polyamide-6 composites. The small volume of the interfacial region requires the use of a ¹³C-enriched compound. Relaxation time measurement of the ¹³C-enriched polysiloxane at the surface of the glass beads indicates the presence of entanglements and interpenetration of the polysiloxane and polyamide networks.¹³⁴ Chemical reaction can also occur between these two polymers.¹³⁴ ¹H NMR affords another approach to the investigation of interfacial material in solid compounds.¹³⁵

3.1.3. Diffusion studies

Self diffusion is a measure of transport due to Brownian motion of molecules in the absence of a concentration gradient. Such determinations for small molecules in gels, polymer matrices or biological materials have been performed. The decrease in the diffusion of solvent molecules compared to the pure solvent results from non-specific kinetic effects associated with the presence of the relatively immobile macrocomponents.^{136,137} In these systems, small molecules diffuse isotropically in the three dimensions and the relationship given in (31) remains applicable. A non-linearity of the logarithmic form of this equation indicates either anisotropy in the diffusion process or a restricted diffusion motion due to the presence of barriers. For a single crystal bilayer stack, this experiment allows the determination of the parallel and perpendicular self-diffusion coefficients when the angle between the bilayer and the external magnetic field equals 0 and 90°, respectively.¹³⁸ In the few recent studies on these systems, water diffusion perpendicular to the bilayer plane is slower by a factor of about 20 than the diffusion parallel to

the bilayer surface.¹³⁷⁻¹³⁹ The echo attenuation has also been derived for polycrystalline samples.¹³⁸ By varying the observation time interval Δ (see (31)), water displacement into different domains of randomly oriented lamellae has been described.¹⁴⁰

Diffusion of fluid in porous alumina has also been performed recently.¹⁴¹ Although restricted diffusion may be differentiated from an anisotropic diffusion,¹⁴² no clearcut interpretation of the results can be deduced.¹⁴¹ Obviously, if the number of molecules affected by the surface is small, it reduces the amplitude of the decrease in the self-diffusion coefficient. Under the fast chemical exchange condition, a weighted-average value is observed (Section 2.4). Nevertheless, information on the heterogeneity of the investigated system or on the hydration of superficial groups of the aggregate is still accessible.¹²⁰

3.2. Ions at an interface

Studies on organic ions use the same NMR probes as those reported in the previous section. Therefore, these works are illustrated by just a few examples here. The location of the inorganic (organic) ion is deduced from changes in quadrupolar splitting as indicated hereafter. Ion relaxation data are discussed for a homogeneous isotropic medium (polyelectrolytes), for an inhomogeneous isotropic medium (silica or clay suspensions) and for an anisotropic medium (liquid crystals). Results on ionic diffusion, using the pulsed field gradient technique or based upon modulation of the intermolecular dipolar interaction are given for isotropic solutions.

3.2.1. Line splitting studies

Most nuclei of inorganic ions are quadrupolar. Because of the high symmetry of their solvated form, a small electric field gradient at the nucleus position is expected. As a consequence, the NMR spectrum of ions often exhibits no quadrupolar splitting. Indeed, one single line is observed for counterions in polyelectrolytes (at low concentration),⁸ in silica suspensions,¹⁴³ in micellar systems² or in clay gels.¹³ However, when the ion is close to a charge surface, a non-zero electric field gradient may arise either from an asymmetric solvation or possibly from a partial desolvation. Because ion binding in mesophase roughly follows the ion-condensation model,¹¹ we expect no dependence of the quadrupolar splitting Δ on the composition when sufficient water is present to fully hydrate the ions. This is observed for sodium alkylsulphates.¹⁴⁴ In contrast with this

behaviour, an increase of the sodium carboxylate concentration induces a decrease in the value of Δ (^{23}Na) to about zero. At higher concentrations the splitting increases again. This can be rationalized by a change in $\langle\theta_{\text{DM}}\rangle$ from values larger to values smaller than that cancelling the geometric term in (12) with η equal to zero.¹⁴⁵

^{23}Na quadrupolar splittings have also been displayed in the highest concentration range of DNA solutions.¹⁴⁶ From its variation with temperature and concentration it has been concluded that the angle θ_{DM} between the DNA helix axis and the principal component of the electrostatic field gradient tensor is about the "magic angle" of 54.7° , which cancels the geometric term in (12) with η equal to zero.

With cationic surfactants, the ^{35}Cl quadrupolar splitting resembles the behaviour of sodium carboxylates in decreasing with composition but differs with the temperature variation.¹¹⁰ No clearcut conclusion can be reached from these observations. The effect of electrolytes on ^{23}Na quadrupolar splitting of zwitterionic surfactant has also been investigated. The variation is strongly dependent on the nature of the anion.¹⁴⁷

In ternary systems a more complicated situation may emerge. This is exemplified with monoglyceride–bile salt–water mixtures. Two binding sites for Na^+ ions characterized by quadrupolar splitting of opposite signs have to be postulated to explain the observations.¹⁴⁸ Quadrupolar splitting can also monitor the competition between ions for the interaction with a charged surface.^{149,150} Any interfacial organic ion, usually deuteriated at specific positions to increase sensitivity, can be studied similarly. For instance, specifically deuteriated tetracain, a local anaesthetic, has been located near the head group of membrane phospholipids.¹⁵¹

^7Li NMR of a saponite clay fully exchanged with lithium cation exhibits a quadrupolar splitting¹¹² (Fig. 5). As with the distribution of the orientation of the clay platelets, an extra broadening is observed for satellite bands which have non-Lorentzian lineshape (Section 2.1). This observation differs from those with other clays^{13–15,111} and probably arises from the different structure of saponite clays.

Chemical shift. Interfacial cations of hydrated aluminosilicates can also be studied by solid state NMR. One would expect a quadrupolar splitting in these spectra. This agrees with the observations on cation-exchanged swelling micas. Taking into account the quadrupolar second-order effect, the chemical shift has been correlated with the hydration state of the cation.¹⁵² For a hydrated CsNa-A zeolite, a synthetic aluminosilicate, the ^{133}Cs (spin $I = \frac{7}{2}$) NMR spectrum shows one single line at room temperature.¹⁵³ Slowing down the temperature results in a two-line spectrum, consonant with a slow exchange between two chemically non-equivalent sites.¹⁵³

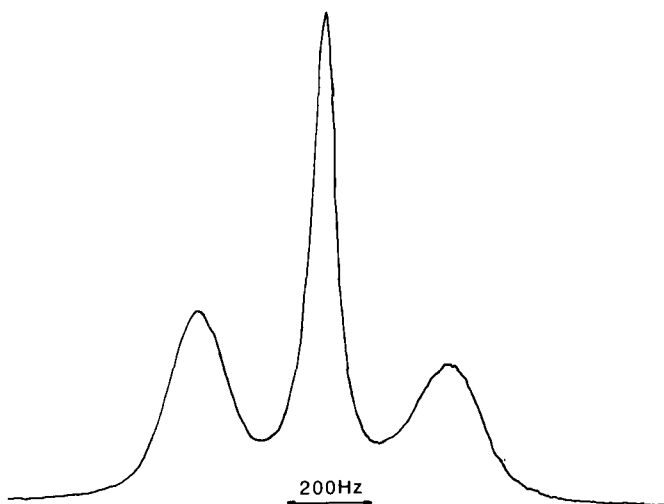


Fig. 5. ^7Li NMR spectrum of lithium-exchanged saponite in heavy water at 294 K (clay content: 28 mg/ml).

3.2.2. Relaxation studies

Numerous studies on the relaxation of quadrupolar counterions have been reported for polyelectrolytes. As these results have some interest for other charged aggregates or solids, I start this section with a brief account of these investigations.

In polyelectrolyte solutions, the counterion relaxation rates R_1 and R_2 are larger than their values for simple electrolyte (salt) solutions. These NMR data have been analysed by assuming a fast exchange between solvated ions and counterions under the direct influence of the polyion. For flexible polyelectrolytes, at low concentration, the extreme narrowing condition $R_1 = R_2$ fails. This corresponds to a slow motion of counterions. Different models have been proposed to explain this observation. The ion can be tightly bound to the polymer¹⁵⁴ and the ion is reoriented at the rate of the segmental motion of the polymer. Alternatively, the time for counterions to escape from a polyion to the neighbouring polymer has also been considered as the origin of the slow process involved in quadrupolar relaxation.¹⁵⁵ However, ^{23}Na NMR studies with DNA are explained in terms of two timescales for the counterion: a local ion motion correlated with the properties of hydration water of DNA (subnanosecond) and a slower motion associated with the mobility of ions in the vicinity of the macromolecule (several nanoseconds).¹⁵⁶ A theoretical model supports these conclusions¹⁵⁷ and gives no argument in line with the two other models.^{154,155}

Similarly, with flexible polyelectrolytes in the semi-dilute regime, the ion relaxation is correlated to the persistence length of the polyion.¹⁵⁸ Therefore, the mobility of condensed cations is associated with the segmental motion of the charged polymer. Although this does not discard the site-binding model, the generality of the above conclusion for different polyelectrolytes does not favour it. Furthermore, using ^7Li relaxation data together with neutron scattering results, it has been deduced that the lithium ion remains fully hydrated in polyacrylate solutions.⁶² Site bindings for divalent cations on DNA seem to coexist with condensed ions as indicated by ^{25}Mg ¹⁵⁹ and ^{43}Ca ¹⁶⁰ NMR studies. In the above systems, the mole fraction p_B (see (25)) of ions neutralizing the polyion agrees with the condensation theory of Manning,¹¹ at least semi-quantitatively, or with the Poisson–Boltzmann treatment.¹² These two theoretical approaches can also reproduce the ^{23}Na relaxation rates for charged polysaccharides such as sodium heparinate¹⁶¹ and sodium polyuronates.¹⁶² The framework of the Poisson–Boltzmann theory has also been extended for counterions condensed around micelles.¹⁶³ Multinuclear relaxation measurements of inorganic cations and anions in agarose gels have also been performed. Although this polysaccharide is uncharged, these studies provide direct evidence for anion binding to agarose gels.¹⁶⁴ The iodide anion but not the potassium cation has also been found to interact with water-soluble polymers.¹⁶⁵

The dynamics of counterions at an interface can be characterized by effective correlation time. Deconvolution of the super-Lorentzian line or longitudinal relaxation rate determination at two different magnetic inductions B_0 gives access to this parameter. The apparent counterion correlation time turns out to be in the nanosecond range.^{158,162} Within a two-state model, values of the same order of magnitude have also been obtained for sodium ions in silica suspensions¹⁴³ and for sodium and lithium cations in laponite (clay) gels.¹⁶⁶ In this latter example, a correlation time of about 1 ns, much shorter than the expected value for the clay platelet reorientation, does not favour a tight cation-binding site.

This correlation time might be associated with the cation residence time at the binding site or with a local cation diffusion motion.¹⁶⁶ With a correlation time in the nanosecond range, the extreme narrowing condition is not fulfilled for interfacial counterions. Multiple-quantum filtration techniques eliminate the signal from the solvated ion, for which the extreme narrowing condition prevails.⁴⁴ The biexponential signal resulting from this filtration technique can be used, as above, to determine the correlation time of the bound ion.¹⁶⁷

All the above results concern counterion relaxation studies in isotropic solutions, i.e. when no residual quadrupolar splittings are displayed in the ion NMR spectrum. In anisotropic media, the spin dynamics, particularly with

spin > 1 (as for most inorganic counterions), are rather complicated. However, recourse to appropriate radiofrequency pulse sequences can solve this problem (Section 2.3). In a recent research on a reverse hexagonal mesophase, a ^{23}Na two-dimensional quadrupolar echo NMR⁵⁵ relaxation study has been performed.¹⁶⁸ The spectral densities $J(\omega_i)$ obtained have been analysed in terms of fast and slow motions. They were assigned to local counterion mobility or collective hydration dynamics and to slow lateral or radial diffusion of the counterion within an aqueous region surrounding the cylindrical aggregates.¹⁶⁸ In the fast motion domain, the ratio of spectral density in mesophase and in water is in the 22–28 range, one order of magnitude larger than that measured for water in the same system.¹¹⁵ With polyelectrolytes, similar ratios are obtained both for water and counterion nuclei.^{158,62} Thus, the physical origin of these motions may be different for polyelectrolytes and for the investigated mesophase. This two-dimensional experiment allows estimation of the counterion surface diffusion, which is reduced by a factor of 3.6 from its value in an infinitely diluted aqueous solution of sodium chloride.¹⁶⁸

Interfacial phenomena also intervene in cation transport across membranes. Based on the magnetization transfer or on the variation of the ion chemical shift,⁴ this translocation process can be followed. In carrier-mediated transport across phospholipid membranes, this describes the cation–ionophore complexation at the water interface.^{169–171}

Study of surfactants at a water–solid interface looks like a promising new area for NMR investigations. Recently, it has been shown for two cationic surfactants that the polar group is anchored at the solid surface but not rigidly attached as indicated by ^2H relaxation determination.¹⁷² The hydrocarbon chain has considerable motional freedom, increasing with the distance from the polar group.¹⁷²

3.2.3. *Diffusion studies*

Pulsed field gradient NMR technique is not appropriate for nuclei characterized by a short relaxation time. Actually, this precludes the observation of most quadrupolar nuclei.¹⁶ Similar self-diffusion coefficients have been found for ^7Li and ^{133}Cs cations in poly(acrylic acid) and poly(methacrylic acid) at different degrees of neutralization. This is consistent with non-specific electrostatic forces between counterions and the polyion.¹⁷³ These data and those with poly(styrenesulfonate)¹⁷⁴ do not substantiate an available theory on counterion diffusion. This NMR technique provides a weighted-average value on each cationic site, including cation in the bulk liquid.

Another diffusion coefficient, describing the cation behaviour near the polymer chain, can be determined without pulsed field gradient accessories,

by adding a small amount of MnCl_2 to the solution. The diffusion coefficient is deduced from the fluctuating dipolar interaction between the paramagnetic cation, which interacts more strongly with the polyion, and the counterion. This parameter is mainly dominated by the fraction of monovalent cations that are near the polymer chain. Both approaches have been used recently to characterize the diffusion of ^7Li cation in poly(acrylic acid) solutions.¹⁷⁵ For the highest degrees of neutralization, the diffusion motion of Li^+ near the chain can be 10 times slower than the overall diffusion.¹⁷⁵ Dipolar nuclei (proton usually) present in organic ions provide another way to study diffusion phenomena in heterogeneous systems. Tetramethylammonium cation has served to monitor the helix-coil transition in polysaccharides.¹⁷⁶ The relative binding strengths of monovalent¹⁷⁷ and divalent¹⁷⁸ carboxylates to a cationic micelle have been reported. The intensity of the electrostatic interaction and the hydrophobicity of the anion play a role in the binding effect. For dicarboxylates, the charge separation between the two negatively charged groups also influences its interaction with micelles. No recent investigations on ion diffusion seem to have been reported in liquid crystals, other than the cited article in the previous section.¹⁶⁸

3.3. Nuclei of superficial groups of phase I components

NMR studies on the polar head group of amphiphilic molecules can be undertaken for different purposes but here we are only concerned with investigations of phenomena occurring at an interface. The structure of the phospholipid polar group has been well-characterized.^{3,34,88,91,179} Therefore, the influence of species in the liquid phase (phase II) on its structure can be readily investigated as shown below with line splitting studies. Interfacial processes as probed by relaxation data are exemplified for chemically modified silica. Finally, diffusion measurements of interfacial species can be determined by modulation of the dipolar interaction between a group fixed on the phase I component and species in the interfacial region. Examples for diffusion in the three-dimensional space or for restricted diffusion are given here.

3.3.1. Line splitting and chemical shielding anisotropy studies

^2H and ^{14}N quadrupolar splitting or ^{31}P chemical shielding anisotropy³⁴ are well-suited to the characterization of interactions between components of phases I and II. Membrane phospholipids have been extensively studied using these NMR parameters. For the last few years, research groups in biochemistry have been studying the electric charge effect on the orientation

of the polar head group of phospholipids. From such studies on phosphatidylcholine, a zwitterionic phospholipid, one main conclusion emerges:^{180,181} in spite of the different nature of the investigated ions (inorganic ions, ionic amphiphiles or local anaesthetics), they all exert qualitatively the same effect on the phosphocholine head group as long as their electric charge has the same sign. A cation moves the N^+ end of this group towards the water phase, whereas an anion displaces the choline group towards the membrane interior.^{180,181} Thus, the electric surface charge is the essential driving force in changing the head group orientation and conformation. Results obtained with phosphatidylserine, an anionic phospholipid, agree with this statement.^{182,183} Biologically active molecules can also perturb the head group orientation as exemplified with benzyl alcohol¹⁸⁴ or other general anaesthetics.¹⁸⁵ Phospholipid-protein interaction includes interfacial processes. It can affect the head group conformation as exemplified with apocytochrome c.¹⁸⁶ ^{31}P chemical shielding anisotropy and ^2H quadrupolar splitting indicate an increased motional freedom of the entire phospholipid head group in the presence of this protein.¹⁸⁶ Earlier results on this subject have been summarized previously.^{3,179}

Another interesting observation in the context of interfacial investigations is the introduction of a chiral phosphorus centre. The $\beta\text{-C}^2\text{H}_2$ signal of the choline group is characterized by two quadrupolar splittings for the *S* isomer and by four quadrupolar splittings for the *R* isomer. These observations are explained by a different average orientation of the two C^2H bonds for both isomers.¹⁸⁷ In addition two slowly exchanging conformational states are present for the *R* isomer.¹⁸⁷

Chemical shift. This parameter has not been often used to investigate interfacial phenomena. The chemical shift of the polar head group nuclei is obviously influenced by the presence of interfacial species. Thus ^{15}N , a dipolar nucleus, is a sensitive probe for this purpose but this approach requires ^{15}N -enriched compounds.¹⁸⁸ Similarly, the chemical shift of the ^{31}P phosphate of phospholipids can be perturbed too. This parameter has also served to determine the transport rate of paramagnetic cations across phospholipid vesicles.⁴ In studies on cationic transport mediated by carboxylic ionophores, interfacial phenomena such as single or hybrid complex formation have been displayed.¹⁸⁹⁻¹⁹¹

3.3.2. Relaxation studies

Although the mobility of the phospholipid head group has been described by relaxation rate measurements of different nuclei,^{3,88,91,179} typical examples are given for other heterogeneous systems.

Interfacial phenomena are involved in product separation by chromatography. NMR studies have been performed on alkyl-modified silica. To investigate the interactions between the solid support and the liquid components of phase II, conventional solution NMR techniques are quite appropriate. Earlier studies have used ^{13}C NMR at natural abundance¹⁹² or on selectively ^{13}C -enriched compounds.¹⁹³⁻¹⁹⁴ An increase in the loading of silica decreases the alkyl chain mobility, as could be anticipated from the interaction between alkyl chains.^{192,193} In $\text{CD}_3\text{CN}/\text{D}_2\text{O}$ mixtures, the hydrocarbon chain mobility is reduced when the water content is higher than 50%.¹⁹² Retention times in chromatography seem to correlate with the alkyl chain mobility.¹⁹²

More recently, ^2H NMR studies on specifically deuteriated hydrocarbon chains have been reported.¹⁹⁵⁻¹⁹⁶ Variation of the longitudinal relaxation rate R_1 with temperature is consistent with a model where at least two different domains of mobility occur along the chain.¹⁹⁵ In agreement with this motional picture, the relaxation rate is linearly related to the square of the linewidth at half-height (approximated to the quadrupolar splitting).¹⁹⁶ The fast reorientations are due to bond rotational isomerizations. Overall chain motion contributes to the slower process. Alkyl chain remains rather flexible in solvents but its mobility drastically decreases in the presence of surfactants or of liquid crystals.¹⁹⁶ The behaviour of alkoxyxilanes immobilized on silica surfaces depends strongly on the used solvent.¹⁹⁷ Hexane and benzene penetrate only to a limited extent into the surface region, while methanol is more deeply inserted into the interfacial domain. Even at high loading levels, the surface appears to be still polar.¹⁹⁷ Also, the structure of poly(ethylenoxide) terminally attached at the polystyrene latex/water interface has been studied by ^1H NMR.¹⁹⁸ Segmental motion is the major contribution of the relaxation rate R_2 for the adsorbed polymer, as is observed for the free polymer. Segments far from the surface are effectively undergoing an isotropic reorientation.¹⁹⁸ Segments near or at the surface are NMR invisible due to their slow motion. Poly(ethylenoxide) and poly(ethylenesulphide) grafted onto macroporous resins have also been investigated by ^1H NMR.^{199,200} High mobility in the polymer chain is observed with pendant ligands, in contrast to difunctional ligands.²⁰⁰ Complexation with mercuric chloride also decreases the chain mobility.¹⁹⁹

3.3.3. Diffusion studies

Pulsed field gradient technique has been applied to such groups to describe the micellization process² or phase transition in anisotropic media,¹⁶ but these experiments do not provide information on interfacial phenomena. Modulation of intermolecular interactions can afford diffusion data in particular

situations. For instance, using attached nitroxide radical to protein²⁰¹ or silica,²⁰² the dominance of electron–proton dipolar relaxation allows the characterization of the translational diffusion of water in the environment of the paramagnetic centre. Values of the order of 10^{-6} cm²/s have been found in both cases.^{201,202}

In contrast to these two situations, restricted diffusion occurs in the lamellar structure. Pyridinium octylhydrogenphosphate in water has been used to illustrate a dipolar relaxation theory in the interlamellar region (a two-dimensional system). The phosphate group moves laterally in an infinite plane whereas the pyridinium cation diffuses within an infinite layer of finite thickness.⁹² The ³¹P longitudinal relaxation rate is governed by a dipolar interaction with the organic ion diffusing within the interlamellar space. Appropriate correlation functions have been calculated and related to diffusion coefficients parallel to and perpendicular to the director of the mesophase.⁹² Reasonable agreement is observed between the values determined in this way and those obtained from a pulsed field gradient technique ($D_{\parallel} = 1.21 \times 10^{-6}$ cm²/s and $D_{\perp} = 2 \times 10^{-8}$ cm²/s).⁹²

4. CONCLUSIONS

A wealth of information on interfacial phenomena results from NMR studies. The determination of quadrupolar splittings, relaxation rates or diffusion measurements provides a detailed picture on the behaviour of molecules and ions at an interface. Broadly speaking, the systems reported in this review can be classified as isotropic homogeneous (e.g. polyelectrolyte or protein solutions), isotropic heterogeneous (e.g. silica suspensions) and anisotropic more or less heterogeneous (e.g. liquid crystals, clay suspensions). In these latter media, quadrupolar splitting and chemical shielding anisotropy data afford a detailed description of the structure and dynamics in the interfacial region.

More recent theoretical works are concerned with these anisotropic media and previous relaxation theories have been adapted for it, taking into account the presence of a residual quadrupolar splitting. Appropriate pulse sequences have been proposed to obtain the different spectral densities. Their application required a homogeneously oriented sample and only a few papers have reported such data. More results are anticipated in the near future. In heterogeneous anisotropic medium (e.g. phospholipids), relaxation rate determination is not so informative but its dependence on orientation with respect to the magnetic induction seems a useful area to study. Investigations of interfacial interactions in phospholipid suspensions should benefit from the recent preparation of compounds with a chiral phosphorus.

In clay suspensions, molecules and ions are in fast exchange between the interface and the bulk liquid. Most interesting data come from quadrupolar splitting and additional results on the effect of counterions are expected for other phyllosilicates. NMR studies of polymers or surfactants adsorbed to a solid particle provide another promising area, according to their technological importance. A few experiments with solid state NMR have been proposed to investigate solid-solid interface or to characterize the behaviour of interfacial cations. Some developments can be foreseen in this area too. Isotropic solutions have been mainly exemplified with polyelectrolytes and, after many years of debate, a convergent picture on the dynamics of interfacial species seems to be emerging, as discussed in the text. Self-diffusion measurements have been chiefly restricted to homogeneous systems until recently. The technology of pulsed field gradients has been boosted by the development of magnetic resonance imaging. Accordingly, future applications on heterogeneous systems (medical and non-medical) are anticipated.

ACKNOWLEDGEMENTS

I am very pleased to express my heart-felt gratitude to Professor P. Laszlo (Liege, Paris) for stimulating discussions during my research work. I also thank Professor P. Stilbs (Stockholm) for providing me with results prior to publication. FNRS (Brussels) is acknowledged for support in our NMR studies.

REFERENCES

1. H. Pfeifer, W. Meiler and D. Deininger, in *Annual Reports on NMR Spectroscopy* (ed. G.A. Webb), Vol. 15. Academic Press, London, 1983.
2. C. Chachaty, in *Progress in NMR Spectroscopy* (ed. J.W. Emsley, J. Feeney and L.H. Sutcliffe), Vol. 19. Pergamon Press, Oxford, 1987.
3. J. Seelig and P.M. MacDonald, *Acc. Chem. Res.*, 1987, **20**, 221.
4. J. Grandjean and P. Laszlo, *Life Sci. Adv. (Biochem.)*, 1987, **6**, 1.
5. S. Forsen, T. Drakenberg and H. Wennerström, *Quart. Rev. Biophys.*, 1987, **19**, 83.
6. L.J. Lynch, in *Magnetic Resonance in Biology* (ed. J.S. Cohen), Vol. 2. Wiley, New York, 1983.
7. M.A. Cohen Stuart, T. Cosgrove and B. Vincent, *Adv. Colloid Interface Sci.*, 1986, **24**, 143.
8. J.C. Leyte, *Makromol. Chem. Macromol. Symp.*, 1990, **34**, 81.
9. W.E.E. Stone, in *Developments in Sedimentology* (ed. J.J. Fripiat), Vol. 34. Elsevier, New York, 1982.
10. N. Boden and S.A. Jones, in *NMR of Liquid Crystals* (ed. J.W. Emsley), p. 473. D. Reidel, Dordrecht, 1985.
11. G.S. Manning, *Acc. Chem. Res.*, 1979, **12**, 443.
12. C.F. Anderson and M.T. Record Jr., *Ann. Rev. Biophys. Biophys. Chem.*, 1990, **19**, 423.
13. J. Grandjean and P. Laszlo, *J. Magn. Reson.*, 1989, **83**, 128.

14. J. Grandjean and P. Laszlo, *Clays Clay Miner.*, 1989, **37**, 403.
15. A. Delville, J. Grandjean and P. Laszlo, *J. Phys. Chem.*, 1991, **95**, 1383.
16. P. Stilbs, in *Progress in NMR Spectroscopy* (ed. J.W. Emsley, J. Feeney and L.H. Sutcliffe), Vol. 19, Pergamon Press, Oxford, 1987.
17. F. Noack, in *Progress in NMR Spectroscopy* (ed. J.W. Emsley, J. Feeney and L.H. Sutcliffe), Vol. 18, Pergamon Press, Oxford, 1986.
18. D.E. Woessner and B.S. Snowden Jr., *J. Chem. Phys.*, 1968, **50**, 1516.
19. H. Wennerström, G. Lindblom and B. Lindman, *Chem. Scr.*, 1974, **6**, 97.
20. E.M. Rose, *Elementary Theory of the Angular Momentum*, Wiley, New York, 1957.
21. W.T. Huntress Jr., *J. Chem. Phys.*, 1968, **48**, 3524.
22. J.S. Blicharski, *Z. Naturforsch.*, 1972, **27a**, 1355.
23. H.R. Falle and G.R. Luckhurst, *J. Magn. Reson.*, 1970, **3**, 161.
24. B. Halle and H. Wennerström, *J. Chem. Phys.*, 1981, **75**, 1928.
25. M.H. Cohen and F. Reif, *Solid State Phys.*, 1957, **5**, 321.
26. A. Saupe, *Z. Naturforsch.*, 1964, **19a**, 161.
27. A.D. Buckingham and K.A. McLauchlan, in *Progress in NMR Spectroscopy* (ed. J.W. Emsley, J. Feeney and L.H. Sutcliffe), Vol. 2, Pergamon Press, Oxford, 1967.
28. P. Diehl and C.L. Khetrapal, in *NMR: Basic Principles and Progress* (ed. P. Diehl, E. Fluck and R. Kosfeld), Vol. 1, Springer Verlag, Berlin, 1969.
29. J.-Ph. Caniparoli, Th. Bredel, C. Chachaty and J. Maruani, *J. Phys. Chem.*, 1989, **93**, 797.
30. H.G. Hertz, *Ber. Bunsenges. Phys. Chem.*, 1973, **77**, 531.
31. M. Holz, in *Progress in NMR Spectroscopy* (ed. J.W. Emsley, J. Feeney and L.H. Sutcliffe), Vol. 18, Pergamon Press, Oxford, 1986.
32. R.G. Barnes and J.W. Bloom, *J. Chem. Phys.*, 1972, **57**, 3082.
33. C. Chachaty and J.P. Quaegebeur, *Mol. Phys.*, 1984, **52**, 1081.
34. J. Seelig, *Biochim. Biophys. Acta*, 1978, **515**, 105.
35. H. Hauser, C. Radloff, R.R. Ernst, S. Sundell and I. Pascher, *J. Am. Chem. Soc.*, 1988, **110**, 1054.
36. S.H. Koenig, *Biophys. J.*, 1988, **53**, 91.
37. B.P. Hills, S.F. Takacs and P.S. Belton, *Mol. Phys.*, 1989, **67**, 903.
38. R. Kimmich, W. Nussler and T. Gneiting, *Colloids Surfaces*, 1990, **45**, 283.
39. J.J. van der Klink, J. Schrieffer and J.C. Leyte, *Ber. Bunsenges. Phys. Chem.*, 1974, **78**, 369.
40. L. Piculell, *J. Chem. Soc., Faraday Trans. 1*, 1986, **82**, 387.
41. L. Piculell and B. Halle, *J. Chem. Soc., Faraday Trans. 1*, 1986, **82**, 401.
42. R. Abragam, *The Principles of Nuclear Magnetism*, Chap. VIII, Clarendon, Oxford, 1970.
43. P.S. Hubbard, *J. Chem. Phys.*, 1970, **53**, 985.
44. G. Jaccard, S. Wimperis and G. Bodenhausen, *J. Chem. Phys.*, 1986, **85**, 6282.
45. W.D. Rooney, T.M. Barbara and C.S. Springer, Jr., *J. Am. Chem. Soc.*, 1988, **110**, 674.
46. T.E. Bull, *J. Magn. Reson.*, 1972, **8**, 344.
47. T.E. Bull, S. Forsen and D.L. Turner, *J. Chem. Phys.*, 1979, **70**, 3106.
48. P.-O. Westlund and H. Wennerström, *J. Magn. Reson.*, 1982, **50**, 451.
49. J.P. Jacobsen, H.K. Bildsoe and K. Schaumburg, *J. Magn. Reson.*, 1976, **23**, 153.
50. R.R. Vold and R.L. Vold, *J. Chem. Phys.*, 1977, **66**, 4018.
51. H.W. Spiess, *J. Chem. Phys.*, 1980, **72**, 6755.
52. S. Emid, J. Konijnendijk, J. Smidt and A. Pines, *Physica B*, 1980, **100**, 215.
53. R.L. Vold, W.H. Dickerson and R.R. Vold, *J. Magn. Reson.*, 1981, **43**, 213.
54. J.R.C. van der Maarel, *Chem. Phys. Lett.*, 1989, **155**, 288.
55. I. Furo, B. Halle and T.C. Wong, *J. Chem. Phys.*, 1988, **89**, 5382.
56. I. Furo and B. Halle, *J. Chem. Phys.*, 1989, **91**, 42.
57. W.T. Huntress Jr., *Adv. Magn. Res.*, 1970, **4**, 1.

58. D.E. Woessner and B.S. Snowden Jr., *Adv. Mol. Relax. Process*, 1973, **3**, 181.
59. C.W.R. Mulder, J. Schrieffer and J.C. Leyte, *J. Phys. Chem.*, 1983, **87**, 2336.
60. B. Halle and L. Piculell, *J. Chem. Soc., Faraday Trans. 1*, 1986, **82**, 415.
61. C.W.R. Mulder, J. de Bleijser and J.C. Leyte, *Chem. Phys. Lett.*, 1980, **69**, 354.
62. J.R.C. van der Maarel, D.H. Powell, A.K. Jawahier, L.H. Leyte-Zuiderweg, G.N. Neilson and M.C. Bellissent-Funel, *J. Chem. Phys.*, 1989, **90**, 6709.
63. R.L. Vold and R.R. Vold, in *Progress in NMR Spectroscopy* (ed. J.W. Emsley, J. Feeney and L.H. Sutcliffe), Vol. 10. Pergamon Press, Oxford, 1978.
64. L.G. Werbelow and D.M. Grant, *Adv. Magn. Reson.*, 1977, **9**, 189.
65. C.J. Hartzell, P.C. Stein, T.J. Lynchk, L.G. Werbelow and W.L. Earl, *J. Am. Chem. Soc.*, 1989, **111**, 5114.
66. K. Elbayed and D. Canet, *Mol. Phys.*, 1989, **68**, 1033.
67. D. Petit, J.-P. Korb, A. Delville, J. Grandjean and P. Laszlo, *J. Magn. Reson.* 1992, in press.
68. B. Halle and H. Wennerström, *J. Magn. Reson.*, 1981, **44**, 89.
69. P.-O. Westlund and H. Wennerström, *J. Magn. Reson.*, 1989, **81**, 68.
70. E. Berggren and P.-O. Westlund, *Chem. Scrip.*, 1989, **29**, 1.
71. E. Berggren and P.-O. Westlund, *J. Magn. Reson.*, 1990, **89**, 161.
72. U. Eliav, A. Baram and G. Navon, *J. Chem. Phys.*, 1988, **89**, 5584.
73. U. Eliav and G. Navon, *J. Magn. Reson.*, 1990, **88**, 223.
74. E. Berggren and P.-O. Westlund, *Biophys. J.*, 1990, **58**, 167.
75. B. Halle and P.-O. Westlund, *Mol. Phys.*, 1988, **63**, 97.
76. M. Mackowiak, G. Liu and J. Jonas, *J. Chem. Phys.*, 1990, **93**, 2154.
77. A. Avogadro and M. Villa, *J. Chem. Phys.*, 1977, **66**, 2359.
78. J.-P. Korb, M. Winterhalter and H.M. McConnell, *J. Chem. Phys.*, 1984, **80**, 1059.
79. J. Tabony and J.-P. Korb, *Mol. Phys.*, 1985, **56**, 1281.
80. M.F. Brown, *J. Chem. Phys.*, 1982, **77**, 1576.
81. P. Ukleja, J. Pirs and J.W. Doane, *Phys. Rev. A*, 1976, **14**, 414.
82. J.H. Freed, *J. Chem. Phys.*, 1977, **66**, 4183.
83. C.G. Wade, *Ann. Rev. Phys. Chem.*, 1977, **28**, 47.
84. M.F. Brown, A.A. Ribeiro and G.D. Williams, *Proc. Natl. Acad. Sci. USA*, 1983, **80**, 4325.
85. D. Doddrell, V. Glushko and A. Allerhand, *J. Chem. Phys.*, 1972, **56**, 3683.
86. M.F. Brown, *J. Chem. Phys.*, 1984, **80**, 2808.
87. J. Seelig, L. Tamm, L. Hymel and S. Fleisher, *Biochemistry*, 1981, **20**, 3992.
88. M.P. Milburn and K.R. Jeffrey, *Biophys. J.*, 1987, **52**, 791.
89. M.F. Brown and J.H. Davis, *Chem. Phys. Lett.*, 1981, **79**, 431.
90. M.C. Jarrell, I.C.P. Smith, P.A. Jovall, H.H. Mantsch and D.J. Siminovitch, *J. Chem. Phys.*, 1988, **88**, 1260.
91. M.P. Milburn and K.R. Jeffrey, *Biophys. J.*, 1989, **56**, 543.
92. J.-P. Korb, Th. Bredel, C. Chachaty and J.R.C. van der Maarel, *J. Chem. Phys.*, 1990, **93**, 1964.
93. E.O. Stejskal and J.E. Tanner, *J. Chem. Phys.*, 1965, **42**, 288.
94. J. Kärger, H. Pfeifer and W. Heink, *Adv. Magn. Reson.*, 1988, **12**, 1.
95. R.M. Cotts, M.J.R. Hoch, T. Sun and J.T. Markert, *J. Magn. Reson.*, 1989, **83**, 252.
96. P. Bendel, *J. Magn. Reson.*, 1990, **86**, 509.
97. J.E.M. Snaar and H. Van As, *J. Magn. Reson.*, 1990, **87**, 132.
98. P.T. Callaghan, *J. Magn. Reson.*, 1990, **88**, 493.
99. D. Canet, B. Diter, A. Belmajdoub, J. Brondeau, J.C. Boubel and K. Elbayed, *J. Magn. Reson.*, 1989, **81**, 1.
100. E.H. Sevilla and A. Sevilla, *J. Magn. Reson.*, 1988, **79**, 534.
101. S. Frey, J. Kärger, H. Pfeifer and P. Walther, *J. Magn. Reson.*, 1988, **79**, 336.

102. G. Jug, *Chem. Phys. Lett.*, 1986, **131**, 94.
103. D.E. Woessner and B.S. Snowden Jr., *Ann. N.Y. Acad. Sci.*, 1973, **204**, 113.
104. R. Mathur-De Vrè, in *Progress of Biophysics and Molecular Biology*, Vol. 35 (ed. D. Noble and T.L. Blundell). Pergamon Press, Oxford, 1980.
105. C. Chachaty and J.P. Quaegebeur, *J. Phys. Chem.*, 1983, **87**, 4341.
106. M.-R. Hakala and T.C. Wong, *Langmuir*, 1986, **2**, 83.
107. W. Guo and T.C. Wong, *Langmuir*, 1987, **3**, 537.
108. K. Rendall and G.J.T. Tiddy, *J. Chem. Soc., Faraday Trans. 1*, 1984, **80**, 3339.
109. K. Rendall, G.J.T. Tiddy and M.A. Trevethan, *J. Chem. Soc., Faraday Trans. 1*, 1983, **79**, 637.
110. E.S. Blackmore and G.J.T. Tiddy, *Liquid Crystals*, 1990, **8**, 131.
111. J. Grandjean and P. Laszlo, in *Spectroscopic Characterization of Minerals and their Surface* (ed. L.M. Coyne, S.W.S. McKeever and D.F. Blake), ACS Symp. Ser. 1990, **415**, 396.
112. J. Grandjean and P. Laszlo manuscript in preparation.
113. J. Breen, D. Huis, J. de Bleijser and J.C. Leyte, *J. Chem. Soc., Faraday Trans. 1*, 1988, **84**, 293.
114. J.R.C. van der Maarel, D. Lankhorst, J. de Bleijser and J.C. Leyte, *Macromolecules*, 1987, **20**, 2390.
115. G. Carlström and B. Halle, *Langmuir*, 1988, **4**, 1346.
116. J. Fripiat, J. Cases, M. François and M. Letellier, *J. Colloid Interface Sci.*, 1982, **89**, 378.
117. D.E. Woessner, *J. Magn. Reson.*, 1980, **39**, 297.
118. G. Carlström and B. Halle, *J. Chem. Soc. Faraday Trans. 1*, 1989, **85**, 1049.
119. M.P. Bozonnet-Frenot, J.P. Marchal and D. Canet, *J. Phys. Chem.*, 1987, **91**, 89.
120. A. Belmajdoub, J.C. Boubel and D. Canet, *J. Phys. Chem.*, 1989, **93**, 4844.
121. A. Yoshino, T. Yoshida, K. Takahashi and I. Ueda, *J. Colloid Interface Sci.*, 1989, **133**, 390.
122. P. Gillis and B. Borcard, *J. Magn. Reson.*, 1988, **77**, 19.
123. P.S. Belton and B.P. Hills, *Mol. Phys.*, 1987, **61**, 999.
124. P.S. Belton, B.P. Hills and E.R. Raimbaud, *Mol. Phys.*, 1988, **63**, 825.
125. R. Blinc, O. Jarh, A. Zidansek and A. Blinc, *Z. Naturforsch.*, 1989, **44a**, 163.
126. D.P. Gallegos, D.M. Smith and J. Brinker, *J. Colloid Interface Sci.*, 1988, **124**, 186.
127. D.P. Gallegos and D.M. Smith, *J. Colloid Interface Sci.*, 1988, **122**, 143.
128. C.L. Glaves and D.M. Smith, *J. Membrane Sci.*, 1989, **46**, 167.
129. J.Y. Bottero, M. Bruant, J.M. Cases, D. Canet and F. Fiessinger, *J. Colloid Interface Sci.*, 1988, **124**, 515.
130. F.D. Blum, B.R. Sinha and F.C. Schwab, *Macromolecules*, 1990, **23**, 3592.
131. T.C. Cosgrove, N. Finch and J. Webster, *Colloids Surfaces*, 1990, **45**, 377.
132. F. Lauprêtre, *Prog. Polym. Sci.*, 1990, **15**, 425.
133. R. Kitamaru, F. Horii and K. Murayama, *Macromolecules*, 1986, **19**, 636.
134. T.P. Huijgen, H.A. Gaur, T.L. Weeding, L.W. Jenneskens, H.E.C. Schuurs, W.G.B. Huysmans and W.S. Veeman, *Macromolecules*, 1990, **23**, 3063.
135. K.J. Packer, I.J.F. Poplett, M.J. Taylor, M.E. Vickers, A.K. Wittaker and K.P.J. Williams, *Makromol. Chem., Macromol. Symp.*, 1990, **34**, 161.
136. F.D. Blum, S. Pickup and K.R. Foster, *J. Colloid Interface Sci.*, 1986, **113**, 336.
137. W. Brown, P. Stilbs and T. Lindström, *J. Appl. Polym. Sci.*, 1984, **29**, 823.
138. P.T. Callaghan, M.A. LeGros and D.N. Pinder, *J. Chem. Phys.*, 1983, **79**, 6372.
139. F.D. Blum, A.S. Padmanabhan and R. Mohebbi, *Langmuir*, 1985, **1**, 127.
140. P.T. Callaghan and O. Soderman, *J. Phys. Chem.*, 1983, **87**, 1737.
141. K.J. Packer and F.O. Zelaya, *Colloids Surfaces*, 1989, **36**, 221.
142. P.T. Callaghan, *Austr. J. Phys.*, 1984, **37**, 359.

143. H.M. Jang and D.W. Fuerstenau, *Langmuir*, 1987, **3**, 1114.
144. I.D. Leigh, M.P. McDonald, R.M. Wood, G.J.T. Tiddy and M.A. Trevethan, *J. Chem. Soc., Faraday Trans. 1*, 1981, **77**, 2867.
145. H. Wennerström, B. Lindman, G. Lindblom and G.J.T. Tiddy, *J. Chem. Soc., Faraday Trans. 1*, 1979, **75**, 663.
146. T.E. Strzelecka and R.L. Rill, *Biopolymers*, 1990, **30**, 803.
147. K. Rendall, G.J.T. Tiddy and M.A. Trevethan, *J. Colloid Interface Sci.*, 1984, **98**, 565.
148. M. Svärd, P. Schurtenberger, K. Fontell, B. Jönsson and B. Lindman, *J. Phys. Chem.*, 1988, **92**, 2261.
149. A. Khan, B. Jönsson and H. Wennerström, *J. Phys. Chem.*, 1985, **89**, 5180.
150. E.T. Fossel, M.M. Sarasua and K.A. Koehler, *J. Magn. Reson.*, 1985, **64**, 536.
151. M. Auger, M.C. Jarrell and I.C.P. Smith, *Biochemistry*, 1988, **27**, 4660.
152. V. Laperche, J.F. Lambert, R. Prost and J.J. Fripiat, *J. Phys. Chem.*, 1990, **94**, 8821.
153. M.-K. Ahn and L.E. Iton, *J. Phys. Chem.*, 1989, **93**, 4924.
154. A. Delville, C. Detellier and P. Laszlo, *J. Magn. Reson.*, 1979, **34**, 301.
155. B. Halle, H. Wennerström and L. Piculell, *J. Phys. Chem.*, 1984, **88**, 2482.
156. L. Van Dijk, M.L.H. Gruwel, W. Jesse, J. de Bleijser and J.C. Leyte, *Biopolymers*, 1987, **26**, 261.
157. M.R. Reddy, P.J. Rossky and C.S. Murthy, *J. Phys. Chem.*, 1987, **91**, 4923.
158. C.J.M. van Rijn, A.J. Maat, J. de Bleijser and J.C. Leyte, *J. Phys. Chem.*, 1989, **93**, 5284.
159. D. Murk Rose, C.F. Polnaszek and R.G. Bryant, *Biopolymers*, 1982, **21**, 653.
160. W.H. Braunlin, T. Drakenberg and L. Nordenskiöld, *Biopolymers*, 1987, **26**, 1047.
161. A. Delville and P. Laszlo, *Biophys. Chem.*, 1983, **17**, 119.
162. H. Grasdalen and B.J. Kwam, *Macromolecules*, 1986, **19**, 1913.
163. A. Delville, L. Herwats and P. Laszlo, *Nouv. J. Chim.*, 1984, **8**, 557.
164. L. Piculell and S. Nilsson, *J. Phys. Chem.*, 1989, **93**, 5602.
165. S.H. Oh, R. Ryoo and M.S. Jhon, *Macromolecules*, 1990, **23**, 1671.
166. J. Grandjean and P. Laszlo, *J. Magn. Reson.*, 1991, **92**, 404.
167. C.-W. Chun and S. Wimperis, *J. Magn. Reson.*, 1990, **88**, 440.
168. I. Furo, B. Halle, P.-O. Quist and T.C. Wong, *J. Phys. Chem.*, 1990, **94**, 2600.
169. F.G. Riddell, S. Arumugam, P.J. Brophy, B.G. Cox, M.C.H. Payne and T.E. Southon, *J. Am. Chem. Soc.*, 1988, **110**, 734.
170. F.G. Riddell and S. Arumugam, *Biochim. Biophys. Acta*, 1988, **945**, 65.
171. D.C. Shungu, D.C. Buster and R.W. Briggs, *J. Magn. Reson.*, 1990, **89**, 102.
172. E. Söderlind and P. Stilbs, *J. Colloid Interface Sci.*, 1991, **143**, 586.
173. R. Rymden and P. Stilbs, *J. Phys. Chem.*, 1985, **89**, 2425.
174. L.G. Nilsson, L. Nordenskiöld and P. Stilbs, *J. Phys. Chem.*, 1987, **91**, 6210.
175. R.H. Tromp, J. de Bleijser and J.C. Leyte, *J. Phys. Chem.*, 1989, **93**, 2626.
176. L. Piculell and R. Rymden, *Macromolecules*, 1989, **22**, 2376.
177. M. Jansson and P. Stilbs, *J. Phys. Chem.*, 1987, **91**, 113.
178. P. Li, M. Jansson, P. Bahadur and P. Stilbs, *J. Phys. Chem.*, 1989, **93**, 6458.
179. J.H. Davis, *Chem. Phys. Lipids*, 1986, **40**, 223.
180. P.G. Scherer and J. Seelig, *Biochemistry*, 1989, **28**, 7720.
181. J. Seelig, P.M. McDonald and P.G. Scherer, *Biochemistry*, 1987, **26**, 7535.
182. M. Roux, J.M. Newmann, R.S. Hodges, P.F. Devaux and M. Bloom, *Biochemistry*, 1989, **28**, 2313.
183. A.I.P.M. de Kroon, J.W. Timmermans, J.A. Killian and B. de Kruijff, *Chem. Phys. Lipids*, 1990, **54**, 33.
184. J.M. Pope, D. Dubro, J.W. Doane and P.W. Westerman, *J. Am. Chem. Soc.*, 1986, **108**, 5426.

185. B.J. Forrest and J. Mattai, *Biochemistry*, 1985, **24**, 7148.
186. W. Jordi, A.I.P.M. de Kroon, J.A. Killian and B. de Kruijff, *Biochemistry*, 1990, **29**, 2312.
187. W.M. Loffredo, R.-T. Jiang and M.-D. Tsai, *Biochemistry*, 1990, **29**, 10912.
188. S. Akoka, C. Tellier and S. Poignant, *Biochemistry*, 1986, **25**, 6972.
189. J. Grandjean and P. Laszlo, *J. Am. Chem. Soc.*, 1984, **106**, 1472.
190. J. Grandjean and P. Laszlo, *J. Am. Chem. Soc.*, 1986, **108**, 3483.
191. J. Grandjean and P. Laszlo, *Biochimie*, 1989, **71**, 183.
192. K. Albert, B. Evers and E. Bayer, *J. Magn. Reson.*, 1985, **62**, 428.
193. R.K. Gilpin and M.E. Gangoda, *Anal. Chem.*, 1984, **56**, 1470.
194. M.E. Gangoda, R.K. Gilpin and B.M. Fung, *J. Magn. Reson.*, 1987, **74**, 134.
195. M.E. Gangoda, R.K. Gilpin and J. Figueirinhas, *J. Phys. Chem.*, 1989, **93**, 4815.
196. M.E. Gangoda and R.K. Gilpin, *Langmuir*, 1990, **6**, 941.
197. E.C. Kelusky and C.A. Fyfe, *J. Am. Chem. Soc.*, 1986, **108**, 1746.
198. T. Cosgrove and K. Ryan, *Langmuir*, 1990, **6**, 136.
199. M. Lauth, Y. Frere, B. Meurer, Ph. Gramain and M. Prevost, *React. Polym.*, 1990, **12**, 155.
200. M. Lauth, Y. Frere, B. Meurer and Ph. Gramain, *React. Polym.*, 1990, **13**, 63.
201. C.F. Polnaszek and R.G. Bryant, *J. Chem. Phys.*, 1984, **81**, 4038.
202. C.F. Polnaszek, D.A. Hanggi, P.A. Carr and R.G. Bryant, *Anal. Chem. Acta*, 1987, **194**, 311.

This Page Intentionally Left Blank

NMR Measurements of Intracellular Ions in Living Systems

JOSEPH C. VENIERO* and RAJ K. GUPTA*,†

*Departments of *Physiology and Biophysics, and †Biochemistry, Albert Einstein College of Medicine of Yeshiva University, Jack and Pearl Resnick Campus, Bronx, NY 10461, USA*

1. Introduction	219
2. Sodium measurements	220
2.1. Shift reagent aided ^{23}Na NMR	220
2.2. ^{19}F NMR of fluorinated indicators	233
2.3. Double-quantum coherence-transfer ^{23}Na NMR	235
3. Potassium measurements	237
3.1. Shift reagent aided ^{39}K NMR	238
3.2. Multiple-quantum filtered ^{39}K NMR	239
3.3. Non-invasive subtraction procedure	240
4. ^{19}F NMR measurements of intracellular free calcium ions	244
4.1. Methodological considerations	244
4.2. General applications	246
4.3. Free calcium changes during cell differentiation	250
5. Magnesium measurements	252
5.1. ^{31}P NMR of intracellular ATP	252
5.2. ^{13}C NMR of intracellular citrate	256
5.3. ^{19}F NMR of fluorinated indicators	257
6. ^{35}Cl NMR spectroscopy	258
6.1. Intracellular chloride ions	258
6.2. Compartmentation of albumin between interstitial and vascular spaces	261
References	262

1. INTRODUCTION

Nuclear magnetic resonance provides a unique methodology for non-invasive physiological measurements in living systems. From the direct visualization of anatomical structure in ^1H magnetic resonance imaging and measurements of flow and intracellular metabolites in whole animals and humans, to spectroscopic measurements of intracellular ions and metabolites

in perfused tissue, organ and cell systems, NMR gives clinicians and researchers access to physiological information unobtainable until recently. The volume of literature concerning these topics is truly staggering, and a comprehensive review of the entire field is beyond the scope of this report. A brief review of NMR of intracellular ions in living systems appeared in this series three years ago.¹

The research interests of our laboratory have been concerned with the development and use of NMR techniques for the measurement of intracellular ions in living systems. Accordingly, this review covers recent advances in the measurement of intracellular ions in cell suspensions, and in perfused tissue, organ and cell systems. While an attempt has been made to provide comprehensive coverage of the literature, it was inevitable that we have drawn on examples from the published and unpublished work of our own laboratory to illustrate the methods and other underlying concepts.

2. SODIUM MEASUREMENTS

Since the discovery of paramagnetic extracellular sodium ion shift reagents in 1982,^{2,3} applications of ^{23}Na NMR to study intracellular sodium ions in cells and tissues have proliferated rapidly. Early work in the field of cellular sodium NMR has been reviewed previously.⁴⁻⁸ In this section we cover more recent applications of ^{23}Na NMR. Earlier work, however, is briefly mentioned, as needed, for the sake of completeness.

2.1. Shift reagent aided ^{23}Na NMR

The most common NMR method for the study of intracellular sodium ions employs membrane-impermeable highly anionic hyperfine shift reagents.^{2,9,10} These paramagnetic reagents, because of their localization in the extracellular compartment and the short range of their paramagnetic effects, interact only with the extracellular sodium ions, shifting their resonance away from the largely unaffected intracellular resonance. (The intracellular resonance may be affected to a small degree by changes in the sample's bulk magnetic susceptibility.⁷) This allows the direct observation of the intracellular ^{23}Na resonance, the intensity of which is proportional to the intracellular sodium ion concentration. The most popular of these reagents have been dysprosium bis(tripolyphosphate) ($\text{Dy}(\text{PPP}_i)_2^{7-}$), which causes an upfield shift, and dysprosium triethylenetetraminehexaacetate (DyTTHA^{3-}), which causes a downfield shift relative to the unperturbed resonance position. Recently, another reagent, proposed for studies of intracellular sodium in perfused

animal hearts but which may have broad usefulness in the study of intracellular sodium in other living systems, has been introduced.¹¹ This reagent, thulium 1,4,7,10-tetraazacyclododecane-*N,N',N'',N'''*-tetra(methylenephosphonate), $\text{Tm}(\text{DOTP})^{5-}$, causes a downfield shift relative to the unperturbed resonance position. The shift produced by this reagent is approximately twice that obtained from $\text{Dy}(\text{TTHA})^{3-}$; this allows the reagent to be used at half the concentration necessary for $\text{Dy}(\text{TTHA})^{3-}$. The lower concentration reduces the potential lanthanide toxicity and reduces any observed magnetic susceptibility effects. The corresponding dysprosium compound, $\text{Dy}(\text{DOTP})^{5-}$, although expected theoretically to give two-fold greater shifts than the thulium compound, produces almost the same shifts in aqueous solutions.¹¹ This discrepancy is possibly due to structural differences between $\text{Tm}(\text{DOTP})^{5-}$ and $\text{Dy}(\text{DOTP})^{5-}$ which may form dimers or trimers in solution.

The magnitude of the shift is proportional to the concentration of the reagent, but the reagents may be toxic at sufficiently high concentrations.¹²⁻¹⁴ If a relatively low concentration of shift reagent is used, the extracellular resonance may not be shifted far enough away from the intracellular resonance to allow accurate measurement of its intensity. Part of the toxicity appears to be due to complexation of free calcium ions by the shift reagents.¹³⁻¹⁵ A large decrease in the free calcium ion concentration in the medium occurs with $\text{Dy}(\text{PPP}_i)_2^{7-}$. Additional calcium is required to replenish the medium and it is possible to maintain free calcium at up to 0.7 mM.¹³ $\text{Dy}(\text{TTHA})$ is quantitatively less affected by calcium ions but its overall induced shifts at comparable concentrations are only about $\frac{1}{4}$ of those induced by $\text{Dy}(\text{PPP}_i)_2^{7-}$.¹⁴

Pike *et al.* have used a Jump and Return selective excitation sequence¹⁶ in an attempt to increase the apparent resolution of the intracellular ^{23}Na resonance.¹⁷ (This involves setting the spectrometer frequency to the position of the extracellular resonance and applying $90^\circ\text{--}\tau\text{--}90^\circ$ pulse sequence where the two 90° pulses are of opposite phase. The sequence effectively reduces the intensity of resonances at the spectrometer frequency and at frequencies $n/(2\tau)$ from the spectrometer frequency). However, in the perfused heart the extracellular resonance intensity was attenuated by only about five-fold and still interfered with quantitation of the intracellular resonance. Elgavish was able to obtain adequate separation of the intra- and extracellular ^{23}Na resonances in isovolumic perfused beating rat heart using 6 mM $\text{Dy}(\text{PPP}_i)_2^{7-}$ supplemented with extra calcium.¹⁴ Burststein and Fossel were able to obtain adequate resolution in frog heart ^{23}Na resonances with only 3 mM $\text{Dy}(\text{PPP}_i)_2^{7-}$. They found it useful to eliminate the extracellular ^{23}Na resonance by continuous rf saturation.¹⁸

A knowledge of the NMR visibility of intracellular sodium ions is essential

for the measurement of intracellular sodium concentration. There are two major explanations given for the lack of full visibility.^{7,19-22} First is the existence in biological tissues of multiple pools of ions with differing correlation times. If the ions in one pool have a long correlation time and are in slow exchange with the other pools, the NMR resonances from this pool may be too broad to detect by conventional methods. Alternatively, only the two outer transitions of the ^{23}Na nucleus ($-\frac{3}{2} \leftrightarrow -\frac{1}{2}$ and $\frac{1}{2} \leftrightarrow \frac{3}{2}$) of all Na^+ pools, which account for 60% of the resonance intensity, may be broadened beyond detectability. Theoretical studies imply that even part of the central transition ($-\frac{1}{2} \rightarrow \frac{1}{2}$), representing the other 40% of the signal, may become invisible under certain conditions.²³ Intracellular sodium has previously been shown to be 80–100% visible in human erythrocytes.^{4,24-26} Invisibility of $17 \pm 3\%$ of the ^{23}Na signal has been documented in packed human erythrocytes^{4,26,27} as well as in *Amphiuma* erythrocytes,¹³ although the ^{23}Na resonance of the freely transportable pool is thought to be nearly 100% visible. Isolated proximal tubules also showed more than 90% visibility of freely transportable internal sodium ions,¹⁵ but in the yeast²⁸ and *E. coli*,²⁹ sodium efflux was accompanied by a 60% increase in intensity of transported sodium ions, and, in amphibian oocytes, the intracellular sodium visibility factor ranged from 17 to 70%, following hormonal and developmental stimuli.³⁰ It has recently been shown that in the Langendorff perfused heart,³¹ and in the perfused kidney,³² more than 90% of the free sodium ions can be observed under certain conditions. Visibility of only about 53% is, however, reported for ^{23}Na ions in rat liver.³³

In order to obtain a measurement of intracellular sodium concentration from the measured intensity of the intracellular sodium resonance, it is essential to know the intracellular volume giving rise to the signal. Since the ^{23}Na signal from the intracellular or extracellular compartment is proportional to its volume and its sodium concentration, and the proportionality constants are equal,

$$\frac{A_{\text{in}}}{[\text{Na}]_{\text{in}} V_{\text{in}}} = \frac{A_{\text{out}}}{[\text{Na}]_{\text{out}} V_{\text{out}}} \quad (1)$$

or

$$[\text{Na}]_{\text{in}} = \frac{A_{\text{in}}}{A_{\text{out}}} \times \frac{V_{\text{out}}}{V_{\text{in}}} \times [\text{Na}]_{\text{out}} \quad (2)$$

where $[\text{Na}]_{\text{in}}$ and $[\text{Na}]_{\text{out}}$ are the intracellular and extracellular sodium concentrations, A_{in} and A_{out} are the areas of the resonances, and V_{in} and V_{out} are the volumes of the two compartments. In the case of a cell suspension as, for example, in the measurement of intracellular sodium in human blood, the total sensitive volume is filled; the fraction of volume not occupied by cells is occupied by extracellular fluid. Thus, the volume ratio $V_{\text{out}}/V_{\text{in}}$ is easily

obtained by taking the ratio of the fractional space occupied by each compartment. For the extracellular compartment, this fraction (S_{out}) is A_{out}/A_o ; where A_o is the area of the ^{23}Na resonance of a sample of medium which fills the sensitive volume. The fractional volume occupied by the intracellular compartment is then simply $(1 - S_{out})$, times a correction factor, W_{in} , which accounts for the fact that the cell is not all water, when it is desirable to express concentrations on cell water basis. Intracellular sodium is then calculated by,^{2,4}

$$[\text{Na}]_{in} = \frac{A_{in}}{A_{out}} \times \frac{S_{out}}{(1 - S_{out})W_{in}} \times [\text{Na}]_{out} \quad (3)$$

W_{in} has been measured to be 0.73 ± 0.02 for red blood cells,³⁴ 0.43 ± 0.01 for amphibian oocytes,³⁵ and 0.77 ± 0.02 for kidney proximal tubules.³⁶

For the measurement of intracellular sodium in perfused organ systems, such as the perfused heart, the necessary volume determinations for use in (2) may be obtained by a combination of ^2H and ^{23}Na NMR. Perfusing the organ with medium containing 1–2% $^2\text{H}_2\text{O}$, which will equilibrate in the intra- and extracellular water pools, gives a measure of total organ-associated water. The V_{in}/V_{out} ratio can then be determined by,³¹

$$\frac{V_{in}}{V_{out}} = \frac{A_{tissue}^D}{A_o^D} \times \frac{A_o^{Na}}{A_{out}^{Na}} - 1 \quad (4)$$

where A_{tissue}^D and A_o^D are the areas of the deuterium resonances of the perfused organ and a medium sample, respectively, and A_o^{Na} is the area of the sodium resonance of the same medium sample (see Fig. 1). It has been argued that small variations in the quality factor, Q , of the rf coil due to differences in sample loading between the perfused organ, which occupies only a fraction of the sensitive volume, and the medium sample which may fill the sensitive volume, are not expected to affect the calculation of the intracellular free sodium ion concentration.³¹

2.1.1. Application to perfused cell systems

The use of hyperfine shift reagents allows the discrimination of a very small intracellular ^{23}Na resonance from the much larger extracellular ^{23}Na resonance in perfused cultured cell systems (see Fig. 2). However, the measurement of intracellular sodium in a system of cultured cells perfused in a hollow fibre bundle or by attachment to beads presents special problems. In this case, the volume occupied by the cells is small (<10%) in comparison to the volume occupied by extracellular fluid. Estimation of a small intracellular volume using the above methods would require obtaining a difference between two nearly equal larger volumes which

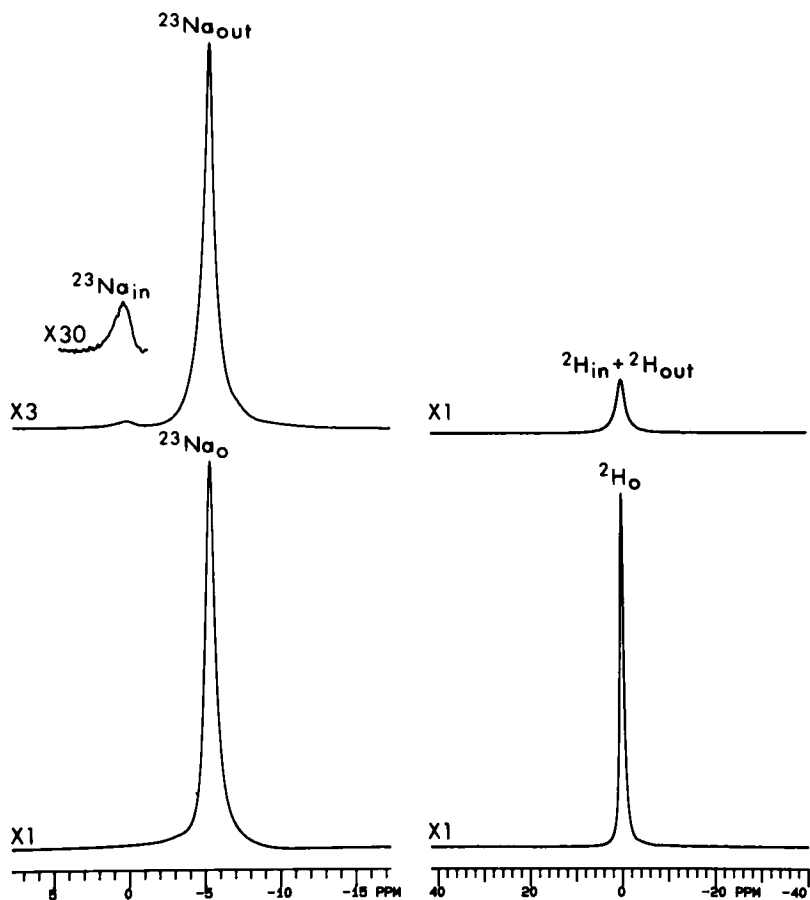


Fig. 1. ^{23}Na (left) and ^2H (right) NMR spectra of the perfused rat heart (upper traces) and perfusate (lower traces) containing 5 mM $\text{Dy}(\text{PPP}_i)_2$. The vertical scale of the ^{23}Na NMR spectrum of the perfused heart is expanded three-fold and the inset showing the intracellular resonance, $^{23}\text{Na}_{\text{in}}$, is again expanded ten-fold. The resonances of intra- ($^{23}\text{Na}_{\text{in}}$) and extracellular Na^+ ($^{23}\text{Na}_{\text{out}}$), the ^{23}Na resonance of the tissue-free perfusate sample ($^{23}\text{Na}_{\text{o}}$), the ^2H resonance of the heart ($^2\text{H}_{\text{in}} + ^2\text{H}_{\text{out}}$), and the ^2H resonance of the tissue-free perfusate sample ($^2\text{H}_{\text{o}}$) are indicated. (From Jelicks and Gupta.³¹)

would have a large error associated with it. In order to measure the small intracellular volume needed for the quantitation of the intracellular sodium in perfused cultured cells, the following method was devised. After a measurement of the basal intracellular ^{23}Na resonance was completed, the internal sodium was raised to equilibrate with that in the extracellular

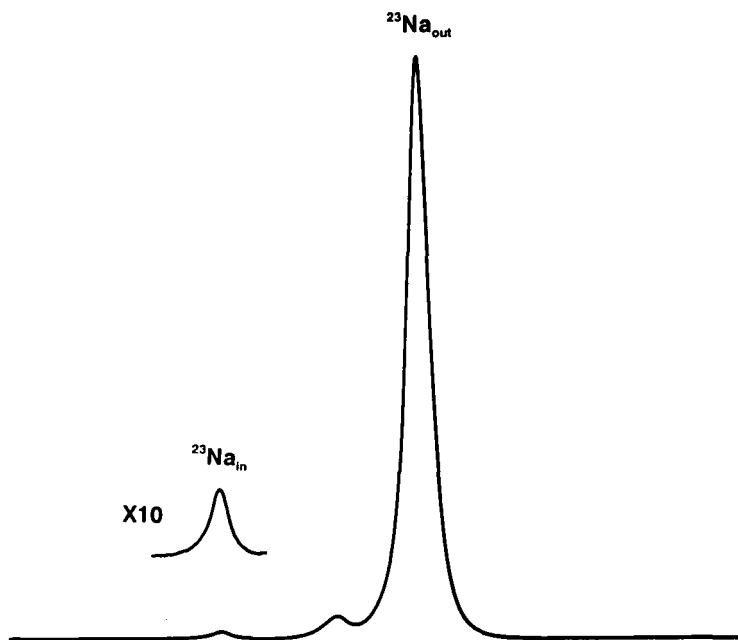


Fig. 2. ^{23}Na NMR spectra of cultured HL-60 cells in a hollow fibre bundle showing the discrimination of the resonances of the very small intracellular sodium ion pool ($^{23}\text{Na}_{\text{in}}$) and the much larger extracellular sodium pool ($^{23}\text{Na}_{\text{out}}$). Spectra were recorded in the presence of 6 mM $\text{Dy}(\text{PPP}_i)_2$ supplemented with additional calcium. The inset is a ten-fold vertical expansion of the intracellular peak. The unlabelled resonance is apparently due to an extracellular compartment in the fibre bundle which maintains a slightly different shift reagent concentration, possibly the intra-fibre extracellular compartment; this peak is present in spectra of empty bundles in the presence of shift reagent.

medium. To achieve this, $\text{Na}^+ - \text{K}^+ - \text{ATPase}$ was blocked with ouabain and sodium entry was increased by the addition of the ionophore monensin. The internal sodium concentration began increasing under these conditions, then became constant and, presumably, equal to that in the perfusion medium. Assuming equal NMR visibility of intra- and extracellular sodium, the intra- to extracellular water volume ratio is merely the ratio of the intensities of the intra- and extracellular ^{23}Na resonances of such sodium-equilibrated cells (see Fig. 3). The intracellular sodium concentration could then be simply calculated from the ratio of the areas of the intracellular sodium resonance intensities in unperturbed and sodium-equilibrated cells via the equation:

$$[\text{Na}]_{\text{in}} = \frac{A_{\text{in}}}{A_{\text{equil}}} \times [\text{Na}]_{\text{out}} \quad (5)$$

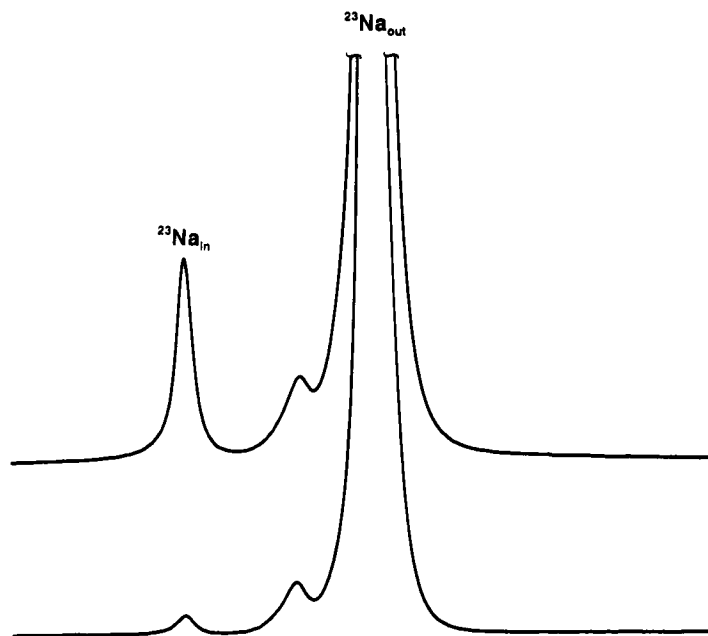


Fig. 3. ^{23}Na NMR spectra of cultured HL-60 cells perfused in a hollow fibre bundle before (lower trace) and after (upper trace) incubation with ouabain and monensin to allow equilibration of intra- and extracellular sodium ion concentrations. Spectra are recorded in the presence of 6 mM $\text{Dy}(\text{PPP}_i)_2$ supplemented with additional calcium. Resonances for intra- ($^{23}\text{Na}_{\text{in}}$) and extracellular ($^{23}\text{Na}_{\text{out}}$) sodium are indicated.

where A_{in} is the area of the unperturbed intracellular ^{23}Na resonance, and A_{equil} is the area of the intracellular resonance after equilibration of the intracellular sodium with that in the medium. This approach does not require knowledge of the NMR-visibility of internal sodium ions, but assumes equal visibility for the unperturbed and sodium equilibrated cells, and should be generally applicable in all situations. We have tested the method with red blood cells, where it yielded a value similar to that obtained by (3). With cultured HL-60 cells perfused in a hollow fibre bundle, a typical sample (see Fig. 3), gave, for intracellular free sodium, a value of approximately 10 mM. HL-60 cells remained visible in the presence of $\text{Dy}(\text{PPP}_i)_2$, which was used to discriminate between intra- and extracellular resonances. A representative set of ^{31}P NMR spectra of the cells run before and 15 min after the addition of the shift reagent, supplemented with calcium to obtain a free calcium concentration of 0.5 mM in the medium, demonstrates maintenance of ATP in these cells in the presence of the shift reagent (see Fig. 4). The ^{31}P resonances

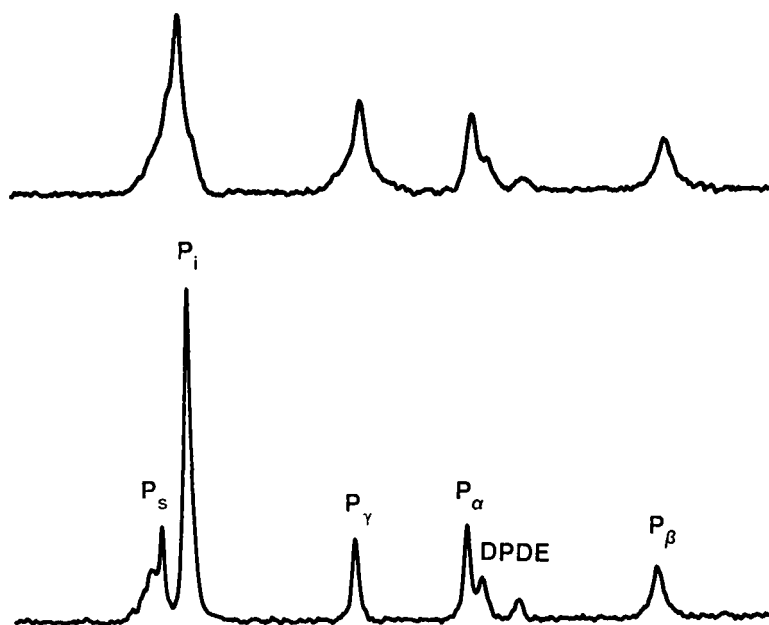


Fig. 4. ^{31}P spectra of HL-60 cells in a hollow fibre bundle before (lower trace) and after (upper trace) 30 min of treatment with 6 mM $\text{Dy}(\text{PPP}_i)_2$. Resonances for sugar phosphates (P_s), inorganic phosphate (P_i), the α , β , and γ phosphates of ATP (P_α , P_β , and P_γ), and diphosphodiester (DPDE) are labelled.

are broadened due to susceptibility effects but their intensities remained stable for a few hours.

2.1.2. Effect of lead on cellular sodium homeostasis

NMR has revealed a derangement of intracellular ion balance in the presence of lead, a toxic heavy metal. Lead exposure remains a major environmental health concern despite the elimination of lead-based paints and the introduction of unleaded gasoline; yet the cellular mechanisms for lead toxicity have still not been adequately defined. Using ^{19}F NMR, lead has been shown to increase intracellular free calcium (*vide infra*) in cultured bone³⁷ and brain cells,³⁸ and in human platelets.³⁹ Because of the critical role of the transmembrane sodium free energy gradient in regulating intracellular free calcium in many types of cells, we have hypothesized that lead may act to increase intracellular free sodium and that an impaired cellular sodium homeostasis may be an important lesion associated with lead toxicity.

To test this hypothesis, ^{23}Na NMR, in combination with $\text{Dy}(\text{PPP}_i)_2$, was

used to measure the intracellular free sodium concentration in human erythrocytes after prior incubation with various concentrations of lead. In a typical experiment, freshly drawn, heparinized human blood (30 ml) was diluted with 75 ml of Hank's balanced salt solution containing 10 mM glucose and was divided into four parts. Lead acetate was added to each of the three parts, to a final concentration of 10, 25 or 100 μM . Each part was then incubated at 37°C in a shaker bath. NMR samples at the various time points were prepared by removing an aliquot of diluted blood (5 ml), and adding $\text{Dy}(\text{PPP}_i)_2$ to a final concentration of 4 mM. Erythrocytes, packed by gentle centrifugation, and supernatant were placed into separate NMR tubes (4 mm o.d.) and the ^{23}Na spectra were recorded on a Varian VXR-500 NMR spectrometer at 132.2 MHz, using 90° pulses, and an acquisition time of 0.205 s.

Representative ^{23}Na NMR spectra of erythrocytes incubated for 24 h at 37°C without and with 25 and 100 μM lead are shown in Fig. 5. To obtain each spectrum, 1024 scans were time-averaged and the FID was Fourier-transformed with a line-broadening of 10 Hz to improve spectral signal-to-noise ratio. The intracellular sodium concentrations from a typical series of experiments, calculated as described above, are summarized in Table 1. As is apparent from the table, in the absence of lead, a low level of intracellular sodium was continuously maintained in control erythrocytes over the observation period of 24 h. Lead-treated samples, however, showed definite increases in internal sodium concentration, the magnitude of which increased with increasing lead concentration and with increasing time following the start of lead treatment. After 24 h of treatment with 10, 25 and 100 μM lead, increases in intracellular sodium of 18, 280 and 414%, respectively, were observed. Experiments on blood from two other donors yielded similar results.

The data clearly demonstrate that lead causes significant increases in intra-erythrocyte sodium. A significant perturbation of cellular sodium homeostasis was apparent even in the presence of 10 μM lead; an 18% increase in intracellular free sodium was observable after 24 h of incubation. While a longer term experiment was not attempted due to sample contamination problems, it is likely that even lower concentrations of lead will cause significant increases in internal sodium over longer periods of incubation, or in more sensitive tissues.

To show that the erythrocytes remained energetically viable and that lead treatment did not deplete the cellular ATP stores, ^{31}P NMR spectra were recorded without lead treatment and with 50 or 100 μM lead. The spectra revealed no significant decline in ATP in lead-treated samples in comparison to their paired controls. Thus, sodium increases are not due to depletion of ATP in the cells.

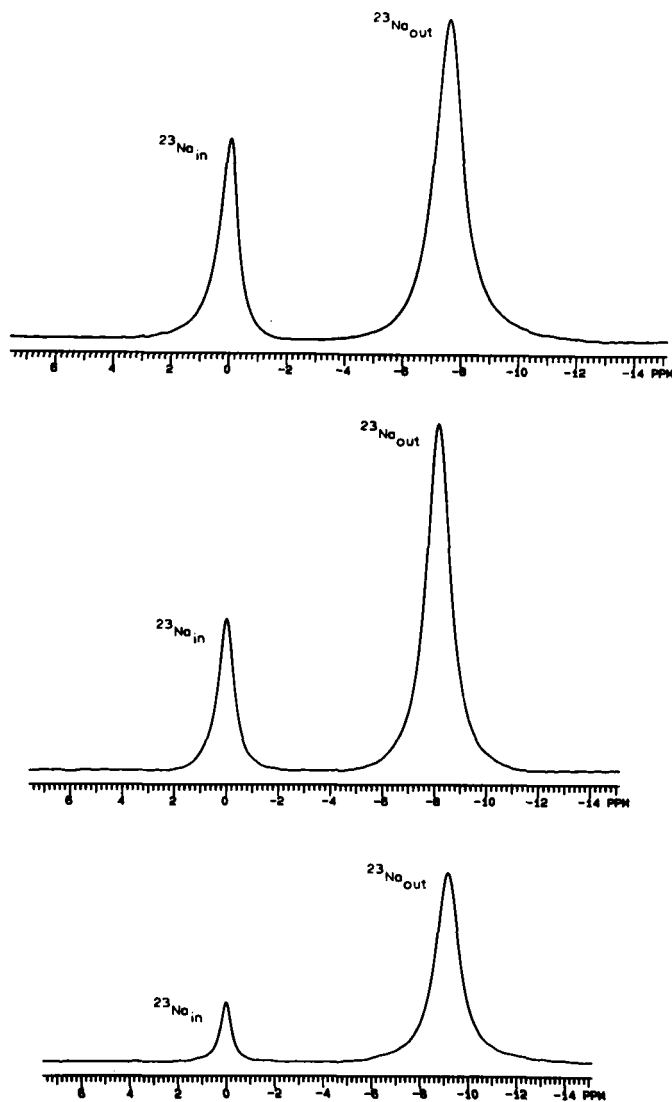


Fig. 5. ^{23}Na NMR spectra of gently packed erythrocytes after 24 h incubation with $100\ \mu\text{M}$ (upper trace) or $25\ \mu\text{M}$ (middle trace) lead or without lead (lower trace). The resonances of intracellular and extracellular sodium ions are labelled as $^{23}\text{Na}_{\text{in}}$ and $^{23}\text{Na}_{\text{out}}$, respectively.

Table 1. Intracellular Na^+ concentration after incubation of erythrocytes with lead acetate.

[Pb^{2+}] (μM)	Intracellular [Na^+] (mmol/litre cells)		
	$t = 3 \text{ h}$	$t = 7 \text{ h}$	$t = 24 \text{ h}$
0	4.7	4.7	4.4
10	4.7	4.7	5.2
25	5.9	8.9	16.7
100	10.8	14.1	22.6

t denotes the incubation time prior to ^{23}Na NMR-measurement.

In order to investigate whether added extracellular divalent cations, or EGTA change the observed effects of lead poisoning on intracellular sodium, experiments were carried out in the presence of an additional 3 mM EGTA or 6 mM Ca^{2+} in the incubation medium. When EGTA (3 mM) was present in the medium, incubation with 100 μM lead did not change the concentration of intracellular sodium significantly from that in untreated control cells, confirming that the increase in intracellular free sodium was caused by the presence of uncomplexed lead in the medium. The presence of an additional 6 mM calcium in the incubation medium also prevented the lead-induced rise in intracellular free sodium. These data indicate that lead caused the increase in internal sodium by binding at calcium sites of the plasma membrane.

^7Li , ^{133}Cs and ^{87}Rb NMR were then used to investigate the mechanism of perturbation of cellular sodium homeostasis by lead. For ^7Li NMR studies, the blood was diluted by a factor of two with a modified Hank's balanced salt solution containing LiCl (137 mM) instead of NaCl. ^7Li spectra were recorded at 194.3 MHz, using 90° pulses, an acquisition time of 0.41 s, and a recycle time of 20 s. For each spectrum, eight scans were collected and the FID was Fourier-transformed with a line-broadening of 40 Hz. The addition of 4 mM $\text{Dy}(\text{PPP}_i)_2$ was adequate to resolve intra- and extracellular ^7Li resonances. For ^{87}Rb NMR studies, the blood was diluted by a factor of two with a modified Hank's balanced salt solution, containing RbCl (5.4 mM) instead of KCl. ^{87}Rb spectra were recorded at 163.6 MHz, using 90° pulses, and an acquisition time of 0.013 s. Each spectrum was the time-average of 10 000 scans and the FID was Fourier-transformed with a line-broadening of 200 Hz. $\text{Dy}(\text{PPP}_i)_2$ was not used since it did not provide adequate resolution, but the small extracellular ^{87}Rb signal could be adequately subtracted using knowledge of haematocrit and the medium

⁸⁷Rb signal. ¹³³Cs experiments were carried out in a manner similar to that described above for ²³Na NMR, except that the blood was diluted by a factor of two with a modified Hank's balanced salt solution, containing 10.8 mM CsCl in place of KCl, before incubation. Because of the lower sensitivity of the ¹³³Cs nucleus, 10 mm o.d. NMR tubes were used. The ¹³³Cs spectra were recorded at 65.6 MHz, using 90° pulses of 40 μs duration, an acquisition time of 0.8 s, and a sequence recycle time of 10 s. Each spectrum was a time-average of 32 scans, and the FID was Fourier-transformed with a line-broadening of 5 Hz. Since the intracellular and extracellular ¹³³Cs resonances are resolved without any shift reagent, no Dy(PPP_i)₂ was added.

No significant change in the transmembrane influx of lithium ions was observed in lead-treated cells in comparison to paired controls. Lithium influx occurred at the initial rate of 2.4 ± 0.07 (mean \pm SE) mmol/litre cells/h in both control and 100 μM lead-treated erythrocytes. Furthermore, no significant effect of lead on intracellular rubidium or cesium influx was observed. Thus, in both control and lead-treated erythrocytes, NMR-measured rubidium and cesium influx occurred at the rate of 0.88 ± 0.04 and 0.65 ± 0.03 (mean \pm SE) mmol/litre cells/h, respectively.

Since lithium substitutes for sodium in Na⁺/H⁺ exchange,⁴⁰ the absence of an effect of lead on lithium influx indicates that lead-induced derangement of intracellular sodium is not due to increased influx via this exchanger. The absence of an effect of lead on influx of rubidium or cesium, which substitute for potassium,^{41,42} in the Na⁺-K⁺-ATPase reaction (sodium pump), suggests that a possible inhibition of the sodium pump by lead is also not responsible for these observations. Thus, it appears that lead must cause an increase in the permeability of the plasma membrane to sodium, and allow greater entry of sodium into the cell in its presence. However, such an ion permeability increase must be selective for sodium, since lithium entry was not enhanced by lead.

The data thus support the hypothesis that impaired cellular sodium homeostasis, involving a sodium-selective increase in membrane permeability, is one of the lesions, at the cellular level, associated with lead-toxicity. Because of the linkage between intracellular sodium and calcium via Na⁺/Ca²⁺ exchange, an elevation of intracellular sodium could lead to increased intracellular free calcium in those cells where this exchanger plays a role in maintaining calcium homeostasis, such as bone, brain and kidney cells, which are natural targets for lead toxicity. Lead-induced increases in internal sodium of vascular smooth muscle cells would cause vasoconstriction and hypertension, and may explain the correlation between blood lead levels and blood pressure.⁴³

2.1.3. General applications

Utilizing ^{23}Na NMR techniques, a variety of other interesting results have recently been reported. Using ^2H and ^{23}Na NMR, in combination with $\text{Dy}(\text{PPP}_i)_2$, Gupta *et al.* have reported the intracellular sodium concentration in the perfused rat kidney to be $27 \pm 2 \text{ mM}$.³² In a study of ionic changes during red cell maturation, Jelicks *et al.* compared intracellular ions in guinea-pig reticulocytes and erythrocytes, and found an increase in intracellular sodium from $5.5 \mu\text{mol/ml}$ cells in reticulocytes to $8.5 \mu\text{mol/ml}$ cells in mature erythrocytes.⁴⁴

Liebling and Gupta have reported a comparison of intracellular sodium in neoplastic and non-neoplastic human tissue.⁴⁵ Using surgical specimens, they compared NMR-measured intracellular free sodium concentrations of uterine leiomyoma and leiomyosarcoma, the benign and malignant tumours of smooth muscle, with their non-neoplastic counterpart myometrium, as well as that of colonic adenocarcinoma, a malignant tumour, with its non-neoplastic counterpart, colonic mucosa. Their results indicate a sizeable difference in the intracellular sodium concentration in neoplastic human tissue relative to its tissue of origin. Further, a direct correlation between the degree of cellular proliferative activity and/or tumour invasiveness and the intracellular sodium concentration was noted, suggesting that the sodium ion concentration may be one spectroscopic criterion for distinguishing benignity from malignancy. In another study of ionic alterations in a disease state, Jelicks and Gupta studied the derangement of intracellular ions in essential hypertension and discovered that the intracellular sodium ion concentration in the aortas of spontaneously hypertensive rats was $21.9 \pm 6.4 \text{ mM}$, two-fold higher than that in normotensive controls where it was only $10.1 \pm 1.8 \text{ mM}$.⁴⁶

In the Langendorff perfused rat heart, Jelicks and Gupta have reported an NMR-visible intracellular sodium concentration, measured using $\text{Dy}(\text{PPP}_i)_2$, of $10 \pm 1.5 \text{ mM}$ which irreversibly rose to $158 \pm 8 \text{ mM}$ or $96 \pm 5\%$ of the extracellular concentration, after prolonged (2 h) ischaemia;³¹ while Malloy *et al.*, using $\text{Tm}(\text{DOTP})$, reported a basal intracellular free sodium concentration of $6.2 \pm 0.5 \text{ mM}$ which was found to rise by about 54% upon brief (10 min) ischaemia, returning to basal values upon reperfusion, and to increase further during longer periods of ischaemia at a rate of 0.53 mM/min .¹¹ Their NMR-measured basal intracellular sodium concentration was only 20% of the total sodium detected by atomic absorption spectroscopy. Pike *et al.* reported a five-fold reversible increase in intracellular sodium in perfused ferret hearts after 20 min of ischaemia which returned to control levels after 35–40 min of reperfusion.¹⁷ The rise in sodium with ischaemia may arise from the fall in the available free energy of hydrolysis of ATP with

accumulation of P_i and ADP, due to the lack of oxygen, and consequent inactivity of $Na^+-K^+-ATPase$, and from an increase in Na^+/H^+ exchange, at the expense of the sodium gradient, at low intracellular pH. A significant role of Na^+/H^+ exchange in increasing intracellular sodium ions has been demonstrated using NMR by Anderson *et al.* who have reported a rate of sodium uptake similar to that seen in ischaemia upon intracellular acidification.⁴⁷ In the perfused frog heart, Powell *et al.* have examined Na^+/Ca^{2+} exchange by studying the effects of extracellular calcium concentration on the intracellular sodium concentration.⁴⁸ They found an inverse relation between extracellular calcium and intracellular sodium, suggesting a role for Na^+/Ca^{2+} exchange in the maintenance of intracellular sodium concentration, in agreement with the findings of Wittenberg and Gupta⁴⁹ on isolated cardiac myocytes. Inhibition of the $Na^+-K^+-ATPase$ along with decreased extracellular calcium resulted in an additive effect on intracellular sodium.

Jans *et al.* have used ^{23}Na NMR with $Dy(PPP)_2$ to show an increase in amiloride sensitive Na^+/H^+ exchange during induced intracellular acidification in a renal epithelial cell line.⁵⁰ They have also detected sodium-glucose cotransport with a stoichiometry of 1:1 in the same system.⁵⁰ Insulin effects on the glucose-induced uptake of sodium in *Neurospora crassa* have been shown by Greenfield *et al.*⁵¹ After an initial increase from 11.9 ± 1.4 mM to more than 14 mM intracellular sodium in the first 2 min of glucose exposure, insulin-treated cells showed a continued accumulation of sodium at the rate of $1.14 \pm 0.39\%/min$ while control cells lost sodium slowly at a rate of $-0.63 \pm 0.29\%/min$.

Cation transport studies of the erythrocytes of uremic patients revealed increased intracellular sodium, due to a defect in the $Na^+-K^+-ATPase$ characterized by a reduced number of enzyme pumps and the presence of an endogenous inhibitor of the ATPase in the plasma of these patients.⁵² ^{23}Na NMR measurements of $Na^+-K^+-ATPase$ activity⁵³ as well as a measurement of the maximal rate of active sodium efflux from human erythrocytes of 10.1 ± 1.0 mmol/h/litre of cells⁵⁴ have been reported.

2.2. ^{19}F NMR of fluorinated indicators

Exogenous fluorinated indicators for the measurement of intracellular sodium have been designed and synthesized by Smith *et al.*⁵⁵ Four characteristics are required of a useful fluorinated intracellular sodium indicator. It must exhibit a measurable change in its spectroscopic characteristics upon sodium binding in normal intracellular concentration ranges. It must have a high selectivity for sodium in the presence of physiological concentrations of competing ions, especially K^+ , Ca^{2+} and Mg^{2+} . It must be retained intracel-

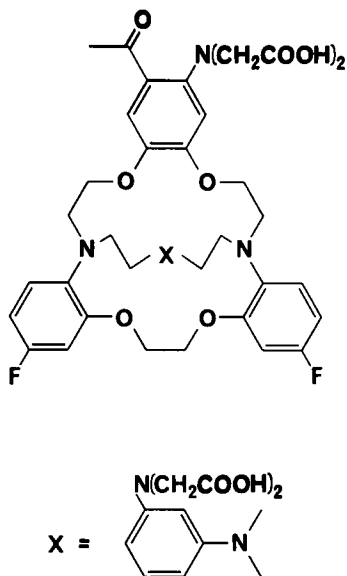


Fig. 6. The structure of FCryp-1.

lularly in concentrations sufficient for rapid NMR detection. Finally, it must not have an effect on cellular physiology or alter intracellular free ion concentrations. They synthesized the compound designated FCryp-1 (see Fig. 6) by incorporating ^{19}F -labelled aromatic rings into a cryptand structure. FCryp-1 has appropriate affinity for sodium ions ($K_d = 50 \text{ mM}$), and exhibits a 2 ppm chemical shift on sodium binding and some selectivity for Na^+ over K^+ (16-fold higher K_d and 50% less induced chemical shift for K^+). The sodium complex is in fast exchange with the uncomplexed indicator and, as a result, one resonance line is observed at the weighted average of the positions of the sodium-bound and unbound indicator. Calcium and magnesium ion complexes are in slow exchange and do not interfere. As a test, FCryp-1 was used to measure intracellular sodium in porcine lymphocytes.⁵⁵ The cells were loaded intracellularly with 0.21 mM FCryp-1 and suspended in a medium containing 10 μM FCryp-1 to provide an extracellular chemical shift reference at a known sodium ion concentration. From the measured ^{19}F chemical shift of intracellular FCryp-1, the intracellular sodium was estimated to be $13.8 \pm 1.8 \text{ mM}$, a value similar to that (17.1 mM) reported^{4,25} for human peripheral blood lymphocytes using ^{23}Na NMR with $\text{Dy}(\text{PPP}_i)_2$. Although calcium and magnesium complexes of FCryp-1 are uncharged and might be expected to be membrane-permeant, there was no detectable leakage of the indicator from lymphocytes over a period of 4 h.

Comparison of NMR-measured free sodium with total sodium measurements indicated that 37–48% of total sodium is free and detectable by this indicator, the rest is either bound or in subcellular compartments not accessible to the indicator. The ^{19}F and ^{23}Na NMR measurements in lymphocytes are consistent with the suggestion that all of the free sodium ions are detectable by NMR and that a strong quadrupolar interaction of a small proportion of free sodium ions does not lead to a loss of 60% of the ^{23}Na signal from the free pool.

2.3. Double-quantum coherence-transfer ^{23}Na NMR

It has been suggested^{56,57} that intracellular sodium may be discriminated from extracellular sodium non-invasively by means of a multiple-quantum coherence filter. It has been shown theoretically and verified experimentally that biexponentially relaxing sodium nuclei ($I = \frac{3}{2}$) can be processed through a state of multiple-quantum coherence by means of appropriate pulse sequences. Biexponential relaxation is to be expected for ^{23}Na ions outside the extreme motional-narrowing regime where the two outer transitions ($-\frac{3}{2} \rightarrow -\frac{1}{2}$ and $+\frac{1}{2} \rightarrow +\frac{3}{2}$) decay more quickly than the central transition ($-\frac{1}{2} \rightarrow +\frac{1}{2}$). A multiple-quantum coherence filter can therefore be used to pass NMR signal from biexponentially relaxing sodium ions and reject signal from monoexponentially relaxing sodium ions. Quantitative analysis of NMR data obtained with a multiple-quantum filter, however, requires that the filtered signal arise solely from the intracellular ions. Using a double-quantum filter, Jelicks and Gupta^{58,59} have recently shown that this is usually not the case and there is a sizeable contribution to the detected signal from extracellular sodium ions which must also relax biexponentially, presumably due to interactions with sites on the cell surface membrane and with plasma proteins. These findings have recently been confirmed by Hutchison *et al.*⁶⁰

In order to eliminate interference from extracellular ^{23}Na ions, Jelicks and Gupta used an anionic relaxation agent, such as gadolinium bis(tripolyphosphate)($\text{Gd}(\text{PPP}_i)_2^-$), to selectively quench the extracellular double-quantum coherence⁵⁹ (see Fig. 7). The quenching phenomenon was ascribed to rapid transverse relaxation of the extracellular ^{23}Na nuclei, via a non-quadrupolar mechanism, in the presence of the paramagnetic $\text{Gd}(\text{PPP}_i)_2$. Pure intracellular double-quantum filtered ^{23}Na NMR signal could be observed in this way.

Jelicks and Gupta also developed a procedure for quantitative measurement of intracellular sodium ion concentration from the double-quantum filtered ^{23}Na signal observed upon paramagnetic quenching of the extracellular coherence. A pulse sequence $90^\circ-\tau/2-180^\circ-\tau/2-90^\circ-\delta-90^\circ-t$ (acquisi-

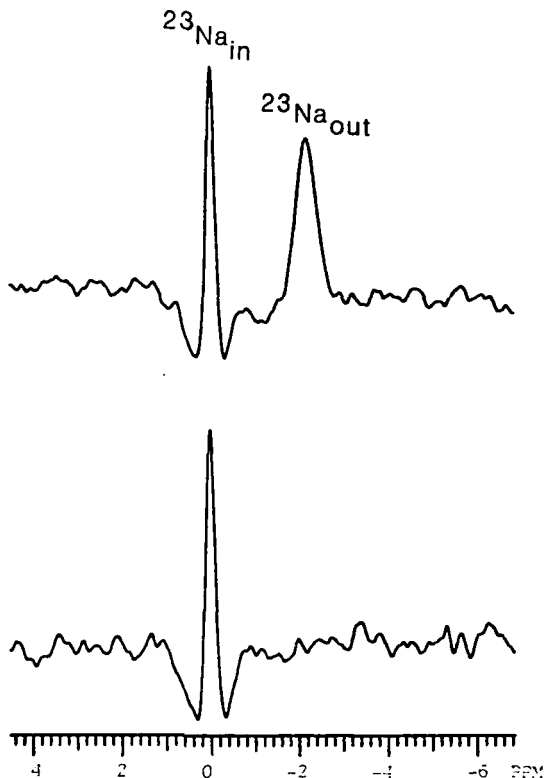


Fig. 7. Double-quantum filtered ^{23}Na NMR spectra of red cells showing an extracellular contribution in the presence of 1.5 mM $\text{Dy}(\text{PPP}_i)_2$ (upper trace). Addition of 1 mM $\text{Gd}(\text{PPP}_i)_2$ results in quenching of the shifted extracellular resonance (lower trace). (From Jelicks and Gupta.⁵⁹)

tion) with a 256-step phase cycling routine was used to obtain double-quantum filtered time-domain signal,

$$f(\tau, t) = M_0 \frac{3}{4} (e^{-\tau/T_{2s}} - e^{-\tau/T_{2f}}) (e^{-\delta/T_{dq}}) \cos 2\Omega\delta (e^{-t/T_{2s}} - e^{-t/T_{2f}}) e^{i\Omega t} \quad (6)$$

where T_{2s} and T_{2f} are the slow and fast transverse relaxation times, T_{dq} is the T_2 of the double-quantum coherence, τ is the double-quantum preparation time, δ is the evolution time, t is the variable time following the last pulse and Ω is the resonance offset.

Because of the low sensitivity of the double-quantum experiment, the data as a function of t were obtained at a fixed τ and were fitted to a difference of two exponentials. The τ , however, was appropriately chosen to be close to, though not necessarily at, the maximum of the function $(e^{\tau/T_{2s}} - e^{\tau/T_{2f}})$.

Since $\delta \ll T_{dq}$, and τ , Ω , and δ were known, the fit yielded M_0 , the equilibrium magnetization which was compared with an albumin standard to obtain the intracellular sodium ion concentration. A concentration of approximately 10 mM was obtained in this way for human red cells. Jelicks and Gupta⁵⁹ also demonstrated that increasing intracellular sodium ions with gramicidin caused a large increase in the double-quantum signal intensity. However, the increase was not proportional to the change in the intracellular sodium ion concentration. This was ascribed to alterations in the efficiency of the generation of the double-quantum filtered signal. A significant contribution of extracellular sodium ions to the double-quantum filtered signal has also been demonstrated in the perfused heart. As with blood, the extracellular signal could be quenched with $Gd(PPP_i)_2$. However, because of poor signal-to-noise of the double-quantum spectra,³¹ no attempt was made towards quantitative analysis in terms of concentrations.

In our experience, the multiple-quantum NMR, while useful for detecting changes in intracellular sodium, is inefficient and inconvenient to use as a quantitative tool. Its major advantage, however, is its non-invasiveness.

3. POTASSIUM MEASUREMENTS

Because of the low sensitivity of the ^{39}K nucleus ($< 1\%$ of that of ^{23}Na), NMR measurements of intracellular potassium have been less popular and researchers have often relied on NMR studies of ^{133}Cs and ^{87}Rb ions as substitutes for ^{39}K to indirectly obtain information on potassium ion transport in living systems. For example, Davis *et al.* have looked at the uptake of ^{133}Cs by erythrocytes and the perfused rat heart.⁶¹ The resulting ^{133}Cs spectra exhibited two sharp resonances, arising from intra- and extracellular cesium ions, separated in chemical shift by 1.0–1.4 ppm. Thus intra- and extracellular ^{133}Cs resonances were resolved without the use of a paramagnetic shift reagent. Although cesium uptake was slower than that of potassium, part of the uptake in erythrocytes did occur via the $Na^+-K^+-ATPase$. Using ^{87}Rb NMR in combination with $Dy(PPP_i)_2$, Williamson examined ^{87}Rb ion flux, in a smooth-muscle-like hamster cell line, induced by an antihypertensive agent which acts by opening potassium channels.⁶² However, the large linewidth of the ^{87}Rb signal in comparison to the $Dy(PPP_i)_2$ -induced shift is a clear disadvantage of this approach. Despite this difficulty, fluxes of ^{87}Rb in the perfused rat heart could be measured by Allis *et al.* where the ^{87}Rb flux was shown to follow the radioactive potassium flux.⁶³ In another paper, Allis *et al.* reported that the NMR-determined unidirectional ^{87}Rb flux was a good measure of net intracellular potassium

influx in the perfused rat kidney.⁶⁴ They also determined the ⁸⁷Rb efflux rate and measured no change in it upon induction of hypoxia.

3.1. Shift reagent aided ³⁹K NMR

As is the case for sodium ions, the measurement of intracellular potassium ions is often accomplished through the use of anionic paramagnetic shift reagents.^{26,28,65-68} Most of the sodium shift reagents also shift the extracellular ³⁹K signal relative to the intracellular signal, resulting in adequate resolution of intra- and extracellular potassium ions.

The NMR visibility, or the NMR detectability,^{22,65} of intracellular potassium has also been addressed in a manner similar to that for the ²³Na nucleus. In erythrocytes potassium appears to be 100% detectable^{26,68,69} while in many other tissues, only 20–40% of intracellular potassium is reported to be detectable.^{28,66,67} As for the sodium nucleus, the proposed explanations for potassium invisibility involve compartmentation of some ions in a slowly exchanging pool or pools with resonances which are too broad to be detected under usual conditions, or the existence of multiple pools in fast exchange exhibiting biexponential transverse relaxation which may result in broadening and loss of up to 60% of the ³⁹K signal. Quadrupole splitting as a mechanism for possible reduction in visibility of the ²³Na, and presumably also ³⁹K, NMR signal, has been excluded in skeletal muscle and cat brain tissues.⁷⁰ Burstein *et al.*, observing ³⁹K NMR, carried out experiments to measure exchange between the NMR detectable pools of intra- and extracellular potassium.⁶⁵ When a ⁴¹K perfusate replaced the normal ³⁹K perfusate in a Langendorff perfused rat heart, the intracellular potassium resonance fell to a level comparable to the noise in approximately 15 min. When the perfusate was switched back to the ³⁹K medium the signal also returned to original levels.

Rashid *et al.* have examined possible causes of the decreased detectability of intracellular potassium.²² They studied rat thigh muscle and initially observed only $57 \pm 5\%$ of the intracellular potassium at a field strength of 7.0 T. The detectability was defined as the amount of potassium detected by NMR divided by the amount of potassium detected by flame photometry. Using standard broadband probes with Helmholtz coils and a one-pulse sequence ($90^\circ\text{-acq-}t$)_n, the NMR detectability of intracellular potassium in excised rat muscle showed a correlation with the magnetic field strength. Specifically, at 4.7, 5.8, 8.0 and 9.4 T, the NMR detectability was $28 \pm 4\%$, $46 \pm 9\%$, $57 \pm 5\%$, and $89 \pm 4\%$, respectively. It was suggested that at lower fields, some of the peak components are broader because of field-dependent relaxation effects; and at higher fields there is better sensitivity and

less baseline roll. They found that the use of common methods for reducing the baseline roll was contributing to the loss of detectability. As expected, increasing the receiver deadtime, the time delay between the excitation pulse and the start of data acquisition, improved baseline but significantly reduced the magnitude of signal from broad resonances. Unfortunately, increasing the receiver deadtime also makes simultaneous phasing of peaks from intra- and extracellular volumes difficult. Other methods used to reduce baseline problems, like baseline subtraction using curve-fitting procedures, can also reduce the signal from broad components of resonances. Upon improving signal-to-noise by using a well-shielded solenoid transmitter/receiver coil probe (which also held the sample in a transverse orientation with respect to the B_0 field), along with a pulse sequence designed to reduce baseline roll, $(90_x^\circ - (\text{acq/add}) - 180_x^\circ - \tau - 90_x^\circ - (\text{acq/subtract}))$, where $\tau = 5 \mu\text{s}$ is short compared to relaxation times), and using a receiver deadtime which was a compromise between signal loss and baseline roll, Rashid *et al.*²² were able to demonstrate improved muscle potassium detectability of $100 \pm 10\%$. These results kindle new hope for the measurement of intracellular potassium in biological tissues.

3.2. Multiple-quantum filtered ^{39}K NMR

The use of multiple-quantum filters to select biexponential relaxing ions can be used to attenuate the resonance of extracellular potassium relative to that of intracellular ^{39}K . This selection occurs because the already larger intracellular ^{39}K NMR signal is transmitted more efficiently through the filter due to the greater degree of its biexponential character. Seo *et al.* studied the perfused rat salivary gland by double-quantum coherence transfer ^{39}K NMR.⁷¹ Most of the double-quantum filtered ^{39}K signal arose from the intracellular potassium and the authors interpreted the existence of only two components of transverse relaxation (T_2) to reflect a single homogeneous population of intracellular potassium. They determined a correlation time of about 2.5×10^{-8} s and a quadrupolar coupling constant of about 1.4 MHz for this potassium ion pool.

Double-quantum filtered ^{39}K NMR studies of Langendorff perfused rat hearts were undertaken by Hiraishi *et al.*; and the data were analysed to obtain transverse relaxation rate constants for intracellular potassium.⁷² The authors confirmed that the observed signal was originating from intracellular potassium by the addition of DyTTHA^{3-} which revealed no shifted extracellular double-quantum signal. As mentioned above for ^{23}Na ,⁵⁸ an already small extracellular double-quantum signal could be further quenched by the

paramagnetic reagent and will be hard to detect. It should be noted that the sensitivity of double-quantum filtered ^{39}K NMR for detecting intracellular ions is an order of magnitude lower than that of single-quantum ^{39}K NMR, which itself is quite insensitive.

3.3. Non-invasive subtraction procedure

Murakami *et al.* have measured the intracellular potassium in perfused rat mandibular salivary gland by an inversion recovery method which takes advantage of the fact that the intracellular signal relaxes faster than the extracellular signal.⁷³ They report changes in intracellular potassium concentrations and fluxes in response to various interventions. However, accurate quantitation of concentrations using this approach requires knowledge of intracellular ^{39}K relaxation times, which are usually unknown. Therefore, we considered the possibility of non-invasively measuring intracellular potassium by estimating and subtracting the contribution of extracellular ions.

Fortunately, unlike the situation with sodium, the extracellular concentration of potassium is low (~ 5 mM) in comparison to intracellular potassium (~ 140 mM) and therefore the contribution of extracellular potassium to the total tissue ^{39}K signal is not dominant. It is possible to estimate the extracellular contribution to the tissue ^{39}K signal from the measured medium ^{39}K signal if the fractional extracellular volume of the tissue is known. The latter could be obtained using ^2H and ^{35}Cl NMR (or ^{23}Na NMR since internal sodium ordinarily contributes very little to the tissue total sodium signal) as described above. We compared the results obtained by this approach for human blood with those reported using $\text{Dy}(\text{PPP}_i)_2$ ⁶⁸ and found them quite acceptable. We have now applied the non-invasive subtraction method to the intact rat aorta which presents a double challenge because of its low tissue mass and the low sensitivity of the ^{39}K nucleus. In the perfused rat aorta the ratio of intracellular to vascular volume is small so that the ^{39}K signal from the extracellular compartment can be on the order of the intracellular signal. The low tissue mass, only 100–200 mg, required that data be acquired for up to 2 h to get an adequate signal-to-noise ratio. For our study, 250–300 g Sprague–Dawley rats were anaesthetized with pentobarbital (100 mg/kg i.p.) and were given heparin (1500 Units/kg i.p.) to reduce clotting. To increase tissue mass for obtaining better spectral signal-to-noise, the aortas from two rats were removed, trimmed, simultaneously cannulated, and perfused as described by Jelicks and Gupta.⁴⁶ The perfusate consisted of a Krebs buffer containing (mM) NaCl (120), KCl (4.8), MgSO_4 (1.2), CaCl_2 (1.3), NaHCO_3 (24), glucose (10), pyruvate (10), and 2% $^2\text{H}_2\text{O}$ maintained at 37°C and

bubbled with a 95% O₂/5% CO₂ gas mixture. All spectra were obtained on a Varian VXR-500 spectrometer operating at 23.3 MHz for ³⁹K, 49.0 MHz for ³⁵Cl, 76.7 MHz for ²H, and 132.2 MHz for ²³Na. For recording ³⁹K spectra, we used 90° pulses, a receiver deadtime of 30 μs and a pulse recycle time of 0.205 s with a spectral width of 10 000 Hz. A total of 30 000 FIDs were accumulated for each spectrum and 50 Hz of exponential line-broadening was applied in processing.

To measure fractional extracellular volume, ³⁵Cl spectra were acquired using 90° pulses, a recycle time of 0.245 s and a spectral width of 5200 Hz. For these spectra, 1000 FIDs were accumulated, and the data were processed using 10 Hz line-broadening. By using an inductor stick in parallel with the tuned circuit, it was possible to record the ²H resonances using the same rf coil used for ³⁹K and ³⁵Cl NMR. This allowed the measurements to be performed without changing the probe and assured that intracellular volume measurements were done on the same region of the aorta as were the potassium measurements. The ²H spectra were recorded using 90° pulses with a spectral width of 5000 Hz, an acquisition time of 0.5 s, and a recycle time of 1.0 s. In this case, 100 FIDs were accumulated, and the data were processed with 30 Hz of exponential line-broadening. The ²³Na spectra were recorded with a spectral width of 10 000 Hz, and a recycle time of 0.205 s. A total of 100 FIDs were recorded and 10 Hz of exponential filtering was applied. For quantitation of ³⁹K signals, a perfusate sample filling the sensitive volume of the coil was run at each nucleus under the same conditions as the aortas.

Representative spectra of each nucleus are shown in Fig. 8; panel (A) shows tissue (left trace) and medium (right trace) ³⁹K signals, panel (B) shows tissue (left trace) and medium (right trace) ²³Na signals, panel (C) shows tissue and medium ²H signals, and panel (D) shows extracellular (left trace) and medium (right trace) ³⁵Cl resonances. As suggested by studies of other tissues,^{34,35,74} the intracellular ³⁵Cl was assumed too broad to detect. The data allow calculation of the total tissue water as a fraction of the sensitive volume of the coil and of the extracellular water as a fraction of the sensitive volume. The extracellular ³⁹K signal then is simply represented by the appropriate volume fraction of the perfusate ³⁹K signal.

Figure 9 shows this extracellular contribution (upper trace) calculated by multiplying the perfusate ³⁹K signal with a factor representing the extracellular chloride space as a fraction of the total sensitive volume (i.e. the ratio of tissue and perfusate ³⁵Cl signals). The extracellular contribution thus calculated is compared with the ³⁹K resonance of the perfused aortic tissue (lower trace). The ²³Na spectra were used to check the ³⁵Cl extracellular volume measurement. Since the aortic intracellular sodium concentration is relatively small (~10 mM) and the intracellular volume is also small, the intracellular sodium peak should be less than 1% of the tissue ²³Na

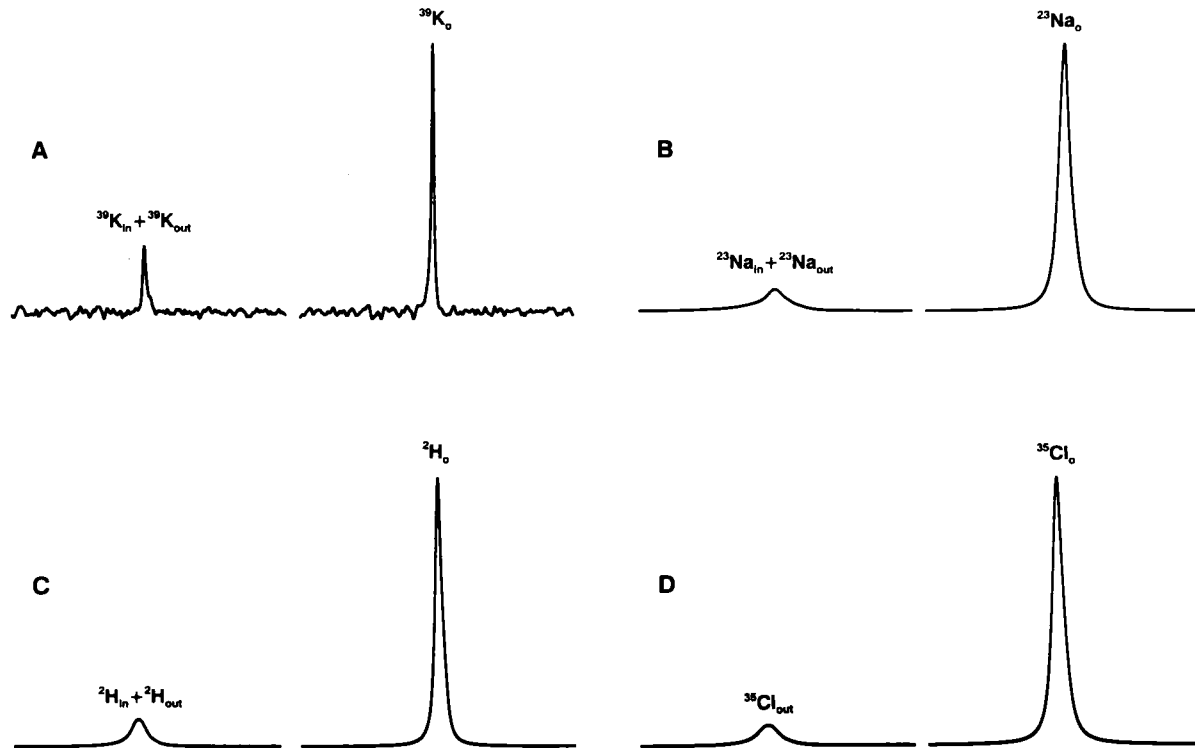


Fig. 8. (A) ^{39}K NMR spectra of potassium (intra- plus extracellular) in the perfused rat aorta (left trace) and potassium in a perfusate sample run under the same conditions (right trace). (B) ^{23}Na spectra of aortic tissue (left trace) and perfusate sample (right trace). (C) ^2H spectra of aorta (left trace) and perfusate sample (right trace). (D) ^{35}Cl spectra of aorta (left trace) and perfusate sample (right trace).

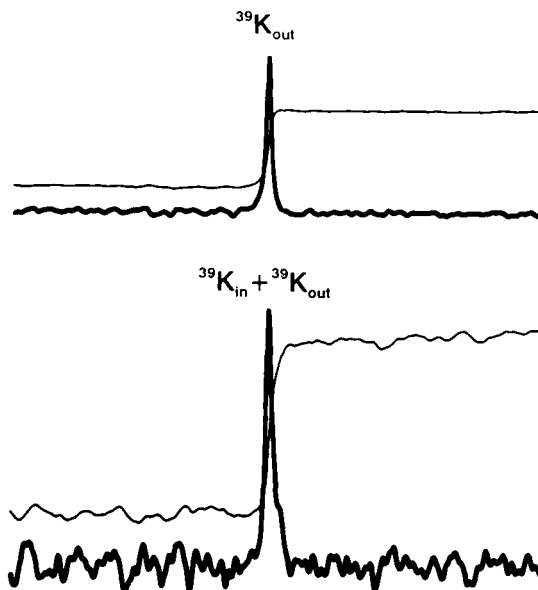


Fig. 9. The ^{39}K resonance of the perfused rat aorta (lower trace, labelled $^{39}\text{K}_{\text{in}} + ^{39}\text{K}_{\text{out}}$) along with the extracellular contribution (upper trace, labelled $^{39}\text{K}_{\text{out}}$). The extracellular signal was derived by multiplying the resonance of the perfusate sample with the factor representing the extracellular volume as a fraction of the sensitive volume, as described in the text.

resonance; therefore the tissue ^{23}Na resonance also provided a good estimate of the extracellular space. The intracellular potassium ion concentration was calculated using the following equation:

$$[\text{K}]_{\text{in}} = \frac{A_{\text{tissue}}^{\text{K}} - \left(A_{\text{o}}^{\text{K}} \times \frac{A_{\text{out}}^{\text{Cl}}}{A_{\text{o}}^{\text{Cl}}} \right)}{A_{\text{o}}^{\text{K}} \times \frac{A_{\text{out}}^{\text{Cl}}}{A_{\text{o}}^{\text{Cl}}}} \times \frac{\frac{A_{\text{out}}^{\text{Cl}}}{A_{\text{o}}^{\text{Cl}}}}{\frac{A_{\text{tissue}}^{\text{D}}}{A_{\text{o}}^{\text{D}}} - \frac{A_{\text{out}}^{\text{Cl}}}{A_{\text{o}}^{\text{Cl}}}} \times [\text{K}]_{\text{out}} \quad (7)$$

where A denotes the area of a resonance peak, the superscript denotes the nucleus, and the subscript identifies the sample. In comparison to (2), the first term represents $A_{\text{in}}/A_{\text{out}}$, and the second term represents $V_{\text{out}}/V_{\text{in}}$. The basis for the calculation of concentration is essentially identical to that presented in (3) for the determination of intracellular sodium ions. An NMR-detectable intracellular potassium ion concentration of 22mM was obtained in this way. The NMR visibility of ^{39}K in the aortic tissue has not been adequately investigated. It should be noted, however, that free intracellular aortic sodium was found to be more than 90% visible in the studies of Jelicks and

Gupta.⁴⁶ The above subtraction procedure should be directly applicable for potassium measurements *in vivo*.

See Note added in proof, on p. 266.

4. ¹⁹F NMR MEASUREMENTS OF INTRACELLULAR FREE CALCIUM IONS

4.1. Methodological considerations

Biological ¹⁹F NMR is almost exclusively used in conjunction with fluorinated compounds which can be introduced into biological systems. The ¹⁹F NMR indicator usually used for the measurement of intracellular free calcium is 1,2-bis(2-amino-5-fluorophenoxy)ethane-*N,N,N',N'*-tetraacetic acid (5F-BAPTA) whose characteristics have been described.⁷⁵ Various divalent cations affect the chemical shift of the 5F-BAPTA ¹⁹F resonance to different degrees and generally shift the resonance downfield. Since the intracellular calcium is in slow exchange with the indicator and is at non-saturating concentrations, two peaks characteristic of free and calcium-bound 5F-BAPTA are observed. The concentration of intracellular free calcium can then be determined by,

$$[\text{Ca}^{2+}]_{\text{in}} = K_d \left(\frac{A_{\text{bound}}}{A_{\text{free}}} \right) \quad (8)$$

where A_{bound} is the area of the ¹⁹F resonance arising from the Ca^{2+} -5F-BAPTA complex, A_{free} is the area of the resonance arising from the uncomplexed 5F-BAPTA, and K_d is the apparent dissociation constant for the complex. The affinity of 5F-BAPTA for Na^+ , K^+ , and Mg^{2+} cations is low and they exchange rapidly on the NMR timescale and thus do not interfere with intracellular free calcium measurement. Zinc, another intracellular divalent cation, is in slow exchange, but gives rise to a distinct Zn-5F-BAPTA resonance which does not interfere in free calcium ion measurements (see Fig. 10).

The K_d of the Ca-5F-BAPTA complex has been a subject of controversy in the literature. In their first paper on the subject, Smith *et al.* reported a K_d for Ca-5F-BAPTA of 710 nM at 37°C in the presence of 1 mM Mg^{2+} using citrate buffer to calibrate free calcium in the solutions used.⁷⁵ Measurements using the fluorescent indicator fura-2 have led to the report of a K_d of 635 nM at 37°C,⁷⁶ but it has been pointed out that the K_d for the Ca-Fura-2 complex itself is somewhat uncertain.⁷⁷ In sharp disagreement with the above, Marban *et al.* have reported a K_d of 308 ± 26 nM at 30°C and pH 7.2^{77,84} using a

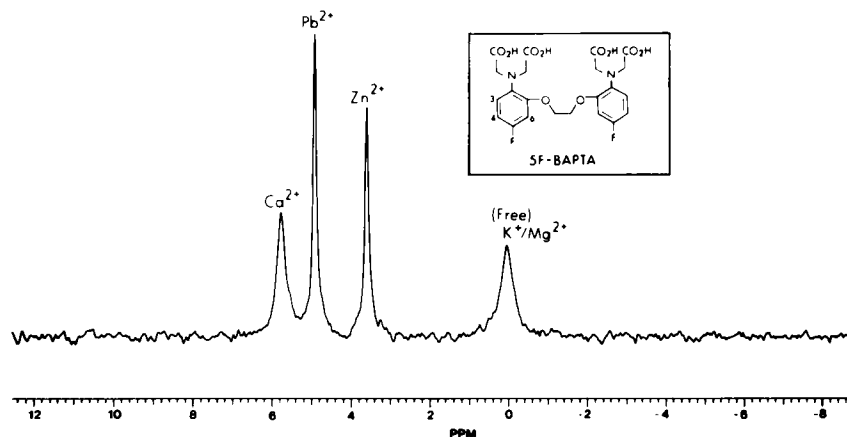


Fig. 10. ^{19}F NMR spectrum of 5F-BAPTA in a solution containing KCl, MgCl_2 , ZnSO_4 , $\text{Pb}(\text{C}_2\text{H}_3\text{O}_2)_2$ and CaCl_2 . The resonance peaks are as indicated for free 5F-BAPTA (K^+ , Mg^{2+}) and each M^{2+} -5F-BAPTA complex are identified. Inset represents the structure of 5F-BAPTA. (From Schanne *et al.*⁷⁸)

computer program to calculate the free calcium concentrations in their solutions from the analytically determined absolute K_d values for the reactions of EGTA with Ca^{2+} and H^+ at the appropriate temperature and ionic strength. To resolve these controversies and to eliminate complications due to possible formation of ternary complexes involving Ca-5F-BAPTA and citrate, Fura-2, or EGTA, Dowd and Gupta³⁹ and Jelicks and Gupta⁴⁶ remeasured K_d using a well-calibrated calcium-selective electrode to directly measure free calcium ions and the ^{19}F NMR to measure the calcium-bound to free 5F-BAPTA concentration ratio in the same solutions. Dowd and Gupta thus obtained a K_d of 554 ± 18 nM at 22°C and Jelicks and Gupta report a K_d of 492 ± 33 nM at 37°C and pH 7.2. The same approach yielded a similar K_d of 500 ± 20 nM at 30°C .⁷⁸ In agreement with these values, a K_d of 540 nM at 30°C and pH 7.1 has been measured by Kirschenlohr *et al.* using UV spectroscopy.⁷⁹ Thus it appears that the controversy is finally resolved and that a K_d value in the range 492–554 nM would be widely acceptable.

The membrane-impermeant 5F-BAPTA is loaded into cells using the membrane-permeable acetoxymethyl ester form (5F-BAPTA-AM). Once inside the cell, endogenous intracellular esterases cleave the ester linkages forming formaldehyde and the free indicator, the 5F-BAPTA acid, which, due to its charge, now cannot readily escape from the cell. Fluorescent calcium indicators are loaded into the cell in the same manner and several concerns have been expressed about the technique, namely incomplete de-esterification, compartmentalization into mitochondria, and disproportionate ac-

cumulation of the indicator in endothelial cells.⁷⁷ Marban *et al.* separated cytosol and mitochondria from homogenates of hearts loaded with 5F-BAPTA. For the cytosolic fraction, the 5F-BAPTA concentration was estimated to be 0.1–0.3 mM from the ¹⁹F spectra. In almost all cases, not enough ¹⁹F was detected in the mitochondrial fraction to accurately measure the 5F-BAPTA concentration. When the mitochondria were lysed with detergent, allowing complete calcium complexation of any 5F-BAPTA present, the concentration of released 5F-BAPTA was estimated to be at most 3% of that in the cytosolic fraction. Marban *et al.* also provided evidence which suggests that partially de-esterified 5F-BAPTA binds calcium with much lower affinity than that of the tetra-anion, so that its presence in a system would cause underestimation of intracellular free calcium. However, by examining ¹⁹F spectra during perfusion of an intact heart with 15 μ M 5F-BAPTA-AM, Marban *et al.*⁷⁷ found simultaneous appearance of free and calcium-bound peaks whose intensity increased with time and there was no evidence for the presence of partially de-esterified 5F-BAPTA in either heart homogenates or perfused whole hearts. Using bradykinin, which increases endothelial cell free calcium, they also showed, from the observed absence of an increase in measured free calcium ions, that in the heart 5F-BAPTA, unlike indo-1, is not more concentrated in endothelial cells and will not give false readings of myocardial calcium. In contrast, Badar-Goffer *et al.* have reported that in 5F-BAPTA loaded superfused cerebral cortical brain slices, about 55% of the 5F-BAPTA-AM was de-esterified, and the remaining 45% was bound as tetraester to membranes so that its resonances would be broadened beyond detectability.⁸⁰ More than 90% of the de-esterified 5F-BAPTA was shown to be in cytosolic fraction of the cells with less than 1% in mitochondria or microsomes. The NMR-visible 5F-BAPTA was found to escape slowly from the tissue with a $t_{1/2}$ of 4 h.

4.2. General applications

Schanne *et al.* have reported the use of 5F-BAPTA in the simultaneous measurement of intracellular free calcium and intracellular free lead in the perfused, cultured osteoblastic bone cell line ROS 17/2.8.⁷⁸ They reported apparent K_d values for Pb^{2+} -5F-BAPTA and Ca^{2+} -5F-BAPTA of 2×10^{-10} M and 5×10^{-7} M, respectively at 30°C, pH 7.1, and 0.5 mM Mg^{2+} . Intracellular free calcium was determined to be 128 ± 14 nM and was found to almost double within the first 30 min upon treatment with parathyroid hormone (PTH) but later returned to baseline levels.⁸¹ The group also measured the initial intracellular indicator concentration in their cells to be less than or equal to 0.5 mM which decreased with an apparent first-order rate

of 12%/h due to leakage of indicator. They, however, noted that their medium flow rate of 2 ml/min would adequately wash away any leaked indicator and thus the extracellular indicator would not interfere with the measurement.

The same group later reported that treatment of osteoblastic bone cells with lead at concentrations of 5 and 25 μM produced sustained 50 and 120% increases in intracellular calcium, respectively, over a 5 h time course.³⁷ At the higher lead concentration, intracellular free lead was measured to be $29 \pm 8 \text{ pM}$. In a further study of the effects of extracellular lead and PTH on ROS 17/2.8 cells, Schanne *et al.* have reported that pretreatment with 5 μM lead, which caused a 50% rise in calcium to $155 \pm 23 \text{ nM}$, diminished the response of the cells to PTH treatment. In the absence of lead, PTH caused the intracellular free calcium concentration of the cells to rise from a basal level of $105 \pm 25 \text{ nM}$ to a concentration of $260 \pm 24 \text{ nM}$. In cells preincubated with lead, the intracellular calcium concentration rose only 25% to $193 \pm 22 \text{ nM}$. It was noted that although treatment with lead reduced the PTH-induced rise in intracellular free calcium, it had no effect on the PTH-induced rise in intracellular cyclic AMP. These data showed that different mechanisms were operative in causing the PTH effects on intracellular calcium and on cyclic AMP and extended the hypothesis that an early toxic effect of lead is perturbation of calcium homeostasis at the cellular level.

Extending these studies further, Schanne *et al.* have reported a basal intracellular free calcium of $106 \pm 14 \text{ nM}$ in the neuroblastoma \times glioma hybrid cell line, NG108-15.³⁸ Two-hour treatment with 5 μM lead gave rise to a two-fold increase in intracellular calcium to $200 \pm 24 \text{ nM}$, a measurable intracellular free lead concentration of $30 \pm 10 \text{ pM}$, and the observation of intracellular free zinc corresponding to zinc concentrations of 1–2 nM using a K_d of 7.9×10^{-9} for the Zn-5F-BAPTA complex.

The observation of a lead-induced rise in intracellular free calcium in a neuronal cell line, provides evidence for a role for calcium in the neurotoxicity of lead. In another study of lead effects on intracellular free calcium, Dowd and Gupta have reported that the treatment of human platelets with extracellular lead at 1, 5, 10 and 25 μM resulted in average increases in intracellular free calcium of 39, 91, 134, and 172%, respectively above the basal level of $172 \pm 8 \text{ nM}$.³⁹ This calcium increase was shown by atomic absorption to be due, in part, to increased influx of extracellular calcium. This is the first report demonstrating that environmental lead concentrations of approximately 1 μM can lead to observable changes in intracellular free calcium after only 3.5 h. The data also provided an explanation for the previously reported effects of lead on platelet reactivity. The authors further suggest that the linkage between blood lead levels and hypertension may

be mediated by a lead-induced increase in intracellular free calcium in vascular smooth muscle cells.

In the first published NMR study of rat aorta, intracellular free calcium was compared in the aortas of normal and spontaneously hypertensive rats by Jelicks and Gupta.⁴⁶ The thoracic aortas of two rats, removed and trimmed of visible fat and other perivascular tissue, were attached to a single perfusion line by means of a Y-joint. The distal ends of the aorta were tied together, forcing the perfusate through the intercostal artery branches. The simultaneous perfusion of two aortas, each of which weighed only 50–100 mg wet, provided adequate signal-to-noise and allowed measurements to be made in reasonable periods of time (an hour). The study has shown that genetic essential hypertension is associated with significantly increased intracellular calcium. Aortic intracellular free calcium in spontaneously hypertensive rats with systolic blood pressures of 159 ± 6 mmHg was 277 ± 28 nM, while normotensive rats with systolic blood pressures of 123 ± 8 mmHg had measured intracellular calcium of only 151 ± 26 nM. It was postulated that these changes may be mediated by decreased Ca^{2+} pump activity, decreased calcium-binding ability of the membranes, alterations in $\text{Na}^+/\text{Ca}^{2+}$ exchange, or may be secondary to observed changes in intracellular sodium in hypertension.

Alterations in intracellular free calcium concentration during red cell maturation were studied by Jelicks *et al.* who reported values of 99 and 33 nM for guinea-pig reticulocytes and mature erythrocytes, respectively.⁴⁴ No evidence for $\text{Na}^+/\text{Ca}^{2+}$ exchange was found in these cells and it was suggested that the increased intracellular calcium in reticulocytes may be due to increased membrane permeability to external calcium.

Extending NMR measurements of intracellular free calcium to cerebral tissue, Bachelard *et al.* report concentrations of 350 and 480 nM in 5F-BAPTA-loaded superfused cerebral cortical brain slices at external calcium concentrations of 1.2 and 2.4 mM respectively.⁸² They showed that membrane depolarization caused by increasing external potassium increased intracellular free calcium, but, at the lower extracellular calcium concentration, 5F-BAPTA-loaded slices showed decreased viability by ^{31}P NMR and an inability to completely recover from high potassium treatment. In another paper by the group, Badar-Goffer *et al.* report an intracellular free calcium of 380 ± 71 nM, at 37°C and 2.4 mM external calcium, which remained stable for over 5 h.⁸⁰ Intracellular free calcium in brain cells was increased by high extracellular potassium, low extracellular sodium, and by the addition of the calcium ionophore A23187. An "overshoot" to lower free calcium concentrations was seen on recovery from high extracellular potassium but the intracellular calcium was resistant to changes in extracellular calcium. Ben-Yoseph *et al.* have looked at the effects of *N*-methyl-D-aspartate (NMDA) on intracel-

lular free calcium in the same cortical slice preparation.⁸³ Treatment with 10 μM NMDA without extracellular magnesium resulted in the expected rise in intracellular calcium and a 42% decrease in phosphocreatine (PCr) along with a 55% increase in the P_i/PCr ratio. The decrease in phosphorylation potential preceded the change in calcium and was irreversible. The presence of 1.2 mM extracellular magnesium prevented the change in free calcium but not the decrease in PCr; thus the decrease in phosphorylation potential is not caused by increased intracellular calcium.

Marban *et al.* loaded ferret hearts with 5F-BAPTA and noted that loading was accompanied by a significant negative inotropic effect.⁸⁴ At 2 mM extracellular calcium, the per cent depressions in developed pressures were 69% at 30°C and 82% at 37°C. This effect is expected because of intracellular calcium buffering by 5F-BAPTA. They found that raising extracellular calcium to 8 mM caused developed force to return to normal levels, presumably because of increased calcium influx during the action potential, although scavenging of other ions may be involved as well.⁷⁹ At 30°C, the hearts maintained a relatively steady intracellular 5F-BAPTA concentration for more than 2 h, while at 37°C there was a slow decrease in the 5F-BAPTA concentration. In their paper examining the changes in intracellular calcium during ischaemia and reperfusion in the perfused ferret heart, Marban *et al.* have noted a resting time-averaged calcium of about 300 nM at 30°C in the presence of 8 mM external calcium.⁷⁷ This value was noted to rise to about 900 nM after 20 min of ischaemia and to return to normal after 5 min of reperfusion. Qualitatively similar but smaller changes were observed at 2 mM external calcium, while at 37°C, the ischaemia-induced rise in free calcium occurred more rapidly. It should be noted that the time-averaged free calcium in the beating heart may be slightly misestimated due to the non-linear response of the fluorinated indicator to changes in calcium concentration and due to the existence of spatial or temporal inhomogeneities in the intracellular free calcium. As a consequence of these systematic errors, time-averaged intracellular free calcium measurements by ^{19}F NMR may provide a lower limit to the true value of intracellular free calcium in the beating heart.⁷⁷

In an application of ^{19}F NMR for the measurement of intracellular free calcium in the perfused rat kidney, Gupta *et al.* have measured an intracellular free calcium of 256 ± 50 nM using a K_d of 545 nM.³² Following a 10 min period of ischaemia, ^{19}F NMR gave an intracellular calcium of approximately 660 nM, which did not completely return to baseline upon reperfusion. This suggests that even short ischaemic periods may lead to irreversible cell injury and derangement of intracellular ions in part of the isolated kidney.

The use of gated ^{19}F NMR with 5F-BAPTA and cardiac pacing has allowed the measurement of calcium transients in the cardiac cycle.^{79,85}

Kirschenlohr *et al.* have broken a cardiac cycle into sixteen 50-ms intervals and collected ^{19}F spectra at these points.⁷⁹ The data show a rise in intracellular calcium from an initial value of $0.5\ \mu\text{M}$ to a value of $1.5\text{--}2.0\ \mu\text{M}$ at 150 ms after stimulation. Marban *et al.* have measured the calcium transients along with gated ^{31}P spectra and have reported that low flow significantly decreases the calcium transient and develops pressure.⁸⁴ This observation, they suggest, could be part of a negative feedback process which reduces the energy demands of the heart under conditions of low flow at the expense of decreased force generation. A decrease in calcium entry during each cardiac cycle would result in less calcium which has to be removed before the next.⁸⁵ During ischaemic contracture, Koretsune and Marban have shown that in the ferret heart although intracellular calcium increases up to $3\ \mu\text{M}$ after 30–35 min of ischaemia, force starts to rise only after 40 min, when the ATP levels are $< 10\%$ of control values.⁸⁶ Upon inhibition of glycolysis, decreases in ATP and consequent increases in force occur before a significant rise in intracellular calcium, arguing for the formation of rigour crossbridges as the force generator and ATP depletion as the primary event in ischaemic contracture. It has also been shown that shortly after peak contracture, reflow can return intracellular calcium to baseline values indicating that the calcium increase precedes lethal myocardial injury and may add to the depletion rate of ATP leading to irreversible cell damage.⁸⁷

4.3. Free calcium changes during cell differentiation

In order to explore changes in the intracellular free calcium during cellular differentiation, we have studied the human leukaemia cell line HL-60. HL-60 cells were maintained in suspension culture in 75-cm^3 flasks in RPMI-1640 medium supplemented with 25 mM HEPES buffer, 27 mM sodium bicarbonate, 10 mM glucose, 40 mg/litre gentamicin, 50 mg/litre fluorocytosine and 5% heat-inactivated fetal bovine serum. The cells were induced to differentiate by the addition of 5 mM *N,N'*-hexamethylene-bis-acetamide (HMBA) for 7 days. They have been shown to be $99 \pm 1\%$ differentiated by Wright-Giemsa staining, and $91 \pm 2\%$ by NBT reduction after 7 days of treatment with HMBA.⁸⁸ The cells were loaded with 5F-BAPTA by incubation with $10\ \mu\text{M}$ of its acetoxymethyl ester derivative for 1 h at 37°C . The cells were then reincubated in a large volume (100–200 ml) of calcium-containing fresh medium for a period of 1 h to allow equilibration of intracellular free calcium either prior to or after loading into a hollow fibre bundle of kidney dialysis fibres (8 mm in diameter, 3.5 cm long). Approximately 1 ml of packed cells are suction-loaded into the fibre bundle; the ends are sealed, the bundle is placed into a 10 mm o.d. NMR tube and superfused at 12 ml/min with

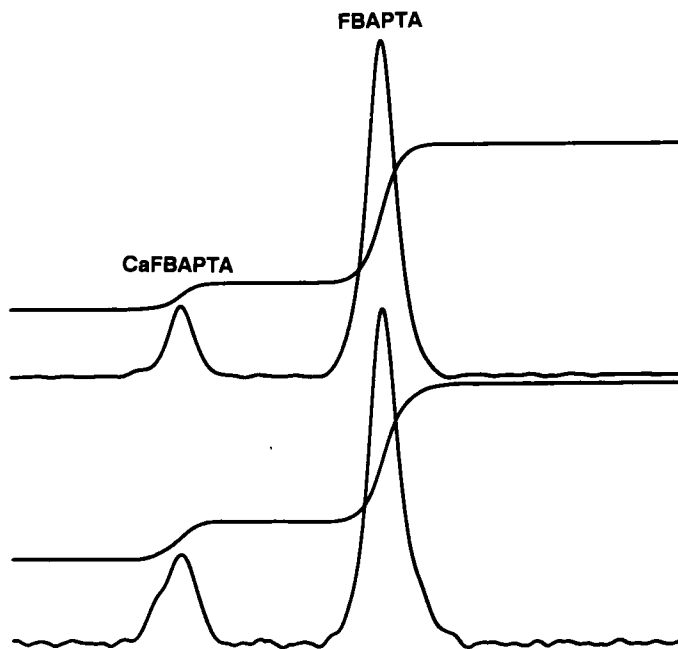


Fig. 11. ^{19}F NMR spectra of 5F-BAPTA-loaded HL-60 cells in a hollow fibre bundle before (lower trace) and after (upper trace) differentiation. The resonances of free 5F-BAPTA (FBAPTA) and calcium-bound 5F-BAPTA (CaFBAPTA) are indicated. Integration of resonance areas is included for convenience.

RPMI-1640 medium bubbled with a humidified 95% O_2 /5% CO_2 gas mixture. NMR spectra were acquired on a Varian VXR-500 spectrometer operating at 470.4 MHz for ^{19}F , at 37°C , using 90° pulses, a spectral width of 10 000 Hz, and a recycle time of 0.8 s. A total of 5000 free induction decays were accumulated for each spectrum and 200 Hz of exponential line-broadening was applied in processing. Figure 11 shows representative ^{19}F spectra of differentiated (upper trace) and control HL-60 cells (lower trace). Integrals have been included for direct comparison of the areas. Using a K_d of $492\ \mu\text{M}$ for the Ca^{2+} -5F-BAPTA complex at 37°C ,⁴⁶ the average value for intracellular free calcium was $104 \pm 7\ \text{nM}$ in differentiated and $145 \pm 7\ \text{nM}$ in proliferating cells. Thus rapidly proliferating cells maintain a significantly higher ($p < 0.01$) free calcium than the corresponding differentiated cells. These observations are consistent with earlier reports⁸⁹ which demonstrated a rise in intracellular free calcium when quiescent cells are stimulated to proliferate.

5. MAGNESIUM MEASUREMENTS

Knowledge of the concentration of cytosolic free magnesium ion, the major divalent cation constituent of all living cells, is of paramount importance for understanding the role of this cation in the regulation of cellular metabolic processes and in the pathophysiology of human disease. Considerable evidence suggests that the free magnesium concentration in many types of cells deviates far from electrochemical equilibrium and is well regulated. A variety of methods have been used to measure intracellular free magnesium. These include the use of Mg^{2+} -selective microelectrodes, measurement of the equilibrium condition for a Mg^{2+} -dependent enzyme reaction, use of a graph of free versus total magnesium generated with the ionophore A23187 and knowledge of membrane potential, null point titrations with metallochromic dyes, NMR spectroscopy, and the use of fluorescent probes. The NMR methods often have the advantage of being non-invasive, although they suffer from the inherent low sensitivity of the technique.

The NMR measurement of intracellular free magnesium is performed indirectly using intracellular indicators. The direct use of ^{25}Mg NMR to make these measurements is hampered by its low natural abundance, its spin- $\frac{5}{2}$ character, high quadrupole moment, and low sensitivity. The indicator most commonly used to measure intracellular free magnesium is the cell's endogenous ATP which can be directly observed by ^{31}P NMR,⁹⁰⁻⁹² however, a method for the measurement of free magnesium has also been described using the ^{13}C NMR of intracellular citrate.⁹³ In addition, an attempt has been made to estimate intracellular free magnesium using resonances from both ATP and ADP under ischaemic conditions which resulted in accumulation of ADP in high enough concentrations to be detectable by ^{31}P NMR.⁹⁴ The introduction of exogenous fluorinated indicators, such as fluorocitrate and 5F-APTRA, has allowed the measurement of free magnesium by ^{19}F NMR and may help to corroborate the values obtained by other methods.

5.1. ^{31}P NMR of intracellular ATP

The most abundant endogenous intracellular magnesium chelator in most cellular systems is ATP. The binding of magnesium to ATP at pH values near neutrality results in shifts in the positions of the P_β and P_γ resonances. The shift of the P_β resonance is due to a change in the conformation of the polyphosphate chain, while that of the P_γ resonance is predominantly due to deprotonation. At non-saturating magnesium ion levels, the chemical shifts of ATP resonances are intermediate between those of MgATP and uncomplexed ATP due to fast exchange of Mg^{2+} on the NMR timescale. Measure-

ment of the chemical shift difference between the magnesium-sensitive P_β resonance and the relatively magnesium independent P_α resonance ($\delta_{\alpha\beta}^{\text{cell}}$) allows a calculation of intracellular free magnesium by,

$$[\text{Mg}^{2+}]_i = K_d^{\text{MgATP}} \left(\frac{1}{\phi} - 1 \right) \quad (9)$$

where,

$$\phi = \frac{\delta_{\alpha\beta}^{\text{cell}} - \delta_{\alpha\beta}^{\text{MgATP}}}{\delta_{\alpha\beta}^{\text{ATP}} - \delta_{\alpha\beta}^{\text{MgATP}}} \quad (10)$$

$\delta_{\alpha\beta}^{\text{ATP}}$ is the chemical shift difference between the P_α and P_β resonances of free ATP and $\delta_{\alpha\beta}^{\text{MgATP}}$ is the difference between the P_α and P_β resonances of fully complexed MgATP under simulated intracellular ionic conditions and pH. K_d^{MgATP} is the dissociation constant for the complex which is both pH- and temperature-dependent. The reported K_d values from different laboratories have shown significant variation. At pH 7.2 and 25°C, Gupta *et al.* reported a value of $50 \pm 10 \mu\text{M}$, which overlaps with the value obtained by them at 37°C ($38 \pm 7 \mu\text{M}$).^{95,96} A more recent study by another group has also reported a value of $51 \mu\text{M}$.⁹⁷

The ^{31}P NMR method for measuring free magnesium from ATP resonances requires knowledge of cytosolic pH, $[\text{Na}^+]$, $[\text{K}^+]$ as well as the K_d for MgATP, and accurate knowledge of chemical shifts of ATP and MgATP, and assumes rapid exchange and the existence of a 1:1 Mg:ATP complex. The rapid exchange condition appears satisfied under physiological ionic conditions and $[\text{ATP}]/[\text{MgATP}]$ ratios at least at 37°C, and at magnetic fields of up to 9.4 T. Further, at the low free Mg^{2+} concentration found in various types of cell, complexation of Mg^{2+} with ATP is predominantly 1:1, but care should be exercised in determining the shift end points corresponding to ATP and MgATP, to take into account the pH-dependence of the former and to minimize the contribution to the latter from higher order complexes. It is also highly desirable to use the K_d of MgATP obtained from ^{31}P NMR shifts of ATP under Mg^{2+} -complexation conditions approximating intracellular values. The K_d value obtained at a certain pH, and under a given set of ionic conditions, can readily be used to derive a value at another pH and under different ionic conditions.

The ^{31}P NMR method based on ATP resonances has been applied to numerous systems including erythrocytes, lymphocytes, platelets, bone cells, skeletal and cardiac muscle, perfused kidney and *in vivo* brain. The presence of readily detectable ATP resonances in most living systems accounts for its wide use. Because, in many cells, the fraction of ATP uncomplexed with Mg^{2+} is in the range of 5–25%, the chemical shift measurements are made in the asymptotic region of the free Mg^{2+} vs. shift curve, where opportunity for

error is high. This is a distinct disadvantage. Nevertheless, with care, the method has proved widely applicable. In combination with imaging and localized spectroscopy techniques, it has the unique capability of determining spatially resolved *in vivo* free Mg^{2+} concentrations.

Jelicks *et al.* have used this technique to compare the intracellular free magnesium in guinea-pig reticulocytes and mature erythrocytes.⁴⁴ The reported free magnesium increased by 65% from 150 μ mol/litre cell water in reticulocytes to 250 μ mol/litre cell water in erythrocytes, seemingly contrasting reports of increased total magnesium in reticulocytes. This discrepancy is most likely due to increased amounts of ATP- and ribosome-bound magnesium in reticulocytes.

The free magnesium in isolated heart cells has been measured by Wittenberg *et al.*⁹⁸ Intracellular magnesium can compete for calcium binding sites and is an important parameter in the study of the cellular physiology of heart cells. The intracellular free magnesium in the superfused myocytes was 0.5 mM using a K_d of 60 μ M at pH 7.1 and 22°C. This value agrees with the level of 0.4 mM recorded in isolated myocytes by ion-selective microelectrodes.⁹⁹

Using the same methods, Borchgrevink *et al.* have looked for changes in the intracellular free magnesium in perfused rat hearts during ischaemia and reperfusion.¹⁰⁰ They noted a rise in magnesium from about 0.5 mM to about 2.5 mM after 6–9 min of ischaemia, then a rapid drop to 0.85 mM upon reperfusion and a gradual decrease to about 0.55 mM after 24 min of reperfusion. Headrick and Willis have reported significant effects of inotropic stimulation on the intracellular free magnesium in perfused rat hearts.¹⁰¹ Upon treatment with isoproterenol, isobutyl-1-methylxanthine, and ouabain, free magnesium rose from a control level of 0.78 ± 0.1 mM to 2.2–3.0 mM and returned to control levels within 10 min after removal of the drug. These changes in the magnesium concentration were found to correlate with the cardiac high-energy phosphate content and a significantly higher free magnesium level was noted in hearts treated with ouabain. This observation supports the existence of a Na^+/Mg^{2+} exchange mechanism in the sarcolemmal membrane for extruding intracellular magnesium ions.⁹¹ The acute changes in magnesium may be important in controlling myocardial metabolism. Intracellular free magnesium has also been examined by Jelicks and Gupta in a study of perfused, spontaneously hypertensive and normotensive rat hearts.¹⁰² Their study revealed depletion of intracellular free magnesium (see Fig. 12) and alterations in cardiac bioenergetics in genetic hypertension. They report a free magnesium level of 452 ± 39 μ M in the hearts of spontaneously hypertensive rats versus 756 ± 52 μ M in normotensive rats. The depletion of free magnesium in hypertension was accompanied by a decrease in cardiac phosphorylation potential without a change in intracellular pH.

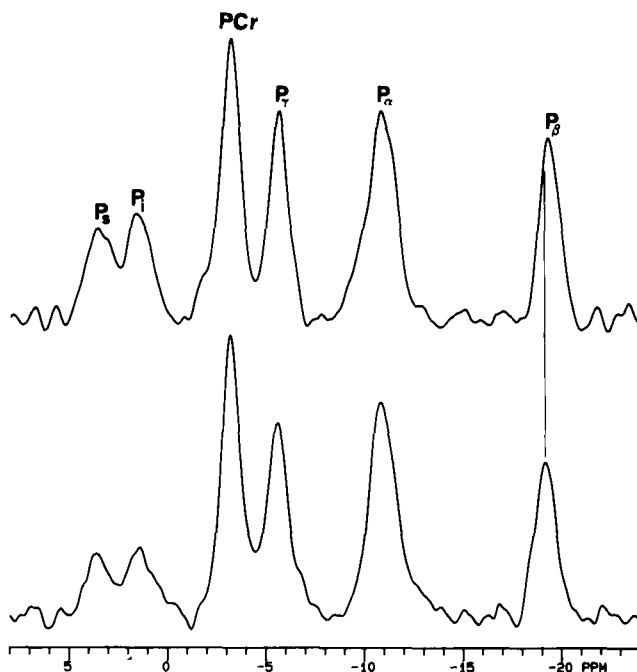


Fig. 12. ^{31}P NMR spectra of Langendorff perfused normotensive (lower trace) and hypertensive (upper trace) rat hearts at 37°C . The resonances of the phosphoryl groups of ATP (P_α , P_β , and P_γ), P-creatine (PCr), sugar phosphates (P_i) and intracellular inorganic phosphate (P_i) are labelled. (From Jelicks and Gupta.¹⁰²)

In a ^{31}P NMR study of perfused rat aorta, Jelicks and Gupta have reported a decreased free magnesium concentration of $180 \pm 38 \mu\text{M}$ in the aorta of spontaneously hypertensive rats in comparison to $246 \pm 76 \mu\text{M}$ from normotensive control rats. Although not statistically highly significant ($p < 0.2$), the trend is consistent with the decreased free magnesium concentration reported by Resnick *et al.*¹⁰³ in a study of human erythrocytes from hypertensive patients. In that study, the intracellular free magnesium in the erythrocytes of hypertensive patients was $183 \pm 9 \mu\text{M}$ versus $251 \pm 9 \mu\text{M}$ in normotensive controls, and there existed a significant inverse relationship between the fasting free magnesium level, and the integrated insulin response to an oral glucose load. Resnick *et al.* hypothesized that hypertension and peripheral insulin resistance may be different clinical expressions of a common abnormal intracellular ionic environment, characterized at least in part by suppressed levels of intracellular free magnesium.

Kopp *et al.* have studied the intracellular free magnesium in single,

perfused porcine carotid artery segments¹⁰⁴ and reported a resting magnesium concentration of 0.54 ± 0.03 mM in flaccid artery segments which increased to 0.99 ± 0.10 mM in the first hour after pressurizing the artery. Pressurization to 95–100 mmHg effectively stretches the muscles. The intracellular free magnesium would then seem to be affected by a change in smooth muscle resting length; and this change in magnesium may be a metabolic trigger for changes in muscle metabolism.

Dowd *et al.* studied free magnesium in cultured osteoblastic bone (ROS 17/2.8) cells using the chemical shifts of intracellular ATP resonances and found a significant (21%) reduction in free magnesium upon treatment of the cells with $10 \mu\text{M}$ lead for 3.5 h.¹⁰⁵ They report a free magnesium concentration of 0.29 ± 0.02 mM in control ROS cells while the average value after 3.5 h of $10 \mu\text{M}$ lead treatment was 0.23 ± 0.02 mM. Since magnesium deficiency has been shown to decrease bone formation, the lead-induced decrease in intracellular free magnesium may contribute to the impairment of bone formation and consequent reduction of stature during lead intoxication.

An attempt has also been made to measure free magnesium from the difference between the chemical shifts of the ADP_β and ATP_γ resonances.⁹⁴ Binding of magnesium to ADP and ATP near neutral pH causes deprotonation of the terminal phosphoryl group resulting in shifts of the ADP_β and ATP_γ resonances. Because of differences in the $\text{p}K_a$ of ADP and ATP, the Mg^{2+} -induced deprotonation causes unequal shifts in the ADP_β and ATP_γ resonances. It should be noted that magnesium-binding in the absence of deprotonation, such as above pH 8, causes negligible shifts in these two resonances. Unfortunately, in most cells, under normal conditions, because of its low concentration and binding to intracellular constituents, the ADP resonances are not identifiable. Under ischaemic conditions, however, breakdown of ATP and sufficient accumulation of ADP may occur, permitting the use of this technique. Burt *et al.* have described and analysed this procedure and have utilized it in the measurement of free magnesium in the ischaemic eye lens and enucleated eye.⁹⁴ The free magnesium reported in ischaemic lens by this method is 0.6 mM. Some values obtained by this method do not fully agree with those obtained by the ATP method. This discrepancy may arise from inaccuracies in the measurement of the chemical shift of the ADP_β resonance due to its overlap with the larger ATP_γ resonance.

5.2. ^{13}C NMR of intracellular citrate

Another method for the indirect measurement of intracellular magnesium using physiological indicators is a ^{13}C NMR method which depends on the

induced shift in the citrate methylene ^{13}C resonance upon magnesium binding.⁹³ Cohen has determined the K_d of the magnesium–citrate complex (K_d^{MgCit}) to be 0.38 ± 0.01 mM. The free magnesium can then be calculated by

$$[\text{Mg}^{2+}]_{\text{in}} = K_d^{\text{MgCit}} \left(\frac{\delta_{\text{cit}} - \delta}{\delta - \delta_c} \right) \quad (11)$$

where δ is the measured shift in the cell system of interest, δ_{cit} and δ_c are the shifts of uncomplexed and fully magnesium-complexed citrate, respectively, under simulated intracellular ionic conditions and pH. Using this method, Cohen has measured a free intracellular magnesium concentration of 0.46 ± 0.05 mM in the perfused rat liver, while Malloy *et al.*¹⁰⁶ report an intracellular free magnesium concentration of 0.68 ± 0.02 mM by the ATP method using a K_d^{MgATP} of $86 \mu\text{M}$. The difference in values is most likely due to the high value of the K_d^{MgATP} used in the latter study. If a K_d^{MgATP} of $50 \mu\text{M}$ is used, the two values are in good agreement.^{95,96}

5.3. ^{19}F NMR of fluorinated indicators

Recently developed fluorinated NMR indicators for the measurement of intracellular free magnesium are based on the magnesium chelators, citrate and *o*-aminophenol-*N,N,O*-triacetic acid (APTRA). While Kirschenlohr *et al.*⁷⁹ have utilized (+)fluorocitrate as a magnesium ion indicator, Levy *et al.* have developed the 4-fluoro, 5-fluoro, and 4-methyl-5-fluoro derivatives of APTRA.¹⁰⁷ The apparent magnesium K_d values for the latter compounds were determined by UV absorption measurements to be 3.1, 0.9, and 0.6 mM, respectively, at 37°C and pH 7.1. The indicators are reported to be insensitive to pH changes near physiological pH, and the K_d values for their calcium complexes are about 2–3 orders of magnitude higher than the intracellular free calcium concentrations so that calcium should not interfere in magnesium measurements. NMR studies of these indicators show magnesium to be in slow exchange with the 5-fluoro and 4-methyl-5-fluoro APTRA derivatives on the NMR timescale, resulting in separate resonances for the free and magnesium-bound forms of the indicator. In this case, the free magnesium concentration may be calculated by multiplying the ratio of free to bound chelator by the K_d for the complex.

The 4-fluoro-APTRA derivative and the (+)-fluorocitrate indicator, on the other hand, are in fast exchange with magnesium on the NMR timescale. This results in one observed ^{19}F resonance whose chemical shift is the weighted average of the chemical shifts of the resonances of free and magnesium-bound indicator. With knowledge of the K_d value of the complex and the chemical shifts of the uncomplexed and fully magnesium-complexed forms

of the indicator, the free magnesium concentration can be calculated from the measured ^{19}F chemical shift of the intact cellular system loaded with the indicator using an equation similar to (11). The indicators are loaded into cellular systems by intracellular hydrolysis of their acetoxymethyl ester derivatives in the same manner as are the ^{19}F calcium indicators. The cellular free magnesium concentration in human erythrocytes using the 4-methyl-5-fluoro-APTRA indicator was determined to be 0.25 mM which is identical to the value of $251 \pm 9\text{ }\mu\text{M}$ reported by Resnick *et al.* using the ATP-based method.¹⁰³ Murphy *et al.* have also measured the intracellular free magnesium concentration in the Langendorff perfused rat heart under normoxic and ischaemic conditions using the fluorinated magnesium indicators described above.¹⁰⁸ An average value of $0.85 \pm 0.10\text{ mM}$ for the basal intracellular magnesium concentration was determined using the three indicators. The value is similar to that obtained for perfused rat hearts using ^{31}P NMR.¹⁰² There was no evidence for a decrease in intracellular free magnesium during loading of the fluorinated indicators as indicated by ^{31}P NMR spectroscopy. During 10–15 min of ischaemia, cardiac ATP levels fell and intracellular free magnesium rose almost three-fold to $2.1 \pm 0.4\text{ mM}$. After 20 min of reperfusion, the magnesium had dropped back only to $1.5 \pm 0.5\text{ mM}$. This sustained increase in free magnesium may inhibit calcium release from the sarcoplasmic reticulum and contribute to the impairment of cardiac function following ischaemia.

The other fluorinated intracellular indicator for the measurement of free magnesium, the stereoisomer (+)fluorocitrate ((+)FCit)^{79,109} has also been used recently. Unlike its diastereomer, (+)FCit does not bind aconitase and block the Krebs cycle. Kirschenlohr *et al.* have used this indicator to measure free magnesium in the perfused rat heart and have reported a value of $1.2 \pm 0.22\text{ mM}$.⁷⁹ They looked for, but found no evidence for, a magnesium transient analogous to the heart's calcium transient.

6. ^{35}Cl NMR SPECTROSCOPY

6.1. Intracellular chloride ions

^{35}Cl is another quadrupolar nucleus with $I = \frac{3}{2}$ which is relatively abundant in biological tissues. Unfortunately, interactions of chloride ions with proteins and other macromolecules can readily cause broadening of its resonance. Because of the large width of its resonance, and the generally low concentration of intracellular chloride ions, the intracellular ^{35}Cl resonance is usually undetectable. An exception to this is the red blood cell, which maintains a high concentration of intracellular chloride ions. It has been

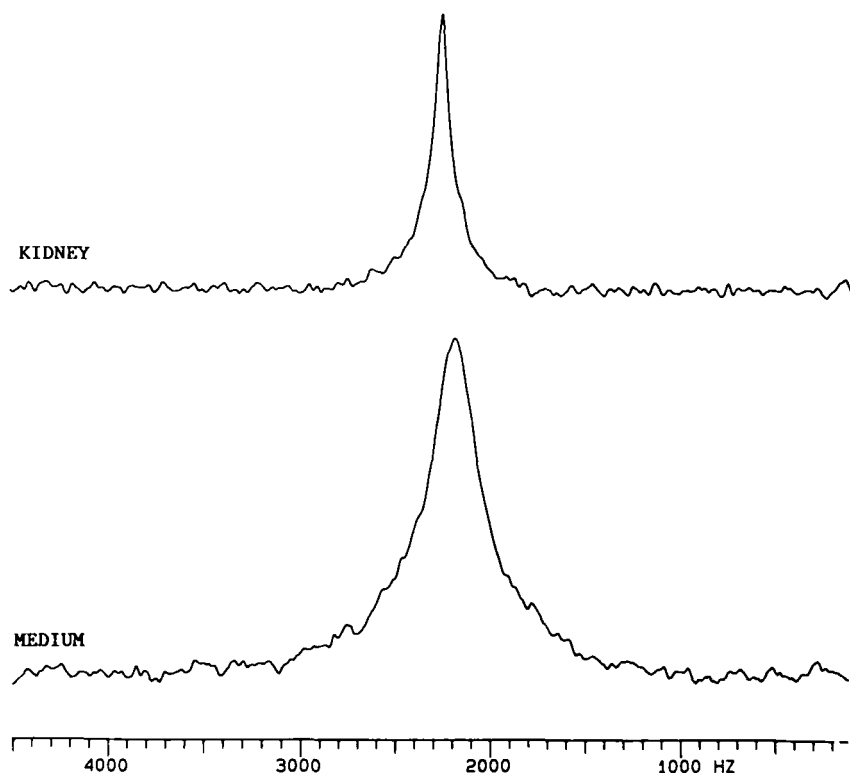


Fig. 13. Comparison of $^{35}\text{Cl}^-$ NMR spectra obtained at 20 MHz and 37°C from the perfused adult (300 g) rat kidney (upper trace) and from 5% albumin-containing perfusate alone (lower trace). (From Gupta *et al.*³²)

shown that the intracellular ^{35}Cl ion resonance in erythrocytes is very broad and not detectable using small (1000 Hz) spectral widths.^{110,111} Recently, we re-examined the ^{35}Cl resonance of intact packed red cells in plasma (approximately 99% haematocrit) using a 100 kHz spectral width (Jelicks, Veniero, and Gupta, unpublished results). We found that a broad intracellular ^{35}Cl resonance was detectable using this spectral width, the linewidth at half height being approximately 1000 Hz. The linewidth of the plasma ^{35}Cl resonance was approximately 250 Hz. It has been possible to quantitate the intracellular and plasma ^{35}Cl concentrations by comparing the integrated areas of their resonances with a calibration standard of known NaCl concentration. An intracellular chloride concentration ($[\text{Cl}^-]_{\text{in}}$) of 75 mM was obtained in this way (assuming the fractional intracellular water volume to be 0.7¹¹²). The serum chloride concentration ($[\text{Cl}^-]_{\text{out}}$) is

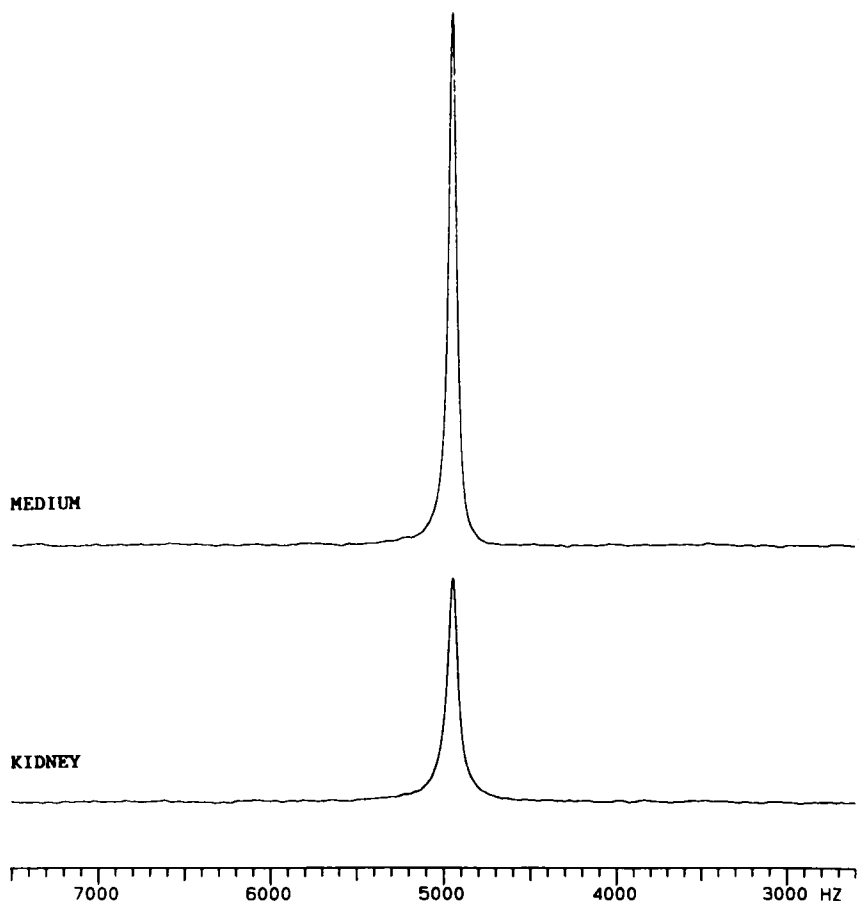


Fig. 14. Comparison of $^{35}\text{Cl}^-$ NMR spectra from the perfused adult rat (300 g) kidney (lower trace) and from albumin-free perfusate (upper trace). (From Gupta *et al.*³²)

approximately 110 mM. Since the transmembrane chloride distribution in red blood cells follows the membrane potential, the latter was determined to be -10.5 mV using the Nernst equation, $E_m = RT/F \ln ([\text{Cl}^-]_{\text{in}}/[\text{Cl}^-]_{\text{out}})$ (at 37°C $RT/F = 26.7$ mV), which is in the range of accepted values. ^{35}Cl NMR, therefore, may offer a non-invasive method for studying red cell membrane potential, which may be altered in some diseased states, in intact blood.

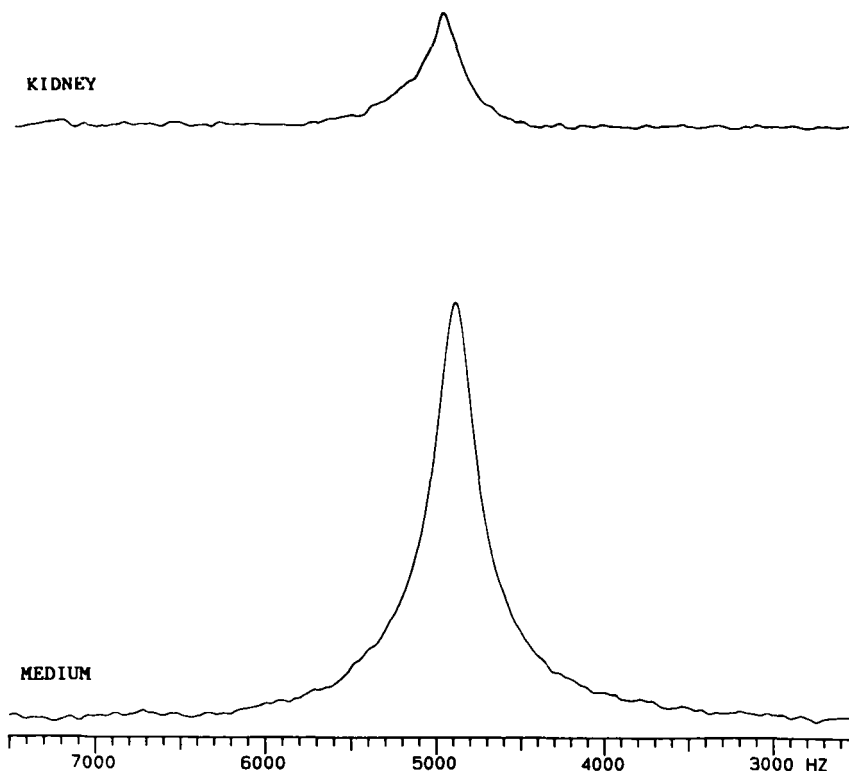


Fig. 15. Comparison of $^{35}\text{Cl}^-$ NMR spectra from a perfused immature kidney removed from a growing rat (90 g) (upper trace) and from 5% albumin-containing perfusate (lower trace). (From Gupta *et al.*³²)

6.2. Compartmentation of albumin between interstitial and vascular spaces

^{35}Cl NMR has also been used to study compartmentation of albumin between interstitial and vascular spaces in the perfused kidney.³² It has been shown that the linewidth of the ^{35}Cl ion resonance of the perfused adult rat kidney was much less than that of the perfusate medium alone (80 vs. 300 Hz, see Fig. 13), when the perfusate contained 5% albumin. The broadening of the perfusate ^{35}Cl resonance was ascribed to binding of the ^{35}Cl ions to albumin. Since the resonance of ^{35}Cl ions in the vascular space was expected to have the same linewidth as that in the perfusate, and intracellular ^{35}Cl was considered invisible, the observed narrower ^{35}Cl resonance of the kidney must arise from the contribution of a narrow resonance of ^{35}Cl ions in the interstitial space, which occupies a sizeable fraction of the total extracellular space

in an *in vitro* perfused kidney. This was interpreted to mean that the interstitial space in an adult rat kidney contains little or no albumin and that albumin remains confined mostly to intravascular space, presumably due to a capillary protein permeability barrier. This interpretation was confirmed by perfusing the kidney with albumin-free medium. As expected, the observed ^{35}Cl resonance from the kidney in this case was about two-fold broader (45 Hz) than that of the albumin-free perfusate (20 Hz) (see Fig. 14). The slightly larger linewidth in the kidney perfused with albumin-free medium is consistent with binding of ^{35}Cl ions to cell surfaces. The above data indicate that ^{35}Cl NMR measures compartmentation of albumin between interstitial and intravascular spaces. In an immature kidney from a growing animal (≤ 90 g rat, ≤ 3 weeks old), the compartmentation of albumin between intravascular and interstitial spaces appeared to be very different. The linewidth of the ^{35}Cl resonance from such a developing kidney (235 Hz) was closer to that from the albumin-containing medium alone (310 Hz) (see Fig. 15), suggesting that the capillary protein permeability barrier responsible for maintaining the albumin concentration gradient between the vascular and interstitial spaces is not fully developed in an immature kidney. The ^{35}Cl resonance thus provides information on the compartmentation of albumin between the vascular and interstitial spaces. ^{35}Cl NMR may also provide a rapid technique to study alterations in the capillary protein permeability barrier in disease states and during development.

ACKNOWLEDGEMENTS

The preparation of this article and some of the research described herein were supported by USPHS NIH Research Grant DK32030 and the NCI Core Grant CA13330.

REFERENCES

1. P.G. Morris, in *Annual Reports on NMR Spectroscopy*, Vol. 20 (ed. G.A. Webb), pp. 1-60. Academic Press, London, 1988.
2. R.K. Gupta and P. Gupta, *J. Magn. Reson.*, 1982, **47**, 344.
3. J.A. Balschi, V.P. Cirillo and C.S. Springer, *Biophys. J.*, 1982, **38**, 323.
4. R.K. Gupta, P. Gupta and R.D. Moore, *Ann. Rev. Biophys. Bioeng.*, 1984, **13**, 221.
5. R.K. Gupta, in *NMR in Living Systems* (ed. T. Axenrod and G. Ceccarelli), pp. 291-308. D. Reidel Publishing, Dordrecht, 1986.
6. R.K. Gupta, in *NMR Spectroscopy of Cells and Organisms*, Vol. II (ed. R.K. Gupta), pp. 1-32. CRC Press, Boca Raton, Florida, 1987.
7. C.S. Springer, *Ann. Rev. Biophys. Biophys. Chem.*, 1987, **16**, 375.
8. R.K. Gupta and L.A. Jelicks, *Indian J. Chem.*, 1988, **27A**, 829.
9. S.C. Chu, M.M. Pike, E.T. Fossel, T.W. Smith, J.A. Balschi and C.S. Springer, *J. Magn. Reson.*, 1984, **56**, 33.

10. D.C. Buster, M.M.C.A. Castro, C.F.G.C. Geraldès, C.R. Malloy, A.D. Sherry and T.C. Siemers, *Magn. Reson. Med.*, 1990, **15**, 25.
11. C.R. Malloy, D.C. Buster, M.M.C.A. Castro, C.F.G.C. Geraldès, F.M.H. Jeffrey and A.D. Sherry, *Magn. Reson. Med.*, 1990, **15**, 33.
12. Z.H. Endre, J.L. Allis and G.K. Radda, *Magn. Reson. Med.*, 1989, **11**, 267.
13. S.E. Anderson, J.S. Adorante and P.M. Cala, *Am. J. Physiol.*, 1988, **254**, C466.
14. G.A. Elgavish, *Invest. Radiol.*, 1989, **24**, 1028.
15. S.R. Gullans, M.J. Avison, T. Ogino, G. Giebisch and R.G. Shulman, *Am. J. Physiol.*, 1985, **249**, F160.
16. P. Plateau and M. Guéron, *J. Am. Chem. Soc.*, 1982, **104**, 7310.
17. M.M. Pike, M. Kitakaze and E. Marban, *Am. J. Physiol.*, 1990, **259**, H1767.
18. D. Burstein and E.T. Fossel, *Magn. Reson. Med.*, 1987, **4**, 261.
19. H.J.C. Berendsen and H.T. Edzes, *Ann. N.Y. Acad. Sci.*, 1973, **204**, 459.
20. M.M. Civan and M. Shporer, *Biol. Magn. Reson.*, 1978, **1**, 1.
21. S. Forsen and B. Lindman, *Meth. Biochem. Anal.*, 1980, **27**, 289.
22. S.A. Rashid, W.R. Adam, D.J. Craik, B.P. Shehan and R.M. Wellard, *Magn. Reson. Med.*, 1991, **17**, 213.
23. V.H. Schmidt, in *Pulsed Magnetic and Optical Resonance* (ed. R. Blinc), pp. 75–83. University of Ljubljana, Ljubljana, 1971.
24. H.J.C. Yeh, F.J. Brinley and E.D. Becker, *Biophys. J.*, 1973, **13**, 459.
25. R.K. Gupta, P. Gupta and W. Negendank, in *Ion, Cell Proliferation, and Cancer*, pp. 1–12. Academic Press, New York, 1982.
26. T. Ogino, G.I. Shulman, M.J. Avison, S.R. Gullans, J.A. den Hollander and R.G. Shulman, *Proc. Natl. Acad. Sci. USA*, 1985, **82**, 1099.
27. D.R. Petrovich and R.K. Gupta, *Fed. Proc.*, 1985, **44**, 1043.
28. T. Ogino, J.A. den Hollander and R.G. Shulman, *Proc. Natl. Acad. Sci. USA*, 1983, **80**, 5185.
29. A.M. Castle, R.M. Macnab and R.G. Shulman, *J. Biol. Chem.*, 1986, **261**, 3288.
30. R.K. Gupta, A.B. Kostellow and G.A. Morrill, *J. Biol. Chem.*, 1985, **260**, 9203.
31. L.A. Jelicks and R.K. Gupta, *J. Biol. Chem.*, 1989, **264**, 15230.
32. R.K. Gupta, T.L. Dowd, A. Spitzer, M. Barac-Nieto, *Renal Physiol. Biochem.*, 1989, **12**, 144.
33. H. Blum, M.D. Osbakken and R.G. Johnson, *Magn. Reson. Med.*, 1991, **18**, 348.
34. D. Hoffman and R.K. Gupta, *J. Magn. Reson.*, 1986, **70**, 481.
35. G.A. Morrill, A.B. Kostellow, D. Hoffman and R.K. Gupta, *Ann. NY Acad. Sci.*, 1987, **508**, 531.
36. D. Hoffman, A.M. Kumar, A. Spitzer and R.K. Gupta, *Biochim. Biophys. Acta*, 1986, **889**, 355.
37. F.A.X. Schanne, T.L. Dowd, R.K. Gupta and J.F. Rosen, *Proc. Natl. Acad. Sci. USA*, 1989, **86**, 5133.
38. F.A.X. Schanne, J.R. Moskal and R.K. Gupta, *Brain Res.*, 1989, **503**, 308.
39. T.L. Dowd and R.K. Gupta, *Biochem. Biophys. Acta*, 1991, **1092**, 341.
40. J.L. Kinsella and R.S. Aronson, *Am. J. Physiol.*, 1980, **238**, F461.
41. L.A. Beaugé and O. Ortiz, *J. Physiol.*, 1970, **210**, 519.
42. L.A. Beaugé and R.A. Sjodin, *J. Physiol.*, 1968, **200**, 459.
43. J.L. Pirkle, J. Schwartz, J.R. Landis and W.R. Harlan, *Am. J. Epidemiol.*, 1985, **121**, 246.
44. L.A. Jelicks, J. Weaver, S. Pollack and R.K. Gupta, *Biochim. Biophys. Acta*, 1989, **1012**, 261.
45. M.S. Liebling and R.K. Gupta, *Ann. NY Acad. Sci.*, 1987, **508**, 149.

46. L.A. Jelicks and R.K. Gupta, *J. Biol. Chem.*, 1990, **265**, 1394.
47. S.E. Anderson, E. Murphy, C. Steenbergen, R.E. London and P.M. Cala, *Am. J. Physiol.*, 1990, **259**, C940.
48. D. Powell, D. Burstein and E.T. Fossel, *Eur. J. Biochem.*, 1990, **193**, 887.
49. B.A. Wittenberg and R.K. Gupta, *J. Biol. Chem.*, 1985, **260**, 2031.
50. A.W.H. Jans, R. Willem, E.R. Kellenbach and R.K.H. Kinne, *Magn. Reson. Med.*, 1988, **7**, 292.
51. N.J. Greenfield, C.N. Cherapack, F. Adebodun and J. Lenard, *Biochim. Biophys. Acta*, 1990, **1025**, 15.
52. J.P. Monti, M. Baz, R. Elsen, Y.F. Berland and A.D. Crevat, *Biochim. Biophys. Acta*, 1990, **1027**, 31.
53. R. Ouwerkerk, C.J. van Echteld, G.E. Staal and G. Rijksen, *Magn. Reson. Med.*, 1989, **12**, 164.
54. T.L. Knubovets, A.V. Revazov, L.A. Sibeldina and U. Eichhoff, *Magn. Reson. Med.*, 1989, **9**, 261.
55. G.A. Smith, P.G. Morris, T.R. Hesketh and J.C. Metcalfe, *Biochim. Biophys. Acta*, 1986, **889**, 72.
56. J. Pekar, P.F. Renshaw and J.S. Leigh, *J. Magn. Reson.*, 1987, **72**, 159.
57. G. Jaccard, S. Wimperis and G. Bodenhausen, *J. Chem. Phys.*, 1986, **85**, 6282.
58. L.A. Jelicks and R.K. Gupta, *J. Magn. Reson.*, 1989, **81**, 586.
59. L.A. Jelicks and R.K. Gupta, *J. Magn. Reson.*, 1989, **83**, 146.
60. R.B. Hutchison, D. Malhotra, R.E. Hendrick, L. Chan and J.I. Shapiro, *J. Biol. Chem.*, 1990, **265**, 15506.
61. D.G. Davis, E. Murphy and R.E. London, *Biochemistry*, 1988, **27**, 3547.
62. M.P. Williamson, *FEBS Lett.*, 1989, **254**, 171.
63. J.L. Allis, C.D. Snaith, A.M. Seymour and G.K. Radda, *FEBS Lett.*, 1989, **242**, 215.
64. J.L. Allis, Z.H. Endre and G.K. Radda, *Renal Physiol. Biochem.*, 1989, **12**, 171.
65. D. Burstein, H.I. Litt and E.T. Fossel, *Magn. Reson. Med.*, 1989, **9**, 66.
66. E.T. Fossel and H. Hoefeler, *Magn. Reson. Med.*, 1986, **3**, 534.
67. D. Burstein and E.T. Fossel, *Am. J. Physiol.*, 1987, **252**, H1138.
68. P.J. Brophy, M.K. Hayer and F.G. Riddell, *Biochem. J.*, 1983, **210**, 961.
69. Y. Boulanger and P. Vinay, *Magn. Reson. Med.*, 1990, **16**, 246.
70. P.M. Joseph and R.M. Summers, *Magn. Reson. Med.*, 1987, **4**, 67.
71. Y. Seo, M. Murakami, E. Suzuki, S. Kuki, K. Nagayama and H. Watari, *Biochemistry*, 1990, **29**, 599.
72. T. Hiraishi, Y. Seo, M. Murakami and H. Watari, *J. Magn. Reson.*, 1990, **87**, 169.
73. M. Murakami, E. Suzuki, S. Miyamoto, Y. Seo and H. Watari, *Pflugers Arch.*, 1989, **414**, 385.
74. B.M. Rayson and R.K. Gupta, *J. Biol. Chem.*, 1985, **260**, 7276.
75. G.A. Smith, R.T. Hesketh, J.C. Metcalfe, J. Feeney and P.G. Morris, *Proc. Natl. Acad. Sci. USA*, 1983, **80**, 7178.
76. L.A. Levy, E. Murphy and R.E. London, *Am. J. Physiol.*, 1987, **252**, C441.
77. E. Marban, M. Kitakaze, Y. Koretsune, D.T. Yue, V.P. Chacko and M.M. Pike, *Circ. Res.*, 1990, **66**, 1255.
78. F.A.X. Schanne, T.L. Dowd, R.K. Gupta and J.F. Rosen, *Environ. Health Perspect.*, 1990, **84**, 99.
79. H.L. Kirschenlohr, J.C. Metcalfe, P.G. Morris, G.C. Rodrigo and G.A. Smith, *Proc. Natl. Acad. Sci. USA*, 1988, **85**, 9017.
80. R.S. Badar-Goffer, O. Ben-Yoseph, S.J. Dolin, P.G. Morris, G.A. Smith and H.S. Bachelard, *J. Neurochem.*, 1990, **55**, 878.

81. F.A.X. Schanne, T.L. Dowd, R.K. Gupta and J.F. Rosen, *Biochim. Biophys. Acta*, 1990, **1054**, 250.
82. H.S. Bachelard, R.S. Badar-Goffer, K.J. Brooks, S.J. Dolin and P.G. Morris, *J. Neurochem.*, 1988, **51**, 1311.
83. O. Ben-Yoseph, H.S. Bachelard, R.S. Badar-Goffer, S.J. Dolin and P.G. Morris, *J. Neurochem.*, 1990, **55**, 1446.
84. E. Marban, M. Kitakaze, H. Kusuoka, J.K. Porterfield, D.T. Yue and V.P. Chacko, *Proc. Natl. Acad. Sci. USA*, 1987, **84**, 6005.
85. E. Marban, M. Kitakaze, V.P. Chacko and M.M. Pike, *Circ. Res.*, 1988, **63**, 673.
86. Y. Koretsune and E. Marban, *Am. J. Physiol.*, 1990, **258**, H9.
87. C. Steinbergen, E. Murphy, J.A. Watts and R.E. London, *Circ. Res.*, 1990, **66**, 135.
88. S.W. Snyder, M.J. Egorin, L.A. Geelhaar, A.W. Hamburger and P.S. Callery, *Cancer Res.*, 1988, **48**, 3613.
89. R.K. Gupta and R.J. Gillies, in *NMR Spectroscopy of Cells and Organisms* (ed. R.K. Gupta), pp. 45–53. CRC Press, Boca Raton, Florida, 1987.
90. R.K. Gupta, J.L. Benovic and Z.B. Rose, *J. Biol. Chem.*, 1978, **253**, 6172.
91. R.K. Gupta and R.D. Moore, *J. Biol. Chem.*, 1980, **255**, 3987.
92. R.K. Gupta and W.D. Yushok, *Proc. Natl. Acad. Sci. USA*, 1980, **77**, 2487.
93. S.M. Cohen, *J. Biol. Chem.*, 1983, **258**, 14294.
94. C.T. Burt, H.M. Cheng, S. Gabel and R.E. London, *J. Biochem.*, 1990, **108**, 441.
95. R.K. Gupta, P. Gupta, W.D. Yushok and Z.B. Rose, *Biochem. Biophys. Res. Commun.*, 1983, **117**, 210.
96. R.K. Gupta, P. Gupta, W.D. Yushok and Z.B. Rose, *Physiol. Chem. Phys.*, 1983, **15**, 265.
97. H. Sigel, *Eur. J. Biochem.*, 1987, **165**, 65.
98. B.A. Wittenberg, J.E. Doeller, R.K. Gupta and R.L. White, in *Biology of Isolated Adult Cardiac Myocytes* (ed. W.A. Clark, R.S. Decker and T.K. Borg), pp. 118–30. Elsevier Science Publishing Co., London, 1988.
99. L.A. Blatter and J.A.S. McGuigan, *Quant. J. Exp. Physiol.*, 1986, **71**, 467.
100. P.C. Borchgrevink, A.S. Bergan, O.E. Bakøy and P. Jynge, *Am. J. Physiol.*, 1989, **256**, H195.
101. J.P. Headrick and R.J. Willis, *Magn. Reson. Med.*, 1989, **12**, 328.
102. L.A. Jelicks and R.K. Gupta, *Am. J. Hypertens.*, 1991, **4**, 131.
103. L.M. Resnick, R.K. Gupta, H. Gruenspan, M.H. Alderman and J.H. Laragh, *Am. J. Hypertens.*, 1990, **3**, 373.
104. S.J. Kopp, J.T. Barron and J.P. Tow, *Biochim. Biophys. Acta*, 1990, **1055**, 27.
105. T.L. Dowd, J.F. Rosen and R.K. Gupta, *J. Biol. Chem.*, 1990, **265**, 20833.
106. C.R. Malloy, C.C. Cunningham and G.K. Radda, *Biochim. Biophys. Acta*, 1986, **885**, 1.
107. L.A. Levy, E. Murphy, B. Raju and R.E. London, *Biochemistry*, 1988, **27**, 4041.
108. E. Murphy, C. Steenbergen, L.A. Levy, B. Raju and R.E. London, *J. Biol. Chem.*, 1989, **264**, 5622.
109. P.G. Morris, G.A. Smith, J.C. Metcalfe and G.C. Rodrigo, in *Works in Progress*, p. 31. Society of Magnetic Resonance in Medicine, 1987.
110. D. Hoffman and R.K. Gupta, *J. Magn. Reson.*, 1986, **70**, 481.
111. M. Brauer, C.Y. Spread, R.A.F. Reitmeir and B.D. Sykes, *J. Biol. Chem.*, 1985, **260**, 11643.
112. J.F. Hoffman, in *Physiology of Membrane Disorders* (ed. T.E. Andreoli, J.F. Hoffman, D.D. Fanestil and S.G. Schultz), Chap. 13. Plenum, New York, 1986.

Note added in proof*3.3.1. Derangement of intracellular potassium ions in hypertension*

There is considerable evidence for derangement in the ability of cells to control the intracellular concentrations of cations in essential hypertension. Previous work has demonstrated significant differences in the intracellular concentrations of free calcium and sodium ions, and suggests changes in the intracellular free magnesium ion concentration in the aortas of normotensive and spontaneously hypertensive rats.⁴⁶ However, little is known about the derangement of intracellular potassium in hypertension even though the importance of dietary potassium in the control of essential hypertension was noted as early as 1925. Total body potassium is significantly decreased in essential hypertension; and raising extracellular potassium produces a significant arteriolar relaxation and a drop in blood pressure.

In an application of the noninvasive subtraction procedure, we have compared the intracellular potassium ion concentrations in the aortas of the normotensive and spontaneously hypertensive rats. The measurements yielded an intracellular free potassium ion concentration of 21.7 ± 1.5 mM in the normotensive aorta (from rats with mean systolic blood pressure of 126 ± 20 mmHg), while in the aorta from spontaneously hypertensive rats (mean systolic blood pressures of 177 ± 8 mmHg), the intracellular potassium was at 12.1 ± 1.8 mM. Assuming that the resonance represents only the central magnetic transition ($\frac{1}{2} \rightarrow -\frac{1}{2}$) for the ^{39}K nucleus, which leads to a 40% visibility for the K^+ in tissues, our measurements could represent an intracellular free potassium ion concentration of about 54 mM in the normotensive and 31 mM in the hypertensive rats. These values are far below those expected for electrochemical equilibrium. However, the results clearly indicate significant depletion of intracellular potassium in vascular smooth muscle tissue in hypertension, which can be measured noninvasively by the subtraction procedure. The decrease in intracellular potassium ion concentration in hypertension is consistent with the previously reported increases in the intracellular free sodium and free calcium ion concentrations in the hypertensive tissue.⁴⁶ Possible mechanisms for the decreased intracellular potassium concentration include a decreased $\text{Na}^+ - \text{K}^+ - \text{ATPase}$ activity in essential hypertension or an increased loss of intracellular potassium ions via calcium-activated potassium channels; or increased passive leak of potassium ions in hypertensive vascular smooth muscle.

^{199}Hg NMR Parameters

BERND WRACKMEYER* and
ROSALINDA CONTRERAS†

**Laboratorium für Anorganische Chemie der Universität Bayreuth, Postfach 101251,
D-8580 Bayreuth, Germany*

†*Centro de Investigacion y de Estudios Avanzados del I.P.N., Departamento de
Química, 07000 Mexico, D.F., Mexico*

1. Introduction	267
2. Experimental	268
2.1. Referencing	268
2.2. Techniques for observing ^{199}Hg resonances	268
3. Nuclear spin relaxation	271
4. Chemical shifts, $\delta^{199}\text{Hg}$	273
4.1. General	273
4.2. Patterns of $\delta^{199}\text{Hg}$ chemical shifts	274
5. Indirect nuclear spin-spin coupling constants $J(^{199}\text{HgX})$	276
5.1. General	276
5.2. Patterns of couplings $J(^{199}\text{HgX})$	277
6. ^{199}Hg NMR of solids	280
7. Conclusions	281
Acknowledgements	281
References	321

1. INTRODUCTION

Many physical properties of mercury,¹ its organic as well as its organo-metallic chemistry,² have fascinated generations of scientists for centuries. Modern insights into its toxicology and environmental aspects have hardly diminished that interest, although the general attitude towards research work on mercury compounds may have changed. Numerous chemical applications of mercury were developed prior to the availability of advanced modern instrumental analysis. Nevertheless, we find a growing impact of such methods and of NMR spectroscopic techniques in particular. In addition to numerous studies of ^1H NMR, ^{199}Hg NMR, together with NMR measurements of other nuclei such as ^{13}C , ^{19}F , ^{29}Si and ^{31}P , have been extremely useful in this context.

This review has several purposes: (i) previous reviews on ^{199}Hg NMR^{3,4} will be updated, aiming for a complete overview on ^{199}Hg chemical shifts ($\delta^{199}\text{Hg}$); (ii) a summary of indirect nuclear spin-spin coupling constants $^nJ(^{199}\text{Hg}-\text{X})$ will be given since these data are widely scattered in the literature;³⁻⁵ (iii) ^{199}Hg nuclear spin relaxation^{3,4} will be discussed; (iv) experimental aspects of ^{199}Hg NMR will be considered, together with some important consequences of the presence of $^{199}\text{Hg}-\text{X}$ isotopomers on NMR spectra of other nuclei X; and (v) applications of solid state NMR to problems in mercury chemistry will be briefly summarized.

There are two magnetically active isotopes, ^{199}Hg and ^{201}Hg , of which the ^{199}Hg nucleus ($I = \frac{1}{2}$, natural abundance 16.84%) is ideally suited for the NMR experiment, at least in liquids (Table 1).

2. EXPERIMENTAL

2.1. Referencing

As for most nuclei other than ^1H or ^{13}C , there is no ideal mercury compound that could serve as an internal reference for ^{199}Hg NMR spectra. The use of capillaries filled with HgMe_2 or a hydrous solution of $\text{Hg}(\text{ClO}_4)_2$ (0.1 M in 0.1 M HClO_4) does not solve the problem, considering the increase in magnetic field inhomogeneity, the reduced sample volume and bulk susceptibility effects. A more convenient procedure uses a distinct frequency as an external reference.⁶ The frequencies most widely used are those for the ^{199}Hg resonance of neat HgMe_2 or of $\text{Hg}(\text{ClO}_4)_2$ (0.1 M in 0.1 M HClO_4) (Section 1). In this review, all $\delta^{199}\text{Hg}$ values are given relative to $\delta^{199}\text{Hg} = 0$ for neat HgMe_2 (a negative sign denotes increased ^{199}Hg nuclear shielding). $\delta^{199}\text{Hg}$ data referred to other reference compounds have been recalculated as accurately as possible. Since the referencing procedures have not always been described in detail (e.g. Refs. 26, 30, 42, 47, 48, 64, 67, 87, 124, 141, 164, 165, 178, 257), some $\delta^{199}\text{Hg}$ values should be used with caution (see also footnotes to the tables).

2.2. Techniques for observing ^{199}Hg resonances

Many ^{199}Hg NMR data have been obtained by INDOR techniques, using cw spectrometers and $^1\text{H}\{^{199}\text{Hg}\}$ heteronuclear double-resonance experiments.⁶⁻⁸ Nowadays, the majority of ^{199}Hg NMR data are observed using the pulse Fourier transform mode. The relatively high sensitivity of ^{199}Hg nuclei to the NMR experiment (Table 1) ensures that direct detection (with or

Table 1. NMR properties of the ^{199}Hg and ^{201}Hg isotopes.

	Spin	Natural abundance	Magnetogyric ratio $\gamma(\text{rad s T})$	$\Xi(^{199}\text{Hg})$ ($\Xi(^1\text{H})$, $\text{Me}_4\text{Si} = 100\text{ MHz}$)	Receptivity $D^{\text{C}} (^{13}\text{C} = 1)$
^{199}Hg	$\frac{1}{2}$	16.84%	4.8458×10^7	17.910 841 ^a 17.870 535 ^b 17.827 146 ^{30c}	5.68
$^{201}\text{Hg}^{\text{d}}$	$\frac{3}{2}$	13.22%	-1.7888×10^7	–	1.12

^a HgMe_2 , neat, reference for chemical shifts $\delta^{199}\text{Hg}$ used throughout this review.

^b $\text{Hg}(\text{ClO}_4)_2$, 0.1 M in 0.1 M HClO_4 .³¹ $\delta^{199}\text{Hg} - 2250$.

^cFree mercury atom:¹⁰⁹ $\delta^{199}\text{Hg} - 4673$.

^dThere are no reports on high-resolution ^{201}Hg NMR measurements.

Table 2. Relaxation times $T_1(^{199}\text{Hg})$ measured under various conditions.

Compound	$T_1(^{199}\text{Hg})$ (s)	Temperature (K)	B_0 (T)	Solvent	Ref.
HgMe_2	1.176	297	1.41	neat	13
	0.87	300	2.35	neat	34
	0.308	297	5.875	neat	19
	0.148	297	9.40	neat	19
$\text{Hg}(\text{CH}_2\text{Ph})_2$	0.074	297	5.875	CDCl_3	19
	0.027	297	9.40	CDCl_3	19
HgPh_2	0.136	273	2.35	$\text{C}_2\text{D}_4\text{Cl}_2/\text{CCl}_4$	12
	0.244	300	2.35	$\text{C}_2\text{D}_4\text{Cl}_2/\text{CCl}_4$	12
	0.087	297	5.875	CDCl_3	19
	0.036	297	9.40	CDCl_3	19
$\text{Hg}(\text{CH}=\text{CH}_2)_2$	0.25	300	2.35	neat	34
$\text{Me-Hg-C}\equiv\text{C-H}$	0.064	298	7.05	C_6D_6	110
HgCl_2	1.4	297	2.114	EtOH	112
	0.281	297	5.875	EtOH	19
	0.113	297	9.40	EtOH	19
$\text{Hg}(\text{CN})_2$	0.184	297	5.875	CD_3OD	19
	0.063	297	9.40	CD_3OD	19
$[\text{HgCl}_4]^{2-}$	6.50	297	5.875	D_2O	19
$[\text{Hg}(\text{CN})_4]^{2-}$	7.0	297	5.875	D_2O	19

without ^1H decoupling) is feasible in most cases (see Figs. 1 and 2). Transfer of ^1H spin polarization to ^{199}Hg (INEPT,⁹ and DEPT¹⁰) is not particularly efficient because of the rather short ^{199}Hg nuclear spin relaxation. However, the so-called indirect or inverse detection of ^{199}Hg resonances via pulsed ^1H $\{^{199}\text{Hg}\}$ experiments¹¹ (the PFT version of INDOR) has shown that organo-mercury compounds can be studied at a very low level of concentration.

As a consequence of efficient chemical shift anisotropy relaxation (*vide infra*) ^{199}Hg resonances are broadened (at least at field strengths $B_0 \geq 4.7$ T) in most cases,^{12,13} except for the complex anions $[\text{HgX}_4]^{2-}$, where the surrounding of the ^{199}Hg nucleus is exactly tetrahedral. Short relaxation times $T_1(^{199}\text{Hg})$ (see Table 1) mean that pulse angles close to 90° and fast pulse repetition rates can be used for direct detection, in contrast to many other spin- $\frac{1}{2}$ nuclei.

Other contributions to the linewidth of the ^{199}Hg resonance signals arise from scalar coupling¹⁴ (e.g. with the halogen nuclei $^{35,37}\text{Cl}$, $^{79,81}\text{Br}$, ^{127}I) and from various exchange processes.²⁴ In addition, there is a considerable dependence of the $\delta^{199}\text{Hg}$ values on small temperature gradients in the sample, which also contributes to the experimental linewidth (see Fig. 3). All these findings indicate that ^{199}Hg NMR studies should also be conducted with respect to variable temperature in order to distinguish between the various

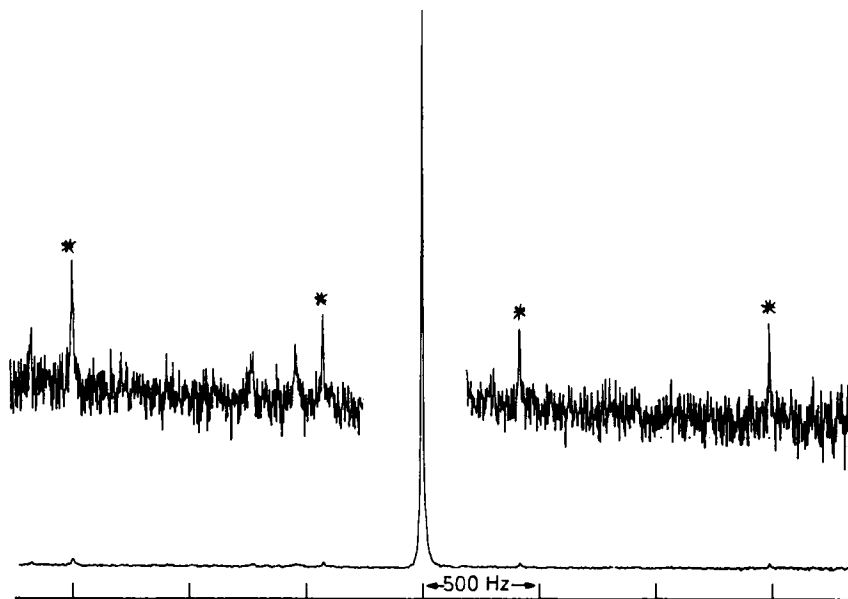


Fig. 1. A 35.85 MHz ^{199}Hg NMR spectrum (35 000 scans, acquisition time 1.2 s, pulse angle $\approx 45^\circ$; ≈ 12 h of spectrometer time) of $\text{Hg}(\text{C}\equiv\text{C}-\text{Cl})$ in DMSO (saturated), showing ^{13}C satellites (*): $\delta(^{199}\text{Hg}) - 1041$; $^1J(^{199}\text{Hg}^{13}\text{C})$ 2991 Hz; $^2J(^{199}\text{Hg}^{13}\text{C})$ 845 Hz. The solubility of this compound is too low and ^{13}C relaxation rates ($T_1(^{13}\text{C})$) are unfavourable (as compared with $T_1(^{199}\text{Hg})$) for observing ^{199}Hg satellites in ^{13}C NMR spectra of the same sample in 12 h.

effects that control the linewidths and the general appearance of ^{199}Hg NMR signals.

3. NUCLEAR SPIN RELAXATION

For diamagnetic compounds, in solution under conditions of motional narrowing limit ($\omega_0^2 \tau_0^2 \ll 1$, where ω_0 is the resonance angular frequency and τ_0 is the correlation time, characterizing molecular motions), the longitudinal relaxation time T_1 is given by¹⁴⁻¹⁶

$$(T_1)^{-1} = (T_1^{\text{dd}})^{-1} + (T_1^{\text{sr}})^{-1} + (T_1^{\text{sc}})^{-1} + (T_1^{\text{csa}})^{-1} \quad (1)$$

Owing to the rather long distances $d_{\text{Hg-H}}$, dipolar interactions (T_1^{dd}) are unimportant. Spin-rotation interactions (T_1^{sr}) have to be considered only for the limited number of small molecules containing mercury, such as HgMe_2 ^{13,34,101} or the Hg^{2+} ion in aqueous solution ($T_1(^{199}\text{Hg}) = 0.5$ s at $B_0 = 2.1 \text{ T}^{52}$). Scalar interactions are less important for T_1^{sc} (except for

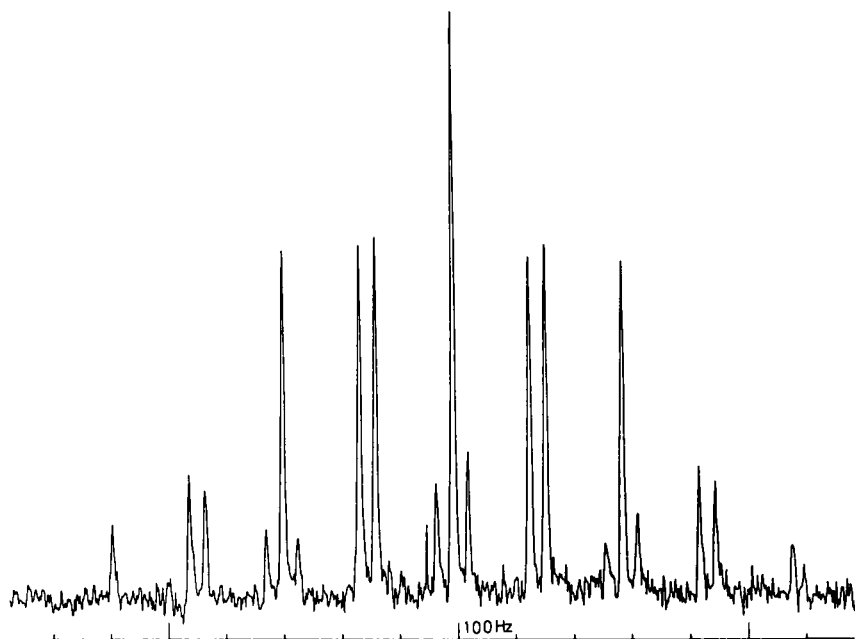


Fig. 2. 35.85 MHz ^1H -coupled ^{199}Hg NMR spectrum of divinylmercury $[\text{Hg}(\text{CH}=\text{CH}_2)_2]$ dissolved in CDCl_3 ($\approx 1\text{m}$) at 27°C . At this field strength ($B_0 = 4.7\text{ T}$) relatively small molecules give rise to reasonably well-resolved spectra which can be analysed for $J(^{199}\text{Hg}^1\text{H})$ values.

compounds containing an $\text{Hg-As}^{17\text{a}}$ or an Hg-I bond, $^{17\text{b}}$ studied at low field strengths B_0) but fairly important for T_2^{sc} , in case of chemical exchange and/or scalar coupling with quadrupolar nuclei 14,18 (e.g. ^{14}N , $^{35,37}\text{Cl}$, $^{79,81}\text{Br}$, ^{127}I , etc.). Finally, the contribution from T_1^{csa} , arising from the anisotropy of nuclear shielding ($\Delta\sigma$), becomes the dominating mechanism (equation (2) for symmetric tensors: $\sigma_{zz} \neq \sigma_{xx} = \sigma_{yy}$), at least at field strengths $B_0 \geq 4.7\text{ T}$, for all mercury compounds with linear, trigonal planar or distorted tetrahedral surrounding of the ^{199}Hg nucleus. 12,13,19

$$(T_1^{\text{csa}})^{-1} = \frac{7}{6}(T_2^{\text{csa}})^{-1} = \frac{2}{15}(\gamma^2 B_0^2)(\Delta\sigma)^2 \tau_c \quad (2)$$

Since the chemical shift anisotropy $\Delta\sigma(^{199}\text{Hg})$ may be in the order of 3000–7500 ppm, 12,19,20 $T_1^{\text{csa}}(^{199}\text{Hg})$ and $T_2^{\text{csa}}(^{199}\text{Hg})$ can be very short ($< 0.1\text{ s}$). Therefore, ^{199}Hg resonances may be broad and couplings to other nuclei may not always be resolved. Of course, the latter is also true for ^{199}Hg satellites in X NMR spectra. 93 Thus, ^{199}Hg satellites are observed as sharp lines, severely broadened, or not at all. This depends on the ^{199}Hg nuclear spin relaxation rate which in turn is related to the structure of the mercury compound, as well

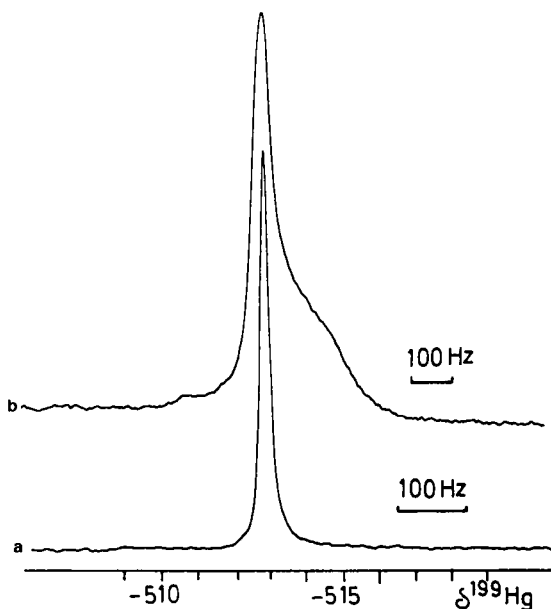


Fig. 3. $^{199}\text{Hg}\{^1\text{H}\}$ NMR spectra of $\text{Me}-\text{Hg}-\text{C}\equiv\text{C}-\text{H}$ in C_6D_6 (0.1 M) at 25°C , measured at two different field strengths (32 scans each). (a) 53.8 MHz. (b) 89.6 MHz: Note the increase in the line width as the result of efficient relaxation via the chemical shift anisotropy mechanism; furthermore, the dependence of $\delta^{199}\text{Hg}$ on temperature gradients in the sample contributes to the linewidth and causes a distorted lineshape.

as on the experimental conditions, namely on B_0 and the temperature. It is important to distinguish between the effect of ^{199}Hg nuclear spin relaxation by the chemical shift anisotropy mechanism and chemical exchange, leading to the elimination of scalar coupling to ^{199}Hg nuclei.

4. CHEMICAL SHIFTS, $\delta^{199}\text{Hg}$

4.1. General

Changes in nuclear shielding of heavy nuclei A are dominated by the paramagnetic term, σ_A^p of the nuclear screening constant σ_A ($\sigma_A = \sigma_A^d + \sigma_A^p$, where σ_A^d is the diamagnetic term). There are numerous non-relativistic empirical and semi-empirical approaches to predict and calculate nuclear shielding. As shown in (3) the problem of calculating origin-dependent molecular terms σ_A^d and σ_A^p is circumvented by using independent electron

molecular orbitals to obtain local terms $\sigma_A^d(\text{loc})$ and $\sigma_A^p(\text{loc})$. Although this expression does not give accurate individual shielding terms, it is useful for the discussion of trends and shows the relation of $\sigma_A^p(\text{loc})$ to the electronic structure of the nucleus A and its immediate surroundings.

$$\sigma_A^p(\text{loc}) = -\frac{\mu_0\mu_B^2}{2\pi}(\Delta E)^{-1}[\langle r^{-3} \rangle_{\text{np}}P_i + \langle r^{-3} \rangle_{\text{nd}}D_i] \quad (3)$$

where the term ΔE is the mean excitation energy (of magnetically active, i.e. magnetic-dipole allowed, electronic transitions), $\langle r^{-3} \rangle_{\text{np}}$ and $\langle r^{-3} \rangle_{\text{nd}}$ are averaged radial expansion terms for the free atom, and P_i , D_i stand for the "imbalance" of the valence electrons in p and d orbitals, respectively, on atom A.

Semi-empirical calculations of ^{199}Hg shielding constants, based on a simplified model, show that the general trends of $\delta^{199}\text{Hg}$ for linear compounds HgR_2 can be reproduced with moderate success.²⁷⁴ In the case of heavy nuclei such as ^{199}Hg , a relativistic analogue to Ramsey's theory of nuclear shielding should be considered.^{168,169}

4.2. Patterns of $\delta^{199}\text{Hg}$ chemical shifts

4.2.1. Mercury compounds containing two-, three- and tetra-coordinate mercury

Chemical shifts $\delta^{199}\text{Hg}$ cover a range of > 5000 ppm ($\delta^{199}\text{Hg} \approx +1700$ for $[\text{Hg}(\text{SiR}_3)_4]^{2-}$ to ≈ -3500 for $[\text{HgI}_4]^{2-}$). The $\delta^{199}\text{Hg}$ values of linear mercury compounds are the result of mutual interactions between two ligands and intermolecular interactions either between the molecular mercury compounds themselves or between the mercury compound and the respective solvent (or other reagents present in the solution). The solvent effects are significant (up to 150 ppm), depending strongly on the electronic structure of the mercury compound. Therefore, the true contribution of a particular ligand R to ^{199}Hg nuclear shielding cannot be straightforwardly deduced from $\delta^{199}\text{Hg}$ values for HgR_2 (as $\delta^{199}\text{Hg}/2$) and is not a constant for the accurate prediction of $\delta^{199}\text{Hg}$ values in compounds with two different groups linked to mercury. However, the concept of linear additivity of $\delta^{199}\text{Hg}$ values can be used as a rough guideline for evaluating expectation-ranges of $\delta^{199}\text{Hg}$ values. It appears that the increase of the coordination number of mercury from 2 to 3 leads to decreased ^{199}Hg nuclear shielding,³¹ irrespective of whether a normal trigonal planar surrounding of the mercury results or a T-shaped structure because of weak interactions. In addition to coordinative bonds there seem to be electrostatic interactions between solvent molecules and the linear mercury compounds, causing an increase in ^{199}Hg nuclear

shielding. In the case of many alkynyl mercury compounds, the solubility proved sufficient in various polar and non-polar solvents to carry out a study of the temperature dependence of $\delta^{199}\text{Hg}$ values for each particular solvent. The results for $\text{Hg}(\text{C}\equiv\text{C}-\text{Ph})_2$ clearly show the competing influence of both types of interactions.⁸⁸ In non-polar as well as in non-coordinating solvents, increasing temperature leads to a decrease in ^{199}Hg shielding⁸⁸ (in agreement with the behaviour of $\text{Hg}(\text{CH}_2\text{SiMe}_3)_2$ ⁸⁷), whereas the ^{199}Hg nuclear shielding increases at higher temperatures for coordinating solvents.⁸⁸ The measurement of the linewidths of ^{35}Cl NMR signals has been suggested as an alternative method for studying coordinative interactions between Cl^- anions and MeHg- or Hg(II) complexes. This is based on efficient quadrupolar relaxation induced by distortion of the electric field gradient associated with the ^{35}Cl nucleus.²⁶¹

Electronegative substituents linked to mercury or to the atom next to mercury tend to increase the ^{199}Hg nuclear shielding, whereas electropositive substituents cause deshielding. In organomercury compounds the replacement of hydrogens β to mercury leads to strongly increased ^{199}Hg nuclear shielding (see, for example, Albright *et al.*⁸⁷ for a large data set):

	$(\text{CH}_3)_2\text{Hg}$	$(\text{CH}_3\text{CH}_2)_2\text{Hg}$	$[(\text{CH}_3)_2\text{CH}]_2\text{Hg}$	$[(\text{CH}_3)_3\text{C}]_2\text{Hg}$
$\delta^{199}\text{Hg}$ (in C_6H_6)	- 50.4	- 294.0	- 595.0	- 828.0

The opposite effect is observed in the case of silyl mercury compounds:^{87,111}

	$(\text{H}_3\text{Si})_2\text{Hg}$	$\text{H}_3\text{Si}-\text{Hg}-\text{SiMe}_3$	$(\text{Me}_3\text{Si})_2\text{Hg}$
$\delta^{199}\text{Hg}$ (in C_6H_6)	+ 196.0	+ 327.0	+ 456.0

The low ^{199}Hg nuclear shielding in many silyl mercury compounds can be explained in terms of the $(\Delta E)^{-1}$ dependence of the paramagnetic screening constant in (2). Indeed, there is a relationship between $\delta^{199}\text{Hg}$ and the lowest observed UV absorption of silyl mercury derivatives.⁸⁷ Since this electronic transition is connected with the Hg-Si σ bond, electronegative substituents at the silicon atom lower the energy of electrons in this bond and lead to an increase in ^{199}Hg nuclear shielding. The replacement of methyl by ethyl groups will have the opposite effect:⁸⁷

	$(\text{Et}_3\text{Si})_2\text{Hg}$	$[\text{Me}_2(\text{Et})\text{Si}]_2\text{Hg}$	$(\text{Me}_3\text{Si})_2\text{Hg}$	$[\text{Me}_2(\text{Cl})\text{Si}]_2\text{Hg}$
$\delta^{199}\text{Hg}(\text{C}_6\text{D}_6/\text{C}_6\text{F}_6)$	+ 849.0	+ 596.0	+ 499.0	- 315.0
	$[\text{Cl}_2(\text{Me})\text{Si}]_2\text{Hg}$	$(\text{Cl}_3\text{Si})_2\text{Hg}$		
	- 658.0	- 1001.0		

In contrast with the shielding of many other nuclei, the so called γ -effect decreases the ^{199}Hg nuclear shielding:

	$(\text{CH}_3\text{CH}_2)_2\text{Hg}$	$(\text{CH}_3\text{CH}_2\text{CH}_2)_2\text{Hg}$	$[(\text{CH}_3)_3\text{CCH}_2]_2\text{Hg}$
$\delta^{199}\text{Hg}$	- 294.0	- 240.0	- 149.4

4.2.2. Isotope-induced ^{199}Hg chemical shifts

Mainly $^2\Delta^{2/1}\text{H}$, $^{187}1.2.3\Delta^{13/12}\text{C}^{69.100.187.194}$ and $^1\Delta^{29/28}\text{Si}^{100}$ isotope-induced shifts of ^{199}Hg resonances have been determined. The unusual observation of a high-frequency shift upon substitution by the heavier isotope indicates that isotope-induced shifts are fairly complex parameters¹⁹⁵ and that competing influences of opposite sign must be considered. Such a behaviour appears to be typical of heavy nuclei such as ^{119}Sn or ^{207}Pb ,²²⁰ whereas the opposite and expected trend is found for light nuclei.¹⁹⁵

5. INDIRECT NUCLEAR SPIN-SPIN COUPLING CONSTANTS $^nJ(^{199}\text{HgX})$

5.1. General

Following Ramsey's non-relativistic treatment, indirect nuclear spin-spin coupling $J(\text{AB})$, mediated by valence electrons, can be traced to several mechanisms, of which the Fermi contact term is generally considered to be of major importance. As for nuclear shielding, knowledge on the excited molecular states is required for an exact treatment. Again, the independent electron model serves in the qualitative discussion:

$$K_{\text{AB}} = \frac{4}{9}(\mu_0^2\mu_{\text{B}}^2)\Psi_{\text{A}}(\text{O})^2\Psi_{\text{B}}(\text{O})^2\Pi_{\text{AB}} \quad (4)$$

where K is the reduced coupling constant [$K_{\text{AB}} = 4\pi^2 J_{\text{AB}}(\gamma_{\text{A}}\gamma_{\text{B}}h)^{-1}$], $\Psi_{\text{A}}(\text{O})^2$ and $\Psi_{\text{B}}(\text{O})^2$ refer to the respective valence s electron densities, and Π_{AB} is the mutual polarizability of the A and B s orbitals, representing the differences of one-electron energies. For heavy nuclei, the mean excitation energy approximation is not valid and a linear relationship between the “ s -character” of the A–B bond (in the case of one-bond couplings) and the magnitude of J_{AB} would be fortuitous. Furthermore, a theoretical treatment of coupling constants involving heavy nuclei such as ^{199}Hg should use the relativistic analogue of Ramsey's theory.¹¹⁰ Qualitatively, the relativistic approach agrees with the dominance of a term corresponding to the contact term. However, the $\Psi(\text{O})^2$ values have to be corrected for relativistic effects.^{170,171} In the case of $^1J(^{199}\text{Hg}^{31}\text{P})$ the anisotropy Δ^1J (see also Pulkkinen *et al.*¹⁸⁵ and Solomin *et al.*²¹³ for the anisotropy of $^1J(^{199}\text{Hg}^{13}\text{C})$ of HgMe_2 partially oriented in a liquid crystalline phase) has been determined from the solid state ^{31}P NMR powder pattern for $\text{Hg}[\text{P}(o\text{-tolyl})_3]_2(\text{NO}_3)_2$. This confirmed the positive sign of this coupling constant^{37,221} and indicated that mechanisms other than the Fermi contact term are important.¹⁸⁴

5.2. Patterns of couplings $^1J(^{199}\text{HgX})$

5.2.1. One-bond couplings $^1J(^{199}\text{HgX})$

Most data on one-bond couplings $^1J(^{199}\text{HgX})$ are available for $\text{X} = ^{13}\text{C}$ (Table 12), ^{29}Si (Table 13) and ^{31}P (Table 9). One-bond couplings between ^{199}Hg and other nuclei (e.g. ^{11}B ,²⁹⁶ ^{15}N ,^{147,223} ^{77}Se ,^{27,149,286} ^{119}Sn ,²²² ^{125}Te ,^{95,166,286} ^{103}Rh ,¹⁶⁵ ^{183}W ,⁵⁰ ^{195}Pt ,¹²⁹ ^{199}Hg ⁸⁹) have been reported but there is no systematic study so far. The largest one-bond coupling constant that has ever been measured was observed for $^1J(^{199}\text{Hg}^{199}\text{Hg})$ in the Hg_3^{2+} cation:⁸⁹ $^1J(^{199}\text{Hg}^{199}\text{Hg}) = 139\,700 \pm 300$ Hz. An example for $^1J(^{199}\text{Hg}^1\text{H})$ (746 Hz) has been observed for the bridging hydrogen in the platinum complex [*trans*-(Et_3P)₂Pt(C_6Cl_5)—H—Hg—CH₂Ph].²⁸¹

A positive sign of coupling constants $^1J(^{199}\text{Hg}^{13}\text{C})$ has been determined for various organomercury compounds. In addition to selective double-resonance experiments,^{7,8,37,174} two-dimensional heteronuclear shift correlations^{218,226} are useful in this context (see Fig. 4). There have been various attempts to relate the “*s*-character” of the Hg—C bond more or less directly with the magnitude of $^1J(^{199}\text{Hg}^{13}\text{C})$.^{25,54,55,58,70,85} Such an approach is valid only for a restricted number of closely related compounds. The magnitude of the $^1J(^{199}\text{Hg}^{13}\text{C})$ is greatly influenced by the nature of the second substituent. Thus in alkynyl mercury compounds of the type $\text{R—C}\equiv\text{C—Hg—X}$, $^1J(^{199}\text{Hg}^{13}\text{C})$ values cover a range of more than 3000 Hz:

$^1J(^{199}\text{Hg}^{13}\text{C}\equiv)$	$\text{Ph—C}\equiv\text{C—Hg—Cl}$	$\text{Ph—C}\equiv\text{C—Hg—C}\equiv\text{C—Ph}$
	3875.0 ⁸⁸	2492.5 ⁸⁸
	$\text{Bu—C}\equiv\text{C—Hg—Me}$	$\text{Bu—C}\equiv\text{C—Hg—SiMe}_3$
	1400.3 ¹⁰⁸	660.0 ¹⁰⁸

The polarizability of the Hg—C \equiv bond is strongly reduced if the second substituent is electronegative, in agreement with the concept of rehybridization.¹⁸³ However, the large range of $^1J(^{199}\text{Hg}^{13}\text{C})$ values is indicative of more complex influences than the “*s*-character” and points towards a significant contribution of relativistic effects to the coupling, involving in particular the mercury 6s electrons.

Labelling with ^{13}C has been used to study the interaction between mercury, linked to the active site of human carbonic anhydrase B, and CN^- .²⁶⁹ Both $\delta^{199}\text{Hg}$ (−910) and the $^1J(^{199}\text{Hg}^{13}\text{C})$ value (3700 Hz) were different from the data for $\text{Hg}(\text{CN})_2$.

In mercury(II)-arene complexes η^1 -bonding accompanied by rapid intramolecular exchange is assumed on the basis of averaged $^1J(^{199}\text{Hg}^{13}\text{C})$ values.²²⁹

The $^1J(^{199}\text{Hg}^{29}\text{Si})$ values measured so far (Table 13) cover a range of ≈ 3500 Hz (432 Hz for $\text{Hg}[\text{Si}(\text{SiMe}_3)_3]_2$ to 3864 Hz for $\text{Hg}(\text{SiCl}_3)_3$ ⁸⁷). A

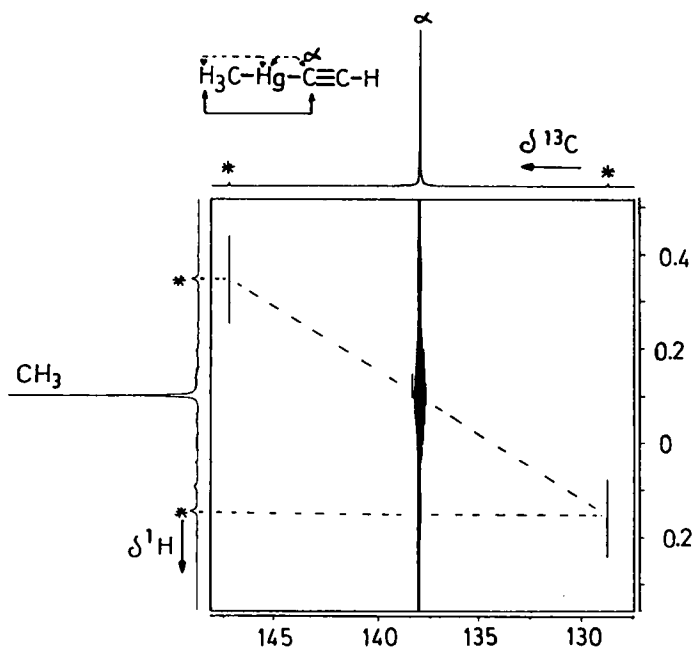


Fig. 4. Two-dimensional $^{13}\text{C}/^1\text{H}$ heteronuclear shift correlation spectrum (Bruker AC 300) showing the $^{13}\text{C}^\alpha$ resonance of $\text{Me}-\text{Hg}-\text{C}\equiv\text{C}-\text{H}$ and the $^1\text{H}(\text{HgMe})$ resonance with the respective ^{199}Hg satellites (marked by asterisks). The experiment is based on the long-range coupling $^3J(^{13}\text{C}^\alpha\text{HgC}^1\text{H})$ (shown in the formula by the solid line). Therefore, the passive nucleus is ^{199}Hg , allowing the signs of $^2J(^{199}\text{HgC}^1\text{H})$ and $^1J(^{199}\text{Hg}^{13}\text{C}^\alpha)$ to be compared (dotted lines in formula). The negative tilt of the cross peaks for the ^{199}Hg satellites proves that the signs of these coupling constants are opposite. Since $^2J(^{199}\text{HgC}^1\text{H})$ has a negative sign,^{7,8,37} the sign of $^1J(^{199}\text{Hg}^{13}\text{C}^\alpha)$ must be positive. Analogous experiments have been carried out, based on $^1J(^{13}\text{C}_{\text{Me}}^1\text{H})$ [relating $^2J(^{199}\text{HgC}^1\text{H})$ (< 0) and $^1J(^{199}\text{Hg}^{13}\text{C}_{\text{Me}})$ (> 0)], $^2J(^{13}\text{C}^\alpha\equiv\text{C}^1\text{H})$ [relating $^3J(^{199}\text{HgC}\equiv\text{C}^1\text{H})$ (> 0) and $^1J(^{199}\text{Hg}^{13}\text{C}^\alpha)$ (> 0)], and $^1J(\equiv^{13}\text{C}^1\text{H})$ [relating $^3J(^{199}\text{HgC}\equiv\text{C}^1\text{H})$ (> 0) and $^2J(^{199}\text{HgC}\equiv^{13}\text{C})$ (> 0)].

negative sign of $^1J(^{199}\text{Hg}^{29}\text{Si})$ (the reduced coupling constant $^1K(^{199}\text{Hg}^{29}\text{Si})$ is positive because of $\gamma(^{29}\text{Si}) < 0$) has been determined for $\text{Hg}(\text{SiMe}_3)_2$ by a two-dimensional $^{199}\text{Hg}/^1\text{H}$ heteronuclear shift correlation, relating $^2K(^{29}\text{SiC}^1\text{H})$ (< 0) and $^1K(^{199}\text{Hg}^{29}\text{Si})$ (> 0).²²⁷ Similar to $^1J(^{199}\text{Hg}^{13}\text{C})$ values, the $^1J(^{199}\text{Hg}^{29}\text{Si})$ data reflect the hybridization at the mercury atom.

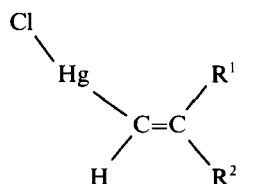
There is an enormous amount of $^1J(^{199}\text{Hg}^{31}\text{P})$ data. In many cases, the $\delta^{199}\text{Hg}$ values have also been measured as can be seen from Table 10. Further $^1J(^{199}\text{Hg}^{31}\text{P})$ values can be found in Refs. 116, 127, 230, 231, 234, 236, 239, 241, 242, 249–253, 255, 289, 290. In general, a positive sign is assumed for $^1J(^{199}\text{Hg}^{31}\text{P})$, consistent with experimental evidence.^{37,221} The $^1J(^{199}\text{Hg}^{31}\text{P})$ data

cover a huge range of more than 17 000 Hz (143 Hz (PPh_3) in $\{[(\text{EtO}_2)(\text{O})\text{P}]_2\text{-Hg}(\text{PPh}_3)_2\}^{43}$ to 17 528 Hz in $\{[(\text{MeO})_3\text{PHg}]^+\text{SO}_3\text{CF}_3^-\}^{128}$). There is a complex dependence on the electronegativity of substituents linked to mercury or to phosphorus, as well as on the coordination number of mercury. Recently, the trends in $^1J(^{199}\text{Hg}^{31}\text{P})$ values have been summarized.²⁹¹

5.2.2. Geminal couplings $^2J(^{199}\text{HgX})$

There is a large data set on $^2J(^{199}\text{Hg}^1\text{H})$, in particular for MeHg -derivatives,^{32,68,264,277,284,287,288} serving in various ways for structural assignments and for the discussion of the bonding situation. The interaction between biologically active molecules and the MeHg^+ ion can be studied, using the magnitude of $^2J(^{199}\text{Hg}^1\text{H})$.^{97,203–207,215–217,228,267} Linear relationships between $^2J(^{199}\text{Hg}^1\text{H})$ and $^1J(^{199}\text{Hg}^{13}\text{C})$ of MeHg derivatives have been established.^{32,39,260}

Many $^2J(^{199}\text{Hg}^{13}\text{C})$ values are known (see Table 12). In some vinyl mercury compounds the sign of $^2J(^{199}\text{Hg}^{13}\text{C})$ has been determined via two-dimensional $^{199}\text{Hg}/^1\text{H}$ shift correlations:⁹⁴

	R^1 R^2 $^2J(^{199}\text{Hg}^{13}\text{C})$
H H	+ 27.3
Cl H	+ 319.5
H Cl	– 115.2

Other data $^2J(^{199}\text{HgX})$ are reported, mainly for $\text{X} = ^{19}\text{F}^{37,172,224}$ and $^{31}\text{P}^{27,51,126,129,143,165,232,233,238,240,244–246,254,256,273,276,282,283,285}$. Some $^2J(^{199}\text{Hg}^{195}\text{Pt})^{281,282}$ and $^2J(^{199}\text{Hg}^{199}\text{Hg})^{292}$ values are known. The sign of $^2J(^{199}\text{Hg}^{19}\text{F})$ is positive in HgCF_3 groups.³⁷ In agreement with other geminal $^2J(^{31}\text{PMX})$ data, the *trans*-coupling $^2J(^{199}\text{HgM}^{31}\text{P})$ across the metal is large and presumably positive. In the SePBu_3 -adducts of mercury halides, a negative sign of $^2J(^{199}\text{HgSe}^{31}\text{P})$ has been determined.²⁷

5.2.3. Vicinal couplings $^3J(^{199}\text{HgX})$

Most data on vicinal couplings are available for $^3J(^{199}\text{Hg}^1\text{H})$. These data show the usual Karplus type of dependency on the respective dihedral angles. Coupling constants of the type $^3J(^{199}\text{HgEC}^1\text{H})$, e.g. $\text{E} = \text{Sn}$, serve for proving the existence of unstable derivatives such as $\text{Bu}'\text{—Hg—SnMe}_3$.⁶⁶

A growing number of $^3J(^{199}\text{Hg}^{13}\text{C})$ values are becoming available (see Table 12) and the expected dihedral dependence has been suggested.²²⁵ There are also various $^3J(^{199}\text{Hg}^{19}\text{F})$ data.^{173,237,243}

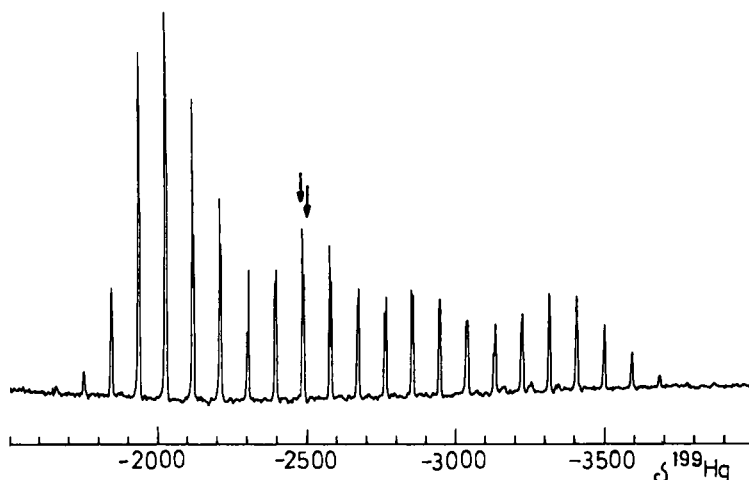


Fig. 5. A 35.85 MHz ^{199}Hg CP/MAS NMR spectrum (spinning speed 3300 Hz, contact time 5 ms, recycle delay 10 s, 4500 transients) of mercury acetate.²¹¹ The isotropic shifts of the two ^{199}Hg sites (at variance with the results of X-ray diffraction²¹⁹) are indicated by arrows. Although the extensive spinning sideband pattern contains valuable information on chemical shift anisotropy and the tensor components of the nuclear screening constant σ , it is obvious that application of ^{199}Hg CP/MAS NMR to more complex systems will not be straightforward.

5.2.4. Long-range couplings $^nJ(^{199}\text{Hg}X)$ ($n > 3$)

Data on long-range coupling constants involving ^{199}Hg are available mostly for $X = ^1\text{H}$, ^{13}C (see Table 12) and ^{19}F . There is no generally valid model for the interpretation of these data.

6. ^{199}Hg NMR OF SOLIDS

Only few NMR data are available for solid mercury compounds. In most cases ^{13}C -^{44,53,75,78,191,258} or ^{31}P CP/MAS^{208,235} (cross-polarization/magic-angle spinning) or MAS NMR has been applied and some powder patterns have been analysed for chemical shifts¹⁶⁷ and direct and indirect ^{199}Hg - ^{31}P ¹⁸⁴ and ^{199}Hg - ^{125}Te couplings.¹⁶⁶ ^{199}Hg CP/MAS NMR of mercury acetate²¹¹ has shown that the enormous anisotropy of the ^{199}Hg nuclear shielding makes it difficult, even at moderate field strengths ($B_0 = 4.7$ or 7.05 T), to measure meaningful spectra using standard equipment (Fig. 5). However, the smaller anisotropy of tetra-coordinate mercury compounds indicates that there are still numerous potential applications for ^{199}Hg CP/MAS or MAS as shown for species containing $[\text{Hg}(\text{SR})_4]^{2-}$ anions.^{98,99} A step towards useful ^{199}Hg

MAS NMR can be done using equipment for high spinning speeds (≥ 12 kHz, sacrificing the advantage of cross-polarization) in order to decrease the number and intensity of spinning sidebands.

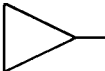

7. CONCLUSIONS

Multinuclear magnetic resonance studies of mercury compounds exploiting various modern NMR techniques are extremely helpful in the synthesis and characterization of mercury compounds. The NMR parameters aid our understanding of chemical bonding as well as of dynamic properties. The data set available for solutions is large and allows, in most cases, the prediction of chemical shifts $\delta^{199}\text{Hg}$ and coupling constants $^nJ(^{199}\text{HgX})$ in an empirical, qualitative way. On the other hand, it appears that a wide field has been left open, in particular for solid state NMR studies. In this field, new developments and numerous applications to the chemistry of mercury can be predicted.

ACKNOWLEDGEMENTS

We gratefully acknowledge the support of this work by the *Deutsche Forschungsgemeinschaft*, the *Fonds der Chemischen Industrie*, the *German Academic Exchange Service (DAAD)*, as well as *CONACYT (Mexico)*.

Table 3. Chemical shifts $\delta^{199}\text{Hg}$ of diorganomercury compounds R_2Hg , RHgR^1 (site of unsaturation removed from mercury).

Compound	$\delta^{199}\text{Hg}$	Solvent	Ref.	Other nuclei	Ref.
Me_2Hg (neat) ^a	± 0	—	—		
(1.00 M)	-50.4	C_6H_6	34		
(1.00 M)	-28.2	CDCl_3	34		
(10%)	-39.0	CH_2Cl_2	69		
(1.00 M)	-108.2	DMSO	34		
Et_2Hg (neat) ^b	-288.6	—	34		
	-294.0	$\text{C}_6\text{F}_6/\text{C}_6\text{D}_6$	50		
(1.00 M)	-364.5	DMSO	34		
(10%)	-330.4	CH_2Cl_2	69		
(2.0 M)	-304.0	CCl_4	103		
Pr_2Hg	-240.0		102		
(1.0 M)	-210.0	CCl_4	103		
Pr^i_2Hg (3.65 M)	-595.0	$\text{C}_6\text{D}_6/\text{C}_6\text{F}_6$	87		
(2.0 M)	-597.0	CCl_4	103		
Bu_3Hg (2.0 M)	-205.0	CCl_4	103		
Bu_3^iHg	-124.6		271		
Bu_3^sHg	-509.6		271		
Bu_3^iHg (0.76 M)	-828.0	$\text{C}_6\text{D}_6/\text{C}_6\text{F}_6$	87		
(conc.)	-862.0	C_6D_6	67		
	-843.7	C_6H_6	69		
	-829.0	toluene, 50%	20a		
$(\text{Bu}^i\text{-Hg-CH}_2\text{C}(\text{CH}_3)_3)$	-132.4	CDCl_3	81		
$[(\text{CH}_3)_3\text{CCH}_2]_2\text{Hg}$	-149.4	CDCl_3	81		
	-153.0	—	20a		
$(\text{C}_6\text{H}_{13})_2\text{Hg}$ (1.92 M)	-206.0	$\text{C}_6\text{D}_6/\text{C}_6\text{F}_6$	87		
( ₂ Hg)	-390.0	$\text{C}_6\text{D}_6/\text{C}_6\text{F}_6$	87		
( ₂ Hg)	-334.0	$\text{C}_6\text{D}_6/\text{C}_6\text{F}_6$	87		


$(C_6H_{11})_2Hg(1.89\text{ M})$	- 218.0	C_6D_6/C_6F_6	87		
$(C_6H_5CH_2)_2Hg(1.0\text{ M})$	- 700.0	CH_2Cl_2	103		
	- 700.0	$CDCl_3/CH_2Cl_2$	30	^{13}C	30
	- 716.5	DMSO	34		
	- 691.7	$CDCl_3$	65	^{13}C	65
$(3-Me-C_6H_4CH_2)_2Hg$	- 693.3	$CDCl_3/CH_2Cl_2$	30	^{13}C	30
$(4-Me-C_6H_4CH_2)_2Hg$	- 690.0	$CDCl_3/CH_2Cl_2$	30	^{13}C	30
$(C_6H_5CH_2CH_2)_2Hg$	- 311.0	—	112		
$Me-Hg-CF_3$	- 799.0	CH_2Cl_2	37	$^{13}C, ^{19}F$	37
$(CF_3)_2Hg^c$	- 1675.0	THF	37	^{19}F	37
	- 1611.0	CH_2Cl_2	37	^{19}F	37
	- 1668.7	THF	182	$^{13}C, ^{19}F$	182
				^{13}C (solid)	191
				$^{13}C, ^{19}F$	192
$(CF_3CH_2)_2Hg$	—	various			
$[(CF_3)_2CF]_2Hg$	- 1542.6	—	100		
$(3-F-C_6H_4CH_2)_2Hg$	- 727.1[14.5]	$CDCl_3/CH_2Cl_2$	30	^{13}C	30
$(4-F-C_6H_4CH_2)_2Hg$	- 696.8[43.9]	$CDCl_3/CH_2Cl_2$	30	^{13}C	30
$(3-CF_3-C_6H_4CH_2)_2Hg$	- 731.4	$CDCl_3/CH_2Cl_2$	30	^{13}C	30
$(2-Br-C_6H_4CH_2)_2Hg$	- 681.5	$CDCl_3$	65	^{13}C	65
$(3-Br-C_6H_4CH_2)_2Hg$	- 718.6	$CDCl_3$	65		
$(4-Br-C_6H_4CH_2)_2Hg$	- 714.6	$CDCl_3$	65	^{13}C	65
$(2,6-Br_2-C_6H_3CH_2)_2Hg$	- 714.7	$CDCl_3$	65	^{13}C	65
$(3,5-Br_2-C_6H_3CH_2)_2Hg$	- 739.3	$CDCl_3$	65		
$(2,4,6-Br_3-C_6H_2CH_2)_2Hg$	- 737.6	$CDCl_3$	65		
$(2,4,6-Cl_3-C_6H_2-OCH_2)_2Hg$	- 741.4	$CDCl_3$	77		
					
$(\text{cyclohexanone-Hg})_2Hg(0.4\text{ M})$	- 296.0	$CDCl_3$	42	^{13}C	42
$PhCH_2-Hg-CH(CN)Ph$	- 1004.0	acetone	275		
$(PhCH_2-Hg)_2C(CN)Ph$	- 888.0	acetone	275		
$Me-Hg-C_3H_5$	- 707.0	$CDCl_3$	196		
$Hg[CH(PPh_2)_2]_2$	- 659	THF	133	^{31}P	133

Table 3. (Continued)

Compound	$\delta^{199}\text{Hg}$	Solvent	Ref.	Other nuclei	Ref.
$\text{Bu}^{\text{t}}\text{-Hg-CH}_2\text{SiMe}_3$	-90.9	CDCl_3	81		
$(\text{Me}_3\text{SiCH}_2)_2\text{Hg}$	-55.4	CDCl_3	81		
(3.63 M)	-58.0	$\text{C}_6\text{D}_6/\text{C}_6\text{F}_6$	87		
$(\text{Cl}_3\text{SiCH}_2)_2\text{Hg}$	^c	—	179	^{29}Si	179
$[(\text{MeO})_3\text{SiCH}_2]_2\text{Hg}$	^d	—	179	^{29}Si	179
$[\text{Me}_2(\text{AcO})\text{SiCH}_2]_2\text{Hg}$	-265.1	CDCl_3	272	^{13}C , ^{29}Si	272
$[\text{Me}(\text{AcO})_2\text{SiCH}_2]_2\text{Hg}$	-371.3	CDCl_3	272	^{13}C , ^{29}Si	272
$[(\text{AcO})_3\text{SiCH}_2]_2\text{Hg}$	-456.8	CDCl_3	272	^{13}C , ^{29}Si	272
$\text{Bu}^{\text{t}}\text{-Hg-CH}_2\text{GeMe}_3$	-65.8	CDCl_3	81		
$(\text{Me}_3\text{GeCH}_2)_2\text{Hg}$	-5.2	CDCl_3	81		
$\text{Bu}^{\text{t}}\text{-Hg-CH}_2\text{SnMe}_3$	-16.3[508]	CDCl_3	81	^{119}Sn	81
$(\text{Me}_3\text{SnCH}_2)_2\text{Hg}$	+100.6[454]	CDCl_3	81	^{119}Sn	81

^a Reference compound Me_2Hg : $\Xi(^{199}\text{Hg}) = 17910841\text{ Hz}$; $\delta^{199}\text{Hg}$ values for a larger variety of solvents are given by Sens *et al.*³⁴

^b For $\delta^{199}\text{Hg}$ values in other solvents, see Sens *et al.*³⁴

^c Referencing not specified; ^{199}Hg resonance is shifted by 424 ppm to lower frequency relative to that of $(\text{Me}_3\text{SiCH}_2)_2\text{Hg}$.

^d Referencing not specified; ^{199}Hg resonance is shifted by 137 ppm to lower frequency relative to that of $(\text{Me}_3\text{SiCH}_2)_2\text{Hg}$.

^e Measured in many different solvents and in five different nematic phases.²⁷⁰

Table 4. Chemical shifts $\delta^{199}\text{Hg}$ of diorganomercury compounds R_2Hg , RHgR^1 (site of unsaturation adjacent to mercury).

Compound	$\delta^{199}\text{Hg}$	Solvent	Ref.	Other nuclei	Ref.
Ph_2Hg (1.0 M)	-742	CH_2Cl_2	103	^{13}C	88
	-750	CDCl_3	64	^{13}C	64
	-749.0	CDCl_3	69		
	-755.8	CH_2Cl_2	69		
	-796.0	THF	176		
	-808.0	acetone	173		
	-789.4	pyridine	56		
$(2\text{-Me-C}_6\text{H}_4)_2\text{Hg}$	-638.0	CDCl_3	64	^{13}C	64
$(3\text{-Me-C}_6\text{H}_4)_2\text{Hg}$	-739.0	CDCl_3	64	^{13}C	64
$(4\text{-Me-C}_6\text{H}_4)_2\text{Hg}$	-708.0	CDCl_3	64	^{13}C	64
$(2,5\text{-Me}_2\text{-C}_6\text{H}_3)_2\text{Hg}$	-629.0	CDCl_3	64	^{13}C	64
$(2,6\text{-Me}_2\text{-C}_6\text{H}_3)_2\text{Hg}$	-503.0	CDCl_3	64	^{13}C	64
$2,4,6\text{-Me}_3\text{-C}_6\text{H}_2)_2\text{Hg}$	-470.0	CDCl_3	64	^{13}C	64
$2\text{-Me-C}_6\text{H}_4\text{-Hg-Ph}$	-694.0	CDCl_3	64	^{13}C	64
$3\text{-Me-C}_6\text{H}_4\text{-Hg-Ph}$	-744.0	CDCl_3	64	^{13}C	64
$4\text{-Me-C}_6\text{H}_4\text{-Hg-Ph}$	-769.1	pyridine	56		
$3\text{-F-C}_6\text{H}_4\text{-Hg-Ph}$	-820.0	pyridine	56		
$4\text{-F-C}_6\text{H}_4\text{-Hg-Ph}$	-786.8	pyridine	56		
	-792.0	THF	176		
$\text{C}_6\text{F}_5\text{-Hg-Ph}$	-829.0	CH_2Cl_2	103		
$3\text{-CF}_3\text{-C}_6\text{H}_4\text{-Hg-Ph}$	-829.0	pyridine	56		
$3\text{-Cl-C}_6\text{H}_4\text{-Hg-Ph}$	-825.8	pyridine	56		
$4\text{-Cl-C}_6\text{H}_4\text{-Hg-Ph}$	-798.0	pyridine	56		
	-826.0	THF	176		
$3,4\text{-Cl}_2\text{-C}_6\text{H}_3\text{-Hg-Ph}$	-829.1	pyridine	56		
$4\text{-MeO-C}_6\text{H}_4\text{-Hg-Ph}$	-751.3	pyridine	56		
	-707.0	THF	176		
$4\text{-Me}_2\text{N-C}_6\text{H}_4\text{-Hg-Ph}$	-713.3	pyridine	56		

Table 4. (Continued)

Compound	$\delta^{199}\text{Hg}$	Solvent	Ref.	Other nuclei	Ref.
Ph-Hg-CH(CN)Ph	-1043.0	acetone	275		
(Ph-Hg) ₂ C(CN)Ph	-929.0	acetone	275		
(C ₆ F ₅) ₂ Hg (sat.)	-920.0	acetone	173		
Me-Hg-Ph	-392.0	CDCl ₃	37	¹³ C	37
CF ₃ -Hg-Ph	-1160.0	CDCl ₃	37	¹³ C, ¹⁹ F	37
CBr ₂ Cl-Hg-Ph (1.00 M)	-1186.9	DMSO	34		
(CH ₂ =CH) ₂ Hg (neat)	-641.9	—	34	¹³ C	88
(1.0 M)	-716.5	DMSO	34		
(2 M)	-648.0	CH ₂ Cl ₂	34, 103		
	-621.0	+ 20% TMS	174		
(CF ₂ =CF) ₂ Hg	-957.0	—	172	¹⁹ F	172
(CCl ₂ =CCl) ₂ Hg	-1167.9	CDCl ₃	118		
(2.0 M)	-1142.0	CH ₂ Cl ₂	103		
Me-Hg-CF=CF ₂	-482.0	—	172	¹⁹ F	172
Ph-Hg-CCl=CCl ₂	-975.1	toluene	118		
(H-C≡C) ₂ Hg	-989.3	CDCl ₃	88	¹³ C	88
(Me-C≡C) ₂ Hg	-884.8	CDCl ₃	88	¹³ C	88
	-928.7	DMSO	88		
(Bu-C≡C) ₂ Hg	-870.0	CDCl ₃	88	¹³ C	88
	-872.0	C ₆ D ₆	88	¹³ C	88
	-917.0	1,4-dioxane	88		
	-827.0	pyridine	88		
	-820.0	Me ₂ S	88		
(Bu ^t -C≡C) ₂ Hg	-848.3	CDCl ₃	88	¹³ C	88
(Ph-C≡C) ₂ Hg	-875.0	CDCl ₃	88	¹³ C	88
	-874.0	C ₆ D ₆	88	¹³ C	88
	-826.0	pyridine	88	¹³ C	88
	-941.0	DMSO	88	¹³ C	88
	-932.0	acetone	88		

	- 940.0	1,4-dioxane	88		
	- 928.0	MeCN	88		
	- 808.0	Me ₂ S	88		
	- 797.0	Et ₂ NH	88		
Bu-C≡C-Hg-C≡C-Ph	- 930.0	1,4-dioxane	88	¹³ C	88
(Cl-C≡C) ₂ Hg	- 986.3	CDCl ₃	88	¹³ C	88
(ClCH ₂ -C≡C) ₂ Hg	- 943.9	CDCl ₃	106	¹³ C	106
(Br-C≡C) ₂ Hg	- 1051.4	DMSO	107	¹³ C	107
(BrCH ₂ -C≡C) ₂ Hg	- 943.0	CDCl ₃	106	¹³ C	106
(2-MeO-C ₆ H ₄ -C≡C) ₂ Hg	- 874.6	CDCl ₃	88	¹³ C	88
(3-MeO-C ₆ H ₄ -C≡C) ₂ Hg	- 886.3	CDCl ₃	88	¹³ C	88
(4-MeO-C ₆ H ₄ -C≡C) ₂ Hg	- 852.5	CDCl ₃	88	¹³ C	88
(Me ₃ Si-C≡C) ₂ Hg	- 1015	C ₆ D ₆	108	¹³ C, ²⁹ Si	108
Me-Hg-C≡C-H	- 496.1	CDCl ₃	88	¹³ C	88
	- 509.6	C ₆ D ₆	88	¹³ C	88
	- 533.5	pyridine	88	¹³ C	88
	- 566.7	DMSO	88	¹³ C	88
Me-Hg-C≡C-Me	- 459.3	CDCl ₃	107	¹³ C	107
Me-Hg-C≡C-Bu	- 461.2	CDCl ₃	88	¹³ C	88
Me-Hg-C≡C-Ph	- 479.7	CDCl ₃	88		
	- 542.0	?	120	¹³ C	120
Me-Hg-C≡C-SiMe ₃	- 514.0	C ₆ D ₆	108	¹³ C, ²⁹ Si	108
Me-Hg-C≡C-Hg-Me	- 480.5	CDCl ₃	88	¹³ C	88
Et-Hg-C≡C-H	- 639.5	CDCl ₃	88	¹³ C	88
Et-Hg-C≡C-Hg-Et	- 627.8	CDCl ₃	88		
Bu-Hg-C≡C-H	- 600.7	CDCl ₃	88	¹³ C	88
Bu ^t -Hg-C≡C-H	—	CDCl ₃	—	¹³ C	25
Bu ^t -Hg-C≡C-Ph	- 833.0	C ₆ D ₆	108	¹³ C	108
Me ₃ CCH ₂ -Hg-C≡C-H	- 623.6	CDCl ₃	88	¹³ C	88
C ₆ H ₁₁ -Hg-C≡C-Bu	- 693.4	—	180		
C ₆ H ₁₁ -Hg-C≡C-C ₆ H ₄ -4-F	- 710.6	—	180		
C ₆ H ₁₁ -Hg-C≡C-Hg-C ₆ H ₁₁	- 730.8	CDCl ₃	88	¹³ C	88

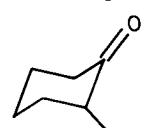
Table 4. (Continued)

Compound	$\delta^{199}\text{Hg}$	Solvent	Ref.	Other nuclei	Ref.
$\text{Me}_3\text{SiCH}_2\text{-Hg-C}\equiv\text{C-H}$	-527.1	CDCl_3	88	^{13}C	88
$\text{Ph-Hg-C}\equiv\text{C-H}$	-859.1	CDCl_3	88	^{13}C	88
$\text{Ph-Hg-C}\equiv\text{C-Bu}$	-814.7	CDCl_3	88		
$\text{Ph-Hg-C}\equiv\text{C-Ph}$	-818.6	CDCl_3	88	^{13}C	88
$\text{Ph-Hg-C}\equiv\text{C-Hg-Ph}$	-750.0	CDCl_3	88	^{13}C	88
$4\text{-Me-C}_6\text{H}_4\text{-Hg-C}\equiv\text{C-C}_6\text{H}_4\text{-4-F}$	-796.2	toluene	181	^{19}F	181
	-825.4	pyridine	181	^{19}F	181
$4\text{-F-C}_6\text{H}_4\text{-Hg-C}\equiv\text{C-Bu}$	-796.7	toluene	181	^{19}F	181
	-782.3	pyridine	181	^{19}F	181
$4\text{-F-C}_6\text{H}_4\text{-Hg-C}\equiv\text{C-Ph}$	-807.3	toluene	181	^{19}F	181
	-836.1	pyridine	181	^{19}F	181
$4\text{-F-C}_6\text{H}_4\text{-Hg-C}\equiv\text{C-CH}_2\text{Cl}$	-841.3	toluene	181	^{19}F	181
	-860.3	pyridine	181	^{19}F	181
$4\text{-F-C}_6\text{H}_4\text{-Hg-C}\equiv\text{C-CO}_2\text{Et}$	-882.7	toluene	181	^{19}F	181
	-890.4	pyridine	181	^{19}F	181
$4\text{-F-C}_6\text{H}_4\text{-Hg-C}\equiv\text{C-CN}$	-943.8	toluene	181	^{19}F	181
	-942.5	pyridine	181	^{19}F	181
$\text{CH}_2=\text{CH-Hg-C}\equiv\text{C-H}$	-831.3	CDCl_3	88	^{13}C	88
$4\text{-MeHg-3-CN-5-Ph-isoxazole}$	-344.0	CDCl_3	120	^{13}C	120

Table 5. Chemical shifts $\delta^{199}\text{Hg}$ of organomercury halides and pseudohalides.

Compound	$\delta^{199}\text{Hg}$	Solvent	Ref.	Other nuclei	Ref.
Me-Hg-Cl	(0.2 M)	$-\text{CDCl}_3$	31		
	(0.1 M)	C_6D_6	31		
	(0.2 M)	DMSO	31		
	(1.00 M)	DMSO	34		
	(0.2 M)	THF	31		
	(0.2 M)	MeOH	31		
	(0.2 M)	$\text{H}_2\text{O}/\text{D}_2\text{O}$	31		
	(0.2 M)	pyridine	31		
Me-Hg-Br		CH_2Cl_2	31		
	(0.49 M)	DMSO	34		
	(1.00 M)	DMSO	34		
Me-Hg-I		CH_2Cl_2	31		
	(1.00 M)	DMSO	34		
Me-Hg-SCN		CH_2Cl_2	31		
		MeOH	31		
	(0.1 M)	D_2O	31		
Me-Hg-CN		THF	37	^{13}C	37
		DMF	206		
		$-\text{DMSO}$	80	$^{13}\text{C}, ^{14}\text{N}$	80
Me-Hg-CNO		THF	80	$^{13}\text{C}, ^{14}\text{N}$	80
		$-\text{DMSO}$	80		
Et-Hg-Cl ^b	(sat.)	$-\text{C}_6\text{H}_6$	31		
	(1.00 M)	DMSO	34		
Et-Hg-Br ^b	(sat.)	$-\text{C}_6\text{H}_6$	31		
Pr-Hg-Cl	(sat.)	$-\text{C}_6\text{H}_6$	31		
Pr-Hg-Br	(sat.)	$-\text{C}_6\text{H}_6$	31		
Bu-Hg-Cl	(sat.)	$-\text{C}_6\text{H}_6$	31		
Bu-Hg-Br	(sat.)	$-\text{C}_6\text{H}_6$	31		
$\text{Me}_3\text{CCH}_2\text{-Hg-Cl}$		THF	176		

Table 5. (Continued)

Compound	$\delta^{199}\text{Hg}$	Solvent	Ref.	Other nuclei	Ref.
$\text{C}_5\text{Me}_5\text{-Hg-Cl}$	-1350.0	CD_2Cl_2	72	^{13}C	72
$\text{CF}_3\text{-Hg-Cl}$	-1638.0	THF	37	^{13}C , ^{19}F	37
	-1578.0	CH_2Cl_2	37		
$\text{CF}_3\text{-Hg-Br}$	-1791.0	THF	37	^{13}C , ^{19}F	37
	-1719.0	CH_2Cl_2	37		
$\text{CF}_3\text{-Hg-I}$	-2062.0	THF	37	^{13}C , ^{19}F	37
	-1979.0	CH_2Cl_2	37		
$\text{CF}_3\text{-Hg-CN}$	-1559.0	THF	37	^{13}C , ^{19}F	37
$\text{Bu}^t\text{OO-CH}_2\text{CH}_2\text{CH}_2\text{-Hg-Br}$	-1319.0	CDCl_3	142	^{13}C	142
$\text{O}(\text{CH}_2\text{CH}_2\text{CH}_2\text{-Hg-Br})_2$	-1258.0	CDCl_3	142	^{13}C	142
$\text{AcO-CH}_2\text{CH}_2\text{CH}_2\text{-Hg-Br}$	-1297.0	CDCl_3	142	^{13}C	142
					
Hg-Cl	-504.0	$\text{CDCl}_3/\text{CH}_2\text{Cl}_2$	42	^{13}C	42
5-Me	-522.4		42	^{13}C	42
1,5-Me ₂	-456.0		42	^{13}C	42
5-Bu ^t	-528.2		42	^{13}C	42
1-Me-5-Bu ^t	-460.4		42	^{13}C	42
5,5-Me ₂	-467.5		42	^{13}C	42
$\text{Me}_3\text{SiCH}_2\text{-Hg-Cl}$	-823.5	CDCl_3	106	^{13}C , ^{29}Si	106
$\text{CH}_2(\text{HgCl})_2$	-758.4	DMSO	259	^{13}C	21
$\text{CH}_2(\text{HgBr})_2$	-889.0	DMSO	259	^{13}C	54
$\text{CH}_2(\text{HgI})_2$	-1109.0	DMSO	259	^{13}C	54
$\text{CH}_2(\text{HgCN})_2$	-646.1	DMSO	259	^{13}C	54
$\text{CH}(\text{HgCl})_3$	-677.3	DMSO	259	^{13}C	21
$\text{CH}(\text{HgBr})_3$	-828.4	DMSO	259	^{13}C	54

CH(HgCN) ₃	− 533.0	DMSO	259	¹³ C	54
C(HgCl) ₄	− 622.7	DMSO	259	¹³ C	21
C(HgBr) ₄	− 795.4	DMSO	259	¹³ C	54
C(HgCN) ₄	− 459.2	DMSO	259	¹³ C	54
PhCH ₂ -Hg-Cl (1 M)	− 1146.0	CDCl ₃	35	¹³ C	35
	− 1120.0	CDCl ₃ /CH ₂ Cl ₂	30	¹³ C	30
(1 M)	− 1184.0	DMSO	35		
(1 M)	− 1109.0	pyridine	35		
PhCH ₂ -Hg-Br	− 1228.0	CDCl ₃	65		
	− 1278.0	DMSO	65	¹³ C	65
	− 1218.4	pyridine	65	¹³ C	65
2-Me-C ₆ H ₄ CH ₂ -Hg-Cl	− 1093.1	CDCl ₃ /CH ₂ Cl ₂	30	¹³ C	30
3-Me-C ₆ H ₄ CH ₂ -Hg-Cl	− 1123.3	CDCl ₃ /CH ₂ Cl ₂	30	¹³ C	30
	− 1172.6	DMSO	35	¹³ C	35
4-Me-C ₆ H ₄ CH ₂ -Hg-Cl	− 1120.4	CDCl ₃ /CH ₂ Cl ₂	30	¹³ C	30
	− 1172.6	DMSO	35	¹³ C	35
3-F-C ₆ H ₄ CH ₂ -Hg-Cl	− 1126.2	CDCl ₃ /CH ₂ Cl ₂	30	¹³ C	30
	− 1182.6	DMSO	35	¹³ C	35
4-F-C ₆ H ₄ CH ₂ -Hg-Cl	− 1122.9	CDCl ₃ /CH ₂ Cl ₂	30	¹³ C	30
	− 1183.2	DMSO	35	¹³ C	35
3-CF ₃ -C ₆ H ₄ CH ₂ -Hg-Cl	− 1129.2	CDCl ₃ /CH ₂ Cl ₂	30	¹³ C	30
3-Cl-C ₆ H ₄ CH ₂ -Hg-Cl	− 1168.2	DMSO	35	¹³ C	35
4-Cl-C ₆ H ₄ CH ₂ -Hg-Cl	− 1128.4	CDCl ₃ /CH ₂ Cl ₂	30	¹³ C	30
	− 1181.0	DMSO	35	¹³ C	35
2-Br-C ₆ H ₄ CH ₂ -Hg-Br	− 1250.0	CDCl ₃	65		
	− 1294.0	DMSO	65	¹³ C	65
	− 1217.6	pyridine	65	¹³ C	65
3-Br-C ₆ H ₄ CH ₂ -Hg-Br	− 1255.0	CDCl ₃	65		

Table 5. (Continued)

Compound	$\delta^{199}\text{Hg}$	Solvent	Ref.	Other nuclei	Ref.
4-Br-C ₆ H ₄ CH ₂ -Hg-Br	-1261.0	CDCl ₃	65		
	-1220.8	pyridine	65	¹³ C	65
2,6-Br ₂ -C ₆ H ₃ CH ₂ -Hg-Br	-1208.0	CDCl ₃	65		
	-1165.2	pyridine	65	¹³ C	65
3,5-Br ₂ -C ₆ H ₃ CH ₂ -Hg-Br	-1262.0	CDCl ₃	65		
2,3,4,6-Br ₄ -C ₆ HCH ₂ -Hg-Br	-1353.0	DMSO	65		
4-MeO-C ₆ H ₄ CH ₂ -Hg-Cl	-1133.2	DMSO	35	¹³ C	35
4-NO ₂ -C ₆ H ₄ CH ₂ -Hg-Cl	-1210.3	DMSO	35	¹³ C	35
PhCH ₂ -Hg-CN	-1010.0	CDCl ₃	35	¹³ C	35
R-Hg-Cl ^d	-1186.2	CDCl ₃	189	¹³ C	189
Me ₂ (MeO)CCH ₂ -Hg-Cl	-1145.0	CHCl ₃ , 40%	198		
Me ₂ (MeO)CCH ₂ -Hg-Br	-1234.0	CHCl ₃ , 40%	198		
Me ₂ (MeO)CCH ₂ -Hg-I	-1386.0	CHCl ₃ , 40%	198		
Me ₂ (MeO)CCH ₂ -Hg-CN	-927.0	CHCl ₃ , 40%	198		
Me ₂ (MeO)CCH ₂ -Hg-SCN	-939.0	CHCl ₃ , 40%	198		
Ph-HgCl (0.5 M)	-1186.6	DMSO	34		
(1.00 M)	-1186.0	DMSO	35	¹³ C	35
(0.75 M)	-1182.6	DMSO	35	¹³ C	35
	-1182.0	DMSO	37		
Ph-Hg-Br	-1287.0	DMSO	37		
Ph-Hg-I	-1459.0	DMSO	37		
Ph-Hg-CN (1.00 M)	-1123.0	DMSO	35	¹³ C	35
	-1119.0	DMSO	35		
	-1007.0	pyridine	263		
Ph-Hg-CNO	-1088.0 ^c	DMSO	80	¹³ C, ¹⁴ N	80
	-1093.0	THF	80	¹³ C, ¹⁴ N	80
3-Me-C ₆ H ₄ -Hg-Cl	-1181.9	DMSO	35	¹³ C	35
4-Me-C ₆ H ₄ -Hg-Cl	-1162.1	DMSO	35	¹³ C	35
(1.0 M)	-1151.0	DMSO	34		

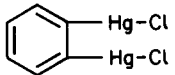
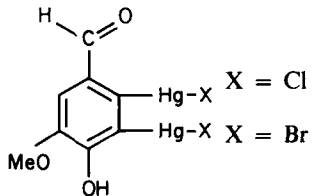
1-C ₁₀ H ₇ -Hg-Cl	- 1096.0	DMSO	148	¹³ C	148
1,8-(ClHg) ₂ -C ₁₀ H ₆	- 958.9	DMSO	148	¹³ C	148
3-F-C ₆ H ₄ -Hg-Cl	- 1206.2	DMSO	35	¹³ C	35
3-CF ₃ -C ₆ H ₄ -Hg-Cl	- 1222.9	DMSO	35	¹³ C	35
3-Br-C ₆ H ₄ -Hg-Cl	- 1234.3	DMSO	35	¹³ C	35
4-Br-C ₆ H ₄ -Hg-Cl	- 1182.4	DMSO	35	¹³ C	35
3-MeO-C ₆ H ₄ -Hg-Cl	- 1129.3	DMSO	35	¹³ C	35
4-MeO-C ₆ H ₄ -Hg-Cl	- 1142.3	DMSO	35	¹³ C	35
4-EtC(O)O-C ₆ H ₄ -Hg-Cl	- 1212.3	DMSO	35	¹³ C	35
3-NO ₂ -C ₆ H ₄ -Hg-Cl	- 1238.1	DMSO	35	¹³ C	35
4-NO ₂ -C ₆ H ₄ -Hg-Cl	- 1231.7	DMSO	35	¹³ C	35
 (0.1 M)	- 1291.0	DMSO	61		
 X = Cl	- 1199.6 (6)	DMSO	90		
	- 1231.6 (5)				
	- 1321.0 (6)	DMSO	90		
	- 1354.0 (5)				
CH ₂ =CH-Hg-Cl	- 1144.8	DMSO	69		
	- 1213.5	acetone	94	¹³ C	94
(E)-ClCH=CH-Hg-Cl	- 1186.8	acetone	94	¹³ C	94
(Z)-ClCH=CH-Hg-Cl	- 1167.9	acetone	94	¹³ C	94
CCl ₂ =CCl-Hg-Cl	- 1335.0	DMSO	118		
(E)-AcO-C(Ph)=C(Me)-Hg-Cl	- 1096.8	CDCl ₃	186, 188	¹³ C	186, 188
	- 1042.7	pyridine	188	¹³ C	188
(E)-AcO-C(Ph)=C(Ph)-Hg-Cl	- 1155.1	CDCl ₃	151	¹³ C	151

Table 5. (Continued)

Compound	$\delta^{199}\text{Hg}$	Solvent	Ref.	Other nuclei	Ref.
(E)-AcO-C(Me)=C(Ph)-Hg-Cl	-1154.2	CDCl ₃	151, 188	¹³ C	151, 188
	-1079.5	pyridine	188	¹³ C	188
(Z)-AcO-C(Me)=C(Ph)-Hg-Cl	-1191.2	CDCl ₃	151, 188	¹³ C	151, 188
	-1106.5	pyridine	188	¹³ C	188
CCl ₂ =CCl-Hg-Br	-1494.9	DMSO	118		
CCl ₂ =CCl-Hg-I	-1797.8	DMSO	118		
CCl ₂ =CCl-Hg-CN	-1281.9	DMSO	118		
CCl ₂ =CCl-Hg-SCN	-1227.4	DMSO	118		
[Me-HgCl ₂] ⁻	-596.0	CH ₂ Cl ₂	31		
[Me-HgBr ₂] ⁻	-688.0	CH ₂ Cl ₂	31		
[Me-HgI ₂] ⁻	-889.0	CH ₂ Cl ₂	31		
[Me-Hg(SCN) ₂] ⁻	-506.0	CH ₂ Cl ₂	31		

^a $^2J(^{199}\text{Hg}^{14}\text{N}) = 90.5 \text{ Hz}$.

^b Also measured in nematic phase;²¹⁴ see Grishin *et al.*²⁹⁴ for other $\delta^{199}\text{Hg}$ values of organomercury chlorides.

^c $^2J(^{199}\text{Hg}^{14}\text{N}) = 106 \text{ Hz}$.

^d R =

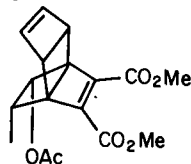


Table 6. Chemical shifts $\delta^{199}\text{Hg}$ of mercury halides and pseudohalides.

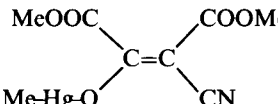
Compound	$\delta^{199}\text{Hg}$	Solvent	Ref.	Other nuclei	Ref.
HgCl_2^a	(1.0 M)	— 1501.6	DMSO	34	
	(1.0 M)	— 1498.8	DMSO	33	
	(0.5 M)	— 1279.5	pyridine	33	
	(0.5 M)	— 1518.6	THF	33	
	(0.5 M)	— 1203.0	H ₂ O	200	
		— 1590	H ₂ O	293	
HgBr_2	(0.5 M)	— 2062.1	DMSO	33	
	(1.0 M)	— 2067.4	DMSO	33	
	(0.5 M)	— 1622.2	pyridine	33	
	(0.5 M)	— 2213.1	THF	33	
HgI_2	(0.5 M)	— 3119.0	DMSO	33	
	(1.0 M)	— 3131.1	DMSO	33	
	(0.5 M)	— 2355.1	pyridine	33	
	(0.5 M)	— 3447.0	THF	33	
$\text{Hg}(\text{CN})_2^b$		— 1386.0	THF	37	¹³ C 80
$\text{Hg}(\text{CNO})_2$	(0.8 M)	— 1245.0 ^c	DMSO	80	¹⁴ N 80
	(0.029 M)	— 1284.0	THF	80	¹⁴ N 80
Cl-Hg-CN		— 1434.0	THF	37	¹³ C 37
		— 1387.0	DMSO	263	
Br-Hg-CN		— 1615.0	THF	37	¹³ C 37
		— 1556.0	DMSO	263	
I-Hg-CN		— 1942.0	THF	37	¹³ C 37
		— 1865	DMSO	263	
$\text{Hg}(\text{SCN})_2$	(0.5 M)	— 992.0	pyridine	262	
$[\text{HgCl}_3]$	(0.5 M)	— 1183.0	CH_2Cl_2	3a	
		— 1148.0	H ₂ O	200	
		— 1298	H ₂ O	293	
		— 1141.0	CH_2Cl_2	22	
$[\text{HgCl}_4]^{2-} [\text{Bu}_4\text{N}^+]_2$		— 808.0	H ₂ O	200	
		— 1170	H ₂ O	293	
		— 3510.0	CH_2Cl_2	22	
$[\text{HgI}_4]^{2-} [\text{Bu}_4\text{N}^+]_2 + 2\text{Bu}_4\text{NCl}$		— 3548.0	CH_2Cl_2	22	

^aSee Fragnals *et al.*²⁶⁶ for $\delta^{199}\text{Hg}$ values of HgCl_2 in DMSO in the presence of amines and sulphides.

^bSee Peringer²⁶³ for $\delta^{199}\text{Hg}$ values of $\text{Hg}(\text{CN})_2$ in various solvents.

^c $^2J(^{199}\text{Hg}^{14}\text{N}) = 260 \text{ Hz}$.

Table 7. Chemical shifts $\delta^{199}\text{Hg}$ of mercury and organomercury chalcogenides.

Compound	$\delta^{199}\text{Hg}$	Solvent	Ref.	Other nuclei	Ref.
$\text{Hg}(\text{OAc})_2$ (1 M)	-2389.0	HOAc	99		
(0.5 M) ^a	-2291.0	DMSO	176		
(0.5 M)	-1936.5	pyridine	176		
	-2490	solid state	99		
$\text{Hg}[\text{OC}(\text{O})\text{CF}_3]_2$ (0.05 M)	-2567.0	$\text{CF}_3\text{CO}_2\text{H}$	136		
	-2395.0	CH_2Cl_2	136		
$\text{Hg}[\text{OC}(\text{O})\text{CF}_3]_2\text{-C}_6\text{Me}_6$	-2387.0	CH_2Cl_2	136		
MeHgOH (0.1 M)	-1028.0	H_2O	199		
$[\text{MeHgOH}_2]^+$ (0.1 M)	-1150.0	H_2O	199		
Me-Hg-OAc (0.5 M)	-1039.0	pyridine	176		
(0.5 M)	-1085.0	DMSO	176		
	-1096.0		120	^{13}C	120
$[\text{CH}_3\text{C}(\text{O})\text{CH}_2\text{-Hg}]^+ \text{NO}_3^-$	-1790.0	H_2O	257		
$[\text{Hg-CH}_2\text{C}(\text{O})\text{CH}_2\text{-Hg}]^{2+}$	-1794.0	H_2O	257		
$[\text{CH}_3\text{C}(\text{O})\text{CHHg}_2]^{2+}$	-1641.0	H_2O	257		
$[\text{Hg-CH}_2\text{C}(\text{O})\text{CHHg}_2]^{3+}$	-1799.0	H_2O	257		
	-1661.0 (Hg_2)				
$[\text{CH}_3\text{C}(\text{O})\text{CHg}_3]^{3+}$	-1569.0	H_2O	257		
$[\text{Hg}_2\text{CHC}(\text{O})\text{CHHg}_2]^{4+}$	-1675.0	H_2O	257		
$[\text{Hg-CH}_2\text{C}(\text{O})\text{CHg}_3]^{4+}$	-1804.0	H_2O	257		
	-1576.0 (Hg_3)				
$[\text{Hg}_2\text{CHC}(\text{O})\text{CHg}_3]^{5+}$	-1688.0	H_2O	257		
	-1588.0				
$[\text{Hg}_3\text{CC}(\text{O})\text{CHg}_3]^{6+}$	-1599.0	H_2O	257		

Me-Hg-OC(O)C(O)O-Hg-Me	- 1094.0				
Ph-Hg-OAc (0.5 M)	- 1365.0				
(0.5 M)	- 1439.5				
Ph-Hg-OC(O)Et (0.5 M)	- 1360.6				
(0.5 M)	- 1434.0				
Ph-Hg-OC(O)-C ₆ H ₄ -2-OH ^f	- 1300.0				
	- 1439.5				
Ph-Hg-OC(O)C(O)O-Hg-Ph	- 1426.0				
[(Ph-Hg) ₂ OH] ⁺ BF ₄ ⁻	- 1466.0				
1,2-[CF ₃ C(O)O-Hg] ₂ -C ₆ H ₄	- 1595.0				
1,2-[CF ₃ C(O)O-Hg] ₂ -C ₆ Me ₄	- 1493.0				
{CF ₂ -1,2-[-CF ₂ C(O)O-Hg] ₂ -C ₆ Me ₄ } ₂	- 1474.0				
2-MeO-1-NO ₂ -C ₆ H ₃ -3,5-[Hg-OC(O)CF ₃] ₂	- 1412.1				
	- 1463.8				
1-C(O)H-3-MeO-4-OH-5,6-[Hg-OC(O)CF ₃] ₂	- 1471.2				
	- 1519.6				
CCl ₂ =CCl-Hg-OAc	- 1619.8				
CCl ₂ =CCl-Hg-O ₃ SCF ₃	- 1594.8				
NC-Hg-OAc	- 1673.0				
NC-Hg-O ₃ SCF ₃	- 1675.0				
[HgPW ₁₁ O ₃₉] ⁵⁻	- 2180.0				
Hg(SET ₂) ₂ (0.5 M)	- 848.3				
Hg(SBu ^t) ₂	- 783.2				
	- 793.0				
	- 665.0				
Hg(SCH ₂ Bu ^t) ₂	- 824.4				
Hg(SPh) ₂ (0.5 M)	- 971.0				
Hg(SCH ₂ SiMe ₃) ₂	- 851.3				
Hg[Sch(SiMe ₃) ₂] ₂	- 831.2				
Hg(S-C ₆ H ₂ -2,4,6-Pr ⁱ) ₂	- 1079.6				
Hg(S-C ₆ H ₄ -2-SiMe ₃) ₂	- 1074.6				
Hg(S-C ₆ H ₃ -2-SiMe ₃ -4-Bu ^t) ₂	- 1072.1				
		pyridine	120	¹³ C	120
		DMSO	176		
		pyridine	176		
		DMSO	176		
		pyridine	176		
		pyridine	176		
		DMSO	120		
		DMSO	138		
		CD ₃ CN	139		
		DMSO	154		
		DMSO	154		
		DMSO	90, 119		
		DMSO	90		
		DMSO	118		
		DMSO	118		
		DMSO	263		
		DMSO	263		
		H ₂ O	177	¹⁷ O, ³¹ P, ¹⁸³ W	177
		pyridine	262		
		CDCl ₃	153	¹³ C	153
		CDCl ₃	99		
		solid state	99		
		CDCl ₃	153	¹³ C	153
		pyridine	262		
		CDCl ₃	153	¹³ C	153
		CDCl ₃	153	¹³ C	153
		CDCl ₃	153	¹³ C	153
		CDCl ₃	153	¹³ C	153
		CDCl ₃	153	¹³ C	153

Table 7. (Continued)

Compound	$\delta^{199}\text{Hg}$	Solvent	Ref.	Other nuclei	Ref.
$\text{Hg}(\text{S-C}_6\text{H}_4\text{-2-SiEt}_3)_2$	-1067.8	CDCl_3	153	^{13}C	153
$\text{Hg}(2\text{-S-C}_5\text{H}_3\text{N-3-SiMe}_3)_2$	-1133.4	CDCl_3	153	^{13}C	153
$\text{Hg}(2\text{-S-C}_5\text{H}_3\text{N-3-SiEt}_3)_2$	-1130.7	CDCl_3	153	^{13}C	153
$\text{Hg}(2\text{-S-C}_5\text{H}_3\text{N-3-SiPhMe}_2)_2$	-1142.0	CDCl_3	153	^{13}C	153
$\text{Hg}(2\text{-S-C}_5\text{H}_3\text{N-6-SiBu}^t\text{Me}_2)_2$	-1112.8	CDCl_3	153	^{13}C	153
$\text{Hg}[2\text{-S-C}_5\text{H}_2\text{N-3,6-(SiBu}^t\text{Me}_2)_2]_2$	-1098.0	CDCl_3	153	^{13}C	153
$[\text{Hg}[2\text{-S-C}_6\text{H}_4)_2\text{O}]_2$	-827.4	CDCl_3	153	^{13}C	153
$\text{Hg}(\text{S-R})_2^k$	-1269.8	$\text{C}_6\text{F}_6/\text{C}_6\text{D}_6$	137	^{13}C , ^{19}F	137
$[\text{Hg}(\text{SBu}^t)_3]^-$	-157.0	DMSO	99		
	-160.0	MeCN	98		
	-158.0	solid state	98, 99		
$[\text{Hg}(\text{SPh})_3]^-$	-354.0	DMSO	99		
	-344.0	solid state	99		
$[\text{Hg}(\text{SMe})_4]^{2-}$	-374.0	H_2O	157		
$[\text{Hg}(\text{SEt})_4]^{2-}$	-302.0	H_2O	157		
$[\text{Hg}(\text{SPr}^i)_4]^{2-}$	-275.0	H_2O	157		
$[\text{Hg}(\text{SCH}_2\text{-CH}_2\text{S})_2]^{2-}$	-60.0	H_2O	157		
$[\text{Hg}(\text{SC}(\text{Me})\text{H-CH}_2\text{S})_2]^{2-}$	-62.0	H_2O	157		
$[\text{Hg}(\text{SC}(\text{Et})\text{H-CH}_2\text{S})_2]^{2-}$	-51.0	H_2O	157		
$[\text{Hg}(\text{SC}(\text{CH}_2\text{OH})\text{H-CH}_2\text{S})_2]^{2-}$	-58.0	H_2O	157		
$[\text{Hg}(1,2\text{-S,S-C}_6\text{H}_3\text{-5-Me})_2]^{2-}$	-19.0	H_2O	157		
$[\text{Hg}(\text{S-C}_6\text{H}_4\text{-4-Cl})_4]^{2-}$	-569.0	DMSO	99		
	-485.0	solid state	99		
$\text{Me-Hg-S}_2\text{O}_3$	-677.0	D_2O	175		
$\text{CH}_2(\text{Hg-S}_2\text{O}_3)_2$	-577.0	D_2O	175		
$\text{CH}(\text{Hg-S}_2\text{O}_3)_3$	-496.0	D_2O	175		
$\text{C}(\text{Hg-S}_2\text{O}_3)_4$	-453.0	D_2O	175		
$\text{Hg}(\text{S}_2\text{COPr}^i)_2$	-1295.0	CH_2Cl_2	155		
$\text{Hg}(\text{S}_2\text{COPr}^i)_3]^-$	-1039.0	CH_2Cl_2	155		

Hg(S ₂ CNMe ₂) ₂	− 1257.0	CH ₂ Cl ₂	130		
Hg(S ₂ CNEt ₂) ₂	− 1260.0	CH ₂ Cl ₂	130		
(0.5 M)	− 1312.0	pyridine	262		
Hg(S ₂ CNPr ₂) ₂	− 1213.0	CH ₂ Cl ₂	130		
+ PBu ₃	− 787.0	CH ₂ Cl ₂	130	³¹ P	130
+ 2PPBu ₃	− 527.0	CH ₂ Cl ₂	130	³¹ P	130
+ P(C ₆ H ₁₁) ₃	− 827.0	CH ₂ Cl ₂	130	³¹ P	130
Hg(S ₂ CNBU ₂) ₂	− 1294.0	CH ₂ Cl ₂	130		
Hg(S ₂ CN(CH ₂) ₅)	− 1262.0	CH ₂ Cl ₂	209		
Hg[S ₂ CN(Me)Ph] ₂	− 1313.0	CH ₂ Cl ₂	130		
[Hg(SPPPh ₂ CH ₂ PPh ₂ S) ₂] ²⁺	− 479.0	CH ₂ Cl ₂	76	³¹ P	76
Hg(dtp ₂) ₂ ^b	− 1082.0	CH ₂ Cl ₂	130	³¹ P	130
+ PBu ₃	− 737.0	CH ₂ Cl ₂	130	³¹ P	130
+ 2PBu ₃	− 517.0	CH ₂ Cl ₂	130	³¹ P	130
Hg(dtpb) ₂ ^b	− 1032.0	CH ₂ Cl ₂	130	³¹ P	130
+ PBu ₃	− 817.0	CH ₂ Cl ₂	130	³¹ P	130
+ 2PBu ₃	− 597.0	CH ₂ Cl ₂	130	³¹ P	130
Hg(dtph) ₂ ^b	− 1077.0	CH ₂ Cl ₂	130	³¹ P	130
+ PBu ₃	− 717.0	CH ₂ Cl ₂	130	³¹ P	130
+ 2PPBu ₃	− 577.0	CH ₂ Cl ₂	130	³¹ P	130
Me-Hg-SPh	− 552.6	CDCl ₃	153	¹³ C	153
	− 620.0	DMF	206		
Me-Hg-S-C ₆ H ₄ -2-SiMe ₃	− 565.5	CDCl ₃	153	¹³ C	153
Me-Hg-S-C ₆ H ₃ -2-SiMe ₃ -4-Bu ⁱ	− 565.8	CDCl ₃	153	¹³ C	153
Me-Hg-S-C ₆ H ₄ -2-SiEt ₃	− 578.2	CDCl ₃	153	¹³ C	153
Me-Hg-S-C ₆ H ₄ -2-SiPh ₃	− 620.6	CDCl ₃	153	¹³ C	153
Me-Hg-S-C ₆ H ₃ -2,6-(SiMe ₃) ₂	− 592.9	CDCl ₃	153	¹³ C	153
Me-Hg-2-S-C ₅ H ₃ N-6-SiPhMe ₂	− 583.4	CDCl ₃	153	¹³ C	153
Me-Hg-2-S-C ₅ H ₃ N-3-SiBu ⁱ Me ₂	− 569.9	CDCl ₃	153	¹³ C	153
Me-Hg-2-S-C ₅ H ₃ N-3,6-(SiBu ⁱ Me) ₂	− 563.8	CDCl ₃	153	¹³ C	153
Me-Hg-S-2-(1-Me-imidazole)	− 717.0	DMSO	115		
Me-Hg-S-Purine ^c	− 621.0	DMSO	115		

Table 7. (Continued)

Compound	$\delta^{199}\text{Hg}$	Solvent	Ref.	Other nuclei	Ref.
Me-Hg-glutathion (0.1 M)	-587.0	H ₂ O, pH = 3	199		
	-585.0	H ₂ O, pH = 9	199		
Hg(glutathion) ₂ (0.25 M)	-993.0	H ₂ O, pH = 7	199		
CCl ₂ =CCHg-SC ₂ H ₅	-985.7	DMSO/pyr.	118		
CCl ₂ =CCHg-SPh	-1144.0	DMSO	118		
NC-Hg-SEt	-932.0	pyridine	263		
NC-Hg-SPh	-999.0	pyridine	263		
Hg(S-PPh ₂ -CH-PPh ₂) ₂	-52.3	THF, -60°C	113	³¹ P	113
(NCS) ₂ Hg(SPBU ₃) ₂	-508.0	CH ₂ Cl ₂	27	³¹ P	27
{[(C ₆ F ₅) ₃ GeS] ₃ Hg} ⁻	-345.0		132	¹⁹ F	132
Hg(SePh) ₂ (0.5 M)	-1401.3	pyridine	262	⁷⁷ Se ^d	262
[(μ-ER) ₆ (HgL) ₄] ²⁻ (ClO ₄ ⁻) ₂ ^m					
E R L					
S Me PPh ₃	-327.0	CHCl ₃	149	³¹ P	149
S Et PPh ₃	-329.0	CHCl ₃	149	³¹ P	149
S Pr PPh ₃	-325.0	CHCl ₃	149	³¹ P	149
S Bu PPh ₃	-326.0	CHCl ₃	149	³¹ P	149
S Pent PPh ₃	-324.0	CHCl ₃	149	³¹ P	149
S Ph PPh ₃	-443.0	CHCl ₃	149	³¹ P	149
S Ph PEt ₃	-392.0	CHCl ₃	149	³¹ P	149
S Ph AsPh ₃	-476.0	CHCl ₃	149		
Se Ph PPh ₃	-702.0	CHCl ₃	149	³¹ P, ⁷⁷ Se	149
Se Ph PEt ₃	-638.0	CHCl ₃	149	³¹ P, ⁷⁷ Se	149
Te Me PPh ₃	-1190.0	CH ₂ Cl ₂	95	³¹ P, ¹²⁵ Te	95
Te Ph PPh ₃	-1073.0	CH ₂ Cl ₂	95	³¹ P, ¹²⁵ Te	95
Te Ph PEt ₃	-1004.0	CH ₂ Cl ₂	95	³¹ P, ¹²⁵ Te	95
[HgSe ₂] ²⁻	-796.0 ^f		286	⁷⁷ Se	286

[Hg(SePh) ₄] ²⁻	-978.0	H ₂ O	157		
Hg(SePPh ₂ CHPPh ₂) ₂	-33.3	THF, -60°C	113	³¹ P	113
[Hg(SePPh ₂ CH ₂ PPh ₂ Se) ₂] ²⁺	-785.0	CH ₂ Cl ₂	76	³¹ P, ⁷⁷ Se	76
Cl ₂ Hg(SePBu ₃) ₂	-970.0	CH ₂ Cl ₂ , -100°C	27	³¹ P, ⁷⁷ Se	27
Br ₂ Hg(SePBu ₃) ₂	-1336.0	CH ₂ Cl ₂	27	³¹ P, ⁷⁷ Se	27
I ₂ Hg(SePBu ₃) ₂	-2162.0	CH ₂ Cl ₂	27	³¹ P, ⁷⁷ Se	27
(NCS) ₂ Hg(SePBu ₃) ₂	-725.0	CH ₂ Cl ₂	27	³¹ P, ⁷⁷ Se	27
Me-Hg-Se-CH ₂ CH(NH ₃ ⁺)COO ⁻	-644.0	H ₂ O	206		
Me-Hg-Se-2-CH ₂ -C ₆ H ₄ -1-COO ⁻	-660.5	D ₂ O	159		
Me-Hg-SePh	-688.0	DMF	206		
NC-Hg-SePh (0.5 M)	-1128.0	pyridine	262		
[(μ-TePh) ₄ (HgL) ₃ (Hg)] ²⁺ (ClO ₄ ⁻) ₂					
<u>L</u>					
PPh ₃	-1098.0	DMF, -59°C	95	³¹ P, ¹²⁵ Te	95
	-875.0				
P(4-Me-C ₆ H ₄) ₃	-1087.0	DMF, -59°C	95	³¹ P, ¹²⁵ Te	95
	-857.0				
[HgTe ₂] ²⁻	-2169.0 ^a		286	¹²⁵ Te	286
[HgTeSe] ²⁻	-1516.0 ^b		286	⁷⁷ Se, ¹²⁵ Te	286
Bu ¹ -Hg-TetBu ¹	-882.7		279	¹³ C, ¹²⁵ Te	279

^aSee Fragnalini *et al.*²⁶⁶ for $\delta^{199}\text{Hg}$ values of Hg(OAc)₂ in DMSO in the presence of amines and sulphides.

^bdtbp = *O,O*-dibutyldithiophosphate; dtpp = *O,O*-diisopropyl-dithiophosphate; dtph = dicyclohexyldithiophosphate.

^cA number of other nucleic acid constituents and their analogues have been studied.

^dOwing to rapid exchange, $^1J(^{199}\text{Hg}^{77}\text{Se})$ was not observed.

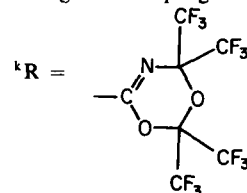
^eSee also Grishin *et al.*²⁶⁵ for $\delta^{199}\text{Hg}$ values of a series of substituted benzoic acids of the type Ph-Hg-OC(O)Ar.

^{f1} $^1J(^{199}\text{Hg}^{77}\text{Se}) = 2258\text{ Hz}$.

^{g1} $^1J(^{199}\text{Hg}^{77}\text{Se}) = 2270\text{ Hz}$; $^1J(^{199}\text{Hg}^{125}\text{Te}) = 6470\text{ Hz}$.

^{h1} $^1J(^{199}\text{Hg}^{125}\text{Te}) = 6500\text{ Hz}$.

ⁱ¹⁹⁹Hg-¹²⁵Te coupling has not been reported.



^mFor $\delta^{199}\text{Hg}$ values of mercury polysulphate complexes, see Bailey *et al.*²⁹⁸

Table 8. Chemical shifts $\delta^{199}\text{Hg}$ of mercury and organomercury nitrogen compounds.^c

Compound	$\delta^{199}\text{Hg}$	Solvent	Ref.	Other nuclei	Ref.
$\text{Hg}[\text{N}(\text{SiMe}_3)_2]_2$	-1056.0	—	41	—	
$\text{Me-Hg-N}(\text{SiMe}_3)_2$	-592.5	C_6D_6	69	^{29}Si	69
$\text{Ph-Hg-N(R)SO}_2\text{Ph}$ (0.1 M)					
R = Me	-1235.2	CDCl_3	212		
R = Et	-1190.6	CDCl_3	212		
R = Pr^i	-1155.5	CDCl_3	212		
R = Bu^t	-1198.1	CDCl_3	212		
R = Ph	-1289.1	CDCl_3	212		
R = 2- $\text{NO}_2\text{-C}_6\text{H}_4$	-1346.1	CDCl_3	212		
R = 4- $\text{NO}_2\text{-C}_6\text{H}_4$	-1294.4	CDCl_3	212		
$[\text{Me-Hg-NH}_3]^+$ (0.1 M)	-943.0	CD_3OD	3a		
$[\text{Me-Hg-pyridine}]^+$	-1233.0	MeOH	197		
$[\text{Me-Hg-2,5-Me}_2\text{-pyridine}]^+$	-1317.0	MeOH	197		
Me-Hg-imidazole ^a	-916.7	DMSO	115		
Me-Hg-(HTu) ^b	-732.1	DMSO	163	^{13}C	163
Me-Hg-(TuSMe) ^b	-918.1	DMSO	163	^{13}C	163
$(\text{Me-Hg})_2(\text{Tu})^b$	-856.0	DMSO	163	^{13}C	163
Ph-Hg-(HTu) ^b	-1072.7	DMSO	163	^{13}C	163
Ph-Hg-(TuSMe) ^b	-1258.0	DMSO	163	^{13}C	163
$(\text{Ph-Hg})_2(\text{Tu})^b$	-1185.8	DMSO	163	^{13}C	163
$\text{CCl}_2=\text{CCHg-N(N-2-Cl-C}_6\text{H}_4)_2$	-1384.9	DMSO/pyr.	118		

^a More $\delta^{199}\text{Hg}$ Hg data are reported for nucleic acid constituents and their analogues; see also Charland *et al.*¹⁴⁶

^b H_2Tu = 2,3-dihydro-2-thioxo-4(1*H*)pyrimidinone; HTuSMe = 2-methylthio-4(1*H*)-pyrimidinone; one or two hydrogen are replaced by RHg; in the crystalline state the mercury is linked to N^3 in Me-Hg-(TuSMe).

^c $\delta^{199}\text{Hg}$ data of N-alkylimine-HgCl₂ adducts, see Al-Showiman.²⁹⁵

Table 9. Chemical shifts $\delta^{199}\text{Hg}$ and coupling constants $^1J(^{199}\text{Hg}^{31}\text{P})$ (Hz) of mercury phosphorus compounds.^a

Compound	$\delta^{199}\text{Hg}$	$^1J(^{199}\text{Hg}^{31}\text{P})$	$\delta^{31}\text{P}$	Solvent	Ref.
$\text{Hg}[\text{P}(\text{O})\text{Bu}^t]_2$	− 942.0	2662	146.5	H_2O	40
	− 961.0	2682	143.4	MeOH	40
	− 873.0	2833	138.8	pyridine	40
	− 967.0	2945	137.6	C_6H_6	40
	− 958.0	3120	136.9	THF	40
$\text{Hg}[\text{P}(\text{O})(\text{OEt})_2]_2$	− 1352.0	7521	107.0	H_2O	62
	− 1242.3	7135	106.0	DMSO	160
	− 1323.3	7375	105.0	MeOH, − 40°C	160
	− 1090.3	7601	103.4	pyridine	161
	− 428.3	5283	129.0	MeOH, − 40°C	160
$\{\text{Hg}[\text{P}(\text{O})(\text{OEt})_2]_3\}^-$	− 475.3	3863	111.0	DMSO	160
$\{\text{Hg}[\text{P}(\text{O})(\text{OEt})_2]_4\}^{2-}$	− 454.3	3975	109.0	MeOH, − 40°C	160
$\text{Hg}[\text{P}(\text{O})(\text{OBu})\text{Ph}]_2$	− 1250.0	5275	—	THF	91
	− 1246.0	5264			
	− 1167.3	5506	111.3	pyridine	161
$\text{Hg}\{\text{PPh}_2[\text{M}(\text{CO})_5]\}_2$					
M = Cr	− 1106.0	640	77.2	CH_2Cl_2	46
M = Mo	− 1094.0	525	50.5	CH_2Cl_2	46
M = W	− 1091.0	725	27.4	CH_2Cl_2	46
$\text{C}_6\text{H}_{11}\text{P}[\text{Cr}(\text{CO})_5]\{\text{HgP}[(\text{C}_6\text{H}_{11})_2\text{Cr}(\text{CO})_5]\}_2$	− 508.3	1002 $[\mu_3\text{-P}]$	38.0	$\text{Et}_2\text{NH/pyr.}$	150
		1302 $[\mu_2\text{-P}]$	66.7		
$\{\text{Hg}[\text{PEt}_2\text{Cr}(\text{CO})_5]_3\}^-$	+ 119.7	921	28.7	THF	134
$\{\text{Hg}[\text{P}(\text{C}_6\text{H}_{11})(\text{H})\text{Cr}(\text{CO})_5]_3\}$	+ 272.7	900	− 12.5		150
	+ 241.7	882, 886	− 13.5, − 15.3		
$\{\text{Hg}[\text{P}(\text{Ph})(\text{H})\text{Cr}(\text{CO})_5]_3\}^-$	+ 20.7	751	− 29.4		150
	+ 66.7	835, 805	− 30.3, − 30.4		
$\text{Ph-Hg-P}(\text{O})\text{Bu}^t$	− 816.0	3094	132.8	pyridine	40

Table 9. (Continued)

Compound	$\delta^{199}\text{Hg}$	$^1J(^{199}\text{Hg}^{31}\text{P})$	$\delta^{31}\text{P}$	Solvent	Ref.
Ph-Hg-P(O)(OBu)Ph	-1028.3	4608	116.7	pyridine	161
Ph-Hg-P(O)(OEt) ₂	-1013.3	5993	112.6	pyridine	161
[Hg(η^1 -dppm) ₂] ²⁺ (O ₃ SCF ₃ ⁻) ₂	-1073.0	2952	13.3	DMSO	60
[Hg(η^2 -dppe) ₂] ²⁺ (O ₃ SCF ₃ ⁻) ₂	-366.0	2295	21.0	DMSO	60
[Hg(PMePh ₂) ₄] ²⁺ (O ₃ SCF ₃ ⁻) ₂	-291.0	2150	6.0	MeOH	60
[Hg(PPh ₂ CH ₂ PPh ₂) ₃] ²⁺	-510.3	1627 (averaged)	6.6	CH ₂ Cl ₂ , -20°C	121
[Hg(dppm) ₂] ²⁺	-889.0	2104	36.7	MeNO ₂ , 35°C	144
	-942.0	2180	31.4	MeNO ₂ , -13°C	144
[Hg(dppm)(dppe)] ²⁺	-549.0	2822 (dppm)	10.2	DMSO	73
		2456 (dppe)	32.2		
	-307.0	1980 (dppm)	34.1	MeNO ₂ , -13°C	144
		2217	28.0		
[Hg(dppm)(dppp)] ²⁺	-448.0	2338 (dppm)	17.6	DMSO	73
		2305 (dppp)	36.2		
	-228.0	1810 (dppm)	25.8	MeNO ₂	144
		2213 (dppp)	30.4		
[Hg(dppe) ₂] ²⁺	-288.0	2172	18.5	MeNO ₂ , 35°C	144
[Hg(dppe)(dppp)] ²⁺	-301.0	1893 (dppe)	18.2	DMSO	73
		2236 (dppp)	15.3		
	-261.0	1899 (dppe)	16.8	MeNO ₂ , 35°C	144
		2198 (dppp)	12.3		
[Hg(dppp) ₂] ²⁺	-250.0	1979	10.5	MeNO ₂ , 35°C	144
[(dppmHg) ₂] ⁴⁺ (O ₃ SCF ₃) ₄ (DMSO) ₄	-983.0 ^c	5530	37.8	acetone	92
	-949.0 ^d	5698	36.1	DMSO	92
[(dppmHg) ₂] ⁴⁺ (SbF ₆ ⁻) ₄	-1003	4496	40.8	MeNO ₂	144
[Hg(PPh ₂ CH ₂ PPh ₂) ₂ Ag] ³⁺	-1026.3	5899	26.1	DMF	140
			-0.9 (AgP)		
	-1006.0	4796	46.8	MeNO ₂ , -13°C	144
			3.7 (AgP)		

$[\text{MeC}(\text{CH}_2\text{PPh}_2)_3\text{Hg-PPh}_3]^{2+}$	- 316.3	4516 (PPh_3) 1278 (P_3)	29.1 3.8	CH_2Cl_2 , 27°C	135
$[\text{MeC}(\text{CH}_2\text{PPh}_2)_3\text{Hg-P}(\text{O})(\text{OEt})_2]^+$	- 455.3	512 (P_3) 10 520 [$\text{P}(\text{O})$]	- 5.6 69.3	CH_2Cl_2 , 27°C	135
$\{\text{Hg}(\text{PBu}_3)_2[\text{P}(\text{O})(\text{OEt})_2]_2\}$	- 334.0	737 5883 [$\text{P}(\text{O})$]	13.8 97.4	CH_2Cl_2	43
$\{\text{Hg}(\text{PPh}_3)_2[\text{P}(\text{O})(\text{OEt})_2]_2\}$	- 391.0	143 6830 [$\text{P}(\text{O})$]	13.8 97.4	CH_2Cl_2	43
$\{\text{Hg}(\text{cis-PPh}_2\text{CH=CHPPh}_2)[\text{P}(\text{O})(\text{OEt})_2]_2\}$	—	690 7321 [$\text{P}(\text{O})$]	8.8 98.9	CDCl_3	49
$\text{Hg}(\text{PR}_3)_n]^{2+} (\text{ClO}_4^-)_2$					
n R					
2 C_6H_{11}	- 956.0	3800	78.7	CH_2Cl_2 , - 60°C	123
2 2-Me- C_6H_4	- 1141.0	4150	51.9	CH_2Cl_2 , - 60°C	123
2 4-Me- C_6H_4	- 1241.0	4836	49.8	CH_2Cl_2 , - 60°C	123
2 4-Cl- C_6H_4	- 1280.0	5329	46.1	CH_2Cl_2 , 0°C	123
	- 1314.0	5273	44.5	CH_2Cl_2 , - 60°C	123
2 4-MeO- C_6H_4	- 1248.0	4775	44.8	CH_2Cl_2 , 0°C	123
2 4-Me ₂ N- C_6H_4	- 1244.0	3947	—	CH_2Cl_2 , 30°C	123
	- 1260.0	3716	47.1	CH_2Cl_2 , - 60°C	123
3 4-Me- C_6H_4	- 505.0	3025	43.3	CH_2Cl_2 , - 60°C	123
3 4-Cl- C_6H_4	- 635.0	3269	42.4	CH_2Cl_2 , - 60°C	123
3 4-MeO- C_6H_4	- 497.0	3040	40.2	CH_2Cl_2 , - 60°C	123
3 4-Me ₂ N- C_6H_4	- 542.0	2880	40.4	CH_2Cl_2 , - 60°C	123
4 4-Me- C_6H_4	- 515.0	2075	31.4	CH_2Cl_2 , - 60°C	123
4 4-MeO- C_6H_4	- 557.0	2068	26.6	CH_2Cl_2 , - 60°C	123
$\text{Hg}[\text{P}(\text{OR})_3]_n]^{2+} (\text{O}_3\text{SCF}_3^-)_2$					
n R					
1 Me	- 1558.3	17 528	98.2	CH_2Cl_2 , - 20°C	128
1 Et	- 1561.3	17 323	90.8	CH_2Cl_2 , - 20°C	128
2 Me	- 1343.3	11 123	120.4	CH_2Cl_2 , - 20°C	128

Table 9. (Continued)

Compound	$\delta^{199}\text{Hg}$	$^1J(^{199}\text{Hg}^{31}\text{P})$	$\delta^{31}\text{P}$	Solvent	Ref.
2 Et	-1353.3	10 645	115.0	CH_2Cl_2 , -20°C	128
3 Me	-662.3	6756	132.3	CH_2Cl_2 , -100°C	128
3 Et	-664.3	6630	128.8	CH_2Cl_2 , -100°C	128
4 Me	-451.3	4410	117.8	CH_2Cl_2 , -100°C	128
4 Et	-419.3	4308	111.5	CH_2Cl_2 , -100°C	128
$[\text{Hg}-\text{P}(\text{C}_6\text{H}_{11})_2]_2^{5+} (\text{HSO}_4)_5$	-890.3	3165	64.3	MeOH	125
$\text{Cl}-\text{Hg}-\text{P}(\text{O})\text{Bu}_2^1$	-1038.0	7000	125.4	pyridine	40
$\text{Cl}-\text{Hg}-\text{P}(\text{O})(\text{OBu})\text{Ph}$	-1153.3	10 525	85.6	pyridine	161
$\text{Cl}-\text{Hg}-\text{P}(\text{O})(\text{OEt})_2$	-1101.3	13 630	69.2	pyridine	161
$[\text{ClHg}(\text{PBu}_3)_2\text{P}(\text{O})(\text{OEt})_2]$	-285.0	2165	15.3	CH_2Cl_2	43
		8003 $[\text{P}(\text{O})]$	101.9		
$[\text{ClHg}(\text{PPh}_3)_2\text{P}(\text{O})(\text{OEt})_2]$	-384.0	1384	22.4	CH_2Cl_2	43
		9882 $[\text{P}(\text{O})]$	90.4		
$[\text{ClHg}[\text{P}(\text{O})(\text{OEt})_2]_2]^- \text{Na}^+$	-1190.0	7718	107.5	H_2O	62
$[\text{Cl}_2\text{Hg}-\text{PH}(\text{C}_6\text{H}_{11})_2]$	-712.0	6978	22.6	CH_2Cl_2	57
$[\text{Cl}_2\text{Hg}-\text{PBu}_3]$	-741.0	7414	34.1	CDCl_3	22
$\text{Cl}_2\text{Hg}[\text{PH}(\text{C}_6\text{H}_{11})_2]_2$	-372.0	4646	15.8	CH_2Cl_2	57
$\text{Cl}_2\text{Hg}(\text{PEt}_3)_2$	—	5117		CDCl_3	49
$\text{Cl}_2\text{Hg}(\text{PBu}_3)_2$	-404.0	5125	28.9	CDCl_3	22
$\text{Cl}_2\text{Hg}(\text{PPh}_3)_2$	-372.0	4829	30.9	CH_2Cl_2 , -60°C	122
$\text{Cl}_2\text{Hg}[\text{P}(4\text{-Me-C}_6\text{H}_4)_3]_2$	-381.0	4808	27.4	CH_2Cl_2 , -30°C	122
	-383.0	4922		CH_2Cl_2 , -60°C	122
$\text{Cl}_2\text{Hg}(\text{cis-PPh}_2\text{CH=CHPPh}_2)$	—	3103	3.1	CDCl_3	49
$\text{Cl}_2\text{Hg}[\text{P}(4\text{-F-C}_6\text{H}_4)_3]_2$	-368.0	4880	28.0	CH_2Cl_2 , -60°C	122
$\text{Cl}_2\text{Hg}[\text{P}(4\text{-Cl-C}_6\text{H}_4)_3]_2$	-364.0	4780	28.4	CH_2Cl_2 , -60°C	122
$\text{Cl}_2\text{Hg}[\text{P}(4\text{-MeO-C}_6\text{H}_4)_3]_2$	-386.0	4942	25.1	CH_2Cl_2 , -60°C	122

Cl ₂ Hg[P(4-Me ₂ N-C ₆ H ₄) ₃] ₂	– 426.0	4990	27.1	CH ₂ Cl ₂ , 0°C	122
	– 421.0	5015	27.1	CH ₂ Cl ₂ , – 30°C	122
	– 415.0	5048	27.1	CH ₂ Cl ₂ , – 60°C	122
Br-Hg-P(O)Bu ₃ ¹	– 1134.0	6363	126.5	pyridine	40
Br-Hg-P(O)(OBu)Ph	– 1252.3	10 288	86.1	pyridine	161
Br-Hg-P(O)(OEt) ₂	– 1200.3	13 313	72.8	pyridine	161
[BrHg(PBu ₃) ₂ P(O)(OEt) ₂]	– 320.0	2100	12.1	CH ₂ Cl ₂	43
		7909 [P(O)]	99.2		
[BrHg(PPh ₃) ₂ P(O)(OEt) ₂]	– 443.0	1286	18.9	CH ₂ Cl ₂	43
		9737	87.9		
[Br ₂ Hg-PH(C ₆ H ₁₁) ₂]	– 1078.0	6078	18.1	CH ₂ Cl ₂	57
[Br ₂ Hg-PBu ₃]	– 1020.0	6623	27.7	CDCl ₃	22
Br ₂ Hg[PH(C ₆ H ₁₁) ₂] ₂	– 553.0	4212	9.7	CH ₂ Cl ₂	57
Br ₂ Hg(PBu ₃) ₂	– 471.0	4829	24.0	CDCl ₃	22
Br ₂ Hg(<i>cis</i> -PPh ₂ CH=CHPPh ₂)	—	2547	– 2.0	CDCl ₃	49
I-Hg-P(O)Bu ₃ ¹	– 1339.0	6492	127.2	pyridine	40
I-Hg-P(O)(OBu)Ph	– 1463.3	9684	89.9	pyridine	161
I-Hg-P(O)(OEt) ₂	– 1401.3	12 563	79.2	pyridine	161
[IHg(PBu ₃) ₂ P(O)(OEt) ₂]	– 334.0	1978	3.5	CH ₂ Cl ₂	43
		7706 [P(O)]	92.4		
[IHg(PPh ₃) ₂ P(O)(OEt) ₂]	– 579.0	1105	11.8	CH ₂ Cl ₂	43
		9425 [P(O)]	84.2		
[I ₂ Hg-PH(C ₆ H ₁₁) ₂]	– 1957.0	4440	– 2.4	CH ₂ Cl ₂	57
[I ₂ Hg-PBu ₃]	– 1729.0	5195	6.2	CDCl ₃	22
I ₂ Hg[PH(C ₆ H ₁₁) ₂] ₂	– 1029.0	3616	– 6.3	CH ₂ Cl ₂	57
I ₂ Hg(PBu ₃) ₂	– 716.0	4101	8.8	CDCl ₃	22
[(Bu ₃ P) ₂ HgI ₂ HgI ₂]	– 572.0	4375	19.1	CH ₂ Cl ₂	22
	– 3507	—	—		
I ₂ Hg(<i>cis</i> -PPh ₂ CH=CHPPh ₂)	—	2170	– 12.6	CDCl ₃	49
[IHgP(C ₆ H ₁₁) ₂] ₄ [Bu ₄ NI]	– 506.0	3095 ^b	49.2	pyridine	57
[NC-Hg-P(O)Bu ₃ ¹]	– 985.0	6199	119.8	pyridine	40
NC-Hg-P(O)(OBu)Ph	– 1130.3	9136	88.1	pyridine	161
NC-Hg-P(O)(OEt) ₂	– 1086.3	11 635	78.5	pyridine	161

Table 9. (Continued)

Compound	$\delta^{199}\text{Hg}$	$^1J(^{199}\text{Hg}^{31}\text{P})$	$\delta^{31}\text{P}$	Solvent	Ref.
$\text{Hg}(\text{CN})_2(\text{cis-PPH}_2\text{CH=CHPPH}_2)$	—	1525	7.2	CDCl_3	49
$\text{NCS-Hg-P}(\text{O})\text{Bu}_2^1$	− 931.0	6626	129.3	pyridine	40
$\text{NCS-Hg-P}(\text{O})(\text{OEt})_2$	− 1001.3	13 127	71.7	pyridine	161
$\text{AcO-Hg-P}(\text{O})\text{Bu}_2^1$	− 1330.0	7191	120.1	pyridine	40
$\text{AcO-Hg-P}(\text{O})(\text{OBu})\text{Ph}$	− 1420.3	10 902	77.5	pyridine	161
$\text{AcO-Hg-P}(\text{O})(\text{OEt})_2$	− 1372.3	14 034	63.8	pyridine	161
$\text{HC}[\text{PPh}_2\text{-Hg}(\text{OAc})_2]_3$					131
$\text{AcOHg-CH}[\text{PPh}_2\text{-Hg}(\text{OAc})_2]_2$	− 1468.3	8773	34.1	MeOH	117
	− 1530.3	265 (Hg-C)			
$(\text{AcOHg})_2\text{C}[\text{PPh}_2\text{-Hg}(\text{OAc})_2]_2$	− 1495.3	8648	43.3	MeOH	117
	− 1443.3	234 (Hg-C)			
$\text{Hg}(\text{OAc})[\text{P}(\text{O})(\text{OEt})_2]\text{PPh}_3$	− 913	11 209	89.8	CH_2Cl_2	43
$\text{Hg}(\text{OAc})[\text{P}(\text{O})(\text{OEt})_2](\text{PPh}_3)_2$	− 583.0	10 711	92.1	CH_2Cl_2	43
$\text{CF}_3\text{SO}_3\text{-Hg-P}(\text{O})(\text{OEt})_2$	− 1380.3	14 580	61.4	pyridine	161
$\text{Hg}(\text{O}_3\text{SCF}_3)[\text{P}(\text{O})(\text{OEt})_2](\text{PBu}_3)_3$		1711	0.6	CH_2Cl_2	43
$\text{Hg}(\text{C}_4\text{H}_4\text{NO}_2)[\text{P}(\text{O})(\text{OEt})_2](\text{PBu}_3)_2$		2170	11.6		
	− 344.0	7899 [P(O)]	102.4	CH_2Cl_2	43
$\text{EtS-Hg-P}(\text{O})(\text{OBu})\text{Ph}$	− 1075.3	7271	98.7	pyridine	161
$\text{EtS-Hg-P}(\text{O})(\text{OEt})_2$	− 964.3	9266	91.7	pyridine	161
$\text{PhS-Hg-P}(\text{O})(\text{OBu})\text{Ph}$	− 993.3	7904	94.2	pyridine	161
$\text{PhS-Hg-P}(\text{O})(\text{OEt})_2$	− 1031.3	10 165	85.4	pyridine	161
$\{\text{Hg}_2[\mu\text{-SP}(\text{C}_6\text{H}_{11})_2]_2[\text{P}(\text{S})(\text{C}_6\text{H}_{11})_2\text{X}_2]\}$					
X = Cl	− 551.0	3498	82.0	CH_2Cl_2	59
		4777	85.1		
X = Br	− 565.0	3438	81.8	CH_2Cl_2	59
		4712	84.9		
X = I	− 555.0	3511	81.6	CH_2Cl_2	59
		4511	81.7		

$\{\text{Hg}_2[\mu\text{-SP}(\text{C}_6\text{H}_{11})_2]_2[\text{P}(\text{S})(\text{C}_6\text{H}_{11})_2]_2\}$		2701	89.9	CH_2Cl_2	59
$[\text{Hg}(\text{dppmS})_2]^{2+}$	— 598	4854	94.7		
		4516	49.5	CH_2Cl_2	76
			23.4		
$\{(\text{Et}_2\text{N-CS}_2)\text{Hg}[\text{P}(\text{O})(\text{OEt})_2]\text{PBu}_3\}$		2797	19.9		
	— 677.0	9669 [P(O)]	93.2	CH_2Cl_2	43
$\{\text{Pr}^i\text{OCS}_2\text{Hg}[\text{P}(\text{C}_6\text{H}_{11})_3]_2\}^+$	— 625.0	3965	56.7	CH_2Cl_2	152
$\{(\text{Et}_2\text{NCS}_2)\text{Hg}[\text{P}(\text{C}_6\text{H}_{11})_3]_2\}^+$	— 590.0	3845	52.1	CH_2Cl_2	152
$[(\text{Et}_2\text{NCS}_2)\text{HgP}(\text{C}_6\text{H}_{11})_3]^+$	— 940.5	5465	45.7	CH_2Cl_2 , — 90°C	210
$[(\text{Et}_2\text{NCS}_2)\text{HgPBu}_3]^+$	— 825.5	5635	18.9	CH_2Cl_2 , — 90°C	210
$[(\text{Pr}^i_2\text{PS}_2)\text{HgP}(\text{C}_6\text{H}_{11})_3]^+$	— 950.0	5410	73.6	CH_2Cl_2	152
$\{(\text{Pr}^i_2\text{PS}_2)\text{Hg}[\text{P}(\text{C}_6\text{H}_{11})_3]_2\}^+$	— 622.0	4040	54.6	CH_2Cl_2	152
$\{(\text{EtO})_2\text{PS}_2\text{Hg}[\text{P}(\text{O})(\text{OEt})_2]\text{PBu}_3\}$		3112	25.5		
	— 811.0	9833 [P(O)]	87.0	CH_2Cl_2	43
$[\text{Hg}(\text{dppmSe})_2]^{2+}$	— 177.0	3750	44.1	CH_2Cl_2	76
			23.2		
$[\eta^2\text{-L-Hg-PtBu}_2]_3^c$	— 430.3	2313	102.0	toluene	45
$[\eta^2\text{-L-Hg-P}(\text{C}_6\text{H}_{11})_2]_3^c$	— 236.0	2352	50.0	THF	45
$[\eta^2\text{-L-Hg-PPh}_2]_4^c$	—	2903	28.0	toluene	45
$[(\text{pyridine})_n\text{Hg-PR}_3]^{2+}$					
R = Bu	— 1185.3	8123	35.2	pyridine, 30°C	114
R = C_6H_{11}	— 1124.3	8123	68.2	pyridine, 30°C	114
R = Ph	— 1217.3	9032	33.1	pyridine, 30°C	114
$(2\text{-R-C}_6\text{H}_4)_2\text{N}_3\text{-Hg-P}(\text{O})(\text{OEt})_2$					
R = H	— 1298.3	11 856	70.4	pyridine	158
R = Me	— 1287.3	11 898	69.1	pyridine	158
R = F	— 1332.3	12 012	66.0	pyridine	158
R = F + PPh_3	— 622.3	10 768 [P(O)]	89.8	CH_2Cl_2 , — 100°C	158
		1839 [PPh ₃]	43.3		

Table 9. (Continued)

Compound	$\delta^{199}\text{Hg}$	$^1J(^{199}\text{Hg}^{31}\text{P})$	$\delta^{31}\text{P}$	Solvent	Ref.
R = Cl	-1291.3	12 617	66.3	pyridine	158
+ PPh ₃	-683.3	11 031 [P(O)] 2039 [PPh ₃]	87.5 43.2	CH ₂ Cl ₂ , -100°C	158
R = Br	-1286.3	12 844	66.8	pyridine	158
R = I	-1281.3	12 920	69.6	pyridine	158
R = NO ₂	-1329.3	13 127	64.2	pyridine	158
(Me ₃ Si) ₂ N-Hg-PBu ₂ ^c	-765.0	—	89.8	toluene or CH ₂ Cl ₂	41
(Me ₃ Si) ₂ N-Hg-P(O)(OEt) ₂ ^f	-1175.3	8749	80.2	toluene or CH ₂ Cl ₂	41

^adppm = Ph₂P-CH₂-PPh₂; dppe = Ph₂P-CH₂CH₂-PPh₂; dppp = Ph₂P-CH₂CH₂CH₂-PPh₂; dppmS = Ph₂P-CH₂-P(S)Ph₂; dppmSe = Ph₂P-CH₂-P(Se)Ph₂; C₄H₄NO₂ = 2,5-pyrrolidinedionato-N.

^b $^2J(^{199}\text{HgP}^{199}\text{Hg}) = 2595\text{ Hz.}$

^c $^1J(^{199}\text{Hg}^{199}\text{Hg}) = 827\text{ Hz.}$

^d $^1J(^{199}\text{Hg}^{199}\text{Hg}) = 699\text{ Hz.}$

^e $\eta^2\text{-L} = 2\text{-F-C}_6\text{H}_4\text{-NNN-(2-F-C}_6\text{H}_4\text{)}.$

^fFor $\delta^{199}\text{Hg}$ and $^1J(^{199}\text{Hg}^{31}\text{P})$ values of other phosphoryl mercury compounds see Bashilov *et al.*²⁹⁷

Table 10. Chemical shifts $\delta^{199}\text{Hg}$ of silyl-, germyl- and stannyl mercury compounds.

Compound	$\delta^{199}\text{Hg}$	Solvent	Ref.	Other nuclei	Ref.
$\text{Hg}(\text{SiH}_3)_2$	+ 196.0	C_6H_6	111	^{29}Si	111
$\text{H}_3\text{Si-Hg-SiMe}_3$	+ 327.0	C_6H_6	111	^{29}Si	111
$\text{Hg}(\text{SiMe}_3)_2$	+ 467.0 ^a	C_6D_6	67	^{13}C , ^{29}Si	67
	+ 499.0 ^b	$\text{C}_6\text{D}_6/\text{C}_6\text{F}_6$	87		
	+ 456.0	C_6H_6	111	^{29}Si	111
	+ 474.0 ^c	C_6D_6	108	^{13}C , ^{29}Si	108
$\text{Hg}(\text{SiMe}_2\text{Et})_2$ (0.99 M)	+ 596.0 ^b	$\text{C}_6\text{D}_6/\text{C}_6\text{F}_6$	87		
$\text{Hg}(\text{SiMe}_2\text{Pr})_2$ (0.58 M)	+ 574.0 ^b	$\text{C}_6\text{D}_6/\text{C}_6\text{F}_6$	87		
$\text{Hg}(\text{SiMe}_2\text{Bu}^t)_2$	^d	—	178	^{29}Si	178
$\text{Hg}(\text{SiEt}_3)_2$	+ 818.0 ^a	C_6D_6	67	^{13}C , ^{29}Si	67
(10.1 M)	+ 849.0 ^b	$\text{C}_6\text{D}_6/\text{C}_6\text{F}_6$	87		
$\text{Hg}[\text{SiMe}_2(\text{CH}_2)_n\text{CH}=\text{CH}_2]_2$					
$n = 0$ (0.53 M)	+ 376.0 ^b	$\text{C}_6\text{D}_6/\text{C}_6\text{F}_6$	87		
$n = 1$ (0.69 M)	+ 491.0 ^b	$\text{C}_6\text{D}_6/\text{C}_6\text{F}_6$	87		
$n = 2$ (0.34 M)	+ 460.0 ^b	$\text{C}_6\text{D}_6/\text{C}_6\text{F}_6$	87		
$n = 3$ (1.32 M)	+ 567.0 ^b	$\text{C}_6\text{D}_6/\text{C}_6\text{F}_6$	87		
$n = 4$ (0.89 M)	+ 572.0 ^b	$\text{C}_6\text{D}_6/\text{C}_6\text{F}_6$	87		
$\text{Hg}(\text{SiMe}_2\text{CH}_2\text{Ph})_2$ (0.44 M)	+ 454.0 ^b	$\text{C}_6\text{D}_6/\text{C}_6\text{F}_6$	87		
$\text{Hg}(\text{SiMe}_2\text{Ph})_2$ (0.27 M)	+ 360.0 ^b	$\text{C}_6\text{D}_6/\text{C}_6\text{F}_6$	87		
$\text{Hg}(\text{SiMePh}_2)_2$ (0.27 M)	+ 294.0 ^b	$\text{C}_6\text{D}_6/\text{C}_6\text{F}_6$	87		
$\text{Hg}(\text{SiMe}_2\text{Cl})_2$ (0.21 M)	− 315.0 ^b	$\text{DME}/\text{C}_6\text{D}_6/\text{C}_6\text{F}_6$	87		
$\text{Hg}(\text{SiMeCl}_2)_2$ (0.23 M)	− 843.0 ^b	$\text{DME}/\text{C}_6\text{D}_6/\text{C}_6\text{F}_6$	87		
(0.17 M)	− 658.0 ^b	$\text{C}_6\text{D}_6/\text{C}_6\text{F}_6$	87		
$\text{Hg}(\text{SiCl}_3)_2$ (0.74 M)	− 1177.0 ^b	$\text{DME}/\text{C}_6\text{D}_6/\text{C}_6\text{F}_6$	87		
(sat.)	− 1001.0 ^b	$\text{C}_6\text{D}_6/\text{C}_6\text{F}_6$	87		
$\text{Hg}(\text{SiMe}_2\text{CH}_2\text{SiMe}_3)_2$ (0.66 M)	+ 493.0 ^b	$\text{C}_6\text{D}_6/\text{C}_6\text{F}_6$	87		
$(-\text{SiMe}_2-\text{CH}_2-\text{SiMe}_2-\text{Hg}-)_2$	+ 740.0 ^b	$\text{C}_5\text{H}_{10}/\text{C}_6\text{F}_6$	87		
$\text{Hg}[\text{Si}(\text{SiMe}_3)_2]_2$ (0.087 M)	+ 987.0 ^b	$\text{C}_6\text{D}_6/\text{C}_6\text{F}_6$	87		
$\text{Li}[\text{Hg}(\text{SiMe}_3)_3]$ (0.54 M)	+ 1137.0	DME	87		

Table 10. (Continued)

Compound	$\delta^{199}\text{Hg}$	Solvent	Ref.	Other nuclei	Ref.
$\text{Li}_2[\text{Hg}(\text{SiMe}_2\text{Ph})_4]$ (0.045 M)	+ 1681.0	C_5H_{10}	87		
Me-Hg-SiMe_3	+ 142.0 ^c	CDCl_3	108	^{13}C , ^{29}Si	108
Et-Hg-SiMe_3	- 4.0 ^c	CDCl_3	108	^{13}C , ^{29}Si	108
Pr-Hg-SiMe_3	+ 67.0 ^a	C_6D_6	67	^{13}C , ^{29}Si	67
$\text{Pr}^i\text{-Hg-SiMe}_3$	- 148.0 ^a	C_6D_6	67	^{13}C , ^{29}Si	67
Bu-Hg-SiMe_3	+ 60.0 ^a	C_6D_6	67	^{13}C , ^{29}Si	67
$\text{Bu}^i\text{-Hg-SiMe}_3$	- 288.0 ^a	C_6D_6	67	^{13}C , ^{29}Si	67
	- 270.0 ^c	C_6D_6	108	^{13}C , ^{29}Si	108
$\text{Me}_3\text{CCH}_2\text{-Hg-SiMe}_3$	+ 110.0 ^c	CDCl_3	108	^{13}C , ^{29}Si	108
$\text{Bu-C}\equiv\text{C-Hg-SiMe}_3$	- 415.0 ^c	CDCl_3	108	^{13}C , ^{29}Si	108
$\text{Ph-C}\equiv\text{C-Hg-SiMe}_3$	- 428.0 ^c	C_6D_6	108	^{13}C , ^{29}Si	108
$\text{Me}_3\text{Si-C}\equiv\text{C-Hg-SiMe}_3$	- 457.0 ^c	C_6D_6	108	^{13}C , ^{29}Si	108
$\text{H}_3\text{Ge-Hg-SiMe}_3$	+ 159.0	C_6H_6	111	^{29}Si	111
$\text{Hg}(\text{GeH}_3)_2$	- 147.0	C_6H_6	111		
$\text{Hg}(\text{GeMe}_3)_2$	^e	—	178		
$\text{Hg}(\text{GeEt}_3)_2$ (0.34 M)	+ 507.3	C_6H_6	71		
$\text{Hg}[\text{Ge}(\text{C}_6\text{F}_5)_3]_2$	- 887.4		190, 193	^{19}F	193
$\{\text{Hg}[\text{Ge}(\text{C}_6\text{F}_5)_3]_2\}^-$ (0.4 M)	+ 93.6	THF	190	^{19}F	190
Et-Hg-GeMe_3	- 188.0 ^a	C_6D_6	67	^{13}C	67
$\text{Pr}^i\text{-Hg-GeMe}_3$	- 331.0 ^a	C_6D_6	67	^{13}C	67
$\text{Bu}^i\text{-Hg-GeMe}_3$	+ 131.0 ^a	C_6D_6	67	^{13}C	67
$(\text{C}_6\text{F}_5)_3\text{GeS-Hg-Ge}(\text{C}_6\text{F}_5)_3$	- 967.5	—	132		
$\{(\text{C}_6\text{F}_5)_3\text{GeS-Hg}[\text{Ge}(\text{C}_6\text{F}_5)_3]\}^-$	- 169.0	—	132	^{19}F	132
$\{[(\text{C}_6\text{F}_5)_3\text{GeS}]_2\text{Hg-Ge}(\text{C}_6\text{F}_5)_3\}^-$	- 323.0	—	132	^{19}F	132
$[(\text{Me}_3\text{CCH}_2)_3\text{Sn}]_2\text{Hg}$	^f	—	178		

^a $\delta^{199}\text{Hg}$ values converted to the HgMe_2 scale by adding - 2460 ppm.^b Original $\delta^{199}\text{Hg}$ data; the frequencies given for ^{19}F -lock (93 653 631 Hz) and for ^{199}Hg (17 913 266 Hz) of a 90: 10 mixture of $\text{HgMe}_2/\text{C}_6\text{F}_6$ do not fit to each other.^c $\delta^{199}\text{Hg}$ values converted to the HgMe_2 scale by adding - 11 ppm.^d Referencing not specified; ^{199}Hg resonance is shifted by 231 ppm to higher frequencies relative to that of $\text{Hg}(\text{SiMe}_3)_2$.^e Referencing is not specified; ^{199}Hg resonance is shifted by 242 ppm to lower frequencies with respect to that of $\text{Hg}(\text{SiMe}_3)_2$.^f Referencing is not specified; ^{199}Hg resonance is shifted by 353 ppm to lower frequencies with respect to that of $\text{Hg}(\text{SiMe}_3)_2$.

Table 11. Chemical shifts $\delta^{199}\text{Hg}^a$ of various mercury-transition metal compounds.

Compound	$\delta^{199}\text{Hg}$	Solvent	Ref.	Other nuclei	Ref.
$\text{Hg}[\text{Cr}(\text{CO})_3\text{C}_5\text{H}_5]_2$	- 80.0	DMSO	50		
$\text{Hg}[\text{Mo}(\text{CO})_3\text{C}_5\text{H}_5]_2$	+ 115.0	DMSO	50		
	+ 236.0	CDCl_3	51	^{13}C , ^{95}Mo	51
	+ 236.0	CH_2Cl_2	79	^{95}Mo	79
$\text{Hg}[\text{Mo}(\text{CO})_3\text{C}_5\text{H}_4\text{Me}]_2$	+ 229.0	CH_2Cl_2	79	^{95}Mo	79
$\text{Hg}[\text{Mo}(\text{CO})_3\text{C}_5\text{HMe}_4]_2$	+ 209.0	CH_2Cl_2	79	^{95}Mo	79
$\text{Hg}[\text{Mo}(\text{CO})_3\text{C}_5\text{Me}_5]_2$	+ 192.0	CH_2Cl_2	79	^{95}Mo	79
$\text{Hg}[\text{Mo}(\text{CO})_3\text{C}_5\text{HPh}_4]_2$	- 4.0	CH_2Cl_2	79	^{95}Mo	79
$\text{Hg}[\text{W}(\text{CO})_3\text{C}_5\text{H}_5]_2$	- 348.0	DMSO	50		
$\text{Cl-Hg-Cr}(\text{CO})_3\text{C}_5\text{H}_5$	- 542.0	DMSO	50		
$\text{Cl-Hg-Mo}(\text{CO})_3\text{C}_5\text{H}_5$	- 617.0	DMSO	50		
	- 574.0	CDCl_3	51	^{13}C , ^{95}Mo	51
	- 574.0	CH_2Cl_2	79	^{95}Mo	79
$\text{Cl-Hg-Mo}(\text{CO})_3\text{C}_5\text{H}_4\text{Me}$	- 577.0	CH_2Cl_2	79	^{95}Mo	79
$\text{Cl-Hg-Mo}(\text{CO})_3\text{C}_5\text{HMe}_4$	- 614.0	CH_2Cl_2	79	^{95}Mo	79
$\text{Cl-Hg-Mo}(\text{CO})_3\text{C}_5\text{Me}_5$	- 645.0	CH_2Cl_2	79	^{95}Mo	79
$\text{Cl-Hg-Mo}(\text{CO})_3\text{C}_5\text{HPh}_4$	- 685	CH_2Cl_2	79	^{95}Mo	79
$\text{Br-Hg-Mo}(\text{CO})_3\text{C}_5\text{H}_5$	- 759.0	CDCl_3	51	^{13}C , ^{95}Mo	51
$\text{Br-Hg-Mo}(\text{CO})_3\text{C}_5\text{H}_4\text{Me}$	- 765.0	CH_2Cl_2	79	^{95}Mo	79
$\text{Br-Hg-Mo}(\text{CO})_3\text{C}_5\text{HMe}_4$	- 776.0	CH_2Cl_2	79	^{95}Mo	79
$\text{Br-Hg-Mo}(\text{CO})_3\text{C}_5\text{Me}_5$	- 807.0	CH_2Cl_2	79	^{95}Mo	79
$\text{Br-Hg-Mo}(\text{CO})_3\text{C}_5\text{HPh}_4$	- 905.0	CH_2Cl_2	79	^{95}Mo	79
$\text{I-Hg-Mo}(\text{CO})_3\text{C}_5\text{H}_5$	- 1107.0	CDCl_3	51	^{13}C , ^{95}Mo	51
$\text{I-Hg-Mo}(\text{CO})_3\text{C}_5\text{H}_4\text{Me}$	- 1135.0	CDCl_3	79	^{95}Mo	79
$\text{I-Hg-Mo}(\text{CO})_3\text{C}_5\text{HMe}_4$	- 1059.0	CH_2Cl_2	79	^{95}Mo	79
$\text{I-Hg-Mo}(\text{CO})_3\text{C}_5\text{Me}_5$	- 1060.0	CH_2Cl_2	79	^{95}Mo	79
$\text{I-Hg-Mo}(\text{CO})_3\text{C}_5\text{HPh}_4$	- 1309.0	CH_2Cl_2	79	^{95}Mo	79
$\text{xant-Hg-Mo}(\text{CO})_3\text{C}_5\text{H}_5^b$	- 481.0	CDCl_3	51	^{13}C , ^{95}Mo	51
$\text{dtc-Hg-Mo}(\text{CO})_3\text{C}_5\text{H}_5^c$	- 401.0	CDCl_3	51	^{13}C , ^{95}Mo	51
$\text{dtp-Hg-Mo}(\text{CO})_3\text{C}_5\text{H}_5^d$	- 427.0	CDCl_3	51	^{13}C , ^{95}Mo	51

Table 11. (Continued)

Compound	$\delta^{199}\text{Hg}$	Solvent	Ref.	Other nuclei	Ref.
$\text{X-Hg-Mo(CO)}_2\text{LC}_5\text{H}_5$					
X L					
Cl P(OMe) ₃	-525.0	CDCl ₃	51	¹³ C, ³¹ P, ⁹⁵ Mo	51
Cl PPh ₃	-530.0	CDCl ₃	51	¹³ C, ³¹ P	51
Br P(OMe) ₃	-662.0	CDCl ₃	51	¹³ C, ³¹ P, ⁹⁵ Mo	51
Br PPh ₃	-668.0	CDCl ₃	51	¹³ C, ³¹ P	51
I P(OMe) ₃	-914.0	CDCl ₃	51	¹³ C, ³¹ P, ⁹⁵ Mo	51
I PPh ₃	-921.0	CDCl ₃	51	¹³ C, ³¹ P	51
dtc ^c P(OMe) ₃	-340.0	CDCl ₃	51	¹³ C, ³¹ P, ⁹⁵ Mo	51
dtc ^c PPh ₃	-347.0	CDCl ₃	51	¹³ C, ³¹ P	51
dtp ^d P(OMe) ₃	-365.0	CDCl ₃	51	¹³ C, ³¹ P, ⁹⁵ Mo	51
dtp ^d PPh ₃	-362.0	CDCl ₃	51	¹³ C, ³¹ P	51
(EtS-Hg) ₂ Mo(C ₅ H ₅) ₂	+202.0	CDCl ₃	162	¹³ C	162
Cl-Hg-W(CO) ₃ C ₅ H ₅	-997.0	DMSO	50		
Br-Hg-W(CO) ₃ C ₅ H ₅	-1200.0	DMSO	50		
I-Hg-W(CO) ₃ C ₅ H ₅	-1529.0	DMSO	50		
NCS-Hg-W(CO) ₃ C ₅ H ₅	-924.0	DMSO	50		
(Pr ⁱ S-Hg) ₂ W(C ₅ H ₅) ₂	+70.0	CDCl ₃	162	¹³ C	162
[(CO) ₄ Co] ₂ Hg	+329.0	CDCl ₃	156		
Cl-Hg-Rh(CCPh)(PPr ₃) ₃ C ₅ H ₅	-1076.4		165	³¹ P	165
[Fe ₄ (HgMe)(CO) ₁₃] ⁻	+1353		145		
	+1449		145		
[Fe ₄ (CO) ₁₃ HgMo(CO) ₃ (C ₅ H ₅) ₃]	+117.4		278		
Hg{Fe ₂ M(μ_3 -COMe)(CO) ₇ (C ₅ H ₅) ₂ } ₂					
M = Co (-50°C)	+891.0	CH ₂ Cl ₂	86	¹³ C	86
(+25°C)	+803.0	CH ₂ Cl ₂	86		
M = Rh ^c (-60°C)	+848.0	CH ₂ Cl ₂	86	¹³ C	86

	+ 588.0 ^f				
	+ 138.0 ^g				
	+ 54.0 ^h				
(μ_3 - η^2 -C ₂ Bu ^t)(CO) ₉ Ru ₃ (μ -Hg)X					
X = Cl	- 203.2	CDCl ₃	156		
X = Br	- 371.5	CDCl ₃	156		
X = I	- 736.0	CDCl ₃	156		
(μ_3 - η^2 -C ₂ Bu ^t)(CO) ₉ Ru ₃ (μ_3 -Hg)ML _n					
<u>ML_n</u>					
Mo(CO) ₃ C ₅ H ₅	+ 748.0	CDCl ₃	156		
Mn(CO) ₅	+ 662.9	CDCl ₃	156		
Re(CO) ₅	+ 676.1	CDCl ₃	156		
Fe(CO) ₂ C ₅ H ₅	+ 60.6	CDCl ₃	156		
Ru(CO) ₂ C ₅ H ₅	+ 329.9	CDCl ₃	156		
Co(CO) ₄	+ 50.2	CDCl ₃	156		
Ph ₃ P(μ_3 - η^2 -C ₂ Bu ^t)(CO) ₈					
Ru ₃ (μ_3 -Hg)Mo(CO) ₃ C ₅ H ₅	+ 700.1	CDCl ₃	156	³¹ P	156
[Cl-Hg-IrCl(SnCl ₃)(CO)(PR ₃) ₂]					
R = Ph	- 2026.0	CDCl ₃	126	³¹ P, ¹¹⁹ Sn	126
R = 4-F-C ₆ H ₄	- 2002.0	CDCl ₃	126	³¹ P, ¹¹⁹ Sn	126
R = 4-MeO-C ₆ H ₄	- 2077.0	CDCl ₃	126	³¹ P, ¹¹⁹ Sn	126
[Cl-Hg-IrCl ₂ (CO)(PR ₃) ₂]					
R = Ph	- 2645.0	C ₆ D ₆ /CH ₂ Cl ₂	126	³¹ P	126
R = 4-F-C ₆ H ₄	- 2595.0	C ₆ D ₆ /CH ₂ Cl ₂	126	³¹ P	126
R = 4-MeO-C ₆ H ₄	- 2712.0	C ₆ D ₆ /CH ₂ Cl ₂	126	³¹ P	126
[Br-Hg-IrBr(SnBr ₃)(CO)(PPh ₃) ₂]	- 2387.0	CDCl ₃	126	³¹ P, ¹¹⁹ Sn	126
[Br-Hg-IrBr ₂ (CO)(PPh ₃) ₂]	- 2814.0	C ₆ D ₆ /CH ₂ Cl ₂	126	³¹ P	126
[I-Hg-IrBr(I)(CO)(PPh ₃) ₂]	- 2964.0	C ₆ D ₆ /CH ₂ Cl ₂	126	³¹ P	126
[I-Hg-IrI ₂ (CO)(PPh ₃) ₂]	- 3093.0	C ₆ D ₆ /CH ₂ Cl ₂	126	³¹ P	126

Table 11. (Continued)

Compound	$\delta^{199}\text{Hg}$	Solvent	Ref.	Other nuclei	Ref.
[AcO-Hg-IrCl(OAc)(CO)(PPh ₃) ₂]	-2584	C ₆ D ₆ /CH ₂ Cl ₂	126	³¹ P	126
Hg[(C ₅ H ₅) ₂ (Ph ₃ Ge)NiHgGePh ₃] ₂	-1063.3(HgNi ₂) -196.7(HgNi)	THF	292		
[Me-Hg-Pd(PPh ₂ CH ₂ CH ₂) ₃ N] ⁺	-606.7	CD ₂ Cl ₂	83	³¹ P	83
[Me-Hg-Pt(PPh ₂ CH ₂ CH ₂) ₃ N] ⁺	-676.7	CD ₂ Cl ₂	83	³¹ P, ¹⁹⁵ Pt	83
<i>cis</i> -[(Ph ₃ P) ₂ Pt(HgGePh ₃)GePh ₃]	-259.1	THF, -49°C	129	³¹ P, ¹⁹⁵ Pt	129
	-281.0	toluene, -40°C	129	³¹ P, ¹⁹⁵ Pt	129
	-349.0	toluene, 90°C	129	³¹ P, ¹⁹⁵ Pt	129
[Hg ₂] ²⁺ [(AsF ₆) ⁻] ₂	-2030.0	SO ₂	89		
[(SO ₃ F) ⁻] ₂ (-70°C)	-1939.0	HSO ₃ F	89		
[(ClO ₄) ⁻] ₂ (sat.) ^j	-1614.0	H ₂ O	89		
[Hg ₃] ²⁺ [(AsF ₆) ⁻] ₂ (-70°C)	-1968.0 ^k -965.0 ^{l,m}	SO ₂	89		
[Hg ₃] ²⁺ [(SO ₃ F) ⁻] ₂ (-70°C)	-1832.0 ^k -895.0 ^{l,n}	HSO ₃ F	89		
[Hg ₄] ²⁺ [(AsF ₆) ⁻] ₂	-1310.0	SO ₂	89		

^aThe $\delta^{199}\text{Hg}$ data from Albright and Oliver⁵⁰ are original data; the frequencies given for ¹⁹F-lock (93 653 631 Hz) and for ¹⁹⁹Hg (17 913 266 Hz) of a 90:10 mixture of HgMe₂/C₆F₆ do not fit to each other.

^bxant = S₂COEt.

^cdtc = S₂CNEt₂.

^ddtp = S₂P(OEt)₂.

^eIsomers; relative abundance *ca.* 1:10:6:2, as judged from the ¹⁹⁹Hg NMR spectrum.

^fDoublet, $J(^{199}\text{Hg}^{103}\text{Rh}) = 279\text{ Hz}$.

^gTriplet, $J(^{199}\text{Hg}^{103}\text{Rh}) = 333\text{ Hz}$.

^hTriplet, $J(^{199}\text{Hg}^{103}\text{Rh}) = 290\text{ Hz}$.

ⁱ $\delta^{199}\text{Hg}$ is dependent on concentration: extrapolated for infinite dilution $\delta^{199}\text{Hg} = -1500$.

^kCentral mercury.

^lTerminal mercury.

^m $J(^{199}\text{Hg}^{199}\text{Hg}) = 139\,700 \pm 300\text{ Hz}$.

ⁿ $J(^{199}\text{Hg}^{199}\text{Hg}) = 139\,600 \pm 1000\text{ Hz}$.

Table 12. Survey of ¹⁹⁹Hg-¹³C spin-spin coupling constants (in Hz).

Compound	Ref.	¹ <i>J</i> (¹⁹⁹ Hg ¹³ C)	² <i>J</i> (¹⁹⁹ Hg ¹³ C)	³ <i>J</i> (¹⁹⁹ Hg ¹³ C)	ⁿ <i>J</i> (¹⁹⁹ Hg ¹³ C)
Me ₂ Hg	69	700.0	—	—	—
Me-Hg-Bu ⁱ	25	597.0 (Me) 760.0 (Bu ⁱ)	—	—	—
Me-Hg-C≡C-H	69	1150.0 (Me) 1395.0 (C≡)	— 398.4	81.0 —	— —
Me-Hg-CF ₃	37	960.0 (Me) 1735.0 (CF ₃)	— —	— —	— —
Me-Hg-Cl	36	1430.7	—	—	—
Me-Hg-Br	36	1393.6	—	—	—
Me-Hg-I	36	1301.3	—	—	—
Me-Hg-NO ₃ /HClO ₄	39	1711–1761	—	—	—
Me-Hg-N(SiMe ₃) ₂	69	1126.0	—	—	—
Me-Hg-SiMe ₃	67	423.4	116.8 (SiMe)	—	—
Et ₂ Hg	69	653.3	22.2	—	—
Et-Hg-Bu ⁱ	25	664.0 (Et) 660.0 (Bu ⁱ)	— —	— 81.0	— —
Et-Hg-C≡C-H	69	1218.5 (Et) 1131.0 (C≡)	31.4 340.6	— —	— —
Et-Hg-SiMe ₃	67	495.5	18.3 109.9 (SiMe)	—	—
Pr ⁱ -Hg-Pr ⁱ	67	633.6	32.0	—	—
Pr ⁱ -Hg-Bu ⁱ	25	731.0 (Pr ⁱ) 582.0 (Bu ⁱ)	— —	— 78.0	— —
Pr ⁱ -Hg-SiMe ₃	67	564.7	104.4 (SiMe)	—	—
Bu ₂ Hg	25	675.0	—	81.0	—
Bu ₂ Hg	69	626.5	—	—	—
(Me ₃ CCH ₂) ₂ Hg	248	684.0	29.0	71.0	—
Me ₃ CCH ₂ -Hg-Cl	248	1514.0	70.0	149.0	—

Table 12. (Continued)

Compound	Ref.	$^1J(^{199}\text{Hg}^{13}\text{C})$	$^2J(^{199}\text{Hg}^{13}\text{C})$	$^3J(^{199}\text{Hg}^{13}\text{C})$	$^nJ(^{199}\text{Hg}^{13}\text{C})$
(1-Norbornyl) ₂ Hg	55	807.0	49.0 (C-2,6) 38.0 (C7)	112.0 (C-4) 94.0 (C-3,5)	—
(Me ₂ NCH ₂ CH ₂ CH ₂) ₂ Hg	82	745.6	41.8	85.8	—
(PhCH ₂) ₂ Hg	30	633.4	72.6	54.1	23.6, 29.2
PhCH ₂ -Hg-Cl	30	1429.0	156.8	105.0	51.3, 63.5
PhCH ₂ -Hg-Br	65	1616.0	157.5	113.6	54.3, 67.2
PhCH ₂ -Hg-CN	35	1310.0	121.0	84.6	40.0, 45.9
PhCH ₂ -Hg-OAc	35	1438.4	157.2	111.3	50.3, 62.5
(CH ₂ =CH-CH ₂) ₂ Hg	58	626.5	—	—	—
3-EtO-1-adamentyl-Hg-Cl	202	1684.7	71.4 (C-2) 68.3 (C-8,9)	232.4 (C-5,7)	26.4 (C-6) 27.2 (C-4,10)
Me(MeO)CHCH ₂ -Hg-Cl	28	1606.0	109.0	—	—
PhSCH ₂ -Hg-Cl	84	2007.5	—	—	—
(Me ₃ SiCH ₂) ₂ Hg	201	545.6	—	—	—
[(Me ₃ Si) ₂ CH] ₂ Hg	201	423.0	—	—	—
[(Me ₃ Si) ₃ C] ₂ Hg	201	334.0	—	—	—
CH ₂ (HgCl) ₂	21	1782.0	—	—	—
CH ₂ (HgBr) ₂	54	1741.0	—	—	—
CH ₂ (HgCN) ₂	54	1488.0 (CH ₂) 1249.0 (C≡N)	—	45.0	—
CH(HgCl) ₃	21	1827.0	—	—	—
CH(HgCN) ₃	54	1455.0 (CH) 1331.0 (C≡N)	—	37.0	—
C(HgCl) ₄	21	1797.0	—	—	—
Ph ₂ Hg	69	1190.0	85.9	100.5	17.5
Ph-Hg-C≡C-Ph	69	1747.7 (Ph) 1550.5 (C≡)	90.4 437.8	136.2	—
Ph-Hg-Cl (DMSO)	38	2634.0	118.6	209.0	37.1

Table 12. (Continued)

Compound	Ref.	¹ J(¹⁹⁹ Hg ¹³ C)	² J(¹⁹⁹ Hg ¹³ C)	³ J(¹⁹⁹ Hg ¹³ C)	ⁿ J(¹⁹⁹ Hg ¹³ C)
2-Me ₂ NCH ₂ -C ₆ H ₄ -Hg-Cl	29	—	— (C-2,6) 11.0 (NMe)	178.0 212.0 (C-5) 101.0 (CH ₂)	— (C-4)
(2-Me-C ₆ H ₄) ₂ Hg	64	1124.8	64.7 (C-2) 83.0 (C-6)	70.8 (C-3) 98.9 (C-5) 101.3 (2-Me)	13.4
2-Me ₂ NCH ₂ -C ₆ H ₄ -Hg-Cl	29	—	— (C-2,6) 11.0 (NMe)	178.0 212.0 (C-5) 101.0 (CH ₂)	— (C-4)
(CH ₂ =CH) ₂ Hg	38	1161.0	36.6	—	—
CH ₂ =CH-Hg-C≡C-H	69	1691.0 (CH=) 1502.3 (C=)	— 425.1 (≡C-H)	—	—
CH ₂ =CH-Hg-Cl	69	2517.4	—	—	—
	94	—	27.3	—	—
(H-C≡C) ₂ Hg	88	2656.0	652.0	—	—
(Me-C≡C) ₂ Hg	88	2509.0	666.5	48.2	—
(Bu ^t -C≡C) ₂ Hg	88	2377.0	610.0	37.0	12.8
(Ph-C≡C) ₂ Hg	88	2492.5	641.4	51.0	16.6
(Cl-C≡C) ₂ Hg	88	2991.0	845.3	—	—
(Br-C≡C) ₂ Hg	107	2773.0	782.5	—	—
(Me ₃ Si-C≡C) ₂ Hg	69	2358.0	538.5	—	—
Me ₃ Si-C≡C-Hg-SiMe ₃	108	650.0	190.0 157.3 (HgSiMe)	—	—
(N≡C) ₂ Hg	37	3142.0	—	—	—

Table 13. Survey of ^{199}Hg - ^{29}Si spin-spin coupling constants (in Hz).

Compound	Ref.	$^1J(^{199}\text{Hg}^{29}\text{Si})$	Compound	Ref.	$^1J(^{199}\text{Hg}^{29}\text{Si})$
$\text{Hg}(\text{SiMe}_3)_2$	67	989.6	$\text{Hg}(\text{SiMe}_2\text{Et})_2$	87	972.0
Me-Hg-SiMe_3	67	1367.0	$\text{Hg}(\text{SiEt}_3)_2$	87	955.0
Et-Hg-SiMe_3	67	1213.0	$\text{Hg}(\text{SiMe}_2\text{CH}_2\text{CHCH}_2)_2$	87	1050.0
Pr-Hg-SiMe_3	67	1234.1	$\text{Hg}(\text{SiMe}_2\text{Ph})_2$	87	1037.0
$\text{Pr}^i\text{-Hg-SiMe}_3$	67	1084.9	$\text{Hg}(\text{SiMe}_2\text{CH}_2\text{SiMe}_3)_2$	87	972.0
$\text{Bu}^i\text{-Hg-SiMe}_3$	67	995.6	$\text{Hg}(\text{SiMe}_2\text{CH}_2\text{Ph})_2$	87	1111.0
$\text{Me}_3\text{CCH}_2\text{-Hg-SiMe}_3$	108	1245.0	$\text{Hg}(\text{SiMe}_2\text{Cl})_2$	87	1392.0
$\text{ClCH}_2\text{-Hg-SiMe}_3$	67	1137.0	$\text{Hg}(\text{SiMeCl}_2)_2$	87	2020.0
$\text{Bu-C}\equiv\text{C-Hg-SiMe}_3$	108	1950.0	$\text{Hg}(\text{SiCl}_3)_2$	87	3864.0
$\text{Ph-C}\equiv\text{C-Hg-SiMe}_3$	108	2001.0	$\text{Hg}[\text{Si}(\text{SiMe}_3)_3]_2$	87	432.0
$\text{Me}_3\text{Si-C}\equiv\text{C-Hg-SiMe}_3$	108	1946.0			

REFERENCES

1. K. Brodersen, *Chem. i.u.Z.*, 1982, **16**, 23.
2. (a) L.G. Makarova and A.N. Nesmeyanov, *The Organic Chemistry of Mercury*. North Holland Publishing Company, Amsterdam, 1967.
(b) R.C. Larock, *Organomercury Compounds in Organic Synthesis*. Springer, New York, 1985.
(c) C.A. McAuliffe, *The Chemistry of Mercury*. Macmillan, London 1977.
(d) H. Staub, K.P. Zeller and H. Leditsche, in *Houben-Weyl—Methoden der Organischen Chemie*, Vol. XIII/2b. Thieme, Stuttgart, 1974.
3. (a) R.G. Kidd and R.J. Goodfellow, in *NMR and the Periodic Table* (ed. R.K. Harris and B.E. Mann), Chap. 8. Academic Press, London, 1978.
(b) R.G. Kidd, *Ann. Rep. NMR Spectrosc.*, 1980, **10A**, 1.
4. R.J. Goodfellow, in *Multinuclear NMR* (ed. J. Mason), pp. 563–89. Plenum Press, London, 1987.
5. V.S. Petrosyan and O.A. Reutov, *J. Organomet. Chem.*, 1974, **76**, 123.
6. W. McFarlane, *Proc. R. Soc. Lond.*, 1986, **A306**, 185.
7. (a) W. McFarlane, in *Annual Reports on NMR Spectroscopy*, Vol. 1 (ed. E.F. Mooney), p. 135. Academic Press, London, 1968.
(b) W. McFarlane, in *Annual Reports on NMR Spectroscopy*, Vol. 5A (ed. E.F. Mooney), p. 353. Academic Press, London, 1972.
8. (a) K.A. McLauchlan, D.H. Whiffen and L.W. Reeves, *Mol. Phys.*, 1966, **10**, 131.
(b) F.A.L. Anet and J.L. Sudmeier, *J. Magn. Reson.*, 1969, **1**, 124.
9. (a) G.A. Morris and R. Freeman, *J. Am. Chem. Soc.*, 1979, **101**, 760.
(b) G.A. Morris, *J. Am. Chem. Soc.*, 1980, **102**, 428.
(c) G.A. Morris, *J. Magn. Reson.*, 1980, **41**, 185.
(d) D.P. Burum and R.R. Ernst, *J. Magn. Reson.*, 1980, **39**, 163.
10. (a) D.T. Pegg, D.M. Doddrell and M.R. Bendall, *J. Chem. Phys.*, 1982, **77**, 2745.
(b) D.T. Pegg, D.M. Doddrell, W.M. Brooks and M.R. Bendall, *J. Magn. Reson.*, 1981, **44**, 32.
11. (a) M.F. Roberts, D.A. Vidusek and G. Bodenhausen, *FEBS Lett.*, 1980, **117**, 311.
(b) D.A. Vidusek, M.F. Roberts and G. Bodenhausen, *J. Am. Chem. Soc.*, 1982, **104**, 5452.
12. D.G. Gillies, L.P. Blaauw, G.R. Hays, R. Huis and A.D.H. Clague, *J. Magn. Reson.*, 1981, **42**, 420.
13. C.R. Lassigne and E.J. Wells, *Can. J. Chem.*, 1976, **55**, 1303.
14. A. Abragam, *The Principles of Nuclear Magnetism*, pp. 333–8. Oxford University Press, Oxford, 1961.
15. R.R. Ernst, F. Bodenhausen and A. Wokaun, *Principles of Nuclear Magnetic Resonance in One and Two Dimensions*. Clarendon Press, Oxford, 1987.
16. J. Kowalewski, in *Annual Reports on NMR Spectroscopy*, Vol. 22 (ed. G.A. Webb), p. 307. Academic Press, London, 1990.
17. (a) P.L. Gogggin, R.J. Goodfellow, S.R. Haddock and J.G. Eary, *J. Chem. Soc. Dalton Trans.*, 1972, 647.
(b) N.S. Ham, E.A. Jeffery and S.N. Stuart, *J. Chem. Soc. Chem. Commun.*, 1967, 254.
18. P. Peringer, *Inorg. Chim. Acta*, 1980, **42**, 129.
19. R.E. Wasylshen, R.E. Lenkinski and C. Rodger, *Can. J. Chem.*, 1982, **60**, 2113.
20. (a) J.D. Kennedy and W. McFarlane, *J. Chem. Soc. Faraday Trans. 2*, 1976, **72**, 1653.
(b) J. Jokisaari and P. Diehl, *Org. Magn. Reson.*, 1980, **5**, 359.
21. D.K. Breitinger, K. Geibel, W. Kress and R. Sendelbeck, *J. Organomet. Chem.*, 1980, **191**, 7.

22. P.L. Goggin, R.J. Goodfellow, D.M. McEwan and K. Kessler, *Inorg. Chim. Acta*, 1980, **44**, L111.
23. P. Peringer, *J. Chem. Res.*, (S) 1980, 194; (M) 1980, 2757.
24. P. Peringer and P.-P. Winkler, *J. Organomet. Chem.*, 1980, **195**, 249.
25. D. Steinborn, R. Taube, R. Radeaglia and W. Höbold, *J. Organomet. Chem.*, 1981, **210**, 139.
26. R. Meyer, L. Gorrichon-Guigon and P. Maroni, *J. Organomet. Chem.*, 1980, **188**, 11.
27. I.J. Colquhoun and W. McFarlane, *J. Chem. Soc. Dalton Trans.*, 1981, 658.
28. T. Iwanayagi, T. Ibusuki and Y. Saito, *J. Organomet. Chem.*, 1977, **128**, 145.
29. A.F.M.J. van der Ploeg, C.E.M. van der Kolk and G. van Koten, *J. Organomet. Chem.*, 1981, **212**, 283.
30. W. Kitching, G.M. Drew, W. Adcock and A.N. Abeywickrema, *J. Org. Chem.*, 1981, **46**, 2252.
31. P.L. Goggin, R.J. Goodfellow and N.W. Hurst, *J. Chem. Soc. Dalton Trans.*, 1978, 561.
32. A.J. Canty, P. Barron and P.C. Healy, *J. Organomet. Chem.*, 1979, **179**, 447.
33. P. Peringer, *Inorg. Chim. Acta*, 1980, **39**, 67.
34. M.A. Sens, N.K. Wilson, P.D. Ellis and J.D. Odom, *J. Magn. Reson.*, 1975, **19**, 323.
35. E. Michel, J. Peril and A. Lattes, *J. Organomet. Chem.*, 1981, **204**, 1.
36. A.J. Brown, O.W. Howarth and P. Moore, *J. Chem. Soc. Dalton Trans.*, 1976, 1589.
37. P.L. Goggin, R.J. Goodfellow, D.M. McEwan, A.J. Griffiths and K. Kessler, *J. Chem. Res.* (M) 1979, 2315.
38. N.K. Wilson, R.D. Zehr and P.D. Ellis, *J. Magn. Reson.*, 1976, **21**, 437.
39. Y. Kawasaki, M. Aritoni and J. Iyoda, *Bull. Chem. Soc. Jap.*, 1976, **49**, 3478.
40. P. Peringer and J. Eichbichler, *J. Inorg. Nucl. Chem.*, 1981, **43**, 2033.
41. J. Eichbichler and P. Peringer, *Trans. Met. Chem.*, 1981, **6**, 313.
42. W. Kitching and G.M. Drew, *J. Org. Chem.*, 1981, **46**, 2695.
43. J. Eichbichler and P. Peringer, *Inorg. Nucl. Chem. Lett.*, 1981, **17**, 305.
44. L.C. Damude, P.A.W. Dean, M.D. Sefcik and J. Schaefer, *J. Organomet. Chem.*, 1982, **226**, 205.
45. J. Eichbichler and P. Peringer, *J. Chem. Soc. Chem. Commun.*, 1982, 193.
46. P. Peringer and J. Eichbichler, *J. Chem. Soc. Dalton Trans.*, 1982, 667.
47. W. Kitching, G.M. Drew and V. Alberts, *Organometallics*, 1982, **1**, 331.
48. P.R. Wells and D.W. Hawker, *Org. Magn. Reson.*, 1981, **17**, 26.
49. H.B. Büergi, E. Fischer, R.W. Kunz, M. Parvez and P.S. Pregosin, *Inorg. Chem.*, 1982, **21**, 1246.
50. M.J. Albright and J.P. Oliver, *J. Organomet. Chem.*, 1979, **172**, 99.
51. M.M. Kubicki, R. Kergoat, J.-Y. le Gall, J.E. Guerchais, J. Douglade and R. Mercier, *Aust. J. Chem.*, 1982, **35**, 1543.
52. R. Bain, *J. Inorg. Nucl. Chem.*, 1981, **43**, 2481.
53. P.F. Barron, *J. Organomet. Chem.*, 1982, **236**, 157.
54. W. Kress, D.K. Breiting and R. Sendelbeck, *J. Organomet. Chem.*, 1983, **246**, 1.
55. V. Dimitrov, K.-H. Thiele and R. Radeaglia, *Z. Anorg. Allg. Chem.*, 1983, **503**, 177.
56. Yu.K. Grishin, Yu.A. Strelenko, Yu.A. Ustynyuk, A.S. Peregudov, L.S. Golovchenko, E.M. Rokhlina and D.N. Kratsov, *Izvest. Akad. Nauk SSSR, Ser. Khim.*, 1982, 1043.
57. J. Eichbichler and P. Peringer, *Chem. Ber.*, 1984, **117**, 1215.
58. F.A. Fedorov, *Zhur. Strukt. Khim.*, 1984, **25**, 43.
59. P. Peringer and N. Baumann, *J. Chem. Soc. Dalton Trans.*, 1985, 223.
60. P. Peringer and M. Lusser, *Inorg. Chem.*, 1985, **24**, 109.
61. J.D. Wuest and B. Zacharie, *Organometallics*, 1985, **4**, 410.
62. P. Peringer, P.-P. Winkler, G. Huttner and L. Zsolnai, *J. Chem. Soc. Dalton Trans.*, 1985, 1061.

63. R.D. Bach, H.B. Vardhan, A.T.M. Rahman and J.P. Oliver, *Organometallics*, 1985, **4**, 846.
64. K.F. Rowland and R.D. Thomas, *Magn. Reson. Chem.*, 1985, **23**, 916.
65. Yu.K. Grishin, K.A. Sokolikova, Yu.A. Ustynyuk, A.A. Ivkina, K.P. Butin and O.A. Reutov, *Izvest. Akad. Nauk. SSSR, Ser. Khim.*, 1985, 793.
66. T.N. Mitchell, *J. Organomet. Chem.*, 1974, **71**, 27.
67. T.N. Mitchell and H.C. Marsmann, *J. Organomet. Chem.*, 1978, **150**, 171.
68. T.F. Schaaf and J.P. Oliver, *Inorg. Chem.*, 1971, **10**, 1521.
69. A. Sebald and B. Wrackmeyer, *J. Magn. Res.*, 1985, **63**, 397.
70. R. Radeaglia, D. Steinborn and R. Taube, *Spectrochim. Acta*, 1983, **39A**, 843.
71. Yu.A. Strelenko, Yu.K. Grishin, V.T. Bychkov and Yu.A. Ustynyuk, *Zh. Obshch. Khim.*, 1979, **49**, 1172.
72. A. Razzavi, M.D. Rausch and H.G. Alt, *J. Organomet. Chem.*, 1987, **329**, 281.
73. P. Peringer and M. Lusser, *Polyhedron*, 1987, **6**, 655.
74. A.M. Bond, R. Colton, A.F. Hollenkamp, B.F. Hoskins and K. McGregor, *J. Am. Chem. Soc.*, 1987, **109**, 1969.
75. G.B. Wulfsberg, J.S. Frye, A.C. Buchanan, III, A. Weiss, C.C.-C. Jui, D.A. Davis, K. Bass and R.W. Todd, *Organometallics*, 1987, **6**, 2363.
76. A.M. Bond, R. Colton and J. Ebner, *Inorg. Chem.*, 1988, **27**, 1697.
77. G.B. Deacon, B.M. Gatehouse and S.C. Ney, *J. Organomet. Chem.*, 1988, **348**, 141.
78. A.M. Hounslow, S.F. Lincoln and E.R.T. Tiekink, *J. Organomet. Chem.*, 1988, **354**, C9.
79. M.M. Kubicki, J.Y. le Gall, R. Pichon, J.Y. Salaun, M. Cano and J.A. Campo, *J. Organomet. Chem.*, 1988, **348**, 349.
80. F. De Sarlo, A. Brandi, I. Fabrizi, A. Guarna and N. Nicolai, *Org. Magn. Reson.*, 1984, **22**, 372.
81. T.N. Mitchell and B. Fabisch, *J. Organomet. Chem.*, 1984, **269**, 249.
82. E. Langguth and K.-H. Thiele, *Z. Anorg. Allg. Chem.*, 1985, **530**, 69.
83. C.A. Ghilardi, S. Midollini, S. Moneti, A. Orlandini, G. Scapacci and D. Dakternieks, *J. Chem. Soc. Chem. Commun.*, 1989, 1687.
84. D. Steinborn and U. Sedlack, *Z. Chem.*, 1985, **25**, 376.
85. D. Steinborn, *Z. Chem.*, 1985, **25**, 412.
86. L.J. Farrugia, *J. Chem. Soc. Chem. Commun.*, 1987, 147.
87. M.J. Albright, T.F. Schaaf, A.K. Howland and J.P. Oliver, *J. Organomet. Chem.*, 1983, **259**, 37.
88. A. Sebald and B. Wrackmeyer, *Spectrochim. Acta*, 1982, **38A**, 163.
89. R.J. Gillespie, P. Granger, K.R. Morgan and G.J. Schrobilgen, *Inorg. Chem.*, 1984, **23**, 887.
90. G.B. Deacon, M.J. O'Connor and G.N. Stretton, *Aust. J. Chem.*, 1986, **39**, 953.
91. J. Eichbichler and P. Peringer, *J. Organomet. Chem.*, 1982, **231**, 95.
92. M. Lusser and P. Peringer, *Chem. Ber.*, 1985, **118**, 2140.
93. R. Benn, H. Günther, A. Maercker, V. Menger and P. Schmitt, *Angew. Chem.*, 1982, **94**, 314; *Angew. Chem. Int. Ed. Engl.*, 1982, **21**, 295.
94. Yu.K. Grishin, D.Z. Bazhenov, V.A. Roznyatovskii, M.A. Kazankova, V.R. Kartashov and Yu.A. Ustynyuk, *Metallorg. Khim.*, 1988, **1**, 335.
95. P.A.W. Dean, V. Manivannan and J.J. Vittal, *Inorg. Chem.*, 1989, **28**, 2360.
96. A.R. Norris, R. Kumar and E. Buncel, *J. Inorg. Biochem.*, 1984, **22**, 11.
97. M.V. Castano, M.M. Plasencia, A. Macias, J.S. Casas, J. Sordo and E. Castellano, *J. Chem. Soc. Dalton Trans.*, 1989, 1409.
98. S.P. Watton, J.G. Wright, F.M. MacDonnell, J.W. Bryson, M. Sabat and T.V. O'Halloran, *J. Am. Chem. Soc.*, 1990, **112**, 2824.
99. M.J. Natan, C.F. Millikan, J.G. Wright and T.V. O'Halloran, *J. Am. Chem. Soc.*, 1990, **112**, 3255.

100. Yu.K. Grishin and Yu.A. Ustynyuk, *Zhur. Strukt. Khim.*, 1982, **23**, 163.
101. Yu. Strelenko, O.K. Sokolikova, Yu.K. Grishin and Yu.A. Ustynyuk, *Dokl. Akad. Nauk SSSR*, 1980, **252**, 924.
102. R.E. Dessy, T.J. Flautt, H.H. Jaffe and G.F. Reynolds, *J. Chem. Phys.*, 1959, **30**, 1422.
103. A.P. Tupciauskas, N.M. Sergeyev, Yu.A. Ustynyuk and A.N. Kashin, *J. Magn. Reson.*, 1972, **7**, 124.
104. Yu.K. Grishin, Yu.A. Strelenko, L.A. Margulis, Yu.A. Ustynyuk, L.S. Golovchenko, A.S. Peregodov and D.N. Kravtsov, *Dokl. Akad. Nauk SSSR*, 1979, **249**, 892.
105. Yu.K. Grishin, V.A. Roznyatovskii and Yu.A. Ustynyuk, *Dokl. Akad. Nauk. SSSR*, 1981, **257**, 919.
106. A. Sebald and B. Wrackmeyer, unpublished results.
107. C. Cauletti, C. Furlani, M.N. Piancastelli, A. Sebald and B. Wrackmeyer, *Inorg. Chem.*, 1984, **23**, 1113.
108. A. Sebald and B. Wrackmeyer, *Spectrochim. Acta*, 1986, **42A**, 1107.
109. H. Krüger, O. Lutz, A. Nolle and A. Schwenk, *Z. Phys., Teil A*, 1975, **273**, 325.
110. P. Pyykkö, *Chem. Phys.*, 1977, **22**, 289.
111. S. Craddock, E.A.V. Ebsworth, N.S. Hosmane and K.M. MacKey, *Angew. Chem. Int. Ed. Engl.*, 1975, **14**, 167.
112. G.E. Maciel and M. Borzo, *J. Magn. Reson.*, 1973, **10**, 388.
113. M. Lusser and P. Peringer, *Inorg. Chim. Acta*, 1987, **127**, 151.
114. P. Peringer and M. Lusser, *Inorg. Chim. Acta*, 1986, **118**, L7.
115. A.R. Norris and R. Kumar, *Inorg. Chim. Acta*, 1984, **93**, L63.
116. D. Dakternieks, *Inorg. Chim. Acta*, 1984, **89**, 209.
117. M. Lusser and P. Peringer, *Organometallics*, 1984, **3**, 1916.
118. P. Peringer and P.-P. Winkler, *Inorg. Chim. Acta*, 1981, **52**, 257.
119. G.B. Deacon, G.N. Stretton and M.J. O'Connor, *J. Organomet. Chem.*, 1984, **277**, C1.
120. F. De Sarlo, A. Guarna, A. Goti and A. Brandi, *J. Organomet. Chem.*, 1984, **269**, 115.
121. M. Lusser and P. Peringer, *Z. Naturforsch. B*, 1985, **40**, 1417.
122. T. Allman and R.G. Goel, *Can. J. Chem.*, 1984, **62**, 615.
123. T. Allman and R.G. Goel, *Can. J. Chem.*, 1984, **62**, 621.
124. A.R. Sanger, *Can. J. Chem.*, 1984, **62**, 822.
125. P. Peringer and J. Eichbichler, *J. Organomet. Chem.*, 1983, **241**, 281.
126. M. Kretschmer, P.S. Pregosin, P. Favre and C.W. Schlaepfer, *J. Organomet. Chem.*, 1983, **253**, 17.
127. A.M. Bond, R. Colton, D. Dakternieks, K.W. Hanck and M. Svestka, *Inorg. Chem.*, 1983, **22**, 236.
128. P. Peringer and D. Obendorf, *Inorg. Chim. Acta*, 1983, **77**, L147.
129. Yu.K. Grishin, V.A. Roznyatovskii, Yu.A. Ustynyuk, S.N. Titova, G.A. Domrachev and G.A. Razuiev, *Polyhedron*, 1983, **2**, 895.
130. A.M. Bond, R. Colton, D. Dakternieks, M.L. Dillon, J. Hauenstein and J.E. Moir, *Aust. J. Chem.*, 1981, **34**, 1393.
131. M. Lusser and P. Peringer, *J. Organomet. Chem.*, 1986, **301**, 269.
132. L.V. Pankratov, L.M. Penyagina, L.N. Zakharov, M.N. Bochkarev, G.A. Razuvaev, Yu.K. Grishin, Yu.A. Ustynyuk and Yu.T. Struchkov, *J. Organomet. Chem.*, 1987, **335**, 313.
133. M. Lusser and P. Peringer, *J. Organomet. Chem.*, 1986, **312**, C61.
134. D. Obendorf and P. Peringer, *J. Organomet. Chem.*, 1987, **320**, 47.
135. P. Peringer and M. Lusser, *Inorg. Chim. Acta*, 1986, **117**, L25.
136. W. Lau and J.K. Kochi, *J. Org. Chim.*, 1986, **51**, 1801.

137. H.W. Roesky, V.W. Pogatzki, K.S. Dhathathreyan, A. Thiel, H.G. Schmidt, M. Dyrbusch, M. Noltemeyer and G.M. Sheldrick, *Chem. Ber.*, 1986, **119**, 2687.
138. B.K. Nicholson and A.J. Whitton, *J. Organomet. Chem.*, 1986, **306**, 139.
139. J.D. Wuest and B. Zacharie, *J. Am. Chem. Soc.*, 1985, **107**, 6121.
140. M. Lusser and P. Peringer, *Polyhedron*, 1985, **4**, 1997.
141. B.L. Khandelwal, A.K. Singh and N.S. Bhandari, *J. Organomet. Chem.*, 1987, **320**, 283.
142. A.J. Bloodworth and C.J. Cooksey, *J. Organomet. Chem.*, 1985, **295**, 131.
143. O. Rossell, M. Seco and I. Torra, *J. Chem. Soc. Dalton Trans.*, 1986, 1011.
144. P.A.W. Dean and R.S. Srivastava, *Can. J. Chem.*, 1985, **63**, 2829.
145. C.P. Horwitz, E.M. Holt, C.P. Brock and D.F. Shriver, *J. Am. Chem. Soc.*, 1985, **107**, 8136.
146. J.-P. Charland, M.T.P. Viet, M. St-Jacques and A.L. Beauchamp, *J. Am. Chem. Soc.*, 1985, **107**, 8202.
147. A.L. Nivorozhkin, E.V. Sukholenko, L.E. Nivorozhkin, N.I. Boisenko, V.I. Minkin, Yu.K. Grishin, O.A. Diachenko, T.G. Takhirov and D.B. Tagiev, *Polyhedron*, 1989, **8**, 569.
148. H. Schmidbaur, H.-J. Öller, D.L. Wilkinson, B. Huber and G. Müller, *Chem. Ber.*, 1989, **122**, 31.
149. P.A.W. Dean, J.J. Vittal and M.H. Trattner, *Inorg. Chem.*, 1987, **26**, 4245.
150. D. Obendorf, P. Peringer, N. Müller and H. Falk, *J. Organomet. Chem.*, 1987, **326**, 375.
151. Yu.K. Grishin, D.V. Bazhenov, Yu.A. Ustynyuk, N.S. Zefirov, V.R. Kartashov, T.N. Sokolova, E.V. Skorobogatova and A.N. Chernov, *Tetrahedron Lett.*, 1988, **29**, 4631.
152. B.F. Abrahams, D. Dakternieks, B.F. Hoskins and G. Winter, *Aust. J. Chem.*, 1988, **41**, 757.
153. E. Block, M. Brito, M. Gernon, D. McGowty, H. Kang and J. Zubieta, *Inorg. Chem.*, 1990, **29**, 3172.
154. F. Nadeau, M. Simard and J.D. Wuest, *Organometallics*, 1990, **9**, 1311.
155. B.F. Abrahams, G. Winter and D. Dakternieks, *Inorg. Chim. Acta*, 1989, **162**, 211.
156. S. Hajela, E. Rosenberg, R. Gobetto, L. Milone and D. Osella, *J. Organomet. Chem.*, 1989, **377**, 85.
157. G.K. Carson and P.A.W. Dean, *Inorg. Chim. Acta*, 1982, **66**, 157.
158. J. Eichbichler and P. Peringer, *Inorg. Chim. Acta*, 1981, **54**, L213.
159. E. Peletier, F. Sauriol and I. Wharf, *Inorg. Chim. Acta*, 1987, **138**, 99.
160. P.-P. Winkler and P. Peringer, *Inorg. Chim. Acta*, 1983, **76**, L59.
161. J. Eichbichler and P. Peringer, *Inorg. Chim. Acta*, 1980, **43**, 121.
162. M.M. Kubicki, R. Kergoat, J.E. Guerschais, C. Bois and P. L'Haridon, *Inorg. Chim. Acta*, 1980, **43**, 17.
163. M.S.G. Tasende, M.I.S. Gimeno, A. Sanchez, J.S. Casas, J. Sordo and E.E. Castellano, *J. Organomet. Chem.*, 1990, **384**, 19.
164. S.A. Mbogo, W.R. McWhinnie and T.S. Lobana, *J. Organomet. Chem.*, 1990, **384**, 115.
165. U. Brekau and H. Werner, *Organometallics*, 1990, **9**, 1067.
166. R. Balz, M. Haller, W.E. Hertler, O. Lutz, A. Nolle and R. Schafitel, *J. Magn. Reson.*, 1980, **40**, 9.
167. W. Koch, O. Lutz and A. Nolle, *Z. Phys., Teil A*, 1978, **289**, 17.
168. P. Pyykkö, *Chem. Phys.*, 1983, **74**, 1.
169. P. Pyykkö, A. Görling and N. Rösch, *Mol. Phys.*, 1987, **61**, 195.
170. G. Breit, *Phys. Rev.*, 1930, **35**, 1447.
171. P. Pyykkö and W. Wiesenfeld, *Mol. Phys.*, 1981, **43**, 557.
172. R.B. Johannesen and R.W. Duerst, *J. Magn. Reson.*, 1971, **5**, 355.
173. W. McFarlane, *J. Chem. Soc. A*, 1968, 2280.
174. K. Hildenbrand and A. Dreiskamp, *Z. Phys. Chem.*, 1970, **69**, 171.

175. D.K. Breitingner, U. Krumphanzl and M. Moll, *J. Mol. Struct.*, 1990, **218**, 27.
176. M. Borzo and G.E. Maciel, *J. Magn. Reson.*, 1975, **19**, 279.
177. M.A. Fedotov, R.I. Maksimovskaya, G.M. Maksimov and K.I. Matveev, *Zh. Neorg. Khim.*, 1987, **32**, 647.
178. M.F. Larin, D.V. Gendin, V.A. Pestunovich, O.A. Kruglaya and N.S. Vyazankin, *Izvest. Akad. Nauk. SSSR, Ser. Khim.*, 1979, 697.
179. M.F. Larin, D.V. Gendin, V.A. Pestunovich, L.I. Rybin, O.A. Vyazankina, N.S. Vyazankin, *Izvest. Akad. Nauk. SSSR, Ser. Khim.*, 1983, 2139.
180. D.N. Kravtsov, A.S. Peregudov, V.F. Ivanov and E.I. Fedin, *Izvest. Akad. Nauk. SSSR, Ser. Khim.*, 1984, 1626.
181. A.S. Peregudov, V.F. Ivanov, E.I. Fedin and D.N. Kravtsov, *Izvest. Akad. Nauk. SSSR, Ser. Khim.*, 1985, 1524.
182. Yu.K. Grishin, V.A. Rozniatovskii, A.A. Solomin and Yu.A. Ustynyuk, *Vestn. Mosk. Univ., Ser. Khim.*, 1984, **25**, 289.
183. H.A. Bent, *Chem. Rev.*, 1961, **61**, 275.
184. G.H. Penner, W.P. Power and R.E. Wasylshen, *Can. J. Chem.*, 1988, **66**, 1821.
185. A. Pulkkinen, Y. Hiltunen and J. Jokisaari, *Liquid Crystals*, 1988, **3**, 737.
186. V.R. Kartashov, T.N. Sokolova, E.V. Skorobogatova, A.N. Tschernov, D.V. Bazhenov, Yu.K. Grishin, Yu.A. Ustynyuk and N.S. Zefirov, *Zh. Org. Khim.*, 1989, **25**, 1846.
187. Yu.K. Grishin, Yu.A. Ustynyuk and E.V. Uglova, *Zh. Org. Khim.*, 1987, **23**, 895.
188. V.R. Kartashov, T.N. Sokolova, E.V. Skorobogatova, Yu.K. Grishin, D.V. Bazhenov, A.N. Tschernov and N.S. Zefirov, *Zh. Org. Khim.*, 1988, **24**, 1684.
189. V.R. Kartashov, T.N. Sokolova, E.N. Skorobogatova, D.V. Bazhenov, V.A. Rozniatovskii, Yu.K. Grishin, A.S. Kozmin and N.S. Zefirov, *Zh. Org. Khim.*, 1987, **23**, 2245.
190. L.V. Pankratov, M.N. Bochkarev, G.A. Razuvaev, L.N. Zakharov, Yu.T. Struchkov, Yu.K. Grishin and Yu.A. Ustynyuk, *Izvest. Akad. Nauk. SSSR, Ser. Khim.*, 1986, 2548.
191. R.D. Kendrick, C.S. Yannoni, R. Aikman and R.J. Lagow, *J. Magn. Reson.*, 1980, **37**, 555.
192. L.A. Fedorov, Z.A. Stutbrechichyute and E.I. Fedin, *Zh. Org. Khim.*, 1975, **11**, 913.
193. M.N. Bochkarev, N.L. Ermolaev, G.A. Razuvaev, Yu.K. Grishin and Yu.A. Ustynyuk, *J. Organomet. Chem.*, 1982, **229**, C1.
194. J. Jokisaari and K. Räsänen, *Mol. Phys.*, 1978, **36**, 113.
195. C.J. Jameson and J.H. Osten, *Ann. Rep. NMR Spectrosc.*, 1986, **17**, 1.
196. R.J. Goodfellow and S.R. Stobart, *J. Magn. Reson.*, 1977, **27**, 143.
197. A.J. Canty, A. Marker, P. Barron and P.C. Healey, *J. Organomet. Chem.*, 1978, **144**, 371.
198. T. Ibuski and Y. Saito, *Chem. Lett.*, 1974, 311.
199. J.L. Sudmeier, R.R. Birge and T.G. Perkins, *J. Magn. Reson.*, 1978, **30**, 491.
200. P.D. Godfrey, M.L. Heffernan and D.F. Kerr, *Aust. J. Chem.*, 1964, **17**, 701.
201. F. Glockling, N.S. Hosmane and V.B. Mahale, *J. Chem. Res.*, (M) 1977, 1201.
202. B.E. Kogai, V.A. Sokolenko, P.V. Petrovskii and V.I. Sokolov, *Izvest. Akad. Nauk. SSSR, Ser. Khim.*, 1982, 1645.
203. A.P. Arnold, A.J. Canty, P.W. Moors and G.B. Deacon, *J. Inorg. Biochem.*, 1983, **19**, 319.
204. A. Pages, J.S. Casas, A. Sanchez, J. Sordo, J. Bravo and M. Gayoso, *J. Inorg. Biochem.*, 1985, **25**, 35.
205. E. Buncel, C. Boone, H. Joly, R. Kumar and A.R. Norris, *J. Inorg. Biochem.*, 1985, **25**, 61.
206. A.J. Canty, A.J. Carty and S.F. Malone, *J. Inorg. Biochem.*, 1983, **19**, 133.
207. A.J. Carty, S.F. Malone, N.J. Taylor and A.J. Canty, *J. Inorg. Biochem.*, 1983, **18**, 291.
208. T. Allman and R.E. Lenkinski, *Inorg. Chem.*, 1986, **25**, 3202.

209. A.M. Bond, R. Colton, M.L. Dillon, J.E. Moir and D.R. Page, *Inorg. Chem.*, 1984, **23**, 2883.
210. A.M. Bond, R. Colton, A.F. Hollenkamp and J.E. Moir, *Inorg. Chem.*, 1986, **25**, 1519.
211. R.K. Harris and A. Sebald, *Magn. Reson. Chem.*, 1987, **25**, 1058.
212. Yu.K. Grishin, Yu.A. Ustynyuk, T.I. Voevodskaya, A.S. Peregudov and D.N. Kravtsov, *Izvest. Akad. Nauk SSSR, Ser. Khim.*, 1985, 1530.
213. A.A. Solomin, V.I. Matislavskii, T.A. Obukhova, Yu.K. Grishin and Yu.A. Ustynyuk, *Vestn. Mosk. Univ. Ser. Khim.*, 1984, **25**, 394.
214. A.A. Solomin, V.I. Matislavskii, A.G. Shakhmatuni, Yu.K. Grishin and Yu.A. Ustynyuk, *Vestn. Mosk. Univ. Ser. Khim.*, 1984, **25**, 78.
215. M.C. Corbeil and A.L. Beauchamp, *Can. J. Chem.*, 1988, **66**, 1379.
216. L. Grenier, J.P. Charland and A.L. Beauchamp, *Can. J. Chem.*, 1988, **66**, 1663.
217. E. Buncel, R. Kumar and A.R. Norris, *Can. J. Chem.*, 1986, **64**, 442.
218. A. Bax and R. Freeman, *J. Magn. Reson.*, 1981, **45**, 177.
219. R. Allmann, *Kristallografiya*, 1973, **138**, 366.
220. S. Kersch, A. Sebald and B. Wrackmeyer, *Magn. Reson. Chem.*, 1985, **23**, 514.
221. N.A. Bell, T.D. Dee, P.L. Goggin, M. Goldstein, R.J. Goodfellow, T. Jones, K. Kessler, D.M. McEwan and I.M. Nowell, *J. Chem. Res. (S)* 1981, 2; (M) 1981, 201.
222. Yu.K. Grishin, V.A. Roznyatovskii, Yu.A. Ustynyuk, M.N. Bochkarev, G.S. Kalinina and G.A. Razuvaev, *Izvest. Akad. Nauk. SSSR, Ser. Khim.*, 1980, 2190.
223. E.H. Curzon, N. Herron and J.P. Moore, *J. Chem. Soc. Dalton Trans.*, 1980, 721.
224. L.A. Fedorov, Z.A. Stutbreichyute and E.I. Fedin, *Zh. Strukt. Khim.*, 1975, **16**, 976.
225. F.A.L. Anet, J. Krane, W. Kitching, D. Doddrell and D. Praeger, *Tetrahedron Lett.*, 1974, 3255; 1975, 759.
226. T.C. Wong, *J. Magn. Reson.*, 1985, **63**, 179.
227. B. Wrackmeyer, unpublished results.
228. J.P. Charland, J.F. Britten and A.L. Beauchamp, *Inorg. Chim. Acta*, 1986, **124**, 161.
229. L.C. Damude and P.A.W. Dean, *J. Organomet. Chem.*, 1979, **181**, 1.
230. E.C. Alyea, S.A. Dias, G. Ferguson and M. Parvez, *Inorg. Chim. Acta*, 1979, **37**, 45.
231. S.O. Grim, D.P. Shah, C.K. Haas, J.M. Ressler and P.H. Smith, *Inorg. Chim. Acta*, 1979, **36**, 139.
232. O. Rossell and M. Seco, *Inorg. Chim. Acta*, 1983, **74**, 119.
233. S.M. Bowen, E.N. Duesler, R.T. Paine and C.F. Campana, *Inorg. Chim. Acta*, 1982, **59**, 53.
234. N.A. Bell, M. Goldstein, T. Jones and I.W. Nowell, *Inorg. Chim. Acta*, 1983, **75**, 21.
235. E.C. Alyea, K.J. Fisher and S. Johnson, *Can. J. Chem.*, 1989, **67**, 1319.
236. N.A. Bell, L.A. March and I.A. Nowell, *Inorg. Chim. Acta*, 1989, **156**, 195.
237. M. Geisel and R. Mews, *Chem. Ber.*, 1987, **120**, 1675.
238. S.O. Grim, P.H. Smith and L.C. Satek, *Polyhedron*, 1982, **1**, 137.
239. W.S. McDonald, P.G. Pringle and B.L. Shaw, *J. Chem. Soc. Chem. Commun.*, 1982, 861.
240. O. Rossell, J. Sales and M. Seco, *J. Organomet. Chem.*, 1982, **236**, 415.
241. P.G. Pringle and B.L. Shaw, *J. Chem. Soc. Chem. Commun.*, 1982, 956.
242. R.W. Kunz, P.S. Pregosin, M. Camalli, F. Caruso and L. Zambonelli, *Helv. Chim. Acta*, 1983, **66**, 1661.
243. I.I. Guerus and Yu.L. Yaguoplskii, *J. Organomet. Chem.*, 1983, **247**, 81.
244. J.A. Iggo and M.J. Mays, *J. Chem. Soc. Dalton Trans.*, 1984, 643.
245. M. Crespo, O. Rossell, J. Sales and M. Seco, *J. Organomet. Chem.*, 1984, **273**, 415.
246. O. Rossell, M. Seco and P. Braunstein, *J. Organomet. Chem.*, 1984, **273**, 233.

247. O. Rossell and M. Seco, *Inorg. Chim. Acta*, 1983, **74**, 119.
248. G. Singh and G.S. Reddy, *J. Organomet. Chem.*, 1972, **42**, 267.
249. D.W. Allen, N.A. Bell, S.T. Fong, L.A. March and I.W. Nowell, *Inorg. Chim. Acta*, 1985, **99**, 157.
250. S.O. Grim, P. Lui and R.L. Keiter, *Inorg. Chem.*, 1974, **13**, 342.
251. H. Schmidbaur and K.-H. R  thlein, *Chem. Ber.*, 1973, **106**, 2491.
252. T. Allman, R.G. Goel and P. Pilon, *Can. J. Chem.*, 1979, **57**, 91.
253. E.C. Alyea and S.A. Dias, *Can. J. Chem.*, 1979, **57**, 83.
254. P.I. van Vliet, J. Kuyper and K. Vrieze, *J. Organomet. Chem.*, 1976, **122**, 99.
255. P. Peringer and J. Eichbichler, *J. Inorg. Nucl. Chem.*, 1981, **43**, 3027.
256. J. Calvet, O. Rossell and M. Seco, *Trans. Met. Chem.*, 1984, **9**, 208.
257. F.A. Johnson and W.D. Perry, *Organometallics*, 1989, **8**, 2646.
258. M. Watanabe, Y. Masuda, I. Motoyama and H. Sano, *J. Coord. Chem.*, 1988, **18**, 141.
259. D.K. Breitinger, W. Kress, R. Sendelbeck and K. Ishiwada, *J. Organomet. Chem.*, 1983, **243**, 245.
260. N. Iwasaki, *Bull. Chem. Soc. Jap.*, 1976, **49**, 2735.
261. J.J. Pesek and J.F. Schneider, *Inorg. Chem.*, 1987, **26**, 3064.
262. P. Peringer, *Monatsh. Chem.*, 1980, **111**, 1245.
263. P. Peringer, *Inorg. Nucl. Chem. Lett.*, 1980, **16**, 205.
264. L.F. Sytsma and R.J. Kline, *J. Organomet. Chem.*, 1973, **54**, 15.
265. Yu.K. Grishin, Yu.A. Ustynyuk, D.N. Kravtsov, A.S. Peregudov and V.F. Ivanov, *Izvest. Akad. Nauk SSSR, Ser. Khim.*, 1983, 809.
266. R. Fr  ginal, N. Barba-Behrens and R. Contreras, *Spectrochim. Acta*, 1989, **45A**, 1385.
267. J.-P. Charland and A.L. Beauchamp, *Inorg. Chem.*, 1986, **25**, 4870.
268. D.L. Rabenstein, *Acc. Chem. Res.*, 1978, **11**, 100.
269. J.L. Sudmeier and T.G. Perkins, *J. Am. Chem. Soc.*, 1977, **99**, 7732.
270. Yu.K. Grishin, A.A. Solomin and Yu.A. Ustynyuk, *Metalloorg. Khim.*, 1989, **2**, 404.
271. V.N. Baidin, Yu.V. Chizhov, M.M. Timoshenko, O.K. Sokolikova, Yu.K. Grishin and Yu.A. Ustynyuk, *Zh. Strukt. Khim.*, 1981, **22**, 164.
272. D.V. Gendin, M.F. Larin, L.I. Rybin, O.A. Vyazankin and N.S. Vyazankin, *Metalloorg. Khim.*, 1989, **2**, 337.
273. H. Schmidbaur and G. M  ller, *Monatsh. Chem.*, 1980, **111**, 1233.
274. D.I. Sheibe, Yu.K. Grishin, V.M. Mamaev and Yu.A. Ustynyuk, *Metalloorg. Khim.*, 1990, **3**, 377.
275. A.S. Peregudov, L.N. Usatova and D.N. Kravtsov, *Metalloorg. Khim.*, 1982, **2**, 695.
276. E. Rosenberg, J. Wang and R.W. Gellert, *Organometallics*, 1988, **7**, 1093.
277. R.D. Bach and A.T. Weibel, *J. Am. Chem. Soc.*, 1976, **98**, 6241.
278. J. Wang, M. Sabat, C.P. Howitz and D.F. Shriver, *Inorg. Chem.*, 1988, **27**, 552.
279. D.C. Harris, R.A. Nissan and K.T. Higa, *Inorg. Chem.*, 1987, **26**, 765.
280. B.S. McGilligan, L.M. Venanzi and M. Wolfer, *Organometallics*, 1987, **6**, 946.
281. G.J. Arsenaault, M. Crespo and R.J. Puddephat, *Organometallics*, 1987, **6**, 2255.
282. P. Braunstein, O. Rossell, M. Seco, I. Torra, X. Solans and C. Miravittles, *Organometallics*, 1986, **5**, 1113.
283. D.V. Khasnis, H. le Dozec, P.H. Dixneuf and R.D. Adams, *Organometallics*, 1986, **5**, 1772.
284. A.P. Arnold, K.-S. Tan and D.L. Rabenstein, *Inorg. Chem.*, 1986, **25**, 2433.
285. S.O. Grim, P.H. Smith, S. Nittolo, H.L. Ammon, L.C. Satek, S.A. Sangokoya, R.K. Khanna, I.J. Colquhoun, W. McFarlane and J.R. Holden, *Inorg. Chem.*, 1985, **24**, 2889.

286. R.C. Burns, L.A. Devereux, P. Granger and G.J. Schrobilgen, *Inorg. Chem.*, 1985, **24**, 2615.
287. A.J. Canty and C.V. Lee, *Organometallics*, 1982, **1**, 1063.
288. A.J. Canty, J.M. Patrick and A.H. White, *Inorg. Chem.*, 1984, **23**, 3827.
289. H.B. Buerger, R.W. Kunz and P.S. Pregosin, *Inorg. Chem.*, 1980, **19**, 3707.
290. E.C. Alyea, S.A. Dias, R.G. Goel, W.O. Ogini, P. Pilon and D.W. Meek, *Inorg. Chem.*, 1978, **17**, 1697.
291. J.G. Verkade and J.A. Mosbo, in *Phosphorus-31 NMR Spectroscopy in Stereochemical Analysis* (ed. J.G. Verkade and L.D. Quin), p. 443. VCH Publishers, Deerfield Beach, Florida, 1987.
292. Yu.K. Grishin, V.A. Rozniatovskii, Yu.A. Ustynyuk, S.N. Titova, G.A. Domrachev and G.A. Razuvaev, *Izvest. Akad. Nauk SSSR, Ser. Khim.* 1985, 1928.
293. M. Delnomdedieu, D. Georgescauld, A. Boudou and E.J. Dufourc, *Bull. Magn. Reson.* 1989, **11**, 420.
294. Yu.K. Grishin, Yu.A. Strelenko, Yu.A. Ustynyuk, A.A. Erdman, I.V. Shchirina-Eingorn and I.I. Kritskaya, *Izvest. Akad. Nauk. SSSR, Ser. Khim.* 1982, 1038.
295. S.S. Al-Showiman, *Orient. J. Chem.* 1989, **5**, 20.
296. Yu.K. Grishin, V.A. Roznyatovskii, Yu.A. Ustynyuk, B.C. Kamel and V.I. Bregadze, *Vestn. Mosk. Univ. Ser. Khim.* 1982, **23**, 488.
297. V.V. Bashilov, A.A. Musaev, Yu.K. Grishin, P.V. Petrovskii and V.I. Sokolov, *Metalloorg. Khim.* 1989, **2**, 854.
298. T.D. Bailey, R.M.H. Banda, D.C. Craig, I.G. Dance, I.N.L. Ma and M.L. Scudder, *Inorg. Chem.* 1991, **30**, 187.

This Page Intentionally Left Blank

Applications of NMR Methods in Coal Research

WOLFGANG MEILER and REINHARD MEUSINGER

Sektion Physik, Universität Leipzig, Linnéstr. 5, 0-7010 Leipzig, Germany

1. Introduction	331
2. NMR investigations of coal structure	332
3. Interactions between solvent molecules and coal surfaces	342
4. Thermal processes	356
Acknowledgements	360
References	361

1. INTRODUCTION

Of the various analytical methods available, NMR spectroscopy has proved to be of special importance in the research of coals, other fossil fuels and derived products. It is possible to determine the structure and properties of different coals in a direct and non-destructive way with respect to basic research as well as to technological conversion processes. Volume 23 of *Annual Reports on NMR Spectroscopy* presents an introduction to the problems of coal physics and chemistry and the background of some NMR spectroscopy methods used in this field of investigation.¹ Some methodical problems like the complex spin-dynamics of coal, the relaxation behaviour, the mobility of coal constituents, the amount of observable carbon content, necessary corrections of spectra intensities and spinning sidebands with regard to determination of quantitative statements, applicability of single-pulse methods for investigation especially of viscous samples and the determination of diffusion coefficients in coal solvent multicomponent systems are discussed. The present paper is, to a certain extent, the continuation of this work.¹

The paper deals with NMR investigations of the coal structure²⁻⁵ as well as with the use of NMR spectroscopy methods for the characterization of elementary steps during the interaction of coal surfaces with organic solvents. More than that, changes in the coal structure and thermoplasticity, the water content and the enhanced mobility of coal constituents caused by thermal

processes are obtained by NMR methods. An important distinction of this work with respect to the majority of published data on coals consists in the investigation of low-rank coals, especially brown coals and lignites. For the fundamental literature on coals⁶⁻⁹ and NMR on coal products, especially multicomponent fractions of coal liquids,^{10,11} the reader is referred elsewhere.

2. NMR INVESTIGATIONS OF COAL STRUCTURE

In this section some results of structure determinations of untreated coals are examined. The application of different NMR methods is illustrated by examples from the literature as well as by measurements on brown coals from westelbian coalfields near Leipzig. The solid state NMR methods of interest are ¹³C cross-polarization magic-angle spinning (CP-MAS), ¹³C CP-MAS dipolar dephasing (DD), ¹³C NMR combined with resolution enhancement procedures or dynamic nuclear polarization and ¹H combined rotation and multiple-pulse spectroscopy (CRAMPS). Examples of NMR studies of other nuclei are presented.

As shown in Fig. 1 ¹³C CP-MAS NMR spectra at lower magnetic field strengths (15.1 MHz) were obtained with relatively good resolution.¹² The spectra indicate the differences in the aliphatic as well as aromatic regions of the ¹³C NMR scale of the individual materials. With respect to the brown coal, and to the bituminous coal, the ¹³C NMR spectrum of the high coalificated anthracite consists essentially of a narrow line due to aromatic carbons.

Intercalations in East German soft brown coals are presented in Fig. 2.¹³ The ¹³C NMR spectrum obtained for a fossilized wax (pyropissite, atomic ratio H/C = 1.87) shows only one sharp signal at about 33 ppm which is typical of long aliphatic (CH₂)_n chains. The spectrum of the fossil resin retinite (H/C = 1.62) consist of intensive signal in the aliphatic range and resonances for *sp*² hybridized carbon atoms. In qualitative agreement with literature data¹⁴ the maceral fusite shows the main resonances in the aromatic range, probably as a result of the unusual thermal process associated with fusinization. "Monkey hairs" are fossilized rubber fibres (fossil caoutchouc, H/C = 1.60), and the ¹³C NMR spectrum consists of signals that are typical of highly polymerized natural rubber with isoprene as a predominant structural element. This interpretation was supported by additional ¹H CRAMPS NMR (BR 24) measurements on the same sample (deposit Geiseltal, westelbian).

Figure 3 presents comparison of ¹³C CP-MAS and ¹H CRAMPS NMR spectra of the same brown coal lithotypes.¹⁵ The ¹³C NMR spectra were recorded in an iron magnet.

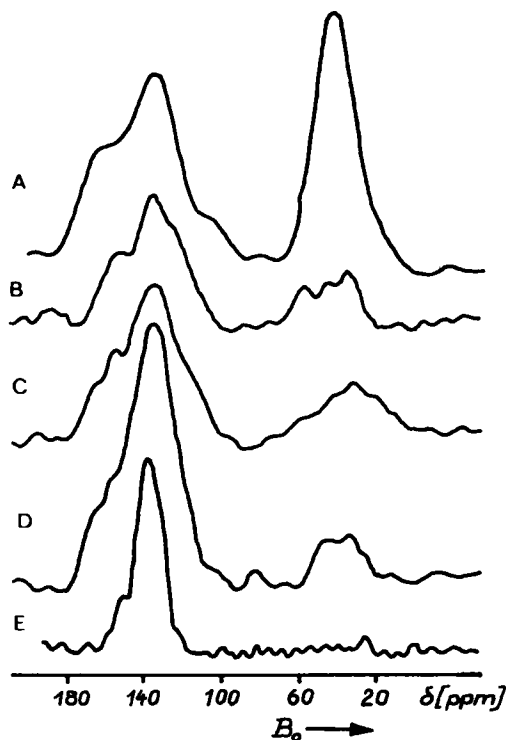


Fig. 1. ^{13}C CP-MAS NMR spectra of humic coals of different rank. Resonance frequency 15.1 MHz. (A) Detrital soft brown coal (Geiseltal, westelbian); (B) xylite-containing soft brown coal (Varpalota, Hungary); (C) bright hard brown coal; (D) high-volatile bituminous coal (Zwickau, westelbian); (E) anthracite (Doberlug-Kirchhain, eastelbian). (From Küstner *et al.*¹²)

With respect of the main contents of this review, the investigation of brown coals, it should be mentioned that recently coals from two of the world's largest and most significant brown coal deposits—the Kansk–Achinsk Basin in Siberia, USSR, and the Latrobe Valley in Victoria, Australia, have been studied by a range of spectroscopic (especially ^{13}C CP-MAS NMR) and chemical techniques.¹⁶ ^{13}C CP-MAS NMR spectra of brown coal samples from the Ulster brown coal deposit are discussed in detail.¹⁷

In recent years the major techniques used in the literature⁸ are CP-MAS and dipolar dephasing experiments. A wide range of simple organic solids of relevance to coal structure have been examined.¹⁸ A selection only of articles is mentioned.^{19–40} Figure 4 illustrates an example of dipolar dephasing CP-MAS spectra from a Gardanne coal at two dipolar dephasing times.³⁶ The

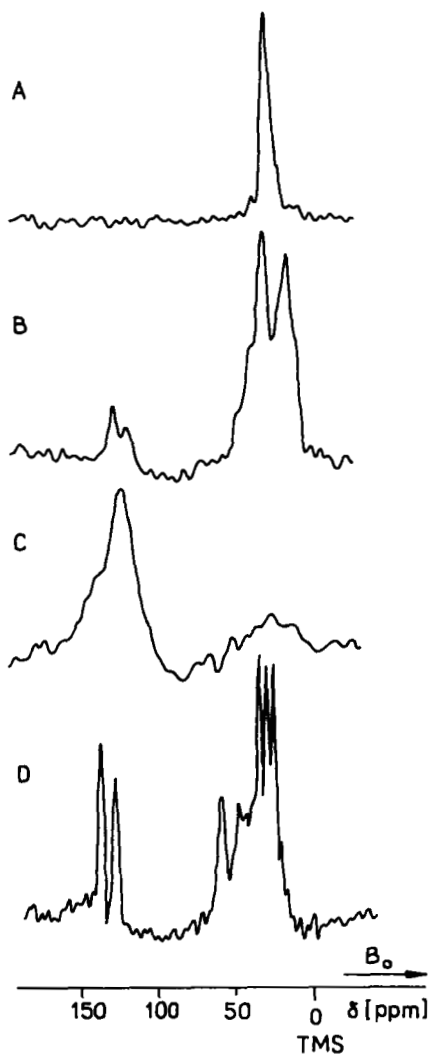


Fig. 2. ^{13}C CP-MAS NMR spectra of some intercalations in German soft brown coals. Resonance frequency 15.1 MHz. (A) Pyropissite; (B) retinite; (C) fusite; (D) "Monkey hairs". (From Ref. 13: H. Rosenberger, G. Scheler and E. Künstner, *Fuel*, 1988, **67**, 508, by permission of the publishers, Butterworth & Co. (Publishers) Ltd ©.)

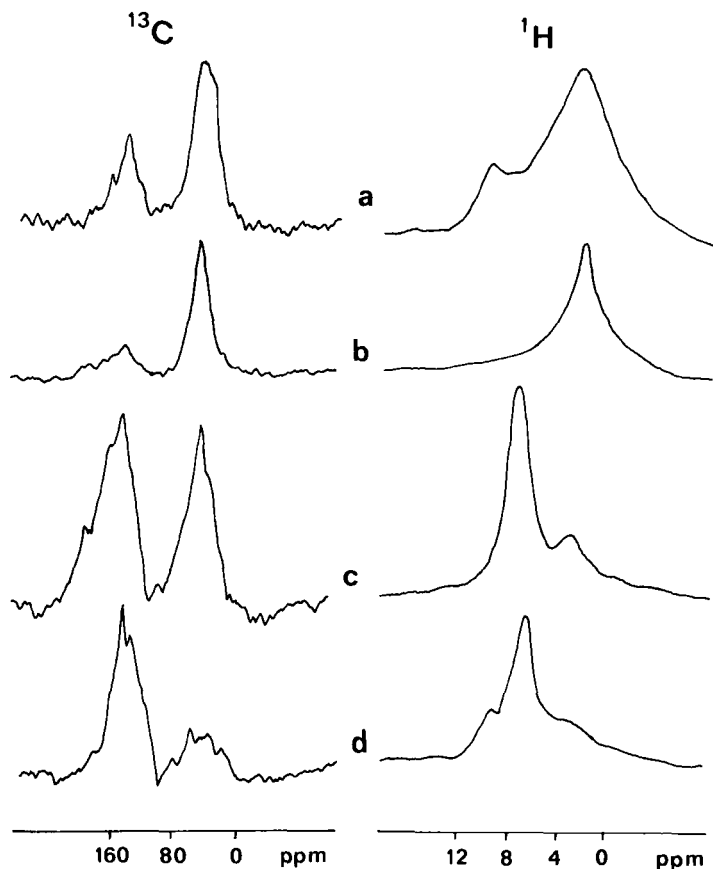


Fig. 3. ^{13}C CP-MAS and ^1H BR 24 MAS NMR (CRAMPS) spectra of lithotypes of brown coal Merseburg-East (westelbian). Resonance frequencies 22.63 and 270 MHz for ^{13}C and ^1H , respectively. CP mixing time 1 ms; repetition time in ^{13}C NMR experiments 0.7 s; number of scans 10 000 . . . 20 000; $f_{\text{rot}}(\text{MAS}) \approx 2.2$ kHz. Repetition time in ^1H NMR experiments 1 s; number of scans 200 . . . 400; $f_{\text{rot}}(\text{MAS}) \approx 2$ kHz. (a) Retinite (fossil resin); (b) yellow coal; (c) black coal; (d) xylite (fossil wood). (From Birke.¹⁵ The ^1H BR 24 MAS NMR measurements were carried out on a home-built spectrometer at the Friedrich Schiller Universität Jena.)

upper spectrum ($T_{\text{DD}} = 0.25 \mu\text{s}$) must result from all carbon atoms, whereas the lower one ($T_{\text{DD}} = 40 \mu\text{s}$) contains predominantly carbons which have not relaxed after this delay, especially non-protonated aromatic and aliphatic methyl carbons with molecular reorientation motion.³⁶ Especially in the case of dipolar dephasing experiments in brown coals with their complicated dynamics, the results of discrimination of molecular groups should be con-

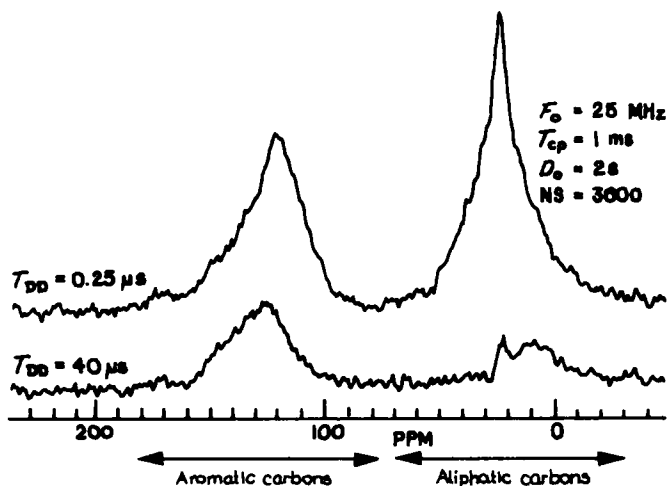


Fig. 4. ^{13}C CP-MAS DD NMR spectra of the Gardanne 1 coal. (From Ref. 36: H. Sfihi, M.F. Quinton, A. Legrand, S. Pregermain, D. Carson and P. Chiche, *Fuel*, 1986, 65, 1006, by permission of the publishers, Butterworth & Co. (Publishers) Ltd ©.)

sidered with care. It could be shown that the decrease of magnetization in the dipolar dephasing experiment depends on the rate of ^1H spin diffusion and on the MAS rotation frequency.⁴¹

An interesting field of investigation is the study of chemically modified coal surfaces.²¹ Figure 5 shows an acetylated as well as a methylated eastelbian brown coal.¹² Distinct additional signals caused by chemical reactions on the coal surface can be seen.

^{13}C CP-MAS NMR spectroscopy has been used to characterize the organic content of 32 low-rank coals from Australia and New Zealand.⁴² Two examples are presented in Fig. 6. The resolution-enhanced spectra were produced by Lorentzian-to-Gaussian transformation,⁴³ involving an exponentially increasing function (time constant 1 ms) and a Gaussian apodization function (time constant 2 ms). The spectra show only some details such as found in those of coals of similar rank.⁴²

An important study by Wind *et al.*⁴⁴ reports the investigation of 60 coal samples of different rank and origin by means of ESR, ^1H NMR, and ^{13}C NMR, the last two in combination with dynamic nuclear polarization (DNP).⁴⁵⁻⁴⁷ In solids containing both a nuclear spin system and unpaired electrons, DNP can be used to transfer the polarization of the electron spins to the nuclei. As a result of this process a considerable enhancement of the NMR signals can be detected (Fig. 7). Moreover, DNP experiments provide information about localization and mobility of the unpaired electrons. As

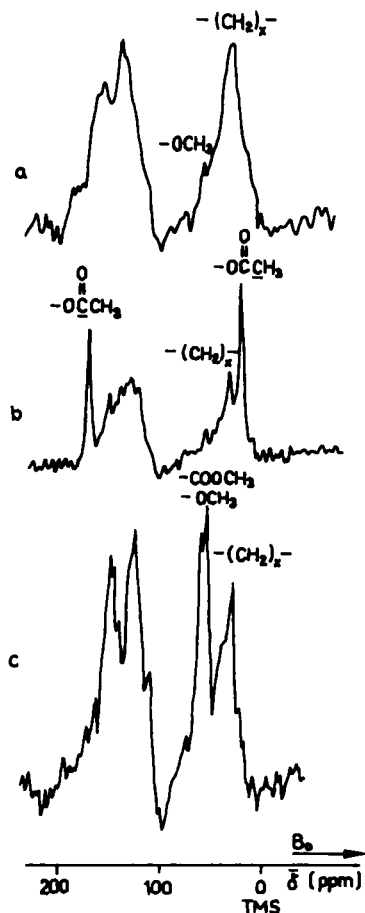


Fig. 5. ^{13}C CP-MAS NMR spectra of chemically modified eastelbian brown coals (demineralized by HCl/HF treatment). Resonance frequency 15.1 MHz. (a) Brown coal; (b) acetylated brown coal; (c) methylated brown coal. (From Künstner *et al.*¹²)

can be seen from Fig. 7(c) and (f), in standard single-pulse NMR experiments including DNP almost no aliphatic carbons are observed. This indicates that in the coal under study the radicals are localized mainly near the aromatic regions of the coal skeleton.⁴⁴

A method of evaluating the ^{13}C CP-MAS NMR spectra and related materials has been developed which permits the quantitative assignment of protonated, substituted and bridged aromatic carbons in addition to alkoxy and aliphatic carbons.⁴⁸ The procedure is based on the numerical evaluation

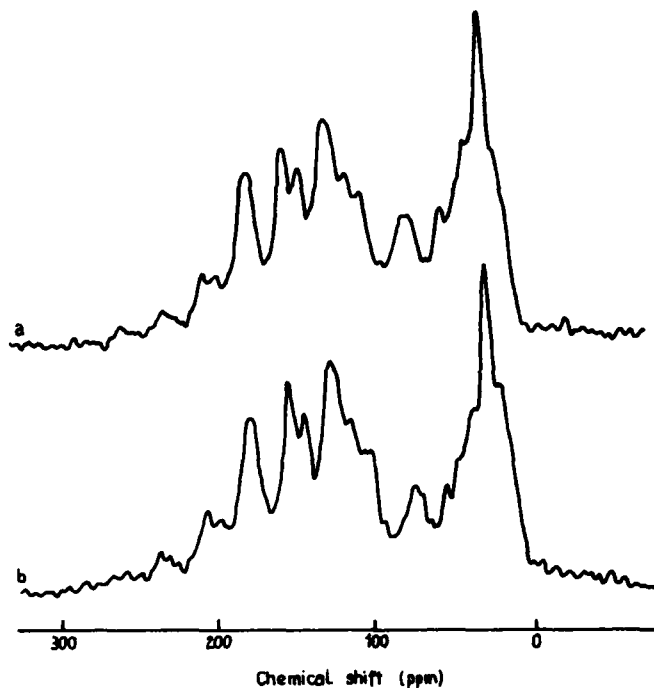


Fig. 6. Resolution-enhanced ^{13}C NMR spectra of Australian brown coals from: (a) Morwell; (b) Loy Yang. (From Ref. 42: R.H. Newman, S.J. Davenport, *Fuel*, 1986, **65**, 533, by permission of the publishers, Butterworth & Co. (Publishers) Ltd ©.)

of the sideband intensities and leads to the possibility of determining the mean degree of aromatic condensation.

The ^{13}C NMR lineshapes for coals were first analysed under conditions of high-power proton decoupling without magic-angle spinning.⁴⁹ If the powder patterns for the chemically distinct species are overlapped, valuable chemical shielding anisotropy information is lost. In a recent study^{50,51} both static and variable angle sample spinning (VASS) lineshapes have been analysed to obtain the chemical shielding anisotropy tensor values and populating factors for the aromatic carbons of coals.

Another method for discrimination between differently substituted carbons consists in selective polarization inversion of resonance signals depending on the polarization transfer rates between protons and carbons.⁵²

A method to eliminate unwanted overlapping of aromatic sidebands with the aliphatic region of the ^{13}C CP-MAS NMR spectrum at high working frequencies (without TOSS)⁵³ consists in the application of a selective saturation sequence.⁵⁴

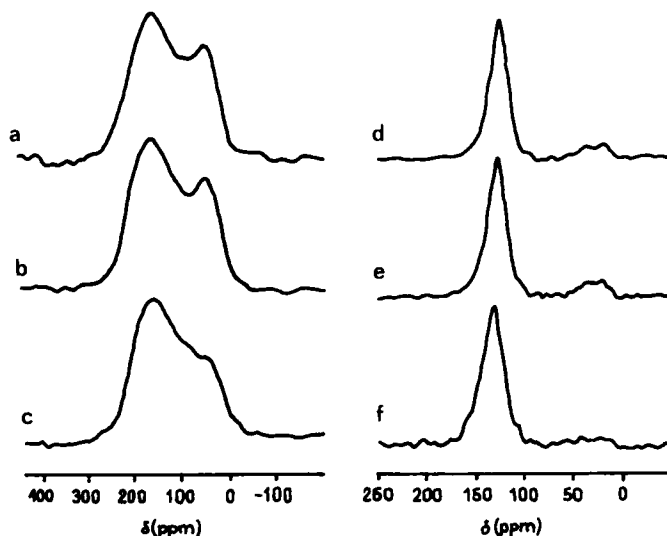


Fig. 7. ^{13}C NMR spectra of coal no. 11 (a low-volatile bituminous German coal) obtained via different experiments. (a) CP, match time 0.9 ms, number of scans 90 000, recycle delay 0.6 s; (b) DNP CP, number of scans 200, other parameters as in (a); (c) DNP FID, number of scans 8, recycle delay 60 s; (d) CP-MAS, number of scans 72 000, other parameters as in (a); (e) DNP CP-MAS, number of scans 500, other parameters as in (a); (f) DNP FID MAS, number of scans 4, recycle delay 60 s. (From Ref. 44: R.A. Wind, M.J. Duijvestijn, C. van der Lugt, J. Smidt and H. Vriend, *Fuel*, 1987, **66**, 876, by permission of the publishers, Butterworth & Co. (Publishers) Ltd ©.)

A fashionable method for a deeper study of coal structure, e.g. for the definition and investigation of reaction sites in coals, is the ^1H , ^{13}C , ^{31}P double cross-polarization (DCP) MAS NMR technique.⁵⁵⁻⁵⁷ In this experiment the ^{31}P nuclei act as a cross-polarization filter. Only carbons with significant ^{31}P - ^{13}C dipolar coupling will polarize during the second magnetization transfer. The radius of the sensitive sphere centred on a ^{31}P atom has been found to be approximately 0.3 nm.

Recently interesting ^1H CRAMPS NMR investigations were undertaken with respect to a line decomposition and the influence of water especially on soft brown coal ^1H NMR spectra.⁵⁸ Opposite to the situation in bituminous coals it could be shown that there is a signal from the remaining water even in carefully dried samples of brown coals. Examples of line deconvolution of a soft brown coal as well as of humic acids from this coal are depicted in Fig. 8.

Besides extensive ^{13}C and ^1H NMR studies other nuclei are of interest for the study of composition of coals and related materials. Figure 9 presents the

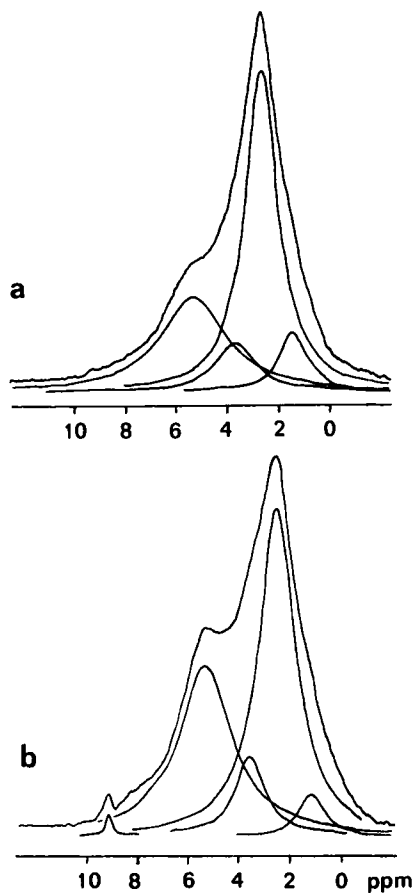


Fig. 8. ^1H MREV-8 MAS NMR (CRAMPS) spectra and line decomposition. Resonance frequency 300 MHz. $f_{\text{rot}}(\text{MAS}) \approx 4$ kHz, number of scans 128, repetition time 1 s. Pulse width ($\pi/2$) and pulse separation in MREV-8 $2\ \mu\text{s}$ and $3.5\ \mu\text{s}$, respectively. Signal assignment (line decomposition): aliphatic H ($-\text{CH}_3$, $-\text{CH}_2-$) ≈ 1.5 , 2.5 ppm; water, $-\text{OCH}_3 \approx 4.0$ ppm; aromatic H ≈ 6.0 ppm; $-\text{COOH} \approx 9.5$ ppm. (a) Brown coal Peres (westelbian); (b) humic acids from brown coal Peres.

^{23}Na MAS NMR spectrum of a dried Australian brown coal (0.28% Na).⁵⁹

^{23}Na MAS NMR spectra have been detected for a variety of coals from both northern and southern hemispheres in the raw as well as the dried state. The differences in the chemical shifts between the raw and the dried coals show the Na^+ to be surface-bound, e.g. to carboxylate groups in the case of brown coals, and hydrated in the raw state. As shown in Fig. 10, ^{27}Al MAS NMR spectra give information about the mineral content, especially

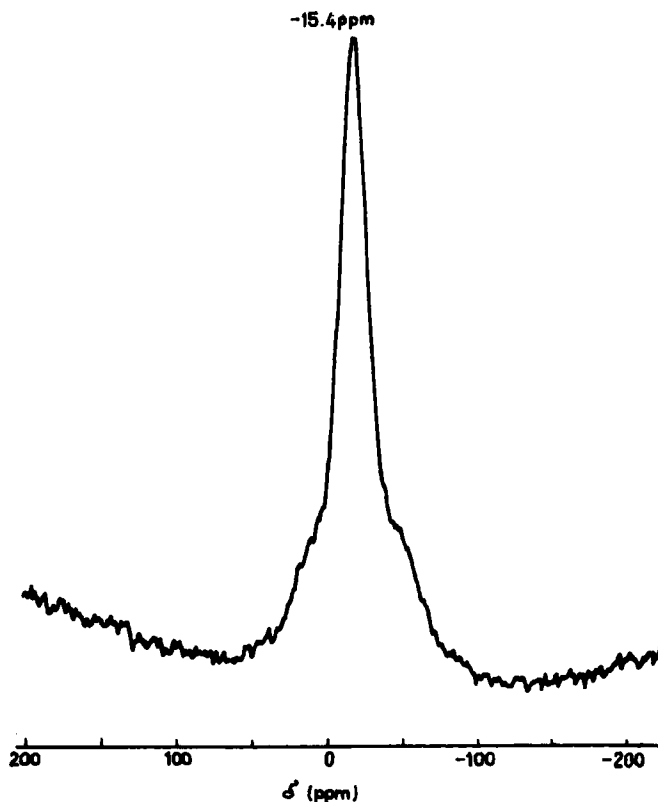


Fig. 9. ^{23}Na MAS NMR spectrum of (dried) Australian brown coal. Chemical shift, δ (ppm), referenced to $\text{Na}_{\text{aq}}^+ = 0$, at infinite dilution. (From Ref. 59; O.W. Howarth, G.S. Ratcliffe and P. Burchill, *Fuel*, 1987, **66**, 34, by permission of the publishers, Butterworth & Co. (Publishers) Ltd ©.)

aluminosilicates, in coals. In the spectrum of Taff Merthyr coal from the United Kingdom a clear distinction exists between tetrahedral (73 ppm) and octahedral (4 ppm) coordinated aluminium, respectively.⁵⁹

^{27}Al as well as ^{29}Si NMR investigations were carried out on clays and layer silicates in coals and heavy oils.^{60,61} An interesting field of research consists of the study of interactions between the insoluble organic matter and the inorganic clays, silica and layer silicates.^{62,63}

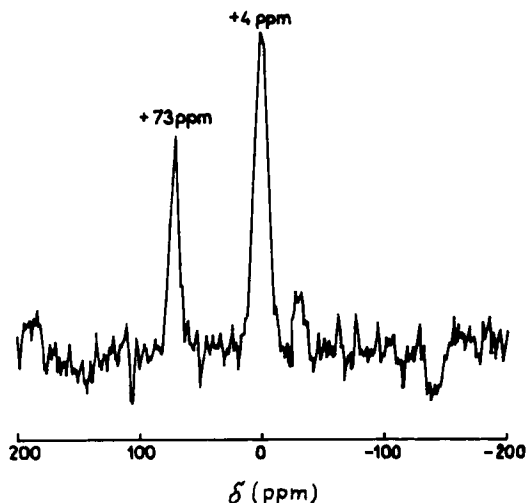


Fig. 10. ^{17}Al MAS NMR spectrum of (raw) Taff Merthyr coal. Chemical shift, δ (ppm), reference to $\text{Al}(\text{H}_2\text{O})_6^{3+} = 0$, at infinite dilution. (From Ref. 59: O.W. Howarth, G.S. Ratcliffe and P. Burchill, *Fuel*, 1987, **66**, 34, by permission of the publishers, Butterworth & Co. (Publishers) Ltd ©.)

3. INTERACTIONS BETWEEN SOLVENT MOLECULES AND COAL SURFACES

This section deals with weak interactions such as sorption and hydrogen bonding between coal surface and molecules, as opposed to strong interactions in which covalent bonds are broken.²¹ Physical and chemical investigation methods play an important role for coal characterization and optimized operating conditions for conversion processes.⁶⁴

A large variety of technical processes for coal conversion, e.g. coal liquefaction,⁶⁵ is based on interactions between solvent molecules and the coal framework. Irrespective of this great practical relevance there is as yet little known about the elementary steps of mass transfer during the process of solvation. The concept of the mobile phase in coals^{66,67} and the proposal of the "host-guest" molecular structure of coal,⁶⁸ in which smaller constituents (< 1000 Da) are embedded in a matrix formed by a three-dimensional macromolecular network, has been supported by ^1H NMR measurements. It is possible to distinguish between mobile and immobile species.⁶⁹ However, also on the basis of such experiments a quantitative determination of the translational mobilities is impossible. Also other conventional techniques, like swelling processes or experiments carried out by introducing

Table 1. Chemical composition of lignite (westelbian, district Leipzig).

Elemental analysis (mass-%, daf ^a)					Aromaticity (f_a)	Mixture (mass-%)		Ash (mass-%)
C	H	N	O	S				
71.5	6.0	1.4	15.2	5.9	0.49 ^b	50.2 ^c	9.7 ^d	13.7 ^e

^aDried ash free.^b¹³C CP-MAS TOSS NMR.^cUntreated coal, determined by microwave damping.^dDried at room temperature, determined by microwave damping.^eDried at room temperature.

labelled molecules ("tracers") give only a few hints of molecular mobility, especially for systems in equilibrium. In a much easier way such experiments may be carried out by NMR field gradient spectroscopy. In the following, some results of a systematic NMR study of diffusion processes in westelbian brown coal are presented.⁷⁰ Table 1 lists the chemical composition of the lignite under study (this composition is representative for many brown coals in westelbian deposits). Applying ¹H NMR, only the diffusivities of the hydrogen-containing species are measured. Therefore, deuterated solvents were used to select the different constituents of the sample. Figure 11 indicates self-diffusion coefficients of water and mobile coal constituents for different imbibed solvents (Fig. 11(a) and (c), respectively), and of different solvent molecules in dependence on the water content of the coal (Fig. 11(b)). It has been found that for sufficiently large concentrations of the solvent and/or residual water (≥ 20 mass-%) the mobility of these three components increases with both increasing humidity and solvent concentration. The transverse relaxation time of residual water (less than 5 mass-% after degassing of coal in vacuum) was too short to yield an observable spin echo for pulsed field gradient measurements, with values for the observation time Δ (cf. Meiler and Meusinger,¹ Figure 12) larger than 2 ms. This is an obvious consequence of the fact that this residual water is very rigidly attached to the coal framework. However, with introducing additional water molecules or solvent molecules, the water mobility increases and leads to an observable spin echo. In order to guarantee that the observed spin echo is in fact due to the water molecules, they must be the only proton-containing mobile species present.

To measure the self-diffusion coefficients of solvents, it is necessary to introduce them in the hydrogen-containing form and water in the deuterated form. Considering the used solvent molecules, one observes the following trend in their mobilities $D_{\text{THF}} \lesssim D_{\text{benzene}} \lesssim D_{\text{methanol}} < D_{n\text{-hexane}}$. This dependence is much more pronounced than one would expect on the basis of the

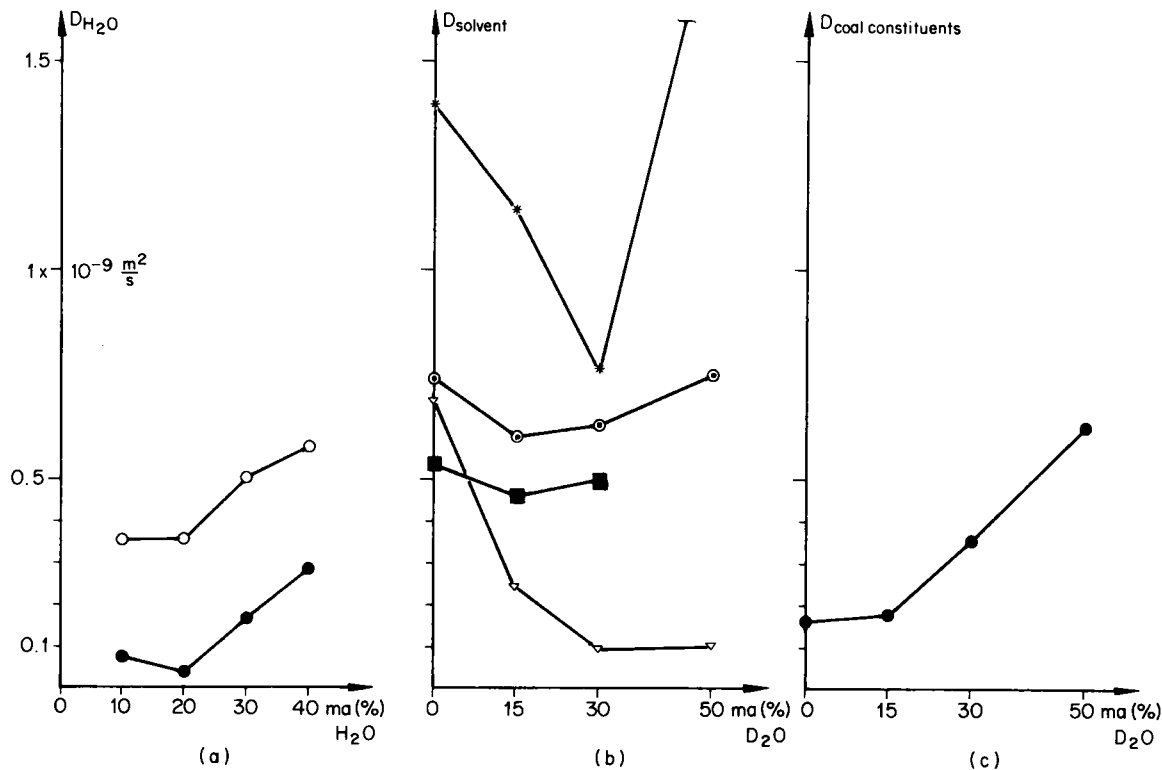


Fig. 11. ^1H NMR self-diffusion measurements in brown coal (westelbian) in dependence on the water concentration in presence of 50 mass-% of solvents: ○ benzene C_6D_6 , ■ benzene C_6H_6 , ● chloroform CDCl_3 , * *n*-hexane, ⊙ methanol CH_3OD , ▽ tetrahydrofuran. Resonance frequency 60 MHz, pulsed magnetic field gradients up to 20 Tm^{-1} . (a) Self-diffusion coefficients of water; (b) different solvent molecules; (c) coal constituents.

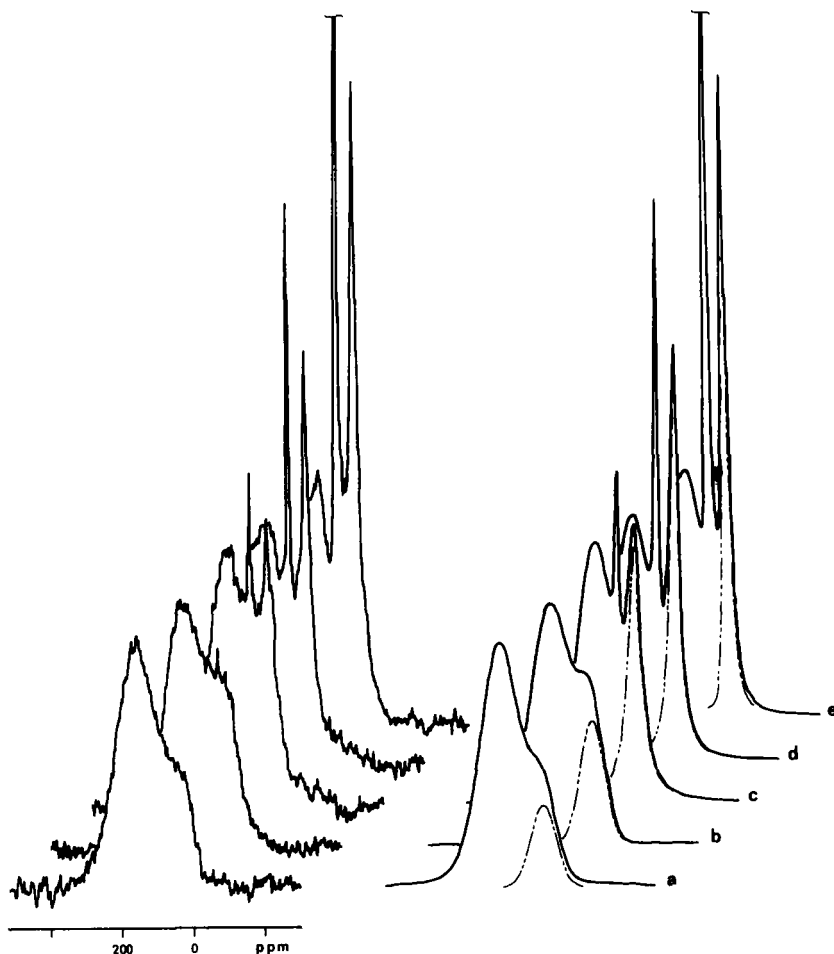


Fig. 12. ^{13}C SP NMR spectra of dried brown coal Delitzsch (westelbian) in interaction with chloroform. Resonance frequency 75.48 MHz, 1000 scans, repetition time 5 s, the line at 77 ppm corresponds to the ^{13}C NMR line of chloroform. (a) Pure lignite; (b) 25 μl ; (c) 75 μl ; (d) 150 μl ; (e) 400 μl chloroform were added to 1 g lignite in each case. Left: experimental spectra; right: spectra after computer-aided line decomposition procedure, the dashed line shows the increasing intensity of the aliphatic line and decreasing of linewidth.

slight differences between the diffusivities in the neat solvents: $2.21 \times 10^{-9} \text{ m}^2/\text{s}$, $2.25 \times 10^{-9} \text{ m}^2/\text{s}$, $2.84 \times 10^{-9} \text{ m}^2/\text{s}$, and $4.32 \times 10^{-9} \text{ m}^2/\text{s}$ for benzene, methanol (CH_3OD), tetrahydrofuran and *n*-hexane, respectively. Moreover, with respect to tetrahydrofuran the sequence in the mobilities is

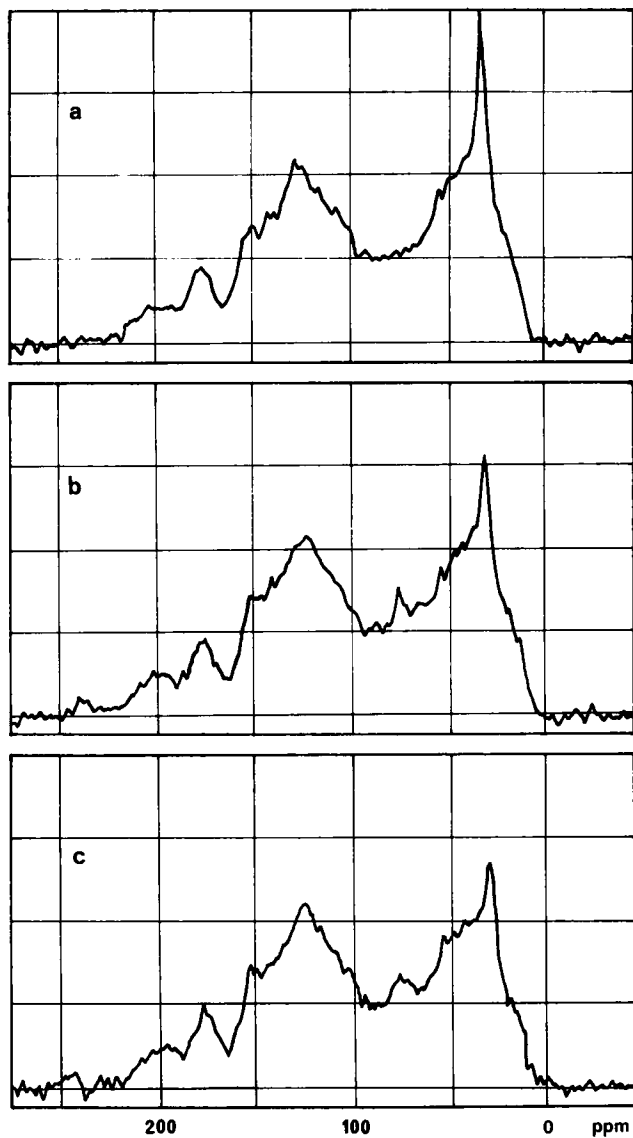


Fig. 13. ^{13}C CP MAS TOSS NMR spectra of dried brown coal Delitzsch (westelbian) in interaction with chloroform. Resonance frequency 75.48 MHz, MAS frequency 2.9 kHz, CP mixing time 1.5 ms, repetition time 1 s. (a) Pure lignite; (b) 75 μl ; (c) 150 μl chloroform were added to 1 g lignite in each case.

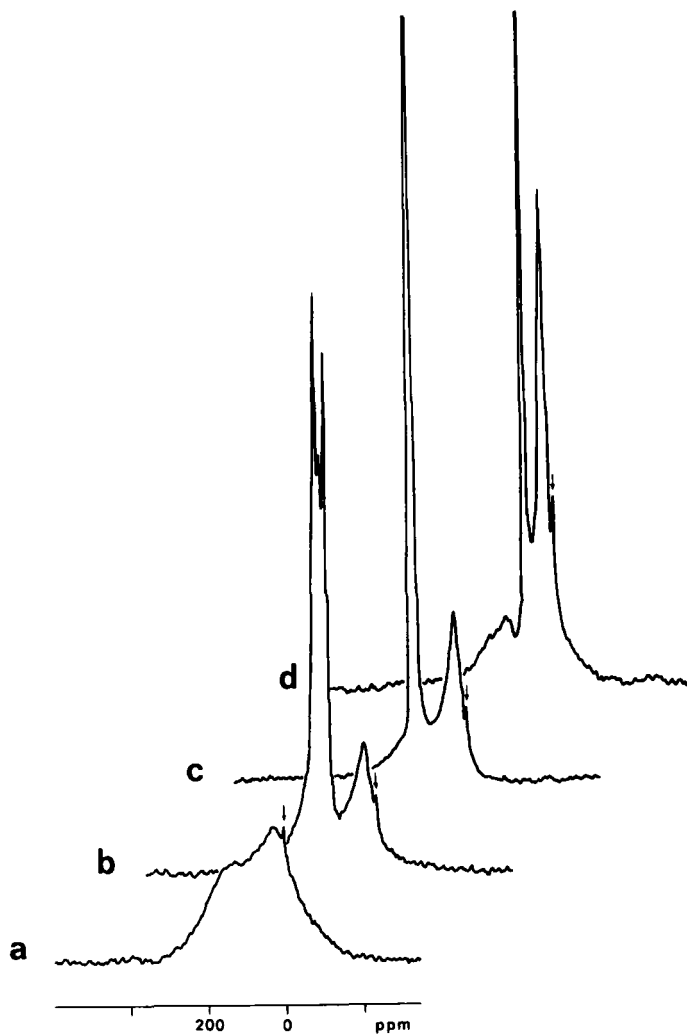


Fig. 14. ^{13}C SP NMR spectra of dried brown coal Espenhain (westelbian) in interaction with solvents. Resonance frequency 75.48 MHz, repetition time 5 s, the arrow denotes the intensity standard polydimethylsiloxane (PDMS). (a) Pure lignite; (b) 300 μl pyridine; (c) 300 μl benzene; (d) 600 μl chloroform were added to 600 mg lignite in each case.

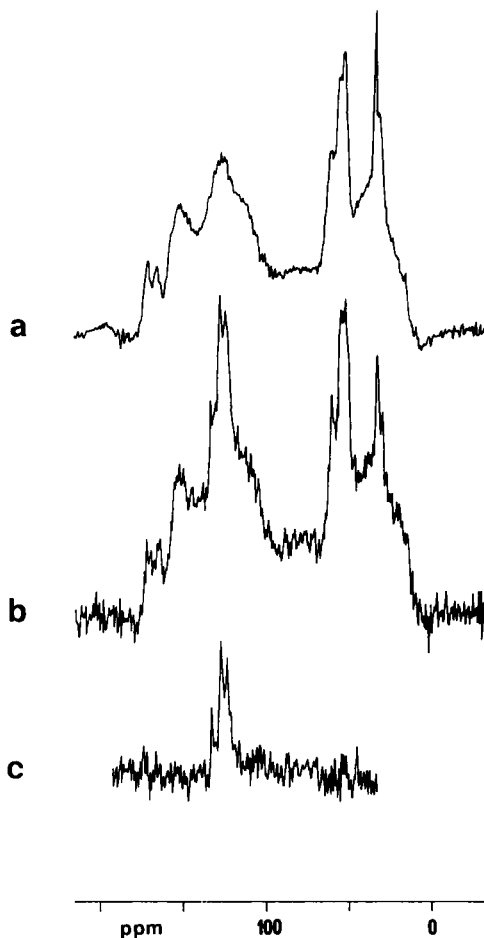


Fig. 15. ^{13}C CP MAS TOSS NMR spectra of methylated lithotype Schleenhain (brown, westelbian) in interaction with imbibed naphthalene molecules. Resonance frequency 75.48 MHz, CP mixing time 2 ms. (a) Methylated lithotype Schleenhain (brown); (b) in vacuum careful dried coal loaded with naphthalene molecules (mass of coal/mass of naphthalene = 1); (c) difference spectrum (b)–(a), the spectrum shows clearly the three ^{13}C NMR lines of naphthalene between 125 and 133 ppm.

even changed. It is concluded that the mobility of the solvent molecules is predominantly controlled by their interaction with the coal network, which is evidently increasing from *n*-hexane to tetrahydrofuran.

Applying a non-hydrogen-containing solvent and deuterated water, the analysis of the observed spin echo did allow the determination of the mobility

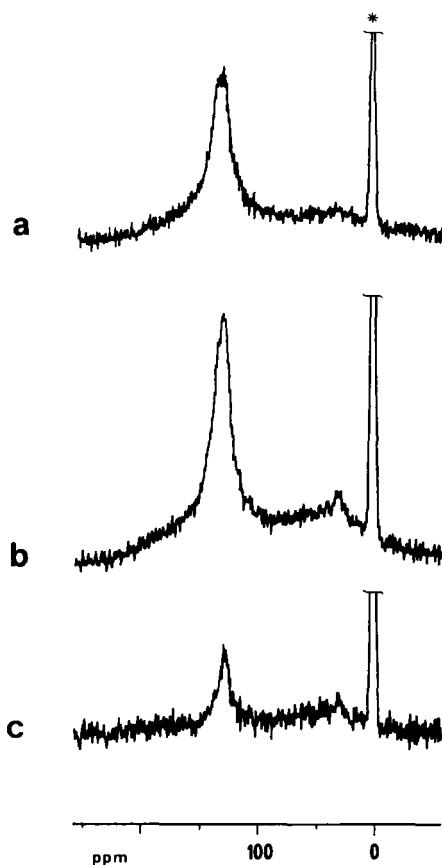


Fig. 16. ^{13}C NMR spectra of methylated lithotype Schleenhain (brown, westelbian) in interaction with imbibed naphthalene molecules. Resonance frequency 75.48 MHz, repetition time 10 s, number of scans 2000, * denotes the intensity standard polydimethylsiloxane (PDMS). (a) Single-pulse (SP), without decoupling; (b) GATED decoupled spectrum of the same sample as in (a); (c) difference spectrum (b)–(a).

of the coal constituents. It is remarkable that the mobility of the coal constituents dissolved in the solvent is significantly enhanced with increasing water content.

In accordance with these self-diffusion measurements ^{13}C SP NMR spectra of mixtures of coal with solvents demonstrate the enhanced mobility of coal constituents caused by the swelling process. Such systems contain considerable amounts of mobile and liquid species. Therefore, in most cases the application of the routine ^{13}C CP-MAS NMR technique fails.⁷¹ ^{13}C SP NMR

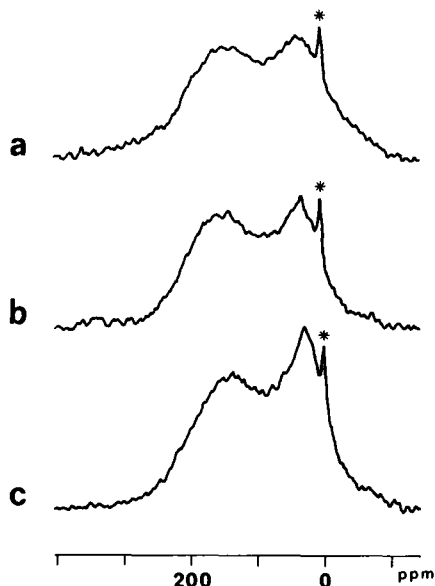


Fig. 17. ^{13}C SP NMR spectra of thermal pretreated brown coal Espenhain (westelbian). Resonance frequency 75.48 MHz, * denotes the intensity standard polydimethylsiloxane (PDMS), repetition time 5 s. (a) Dried at room temperature up to the value of constancy of mass; (b) 1 h dried at 100°C; (c) 1 h dried at 220°C.

investigations prove to be a powerful tool for the study of species with molecular mobilities between the limiting cases of rigid solids and non-viscous liquids. The method works in a direct and non-destructive manner. Modifications within the coal framework can be detected directly in the ^{13}C NMR spectrum of the recorded portion of the sample. This spectrum should originate from carbons with weak dipole interaction: carbons which are not directly bound to protons, methyl groups and mobile species.

Figure 12 shows the interaction of dried brown coal with chloroform. The ^{13}C NMR line of chloroform at 77 ppm can be distinguished clearly from the aromatic as well as the aliphatic regions of the coal spectrum. In this way with the enhancement of the chloroform concentration, the increase of the intensity and the decrease of the aliphatic linewidth can be observed simultaneously (dashed lines). These effects may be caused by a progressive amount of mobile aliphatic carbon atoms in coal.

The existence of the samples containing only a small amount of chloroform allow one to measure these samples by ^{13}C CP-MAS NMR.⁷² The results are given in Fig. 13. In contrast to Fig. 12 the ^{13}C CP-MAS TOSS NMR spectra indicate a decrease of the aliphatic signal intensity. Obviously, this is due to the prolongation of the cross-relaxation time T_{CH} caused by the enhanced

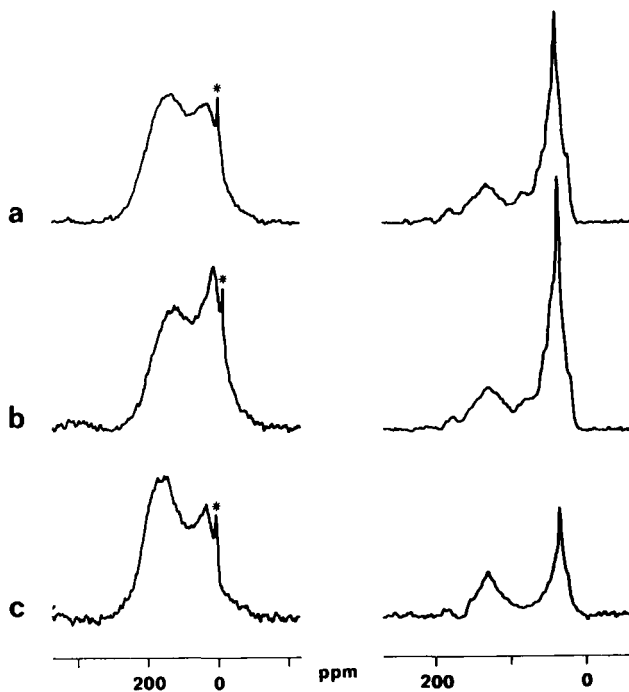


Fig. 18. ^{13}C SP (left) and ^{13}C CP MAS TOSS (right) NMR spectra of thermal pretreated brown coal Espenhain (westelbian). Resonance frequency 75.48 MHz, * denotes the intensity standard polydimethylsiloxane (PDMS), SP repetition time 5 s, CP mixing time 1 ms, number of scans in CP experiments 1200. (a) Dried at room temperature, $f_a(\text{CP}) = 0.34$; (b) 1 h dried at 220°C , $f_a(\text{CP}) = 0.35$; (c) 1 h dried at 350°C , $f_a(\text{CP}) = 0.61$.

mobility of the corresponding species. In summary, the experiments demonstrate the reduction of the observed carbon of the coal structure in ^{13}C CP-MAS NMR experiments. This is contrary to the ^{13}C SP NMR investigations in which the amount of observed coal constituents increases if the coal matter interacts with solvent molecules.

Figure 14 depicts the ^{13}C SP NMR spectra of a brown coal rich in bitumen with different imbibed solvents: pyridine, benzene and chloroform, respectively. It appears from Fig. 14 that the solvent molecules have a considerable influence upon the coal spectra, especially of the aliphatic region. In the case of chloroform slight changes in the aromatic part of the coal spectrum can be observed also. For a quantitative determination of coal components such samples contain a known weight of polydimethylsiloxane (PDMS, cf. Fig. 14). It is well known that pyridine interacts strongly with coal and causes swelling and partial dissolution. When pyridine is sorbed onto coal it can be

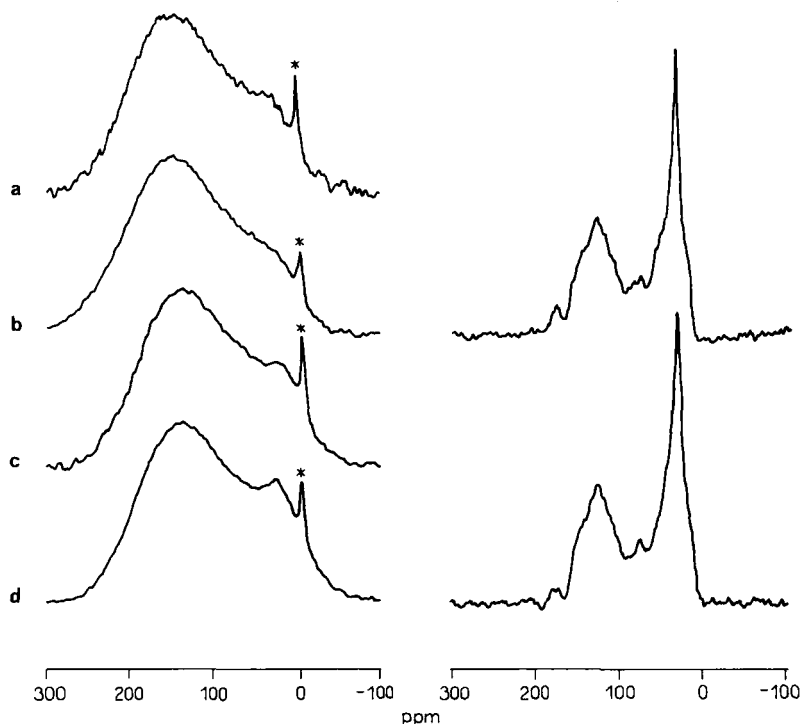


Fig. 19. ^{13}C SP (left) and ^{13}C CP MAS TOSS (right) NMR spectra of thermal pretreated brown coal Delitzsch (westelbian). Resonance frequency 75.48 MHz, * denotes the intensity standard polydimethylsiloxane (PDMS), SP repetition time 5 s, CP mixing time 1 ms. (a) Raw brown coal, water content 50.2 mass-%; (b) dried at room temperature, water content 9.7 mass-%; (c) 1 h dried at 100°C, water content 8.6 mass-%; (d) 1 h dried at 220°C, water content 5.5 mass-%.

observed using ^{13}C CP NMR.^{21,73} By the use of MAS experiments it can be demonstrated that aliphatic groups in coal become conformationally less rigid and this allows additional resolution.⁷³ Using a special difference technique, only the mobile “liquid-like” spins in a pyridine-soaked coal can be measured. In the coal under study it can be seen that there are sharp resonance lines from free pyridine molecules, and a broad aromatic line from those structures which have been freed from the solid matrix by the swelling action of pyridine.²¹

The interaction between ^{15}N -enriched pyridine molecules and both fresh and oxidized bituminous coal was studied by means of ^{15}N CP-MAS NMR.⁷⁴ In fresh bituminous coal, pyridine interacts only weakly through physical adsorption. Also, hydrogen-bonded complex formations are possible. But in

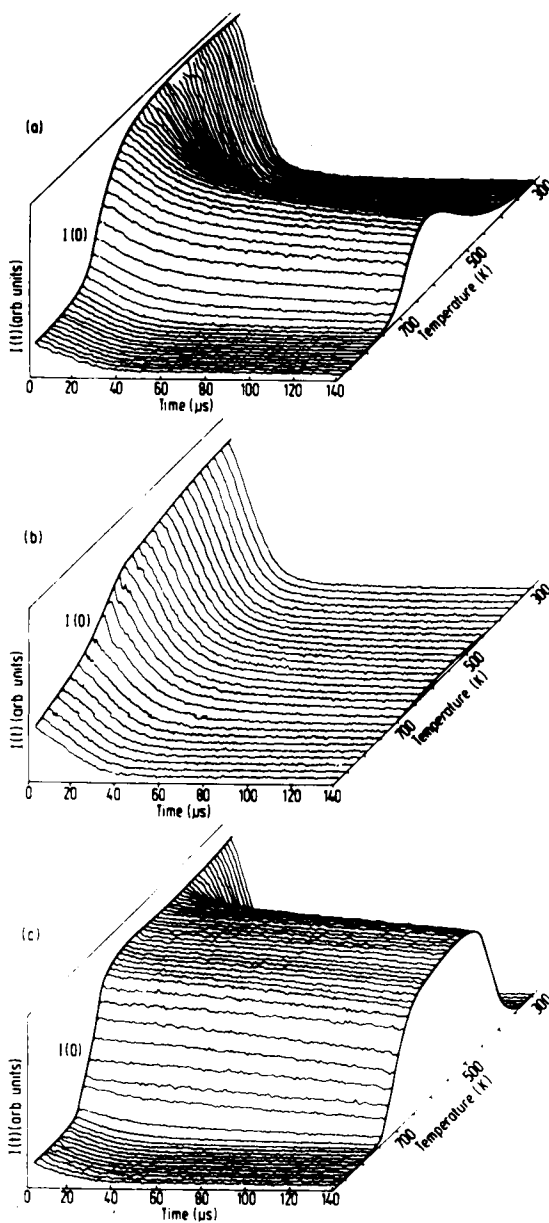


Fig. 20. Stacked plots of signals obtained from ^1H NMR thermal analysis of: (a) a Bacchus Marsh brown coal; (b) the residue after treatment at 593 K with decalin, followed by room temperature extraction with dichloromethane;⁹⁵ (c) the dichloromethane-soluble, pentane-insoluble fraction of the 593 K extract. The signals have been interpolated to 10 K intervals. (From Ref. 78: L.J. Lynch, R. Sakurovs, D.S. Webster and P.J. Redlich, *Fuel*, 1988, **67**, 1036, by permission of the publishers, Butterworth & Co. (Publishers) Ltd ©.)

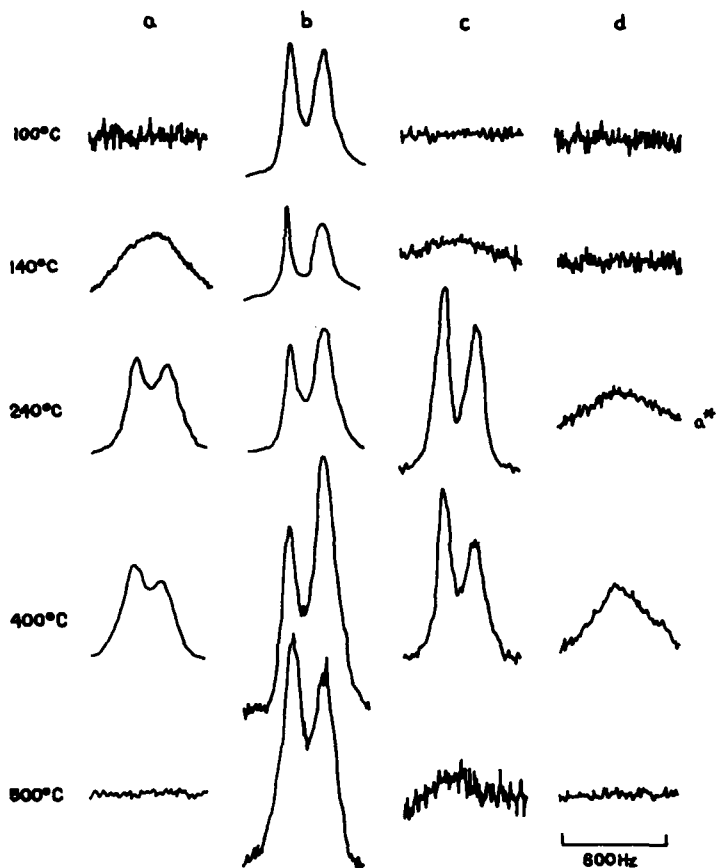


Fig. 21. Temperature dependence of ^1H NMR spectra for original pitch A and its corresponding fractions: (a) original pitch A; (b) BS-HS fraction; (c) BS-HI fraction; (d) BI-PS fraction (a*, 315°C). (From Ref. 84: H. de Lopez, T. Yokono, N. Takahashi and Y. Sanada, *Fuel*, 1988, **67**, 301, by permission of the publishers, Butterworth & Co. (Publishers) Ltd ©.)

oxidized bituminous coal and fresh sub-bituminous coal the presence of both pyridinium ions and physically sorbed pyridine was observed. The occurrence of proton transfer to pyridine suggests that strongly acidic functionalities are generated during the process of coal oxidation.⁷⁴

A combined ^{13}C CP-MAS, ^1H CRAMPS and ^1H liquid state NMR study of the pyridine and tetrahydrofuran extraction of coal should be mentioned.⁷⁵

Naphthalene molecules adsorbed on a carefully vacuum-dried brown coal (mass ratio coal:naphthalene = 1:1) were studied as a model system for the

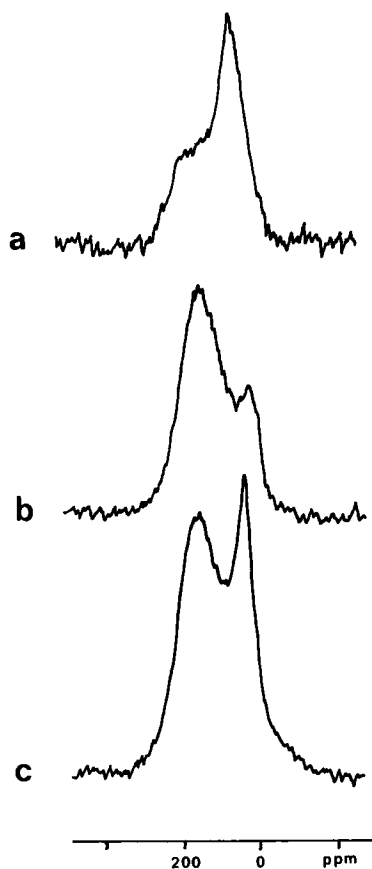


Fig. 22. ^{13}C SP NMR spectra after thermal pretreatment of coal in presence of *n*-hexane molecules. (a) Brown coal Schleenhain (westelbian), 1 g; (b) coal as in (a), thermal pretreatment (12 h) at 320°C ; (c) coal as in (a), 1 ml *n*-hexane added, thermal pretreatment (12 h) at 320°C .

two-component structure of coal.^{71,76} The coal used was a methylated lithotype from Schleenhain. The preparation procedure for the samples was the following: degassing at room temperature, 48 h at 95°C , sorption of naphthalene molecules by breaking off a glass ampoule, melting of the ampoule, tempering the samples 48 h at 95°C (the melting point of naphthalene is 81°C). It should be noted that solid naphthalene cannot be measured both with ^{13}C SP NMR and CP (T_1 of protons about 1000 s). The results are shown in Figs. 15 and 16. It appears from Fig. 15 that the three ^{13}C NMR lines of naphthalene are superimposed on the well-resolved ^{13}C

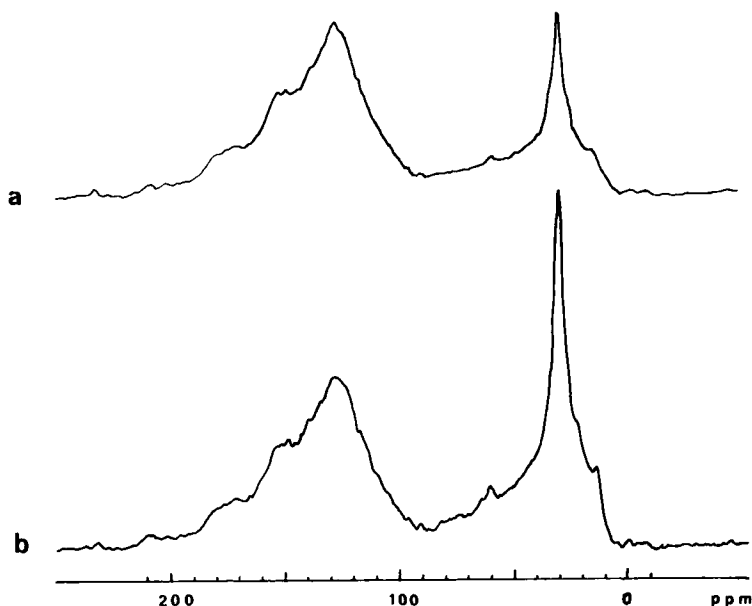


Fig. 23. ^{13}C CP MAS TOSS NMR spectra after thermal pretreatment of brown coal Schleenhain (westelbian). Resonance frequency 75.48 MHz, CP mixing time 1.5 ms, MAS frequency 3.2 kHz. (a) Thermal pretreatment (12 h) at 320°C; (b) thermal pretreatment (12 h) at 320°C in presence of *n*-hexane.

CP-MAS TOSS NMR spectra of the methylated coal. The difference between the spectra (a) and (b) leads to a value of 5–10% of the whole signal of the loaded coal which can be ascribed to the naphthalene molecules. From ^{13}C SP NMR experiments including GATED decoupling follows (cf. Fig. 16) a nuclear Overhauser factor of 1.4 for the adsorbed naphthalene molecules (about 25% of the naphthalene molecules were observed by the SP experiment).

Thus it is concluded that in fact a non-negligible amount of highly mobile species are present in the coal structure; this amount is underestimated in the CP-MAS experiment.^{71,76}

4. THERMAL PROCESSES

Thermal pretreatment processes take place in thermal-mechanical upgrading of coal and are necessary for coal refinement processes. The drying of coal represents a process of a complicated nature. This results from some of the following facts. Water exists in coal in different mobile and adsorbed states,

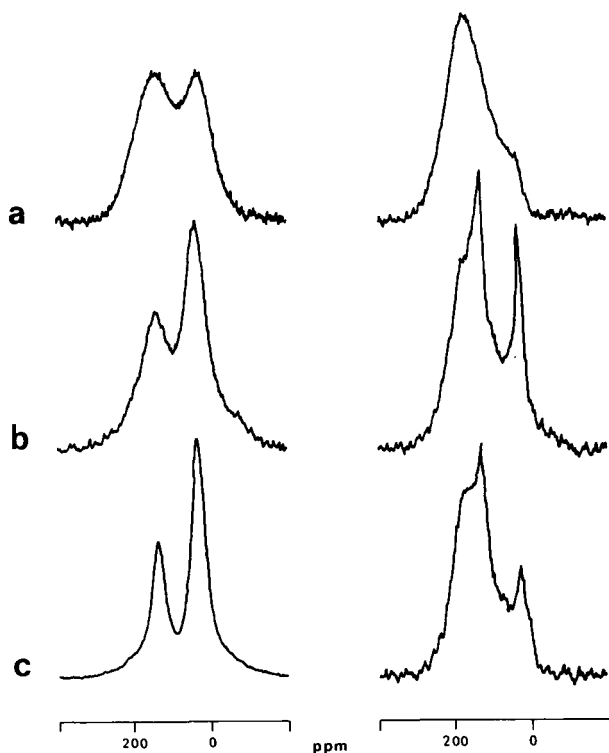


Fig. 24. ^{13}C SP NMR spectra of dry liquefaction of brown coals Espenhain (westelbian, left) and Peres (westelbian, right). Resonance frequency 75.48 MHz, repetition time 5 s. (a) Dried at room temperature; (b) liquefaction products after 0 min liquefaction time (the experiment was finished at the temperature of liquefaction); (c) liquefaction products after 30 min liquefaction time.

several interactions occur between water and both the organic skeleton and the pore system. Different methods of removal of water, often in combination with swelling procedures using organic solvents and oils, affect the behaviour of drying of coal and coal-oil mixtures. Thermal pretreatment of coal samples leads to changes in the composition of coals. During recent years considerable progress has been made in the characterization of thermal processes, the resulting products and residues by means of NMR methods.⁷⁷⁻⁹⁵

The examples in this section are concerned with NMR investigations of coals, coal-tar pitch, pyrolysis products and coal solvent mixtures in thermal processes.

It appears from Figs. 17, 18 and 19 that changes in the coal structure due

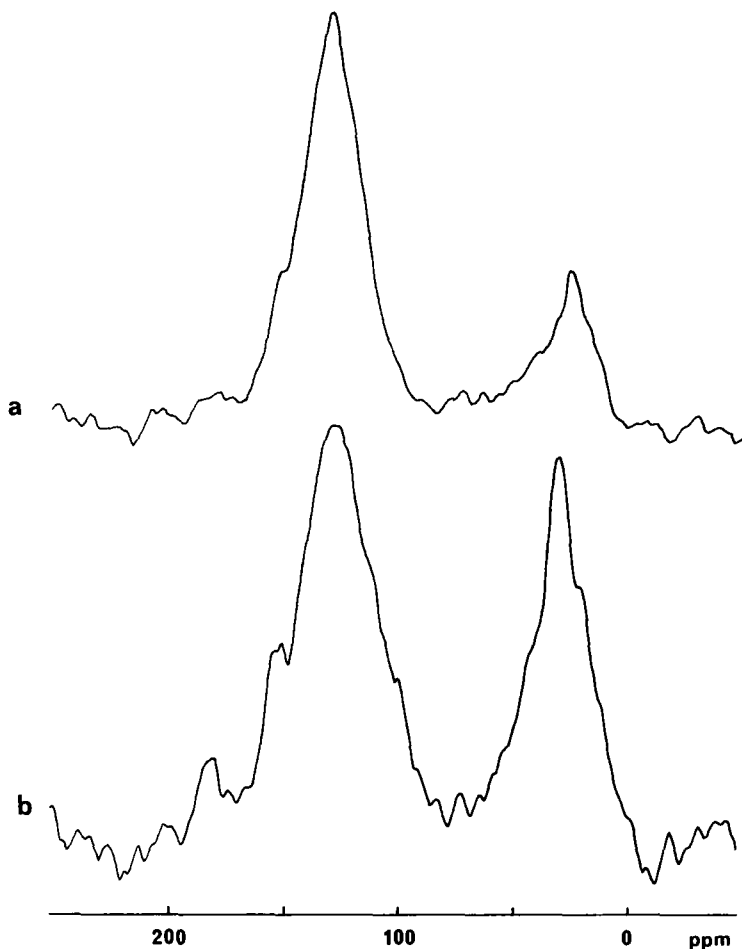


Fig. 25. ^{13}C CP MAS TOSS NMR spectra of residues from hydrolification of thermal pretreated brown coal Espenhain (westelbian). Resonance frequency 75.48 MHz, CP mixing time 1.5 ms. (a) Residue of thermal pretreated coal (75°C), $f_a = 0.81$; (b) residue of thermal pretreated coal (100°C), $f_a = 0.69$.

to thermal processes can be obtained in ^{13}C NMR spectra. Figures 17 and 19 show ^{13}C SP NMR spectra of dried brown coals. It can be seen that the aliphatic linewidth increases up to drying temperatures of 220°C if the water content decreases. If chemical reactions do not occur in this temperature region, the effect could arise from the enhancement of mobility of aliphatic groups, especially $-\text{CH}_2-$. A line deconvolution shows a decreased linewidth too. This effect of an enhanced mobility of coal constituents if the

water content reaches a limit cannot be observed by other methods (e.g. IR spectroscopy). Also, ^{13}C CP-MAS TOSS NMR spectra give no hints of this process as can be seen in Fig. 18(a) and (b). If the temperature is higher than 250°C , distinct modifications can be observed in the ^{13}C SP as well as in the ^{13}C CP NMR spectra. The aromaticity of the coal increases if volatile matter and aliphatic structures are removed. This observation is supported by thermogravimetric experiments.

With respect to the host/guest model of brown coals one can find interesting ^1H NMR investigations.⁷⁷⁻⁸¹ The proposal that low-rank coals like brown coals consist of a two-component molecular structure (host/guest) has been investigated by *in situ* ^1H NMR measurements of a suite of Australian and New Zealand brown coals, Morwell brown coal lithotypes, and extracts and extract residues of some of these coals.⁷⁸ Figure 20 illustrates stacked plots of signals obtained from *in situ* ^1H NMR thermal analysis during heating up to 600°C .⁷⁸ The transverse relaxation signal taken as the peak of the solid echo is shown for a brown coal, its residue (host) after treatment at 320°C with decalin and the dichloromethane-soluble pentane-insoluble fraction of the 320°C extract (guest). After an analysis such data provide parameters for a quantitative description of the composition and molecular dynamics of the specimens during heating. The initial intensity $I(0)$ of the transverse relaxation signal gives an estimate of the residual hydrogen content of the specimens. The signals can be resolved (cf. Meiler and Meusinger¹) in a slowly relaxing exponential component fitted at longer times (the "mobile" component), and a rapidly relaxing Gaussian-like residual signal (the "rigid" component). The interpretation of the ^1H NMR signals inclusive of determined second moments of each recorded NMR signal $I(t)$ leads to the following statements concerning the example in Fig. 20. The whole coal specimen passes through a well-defined maximum of 60% mobile structure near 600 K. The extract is fully mobilized on heating above 460 K and the residue reaches a maximum of 15% mobile structure components near 600 K.⁷⁸

Coal-tar and petroleum pitches and their solvent fractions were studied by high-temperature ^1H NMR.⁸⁴ The corresponding ^1H NMR spectra for a hydrogenated coal-tar pitch, its benzene-soluble hexane-soluble (BS-HS), benzene-soluble hexane-insoluble (BS-HI) and benzene-insoluble pyridine-soluble (BI-PS) fractions are given in Fig. 21. It should be mentioned that no signal was found for the original pitch at room temperature. As the heat treatment temperature is increased, a broad peak appears at 140°C . This temperature corresponds to the softening point of the pitch. At 240°C , a doublet due to the aromatic and aliphatic protons became visible. Then a broadening of the signal indicates the decreasing mobility of the molecules within the system above 400°C . At 500°C the temperature corresponds to the

solidification temperature of this pitch and the ^1H NMR signal disappears. The discussion of the spectra concerning the fractions is similar.

Further interesting ^1H NMR results concerning thermal processes can be found in the literature.⁸⁵⁻⁸⁸

Of special interest proves to be the behaviour of coals in interaction with solvents in thermal processes. ^{13}C NMR spectra of such systems and residues are presented in Figs. 22-25. Figures 22 and 23 show the ^{13}C SP NMR and the ^{13}C CP-MAS TOSS NMR spectra of the system coal/*n*-hexane. The thermal treatment of the coal leads to the decreasing of aliphatic intensity in the spectra. If the thermal treatment was carried out in the presence of *n*-hexane and assuming that the introduced *n*-hexane molecules after 12 h at 320°C are removed from the sample both in the ^{13}C SP NMR and the ^{13}C CP-MAS NMR spectra, a higher amount of aliphatic structures than in the initial coal is observed.

Figure 24 shows ^{13}C SP NMR spectra of liquefaction experiments on two brown coals which differ in aromaticity. The coal from deposit Espenhain (Fig. 24 left) is characterized by a high content of aliphatic structures. The hydrogenation was carried out without solvents or oil at higher temperatures in a hydrogen atmosphere. The spectra show the increased mobility of the products and the changes in the intensities due to the chemical reactions. It should be mentioned that in the case of the coal possessing the higher aromaticity (Fig. 24 right) the relative portion of observed aliphatics decreases with longer liquefaction times. Residues from hydrol liquefaction of brown coals are seen in Fig. 25. The ^{13}C NMR spectra indicate the residual organic content of the coal matter after liquefaction. As shown in Fig. 25, strong differences in the ^{13}C CP-MAS TOSS NMR spectra of residues were obtained after liquefaction of coals, depending on the thermal pretreatment of the hydrogenated coals. The spectra correspond to the larger amount of coal-derived oil in the case of the 75°C pretreated coal. But it should be mentioned that in many cases the ^{13}C CP NMR measurement of residues fails due to the small amount of hydrogen, relaxation mechanisms and electric conductivity of graphite structures, respectively.

Examples of ^{13}C NMR studies in thermal processes including residues can be found in many current papers.⁸⁹⁻⁹⁵

ACKNOWLEDGEMENTS

The authors wish to express gratitude to Professor Dr Dr h. c. H. Pfeifer, Professor Dr D. Michel and Professor Dr H. Siegel for permanent interest and many stimulating discussions on the subject of this work. We acknowledge the cooperation and considerable help of the people who made the

article "NMR of Coals and Coal Products" in Vol. 23 of *Annual Reports* and this article possible. We are especially grateful to Mrs K. Bienert, F. Birke, W. Böhlmann, Dr F. Engelke, Dr H. Ernst, Doz. Dr D. Fenzke, Dr A. Germanus, R. Graebert, Dr W.-D. Hoffmann, Professor Dr J. Kärger, Dr H. Metz, L. Moschkowitz, Dr U. Müller, Dr H.-E. Müller, T. Schaller, Dr D. Schulze, Dr B. Staudte, Dr J. Witt and to the members of Professor Pfeifer's experimental physics group for preparation and service of NMR facilities. We acknowledge with sincere thanks the permission granted by the authors and Butterworths Publishers for allowing us to reproduce some of the figures that appear in the text. It is a pleasure to thank Mrs U. Krause for her expert technical assistance throughout this work.

REFERENCES

1. W. Meiler and R. Meusinger, in *Annual Reports on NMR Spectroscopy*, Vol. 23 (ed. G.A. Webb), pp. 375-410. Academic Press, London, 1991.
2. D.W. van Krevelen, *Coal*. Elsevier, Amsterdam, 1961.
3. A. Volborth (ed.), *Coal Science and Chemistry*. Elsevier, Amsterdam, 1987.
4. R.A. Meyers (ed.), *Coal Structure*. Academic Press, New York, 1982.
5. N. Berkowitz, *The Chemistry of Coal*. Elsevier, Amsterdam, 1985.
6. L. Petrakis and J.P. Fraissard (eds), *Magnetic Resonance—Introduction, Advanced Topics and Applications to Fossil Energy*, Reidel, Dordrecht, 1984.
7. P.H. Given, A. Marzec, W.A. Barton, L.J. Lynch and B.C. Gerstein, *Fuel*, 1986, **65**, 155.
8. C.E. Snape, D.E. Axelson, R.E. Botto, J.-J. Delpuech, P. Tekely, B.C. Gerstein, M. Pruski, G.E. Maciel and M.A. Wilson, *Fuel*, 1989, **68**, 547.
9. F. Derbyshire, A. Marzec, H.-R. Schulten, M.A. Wilson, A. Davis, P. Tekely, J.-J. Delpuech, A. Jurkiewicz, C.E. Bronnimann, R.A. Wind, G.E. Maciel, R. Narayan, K. Bartle and C. Snape, *Fuel*, 1989, **68**, 1091.
10. L. Petrakis and D. Allen, *NMR for Liquid Fossil Fuels*. Elsevier, Amsterdam, 1987.
11. L. Petrakis, D.T. Allen, G.R. Gavalas and B.C. Gates, *Anal. Chem.*, 1983, **54**, 1557.
12. E. Künstner, K.-H. Rentrop, H. Rosenberger, G. Scheler and H. Schmiere, Konstitutionsaufklärung von Kohlen und verwandten Produkten, Erkenntnisstand und Fortschritte durch die hochauflösende Festkörper-NMR-Spektroskopie, Freiburger Forschungshefte, A 742, Dt. Verlag f. Grundstoff-industrie, Leipzig, 1985.
13. H. Rosenberger, G. Scheler and E. Künstner, *Fuel*, 1988, **67**, 508.
14. H.L. Retcofsky and T.A. Link, in *Analytical Methods for Coal and Coal Products*, Vol. II (ed. C. Karr), p. 161. Academic Press, New York, 1978.
15. F. Birke, diploma work, Leipzig, 1985.
16. P.J. Redlich, W.R. Jackson, F.P. Larkins, A.L. Chaffee, A.A. Krichko, E.A. Grigoryeva and S.N. Shatov, *Energy & Fuels*, 1990, **4**, 28.
17. A.H. Fawcett, J. Grimshaw, J. Trocha-Grimshaw, F. Donnelly and B.J. Say, *Fuel*, 1990, **69**, 415.
18. M.A. Wilson, A.M. Vassallo, P.J. Collin and H. Rottendorf, *Anal. Chem.*, 1984, **56**, 433.
19. E.W. Hagaman, R.R. Chambers and M.C. Woody, *Anal. Chem.*, 1986, **58**, 387.
20. K.J. Packer, R.K. Harris, A.M. Kenwright and C.E. Snape, *Fuel*, 1983, **62**, 999.
21. M.A. Wilson and A.M. Vassallo, *Org. Geochem.*, 1985, **8**, 299.

22. A.D. Alekseev, H.H. Serebrowa, E.B. Uljanowa and W.J. Proschko, *Dokl. Akad. Nauk Ukr. SSR*, 1987, **3**, 3.
23. S. Derenne, C. Largeau, E. Casadevall and F. Lauprêtre, *Fuel*, 1987, **66**, 1084.
24. Y. Chaohui, R.A. Wind and G.E. Maciel, *Scientia Sinica*, 1988, **31**, 968.
25. P.I. Premović, B.V. Komatinović, R.J. Pugmire and W.R. Woolfenden, *Naturwissenschaften*, 1988, **75**, 98.
26. R. Hayatsu, R.E. Botto, R.L. McBeth, R.G. Scott and R.E. Winans, *Energy & Fuels*, 1988, **2**, 843.
27. M.S. Solum, R.J. Pugmire and D.M. Grant, *Energy & Fuels*, 1989, **3**, 187.
28. I.J. Lindberg and B. Hortling, *Adv. Polym. Sci.*, 1985, **66**, 1.
29. S.-C. Shin, R.M. Baldwin and R.L. Miller, in *Coal Characterization for Conversion Processes II, Proceedings of the Second International Rolduc Symposium on Coal Science*, Rolduc, the Netherlands, 1989 (ed. W. Prins *et al.*); *Fuel Process. Technol.*, 1990, **24**, 135.
30. G. Harrison and P. Cahill, in *Coal Characterization for Conversion Processes II, Proceedings of the Second International Rolduc Symposium on Coal Science*, Rolduc, the Netherlands, 1989 (ed. W. Prins); *Fuel Process. Technol.*, 1990, **24**, 143.
31. M.A. Wilson, R.J. Pugmire, J. Karas, L.B. Alemany, W.R. Woolfenden, D.M. Grant and P.H. Given, *Anal. Chem.*, 1984, **56**, 933.
32. N. Cyr and M.L. Selucky, *Liquid Fuels Technol.*, 1985, **3**, 377.
33. O. Ito, S. Akiho, T. Nozawa, M. Hatano and M. Jino, *Fuel*, 1989, **68**, 335.
34. R. Gerhards, I. Kasüschke, in *1987 International Conference on Coal Science* (ed. J.A. Moulijn *et al.*), p. 33. Elsevier, Amsterdam, 1987.
35. I. Kasüschke, W. Riepe and R. Gerhards, *Erdöl & Kohle-Erdgas-Petrochemie/Hydrocarbon Technol.*, 1989, **42**, 209.
36. H. Sfihi, M.F. Quinton, A. Legrand, S. Pregermain, D. Carson and P. Chiche, *Fuel*, 1986, **65**, 1006.
37. N.K. Sethi, R.J. Pugmire, J.C. Facelli and D.M. Grant, *Anal. Chem.*, 1988, **60**, 1575.
38. D.J. Cookson, C.P. Lloyd and B.E. Smith, *Fuel*, 1986, **65**, 1247.
39. B.W. Pestrakov, *Chim. Tverd. Topl.*, 1987, No. 1, 11.
40. M.A. Wilson, A.M. Vassallo, Y.L. Liu and L.S.K. Pang, *Fuel*, 1990, **69**, 931.
41. J. Witt, thesis, Leipzig, 1991.
42. R.H. Newman and S.J. Davenport, *Fuel*, 1986, **65**, 533.
43. A.G. Ferrige and J.C. Lindon, *J. Magn. Reson.*, 1978, **31**, 337.
44. R. Wind, M.J. Duijvestijn, C. Van der Lugt, J. Schmidt and H. Vriend, *Fuel*, 1987, **66**, 876.
45. R.A. Wind, J. Trommel and J. Smidt, *Fuel*, 1979, **58**, 900.
46. R.A. Wind, F.E. Anthonio, M.J. Duijvestijn, J. Smidt, J. Trommel and G.M.C. deVette, *J. Magn. Reson.*, 1983, **52**, 424.
47. R.A. Wind, M.J. Duijvestijn, C. Van der Lugt, J. Smidt and J. Vriend, in *Magnetic Resonance, Advanced Topics and Applications to Fossil Energy* (ed. L. Petrakis and J.P. Fraissard), p. 461. Reidel, Dordrecht, 1984.
48. M.I. Burgar, *Fuel*, 1984, **63**, 1621.
49. D.E. Wemmer, A. Pines and D.D. Whitehurst, *Phil. Trans. R. Soc. (Lond.) A*, 1981, **300**, 15.
50. N.K. Sethi, R.J. Pugmire, D.M. Grant, in *1987 International Conference on Coal Science* (ed. J.A. Moulijn *et al.*), p. 41. Elsevier, Amsterdam, 1987.
51. N.K. Sethi, R.J. Pugmire, J.C. Facelli and D.M. Grant, *Anal. Chem.*, 1988, **60**, 1574.
52. P. Tekely and J.J. Delpuech, *Fuel*, 1989, **68**, 947.
53. P. Tekely, J. Brondeau, J.-P. Marchal and J.-J. Delpuech, *Fuel*, 1986, **65**, 997.
54. P. Caravatti, G. Bodenhausen and R.R. Ernst, *J. Magn. Reson.*, 1983, **55**, 88.
55. E.W. Hagaman, *J. Am. Chem. Soc.*, 1988, **110**, 5594.

56. E.W. Hagaman, R.R. Chambers, F.M. Schell and M.C. Woody, in *1987 International Conference on Coal Science* (ed. J.A. Moulijn *et al.*), p. 23. Elsevier, Amsterdam, 1987.
57. E.W.J. Hagaman, *Energy & Fuels*, 1988, **2**, 861.
58. W.-D. Hoffmann, T. Schaller and D. Michel, *Fuel*, 1990, **69**, 810.
59. O.W. Howarth, G.S. Ratcliffe and P. Burchill, *Fuel*, 1987, **66**, 34.
60. A.R. Thompson and R.E. Botto, *Symposium on Research on Argonne Premium Coal Samples*, New Orleans, 1987.
61. D.E. Axelson, *Fuel Sci. Technol.*, 1987, **5**, 561.
62. L.S. Kotlyar and J.A. Ripmeester, *Reprints of the Symposium on Characterization and Chemistry of Tar Sand*, Toronto, 1988, p. 253.
63. D.E. Axelson, *Fuel*, 1987, **66**, 40.
64. W. Prins, K.A. Nater, H.A.G. Chermin and J.A. Moulijn (eds), *Coal Characterization for Conversion Processes II, Proceedings of the 2nd International Rolduc Symposium on Coal Science*, Rolduc, the Netherlands, 1989; *Fuel Process. Technol.*, 1990, **24**, 3-466.
65. F. Bergius, *Z. Angew. Chem.*, 1921, **34**, 341.
66. M.T. Terror and F.J. Derbyshire, *The Mobile Phase in Coals: Its Nature and Modes of Release, Structural Interferences from Dry Catalytic Hydrogenation of a Subbituminous Coal*, Final Report Part 1. Coal Research Section, Pennsylvania State University, 1986.
67. P.H. Given, *The Mobile Phase in Coals: Its Nature and Modes of Release, Efforts to Better Define the Nature and Magnitude of the Mobile Phase*, Final Report Part 2. Coal Research Section, Pennsylvania State University, 1987.
68. M. Vahrman, *Fuel*, 1970, **49**, 5.
69. L.J. Lynch, R. Sakurovs, D.S. Webster and P.J. Redlich, *Fuel*, 1988, **67**, 1036.
70. R. Meusinger, F. Dennhardt, J. Kärger, W. Meiler and H. Pfeifer, *Fuel*, 1990, **69**, 1249.
71. D. Schulze, H. Ernst, D. Fenzke, W. Meiler and H. Pfeifer, *J. Phys. Chem.*, 1990, **94**, 3499.
72. D. Schulze, thesis, Leipzig, 1990.
73. A.M. Vassallo and M.A. Wilson, *Fuel*, 1984, **63**, 571.
74. J.A. Ripmeester, R.E. Hawkins, J.A. MacPhee and B.N. Nandi, *Fuel*, 1986, **65**, 740.
75. M.F. Davis, G.R. Quinting, C.E. Bronnimann and G.E. Maciel, *Fuel*, 1989, **68**, 763.
76. D. Schulze, J. Witt, W. Meiler, R. Meusinger and H. Pfeifer, *International Conference on Coal Structure*, Jadwisin, 1989; and MARECO, Reinhardsbrunn, 1989.
77. L.J. Lynch, D.S. Webster and W.A. Barton, *Adv. Magn. Res.*, 1988, **12**, 385.
78. L.J. Lynch, R. Sakurovs, D.S. Webster and P.J. Redlich, *Fuel*, 1988, **67**, 1036.
79. R. Sakurovs, L.J. Lynch, T.P. Maher and R.N. Banerjee, *Energy & Fuels*, 1987, **1**, 167.
80. A. Jurkiewicz, S. Idziak and N. Pislewski, *Fuel*, 1987, **66**, 1066.
81. L.J. Lynch, D.S. Webster, R. Sakurovs, W.A. Barton and T.P. Maher, *Fuel*, 1988, **67**, 579.
82. W.A. Barton and L.J. Lynch, *Energy & Fuels*, 1989, **3**, 402.
83. N.A. Bacon, W.A. Barton, L.J. Lynch and D.S. Webster, *Carbon*, 1987, **25**, 669.
84. H. de Lopez, T. Yokono, N. Takahashi and Y. Sanada, *Fuel*, 1988, **67**, 301.
85. K. Azami, T. Yokono, Y. Sanada and S. Uemura, *Carbon*, 1989, **27**, 177.
86. C.E. Snape, A.M. Kenwright, J. Bermejo, J. Fernandez and S.R. Moinelo, *Fuel*, 1989, **68**, 1605.
87. J.S. Hayward, B. Ellis and B. Rand, *Carbon*, 1988, **26**, 71.
88. T. Yokono, S. Iyama, Y. Sanada, S. Shimokawa and E. Yamada, *Fuel*, 1986, **65**, 1701.
89. A.M. Vassallo, M.A. Wilson and J.H. Edwards, *Fuel*, 1987, **66**, 622.
90. P. Tekely, R. Bacaud, H. Charcosset, J.-J. Delpuech, J. Kister, D. Nicole and M. Oberson, *Fuel*, 1988, **67**, 932.

91. V. Calemma, E. Giradi, R. Rausa and S. Ghelli, *1987 International Conference on Coal Science* (ed. J.A. Moulijn *et al.*), p.423. Elsevier, Amsterdam, 1987.
92. W.S. Kalema and G.R. Gavalas, *Fuel*, 1987, **66**, 158.
93. P.J. Redlich, W.R. Jackson and F.P. Larkins, *Fuel*, 1989, **68**, 1544.
94. P.J. Redlich, W.R. Jackson, F.P. Larkins, A.L. Chaffee and I. Liepa, *Fuel*, 1989, **68**, 1549.
95. P.J. Redlich, W.R. Jackson and F.P. Larkins, *Fuel*, 1985, **64**, 1383.

Index

- Acetonitrile-d₃, residual anisotropies, 187
- Adiabatic demagnetization in the rotating frame (ADRF), 5–7
- ²⁷Al nuclei, imaging, 168, 170
- Albumin compartmentation, ³⁵Cl NMR studies, 261–262
- ALPHA-3 pulse sequence, 28, 29
- Alumina, porous, diffusion study, 203
- Aluminosilicate suspensions, nucleus splitting, 199
- ATP, as intracellular magnesium indicator, 252–256
- ³¹P NMR method, 253–255
- Average Hamiltonian theory (AHT), 118–120

- Back-projection reconstruction, 106, 108
- Bentonite suspensions
 - exchangeable cations, and nuclei splitting, 199
 - ²H NMR spectrum, 183, 193–194
- Benzene, coal interaction, 347, 351
- BLEW pulse sequences, 28
- Blood cells, *see* Erythrocytes
- Bone, ³¹P NMR imaging, 173
- Bone cells, magnesium in, and lead in, 256
- BR-24 pulse cycle, 28
 - in solid state imaging, 131
- Bromobenzoic acid, ammonia reaction, NMR imaging, 171–172

- ¹³C NMR
 - of coals, cross-polarization mass spectra, 332–338
 - double-quantum coherences, 71–72
 - for intracellular magnesium measurement, 256–257
 - magic-angle spinning in, 68
 - solid state imaging, 165–166, 167
 - ¹³C-¹⁹⁹Hg spin-spin coupling constants, 317–319
 - ¹³C-¹⁵N dipolar coupling, pi pulse modulation, 34–36
- Calcium, cellular
 - intracellular, ¹⁹F NMR measurements, 244–251
 - applications, 246–250
 - in cell differentiation, 250–251
 - methodological considerations, 244–246
 - sodium exchange and lead, 231
 - NMR studies, 233
- Calcium sulphate, Pake doublet at low temperature, 4, 5
- Carboxylates, cationic micelle binding, 208
- Cardiac cycle, calcium transients, ¹⁹F NMR studies, 249–250
- Carr–Purcell cycle in solid state imaging, 120–122, 124, 125
 - with gradient modulation, 123, 125–126
- Cell differentiation, free calcium in, ¹⁹F NMR studies, 250–251
 - see also* Intracellular ions in living systems
- Ceramics, NMR imaging, 173
- Chemical shift anisotropy, 96
 - correlation of chemical shift, 25
 - dynamic processes, 20–24
 - interfacial, 189–190
 - magic-angle spinning, 11–15

- Chemical shift anisotropy (*cont.*)
 tensor determination, 15, 17–20
see also Shift reagent aided NMR for cellular studies
- Chloroform, coal interaction, 345, 346, 347, 350–351
- Chromatography, interfacial processes in, 210
- Citrates, fluorinated, as indicators for magnesium, 257, 258
- ^{35}Cl NMR spectroscopy
 for albumin compartmentation, 261–262
 erythrocyte studies, 258–262
 splitting studies with surfactants, 204
- clay suspensions
 bentonite
 exchangeable cations, and nuclei splitting, 199
 ^2H NMR spectrum, 183, 193–194
 interfacial phenomena, 212
 nuclei splitting studies, 199–200
 quadrupolar splittings, 182–183
see also Zeolites
- CMG-48, for pulsed gradients, 138
- Coal research, 331–364
 coal structure, 332–341
 solid state NMR imaging, 172–173
 solvent-molecules/coal-surface interactions, 342–356
 ‘host-guest’ molecular structure, 342
 thermal processes, 356–360
 and *n*-hexane treatment, 355, 356, 360
 and ‘host-guest’ model, 353, 359
 liquefaction experiments, 357, 358, 360
 pitches, 354, 359–360
 and structure, 350, 351, 352, 357–359
- Coal-tar pitch, high-temperature ^1H NMR, 354, 359–360
- COMARO decoupling pulse sequence, 28–29
- Combined rotation and multiple-pulse spectroscopy (CRAMPS)
versus magic-angle spinning, 11, 12
 brown coal spectra, 332–338
 solid state imaging, 150
- COSY pulse sequence, 25
- Cross-polarization in solid state NMR, 5–10
 advantages, 8, 10
 methods, 5–8
 quantification of spectra intensities, 8
- Cross-polarization MAS spectra, of brown coals, 332–338
- Crystal chemistry, NMR imaging for, 171–172
- ^{133}Cs ion, as study substitute for cellular potassium, 237
- ^{133}Cs NMR
 for cellular homeostasis study, and lead, 231
 of CsNa-A zeolite, 204
- DANTE pulse sequence
 for solid imaging slice selection, 160, 161–164
 for spin diffusion study, 40
- Deconvolution, in solid state imaging, 100
- Deuterium, *see* ^2H NMR
- Diffraction of NMR, 64
- Diopside, ^{17}O NMR spectrum, 46
- Dipolar interactions, versus chemical shift, 20–21
- Dipole–dipole coupling, 25–41
 line-broadening effects, 26
 nutation spectroscopy for, 38–39
 reintroduction, 29–38
 homonuclear decoupling, 30–33
 π pulse modulation, 33–36
 rotational resonance, 37
 weak cw irradiation, 37–38
 removal, 27–29
 spin diffusion, 39–41
 pulse sequences for study, 40–41
 transition energy conservation in, 39–40
 uses, 41
- DNA
 counterion relaxation studies, 205–206
 ^{23}Na line splitting studies, 204
- Double cross-polarization (DCP) MAS, for coal structure, 339
- Double-angle rotation, for quadrupolar nuclei study, 47

- Double-quantum coherence-transfer
²³Na NMR, for intracellular sodium, 235–237
- Double-quantum filtered ³⁹K NMR, for intracellular potassium, 239–240
see also Multiple-quantum NMR
- Dynamic nuclear polarization (DNP), 10–11
 for coal structure studies, 336–337
 in rare-spin imaging, 70
- Dysprosium shift reagents, 220
see also Shift reagent aided ²³Na NMR for intracellular Na
- Erythrocytes
³⁵Cl NMR spectroscopy, 258–260
 calcium in, 248
 sodium in
 lead effects, ²³Na NMR studies, 228–231
 measurement, 226
- ¹⁹F NMR
 of fluorinated intracellular sodium indicators, 233–235
 for intracellular calcium measurement, 244–251
 applications, 246–250
 in cell differentiation, 250–251
 methodological considerations, 244–246
- FCryp-1 intracellular sodium indicator, 234
- Fluorinated intracellular indicators, for magnesium, 257–258
- Fusite, ¹³C NMR spectrum, 332, 334
- Gadolinium bis(tripolyphosphate) (GdPPP)₂ relaxation agent, 235
- Goldman–Shen pulse sequence, in spin diffusion studies, 41
- ¹H NMR
 imaging, magic-angle spinning in, 67–68
 for pitches, high-temperature, 354, 359–360
- ²H NMR
 bentonite spectrum, 183, 193–194
 for quadrupolar nucleus imaging, 168, 169, 170
 quadrupole echo, 50–54
 composite pulses, 53
 paramagnetic compounds, 53–54
 two-dimensional exchange experiment, 51–53
 surfactant systems, 198–199
- Hectorites, quadrupolar splittings, 199–200
- n*-Hexane, and coal behaviour, and thermal processing, 355, 356, 360
- ¹⁹⁹Hg NMR, 268–329
 chemical shift tables, 282–316
 diorganomercury compounds, 282–288
 mercury halides/pseudohalides, 295
 mercury-transition metal compounds, 313–316
 mercury/organomercury
 chalkogenides, 296–301
 mercury/organomercury nitrogen compounds, 302–303
 organomercury halides/pseudohalides, 289–294
 silyl/germyl/stannyl mercury compounds, 311–312
 chemical shift/coupling constants
 ⁿJ(¹⁹⁹HgX) table, mercury phosphorus compounds, 304–310
 chemical shifts, 273–276
 nuclear shielding theory, 273–274
 patterns, 274–276
 coupling constants ⁿJ(¹⁹⁹HgX), 276
 geminal couplings, 279
 long-range couplings, 280
 one-bond couplings, 277–279
 vicinal couplings, 279
 coupling constants tables, spin-spin, 317–320
 ¹⁹⁹Hg-¹³C, 317–319
 ¹⁹⁹Hg-²⁹Si, 320
 experimental aspects
 referencing, 268
 resonance observation, 268, 270–271
 nuclear spin relaxation, 271–273

- ¹⁹⁹Hg NMR (cont.)
 of solids, 280–281
see also Mercury
- 'Host-guest' model of coal, 342
 investigations, 353, 359
- Hydrocarbon chains, interfacial
 phenomena, relaxation studies,
 210
- Hypertension, and intracellular
 magnesium, ³¹P NMR studies,
 255
- Imaging, 88
see also Solid state NMR imaging
- INADEQUATE experiment, 71, 73
- Inotropic effect of calcium, 249
- Insulin, and cell sodium uptake, and
 glucose, 233
- Interfacial phenomena, study results,
 197–212
 amphiphilic molecule head groups,
 208–211
 diffusion, 210–211
 line splitting, 208–209
 relaxation, 209–210
 future developments, 211–212
 interfacial ions, 203–208
 diffusion, 207–208
 line splitting, 203–205
 relaxation, 205–207
 interfacial molecules, 198–203
 diffusion, 202–203
 line splitting, 198–200
 relaxation, 200–202
 types of NMR studies, 181–182
- Interfacial phenomena, theory, 181–197
 chemical shielding anisotropy, 189–
 190
 interfacial region, 181, 182
 line splitting, 185–189
 amphiphilic aggregate nuclei, 188–
 189
 counterions, 188
 interfacial molecules, 185–188
- NMR parameters, 182
- quadrupolar splittings, 182–183
 relaxation, 190–196
 counterions, 194–195
 head group nuclei, 195–196
 interfacial molecules, 190–194
 self diffusion, 196–197
- Internuclear distance measurement
 rotational resonance, 37
 spin diffusion, 39, 40
- Intracellular ions in living systems,
 219–265
 calcium ¹⁹F NMR measurements,
 244–251
 applications, 246–250
 in cell differentiation, 250–251
 methodological considerations,
 244–246
- ³⁵Cl NMR spectroscopy, 258–262
 albumin compartmentation studies,
 261–262
 erythrocyte studies, 258–260
 magnesium measurements, 252–258
¹³C NMR method, 256–257
 endogenous indicators, 252–256
 fluorinated indicators, 257–258
 potassium measurements, 237–244
 Cs/Rb substitutes, 237–238
 multiple-quantum filtered ³⁹K
 NMR, 239–240
 non-invasive subtraction, 240–244
 shift reagent aided ³⁹K NMR, 238–
 239
 sodium measurements, 220–237
 fluorinated indicators, ¹⁹F NMR
 of, 233–235
 shift reagent aided ²³Na NMR,
 220–233
- Ion studies, interfacial
 diffusion, 207–208
 line splitting, 203–205
 relaxation, 205–207
see also Intracellular ions in living
 systems
- Ischaemia
 and intra/extracellular calcium, 249,
 250
 and intracellular magnesium
 ADP/ATP resonance studies, 256
 fluorinated indicator studies, 258
³¹P NMR studies, 254
 and intracellular sodium, ²³Na NMR
 measurement, 232–233
- Jeneer–Broekaert sequence, in solid
 echo imaging, 63–64

- ³⁹K NMR for intracellular potassium study
multiple-quantum filtered, 239–240
shift reagent aided, 238–239
see also Potassium measurement, intracellular
- Lead, cellular effects
on calcium, ¹⁹F NMR studies, 246–248
on magnesium, bone cell studies, 256
on sodium homeostasis, ²³Na NMR studies, 227–231
- ⁷Li cation, diffusion in polyelectrolyte solution, 208
- ⁷Li NMR
for cellular homeostasis study, and lead, 230–231
saponite clay spectrum, 204, 205
- Living systems, *see* Intracellular ions in living systems
- LOS Y slice selection scheme, 164
- Low-temperature NMR, and sensitivity, 4–5
- LW-24 pulse cycle, for pulsed gradients, 138
- Magic-angle nutation (MAN) pulse sequence, 71
- Magic-angle rotating frame (MARF) imaging, 68–70
in solid state imaging, 154–157, 158
- Magic-angle spinning (MAS), 11–15
applications, 14
in chemical shift tensor determination, 17–18
versus CRAMPS, 11, 12
and spinning sidebands, 13–14
in homonuclear decoupling experiments, 30–31
multiple-quantum coherence in, 73
partially ordered material, 14–15, 16
in solid state imaging, 67–68, 126–127, 144–150
advantages, 145
CRAMPS method, 150–152
static gradient methods, 152, 153
synchronously rotating gradient method, 145–150, 151
- Magnesium, intracellular measurement methods other than NMR, 252
NMR methods, 252–258
¹³C NMR, 256–257
endogenous indicators, 252–256
fluorinated indicators, 257–258
- Magnets in imaging
solenoid, large-gradient region, 111
superconducting, for solid state imaging, 59–60
- Malignancy, and intracellular sodium, 232
- MAN pulse sequence, 71
- Medical applications of NMR
imaging, 88
intracellular sodium measurements, 232–233
- Membranes, cation transport, 207
see also Intracellular ions in living systems
- Mercury, 267
isotopes, 268, 269
see also ¹⁹⁹Hg NMR
- Mercury acetate, ¹⁹⁹Hg NMR, 280
- Metals, skin depth imaging, 159–160
see also by particular metal
- MG-8 pulse cycle in solid state imaging, 121, 122–123, 124, 125
with gradient modulation, 126
- ‘Monkey hairs’, ¹³C NMR spectrum, 332, 334
- Montmorillonite, *see* Bentonite suspensions
- MREV-8 pulse sequence, 28
in homonuclear decoupling, 31
in solid state imaging, 65–66, 121, 122, 124, 125
with pulsed gradients, 134, 135, 136, 138
resolution, 139, 141
with static gradients, 127–131
- Multiple-quantum NMR, 116–117
phase incrementation, 74
for solid imaging, 66–67, 71–74
double-quantum coherences, 71–73
phase incrementation, 74
spin clusters, 73–74
see also Double-quantum coherence-transfer ²³Na NMR; Double-quantum filtered ³⁹K NMR, for intracellular potassium

- ¹⁴N NMR, 49–50
 - overtone NMR, 50
- ¹⁵N-¹³C dipolar coupling pi pulse modulation, 34–36
- ²³Na NMR
 - double-quantum coherence-transfer, for intracellular Na, 235–237
 - line splitting, in electrolytes, 204
 - relaxation
 - in anisotropic media, 207
 - in polyelectrolytes, 205–206
 - shift reagent aided, for intracellular sodium, 220–233
 - applications, general, 232–233
 - lead effects on sodium
 - homeostasis, 227–231
 - for perfused cell systems, 223–227
 - reagents, 220–221
 - resolution, 221
 - sodium concentration/volume determination, 222–223
 - and sodium ion NMR visibility, 221–222
 - toxicity of reagents, 221
 - see also* Sodium measurement, intracellular
- Naphthalene, coal interaction, 348, 349, 354–356
- Neoplastic tissue, intracellular sodium measurement, 232
- Noise in solid state imaging, 100–101
 - and contrast, 109–110
 - see also* Signal-to-noise in solid state imaging
- Non-destructive evaluation (NDE), 92–93, 173
- Nutation NMR
 - for dipole-dipole coupling, 38–39
 - for metal skin depth imaging, 159–160
 - for quadrupole nucleus study, 47–49
- Nylon imaging, 144, 174
- ¹⁷O diopside spectrum, 46
- Odd dipolar rotational spin-echo (ODRSE), 36
- Optical detection of magnetic resonance (ODMR), 3
- Overtone NMR, for quadrupolar nuclei, 49–50
- ³¹P NMR
 - in solid state imaging, 166–167
 - for bone, 173
 - for intracellular magnesium measurement, 253–255
- ³¹P nucleus in phospholipid head group chemical shielding, 189–190
- relaxation, 196
- Pake doublet, calcium sulphate, 4, 5
- Phosphatidylcholine, polar group, interfacial processes, 209
- Phospholipids
 - head group
 - interfacial processes, 208–209
 - nuclei relaxation, 196
 - phosphorus nuclear chemical shielding anisotropy (CSA), 189–190
- Physiological measurements, *see* Intracellular ions in living systems
- Pi pulses, in dipole–dipole coupling modulation, 33–36
- Pitches, high-temperature ¹H NMR, 354, 359–360
- Polarization transfer, and solid state NMR sensitivity, 3, 5–11
 - cross-polarization, 5–10
 - dynamic nuclear spin polarization, 10–11
- Polyelectrolyte solutions, counterion relaxation studies, 205–206
- Polymers
 - adsorption from solution, 201–202
 - interfacial phenomena, relaxation studies, 210
 - solid state imaging, 59, 91, 94, 173–174
 - ²H NMR, 168, 170
 - with magic-angle spinning, 150, 151
 - resolution, 144
 - high-temperature, 60, 62
 - sensitive slice methods, 61
 - spin diffusion studies, 41
- Potassium measurement, intracellular, 237–244
 - Cs/Rb substitutes, 237–238
 - multiple-quantum filtered ³⁹K NMR, 239–240
 - non-invasive subtraction, 240–244

- shift reagent aided ^{39}K NMR, 238–239
- Pulsed field gradient NMR, and interfacial ion diffusion, 207
- Pyridine, coal interaction, 347, 351–352, 354
- Pyridinium octylhydrogenphosphate, aqueous, diffusion, 211
- Pyropissite, ^{13}C NMR spectrum, 332, 334
- Quadrupolar nuclei, imaging, 168–171
 - solid state, 59
- Quadrupolar splittings in clay suspension, 182–183
- Quadrupole coupling, 41–54
 - ^2H quadrupole echo, 50–54
 - composite pulses, 53
 - paramagnetic compounds, 53–54
 - two-dimensional exchange experiment, 51–53
 - and integer/half-integer spins, 41–42
 - multiple-quantum excitation, 54
 - nutation NMR, 47–49
 - overtone NMR, 49–50
 - reduction/removal, 43–47
 - spin-half nuclei effects, 42–43
 - uses, 42
- ^{87}Rb ion, as study substitute for cellular potassium, 237–238
- ^{87}Rb NMR, for cellular homeostasis, and lead, 230–231
- Reciprocal space, in solid state imaging, 99–101
- Refocused gradient imaging (RGI), 65–66
- Retinite, ^{13}C NMR spectrum, 332, 334
- Reversed effective field (REF) sequence, 65–66
- Rotational-echo double resonance (REDOR) sequence, 35–36
- Rubbers, imaging, 91
- Saponites, quadrupolar splittings, 199–200
- SEEING (skin effect imaging), 159–160
- SEMUT sequence, 29
- Shift reagent aided NMR for cellular studies
 - ^{39}K NMR, 238–239
 - ^{23}Na NMR, 220–233
 - applications, general, 232–233
 - lead effects on sodium homeostasis, 227–231
 - for perfused cell systems, 223–227
 - reagents, 220–221
 - resolution, 221
 - sodium concentration/volume determination, 222–223
 - and sodium ion NMR visibility, 221–222
 - toxicity of reagents, 221
 - see also* Chemical shift anisotropy
- SHRIMP pulse cycle, in solid state imaging, 133, 140–141
- ^{29}Si - ^{199}Hg spin-spin coupling constants, 320
- Signal-to-noise in solid state imaging
 - constant time imaging, 115
 - and contrast, 109–110
 - and resolution limits, 102–104
 - see also* Noise in solid state imaging
- Skin effect imaging (SEEING), 159–160
- Sodium measurement, intracellular, 220–237
 - double-quantum coherence-transfer ^{23}Na NMR, 235–237
 - fluorinated indicators, ^{19}F NMR of, 233–235
 - shift reagent aided ^{23}Na NMR, 220–233
 - applications, general, 232–233
 - lead effects on sodium homeostasis, 227–231
 - for perfused cell systems, 223–227
 - reagents, 220–221
 - resolution, 221
 - sodium concentration/volume determination, 222–223
 - and sodium ion NMR visibility, 221–222
 - toxicity of reagents, 221
 - see also* ^{23}Na NMR
- Solid state NMR
 - chemical shift anisotropy
 - correlation of chemical shift, 25
 - dynamic processes, 20–24
 - magic-angle spinning, 11–15

- Solid state NMR, chemical shift**
 anisotropy (*cont.*)
 tensor determination, 15, 17–20
dipole-dipole coupling, 25–41
 line-broadening effects, 26
 nutration spectroscopy for, 38–39
 reintroduction, 28–38
 removal, 27–29
 spin diffusion, 39–41
imaging, *see* Solid state NMR imaging
multiple-quantum methods, 71–74
 double-quantum coherences, 71–73
 phase incrementation, 74
 spin clusters, 73–74
quadrupole coupling, 41–54
 ^2H quadrupole echo, 50–54
 and integer/half-integer spins, 41–42
 multiple-quantum excitation, 54
 nutration NMR, 47–49
 overtone NMR, 49–50
 reduction/removal, 43–47
 spin-half nuclei effects, 42–43
 uses, 42
sensitivity, 3–11
 low-temperature NMR, 4–5
 polarization transfer, 3, 5–11
 technical approaches to, 3–4
zero field, 54–57
 direct detection, 54–55
 fictitious spectra, 57
 indirect detection, 55
 resolution, 55–57
Solid state NMR imaging, 57–71, 87–180
 applications, 59, 92–93, 171–174
 bone studies, 173
 ceramic processing, 173
 coal characterization, 172–173
 crystal chemistry, 171–172
 polymer processing, 173–174
 basics, 94–110
 contrast, 109–110
 nuclear spin Hamiltonians, 95–98
 reciprocal space and one-dimensional imaging, 98–101
 resolution limits, 102–104
 three-dimensional imaging, 107
 two-dimensional images, 104–107, 108
 volume selected spectroscopy, 107
 ^{13}C imaging, 165–166, 167
 constant time imaging, 58–59
 field gradient application, 57–58
 Hamiltonian manipulation, 89, 118–127
 average Hamiltonian theory, 118–120
 gradient modulation, 123, 125–126
 magic-angle sample spinning, 126–127
 multiple-phase methods, 120–123, 124
 high-temperature, 60
 incremental time imaging, 58
 magic-angle rotating frame, 68–70
 with magic-angle spinning, 67–68, 144–152
 advantages, 145
 CRAMPS method, 150–152
 static gradient methods, 152, 153
 synchronously rotating gradient method, 145–150, 151
 metal skin effect imaging, 159–160
 multiple-phase sequences, 64–67
 for forced precession, 67
 for line-narrowing, 65–66
 for multiple quantum coherences, 66–67
 off-resonance effects, 64
 pulse length effects, 65
 with multiple-pulse line-narrowing, 127–144
 oscillating gradients, 132–133
 pulsed gradients, 134–139, 140–1, 142
 resolution/sensitivity, 139, 141–144
 static gradients, 127–132
 non-rigid solids, 91
 ^{31}P imaging, 166–167
 for bone, 173
 quadrupolar nuclei, 168–171
 ^{27}Al , 168, 170
 ^2H , 168, 169, 170
 temperature/pressure sensitivity, 171
 range of NMR spatial techniques, 90–91
 rare spins, 70
 rotating frame, 152, 154–157
 magic-angle rotating frame

- imaging, 154–157, 158
- sample handling/treatment, 89–90
- slice selection methods, 160–165
 - adiabatic sweeps, 165
 - DANTE sequence, 160, 161–164
 - sensitive slice, 59–60, 61
 - spin-locking approach, 164–165
- solid echo, 60, 63–64
- surface coils, 71
 - for large samples, 157–159
- wide-line methods, 110–117
 - constant time, 114–116
 - multiple-quantum, 116–117
 - STRAFI, 110–114
- Spectral editing, homonuclear decoupling for, 29
- Spin diffusion, 39–41, 90–91
 - pulse sequences for, 40–41
 - transition energy conservation in, 39–40
 - uses, 41
- Spin-half nuclei, quadrupole coupling effects, 42–43
- Spin-lattice relaxation, increase at low temperature, 4
- Spin-locking slice selection, 164–165
- Spin-warp imaging, 106
- Squaric acid, zero field NMR spectra, 55, 56
- SQUID, 3
- Stray field imaging (STRAFI), 110–114
- Super-conducting quantum interference device (SQUID), 54–55
- Surfactant systems
 - ^2H nucleus splitting studies, 198–199
 - line splitting studies, interfacial ions, 204
 - water/solid interface studies, 207
- Thulium, 221
 - see also* Shift reagent aided NMR for cellular studies
- TOSS, sideband suppression sequence, 13
- TREV-8 pulse sequence, 28
- WAHUHA pulse sequence, 28
 - in solid state imaging, 131
- Water molecules, interfacial diffusion studies, 202–203
 - line splitting, 185–187
 - studies, 198–199
 - relaxation, 190–193
 - studies, 200–201
- Waxes, imaging, 91
- XDM-R2 two-pulse sequence, 36
- Zeeman interaction, 95
- Zeolites
 - chemical shift correlation, 25
 - nutration NMR, 48
 - see also* Clay suspensions
- Zero field NMR, 54–57
 - direct detection, 54–55
 - fictitious spectra, 57
 - indirect detection, 55
 - resolution, 55–57

This Page Intentionally Left Blank